AD-A174 754

FINAL TECHNICAL REPORT

1 November 1983 - 30 June 1986

DTIC
ELECTE
DEC 0 1 1986
S D

AFOSR-TR- 86-1091

ARPA Order:	4983
Program Code:	5D60
Name of Grantee:	The Regents of the University of California University of California, San Diego Scripps Institution of Oceanography La Jolla, California 92093
Effective Date of Grant:	1 November 1983
Grant Expiration Date:	30 June 1986
Amount of Grant Dollars:	$331,014
Grant Number:	AFOSR-84-0043
Principal Investigator:	Dr. John A. Orcutt (619) 534-2887
Program Manager:	Dr. Henry Radoski (202) 767-4904
Short Title of Work:	Analysis of MSS and OBS Data Collected During the NGENDEI Seismic Experiment

Approved for public release;
distribution unlimited.

DTIC FILE COPY

Sponsored by
Advanced Research Projects Agency (DOD)
DARPA Order No. 4983
Monitored by AFOSR/PKZ
Under Grant No. AFOSR-84-0043

DISTRIBUTION STATEMENT A
Approved for public release;
Distribution Unlimited

AIR FORCE OFFICE OF SCIENTIFIC RESEARCH (AFSC)
NOTICE OF TRANSMITTAL TO DTIC
This technical report has been reviewed and is
approved for public release IAW AFR 190-12.
Distribution is unlimited.
MATTHEW J. KELLY
Chief, Technical Information Division

The views and conclusions contained in this document are those of the authors and should not be interpreted as necessarily representing the official policies, either expressed or implied, of the Defense Advanced Research Projects Agency or the U.S. Government.

86 11 26 055

UNCLASSIFIED

SECURITY CLASSIFICATION OF THIS PAGE

REPORT DOCUMENTATION PAGE

1a. REPORT SECURITY CLASSIFICATION: UNCLASSIFIED	1b. RESTRICTIVE MARKINGS
2a. SECURITY CLASSIFICATION AUTHORITY	3. DISTRIBUTION/AVAILABILITY OF REPORT: Approved for public release; distribution unlimited
2b. DECLASSIFICATION/DOWNGRADING SCHEDULE	
4. PERFORMING ORGANIZATION REPORT NUMBER(S)	5. MONITORING ORGANIZATION REPORT NUMBER(S): AFOSR-TR-86-1091
6a. NAME OF PERFORMING ORGANIZATION: Univ. of California, Scripps Inst. of Oceanography; 6b. OFFICE SYMBOL (If applicable)	7a. NAME OF MONITORING ORGANIZATION: AFOSR
6c. ADDRESS (City, State and ZIP Code): Scripps Inst. of Oceanography, La Jolla, CA 92093	7b. ADDRESS (City, State and ZIP Code): AFOSR, Bldg. 410, Bolling Air Force Base, DC 20332
8a. NAME OF FUNDING/SPONSORING ORGANIZATION: AFOSR; 8b. OFFICE SYMBOL (If applicable): NP	9. PROCUREMENT INSTRUMENT IDENTIFICATION NUMBER: AFOSR-84-0043
8c. ADDRESS (City, State and ZIP Code): AFOSR, Bldg 410, Bolling AFB, DC. 20332	10. SOURCE OF FUNDING NOS. — PROGRAM ELEMENT NO.: 61102F; PROJECT NO.: 2309; TASK NO.: A1; WORK UNIT NO.:
11. TITLE (Include Security Classification): Analysis of MSS and OBS Data Collected During the NGENDEI Seismic Experiment	
12. PERSONAL AUTHOR(S): John A. Orcutt	
13a. TYPE OF REPORT: Final technical; 13b. TIME COVERED: FROM 11/1/83 TO 6/30/86; 14. DATE OF REPORT (Yr., Mo., Day): August 1986; 15. PAGE COUNT: 574	
16. SUPPLEMENTARY NOTATION	

17. COSATI CODES			18. SUBJECT TERMS (Continue on reverse if necessary and identify by block number)
FIELD	GROUP	SUB. GR.	

19. ABSTRACT (Continue on reverse if necessary and identify by block number)

The results of the data analysis employing data collected during the NGENDEI Seismic Experiment in the southwest Pacific are presented. This experiment tested the DARPA Marine Seismic System (MSS) and verified the improved signal-to-noise ratio achieved by burying the instrument within the oceanic crust. Generally, all the goals of the experiment were achieved and a number of very exciting results are reported.

20. DISTRIBUTION/AVAILABILITY OF ABSTRACT: UNCLASSIFIED/UNLIMITED ☑ SAME AS RPT. ☑ DTIC USERS ☐	21. ABSTRACT SECURITY CLASSIFICATION: UNCLASSIFIED
22a. NAME OF RESPONSIBLE INDIVIDUAL: John F. Prince	22b. TELEPHONE NUMBER (Include Area Code): (202) 767-4908; 22c. OFFICE SYMBOL: NP

DD FORM 1473, 83 APR — EDITION OF 1 JAN 73 IS OBSOLETE.

UNCLASSIFIED

SECURITY CLASSIFICATION OF THIS PAGE

FINAL TECHNICAL REPORT

1 November 1983 - 30 June 1986

ARPA Order:	4983
Program Code:	5D60
Name of Grantee:	The Regents of the University of California University of California, San Diego Scripps Institution of Oceanography La Jolla, California 92093
Effective Date of Grant:	1 November 1983
Grant Expiration Date:	30 June 1986
Amount of Grant Dollars:	$331,014
Grant Number:	AFOSR-84-0043
Principal Investigator:	Dr. John A. Orcutt (619) 534-2887
Program Manager:	Dr. Henry Radoski (202) 767-4904
Short Title of Work:	Analysis of MSS and OBS Data Collected During the NGENDEI Seismic Experiment

Sponsored by
Advanced Research Projects Agency (DOD)
DARPA Order No. 4983
Monitored by AFOSR/PKZ
Under Grant No. AFOSR-84-0043

The views and conclusions contained in this document are those of the authors and should not be interpreted as necessarily representing the official policies, either expressed or implied, of the Defense Advanced Research Projects Agency or the U.S. Government.

ABSTRACT

The results of the data analysis employing data collected during the NGENDEI Seismic Experiment in the southwest Pacific are presented. This experiment tested the DARPA Marine Seismic System (MSS) and verified the improved signal-to-noise ratio achieved by burying the instrument within the oceanic crust. Generally, all the goals of the experiment were achieved and a number of very exciting results are reported.

Introduction

This Final Report provides an update on progress in the analysis of the seismic data collected during the NGENDEI Experiment sponsored by DARPA in early 1983 in the southwest Pacific. The experiment, which took place on the Deep Sea Drilling Project Leg 91, was designed to test the MSS in a realistic environment near an active trench. An earlier test of the system in the northwest Pacific had been unsuccessful because of difficulties in drilling an acceptable borehole on the seafloor. The Scripp's ship, the R/V Melville, was used in addition to the D/V Glomar Challenger for tasks related to site surveying, ocean bottom seismograph (OBS) deployment and refraction shooting. Chief Scientists on the expedition were John Orcutt and Tom Jordan on the Melville and Bill Menard and Jim Natland on the Challenger. The experiment was quite successful, as is evident when reviewing the results outlined in the Annual Report, and accomplished all major goals. The MSS was recorded aboard the D/V Glomar Challenger for several days of earthquake, refraction and environmental noise experiments. The subsequent deployment of an autonomous recording package on the seafloor was successful, but a leak in one of the spheres housing the batteries resulted in a power loss after approximately two days. The OBS's launched several times during the course of the experiment operated correctly in all instances including the 45 day teleseismic recording phase at the end. The MSS recording package as well as the six OBS's were recovered at the end of the experiment by the R/V Melville. The MSS was left in the borehole and the coaxial cable was terminated in a dummy load. The mooring system used for recovery was redeployed in the event a future experiment became necessary or desireable.

The sixteen chapters of this report are composed of papers which have been submitted for publication, are *in press* or have been published in various journals including the Initial Reports of the Deep Sea Drilling Project. Chapter 1 reports on the surveying conducted by both the D/V Glomar Challenger and the R/V Melville in support of site selection for the borehole. The greatest challenge encountered in this phase of the experiment was finding a location in the southwest Pacific Basin which was sufficiently heavily sedimented to support the reentry cone required for the successful emplacement of the MSS. In addition to this operational requirement, the two ships conducted as much detailed surveying as possible in order to place constraints on the poorly understood tectonics in the region. The lithosphere at the site may be as old as 140,000,000 years; The thin layer of sediments results largely from a plate history which excluded passage beneath any highly productive waters.

Chapter 2 briefly outlines the operation of the MSS during the experiment. The instrument returned exceptionally high quality data with excellent signal-to-noise. Only the loss of one of the installed horizontal sensors and the failure of the battery package imposed limitations on the experimental results. Two digitizing schemes were employed during the shipboard recording phase of the experiment. One of these (Teledyne) used a 14-bit analog-to-digital converter with gain ranging while the second (Gould) employed a new 24-bit digitizer. The performance of these two converters is reviewed in some detail in this chapter. Additional testing of the 24-bit instrument is recommended prior to any large-scale employment in the field.

Chapter 3 is a review of the operation of the OBS's. All the OBS's deployed were recovered and data were satisfactorily collected on all the instruments. The temperature-compensated clocks in the capsules provided excellent timing throughout even the 45 day deployment. The horizontal sensors frequently exhibited resonances generally associated with seafloor coupling problems and, in a few cases, the hydrophones did not operate correctly. The

OBS's were accurately located on the bottom with acoustic transponders. The proximity of the MSS and OBS's in the central array provided excellent data for instrument intercomparisons and propagation studies.

The experiment provided reliable estimates of seafloor and subseafloor seismic noise levels and coherence and these are detailed in Chapter 4. The noise levels within the borehole were reduced by as much as 20 db below levels at the seafloor as earlier predicted by our physical model for the generation and propagation of seafloor noise. Although noise levels in the vicinity of the microseism peak were quite high, the levels above a frequency of 4 Hz approached measurements at very quiet contiental sites. The microseismic noise was found to be coherent over baselines of one kilometer and the levels at frequencies in excess of 3-4 Hz were dominated by ship-generated noise.

One of the primary goals of the experiment was to measure the signal-to-noise ratios at seafloor and sub-seafloor locations. Chapter 5 compares these levels for explosion and teleseismic arrivals at a variety of phase velocities. In all cases, the absolute signal levels at the MSS and the OBS's were comparable and, given the reduction in noise, the MSS receiver achieved a considerable signal-to-noise advantage. In general, not only were signal levels comparable on the various instruments, but the signals were coherent over long periods of time.

Preliminary results from the seismic refraction study are reported in Chapter 6. This paper includes plots of the travel time data from the explosion studies using the MSS and extremal velocity bounds for the structure are presented. Chapter 7 reviews the seismic refraction data from the OBS's and record sections observed by all the instruments and all components are plotted. An apparent anisotropy in upper mantle compressional velocity is discussed.

Chapter 8 is a detailed analysis of the MSS and OBS travel time data. An upper mantle anisotropy is reported and, for the first time in marine seismology, clear constraints on anisotropy in the upper crust are available. The two directions of maximum velocity are found to be perpendicular. The anisotropy in the upper mantle is attributed to the alignment of olivine crystals by the spreading process while that in the upper crust is produced by thin, fluid-filled cracks parallel to the sheeted dikes which feed the seafloor extrusives at the rise axis. This chapter has been published in the *Geophysical Journal of the Royal Astronomical Society* [Shearer, P. and J. Orcutt, Anisotropy in the oceanic lithosphere - theory and observations from the Ngendei seismic refraction experiment in the south-west Pacific, *Geophys. J. R. Astron. Soc., 80*, 493-526, 1985.]

Strong regional P_n and S_n phases were recorded by the MSS and OBS's for events located at all depths within the Tonga-Kermadec Trench. We have successfully computed synthetic seismograms which match most features of these long, ringy wavetrains without resort to scattering from inhomogeneities within the lithosphere. Chapter 9 is a paper on the synthetics and the NGENDEI observations which has been published in *Nature* (Sereno, T. and J. Orcutt, Synthetic seismogram modelling of the oceanic P_n phase, *Nature*, *316*, 246-248, 1985). A more detailed presentation of these results is found in Chapter 10 and this chapter has been published in the *Journal of Geophysical Research* (Sereno, T. and J. Orcutt, Synthesis of realistic oceanic P_n wave trains, *J. Geophys. Res.*, *90*, 12755-12776, 1985). The acoustics implications of the P_n and S_n observations and the observations of the oceanic T phase are described in Chapter 11 and the research has been published in the proceedings volume of a conference on seismo-acoustics held in La Spezia, Italy (Sereno, T. and J. Orcutt, The propagation of P_n, *In:* Akal, T. and J.M. Berkson, eds., *Ocean Seismo-Acoustics*, 579-587, Plenum Publishing Company, 1986).

The preliminary work on seafloor noise, outlined in Chapter 4, was continued and the results are outlined in Chapter 12. A detailed study of the coherence and phase spectra between adjacent OBS's has confirmed the surface wave propagation mode of low frequency seismic noise and a clear correlation between wind speed and direction and the level of seafloor noise is shown.

This work has been published in the *Journal of the Acoustical Society of America* (Adair, R.G., J.A. Orcutt and T.H. Jordan, Low frequency ocean-bottom noise observations in the deep sea, *J. Acoust. Soc. Am., 80*, 633-645, 1986).

The seismic profiles collected during the NGENDEI seismic experiment also recorded strong converted shear wave arrivals. Chapter 13 is a detailed study of the evidence for crustal and uppermost mantle shear wave anisotropy. In general, the upper crust was found to be anisotropic for shear waves while the lower crust was essentially isotropic. These observations are consistent with physical models for the oceanic crust and upper mantle based on cracking in the shallow crust and olivine crystal alignment in the mantle. This work is *in press* in the *Geophysical Journal of the Royal Astronomical Society* (Shearer, P.M. and J. Orcutt, Compressional and shear wave anisotropy in the lithosphere: The Ngendei seismic refraction experiment, *Geophys. J.R. Astron. Soc.*, in press, 1986).

The seafloor noise data collected during the experiment were compared to quantitative predictions of noise levels from various physical models. Previous work on the noise levels generated by atmospheric turbulence at high frequencies (>4 Hz) was found to be in error and a correction to the equations resulted in an increased consistency between observations and data. This research is outlined in chapter 14 and a paper is *in press* in the *Journal of the Acoustical Society of America* (Adair, R.G., Comments on the absolute levels of very-low frequency acoustic noise predicted by Wilson's modification of Isakovich and Kur'yanov's theory, *J. Acoust. Soc. Am.*, in press, 1986).

The regional distance seismic data were used to estimate the suitability of an instrument like the MSS for seismic discrimination and detection work. Chapter 15 describes the regional data collected and demonstrates that the detection threshold for regional events ($<30^{o}$) is approximately 3.7. This chapter was published in a book reviewing 25 years of progress in the Vela Program (Orcutt, J. and T.H. Jordan, MSS and OBS data from the Ngendei experiment in the southwest Pacific, *In:* Kerr, A., ed., *The VELA Program,* 758-770, Defense Advanced Research Projects Agency, Washington, D.C., 1985).

While chapters 9 and 10 describe the propagation and modeling of the P_n phase, these results were not entirely consistent with the S_n observations. Modeling of the S_n phase is described in detail in Chapter 16. We found that it was essential to introduce an absorption band rheology for the oceanic lithosphere in order to parameterize the apparent frequency dependence of Q. The data require a very high Q at high frequencies although realistic data are shown to be inadequate for discriminating between Q's of 1,000 and 20,000. A manuscript describing this work has been submitted to the *Journal of Geophysical Research* (Sereno, T. and J. Orcutt, Synthetic P_n and S_n phases and the frequency dependence of Q of oceanic lithosphere, *J. Geophys. Res.*, in press, 1986).



Accesion For
NTIS CRA&I ☑
DTIC TAB ☐
U..announced ☐
Justificatio.
By
Dist ibution/
Availability Codes
Dist | Avail a..d/or Special
A-1

CHAPTER 1

SEISMIC REFLECTION SITE SURVEY: CORRELATION WITH PHYSICAL PROPERTIES, LEG 91, DEEP SEA DRILLING PROJECT

Isaac I. Kim
Institute of Geophysics and Planetary Physics,
Scripps Institution of Oceanography

Deborah K. Smith
Geological Research Division,
Scripps Institution of Oceanography

H. William Menard
Institute of Marine Resources, Geological Research Division,
Scripps Insitution of Oceanography

John A. Orcutt
Institute of Geophysics and Planetary Physics,
Scripps Institution of Oceanography

Thomas H. Jordan
Department of Earth, Atmospheric, and Planetary Sceiences,
Massachusetts Institute of Technology

INTRODUCTION

Leg 91 of the Deep Sea Drilling Project (DSDP) deployed and recovered the Defense Advanced Research Project Agency's (DARPA) Marine Seismic System (MSS). An attempt to deploy the MSS during Leg 88 off Kamchatka was aborted due to drilling difficulties in a high sea state. The MSS featured a Borehole Instrument Package (BIP) which was emplaced beneath pelagic sediments 70 meters into the oceanic crust by the D/V Glomar Challenger. Earthquakes, refraction shots, and microseismic noise were recorded by a triaxial seismometer and hydrophone located in the BIP, as well as by an ocean bottom seismometer (OBS) array surrounding the drilling site. The primary scientific objective of Leg 91, referred to as the Ngendei expedition, was to compare the instrument response of these downhole seismometers to the OBS's and to determine how much improvement in signal-to-noise would be obtained by placing a seismometer beneath ocean sediments in an apparently quieter environment. The site survey for Leg 91 was performed by the R/V Melville of the Scripps Institution of Oceanography (SIO) and included magnetics, 12.5 kHz bathymetry, and 3.5 kHz profiling and digital watergun seismic reflection profiling.

PRELIMINARY SITE SELECTION

The drilling site was located at a latitude of 24 degrees South, 1000 kilometers east of the Tonga Trench (see Figure 1, designated MSST-5). The site was chosen to be proximal to the Tonga-Kermadec Trench, the most seismically active area in the world. Deep seismicity, that is earthquakes with hypocenters located below 300 kilometers, accounts for 20 percent of all events (above Mb 3.5) in the Benioff zone, according to 1981 International Seismic Centre (ISC) data. The distance from the trench was chosen so that the teleseismic rays from deep and intermediate focus earthquakes would bottom in and around the 400 kilometer and 670 kilometer seismic discontinuities. This purely oceanic path is rarely sampled and could potentially contribute significantly to knowledge of the upper mantle beneath the Southwestern Pacific Basin (see Jordan et.al. this volume). In addition, mid-plate earthquakes associated with French Polynesian volcanism (Okal, et.al., 1980) would be recorded. The site also happened to lie 25 degrees west of the French nuclear test site.

Little is known about the tectonic history of this portion of the South Pacific given there are only a few widely-spaced shiptracks through the area. From hot spot traces, we can assume that this crust was produced from a fast spreading ridge at a high southern latitude in the late Cretaceous (140 MY). This would place the site's origin somewhere in the center of the Mesozoic world ocean (present-day Pacific) when the Atlantic started its present-day opening phase. As this portion of oceanic crust migrated across the Pacific, it was far removed from

any source of continental sediments, and never passed under the highly productive equatorial zone. Therefore, even though this oceanic crust is quite old, we anticipated and found very thin sediment cover.

Engineering constraints required that the site be located in water less than 5500 meters deep and have at least 100 meters of sediment for lateral support of the bottom hole assembly. Seismic reflection profiles from the 1969 R/V Eltanin and 1972 R/V Conrad expeditions were used to pick a primary target (MSST-5 in Figure 1) and an alterate site (MSST-3 in Figure 1). Two storm sites (SS-1 and SS-2 in Figure 1) were also chosen at a lower latitude in case of inclement weather at the primary target. The R/V Melville was to survey the primary target area in detail with its digital watergun reflection system to locate a site sufficiently shallow in depth and with thick enough sediments to satisfy the drilling requirements.

It was hoped that the orientation of abyssal hills in the area would indicate the spreading direction at the time of crustal formation. Knowledge of the spreading direction would be crucial to the design of the refraction survey. Also, locating a site with relatively low topographic relief would make the interpretation of refraction results less complicated. The refraction survey was designed to investigate azimuthal anisotropy in the oceanic crust and upper mantle and relate this to the spreading direction (see Shearer, et.al., this volume).

Underway geophysical data were acquired by the D/V Glomar Challenger and R/V Melville during transits both to and from the site. Most of the surveying at the site, however, was performed by the R/V Melville.

D/V CHALLENGER UNDERWAY DATA COLLECTION

Depth, magnetic and watergun profiler records were recorded during the transit of the D/V Challenger from New Zealand to the proposed drill site . After leaving Wellington, an abrupt increase in seafloor depth indicated that the Challenger had crossed the limit of the New Zealand continental crust. A 700 meter scarp (see Figure 2) descended to a region with depths commonly as great as 5400 - 5800 meters. In this region, bounded to the north by the Louisville Ridge, the Challenger crossed a group of highs and lows with relief as great as 1000 meters. This relief is partly concealed by as much as 500 meters of sediment in the lows. Bathymetric trends in this region appear on SIO bathymetric maps (Mammerickx,et al., 1975) and are interpreted to be approximately parallel to the trend of the Louisville ridge (see Figure 1).

The Challenger's track across the Louisville Ridge was chosen to supplement track lines of previous expeditions. In this area SIO bathymetric maps (Mammerickx et al., 1975) show an elongate, sinuous ridge,

but the Challenger's sounding line (see Figure 3) in conjunction with a sounding line by R/V Eltanin indicates that the ridge at this point is probably a circular volcano instead of a local high on an elongate ridge.

From the Louisville Ridge to the proposed drill site, the ship sailed on course to confirm the existence of a narrow trough trending southwest- northeast and reaching a basement depth of nearly 6950 meters. The Challenger verified the existence and southwesterly trend of this trough. The along- track morphology shows two asymmetrical ridges separated by a deep trough reaching a basement depth of 6000 meters, far below common regional depths of about 5500 meters (see Figure 4) and indicates a probable deepening of the trough to the southwest.

As seen from the D/V Challenger, relief of the seafloor near the drill site is low: less than 150 meters, and digital watergun profiler records show sediment thicknesses of approximately 30 meters. Drilling results along with R/V Melville's records subsequently showed that the D/V Challenger's watergun data, which were recorded through a high pass filter, was reflecting off the top of thin chert and porcellanite stringers and was not penetrating the total sediment thickness of approximately 70 meters.

The Glomar Challenger left the drill site on February 2, for Papeete, Tahiti, with a transit course through the Cook Island chain. Numerous seamounts and guyots were crossed during the transit.

R/V MELVILLE SITE SURVEY

The R/V Melville left Honolulu on January 9, 1983, one week before the D/V Glomar Challenger left Wellington, and arrived at the proposed site 36 hours before the arrival of the D/V Challenger.

The seismic reflection source used was a 50 cubic inch watergun, which is a high frequency implosive source that does not generate a bubble pulse, and thus reverberates less than a conventional airgun. The receiver was a 50 hydrophone (spaced at one meter intervals) single-channel streamer towed 275 meters behind the R/V Melville. The reflection data were recorded digitally at a sampling rate of 2 milliseconds on an IBM 1800 with bandpass filters set at 15 and 125 Hertz, and displayed in real time on a Tektronix screen. Real time processed (automatic gain control, trace equalization) reflection profiles were used by the Melville scientists to determine the final drilling site. Altogether, 500 kilometers of digital seismic reflection data were collected. The reflection site survey shiptrack, along with the surveyed bathymetry are shown in Figure 5. Details of the individual site survey lines are shown in Figures 6, 19, and 29.

The site survey was broken into eight lines and these are displayed in Figures 7-31. These profiles have been reprocessed at Scripps using a partial deconvolution. A watergun source function is not minimum phase due to a low frequency precursor and thus precluded the use of a conventional spiking deconvolution algorithm. The partial deconvolution used prewhitens the amplitude spectrum, but does not alter the phase spectrum. Actually, we found this process did very little to change the appearance of the seismic data and only marginally increased the freqency content. In the future, watergun source functions digitized on board ship at a sampling interval of 20 microseconds will be used to obtain spectral estimates of the watergun source. These estimates will allow a deterministic deconvolution to be applied to these data in order to increase the spectral resolution and thus improve the sediment interpretation. Migration of these seismic profiles would collapse strong hyperbolas noticeable on some of the basement reflections, but would do little to improve the sediment interpretation since most of these reflections are nearly horizontal.

LINE 1 (Jan 20/17:40Z - Jan 21/2:30Z) (Figures 7-12)

This was a long N-S line, the first running through the proposed initial survey area. Two sites along this line were considered:

A) 1800Z-1925Z (see Figure 7): The sediment reflections look very flat and undisturbed.

B) 2100Z-0045Z (see Figure 9): The sediment reflections are poorer, but there is less large scale topography in the vicinity.

At both sites, the two-way travel time was 7.5 seconds which translates to a water depth of 5625 metres (using 1500 m/s water velocity); 125 meters deeper than our target depth. The sediment thickness at both sites was about 90 meters. This estimate was based on a two-way travel time of .12 seconds from the first arrival to what appeared to the basement reflector (chosen on the strength of that reflector and the lack of any clear reflections below it). However, because of the error in picking exactly where in the broad wavelet the actual basement lies, the sediment thickness estimate represents an upper bound. It was decided to survey Site B in greater detail since the lack of topography would benefit the interpretation of refraction survey data. The deep hyperbola at 1945Z at about 8.1 seconds (see Figure 8) is most likely an out-of-plane reflection, since it is found below the basement reflector. This part of the line was clearly collected in an area of relatively rough topography.

LINE 2 (Jan 21/2:30Z - Jan 21/7:45Z) (Figures 13-15)

After completing Line 1, we maneuvered the ship to obtain a perpendicular crossing through Line 1 at Site B. The sediments seemed to be about the same thickness as previously observed in Line 1 with the same bumpy, uneven basement reflection. The strong hyperbolas along the

basement reflection are most likely from small faults in the upper part of the basalt. Again, migration would collapse these hyperbolas and concentrate the scattered energy at the apex of the hyperbola, making the basement reflector much stronger. We passed by a large topographic feature which was not recorded in the seismic record because the delay switches were not adjusted sufficiently rapidly (see Figure 14). All the sediments appeared to very flat, indicating a pelagic source.

LINE 3 (Jan 21/7:45Z - Jan 21/11:45Z) (Figures 16-18)

This is the W-E cross line through Site B. Other than the bathymetric high at 015Z (see Figure 16), the topography was relatively flat. The sediments seemed to thicken and thin slightly as the basement reflector moved slightly up and down. Again, we saw many hyperbolas in the top of the basalt reflection, indicating a rough basement. There appeared to be a thick mound of sediments at 1055Z (see Figure 18); Line 1 passed near this mound, yet no such feature was seen on Line 1. This region near the mound exhibited the thickest observed sediments but these thick sediments are very localized.

LINE 4 (Jan 21/11:45Z - Jan 21/15:15Z) (Figures 20-21)

This portion of the survey was run to determine if the sediments thickened south of Line 3. The line ran south slightly and then east crossing Line 1. The sediments were of the same thickness although the sediment reflections looked a little flatter and less disturbed than the sedment reflections on Line 3. However, the surrounding topography seemed to be rougher, as indicated by the exceptional out-of-plane reflection at 8.5 seconds (see Figure 21).

LINE 5 (Jan 21/15:15Z - Jan 21/19:15Z) (Figures 22-24)

The ship was steered back though Site B in a NW direction for one final check. Again, the mound was evident although the sediments were still marginal in thickness (see Figure 23). There was disagreement over the initial sediment thickness estimation of 90 meters, from the D/V Challenger which by now had arrived in the area. The Challenger's seismic reflection system recorded a much thinner sediment thickness. The discrepancy between the observations was soon explained by differences in the recording settings used on the two ships. Both ships were using a watergun as their seismic source and were recording digitally. The R/V Melville, however, was using a greater bandwidth which extended to lower frequencies and yielded greater penetration. During the actual drilling, cherts were encountered about midway in the sediments. A high reflection coefficient existed between the hard cherts and the soft overlying pelagic sediments. The Challenger mistook the chert reflection for a basement reflection, since their filters were set to record much higher frequencies. The D/V Challenger passed over the chosen site and dropped the positioning beacon at 1700Z for the first exploratory hole

(595) in the vicinity of the sediment mound seen in Line 3.

LINE 6 (Jan 21/19:15Z - Jan 22/1:00Z) (Figures 25-28)

The R/V Melville surveyed north of Site B during the early drilling operations and encountered rougher topography (see figure 26). As the ship returned to the site, the sediments thickened slightly. During the drilling of Hole 595, the expedition Chief Scientists met on the Challenger with copies of the seismic profiles to discuss the site and examine the initial cores. These results showed that the sediments were soft and perhaps too thin. Apparently, the Challenger was drilling at the peak of the mound seen on the seismic data where the sediments appeared to be thinnest. Line 3 indicated thicker sediments just off the mound and slightly to the east (see Figure 18); this accumulation could be attributed to sediment slumping from the mound. The Challenger moved 460 metres to the east to drill the second exploratory hole (595A), while the Melville continued to survey to the south.

LINE 7 (Jan 22/7:00Z - Jan 22/8:45Z) (Figure 30)

The Melville survey to the south, conducted during the drilling of Hole 595A, failed to find any evidence of increased sediment thickness necessary for setting a reentry cone. The Melville returned to Site B.

LINE 8 (Jan 22/8:45Z - Jan 22/10:45Z) (Figure 31)

During this survey leg, which extended north to the Challenger, it was decided that the present site was the best available within the site survey area. Drilling operations continued even though results from the second exploratory hole indicated only 70 meters of sediments. While the D/V Glomar Challenger started to drill reentry hole 595B (location: 23 49' S, 165 32' W) the R/V Melville moved off to deploy the OBS's for the initial teleseismic recording experiment.

The bathymetric survey using the 12 kHz and the 3.5 kHz echosounders continued as the Challenger drilled Hole 595B and deployed the BIP. From the orientation of a distinct series of abyssal hills northwest of the site, the direction of spreading at the time of crustal formation was estimated to be N45W (see Figure 5). The refraction program was then set up with two lines parallel and two lines perpendicular to this spreading direction. The layout of the refraction experiment was designed to test the spreading direction hypothesis: the higher upper mantle velocities would lie in the direction parallel to the original direction of spreading, and the higher crustal velocities would lie in a direction perpendicular to the original spreading direction, due to the orientation of sheeted dikes in Layer 2.

CORRELATION WITH PHYSICAL PROPERTIES

Lithological analysis and physical properties measurements of the cored sediments from Hole 595 and 596 revealed two major stratigraphic units (see Figure 32). The first 40 meters consisted of a homogeneous layer of zeolitic pelagic clays. There was a high percentage of recovery in this unit and all measurements of physical properties were very consistent. Sonic velocities measured at 400 kHz with a Hamilton Frame Velocimeter varied only slightly from 1.5 kilometers/second in the pelagic clays. Wet bulk density measurements using a Gamma Ray Attenuation Porosity Evaluator (GRAPE) averaged 1.29 Mg/m**3. Below 40 meters, the dominant sediment was still pelagic clays, but thin stringers (up to ten meters) of porcellanite and chert were encountered. Core recovery in this unit was very poor because of the difficulty in drilling through the very hard stringers. Only one sample of chert recovered was large enough for physical properties measurements. This sample gave a much higher sonic velocity of 3.8 kilometers/second and a wet bulk desity of 2.46 Mg/m**3. A thin layer of metalliferous sediments was encountered immediately above the basalts but no physical properties measurements were taken. Basalt samples tested exhibited a mean sonic velocity of 4.7 kilometers/second. Lower velocities seemed to be associated with veined basalt cores and higher velocities associated with massive, uncracked, and unveined basalts. The GRAPE wet bulk density measurements in the basalts averaged 2.70 Mg/m**3.

A comparison of downhole lithology and physical properties with watergun reflection data recorded proximal to the site by the R/V Melville is shown in Figure 5. The watergun data shows a stong basement reflection from the top of the basalt layer. However, no strong reflection is seen where the interbedded cherts begin, even though a large velocity contrast and thus a large reflection coefficient exists between the cherts and the surrounding pelagic clays. This lack of a strong chert reflection resulted from the chosen frequencies recorded by the Melville's digital reflection system, which extended from 15 to 125 Hertz. Much of the low frequency energy from the watergun source passed through this reflector. At a frequency of 50 Hertz, the seismic wavelength is about 30 meters, and thus the thin layering in the cherts is practically invisible. However, a stong reflection corresponding to the top of the interbedded chert layer is seen in the 3.5 kHz data.

3.5 kHz data near the drill site are also shown in Figure 5. The two- way travel time between the first reflection from the bottom and the only other stong reflector in the 3.5 kHz record is .05 seconds. This corresponds to a depth of 38 meters if a velocity of 1.5 kilometers/second is used. This depth is far too shallow for this strong reflection to correspond to the top of the basalts. Because the length of the 3.5 kHz wave is .4 meters (compared to 30 meters for the watergun wavelength), a thin 10 meter stringer of cherts would easily produce a strong reflection on the 3.5 kHz record. Also, because higher frequency

acoustic energy attentuates much quicker, little energy remained to reflect off the basalts. The 3.5 kHz record indicates that these thin chert stringers do not pinch out locally, but are quite extensive laterally.

REVERBERANT LAYER

Work done at Lamont-Doherty (see Houtz and Ludwig, 1979) indicates the likely presence of a 'reverberant layer' in the seismic profiles for this region. This reverberant layer hypothesis resulted from a series of high amplitude stratified reflections seen in earlier recorded large volume airgun data throughout the Southwest Pacific Basin. Houtz and Ludwig explained this phenomena as reflections from very hard thinly-layered sediments such as those found in calcarious beds and volcanoclastic aprons. They have mapped the extent and thickness of this reverberant layer thoughout the Pacific and, according to their maps, we would have expected to find 60-100 metres of acoustically transparent material followed by 100-120 metres of highly reflective material in the drill hole. No reverberant layer was noticed in the watergun reflection profiles collected during the site survey. 70 metres of acoustically transparent sediments were drilled, but then basement was encountered. We agree with Shipley, et.al. (1983) that the reverberant layer is strictly an instrumentation effect caused by using narrow-band sources (airguns) and receivers. When this airgun source wavelet reflects off the hard basement reflector, the ringing wavetrain gives the impression of a well-layered stack of high amplitude sediment reflections.

CONCLUSION

The Site Survey conducted immediately prior to the arrival of the D/V Glomar Challenger successfully located a site with sufficiently shallow water depth and thick sediment cover to allow setting a reentry cone. The data collected were subsequently correlated with the sediments drilled at the site and the presence of the unexpected chert-bearing sediments provided a satisfactory explanation for the differences between the reflection data gathered on the R/V Melville and the D/V Glomar Challenger. What appeared to be a shallow basement reflection on the narrow- band Challenger and 3.5 kHz transducer profiles was simply high frequency energy reflected off the top of chert and porcellanite stringers. The 'reverberant layer' of Houtz and Ewing was not observed in the survey data and was not drilled. The reverberant layer, in this area, must simply be an artifact of the narrow band analog recording typical of early reflection systems.

REFERENCES

Houtz, R. E., and Ludwig, W. J., 1979. Distribution of Reverberant Subbottom Layers in the Southwest Pacific Basin. J. Geophys. Res., 84: 3497-3504.

Okal, E. A., Talandier, J., Sverdrup, K. A., and Jordan, T. H., 1980. Seismicity and Tectonic Stress in the South-Central Pacific. J. Geophys. Res., 85: 6479-6495.

Shipley, T. H., Whitman, J. M., Duennebier, F. K., and Petersen, L. D., 1983. Seismic Stratigraphy and Sedimentation History of the East Mariana Basin, Western Pacific. Earth Planet. Sci. Lett., 64: 257-275.

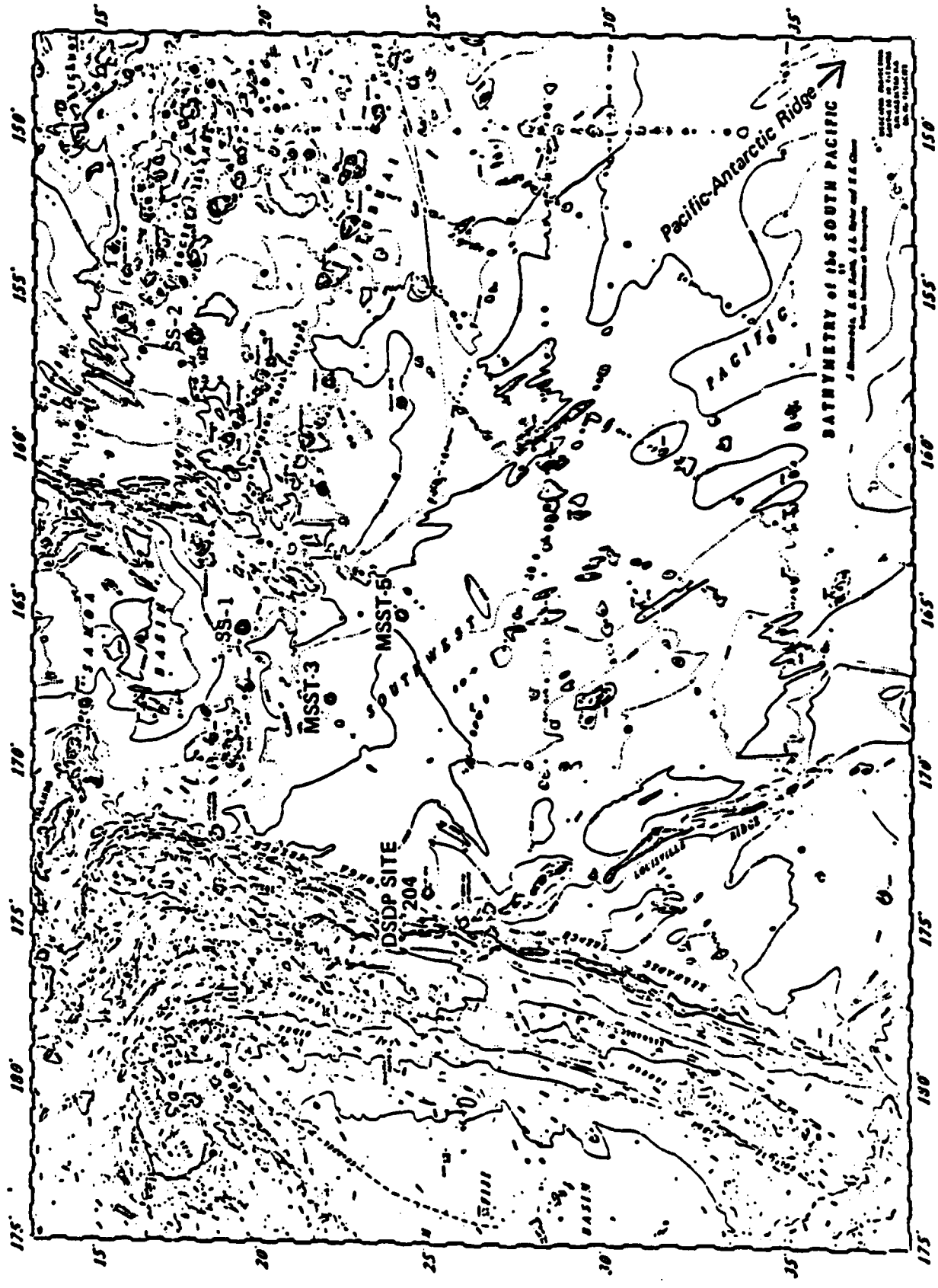


Figure 1. Location of preliminary site survey areas MSST-5 (primary) and MSST-3 (alternative), contingency "storm" sites SS-1 and SS-2, and DSDP Site 204 in the southwest Pacific. A suitable site for Leg 91 was found at MSST-5.

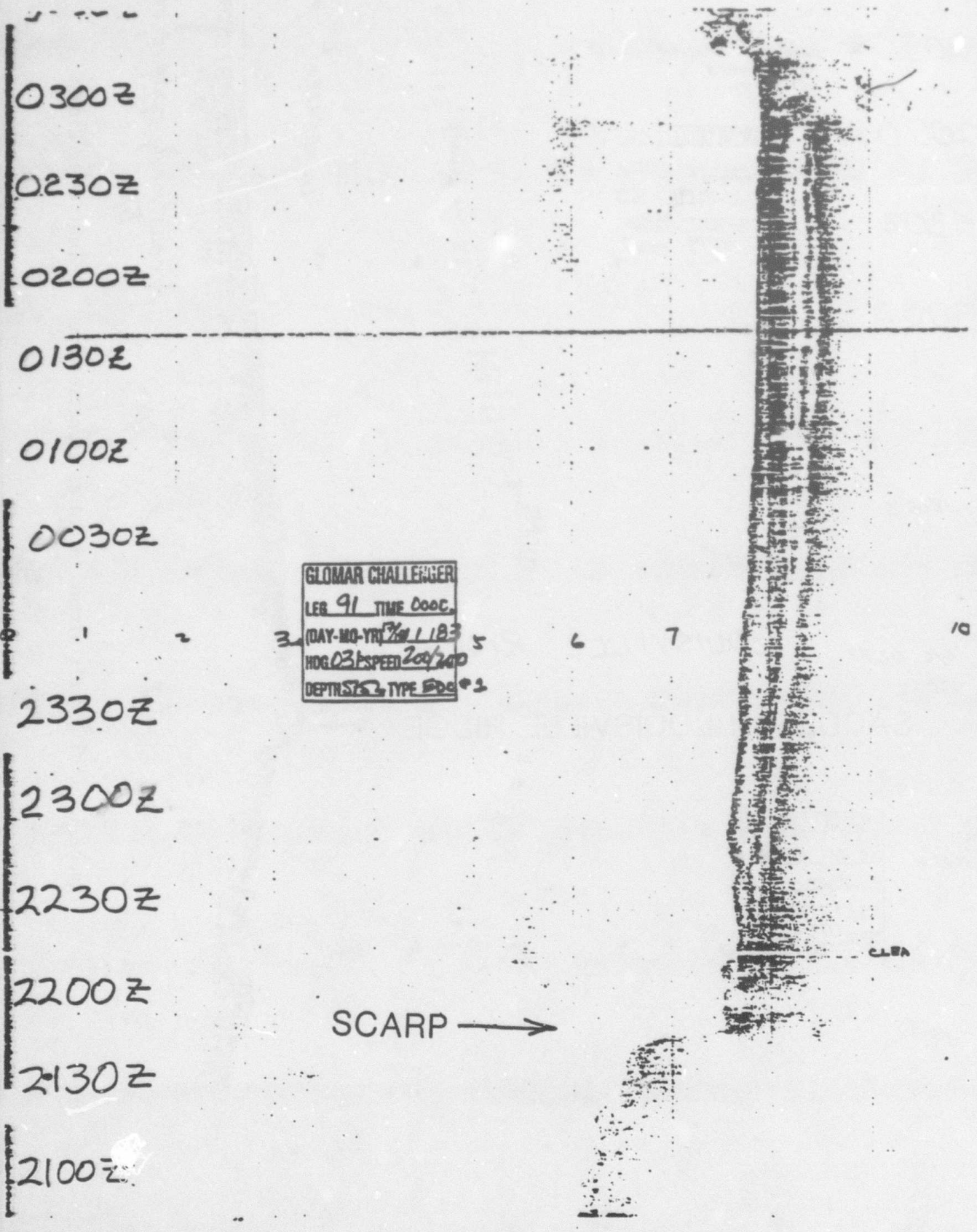


Figure 2. Airgun record of the D/V Glomar Challenger as it leaves the New Zealand shelf. Exact location of the edge of the shelf indicated by the 700 m scarp.

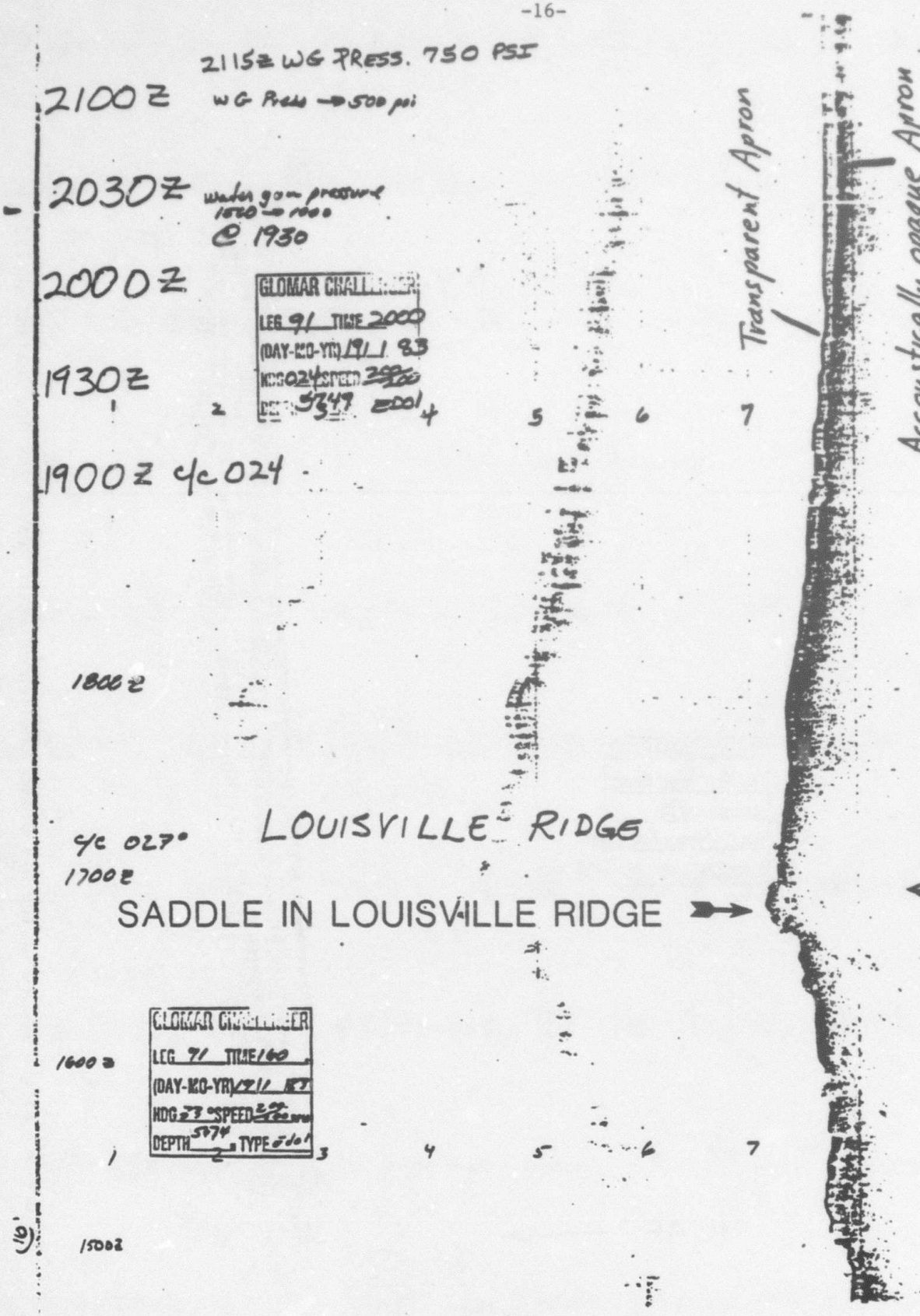


Figure 3. Challenger's airgun record as it passes over the Louisville Ridge.

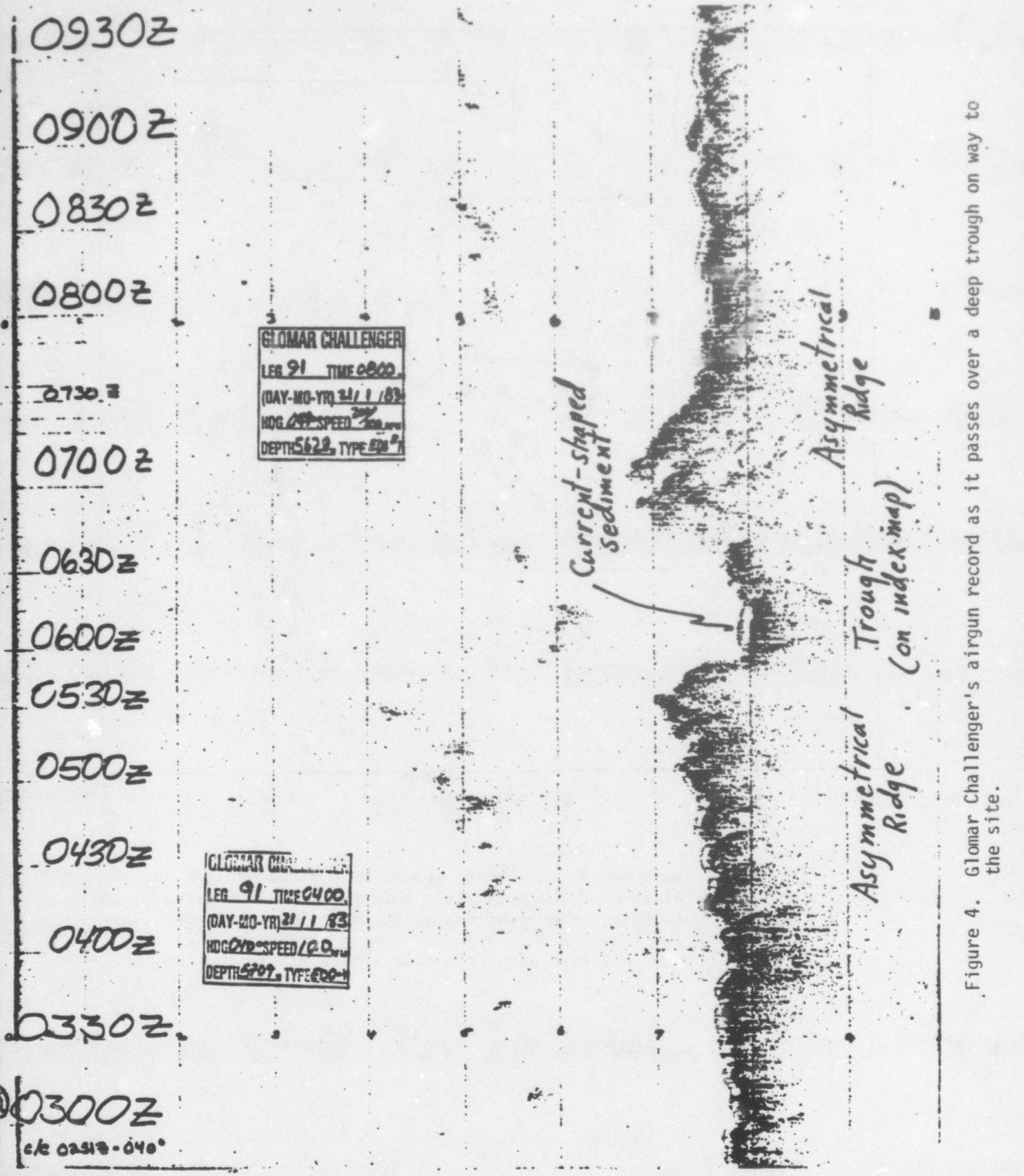


Figure 4. Glomar Challenger's airgun record as it passes over a deep trough on way to the site.

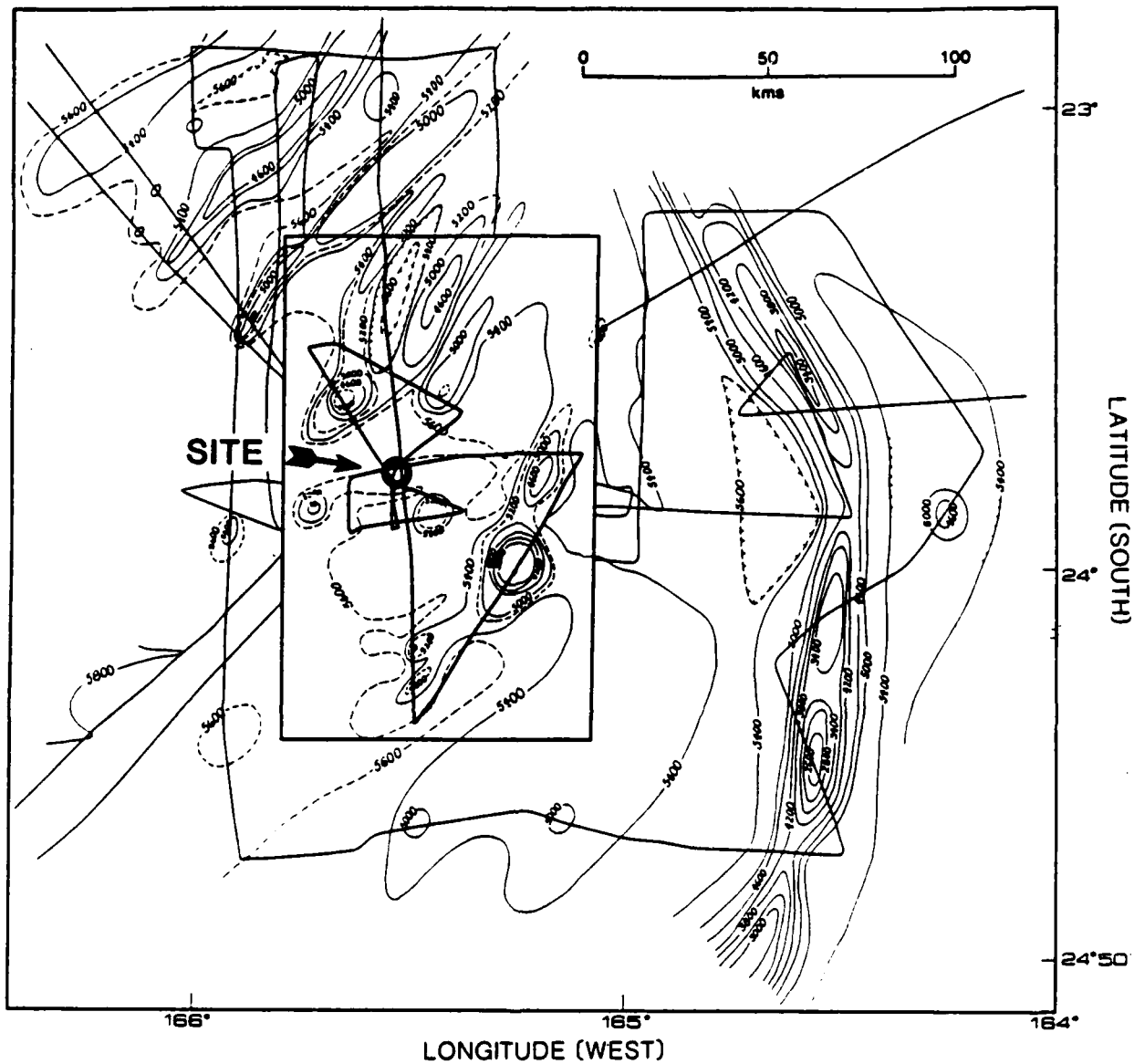


Figure 5. Bathymetry (in meters) around DSDP sites 595 and 596 along with the Melville's shiptrack. Boxed in area indicates extend of the watergun reflection survey. 500 kilometers of digital seismic reflection data was collected along the darker line within the box.

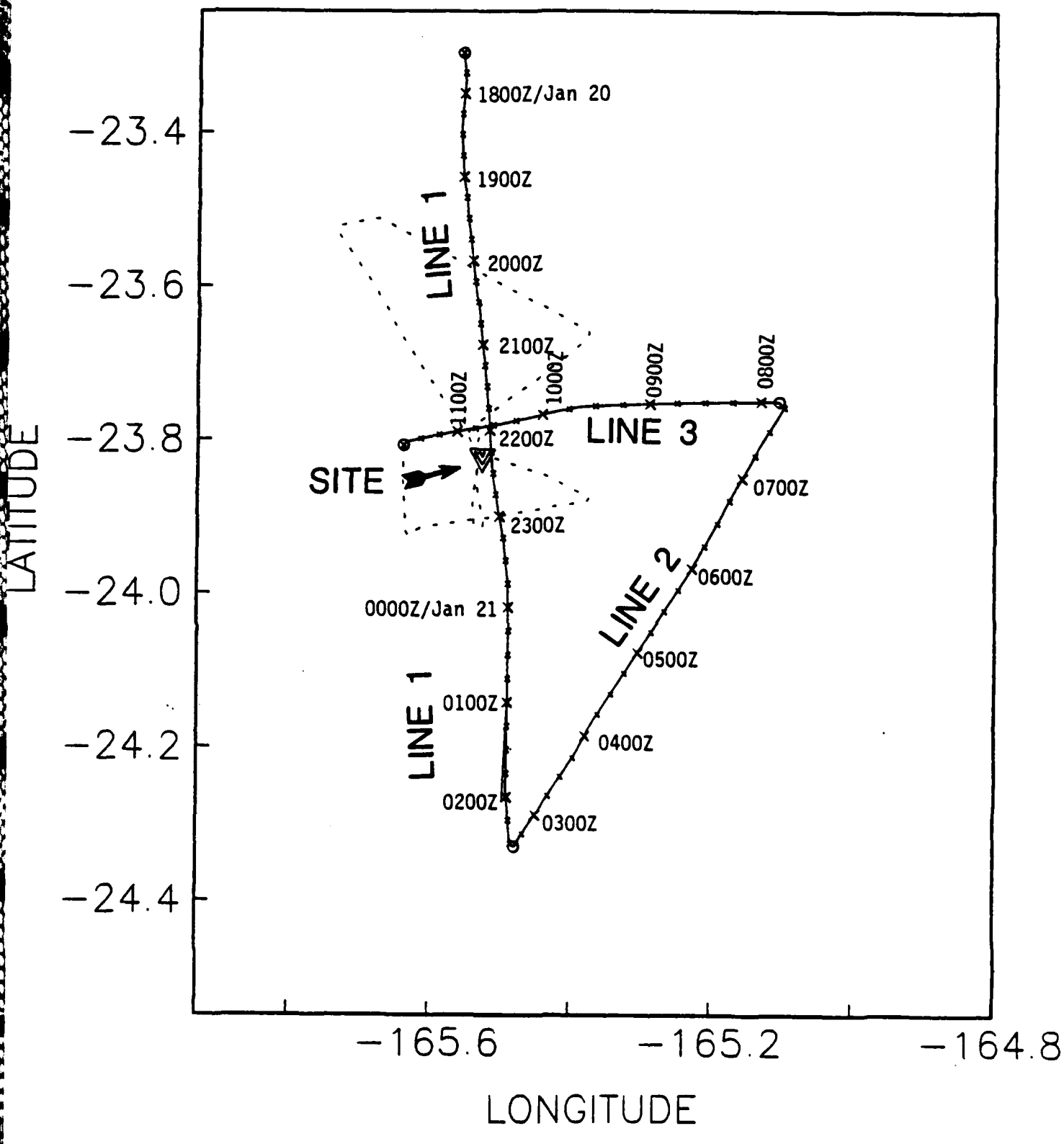


Figure 6. Location of site survey reflection lines 1-3. Filled triangle indicates the location of the chosen drill site. The remainder of the survey is shown by the dashed lines.

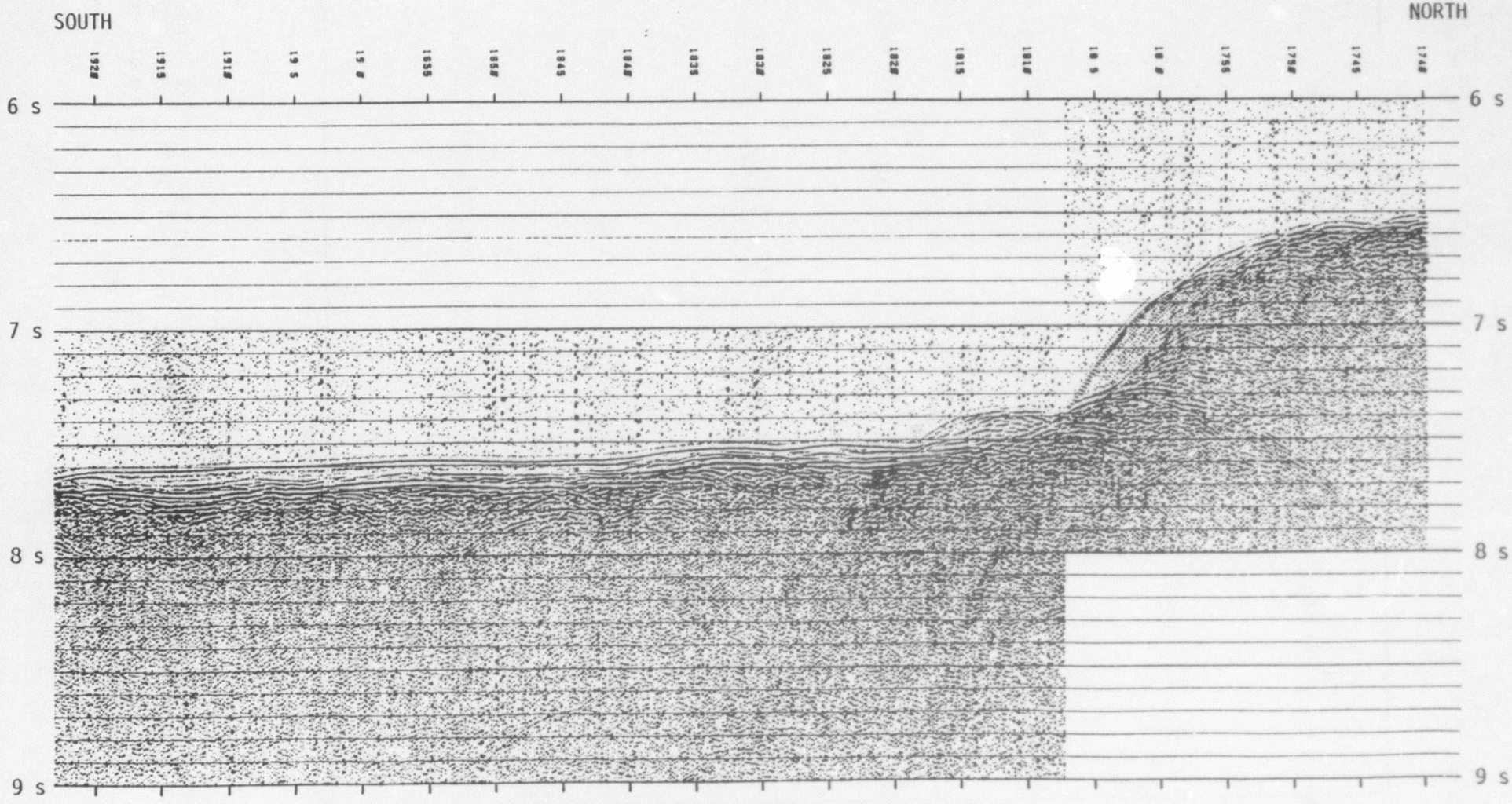


Figure 7. The beginning of Line 1 of Leg 91's watergun reflection site survey. Two-way travel time is displayed in the margins. The first site considered lies between 1820Z and 1920Z.

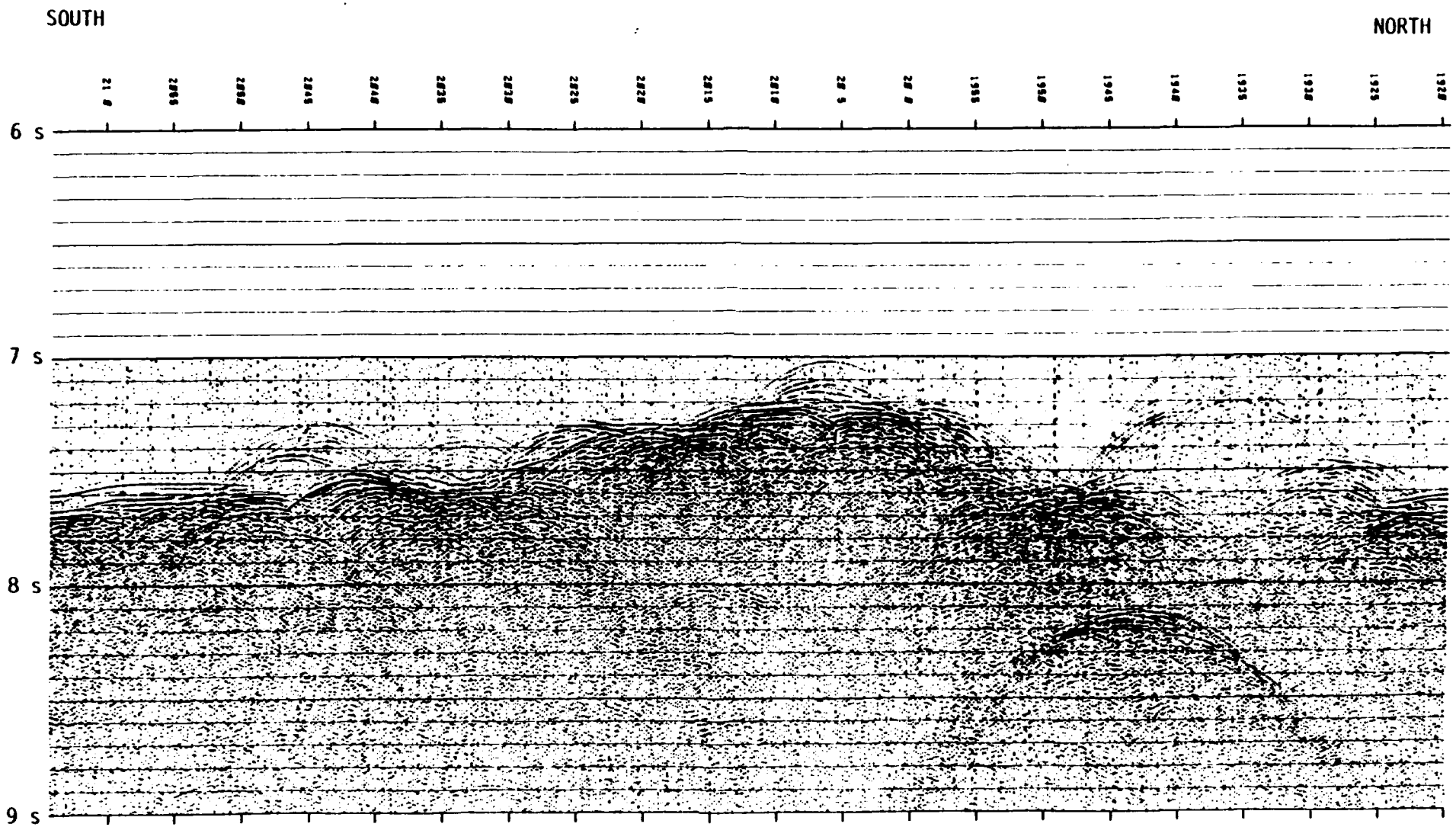


Figure 8. Line 1 (continued). Here the bathymetry has become much rougher, especially noticeable by the out-of-plane reflection at 1940Z at 8.2 seconds.

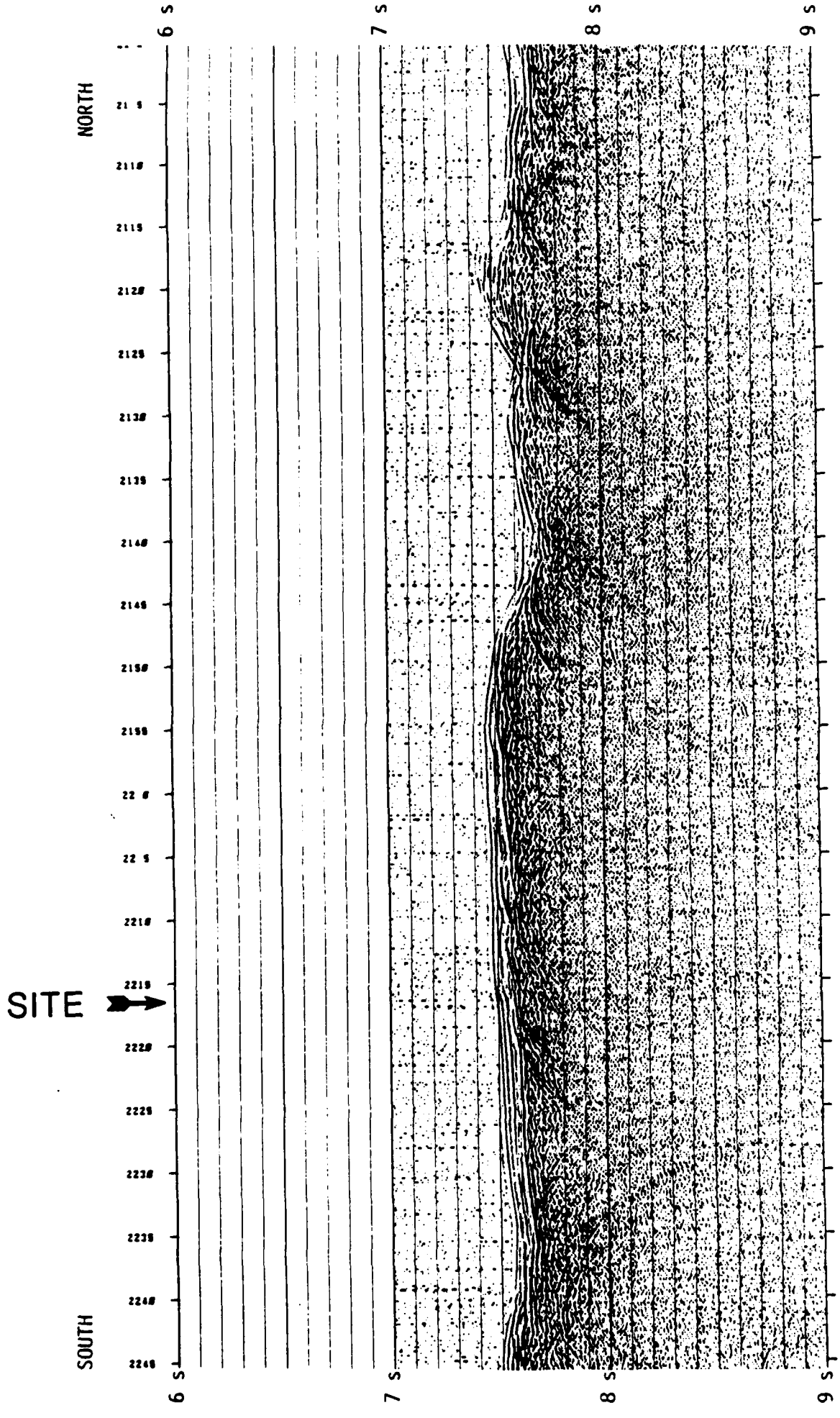


Figure 9. Line 1 (continued). This profile shows the second site considered which eventually became the actual drill site indicated by the arrow. The sediment thickness at the site was estimated at 90 m using a sediment velocity of 1500 m/s.

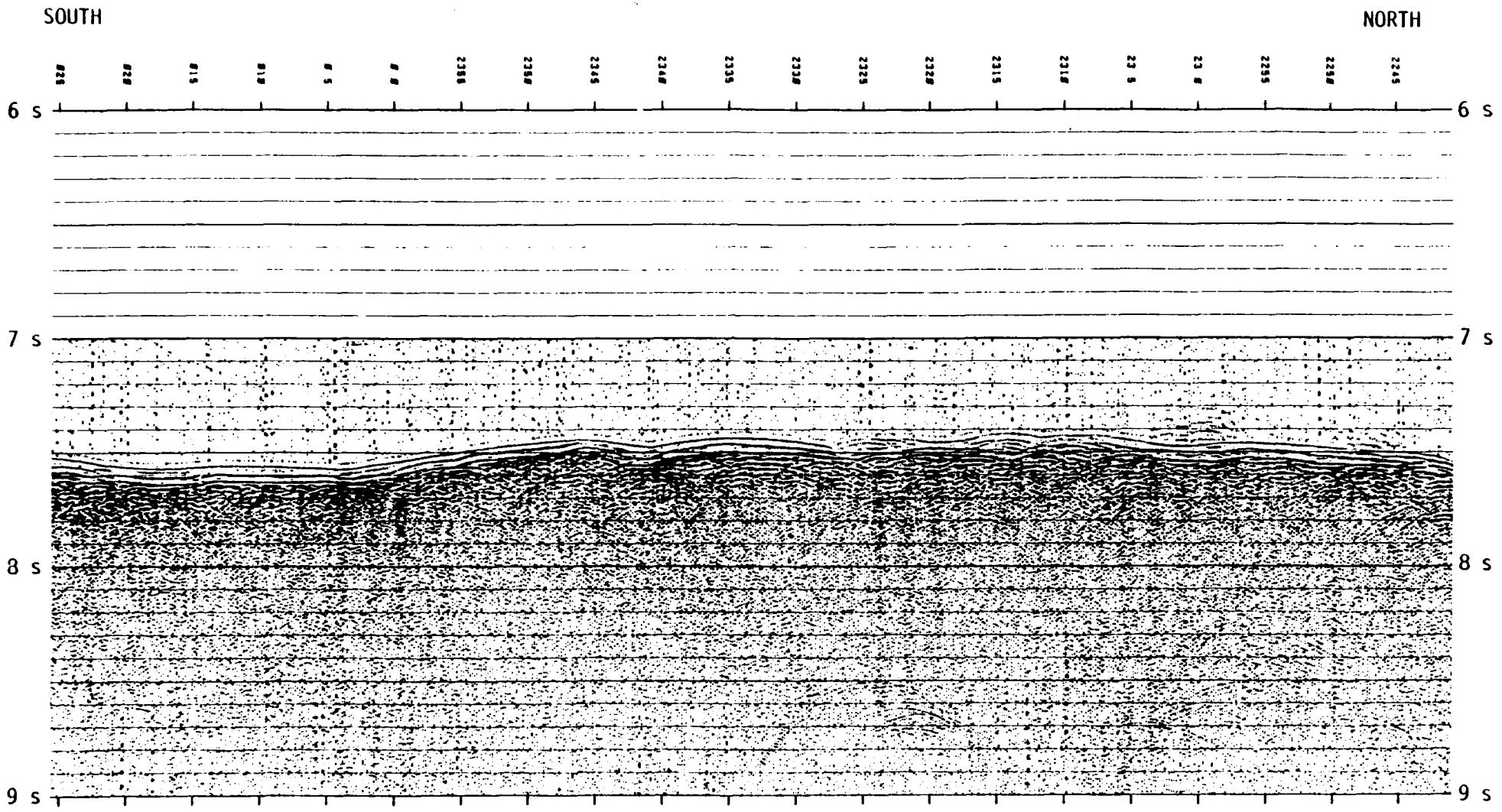


Figure 10. Line 1 (continued) further south of the site. The sediments here appear to be slightly thinner than at the chosen site.

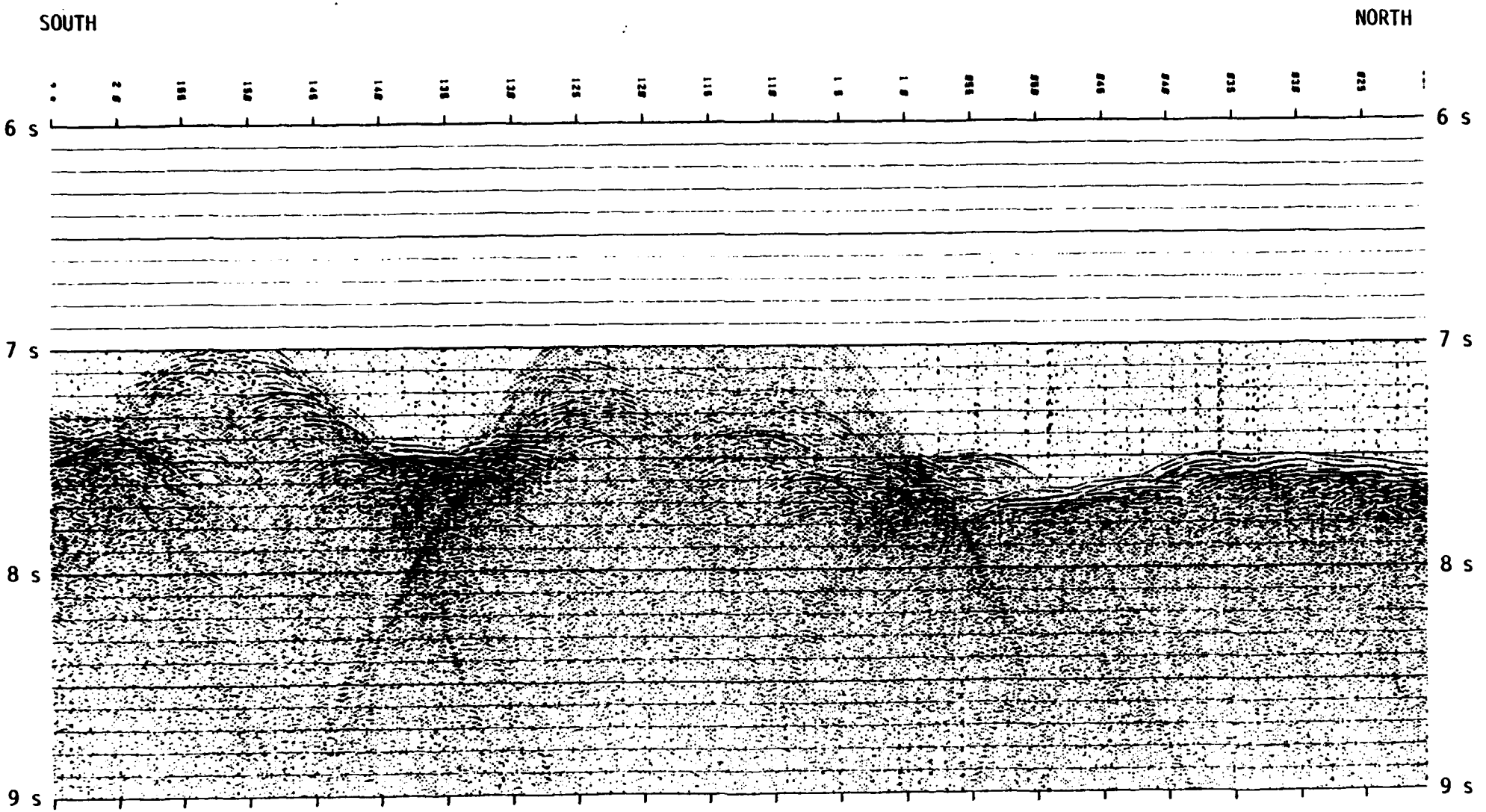


Figure 11. Line 1 (continued). The profile indicated that the topography becomes much rougher further south of the site.

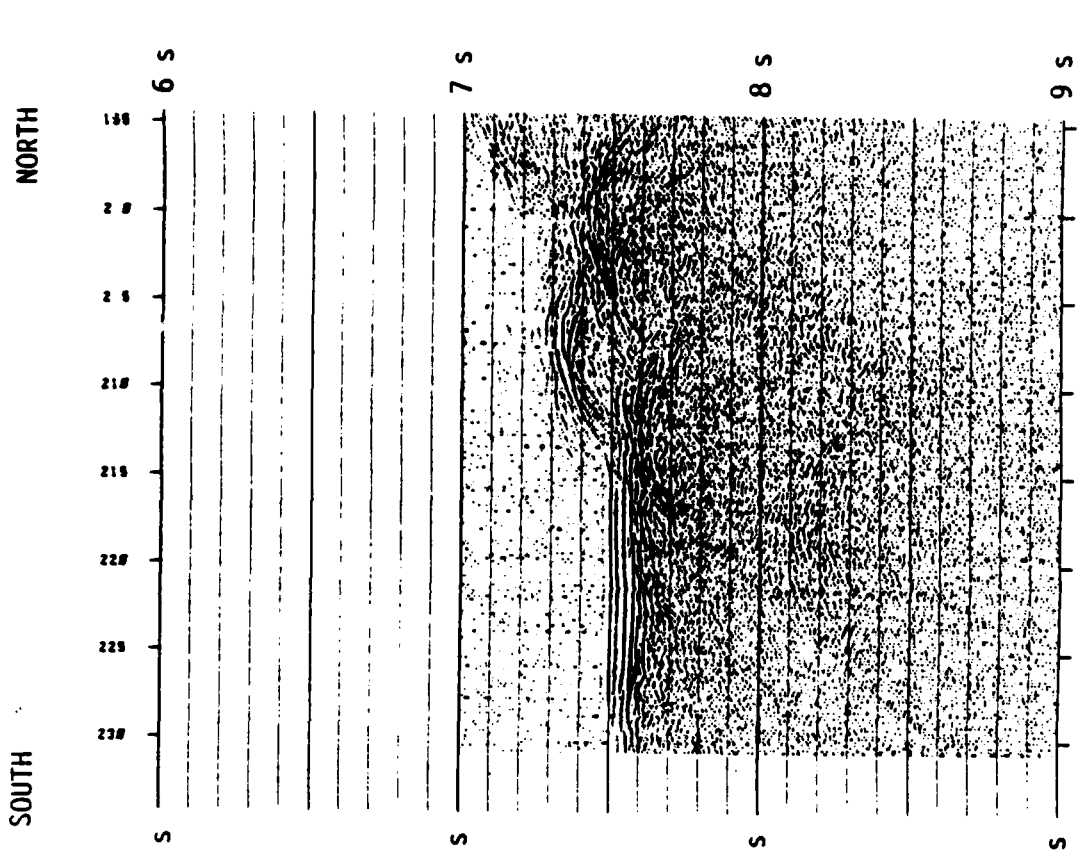


Figure 12. The end of Line 1 of the site survey.

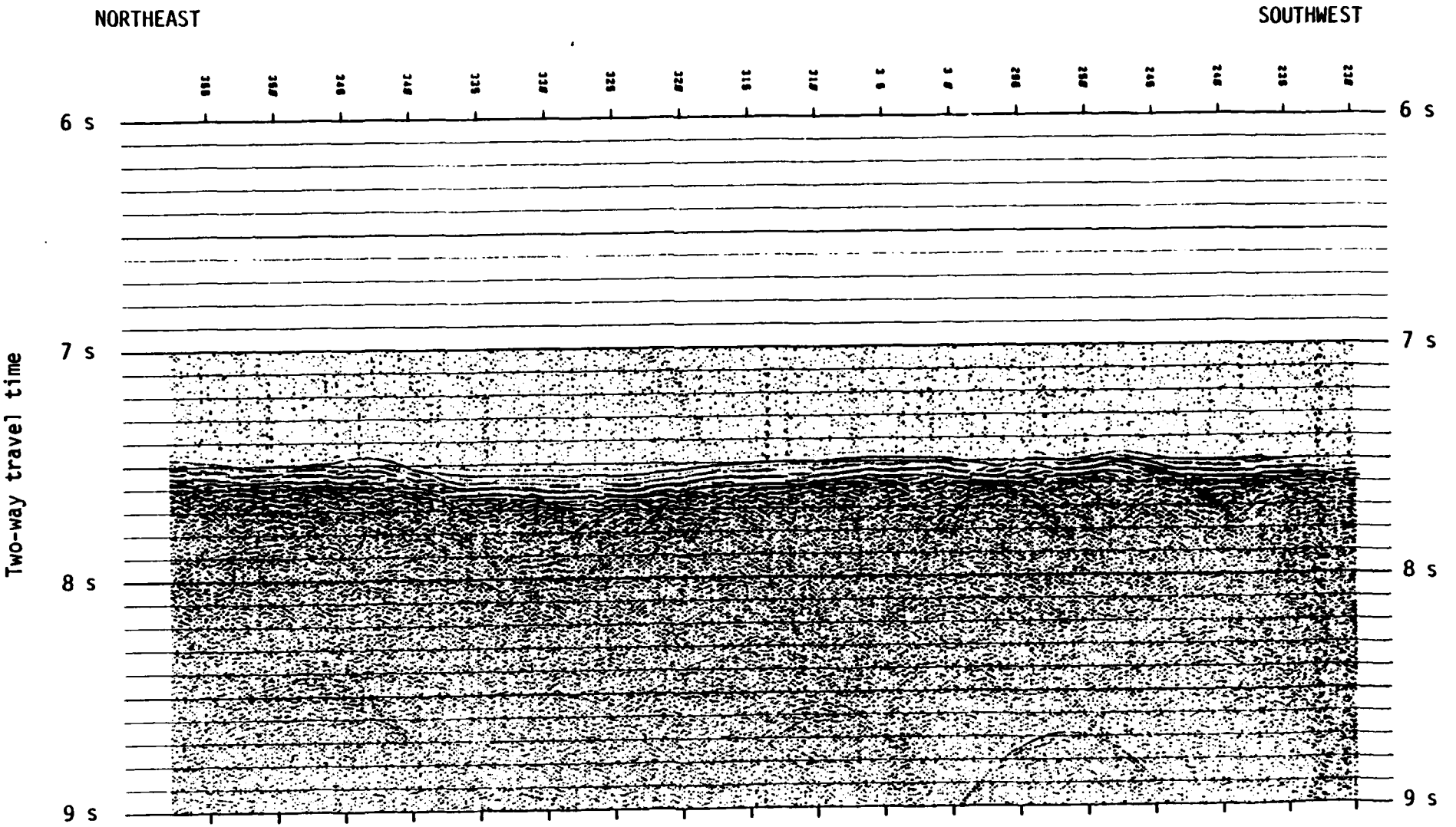


Figure 13. The start of Line 2 as the ship turns to the northeast. Hyperbolic reflections in the basement reflection indicates possible small faults in the upper part of the basalt.

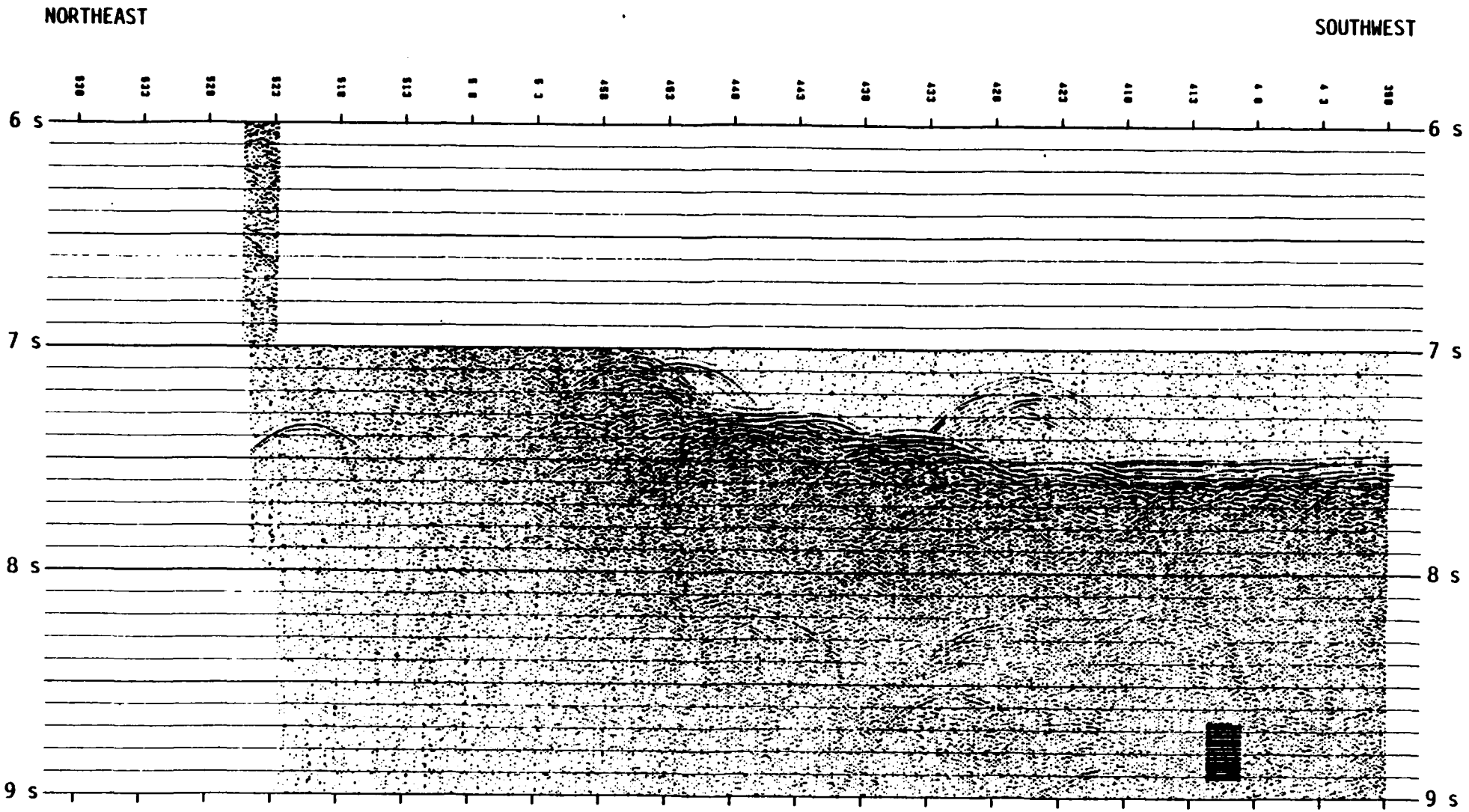


Figure 14. Line 2 (continued) as the ship maneuvers for a perpendicular crossing of the second site. Here the profile goes off scale as the delay switches were not adjusted quick enough.

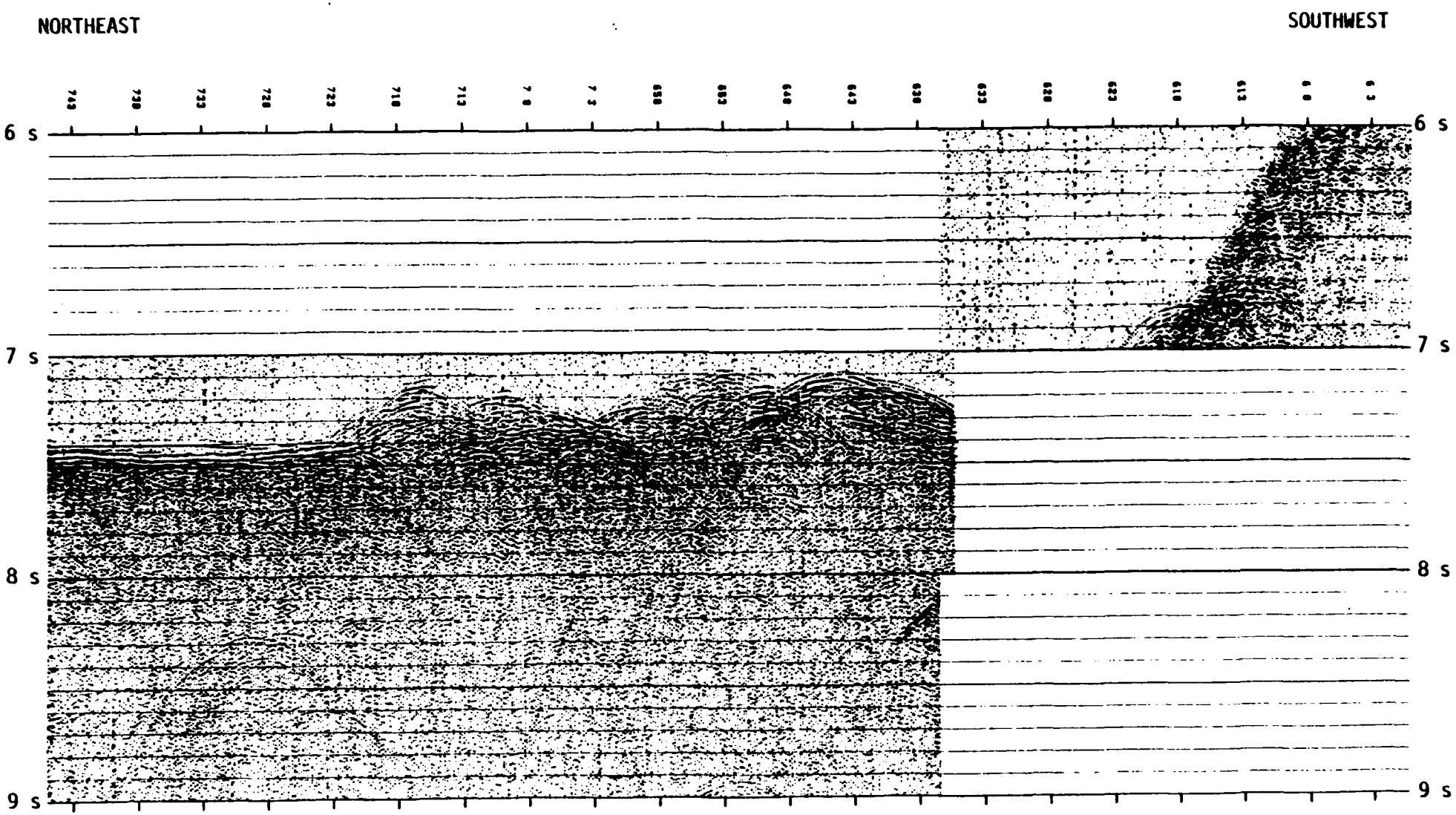


Figure 15. Line 2 (continued) as the ship comes off the large bathymetric high back into the flatter area.

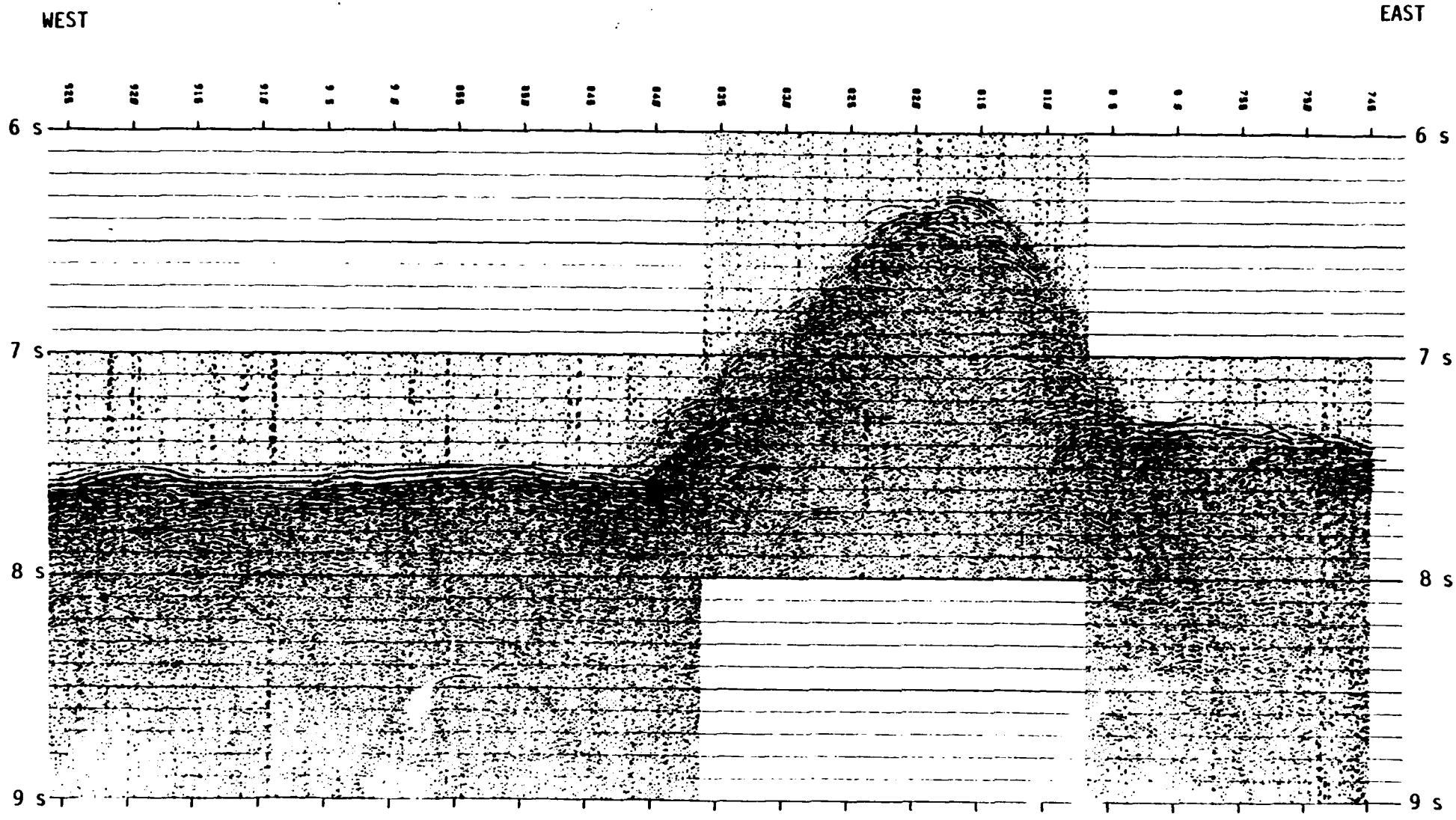


Figure 16. The start of Line 3 of the site survey as the ships back towards the site.

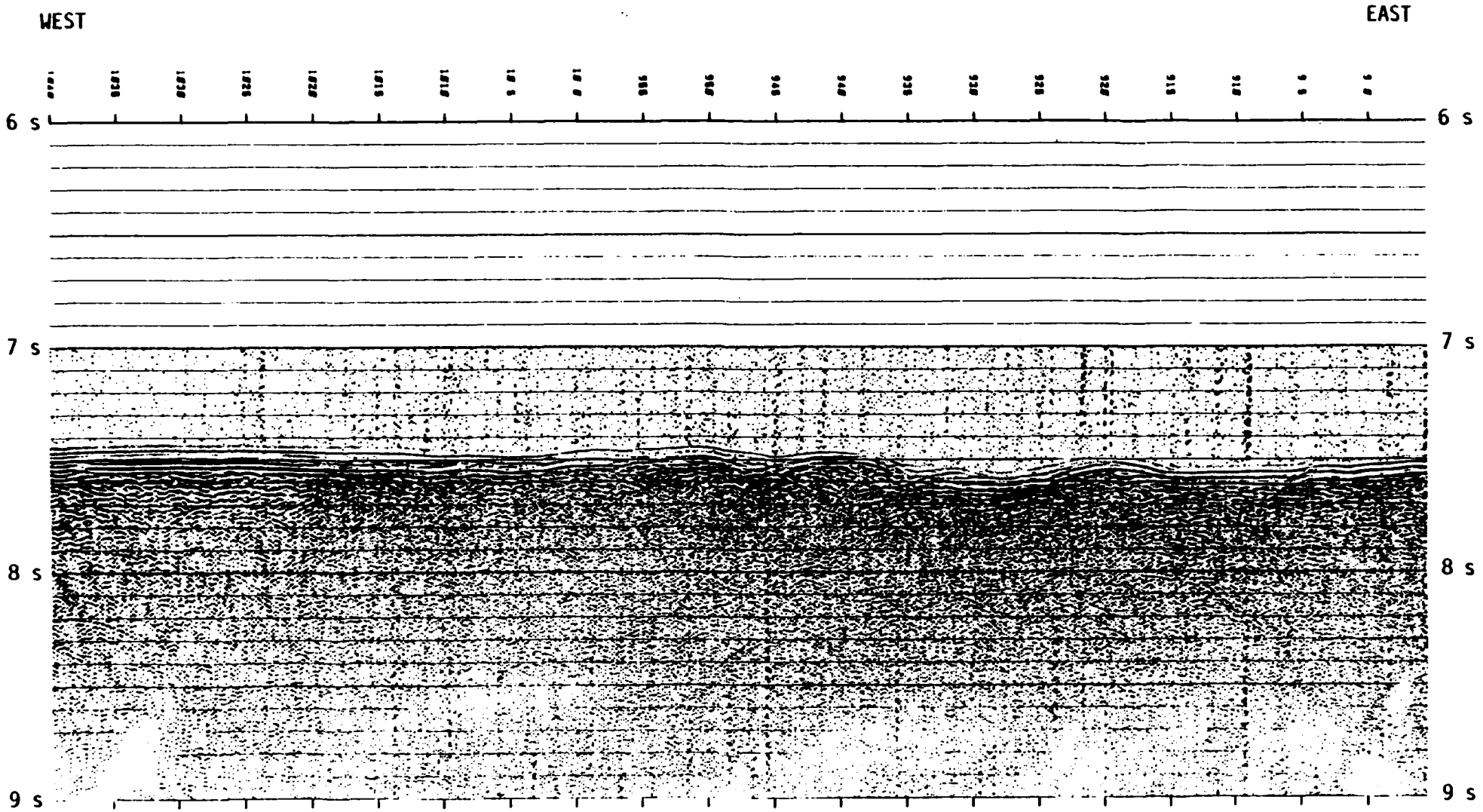


Figure 17. Line 3 (continued). The topography appears to be much flatter than the rougher areas seen in Line 2.

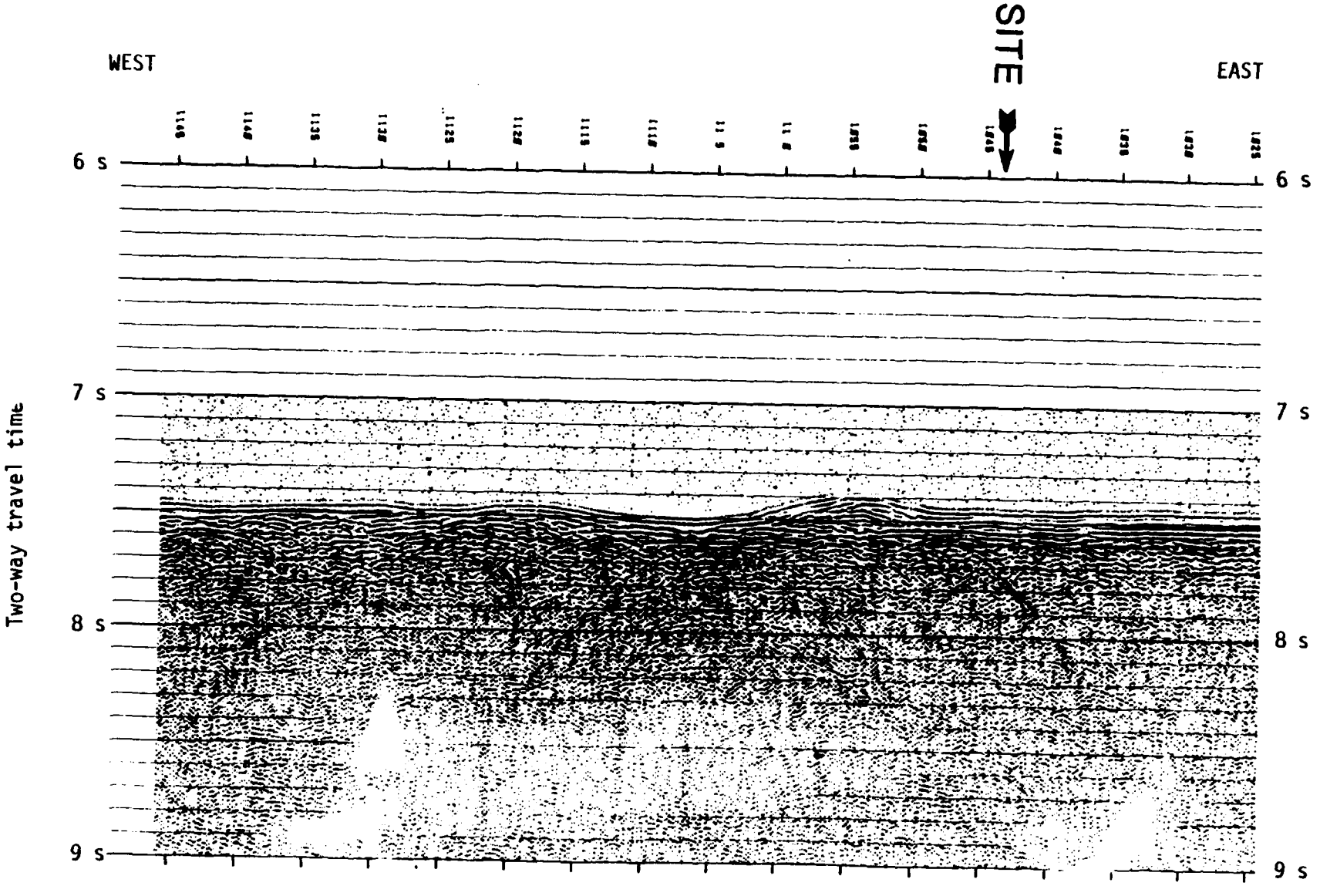


Figure 18. The end of Line 3. This profile shows a perpendicular crossing through the site. A mound is evident near the site that was not seen in Line 1. The sediments also appear to be thickess around this mound.

NGENDEI SITE SURVEY: LINES 4-6

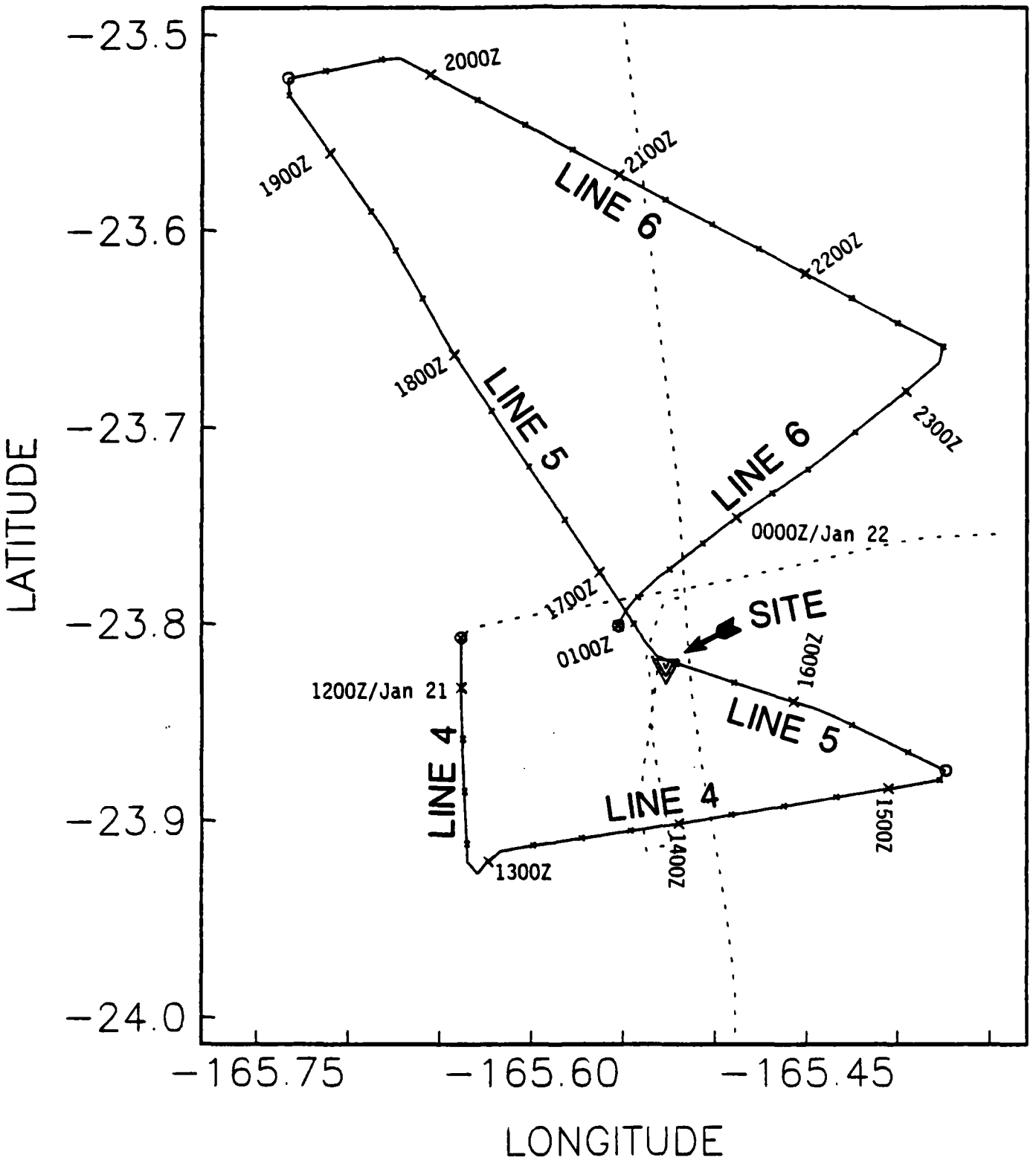


Figure 19. Location of site survey reflection lines 4-6. Filled triangle indicates the location of the chosen drill site. Parts of the rest of the survey is denoted by the dashed lines.

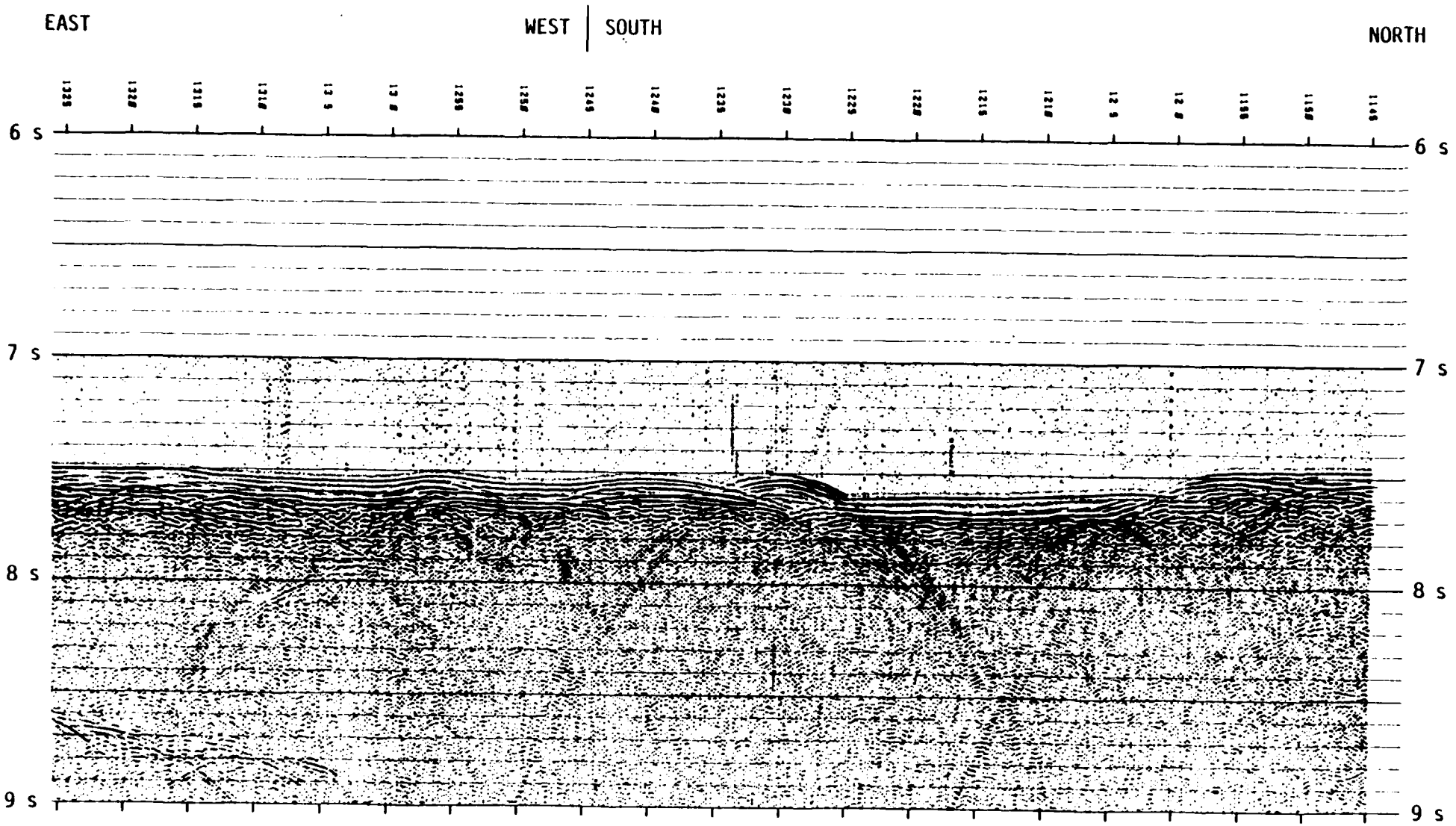


Figure 20. The start of Line 4 of the watergun site survey to investigate the sediments slightly south of the site. Deep reflection at 8.8 seconds from 1305Z to 1325Z is mostly likely an out-of-plane reflection since it is found well within the basement.

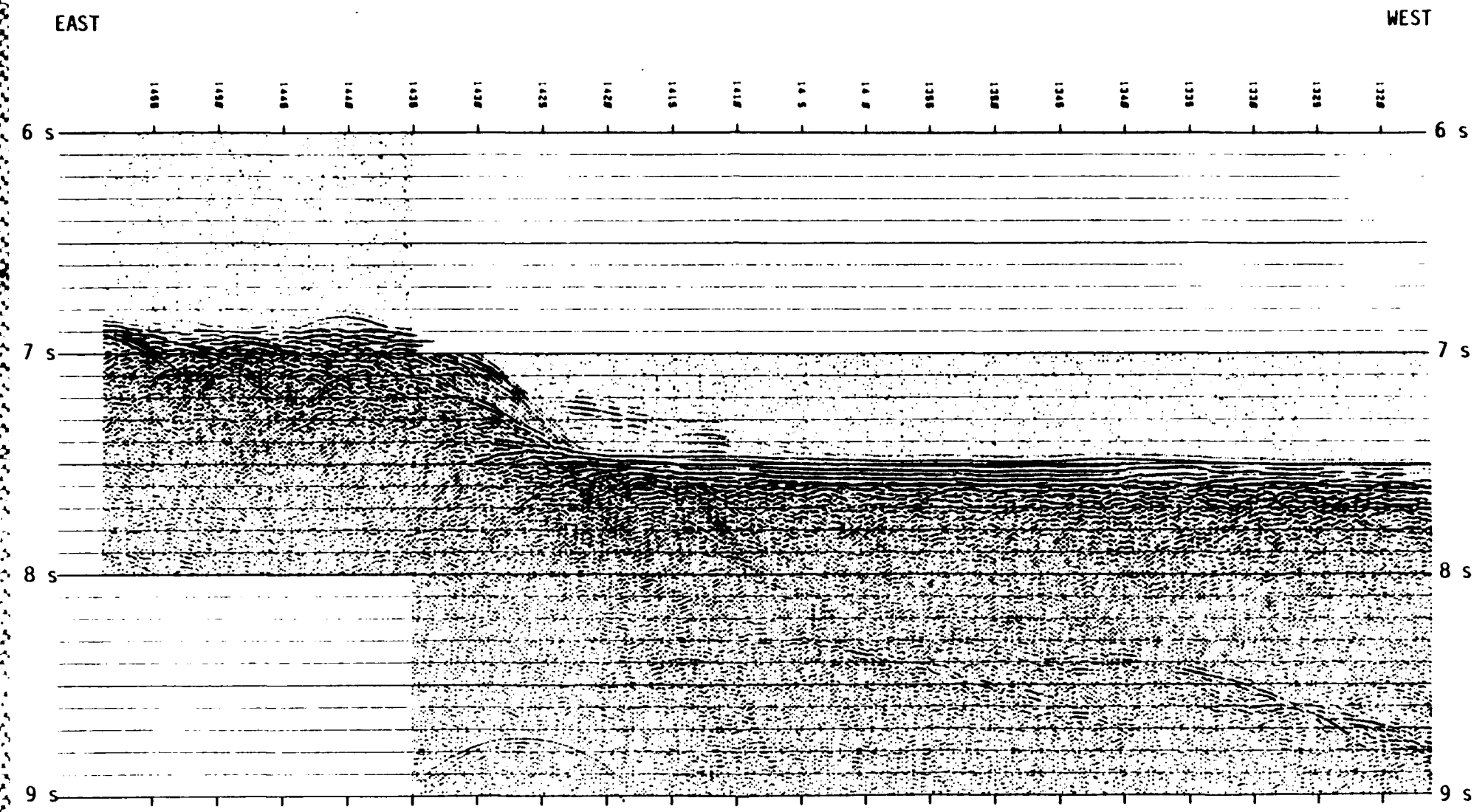


Figure 21. Line 4 (continued). As the ship moved further east, the bathymetry became rougher so the ship was turned back to the northwest. The out-of-plane reflection seen in Figure 20 continues at about 8.5 seconds from 1320Z to 1400Z.

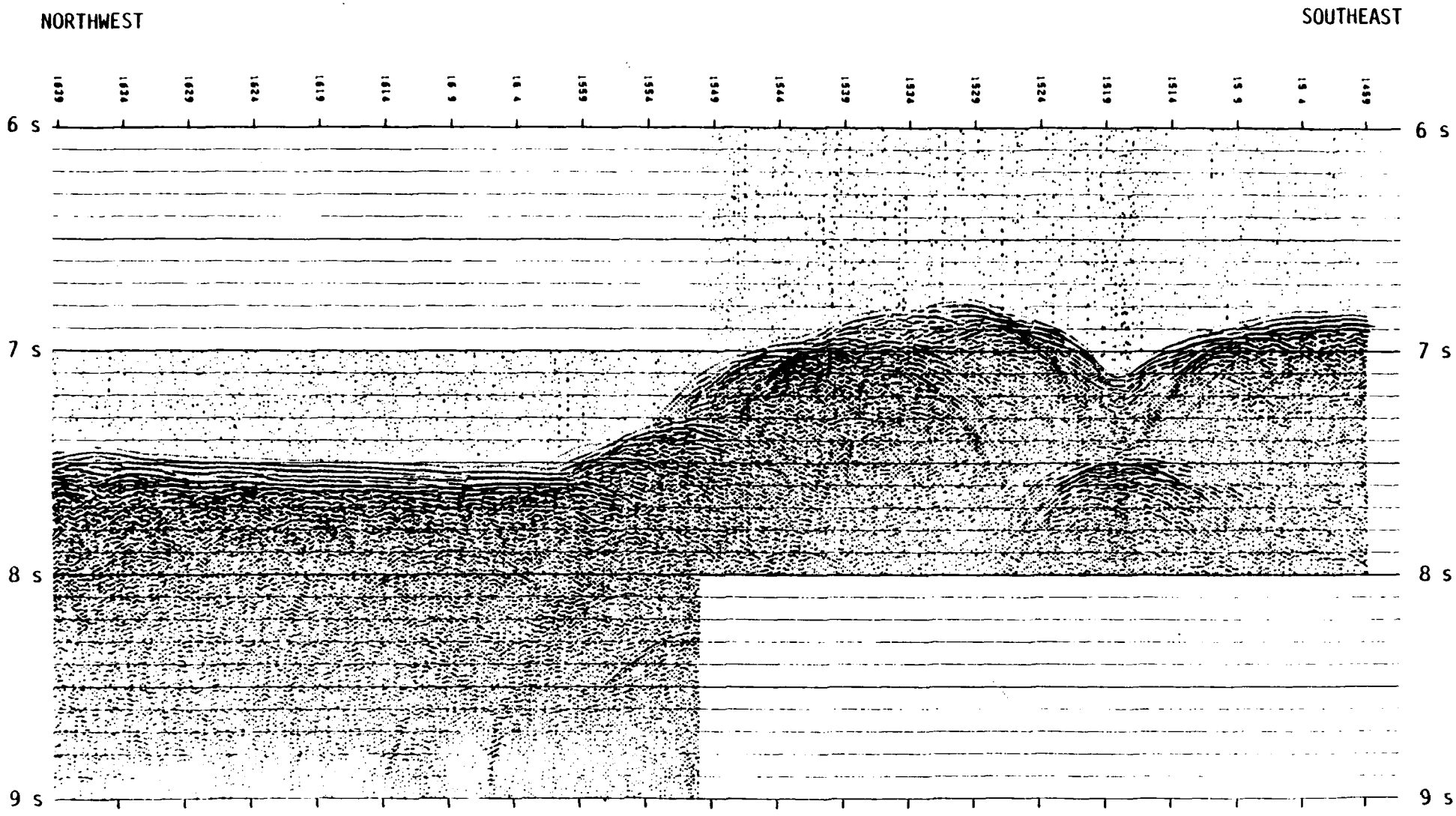


Figure 22. The start of Line 5 of the reflection site survey. Here the ship comes off of the bathymetric high and back into the flatter topography.

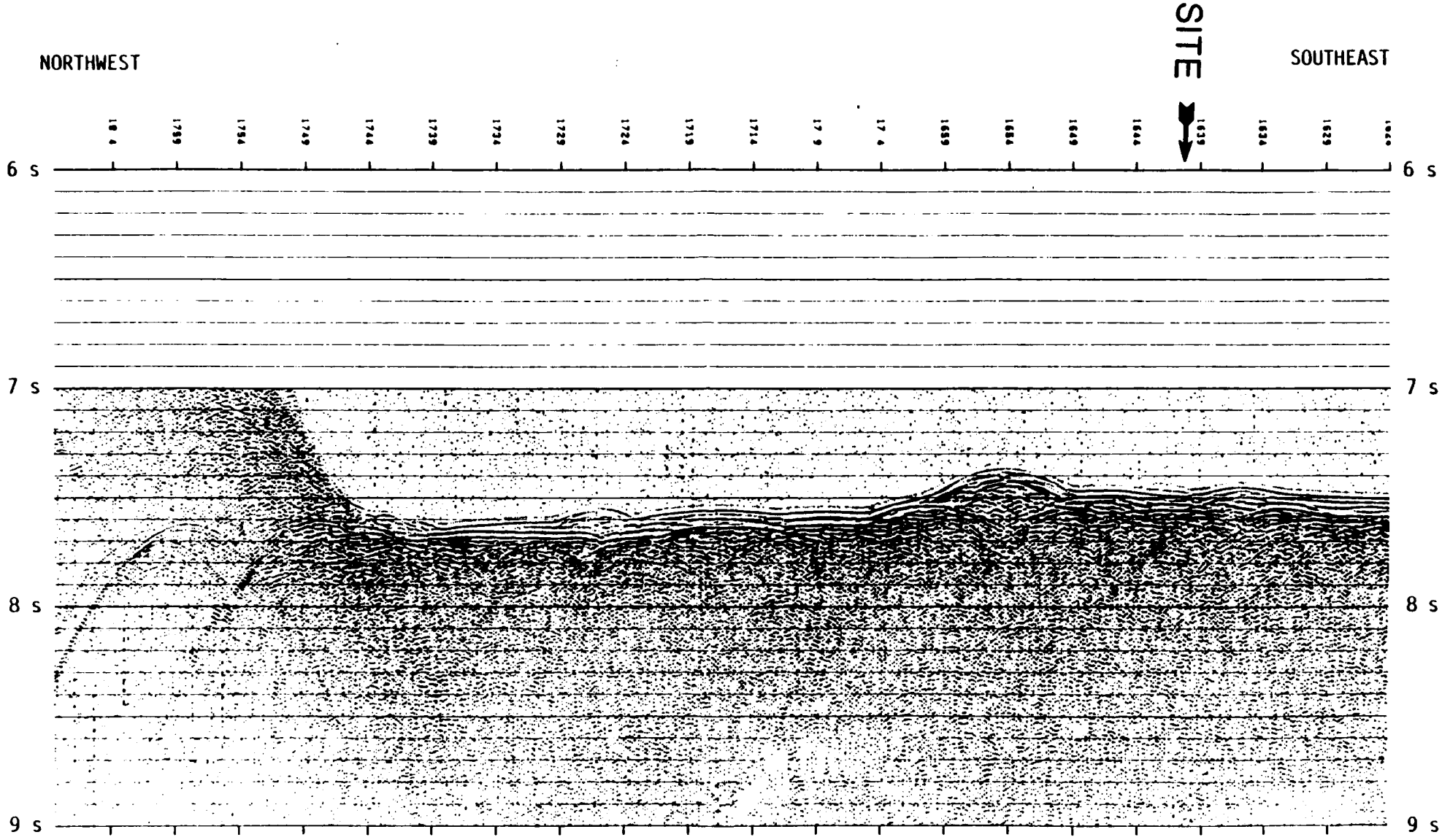


Figure 23. Line 5 (continued) as the ship passes through the site in a northwest direction. Again the mound seen in Line 3 (Figure 18) is evident. Higher bathymetry is seen northwest of the site.

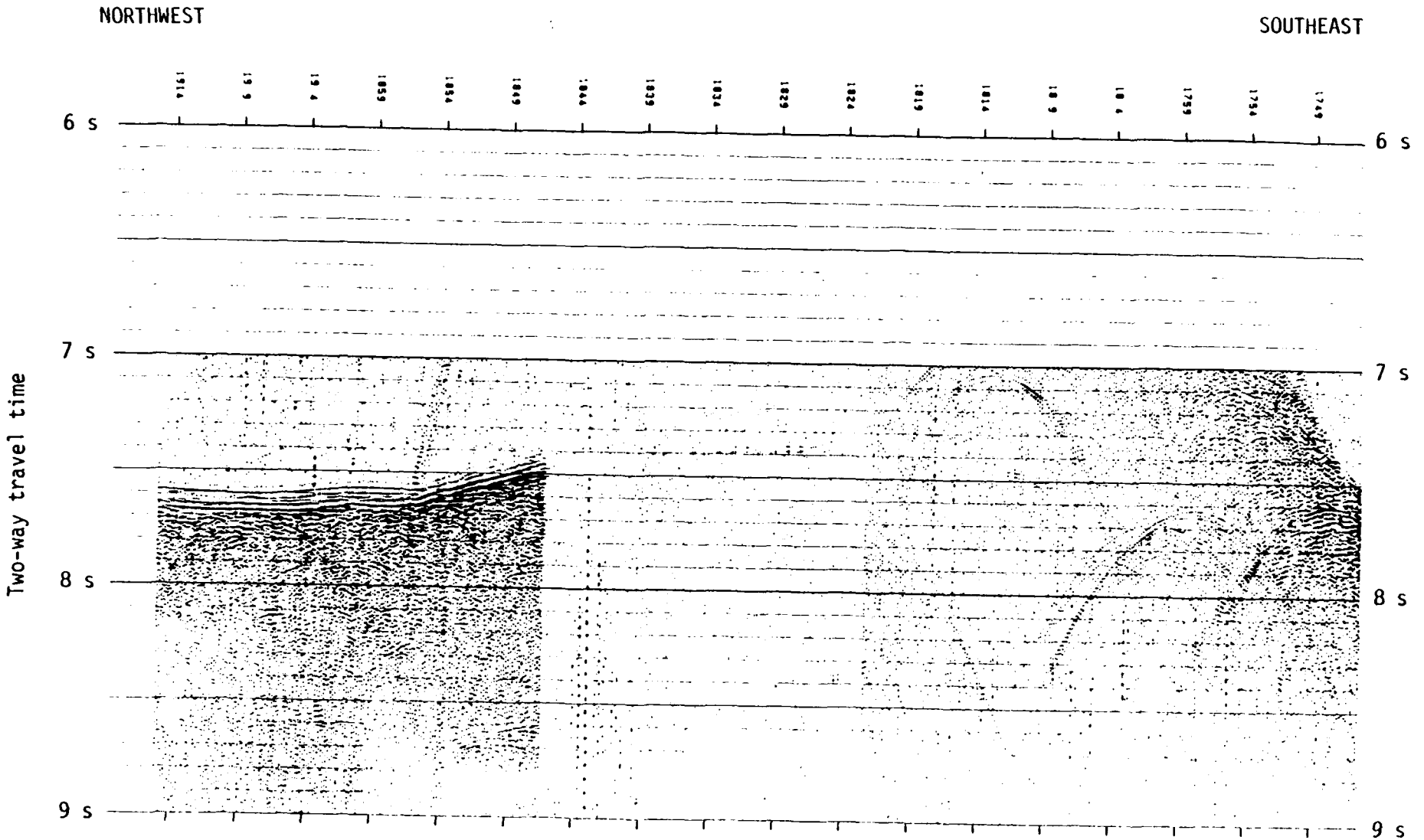


Figure 24. End of Line 5 as the ship passes back down into a flatter area. Data loss from 1749Z to 1823Z due to incorrect delay setting and data loss from 1823Z to 1848Z due to recording failure. At the end of Line 5, the ship turned back to survey north of the site.

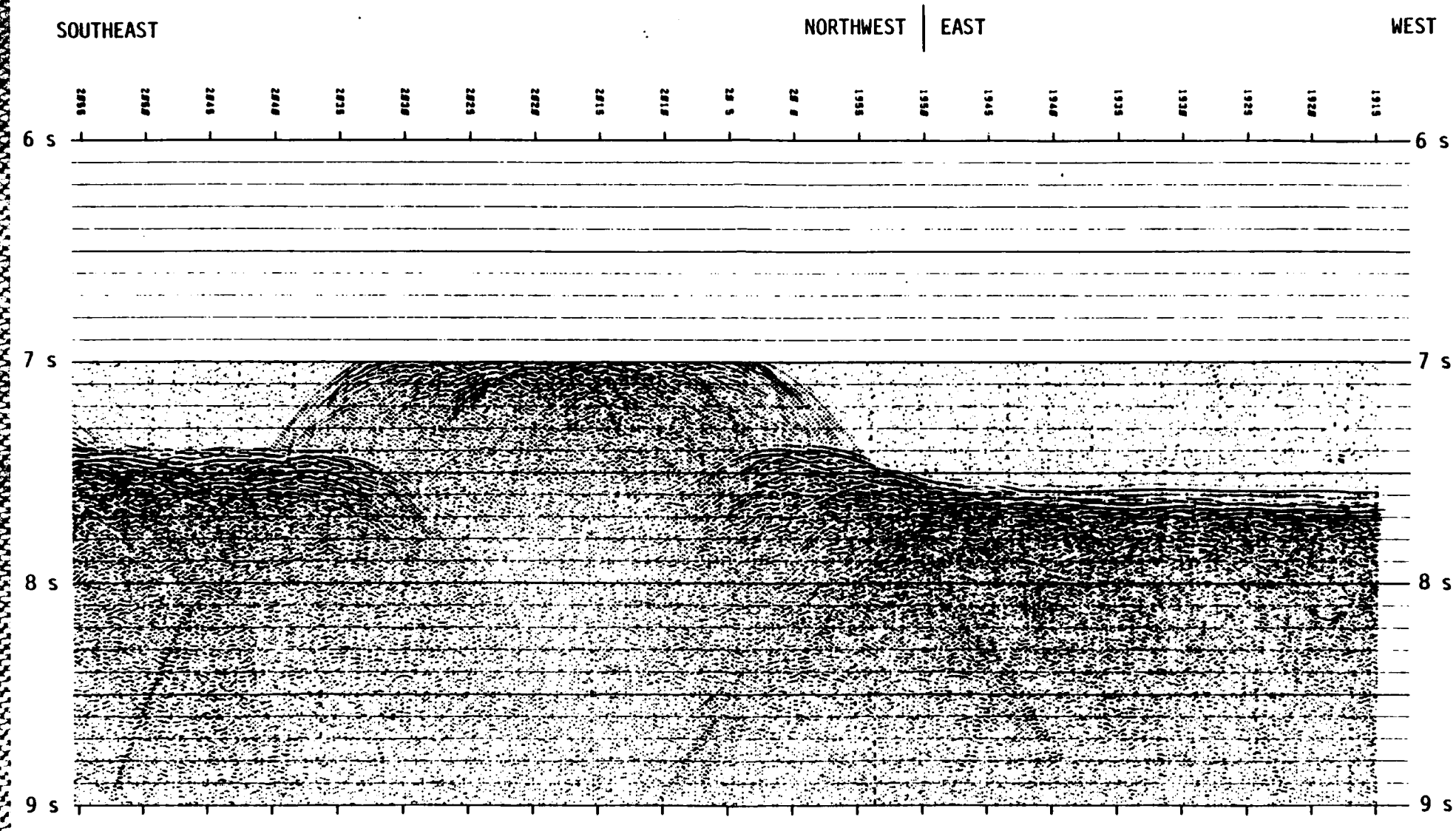


Figure 25. The start of site survey Line 6. The Melville first started east and then turned to the southeast.

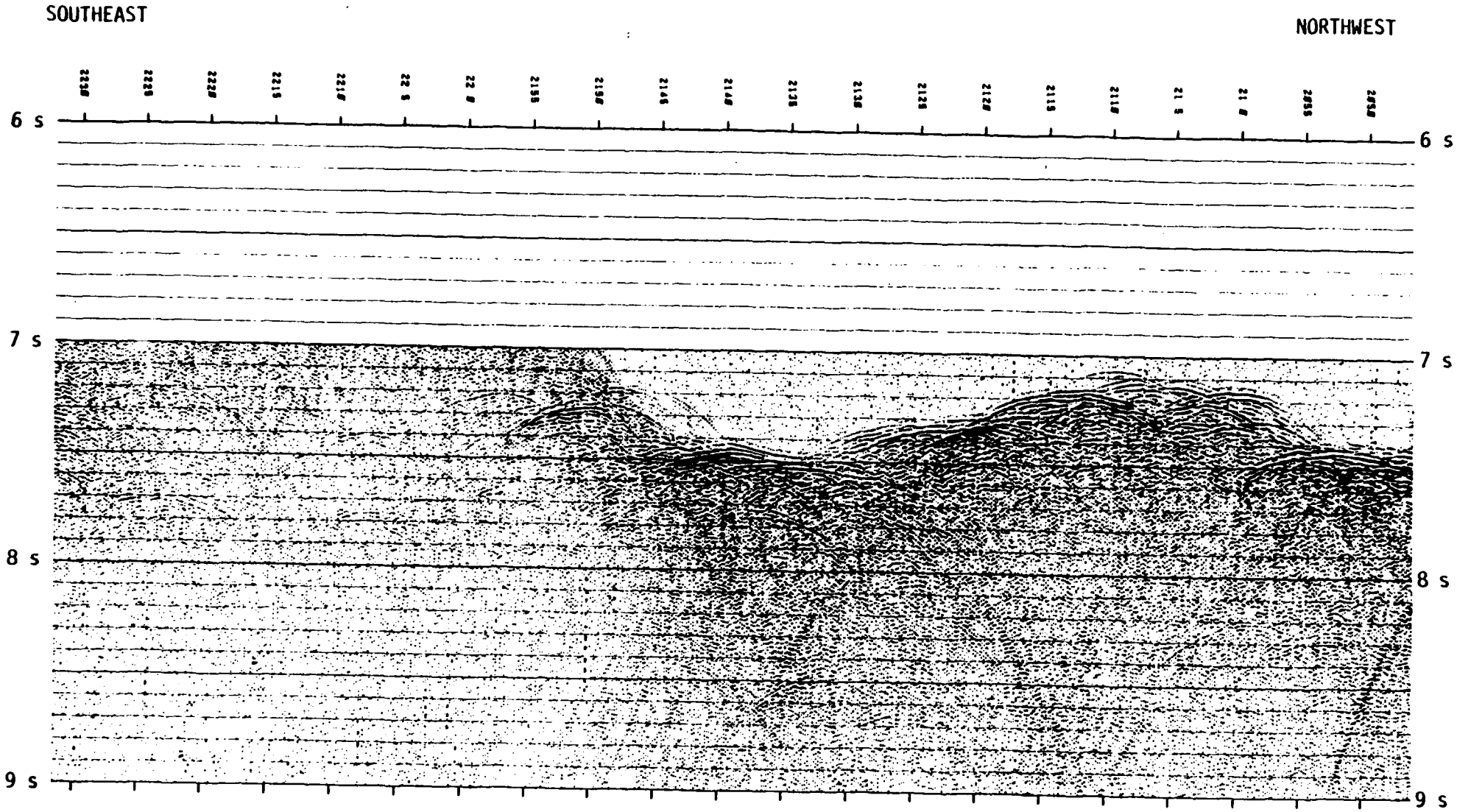


Figure 26. Line 6 (continued). Much rougher topography was encountered in this portion of the survey.

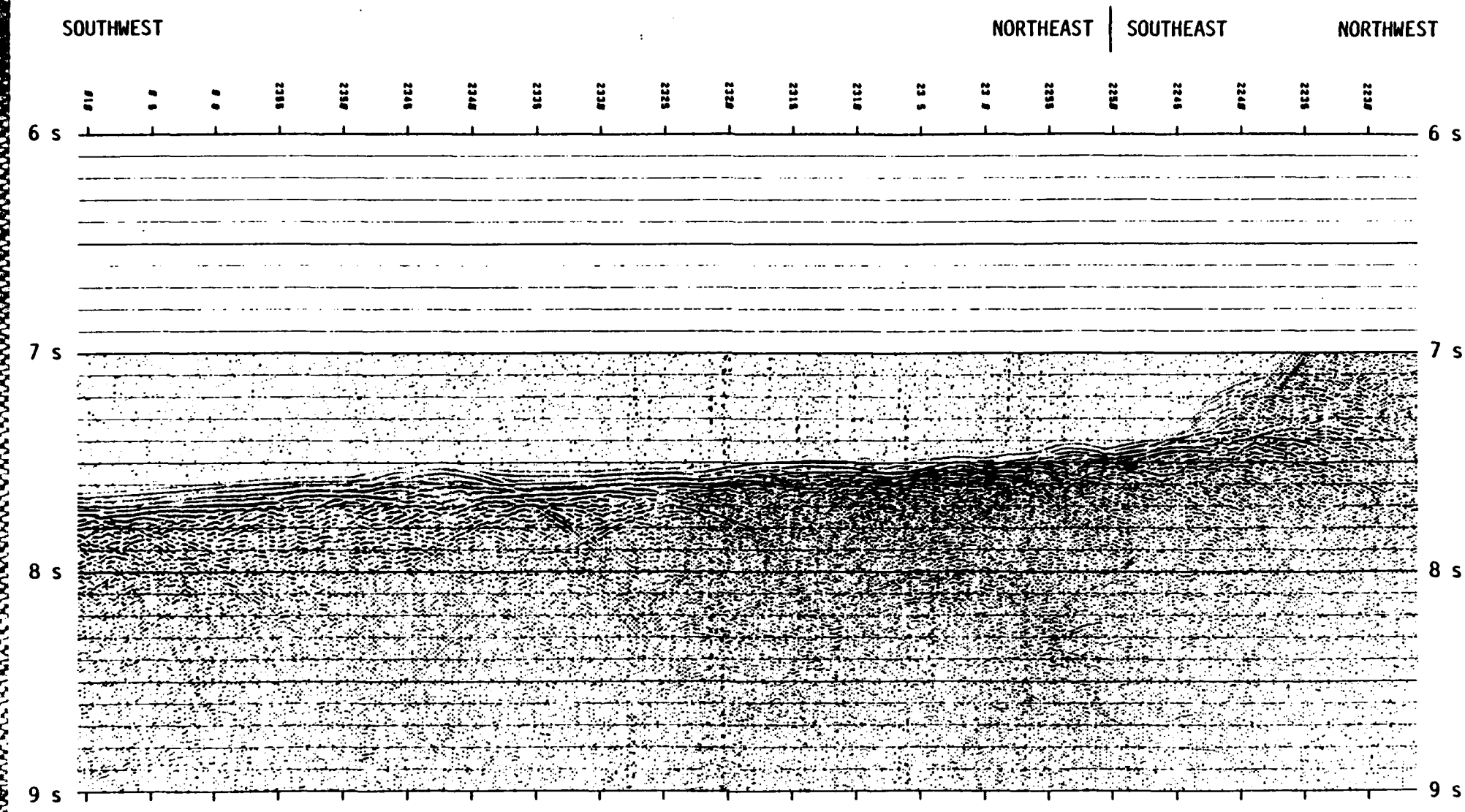


Figure 27. Line 6 (continued). This ship turned back towards the site since no area of greater sediment thickness was found north and east of the site. The sediments appear to thicken slightly as the ship moved southeast.

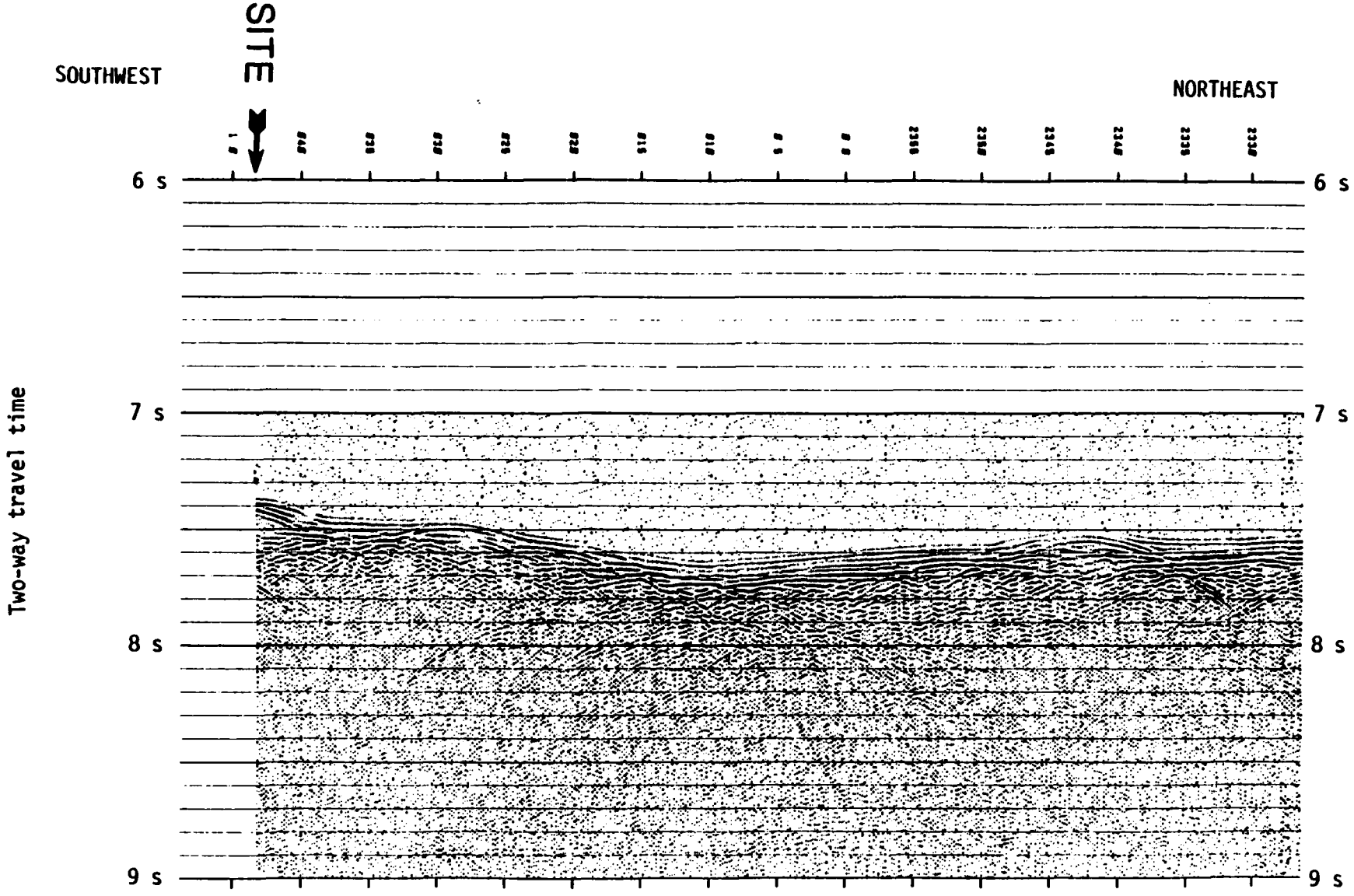


Figure 28. The end of Line 6 as the Melville approached the site from the northeast. Since no area was found with any greater sediment thickness, the second site on Line 1 was chosen for the drill site.

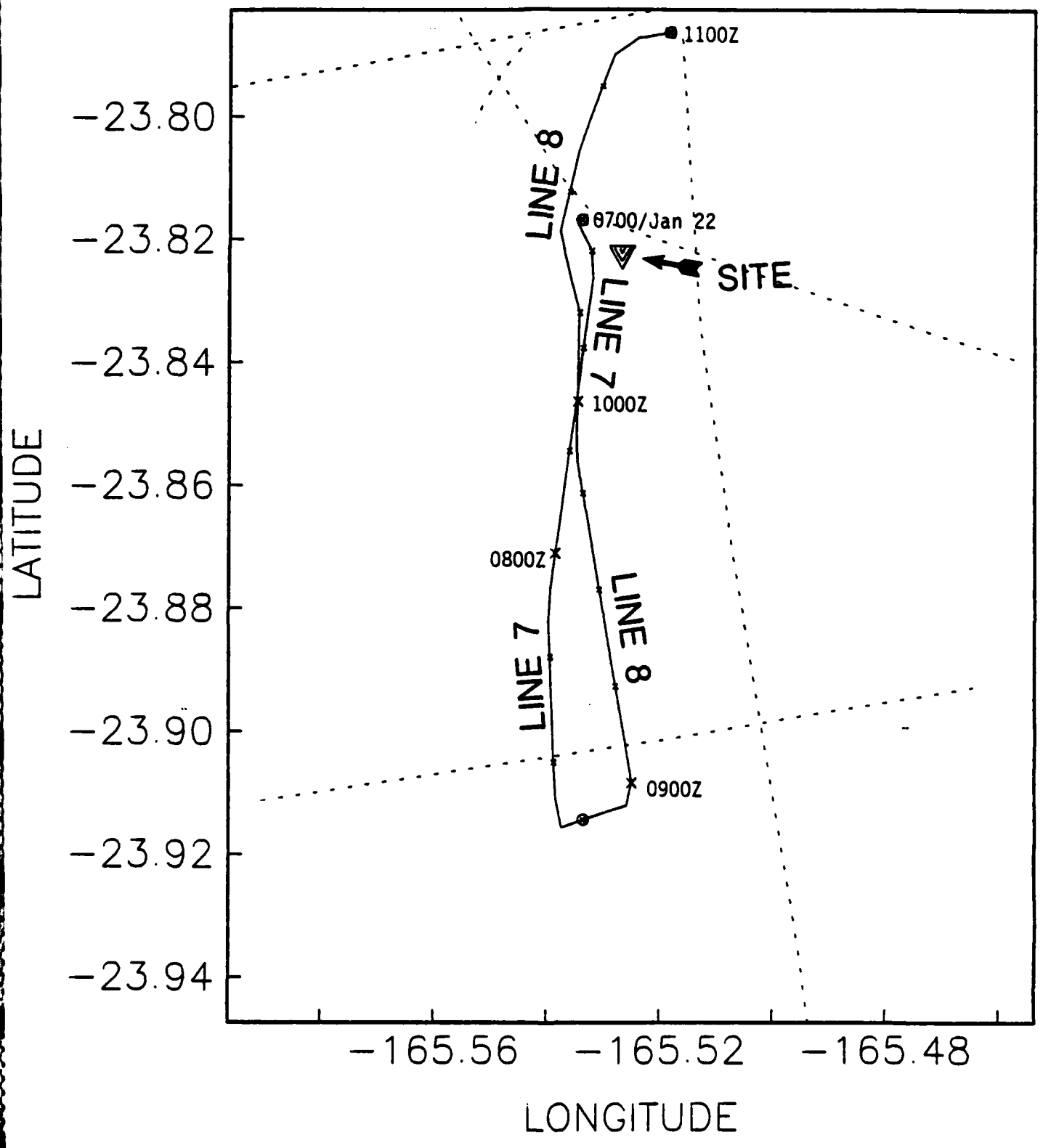


Figure 29. Location of site survey lines 7 and 8 immediately below the site (located by the filled triangle). Dashed lines show part of the rest of the seismic reflection site survey.

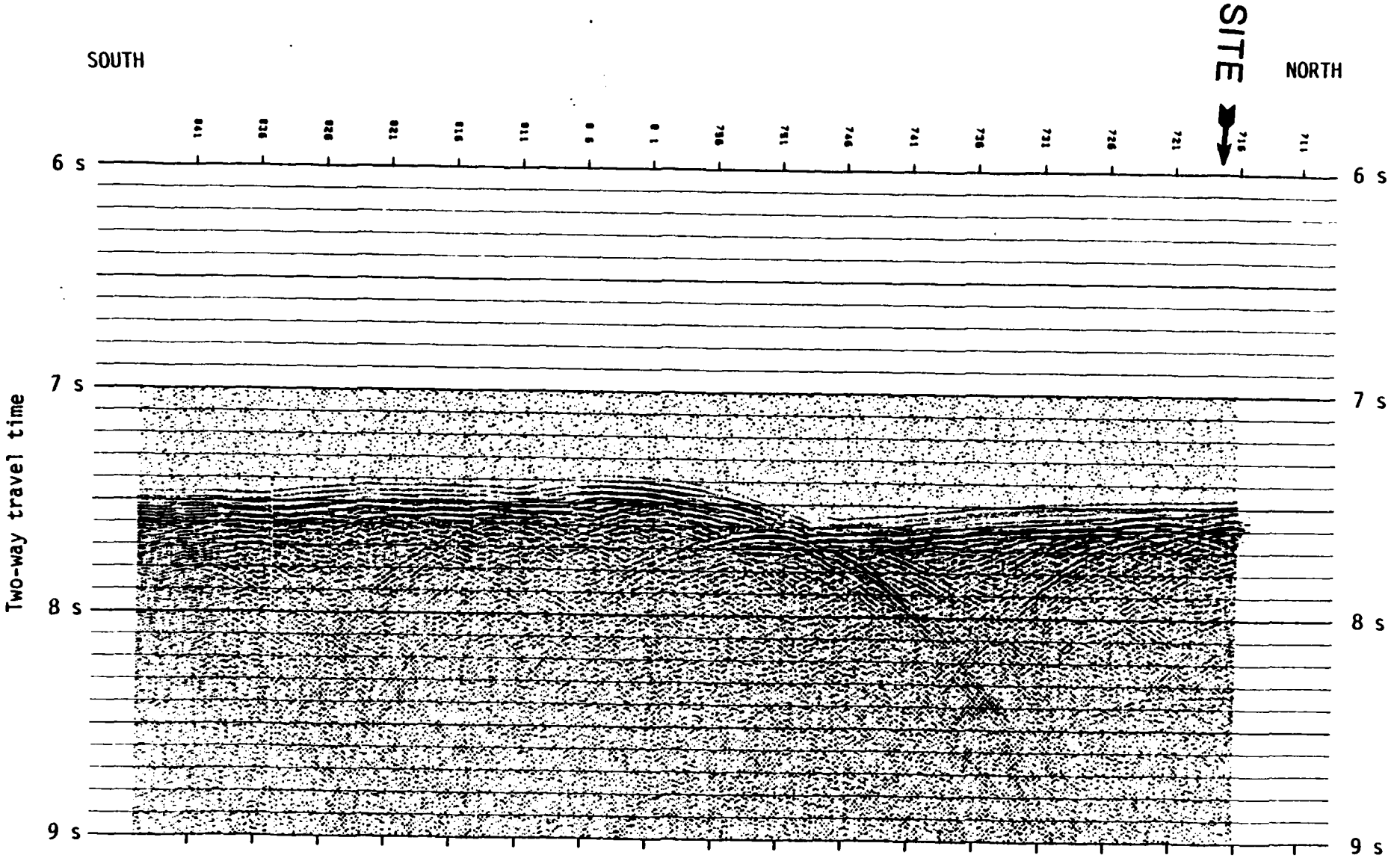


Figure 30. Line 7 of the watergun site survey. The ship travelled due south of the site but no apparent increase in thickness was seen.

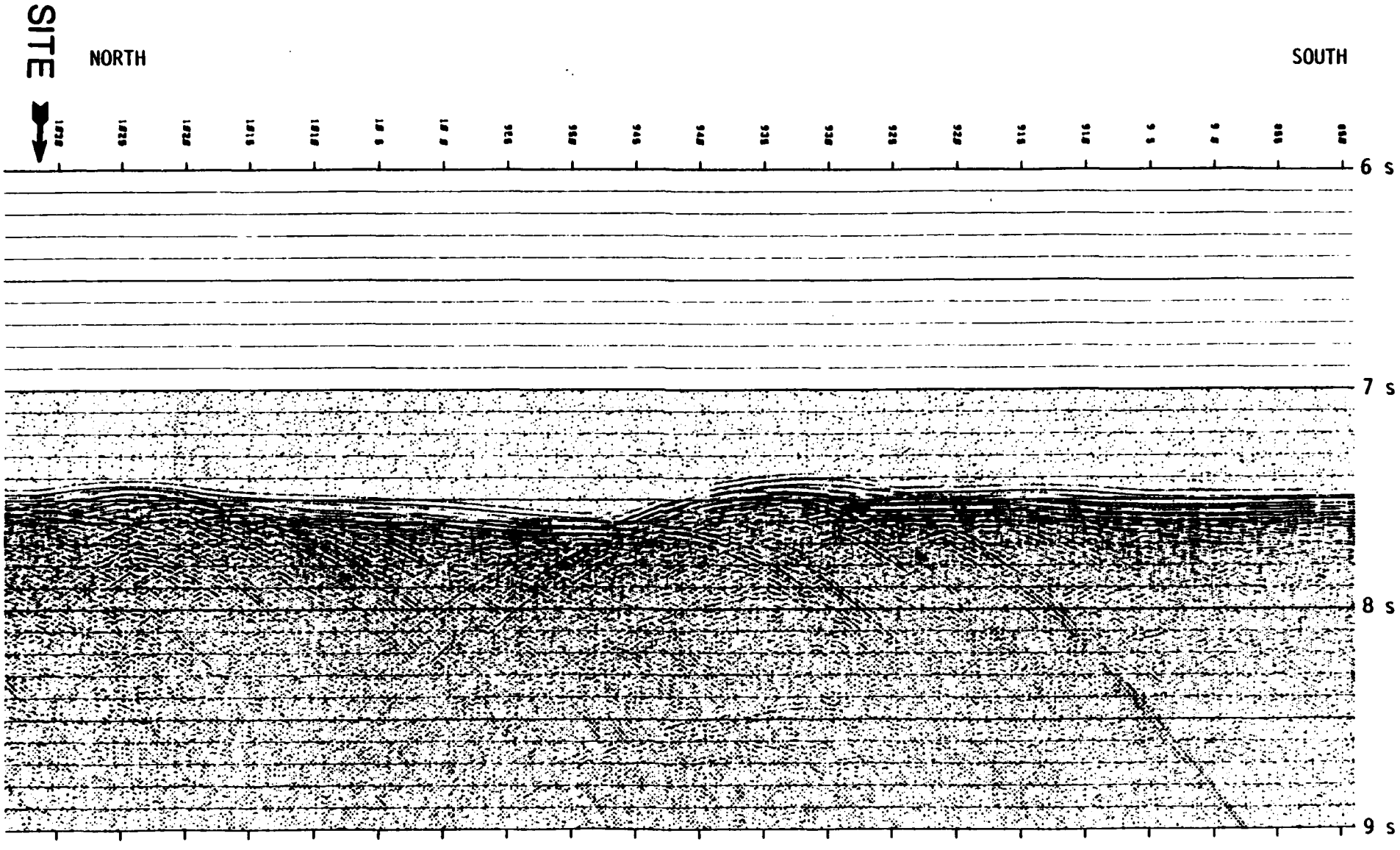


Figure 31. Line 8 of Leg 91's site survey. This line parallels Line 7 as the Melville ruturned to the site to terminate the site survey.

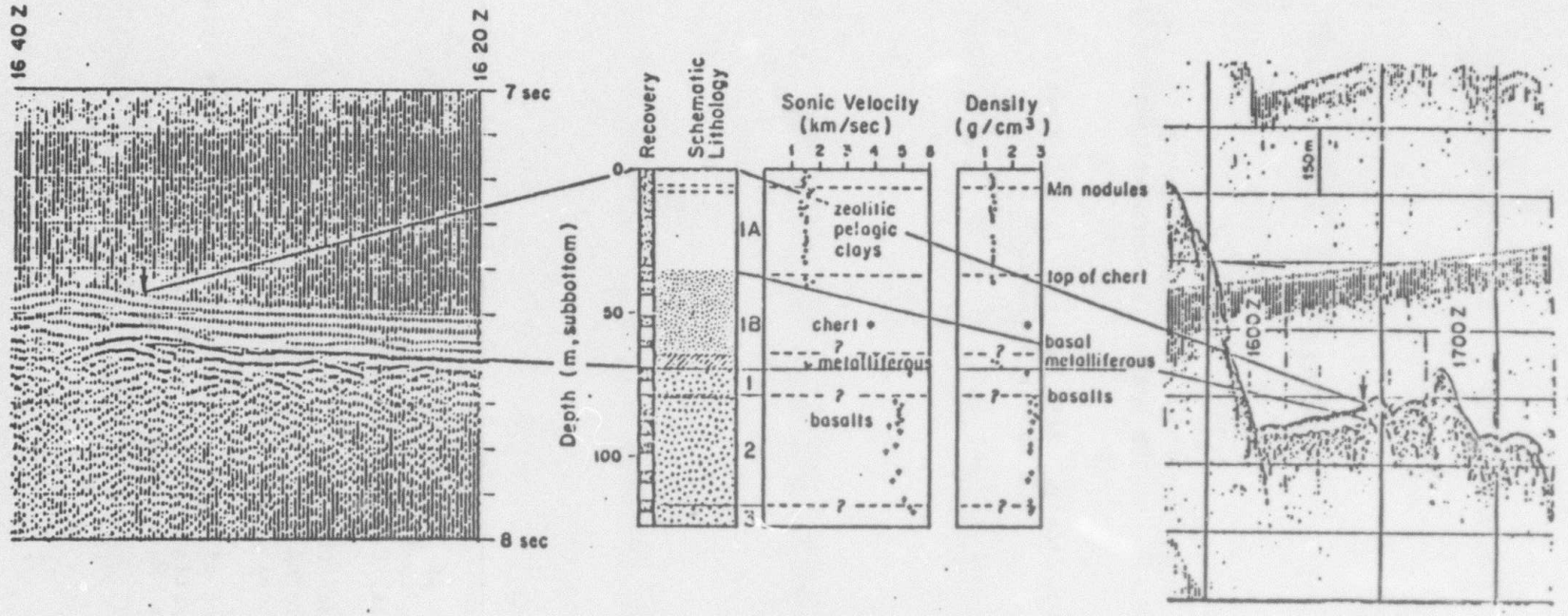


Figure 32. Correlation of physical properties and sediment lithology with watergun reflection data and 3.5 kHz sounding data. Reflections off the chert layer and the top of the oceanic crust are seen in the reflection data, but only the chert reflection is seen in the 3.5 kHz data. The chert reflection was interpreted by the Challenger as the basement reflection, therefore explaining the Challenger's much shallower sediment thickness prediction at the site.

CHAPTER 2

DESCRIPTION AND PERFORMANCE OF THE MARINE SEISMIC SYSTEM DURING THE NGENDEI EXPERIMENT

Richard G. Adair,[1] Mike Harris,[2] John A. Orcutt,[1]
and Thomas H. Jordan[3]

---

1 Institute of Geophysics and Planetary Physics,
Scripps Institution of Oceanography
La Jolla, California 92093

2 NORDA Code 500
NSTL Building 1100
Bay St. Louis, Mississippi 39529

3 Department of Earth, Atmospheric, and Planetary Sciences
Massachusetts Institute of Technology
Cambridge, Massachusetts 02139

INTRODUCTION

The Marine Seismic System (MSS) was designed to record broadband, triaxial, seismic data automatically for extended periods while deployed in a Deep Sea Drilling Project (DSDP) borehole. This paper describes the MSS and its deployment and retrieval equipment, as well as the modifications made to the original system during Leg 91 to accommodate equipment failures and operational realities. Calibrations and other data related to actual system performance are presented.

As a part of the ongoing program to discriminate nuclear explosions from natural seismic events through seismic means, the Defense Advanced Research Projects Agency (Darpa) had tested the use of ocean bottom seismographs (OBS's) for monitoring during the late 1960's and early 1970's. It was hoped that deep-ocean monitoring would yield increased geographic coverage of seismic signals from both earthquakes and explosions, perhaps at lower ambient seismic noise levels than obtained by typical continental stations. Unfortunately, noise levels at the seafloor were found to be substantially higher than at moderately quiet land sites and, as such, ocean bottom seismographs were limited in their capabilities for seismic discrimination. The noise levels on continents were found to be dominated by surficial sources and to be generally reduced by burial of the sensors in a deep borehole. Similar noise reductions might be achieved by borehole seismometer emplaced below the unconsolidated sediments at the seafloor. Darpa, in order to test this concept, began an ambitious program to deploy an instrument package in a reentrable hole drilled into basement rock in the deep ocean.

The primary design criterion for the instrumentation package was ease of deployment. This meant interfacing the system with current DSDP hole reentry techniques involving the use of a reentry cone and sonar device. The package also had to fit in the 12.25 inch open hole that could be drilled in competent basement rock. To facilitate coupling between the seismic sensor and the ground, a holelock mechanism was desirable. A minor consideration was the accommodation of vessel motion when the shipboard recording system was in use.

A triaxial, broadband, short period sensor was needed to maximize the likelihood of detection of seismic signals. A large dynamic range with adequate resolution was required to record the anticipated signal amplitudes ranging from ambient seismic noise (a few nanometers of ground motion) to regional earthquakes (millimeters of ground motion). Because the goal of the MSS was to record low-amplitude signal with good fidelity, instrument noise had to be small.

The recording package was to be self-contained when installed at the ocean bottom and was to continuously record data for as long as possible. A deep-water, all weather mooring system was to be developed to facilitate MSS deployment and recovery under adverse conditions.

The above criteria were achieved through a composite effort coordinated by the Naval Ocean Research Development Activity (NORDA). Teledyne Geotech, Inc., developed the borehole instrumentation, and Gould, Inc., the ocean bottom recording system. Global Marine designed and established operating procedures for the reentry tools, and the Naval Civil Engineering Laboratory (NCEL), in cooperation with NORDA, developed the mooring system.

SYSTEM DESCRIPTION

When installed (see Figure 1), the MSS comprises a borehole instrumentation package (BIP), which contains the seismic sensors and is connected by coaxial cable to an ocean bottom recording system, the Bottom Processing Package (BPP). After BIP emplacement, data can be recorded on two shipboard consoles distinguished by different digitization schemes and post-digitization processing. One of these, the Test Equipment Rack (TER), referred to here as the 'Gould system,' emulates most of the BPP functions. The other, the Shipboard Test Console (STC), referred to as the 'Teledyne system', monitors the BIP and provides redundant data logging. The BIP has separate electronics bays for communication with both consoles, each of which can initiate BIP calibrations, play back seismic data on strip charts, and supply BIP power. Following a satisfactory checkout of the BIP and period of shipboard data recording, the BIP is connected to the BPP, which is then lowered to the seafloor for a maximum of 45 days of operation. A submerged mooring, the Installation, Recovery, and Reinstallation (IRR) system, facilitates BPP deployment and recovery.

The 997.3 cm-long, 20.3 cm outside-diameter BIP mechanical structure (Figure 2) comprises a 609.6 cm-long pressure vessel housing the borehole instrumentation, a 343.9 cm-long cable terminator, and a 43.8 cm-long impact tip. The borehole instrumentation includes the seismic sensors, a triaxial accelerometer monitoring forces on the tool, a pressure transducer and temperature monitors. The terminator includes a cable-isolator designed to decouple cable and BIP motions by means of a telescoping length of clamped, coiled cable, and toothed pawls which lock into the borehole. The pressure vessel hangs pendulously from the isolator. Rigid rubber collars on the terminator retard its motion in the hole.

A triaxial set of Teledyne Model S-750 seismometers (orthogonal horizontals, X and Y, and one vertical, Z) and a redundant, backup vertical component (B) compose the MSS seismic sensors. The S-750 is a short-period piezoelectric seismometer frequently used for seismic exploration and local earthquake recording. (Throughout MSS operations, the horizontal sensors X and Y were referred to as 'east' and 'north', respectively; these designations are not used here because the seismometer orientations are not well known.) Backup sensor B was configured 175.5 cm below the primary vertical sensor Z. Output from each of the

primary sensors is split into mid-period (MP) and short-period (SP) passbands that span the frequency intervals 0.1-2.0 Hz and 0.5-20.0 Hz, respectively, while the redundant vertical is passed through the SP band only. The resulting seven data streams, labelled MZ, MX, MY, SZ, SX, SY, and SB, are then digitized and transmitted to logging devices over the coaxial cable as a frequency-shift-keyed (FSK) signal.

Teledyne System

Output destined for the shipboard Teledyne system is digitized as floating-point numbers at one of four gain ranges (x1, x8, x32, x128) and represented as a 16-bit word, including 2 bits which encode the gain range. This achieves a 21-bit dynamic range with 14-bit resolution. MP data are routinely digitized at 4 samples/second (s/s), and SP data at 40 s/s, although either of the SP vertical channels may be sampled 80 s/s by excluding the other. One of three framing formats is used to multiplex seismic data for transmission while nine other formats represent various diagnostic and calibration data. A data frame spans one second and comprises 20 subframes of 12 16-bit words, a total of 240 words. In the seismic formats, words 1 and 2 compose a synchronization pattern, words 3-6 and 9-12 are SP data, word 7 is MP data, and word 8 is a state-of-health datum.

The three MP channels are consecutively sampled once per subframe over five subframes in the order MY, MX, and MZ, and SP data twice per subframe in every subframe, except in the case of SP vertical-component 80 s/s mode, where one of SZ or SB is sampled four times per subframe. When recording SZ or SB at 80 s/s, SP channels are sampled in the order SZ or SB, SY, SX, SZ or SB; otherwise they are sampled in the order SZ, SY, SX, SB. The MP data times are consequently skewed by the duration of one subframe (1/20 second), and the SP by one subframe word (1/240 second); the skewed times are written with the data.

The shipboard Teledyne system records data, including timing information generated in the BIP, as a PCM (pulse-code modulated) digital stream on one of seven tape tracks of an Ampex model PR-2230 bit stream recorder. This stream may also be applied to a Conic D-PAD-III decommutator for diagnostic display and then to a digital-to-analog converter for output to a strip chart. IRIG (inter-range instrumental group) B time-code synchronized with Universal Standard Time may be written simultaneously with strip chart data.

Gould System and BPP

Data to be transmitted to the BPP and its shipboard counterpart (the Gould system) are represented with an enhanced delta modulator encoding (EDME) technique. In essence, this digitizing method (see, e.g., Claasen et al., 1980) oversamples (by 256 times) the integrated signal, which, after transmission, is recovered from first differences

of the digital data. The resulting sampling noise spectrum is essentially proportional to the ratio of frequency and the oversampling factor. Hence, an appropriate choice of the oversampling factor ensures that sampling noise is sufficiently small over the desired passband, and that the dynamic range is increased over that of straightforward digital representation of amplitudes.

The encoded, oversampled streams are then sent to the recording unit where they are digitally convolved with a finite-impulse response (FIR) low-pass filter, resampled at their proper rates (4 and 40 s/s for the MP and SP data, respectively), and decoded as a 24-bit integer, yielding 144 dB of dynamic range with a 24-bit resolution. The rich oversampling obviates timing skew (1/256 of a sample interval), which is therefore neglected in data buffering. The FIR filter weights are derived from an IEEE signal analysis program (McClellen et al., 1973), and modified to yield a low-ripple, nearly flat (amplitude variation of $\pm$ 0.01 dB), zero phase-shift response to 75% of the ultimate Nyquist frequency, and thereafter a 160 dB fall-off at 125% of the Nyquist frequency, a decline of approximately 720 dB/decade. Each of the resultant filter weights, generated assuming eightfold oversampling is padded with 31 zero weights to achieve the 256-fold oversampling. Sixfold convolution with a 32-point boxcar suppresses unwanted peaks in the filter's amplitude spectrum introduced by the zero-padding. This convolution is equivalent to multiplying the filter's amplitude spectrum by $\mathrm{sinc}^6(f/320)$, where $\mathrm{sinc}(x) \equiv \sin(\pi x) / (\pi x)$. Prior to this, however, the weights are smoothed with a three-point running mean (weights of -0.25392, +1.50784, and -0.25392) to compensate a droop within the desired passband introduced by the subsequent boxcar convolutions.

The BPP (Figure 4) is the primary MSS recording system. It acquires digital data from the BIP, low-passes, resamples at a lower rate and decodes the seismic data, formats buffers comprised of seismic data, timing and system status, and writes the buffers to 67.1 megabyte-capacity tape cartridges (3M model DC600HC) on one of twenty tape drives (3M model HCD-75). Each cartridge is initialized with sensor and digitizer calibrations. Status information includes leak detection, various BIP and BPP state-of-health monitors. Timing is set just prior to deployment. Over a 45-day maximum operation period, the BPP can record three channels each of MP and SP data, and one of hydrophone (sampled at the SP rate) with scheduled shut-offs of the SP horizontals after 22 days, and of the hydrophone after 37 days. Output from the hydrophone replaces one of the SP vertical channels (SZ or SB), both of which may be recorded by the BPP's shipboard console. The BPP powers down after the last tape is filled. Power from two zinc-silver battery packs and commands are transmitted to the BIP on the coaxial cable.

The data-processing electronics and the two battery packs are each housed in spheres made of 5.08 cm-thick, 85.1 cm inner-diameter yoked aluminum hemispheres salvaged from OBS's employed by Texas Instruments

in the 1960's for an earlier generation of discrimination research. The three spheres and various hydro-acoustic instruments are mounted on an aluminum structure comprised of a 254.0 cm x 223.5 cm platform and its 248.9 cm-high framework. A sediment-penetrating flange rims the platform to secure the BPP on the seafloor; subsequent corrosion of the magnesium-alloy bolts binding the flange allows detatchment of the BPP superstructure for recovery. The coaxial cable is terminated in a spring-loaded strain-relief arm on the platform's underside, and thence to the instrument sphere.

Seismic Instrument Response

Figure 3 illustrates the net displacement responses of the MP and SP passbands; the dashed lines at the high ends depict the FIR filter modification. The MP response is peaked at approximately 1.2 Hz and falls off at 40 and 150 dB/decade towards lower and higher frequencies, respectively, while the SP response is peaked at approximately 15 Hz and declines gently towards lower and higher frequencies at 40 and 45 dB/decade, respectively. At the Nyquist frequencies, in the absence of the FIR filters, the MP response is down 28 dB from its peak, while the SP response is down only 1.5 dB from its peak; in the case of the 80 s/s SP vertical data recorded on the Teledyne system, the response is down 11.5 dB.

Deployment and Recovery Tools

Special tools and equipment facilitate deployment and retrieval of the MSS. A reentry sub (i.e. substitute drill string section) employed at the drill string's bottom end installs the BIP, the outer diameter of which prohibits its deployment within the drill string.

The 15.7 km-long IRR mooring facilitates BPP emplacement and retrieval. The various MSS-related cables and lines are passed from a winch through a sheave block mounted on a heave-compensated A-frame equipped with tension monitors. A network of acoustic transponders, the Acoustic Transponder Navigation (ATNAV) system, facilitates MSS location and recovery.

The reentry sub (Figure 5) comprises the BIP carriage, carriage housing, stinger, control sub, packer/sonar tool adaptor, and release hydraulics. The carriage, bearing the BIP with the coaxial cable attached, rides to the seafloor in the off-axis carriage housing, and is shifted on-axis with the release hydraulics after the sub's stinger tip is seated in the reentry cone throat. During the trip down, the cable is arced downstream of the drill string to avoid entanglements. When the reentry sub nears the ocean bottom, a sonar tool is lowered through the drill string and reentry sub to guide the stab into the cone, where the stinger assembly directs and seats the sub in the cone throat. The sonar tool is then retrieved and a packer lowered to the control sub at

the top of the reentry sub to activate the release hydraulics. The packer/sonar tool adaptor is subsequently raised from the stinger tip to the control sub where it seals the hydraulics. The hydraulics shear aluminum release pins and shift the BIP carriage over the borehole. Coaxial cable pay out then lowers the BIP to the hole bottom. After the reentry sub is raised clear of the cone, the hydraulics actuate release of the cable from a protective sheath in the stinger. The cable is then freed through a slit running the entire length of the reentry sub. The cable is of sufficient mechanical strength to be winched-in for BIP recovery and is therefore referred to as electro-mechanical (EM) cable.

When deployed with the BPP at one end and a clump anchor at the other, the submerged IRR mooring has a roughly trapeziform configuration (see Figure 1) with its crown (a grapnel leg) buoyed by floats at either vertex, the shallowest of which is nearer to the BPP than the anchor. The mooring comprises, in order, an isolation link of 2.9 cm (1 1/4 in) wire cable, a riser leg of 4.4 cm (1 3/4 in) power braid, and grapnel and anchor legs of 2.2 cm (7/8 in) power braid. The approximate lengths of these segments are, respectively, 0.5 km, 6.6 km, 3.1 km, and 5.5 km, a total of 15.7 km. A pair of release mechanisms equipped with ATNAV transponders link the grapnel and anchor legs, while all other mooring segments are spliced. The transponders and flashing beacons at each of the crown vertices aid in finding the mooring location once the grapnel leg surfaces.

SYSTEM PERFORMANCE DURING LEG 91 OPERATIONS

Figure 6 summarizes the event chronology pertinent to MSS system performance. Operations progressed with BIP deployment and on-deck recording, BPP deployment, and BPP recovery. These periods are respectively referred to elsewhere in this volume as MS1, MS2, and MS3. The initial BIP deployment, using BIP-1, was aborted at 1428Z, 1 Feb, 1983, when, after tripping only 213 meters of drill string, an instrumentation malfunction was detected (Figure 6, point 1a). The malfunction was attributed to damage to the coiled EM cable in the terminator's cable isolator, which isolated the cable and instrument from vessel motion. This mechanism, as well as an associated holelock arrangement and motion-retarding rubber disk collars were disabled in the subsequently deployed BIP-2, both to prevent cable damage and to improve the BIP fit within the reentry sub's BIP carriage. BIP-2's triaxial accelerometer, which monitors the forces it encounters, probably malfunctioned as no observations exceeded 1 g (= 9.8 m/s/s), an unlikely situation in light of the 2-4 g's experienced by a prototype BIP installed during DSDP Leg 78B (Ballard et al., 1984). Acceleration data would have been useful in ascertaining why the bolts binding the stinger, which was missing when the reentry sub was recovered, sheared.

BIP installation at the hole bottom, a depth of 124 m below the seafloor, and 54 m into the basement rock, was successfully completed by

1115Z, 6 Feb. and the five-day period of on-deck recording of seismic data began five minutes earlier (Figure 6, point 2). Data were continuously recorded except for breaks due to system maintenance or malfunction. Channel SZ of the Gould system was not used because an unknown shipboard source of electrical noise dominated its output. Sensor calibrations indicated Y-sensor malfunction. During this on-deck period, the Teledyne system collected approximately 114 hours of seismic data (1000Z, 6 Feb-0957Z 11 Feb), and the Gould system approximately 71 hours (1200Z, 6 Feb-2357Z, 10 Feb) (Figure 6, points 2a and 2b). These data include observations of ambient noise, earthquakes, and signals from refraction shots, many of which were simultaneously recorded on a proximate array of six OBS's.

BPP deployment operations (Figure 6, point 3a) began at 0235Z, 11 Feb with transfer of the BPP to the staging area and ended at 2311Z, 12 Feb, with the confirmed emplacement of the IRR mooring. The BPP touched down on the seafloor at 0920Z, 12 Feb. (Figure 6, point 3b). Data recording started at 2142Z, 11 Feb, (Figure 6, point 3d) before the BPP was in the water (Figure 6, point 3b), and ended approximately two days later at 1805Z, 13 Feb, after approximately 43 hours of data collection, when a water leak in one of the power spheres caused a total BPP shutdown. Neither calibrations nor channel MZ are available in the recovered BPP data because of a failure of the electronics in the BIP bay containing both the calibration initiator and Gould's channel MZ digitizing unit. Figure 7 shows the final configuration of the MSS and the various navigational transponders.

BPP recovery operations (Figure 6, point 4a) proceeded smoothly following the successful recovery of the six OBS's, and the BPP was brought aboard Melville at 1934Z, 24 March, at which time the BPP failure was discovered. On-deck data recording (Figure 6, point 4b) began shortly after this, yielding approximately 5.5 and 12.75 hours of data from the Teledyne and Gould shipboard systems, a total of approximately 120 and 127 hours, respectively, from the two types of systems (including BPP data). BPP recovery ended at 1820Z, 26 March, after the replacement of the BPP with a dummy load, and the redeployment of the IRR (Figure 6, point 4c) to facilitate future use of the BIP, which remains in Hole 595B.

Recovered data from the two systems are available from the Darpa-funded Center for Seismic Studies (CSS; see Berger et al., 1984 for a brief description) on nine-track tapes in a format which multiplexes simultaneous blocks of both MP and SP data; these tapes arbitrarily identify the X and Y BIP sensors as East (E) and North (N), respectively. Brief gaps of approximately 15 seconds due to the establishment of playback synchronization pepper the retrieved, formatted Teledyne data. The Teledyne data have been corrected for the clock drift shown in Figure 8; Gould shipboard data timing was slaved to Teledyne's. BPP data timing, maintained by internal clocks, was erroneously set six

hours earlier than CUT time at deployment, consequently six hours must be added to the time given in the CSS transcriptions of the BPP data. Figures 9 and 10 depict a typical sample of the Teledyne and Gould system recordings. (The data means have been removed prior to being plotted, a particularly essential step for the 24-bit Gould data, in which signal amplitudes are two-to-three orders of magnitude smaller than the digital DC offset.) The noisy, transient-ridden character of both passbands of the Y sensor as well as their insensitivity to signal apparent on all other channels is due to sensor malfunction. Sensor malfunction is also indicated by the mismatch observed in the Teledyne sensor calibrations of channels SY and MY (Figure 11 during both the installation and recovery shipboard recording periods. All other MP channels were well-calibrated between 0.2-1.0 Hz, and the other SP channels were well-calibrated between 0.2-15 Hz.

Analysis of the recovered data reveals a systematic timing skew and amplitude mismatch between the Teledyne and Gould data. The timing skew amounts to a nominal 16-sample delay of the Gould data with respect to the Teledyne data on both the SP and MP channels. Comparison of refraction signals recorded on the Teledyne system with analog tracings on which WWV timing is superposed indicate that the Gould data timing is in error.

The amplitude mismatch is evident from least-squares fits of Gould data, corrected for the aforementioned timing skew, against Teledyne data. The ratio of Teledyne and Gould amplitudes is approximatley 3 dB lower than that expected from dynamic range differences. Gould amplitudes should be eight times greater that Teledyne amplitudes, but are observed to be only approximately 5.5 times greater. Teledyne sensor calibrations are within 3 dB of the calculated norm, implying that Gould amplitudes are in error.

Short-period recordings of signals from near shots (within 10 km) on the Gould system (Figure 12, between 0.1 and 0.35 sec) have an 18 Hz (approximately) precursor to water waves which is absent in Teledyne data and precedes any possible physical arrival. Gould's FIR filter is most likely responsible for these acausal oscillations because it is a zero-phase shift, digitally-implemented filter. The precursor's frequency is near the filter's extremely sharp corner at 15 Hz.

Also evident in Figure 12 is Teledyne data aliasing between 0.5-0.6 seconds. Peaks of the oscillation just after the largest amplitudes of the water wave which are present in the Teledyne data (dashed), but not

the Gould data (solid), occur at the sampling rate.

SUMMARY AND CONCLUSIONS

The components of a marine borehole seismograph system, the MSS, and their performance during the Ngendei Experiment have been described. The MSS comprises a borehole instrumentation package (BIP) connected by coaxial cable to an ocean-bottom recording system, the BPP. Data were also recorded by two shipboard consoles, one of which (the Gould system) emulated most BPP capabilities, and the other of which (the Teledyne system) provided redundant data logging and BIP monitoring.

The BIP rested unclamped at the bottom of Hole 595B approximately 52 meters within basement rock overlain by 70 meters of sediment. The BIP holelock mechanism had to be disabled because it was found to cause coaxial cable damage. However, 0.5 km of slack cable was payed out on the seafloor to dampen cable motions.

Seismic data were obtained from the mid-period (MP) and short-period (SP) passbands of a triaxial set of sensors (two horizontal components X and Y, and a vertical component Z) and the SP passband of a backup vertical-component sensor (B). The resultant seven data channels are referred to as MX, MY, MZ, SX, SY, SZ, and SB.

MSS operations, summarized by the three time periods labelled MS1, MS2, and MS3, progressed with BIP deployment and shipboard data recording (MS1), BPP deployment (MS2), and BPP recovery and further on-deck recording (MS3).

A total of approximately 120 and 84 hours of data were recorded by the Teledyne and Gould systems, respectively. The BPP failed after collecting approximately 43 hours of data.

Limitations of the data are listed below:

MSS
- The Y-sensor malfunctioned for unknown reasons.

Teledyne system
- Approximately 115 and 5 hours of data were recorded during MS1 and MS3, respectively.
- SP data are aliased because of inadequate low-pass filtering.

Gould system
- Approximately 71 and 13 hours of data were recorded during MS1 and MS3, respectively.
- Channel SZ was unavailable during MS1 and MS3 due to radio

interference.

- Amplitudes are approximately 3 dB too low.

- The data timing is delayed by a nominal 16 samples in both the SP and MP bands.

BPP

- The system failed after recording approximately 43 hours of data.

- The absolute data timing is set for six hours too early.

- Channel SB was replaced by hydrophone channel SH.

- The 16-sample timing skew and 3 dB amplitude mismatch observed in the Gould shipboard data probably afflict the BPP data as well.

Gould system and BPP

- The digital implementation of the low-pass, FIR filter introduces acausal precursors which are most apparent in recordings of impulsive, high-amplitude signals.

- Gould-initiated calibrations and channel MZ were unavailable during MS2 and MS3 due to a BIP electronics failure.

The MSS was a qualified success. Although its ocean-bottom recording system malfunctioned shortly after emplacement and therefore precluded the long-term earthquake and noise studies, the large amount of digital data retrieved from the various MSS recording systems, approximately five days from each, are sufficient to address the goals of the Ngendei experiment. With the exception of the cable-isolating/holelock mechanism of the borehole package, the installation and operational procedures of the various MSS components were effective. The Gould recording scheme suffered from several defects, the most serious of which was the introduction of acausal signal by its anti-aliasing filter.

References

Ballard, J. A., Mulchahy, C. C., Wallerstedt, R. L., and Kiser, E. L., 1984. The borehole seismic experiment in Hole 395A: Engineering and installation, In Hyndman, R. D., Salisbury, M. H., et al., Init. Repts. DSDP, 78: Washington (U.S. Govt. Printing Office), 743-758.

Berger, J., R. G. North, R. C. Goff, and M. A. Tiberio, 1984. A

seismological data base management system, Bull. Seism. Soc. Am., 74, 1849-1862.

Claasen, Theo A. C. M., Wolfgang F. G. Mechlenbraüker, J. B. H. Peek, and Nicolaas van Hurck, 1980. Signal processing method for improving the dynamic range of A/D and D/A converters, IEEE Trans. Acoust., Speech, Signal Processing, ASSP-28, 5, 529-537

McClellan, J. H., Parks, T. W., and Rabiner, L. R., 1973. A computer program for designing optimum FIR linear phase digital filters, IEEE Trans. Audio and Electroacous., AU-21 506-525.

FIGURE CAPTIONS

Figure 1 Cartoon of the MSS configuration as deployed on the sea floor. The borehole instrumentation package (BIP) is connected to the ocean-bottom recording system (the BPP, Bottom Processing Package) by a mechanically-strong coaxial cable. The BPP in turn is connected to a 15.7 km submerged mooring which permits its emplacement and recovery.

Figure 2 Schematic representation of the BIP showing the seismic sensor locations.

Figure 3 External view of the MSS's ocean-bottom recording system. Most of its recording and control instrumentation is located in the foreground sphere, and the two rear spheres hold zinc-silver batteries which power both the BIP and BPP. Mounted on the BPP's base is a short-period hydrophone and an acoustic transponder. The transponder permits monitoring of BPP status and depth during its emplacement.

Figure 4 Displacement responses of the MSS. The Gould and Teledyne systems have identical responses over both mid-period (MP) and short-period (SP) bands below 1.5 and 15 Hz, respectively. Above these frequencies the Gould systems are augmented by a low-pass, FIR (Finite Impulse Response) digital filter. The Nyquist frequencies for the MP and SP bands are 2 and 20 Hz, respectively.

Figure 5 Schematic illustration of the BIP's reentry tool. The left portion of this figure shows an exploded view of the tool, and the right portion shows the configuration of the BIP in the tool at reentry and release.

Figure 6 Chronology of events during the MSS deployment. Coordinated Universal Time (CUT) data is given along the bottom axis, with a break between mid-February, 1983, and late March, 1983, when the teleseismic experiment took place and noise samples were recorded by each OBS at 24-hour intervals. See text for explanation.

Figure 7 Configuration of the MSS as actually deployed. The BIP is denoted by an asterisk, portions of the BPP and IRR mooring by circles, and navigational transponders by boxes. Reference latitudes and longitudes are shown in degrees south and west, respectively.

Figure 8 Clock drift of the Teledyne system during the shipboard recording period. A drift value of zero denotes clock reset to Coordinated Universal Time (CUT).

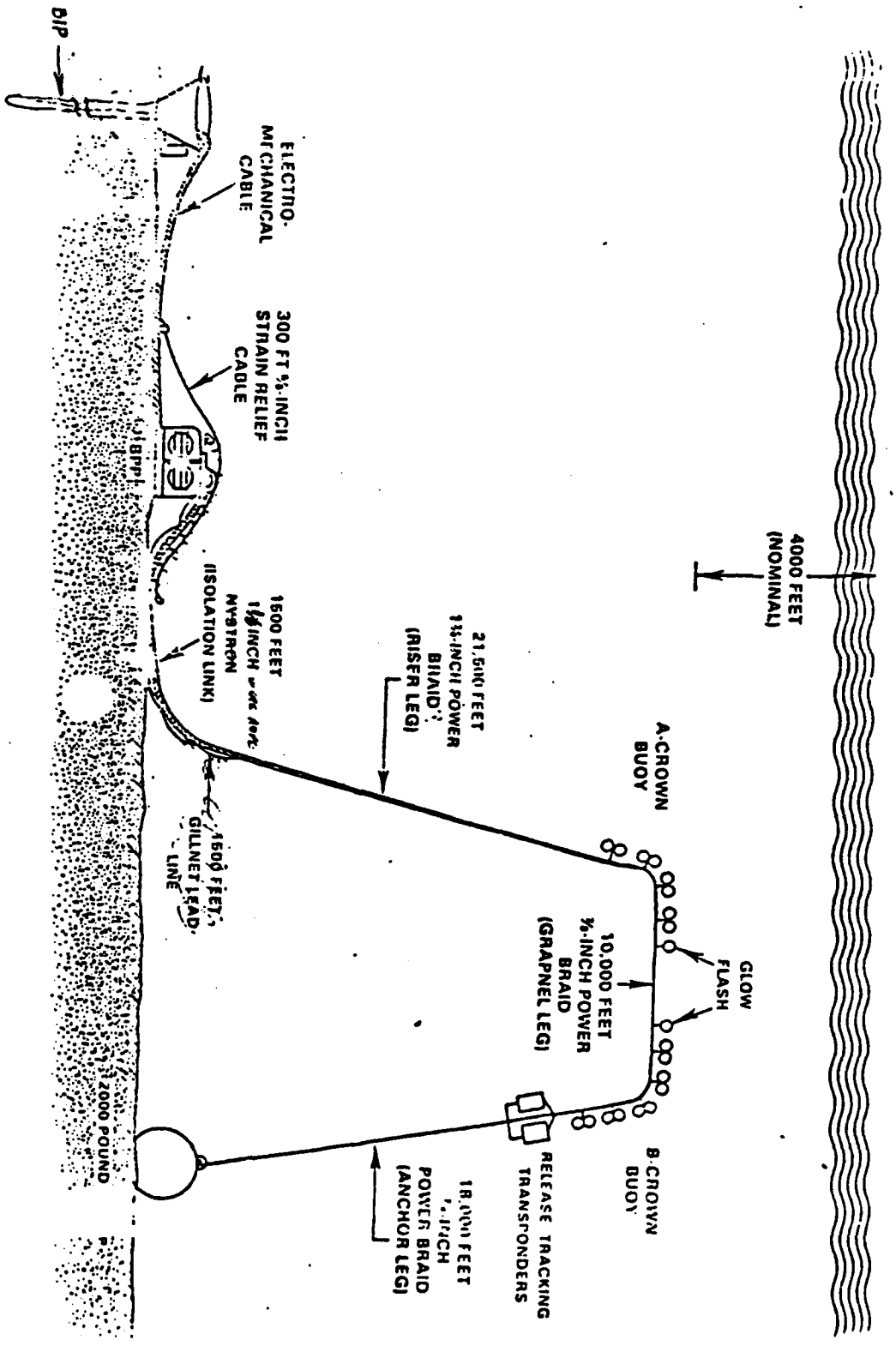
Figure 9 Typical example of seven-channel data from the Teledyne system during MS1. The recording interval is listed across the top, and the time in minutes after the hour is given across the bottom. Channel identifications and amplitudes in digital counts are along the left-hand side. The event number refers to lengths of uninterrupted data present on the tapes available from the CSS (see text).

Figure 10 Typical example of seven-channel data from the Gould system during MS1. See Figure 9 for explanation.

Figure 11 MSS sensor calibrations recorded by the Teledyne system during MS1 (a and b) and MS3 (c and d). Channels MZ and MX were well-calibrated between 0.2 and 1.0 Hz (a and c), as were channels SZ, SX, and SB between 0.2 and 15 Hz (b and d). Y-sensor channels MY and SY were poorly-calibrated at all times.

Figure 12 Illustration of the acausality due to Gould's low-pass filter and of aliasing in the Teledyne data. Shown are simultaneous recordings on the Teledyne (dashed) and Gould (solid) systems of signals from a one pound shot, c 1920Z, 7 February, 1983, withing 4 km of the borehole. The boxed inset is an enlargement of the boxed portion of the seismogram section immediately above it. The time scale is given at the bottom. The large-amplitude arrival is the direct water wave. An 18 Hz (approximately) precursor to the water wave is seen in the Gould data, but not in the Teledyne data. This precursor precedes any physical arrival, and is therefore a relict of the Gould recording scheme. Note also the effect of aliasing in the Teledyne data, in which an extra peak near 0.55 seconds is seen which is not present in the Gould data.

FIGURE 1


DIP
ELECTRO-MECHANICAL CABLE
300 FT ⅝-INCH STRAIN RELIEF CABLE
1500 FEET 1¼-INCH NYBTRON (ISOLATION LINK)
21,500 FEET 1¼-INCH POWER BRAID (RISER LEG)
4000 FEET (NOMINAL)
A-CROWN BUOY
GLOW FLASH
10,000 FEET ⅝-INCH POWER BRAID (GRAPNEL LEG)
RELEASE TRACKING TRANSPONDERS
B-CROWN BUOY
POWER BRAID (ANCHOR LEG)

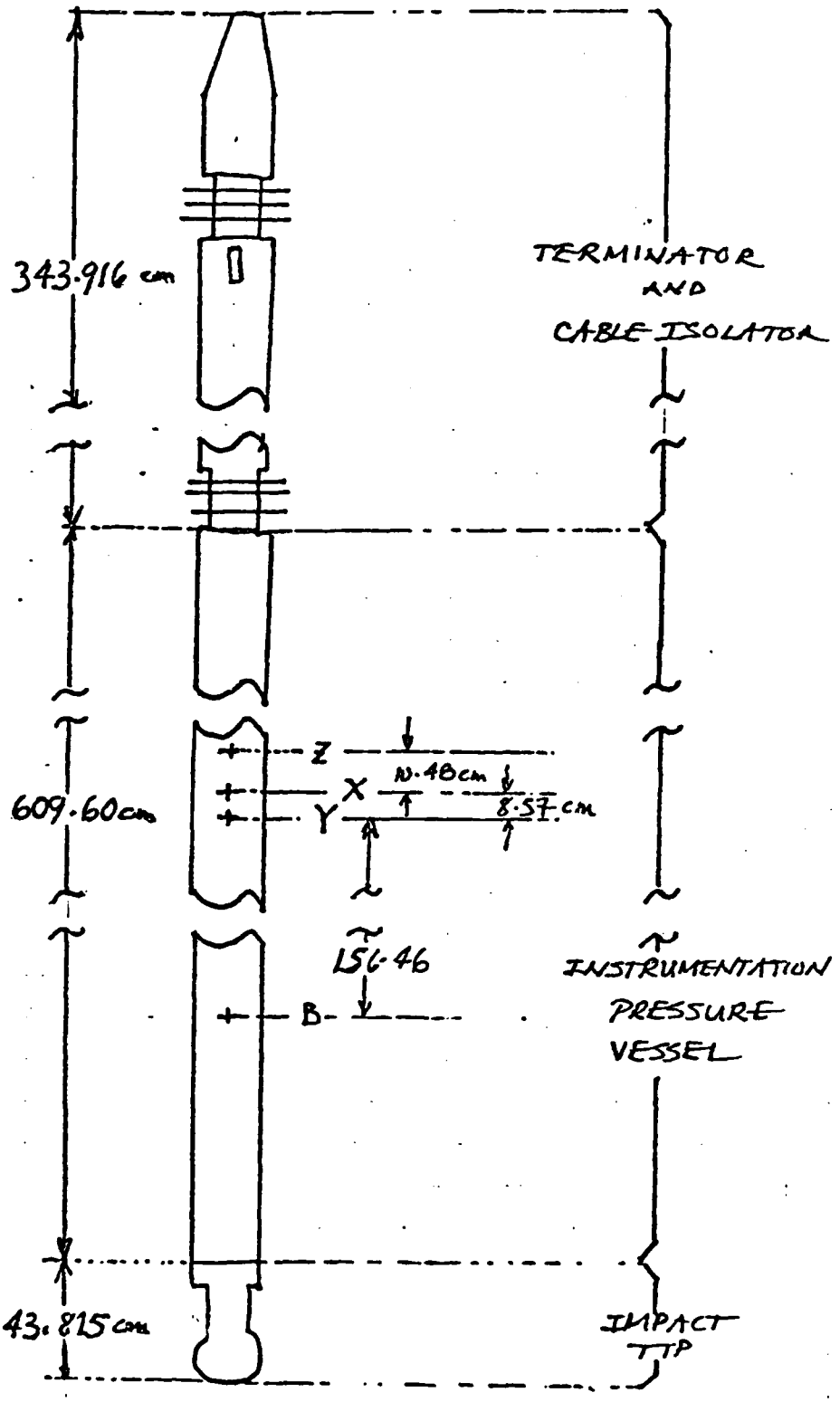

343.916 cm
TERMINATOR
AND
CABLE ISOLATOR
609.60cm
Z
X
Y
10.48cm
8.57cm
156.46
B
INSTRUMENTATION
PRESSURE
VESSEL
43.815cm
IMPACT
TIP

FIGURE 2

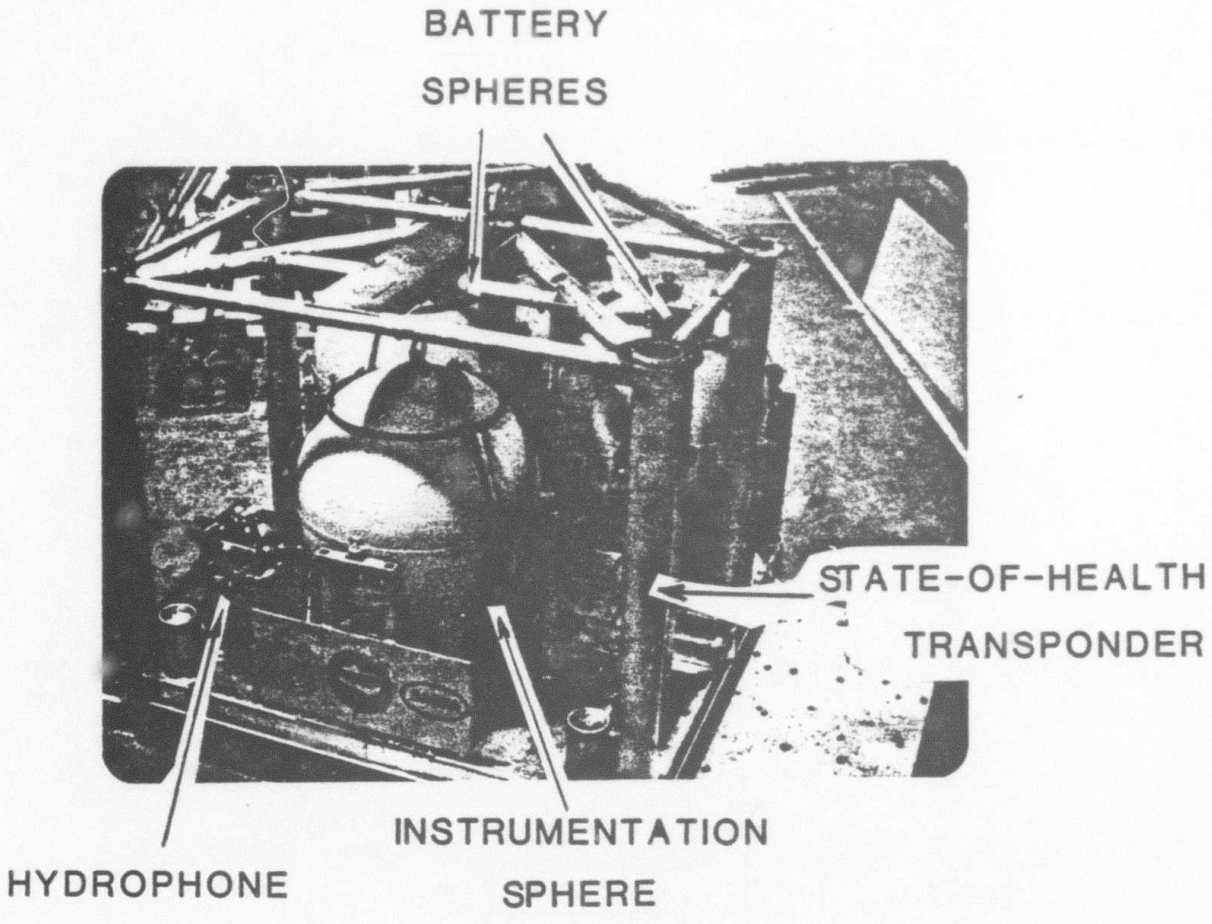
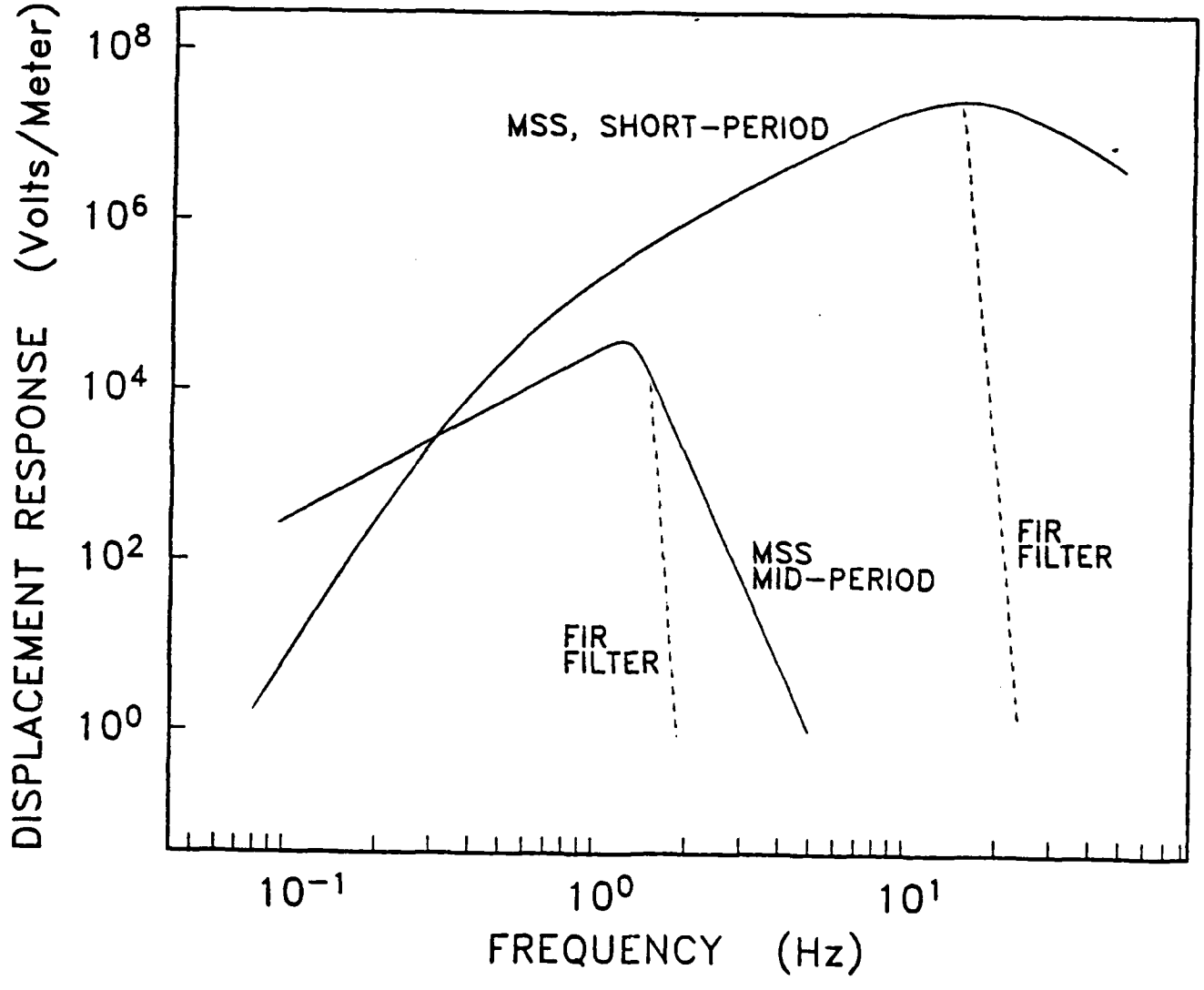

BATTERY
SPHERES
STATE-OF-HEALTH
TRANSPONDER
HYDROPHONE
INSTRUMENTATION
SPHERE

FIGURE 3

FIGURE 4


DISPLACEMENT RESPONSE (Volts/Meter)
10^8
10^6
10^4
10^2
10^0
MSS, SHORT-PERIOD
MSS
MID-PERIOD
FIR
FILTER
FIR
FILTER
10^{-1}
10^0
10^1
FREQUENCY (Hz)

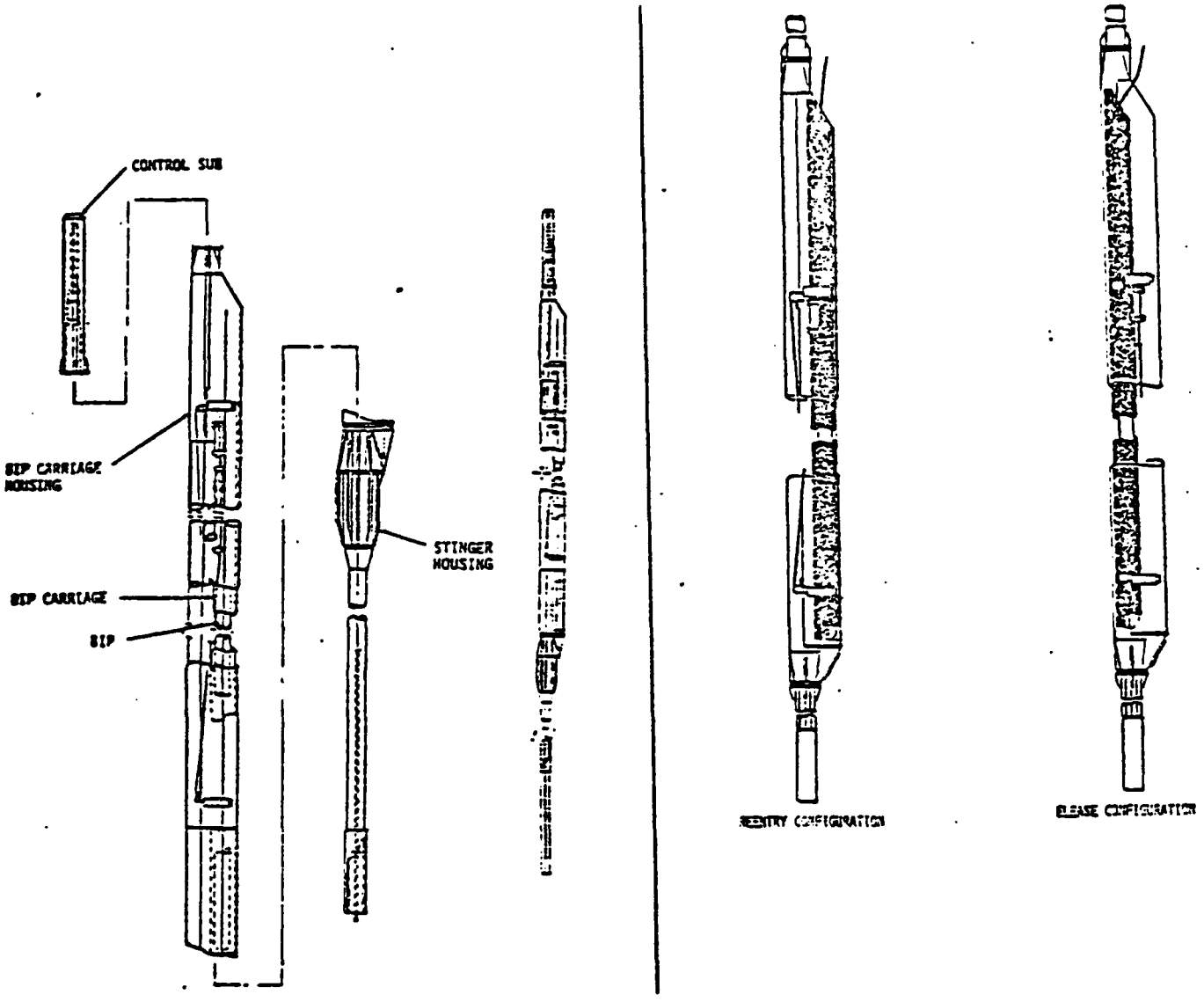

CONTROL SUB
BIP CARRIAGE HOUSING
BIP CARRIAGE
BIP
STINGER HOUSING
RETRY CONFIGURATION
RELEASE CONFIGURATION

FIGURE 5

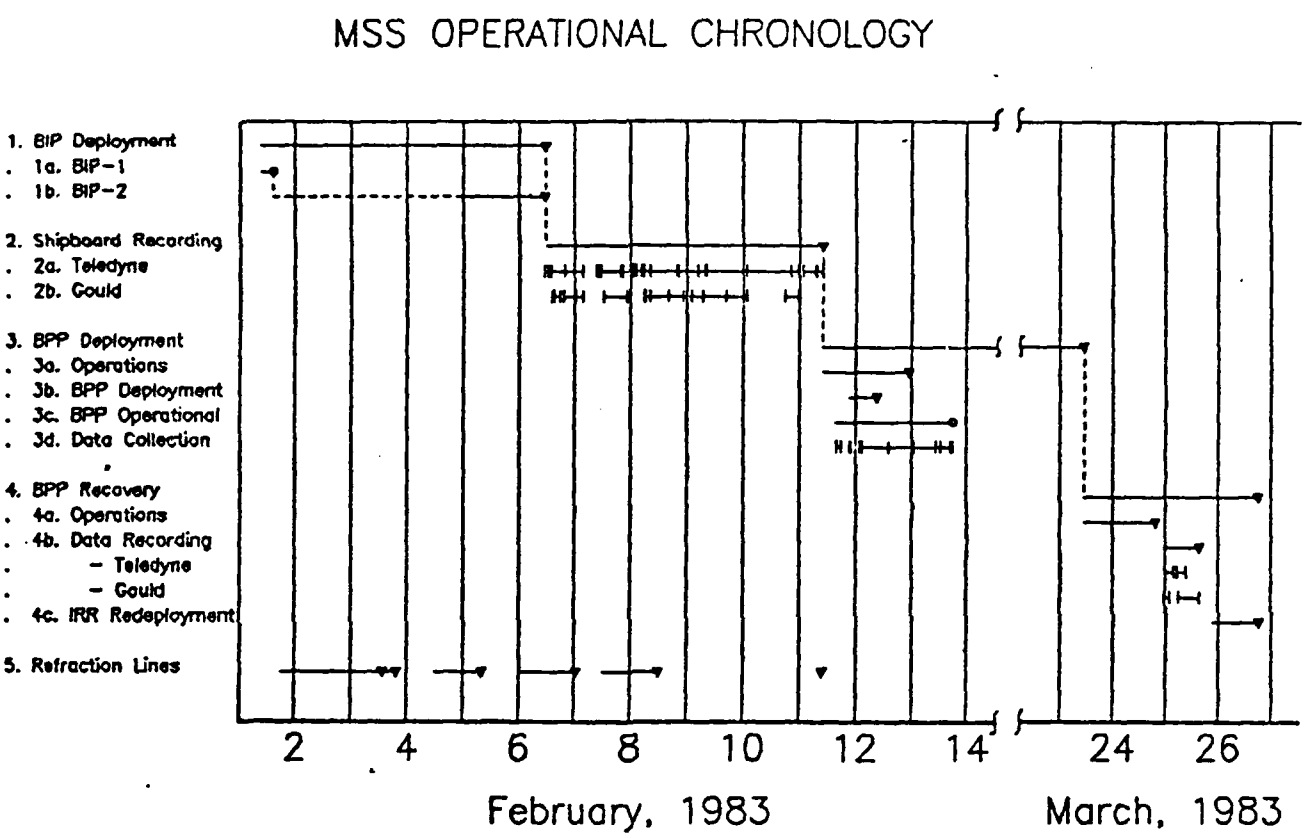

MSS OPERATIONAL CHRONOLOGY
1. BIP Deployment
. 1a. BIP-1
. 1b. BIP-2
2. Shipboard Recording
. 2a. Teledyne
. 2b. Gould
3. BPP Deployment
. 3a. Operations
. 3b. BPP Deployment
. 3c. BPP Operational
. 3d. Data Collection
4. BPP Recovery
. 4a. Operations
. 4b. Data Recording
. - Teledyne
. - Gould
. 4c. IRR Redeployment
5. Refraction Lines
2
4
6
8
10
12
14
24
26
February, 1983
March, 1983

FIGURE 6

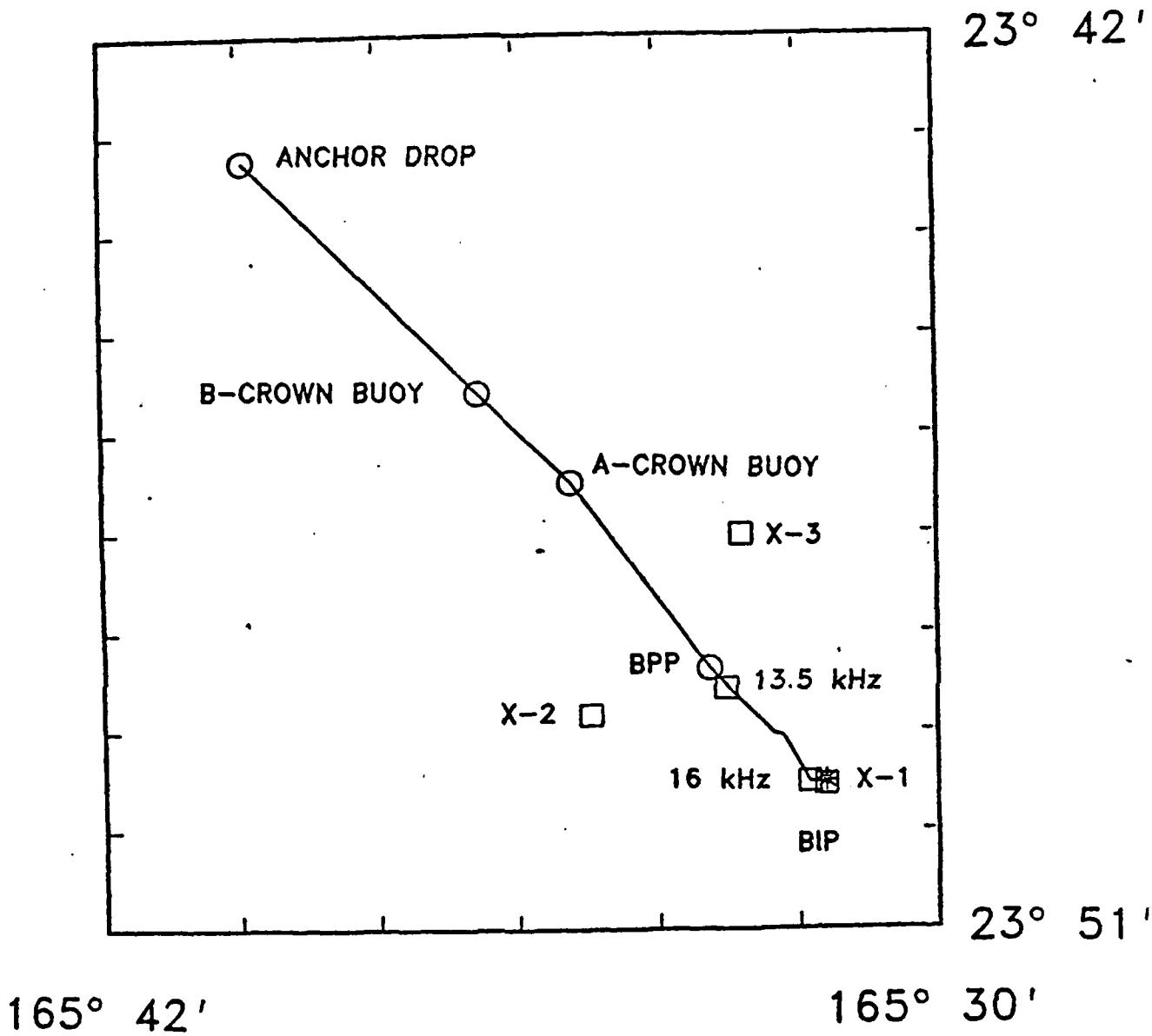

23° 42'
ANCHOR DROP
B-CROWN BUOY
A-CROWN BUOY
X-3
BPP
13.5 kHz
X-2
16 kHz
X-1
BIP
23° 51'
165° 42'
165° 30'

FIGURE 7

FIGURE 8

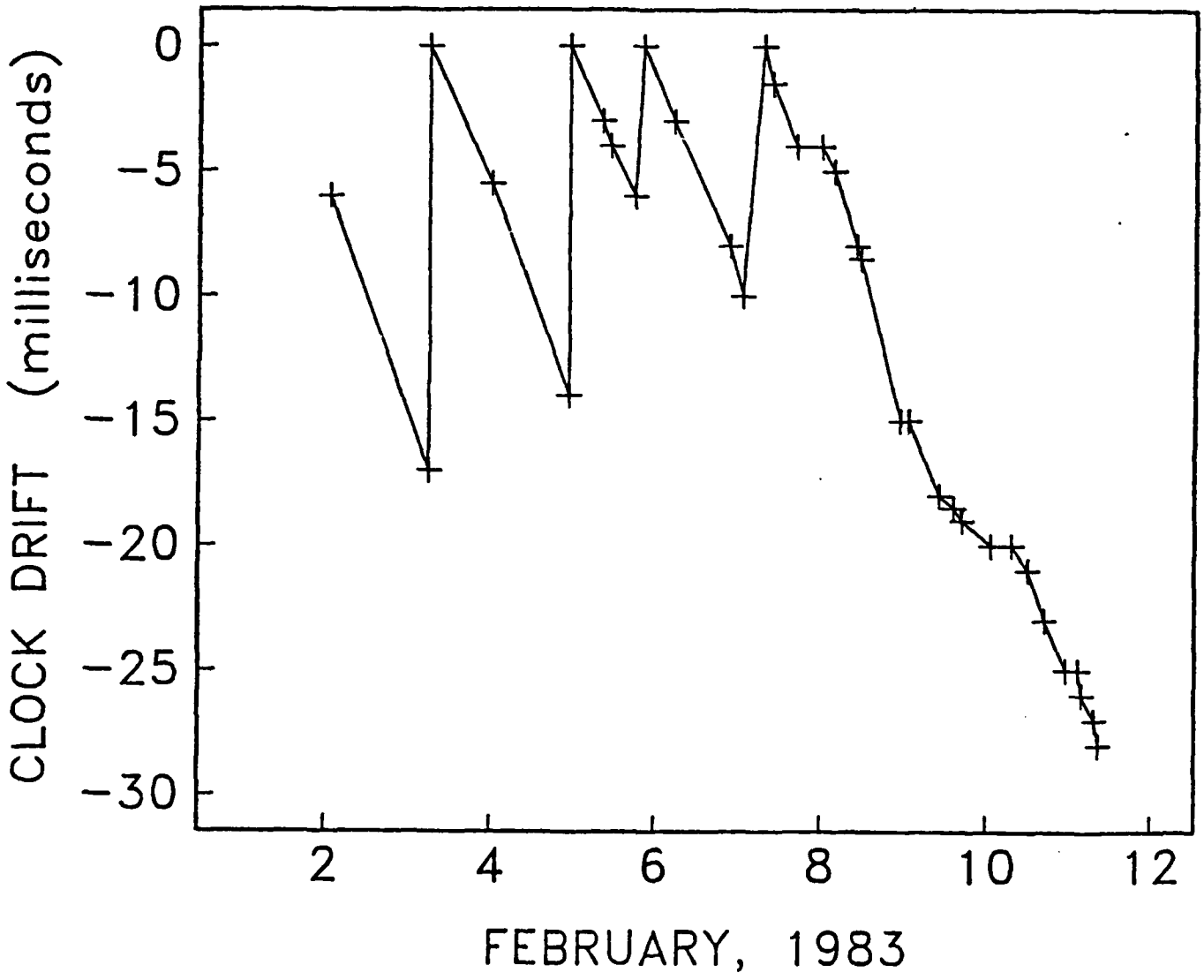

CLOCK DRIFT (milliseconds)
0
-5
-10
-15
-20
-25
-30
2
4
6
8
10
12
FEBRUARY, 1983

FIGURE 9

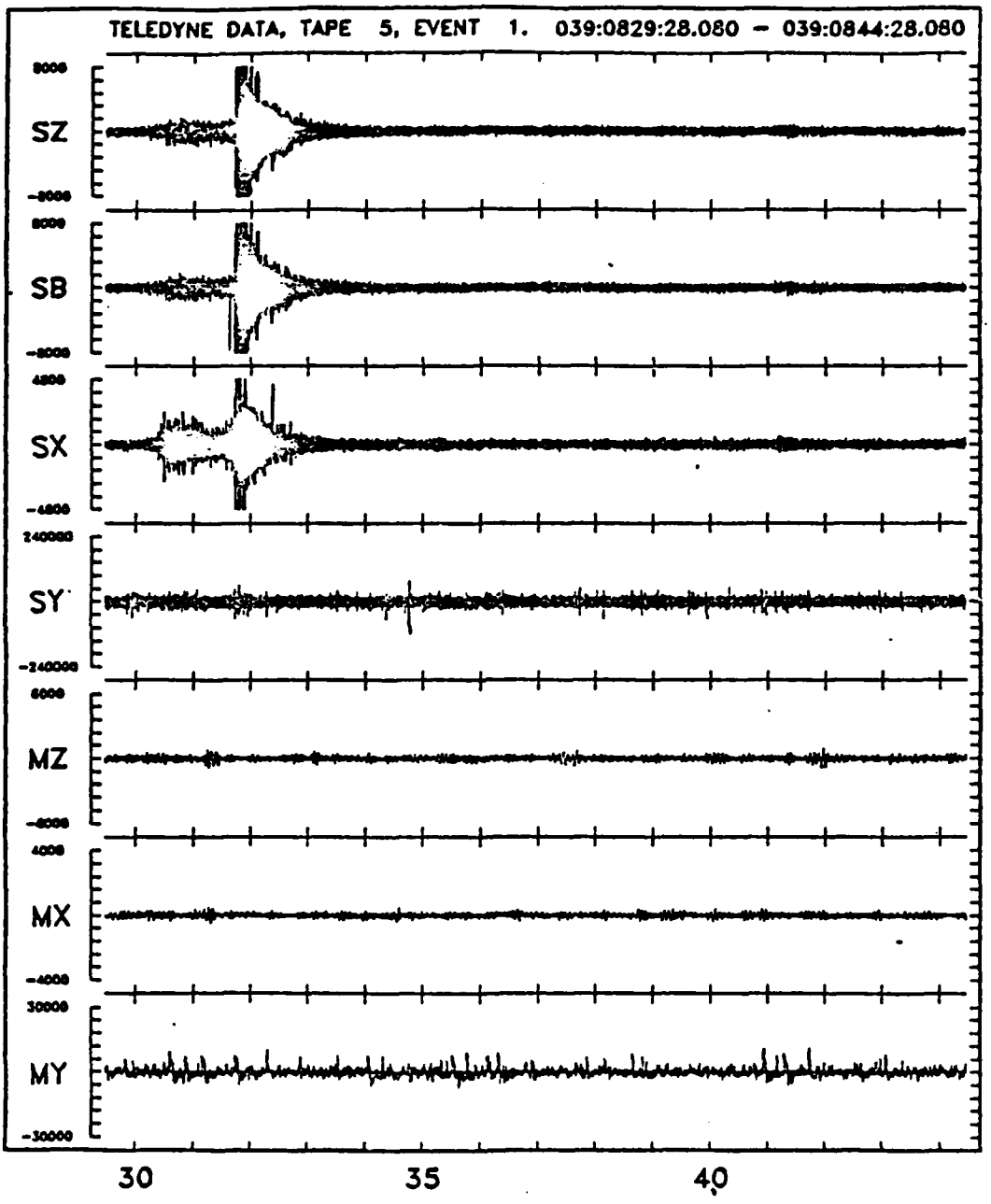
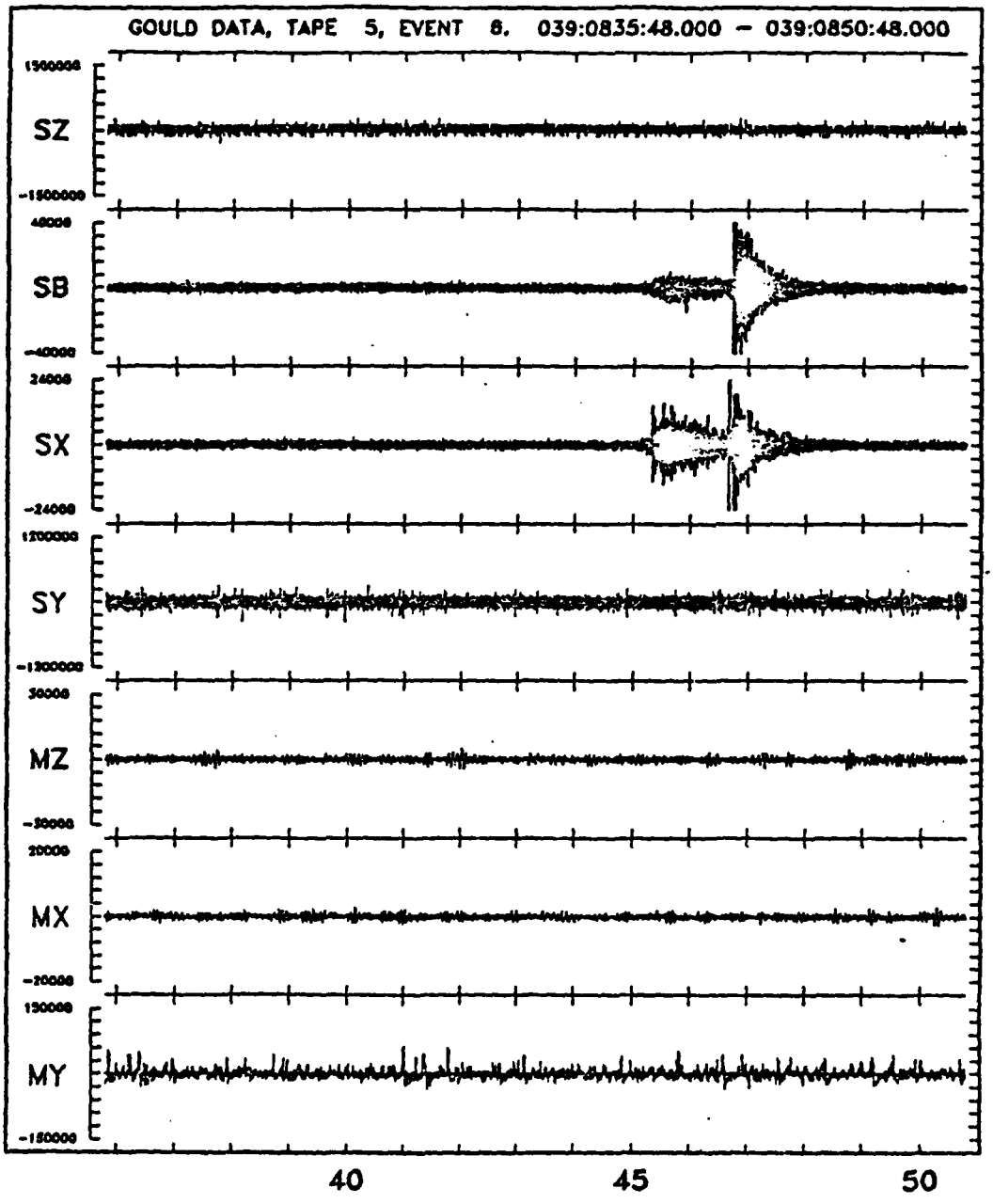
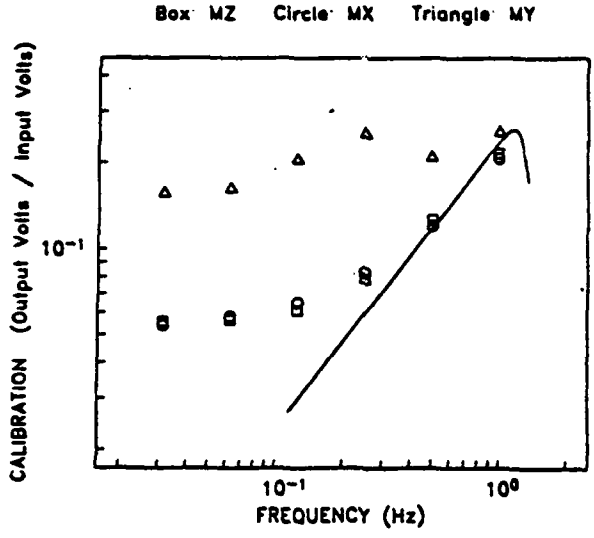

TELEDYNE DATA, TAPE 5, EVENT 1. 039:0829:28.080 - 039:0844:28.080
SZ
SB
SX
SY
MZ
MX
MY
30
35
40

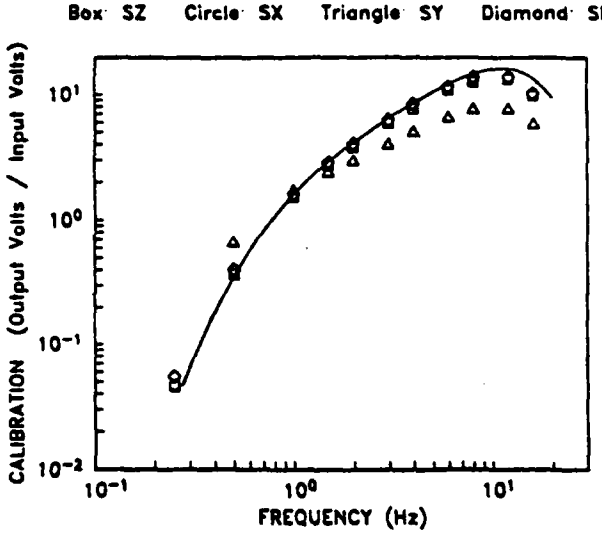
FIGURE 10


GOULD DATA, TAPE 5, EVENT 8. 039:0835:48.000 - 039:0850:48.000
SZ
SB
SX
SY
MZ
MX
MY
40
45
50

SHIPBOARD RECORDING PERIOD

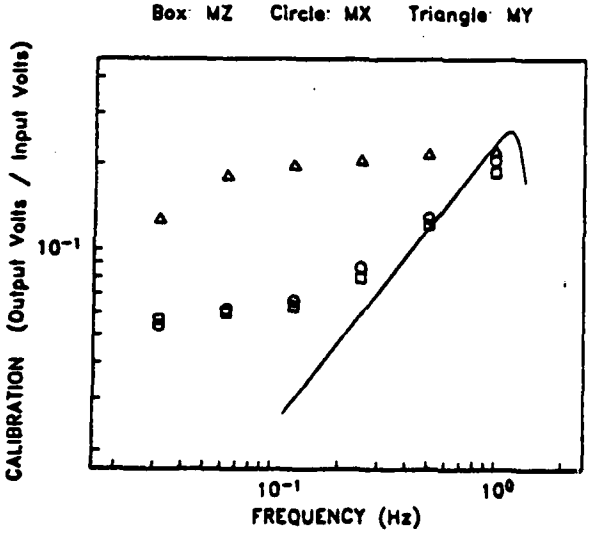


(a)

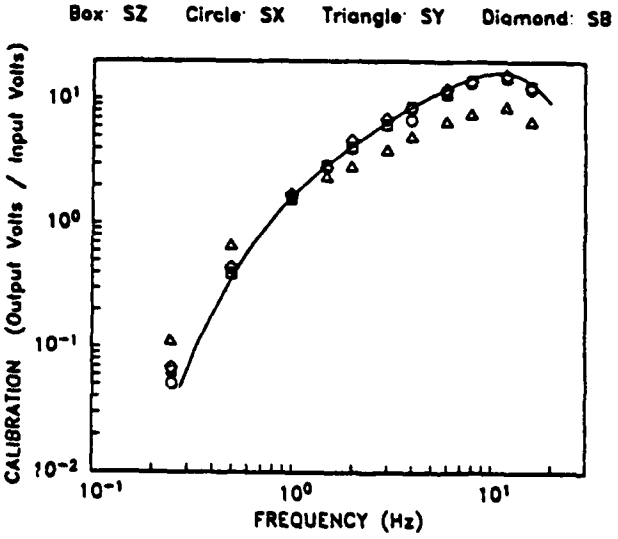


(b)

RECOVERY PERIOD



(c)



(d)

FIGURE 11

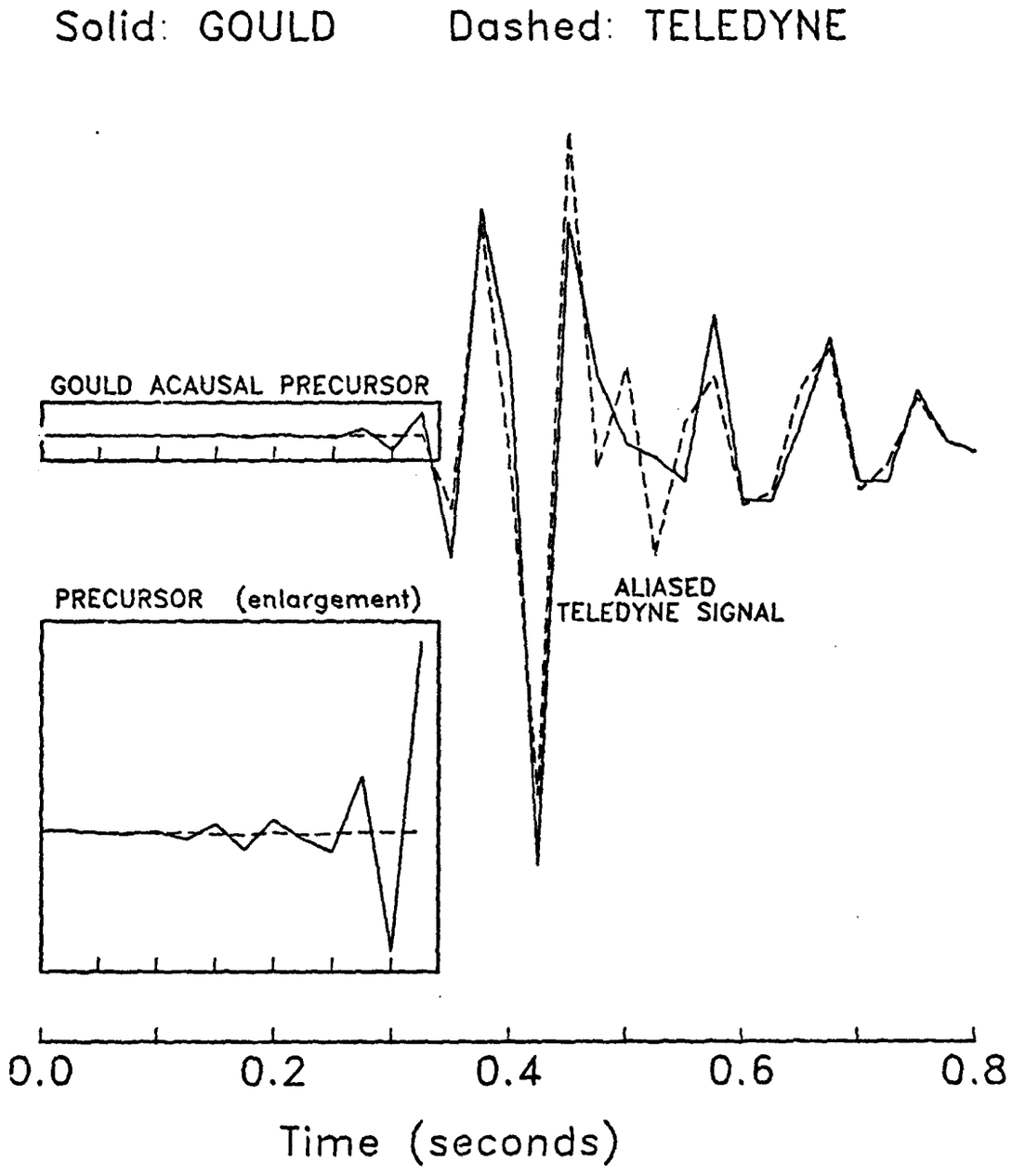

Solid: GOULD
Dashed: TELEDYNE
GOULD ACAUSAL PRECURSOR
PRECURSOR (enlargement)
ALIASED
TELEDYNE SIGNAL
0.0
0.2
0.4
0.6
0.8
Time (seconds)

FIGURE 12

CHAPTER 3

DESCRIPTION AND PERFORMANCE OF THE SCRIPPS OCEAN BOTTOM SEISMOGRAPHS DURING THE NGENDEI EXPERIMENT

John A. Orcutt[1]
Robert D. Moore[2]
Thomas H. Jordan[3]

[1]Institute of Geophysics and Planetary Physics (A-025)
Scripps Institution of Oceanography
La Jolla, CA 92093

[2]RD Moore Associates
7868 Camino Raposa
San Diego, CA 92122

[3]Department of Earth, Atmospheric and Planetary Sciences
Massachusetts Institute of Technology
Cambridge, MA 02139

ABSTRACT

Six ocean bottom seismographs from the Scripps Institution of Oceanography were employed in the NGENDEI experiment in conjunction with the Marine Seismic System. The systems used had been modified in a number of significant ways in order to meet the special requirements of this experiment. Significant buffer memory was added to several of the instruments in order to eliminate the effects of a rotating tape recorder housed in the same capsule as the inertial sensors. In addition, the response of the instruments was modified for the triggered portion of the experiment to maximize the likelihood of triggering on low frequency teleseismic signals. Finally, the software used by the seismograph's CPU was modified to allow simple, but important, modifications to the operating characteristics immediately prior to launch. Each of the instruments were deployed several times and all capsules were recovered. Several deployments were found to be unsuccessful through acoustic diagnostics and several capsules returned to the surface shortly after launch due to small leakages revealed by the leak detectors. Nevertheless, the deployments which followed the correction of these faults were all successful in that data were returned in each instance. This paper outlines the operating characteristics of each instrument, describes the instrument response functions, lists the locations of the seismographs on the seafloor and enumerates the events recorded by each of the capsules.

INTRODUCTION

The ocean bottom seismographs (OBS) used in this experiment were developed and constructed at the Scripps Institution of Oceanography. The design of these instruments was originally described by Moore, et al. (1981) although a number of important changes were made to meet the operational requirements of the NGENDEI expedition.

The sensors in the ocean bottom seismographs consist of a triaxial inertial sensor (Mark Products L-4-3D; Mark Products, Inc., 10507 Kinghorst Drive, Houston, TX 77072) and a deep water hydrophone (Ocean and Atmospheric Science, Inc. model E-2PD; Ocean and Atmospheric Science, Inc., 45 Palisade St., Dobbs Ferry, NY 10522). The natural period of the seismometers is 1 Hz, the lowest free period currently in use in any operational bottom seismometer system.

The output of the seismometers, as well as the external hydrophone, is amplified by a broad band, low power CMOS device with software selectable gains of 2^N where N can range from 0 to 9 for a total gain range of 1 to 512. The gains are controlled by the microcomputer which seeks to maintain the long term average of the noise amplitude between a specified upper and lower level of the output of the analog-to-digital converter. This practice ensures that the instrument will record ground noise at some level, but will make the bulk of the instrument's dynamic

range available for recording large amplitude signals. The 12-bit analog-to-digital converter with the 9-bit gain ranging provides an overall dynamic range of 120 db.

The conservation of high dynamic range across a wide range of frequencies requires that the recorded noise be as flat as possible. Figure 1 illustrates the seafloor noise as recorded by the MSS for a period of time during the NGENDEI experiment and is typical of seafloor noise in general. The power spectrum has been corrected for the response of the instrument and is demonstrably red largely due to the substantial "microseismic" noise generated on the seafloor by weather patterns and resultant long period gravity waves at the surface. The OBS is equipped with a notch filter within the microseism band below 1 Hz to depress the low frequency noise and boost the higher frequencies.

Prior to the NGENDEI experiment, we added additional buffer memory to the system to postpone tape recorder startup until after the arrivals of interest were already recorded in the buffer. The UHER tape recorders used in the system to record digital data in a serial format tend to shake the capsule during operation thereby limiting the sensitivity of the instrument. Each of the buffer memories can store 64 Kwords of data which, at the nominal 128 samples/s digitizing rate, is equivalent to 113 seconds of data on all four channels. As many as four of these boards can be used in any given instrument for a total of almost 8 minutes of solid state recording. Because this facility was quite new and since our experience with refraction programs indicated the buffer memory was not absolutely essential, we elected to use the buffer capabilities only for the teleseismic portion of the experiment.

The OBSs, when on the sea floor, can communicate with the parent ship through an acoustic link. This link, in its most simple mode, acts as a transponder and is used to accurately pinpoint the instrument on the seafloor. The acoustic link is also used as a telemetry link for sending capsule diagnostics to the ship regarding battery voltages, number of triggered events, the tilt status of the seismometers, the seafloor noise level, channel gain, etc. Finally, the telemetry link is used to command instrument release by firing one of the two available explosive bolts connecting the spherical package to the tripod anchor through a mechanical 'OR' circuit. An independent pair of timed releases serve as a backup in the

Operational Summary

Each OBS was deployed several times to accomplish the goals of the experiment. The drops, launch goals, a summary of performance and an identifier code are listed in Table 1.

The locations of the OBSs are enumerated in Table 2 and depicted in Figures 2-5. These locations were determined using the OBS acoustics

system and estimates of the ship's position obtained from satellite fixes as outlined by Creager and Dorman (1982). In most cases the position of the ship at drop time is included to give an idea of the horizontal drift of the instruments during the transit to the seafloor. The position of LY2 on the seafloor is poorly known since time was not available for accurately locating the OBS

Sensors and Signal Conditioning

The inertial sensors used in the Scripps' OBS are standard seismometers with moving coil transducers. The output of these 'velocity transducers' is further conditioned by active filters and preamplifiers to provide adequate levels for digitizing, to pre-whiten the earth noise present on the seafloor and to provide adequate protection against aliasing.

The analog data streams for the seismometers and hydrophone are shown in Figure 6. The two systems are quite similar except for the lack of a 'notch filter' for the hydrophone. The output of the seismometer is given by the standard form:

$$e_o = \frac{-2\pi iGf\ (f/f_o)^2}{1-(f/f_o)^2+if/f_oQ}X$$

e_o = output voltage
f_o = seismometer natural frequency (Hz) = 1 Hz
G = seismometer generator constant = 417 volts/m/s
Q = 'quality factor' = 0.707
X = ground displacement (m)

f_o, G and Q have been obtained from the equipment manufacturer, Mark Products, and were not explicitly measured at Scripps prior to the conduct of the NGENDEI experiment.

The preamplifier is essentially flat at all the frequencies of interest within the seismic passband and the gain is set by the OBS microcomputer in response to seismic noise levels on the seafloor. The gain is given by:

$$e_o = \frac{-2^n}{1+if2^n/f_1} \qquad n = 0,1,\ldots,9$$

where f_1 is approximately 1.44×10^5 Hz and e_i is the input voltage. In the worst case, this gives a corner frequency of 282 Hz at a gain of 9. This rolloff can, obviously, be neglected when computing the system response.

Anti-aliasing protection is provided by a total of 5 poles of low-pass filtering at a frequency of approximately 30 Hz. One of these poles is included in the 'notch filter' to be discussed next while the other four poles arise from the action of two two-pole active filters. The response of the first of these is given by:

$$e_o = \frac{-54.4if}{1+19.4if-0.650f^2-0.0218if^3}e_i$$

while that of the second can be calculated from:

$$e_o = \frac{-2.80}{1+if/30-(f/30)^2}e_i$$

The Nyquist frequency of the Scripps' OBSs is 64 Hz. In the range from 0 to 30 Hz, the worst case aliasing occurs at 30 Hz from frequencies at 64 + (64 - 30) = 98 Hz. This level is reduced, through the anti-aliasing filters, by 51.4 db. The dynamic range of the analog to digital converter is 66 db so the anti-aliasing protection should be adequate for most purposes.

The 'notch filter' is introduced in the seismometer channel to pre-whiten the input noise available to the analog-to-digital converter and to prevent the markedly 'red' seafloor noise spectrum from controlling the bulk of the dynamic range of the 12-bit converter. The response of the notch filter is given by:

$$e_o = -1.97\frac{1+if/0.504}{1+if/0.10}\cdot\frac{1+if/1.52}{1+if/5.03}\cdot\frac{1}{1+if/32.2}\cdot\frac{(1+if/1.52)^2}{(1+if/5.03)(1+if/5.12)}e_i$$

The modulus of this filter is plotted in Figure 7. The bottom of the notch occurs at a frequency of about 0.6 Hz and the maximum high frequency boost is achieved at a frequency of 15 Hz. The action of the single pole of anti-aliasing filtering can be seen at higher frequencies. This filter is very well-suited to recording explosion sources in a refraction experiment when the primary frequencies of interest lie at 5 Hz and higher. In this case the low frequencies in the vicinity of the microseism peak are of little interest and the notch filter actively suppresses these contributions. The filter is, however, poorly suited to triggering on and recording distant earthquakes. Experience with the use of the Scripps' OBSs in the past for earthquake recording had indicated that triggering on microearthquakes was quite straightforward and no events were missed when compared to recordings obtained from a continuously recording analog instrument (Riedesel, et al. 1982). On the other hand, the instruments rarely triggered on teleseisms. Following discussions with Dr. William Prothero, who had designed an effective trigger for teleseisms (Prothero, 1979), we elected to remove the notch filter for the teleseismic recording portion of NGENDEI. This removes

the high frequency boost and emphasizes the low frequency portion of the spectrum. Figure 8 illustrates the overall response of the Scripps' OBS before and after the removal of the notch filter. The teleseismic recording portion of the experiment was very successful as discussed later in this volume.

The output of the hydrophone is given by:

$$e_o = 25.1 \times 10^{-7} \frac{0.0314if}{1+0.0314if} P$$

where P is the pressure in Pascals. The hydrophone preamp response can be calculated from:

$$e_o = \frac{87.4if}{1+43.7if-1.51f^2-0.052if^3} e_i$$

This hydrophone preamplifier is followed by the same preamplifier as discussed above for the seismometers and by two active anti-aliasing filters. The response of the hydrophone channel is illustrated in Figure 9.

OBS Acoustics

The acoustics system on the Scripps' ocean bottom seismographs is designed to accomplish a number of functions. The acoustics were designed and constructed at Scripps after a long history of difficulties with a popular commercial system. The most rudimentary function of the system involves service as an acoustic transponder. This is extremely useful in locating the individual instruments on the seafloor and can be accomplished to an accuracy on the order of ten meters using a least squares algorithm (Creager and Dorman, 1982). The use of OBSs on the seafloor in array studies requires extremely accurate locations for the sensors which cannot be provided by ship's navigation at launch time or the relatively inaccurate timing provided by low frequency explosions. We found, during the NGENDEI experiment, that an OBS could drift by more than a kilometer from the time of release until it settled on the seafloor. Recordings of explosions can be used to locate the seismographs on the bottom, but the accuracy is limited both by the frequencies detected by the seismic recording system on board the seafloor instrument and the not negligible timing inaccuracies associated with the shot times and the clock times in the recorder. The acoustic system also allows the ship to send transpond commands throughout the time that a transit satellite is above the horizon and to interpolate the replies to the actual time of the fix. This timing is particularly cumbersome if explosions are being used for locations. The acoustics system also permits low speed telemetry from the instrument which can be useful for checking the 'health' of the electronics and to assess the need for early recovery and relaunch. Finally, because the system is able to

recognize specific commands, the acoustics are used for affecting release. This acoustic release system is considered the primary means for recalling the OBSs while timed release is regarded as a backup system. The instrument is also released automatically if a leak into the capsule is detected. The flexibility afforded by the release upon command feature is very helpful in executing an experiment; large numbers of hours of ship time can be lost while waiting on a timed release.

The OBSs are interrogated on the seafloor at a frequency of 12.5 KHz and reply at frequencies between 8.0 and 15.5 KHz. Given the discrete reply frequencies, individual instruments can be readily identified by the ship's electronics. The collection of a number of ranges during several satellite fixes with the ship at different positions with respect to the seafloor array allows the accurate determination of the instrument locations. The locations of individual instruments during the NGENDEI experiment are given in the subsequent chapters which discuss specific portions of the program.

Following a diagnostics command on the seafloor, the OBSs reply to the command with strings of twelve bits which comprise four octal words. A one is denoted by two 'pings' while a zero is a single 'ping'. The diagnostics which are sent by the OBS depend upon the time elapsed since the capsule was launched. The first diagnostics command is sent to the OBS after it has undergone final preparations, but is still sitting in the checkout van. The reply to this first command is two strings of octal 2's, 2222 2222, or 010010010010 010010010010. Subsequent diagnostics commands result in replies of 0007 0007 0007 0007 until the seismometer is first leveled on the bottom. The time interval between the first set of diagnostics and the leveling is set by the computer software, but is generally three hours. This period is measured by the OBS computer in seconds so that three hours easily overflows the IM6100's 12-bit word. This is true of many of the variables which the computer must use so that a 'double-precision' 24-bit word becomes necessary. The two 12-bit words which hold the bits for this time delay are called WAITLL and WAITMM.

Following the initial wait which is designed to ensure the instrument has reached the seafloor in the study area, the seismometer is leveled and the instrument enters into a setup period. This setup period is also controlled by the computer and the time interval is entered in the two variables RUNTML and RUNTMM to comprise another double precision variable. This time is generally set to 4096 s to correspond to four time constants of the algorithm which is used to calculate the long term average (LTA) of the seafloor noise. The LTA is used to individually set channel gains and to remove any analog amplifier offset voltage. This variable is discussed in greater detail below. During the setup period the acoustic diagnostics reply with 3333 3333 3333 3333 if the system it tilted by less than 15 degrees and leveling has been successful or by 7171 7171 7171 7171 if the capsule is tilted by more than 15

degrees and leveling is impossible. The investigator must at this time make a decision about whether to recall the seismograph and relaunch or realize that much of the horizontal information will be lost and that even the vertical channel may be badly degraded. None of the OBSs launched during the NGENDEI experiment had to be recalled to correct excessive tilt problems.

The computer activates the 'normal' diagnostics sequence once the setup is complete. These diagnostics consist of eleven groups of four digit octal words which report on the health of the system in detail. The words look like:

7007	1	1	1	0	0	0	0	0	0	1	1	1
Status Word	0	0	0	B3	B4	B5	B6	B7	B8	B9	B10	B11
Trigger Count	-	-	-	-	-	-	-	-	-	-	-	-
Trigger Ratio	-	-	-	-	-	-	-	-	-	-	-	-
Gains	0	0		[Channel 0]			0	0		[Channel 1]		
Gains	0	0		[Channel 2]			0	0		[Channel 3]		
+6 V. Supply	-	-	-	-	-	-	-	-	-	-	-	-
+5 V. Supply	-	-	-	-	-	-	-	-	-	-	-	-
+12 V. Supply	-	-	-	-	-	-	-	-	-	-	-	-
-12 V. Supply	-	-	-	-	-	-	-	-	-	-	-	-
7007	1	1	1	0	0	0	0	0	0	1	1	1
Silence												

The 7007 words at the beginning and end of the sequence are used to allow the listener to arrange the intervening words in correct order and to identify the beginning and end of the diagnostics. This is critically important in situations which constantly arise when the signal-to-noise ratio is marginal and the individual bits are difficult to detect. The bits are sent at exact intervals of 4 s. The bits B3-B11 in the status word are decoded as:

B3 = 1 if a watchdog timer reset has occurred.
B4 = 1 if acoustic release #2 has not fired.
B5 = 1 if acoustic release #1 has not fired.
B6 = 1 if capsule is not leaking.
B7 = 1 if tilt is less than 15 degrees.
B8 = 1 if time release B has not fired.
B9 = 1 if time release A has not fired.
B10 = 1 if time release B is 'on'.
B11 = 1 if time release A is 'on'.

The normal state while on the bottom is 000 011 111 111. The watchdog timer is a software device used to reset the program in the computer if, for some reason, the program has crashed. This timer checks to ensure that several specific instructions have been performed within a specific time period and resets and reinitializes the program if a problem is noted. The operation of the real-time clock is not affected by the computer reset. Normally, the computer should indicate no watchdog timer

resets and none were noted throughout the duration of the NGENDEI experiment on any of the capsules.

The instrument can be released from the bottom by an acoustic release command. The computer returns the words 6314 6314 upon the receipt of a release command and subsequent diagnostics commands from the ship return the same pair of words. Finally, the instrument will release its anchor upon detecting a leak in the capsule. When the leak is detected, the instrument sends the words 0421 0421 every 128 s for eight times. Subsequent diagnostics result in the words 0421 0421 to notify the ship that a recovery is imminent.

The Scripps' OBSs at one time used an acoustics command system which depended upon the temporal relationship of an 'arm' and a frequency-encoded 'command' pulse. Any signals arriving in the brief period (1 s) between the arm and command signals would 'disarm' the acoustics unit. Such a system works quite nicely when the acoustic transceiver is several meters off the seafloor or if the seafloor is well-sedimented. However, in a rough seafloor environment, reverberations from the bottom and surrounding topography frequently disarm the acoustics system. This 'temporal' approach was replaced during the past two years with a'frequency-domain' system which is sensitive to eight frequencies:

A: 12.650 KHz	B: 12.850 KHz
C: 13.050 KHz	D: 13.250 KHz
E: 13.650 KHz	F: 13.850 KHz
G: 14.050 KHz	H: 14.250 KHz

Each capsule is programmed to recognize two acoustics commands consisting of a combination of four frequencies on and four frequencies off. Any other command combination is ignored. The number of frequencies allows us to work with a large number of capsules and additional commands could be added for specific experiments. The new system also avoids the difficulties associated with the 'temporal' approach and is extremely reliable.

Ocean Bottom Seismograph Computer and Operational Software

The microcomputer chip used in the Scripps' OBSs is an Intersil IM6100 CMOS device which we have chosen to clock at a relatively low speed of 2 MHz. This frequency was chosen as a reasonable compromise between current drain and computational speed. The IM6100 was one of the few CMOS microprocessors available at the time the OBSs were originally designed and had the advantage of a 12-bit word and compatibility with the Digital Equipment Corporation's PDP8/E minicomputer. This compatibility allowed the use of the OS/8 operating system with attendant editors, assemblers and FORTRAN and BASIC high-level languages. (PDP8/E and OS/8 are trademarks of the Digital Equipment Corporation.) In

addition a development system was available from Pacific Cyber Metrix (Pacific Cyber Metrix, 3120 Crow Canyon Road, San Ramon, CA 94583) which included interfaces for floppy and hard discs, line printers and RS232 communications.

The oscillator used to clock the computer is a temperature compensated crystal oscillator rather than an oven-controlled system which would have required substantially more power. The drift rates observed for all the instruments is given in the OBS operational summary in Table I. We do not attempt to set the frequency of the oscillators to match Universal Coordinated Time exactly so that each OBS has a net drift with respect to the correct time. The operational summary shows that this rate of drift from launch to launch is nearly constant and that the required time corrections are quite accurate. The computer real time clock counts seconds with a double precision 24-bit word. The memory in the system is composed of three 4K word blocks of CMOS memory. One of these blocks is reserved for program storage and operation and can be write-protected in 1 K sections. Although the data are sampled at 128 samples/s, the computer actually writes 144 words/s to the tape in order to provide timing, gain and other checks. The available memory, the 8K words remaining outside the program area, is thus filled every 2x4096/(144x4) = 14.2 s. Without additional memory, the system can record only for this period of time before turning the noisy tape recorder on. The Uher tape recorder can record data for approximately 6.5 hours in a serial format on 1/4 inch magnetic tape. The total capacity of the system is about 159 Mbits which contrasts with 368 Mbits on a 2400 ft, 9 track tape written at 1600 BPI.

The software which operates the seismographs is written in assembly language to ensure compact storage and efficiency. A number of control variables can be changed at checkout time to allow considerable flexibility in experiment design and execution. Many of these variables must be written in double precision and some of the calculations done in the determination of noise levels require triple precision or 36 bits. A good initial example of a control loop in the OBS computer involves the collection of periodic noise records on the seafloor. This portion of the program referred to as 'Auto Noise Record' is controlled by three variables. The first variable is a double precision entity composed of the words ANRLSB and ANRMSB where LSB and MSB denote the least and most significant words of the pair. These two words determine the time of the first automatic noise recording with respect to the time the clock in the OBS is reset prior to launch. This pair of variables was set on each OBS during the teleseismic recording portion of the experiment to ensure the noise windows opened simultaneously to allow later processing for coherence across the array. The next variable (ANRTML, ANRTMM) specifies the intervals for repetition of the recording and is normally set to 4 hours. We did change this variable for the NGENDEI experiment to ensure that tape usage for noise recording did not seriously affect the number of teleseisms we could record. The last variable controlling

the automatic noise recording is the single work ANRREC which is the duration in seconds of the noise recordings.

Prior to the NGENDEI experiment we added considerable CMOS memory to the system to allow recording noise and teleseisms without interference from the rotation of the tape recorder. Additional 64 Kword memory boards can be added to the recorder up to a maximum of 4 boards. The single precision variable KPTR describes the number of boards installed; each board adds approximately 113 s of memory for all four channels and greatly extends the noiseless recording time available to the system. When the capsule is configured with the expanded memory area, the 8K memory boards usually in use are removed. The 12 bit word of the computer normally permits only 4096 (4K) words to be addressed in memory. An additional 'memory extender' card is added to permit a larger address space; during operation with the 64K word boards this board is also removed. The large memory boards are not treated as RAM, as was the case with the normal 8K CMOS memory, in that the software and hardware permit only serial writes and reads in a circular fashion within the augmented memory space. The controller board for the large scale memory keeps pointers available to the current read and write positions, but arbitrary access is not facilitated. This practice eliminates the need for an enormously expanded address space, does not require additional computer power to operate the memory extender which would otherwise be required and reduces the power supply load. The full complement of 64K word boards actually draws *less* power than the normal 8K words used as RAM! Because the system was new for this experiment, it was used only during the teleseismic portion of NGENDEI and then only on four of the six available capsules. The added memory worked without encountering any problems and is now a routine part of capsule operations.

The setup of the seismographs was outlined in the earlier acoustics section and the function of the two variables (WAITLL, WAITMM) and (RUNTML, RUNTMM) was discussed. The setup portion of the program also controls the interval between subsequent leveling sequences through the double precision variable (TPTML, TPTMM). Normally this is set at 24 hours, but can be changed if desired. The system is periodically leveled to ensure that settling in the sediments does not introduce tilt.

The seismograph changes gain on the seafloor in response to changing noise levels in order to ensure that seismic noise does not consume the entire dynamic range of the system and, on the other hand, to ensure the system is limited by ground noise at all times in order to maintain high sensitivity. The detection of noise levels on the seafloor requires that the system average detected levels over sufficiently long times that a stable estimate of noise is available for setting these gains. This process involves the calculation of both short term averages (STA) and long term averages (LTA); the LTA is actually calculated using the results of the STA. The STA is calculated by summing the absolute levels (128 of them for each channel) over the period of a

second. The LTA is then updated by the most recent STA. The computer updates the gain of each channel individually every GANWAT seconds where GANWAT is normally 512 s. The gain is adjusted to ensure that the value of the LTA lies within a pair of bounds specified by the investigator. The two double precision variables are (LOBNDL, LOBNDM) and (UPBNDL, UPBNDM) and are normally set to $8x2^7$ and $20x2^7$ where the 2^7 multiplier is a constant used in the calculation and the digital levels are 8 and 20 counts. During a noise study it might be desirable to raise these levels in order to keep the gain high enough to record all frequencies of interest at amplitudes in excess of the digitizing noise level. The STA and LTA are also calculated using the true rather than the absolute values of the levels for each channel. These averages should be zero, but may vary because of offsets in the analog amplifiers. This average is subtracted from the data prior to recording and trigger calculations.

The recording capacity of the seismograph is obviously limited by the tape storage so that triggering on earthquakes is necessary. The trigger system on the Scripps' OBSs is relatively simple although it is adaptive to ensure that a given experiment will come as close as possible to filling the tape. If the STA mentioned above exceeds RxLTA for two consecutive seconds on the vertical channel, a trigger occurs, the auxiliary memory is energized and the recorder is turned on some time later. The variable R is adjusted by the computer and can vary from 2 to 15. Two single precision variables control the setting of R and are called TRGMIN and TRGMAX. If the number of triggers exceeds TRGMAX in a specified time period, the ratio R is increased by one and if the triggers are less than TRGMIN, R is decreased by one. The time interval involved is controlled by the double precision variable (TRGTML, TRGTMM) and is normally set to 24 hours. The investigator must choose these variables to ensure that the required number of triggers will approximately fill the available recording capacity for the length of the experiment. Experience at the NGENDEI site showed that the noise was sufficiently stationary that the trigger ratio should be 3 at all times. The variable TRGMIN was set to 2-4 and TRGMAX was set to a very large number to ensure that the trigger ratio was actually driven to 3 and remained there. Two variables had to be changed to ensure the trigger ratio did not drop below three. These single precision variables, RATIO1 and RATIO2, are normally set to 2 and -3. When an adjustment is to be made to the trigger ratio, the current value minus 1 is compared to -(-3). If this is greater than -(-3) the trigger ratio is decremented, but if it is less than or equal to -(-3) the trigger ratio is set to 2. The values of RATIO1 and RATIO2 were changed to 3 and -4 for the teleseismic portion of the NGENDEI experiment. A final variable TRIGRAT controls the initial trigger level of the system. This is normally set to 4, but some OBSs were set up with TRIGRAT = 3 in order to minimize the time period the instruments required for reaching the desired trigger level. When experience with a particular site is not available prior to an extended launch, the 'intelligence' built into the trigger could be very helpful.

The conduct of an explosion seismology experiment with a digital OBS requires that the capsule recognize a shooting schedule to ensure that seismograms will be recorded at the correct times. The computer in the OBS recognizes a refraction schedule composed of a series of four variables. The first variable is a double precision number and contains the time, following capsule time reset during launch preparation, at which a recording series is to be started. The second word is a single precision variable which contains the duration of the recording interval in seconds. The third word contains the time interval between shots and the fourth indicates the number of shots.

The final set of variables contain times which control the action of the tape recorder with respect to the data which is in memory. Recall that NPTR X 113 is the number of seconds in the auxiliary memory. The single precision variable RECDLY is the number of seconds from a trigger decision until the recorder is turned on; normally this is set to 100 s when one memory board is in place. The system must also know how long to record after the STA is no longer able to assure a trigger condition. This must inevitably occur for a signal of any size since the LTA, with a time constant of 1024 s, will eventually grow and approximate the size of the STA. This recording time is set in the single precision variable MTRMS and is calculated from the relationship MTRMX = Buffer Size + Post Trigger Recording Interval + 1. Finally a single precision variable TRGDLY locks out the trigger algorithm for TRGDLY - 5 s after the tape recorder turns off. Normally TRGDLY is set to 12 s to ensure the tape recorder turnoff transient does not cause another false trigger. This is very important given that MTRMX is usually quite large to ensure that most of the teleseismic wavetrain is recorded.

In summary, the important variables, their functions and default values are:

Variable	Function	Default
ANREC	Length of auto noise rec	60 s
ANRLSB, ANRMSB	time from clock reset to first auto noise rec	0 s
ANRTML, ANRTMM	Time interval between auto noise rec	12 Hr
GANWAT	Length of time between gain adjustments	512 s
KPTR	Number of auxiliary memory boards	1
L	Number of consecutive s for trigger	2
LOBNDL, LOBNDM	Min number of triggers in specified time period	8x2
MTRMAX	Used to compute # seconds of rec after trigger end	154 s
RECDLKY	# of seconds after trigger for recorder start	100 s
RATIO1	Used to set the minimum trigger ratio of the	2
RATIO2	system	-3
RUNTML, RUNTMM	Number of seconds in setup run	4096 s
TPTML, TPTMM	Time interval betweeen seis levelings	24 Hr
TRIGRAT	Beginning trigger ratio	4
TRGDLY	Calculates # s after rec turnoff for trig restart	12 s

TRGMIN	Minimum # triggers in specified period	1
TRGMAX	Maximum # triggers in specified period	4
TRGTML, TRGTMM	Time interval over which to check trigger #	24 Hr
UPBNDL, UPBNDM	Max # of triggers in a specified time period	20x2
WAITLL, WAITMM	time interval from first diagnostics to leveling	3 Hr

The assignment of the variables for the OBS launches during NGENDEI are given below for the variables which were different from the default values:

OBS REFRACTION

OBS	Launch Date	Variable	Value
KAREN	28Jan83	No changes	
JUAN	29Jan83	LOBNDL, LOBNDM	$16x2^7$
		UPBNDL, UPBNDM	$40x2^7$
SUZY	29Jan83	No changes	
LYNN	30Jan83	LOBNDL, LOBNDM	$16x2^7$
		UPBNDL, UPBNDM	$40x2^7$

INITIAL TELESEISMIC RECORDING

OBS	Launch Date	Variable	Value
PHRED	23Jan83	ANRLSB, ANRMSB	7 Hr 50 min
		ANRTML, ANRTMM	3 Hr
		TRGMIN	6
		TRGMAX	18
JANICE	24Jan84	ANRLSB, ANRMSB	7 Hr 40 min
		ANRTML, ANRTMM	3 Hr
		TRGMIN	4
		TRGMAX	12

TELESEISMIC RECORDING PERIOD

OBS	Launch Date	Variable	Value
JANICE	5Feb83	ANRLSB, ANRMSB	85 Hr 30 min
		ANRTML, ANRTMM	24 Hr
		RATIO 1	3
		RATIO2	-4
		TRGMIN	2
		TRGMAX	6
PHRED	9Feb83	ANRLSB, ANRMSB	30 Hr 20 min
		ANRTML, ANRTMM	24 Hr
		RATIO1	3
		RATIO2	-4

		TRGMIN	4
		TRGMAX	16
		TRIGRAT	3
SUZY	10Feb83	ANRLSB, ANRMSB	29 Hr 30 min
		ANRTML, ANRTMM	24 Hr
		RATIO1	3
		RATIO2	-4
		TRGMIN	4
		TRGMAX	16
		RECDLY	90 s
JUAN	11Feb83	ANRLSB, ANRMSB	15 Hr 50 min
		ANRTML, ANRTMM	24 Hr
		RATIO1	3
		RATIO2	-4
		TRGMIN	4
		TRGMAX	16
KAREN	11Feb83	ANRLSB, ANRMSB	27 Hr 25 min
		ANRTML, ANRTMM	24 Hr
		MTRMAX	240 x
		RATIO1	3
		RATIO2	-4
		TRGMIN	2
LYNN	12Feb83	ANRLSB, ANRMSB	3 Hr 29 min
		MTRMAX	300 s
		RATIO1	3
		RATIO2	-4
		TRGMIN	2

OBS POWER SUPPLY

The Scripps' OBSs are powered from a combination of alkaline and Li/SO_4 cells. The bulk of the power is obtained from high capacity lithium cells to minimize space and weight requirements although this choice of chemistry demands care in handling the batteries. The power packs have been especially designed to minimize the chances of inappropriate handling.

The 6 Volt power supply consists of a pair of 3 Volt, 30 Ampere-Hour cells in series. The 12 volt power supply is obtained from another pair of these cells driving an inverter. The power for the leveling mechanism and the tape recorder is taken from three 10 Ampere-Hour cells in series to provide the 7.5 volts required by the Uher tape recorder.

The alkaline cells power the acoustics, the timed releases and the board used to detect the acoustic command for release. 24 AA cells and 4 C cells power the acoustics while 4 AA cells are used for each of the release boards. The power for firing the explosive bolts is provided by three 9 volt alkaline batteries connected in series; each timed release board contains one of these power packs while the acoustics release

board uses two of the packages. The power for the release boards is entirely separate and the electronics and required oscillators are isolated from the main computer to ensure a maximum amount of reliability through redundancy. None of these instruments have ever been lost at sea largely because of the care given to this design.

The OBSs were left on the bottom for in excess of 45 days during the teleseismic recording portion of the NGENDEI experiment. The instruments draw less than 400 mW when not actually recording and, given the conservatism of the manufacturer's specifications for battery capacity, the seismographs are capable of deployments at least as long as 60 days with the current battery complement.

CONCLUSIONS

The ocean bottom seismographs from the Scripps Institution of Oceanography performed exceptionally well during the course of the NGENDEI seismic experiment. Several deployments lasted for more than 45 days and, in each case, the capsules returned high-quality data. Difficulties with the response of the horizontal channels were encountered in a number of instances as described in other papers in this volume and a satisfactory solution to this instrumentation problem has not been found. The use of software to control the operating characteristics of the seismographs was largely successful although the flexibility of the system is still limited by the rather primitive nature of the processor being used for capsule operation. Many of the water waves recorded by the instruments were clipped in the digitization process. We have found such data to be extremely valuable in evaluating the structure of the shallow seafloor. Modifications to the system to permit "dynamic" gain ranging or, equivalently, a floating-point digitizing scheme would be very welcome.

Creager, K.C. and L.M. Dorman, 1982. Location of instruments on the seafloor by joint adjustment of instruments and ship positions, J. Geophys. Res., 87, 8379-8388.

Prothero, W.A., 1979. Earthquake signal processing and logging with a battery-powered microcomputer, Bull. Seism. Soc. Am., 70, 2275-2290.

Riedesel, M., J.A. Orcutt, K.C. Macdonald and J.S. McClain, 1982. Microearthquakes in the black smoker hydrothermal field, East Pacific Rise, J. Geophys. Res., 87, 10613-10623.

TABLE 1
OBS OPERATIONAL SUMMARY

OBS	Time	Date	Purpose of Deployment	Code
PHRED	0640	23Jan	Teleseismic and noise level recording	PH1
JANICE	0626	24Jan	Teleseismic and noise level recording	JA1
KAREN	0102	29Jan	Seismic refraction and noise level recording	KA1
JUAN	1104	29Jan	Seismic refraction and noise level recording	JU1
SUZY	0039	30Jan	Seismic refraction and noise level recording	SU1
LYNN	1124	30Jan	Seismic refraction and noise level recording	LY1
JANICE	0455	1Feb	Teleseismic and noise level recording	JA2
JANICE	1433	5Feb	Teleseismic and noise level recording	JA3
PHRED	2045	9Feb	Teleseismic and noise level recording	PH2
JUAN	1136	10Feb	Teleseismic and noise level recording	JU2
SUZY	2247	10Feb	Teleseismic and noise level recording	SU2
JUAN	1124	11Feb	Teleseismic and noise level recording	JU3
KAREN	2142	11Feb	Teleseismic and noise level recording	KA2
LYNN	1357	12Feb	Teleseismic and noise level recording	LY2

Code	Time and Date Recovered		# Events Recorded	Comments
PH1	0850	7Feb	358	
JA1	0715	31Jan	91	Fired 2nd bolt on leak indication upon recovery. Apparently leaked a drop of seawater by O-ring at low pressure.
KA1	0807	9Feb	758	
JU1	0535	9Feb	789	Horizontal channels did not record properly probably due to excessive tilt.
SU1	0556	10Feb	894	
LY1	0817	10Feb	898	Horizontal channel 2 did not record properly probably due to excessive tilt.
JA2	0815	3Feb	0	A/D board had been placed in wrong slot in card cage upon checkout. This is only card requiring a specific location.
JA3	1520	22Mar	114	
PH2	0905	23Mar	158	
JU2	0250	11Feb	4	Recalled after teleseismic launch when acoustics indicated one horizontal gain was extremely high (9). Seismometer might have been tilted.
SU2	0531	22Mar	153	
JU3	1100	22Mar	119	
KA2	0600	23Mar	112	
LY2	1040	23Mar	282	

Code	Clock Drift (ms/day) All slow
PH1	73.609
JA1	44.189
KA1	105.791
JU1	43.712
SU1	133.991
LY1	34.112
JA2	-
JA3	36.669
PH2	75.217
JU2	21.878
SU2	133.719
JU3	39.420
KA2	103.999
LY2	31.655

TABLE 2
OBS SEAFLOOR POSITIONS

DEPLOY	LAT	LONG	DEP(m)	ABS ERROR ELL. 1 S.D. (km) s-maj	s-min	azi	REL. ERROR ELL. 1 S.D. (km) s-maj	s-min	azi
KA1 ref	-23.81733	-165.52758	5612	0.115	0.079	148	0.027	0.014	139
JU1 ref	-23.82024	-165.53244	5618	0.133	0.080	143	0.037	0.014	135
SU1 ref	-23.81737	-165.52745	5612	0.119	0.081	151	0.027	0.019	122
LY1 ref	-23.82077	-165.53115	5603	0.126	0.082	145	0.027	0.019	122
PH1 tele1	-23.94182	-165.76130	5676	0.115	0.073	162	0.160	0.071	138
JA1 tele1	-23.93398	-165.78653	5704	0.458	0.191	137	0.315	0.138	138
JA2 tele1	-23.93612	-165.76672	5717	0.124	0.085	170	0.161	0.078	139
JA3 tele2	-23.81823	-165.52578	5605	0.080	0.062	158	0.071	0.047	139
PH3 tele2	-23.82394	-165.53820	5544	0.149	0.075	136	0.106	0.024	125
KA2 tele2	-23.80939	-165.54157	5593	0.145	0.103	115	0.116	0.056	119
LY2 tele2	-23.81230	-165.55120	5503	(Posit. based on drop point)					
SU2 tele2	-23.85997	-165.29674	5654	0.292	0.190	10	n.a.		
JU3 tele2	-24.04531	-165.53030	5579	0.151	0.118	69	n.a.		

Figure 1: Displacement power spectrum for MSS for a period of time during NGENDEI experiment. Spectral estimate has been stabilized by stacking over ten realizations of the noise.

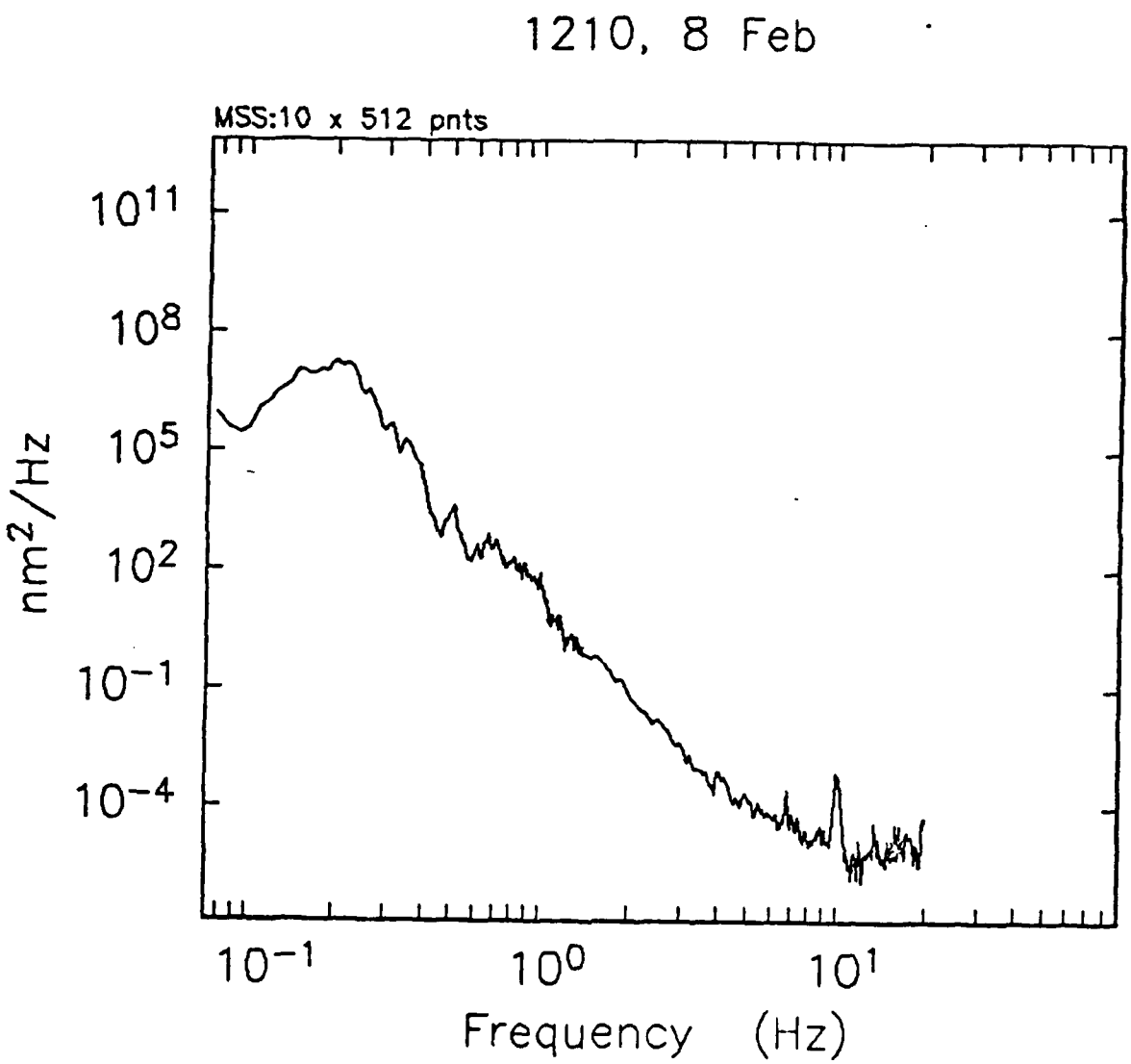


Figure 2: OBS locations for the refraction experiment relative to a common center of mass. Error ellipses are 95% confidence limits. Diamonds show the approximate location of the OBS drop points. The OBS locations are keyed with the notations (eg PH1) from the text.

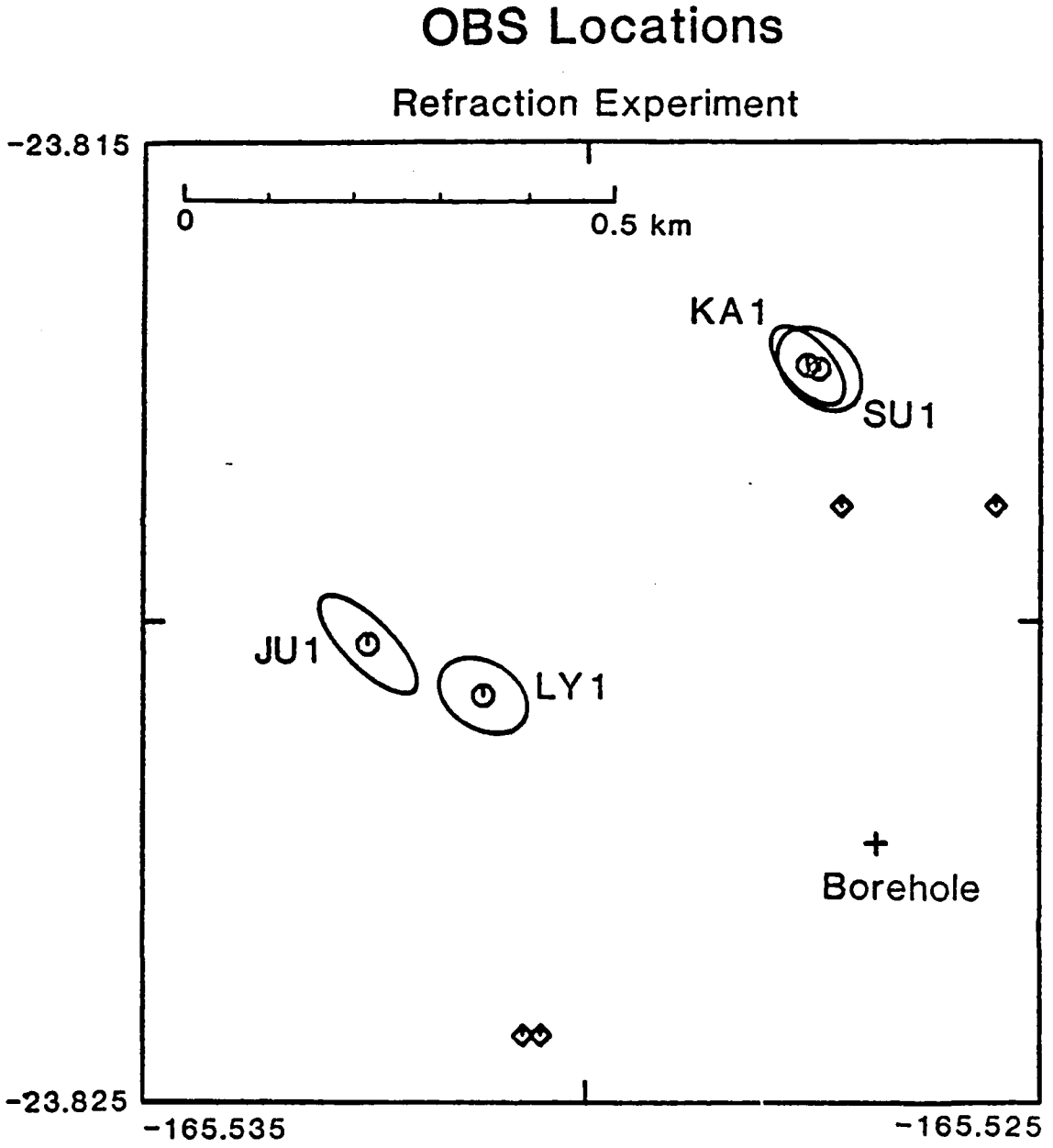


Figure 3: Absolute OBS locations for the initial teleseismic experiment. Error ellipses are 95% confidence limits; drop points are shown as up-arrows.

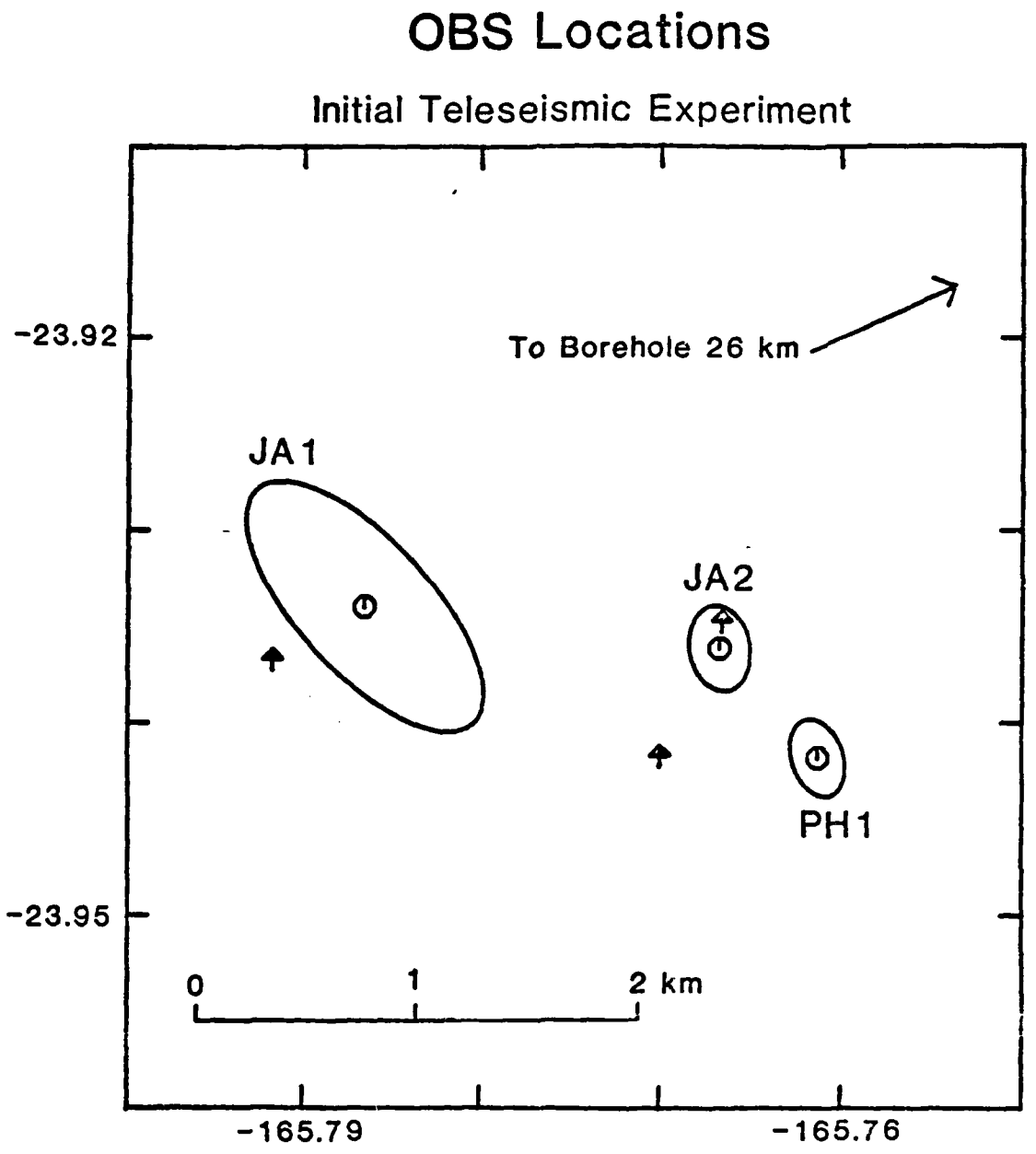


Figure 4: Absolute OBS locations near the borehole for the 45 day teleseismic experiment. Error ellipses are 95% confidence limits; drop points are shown as diamonds. The location for LY2 is approximate because no joint ranging information is available for this deployment.

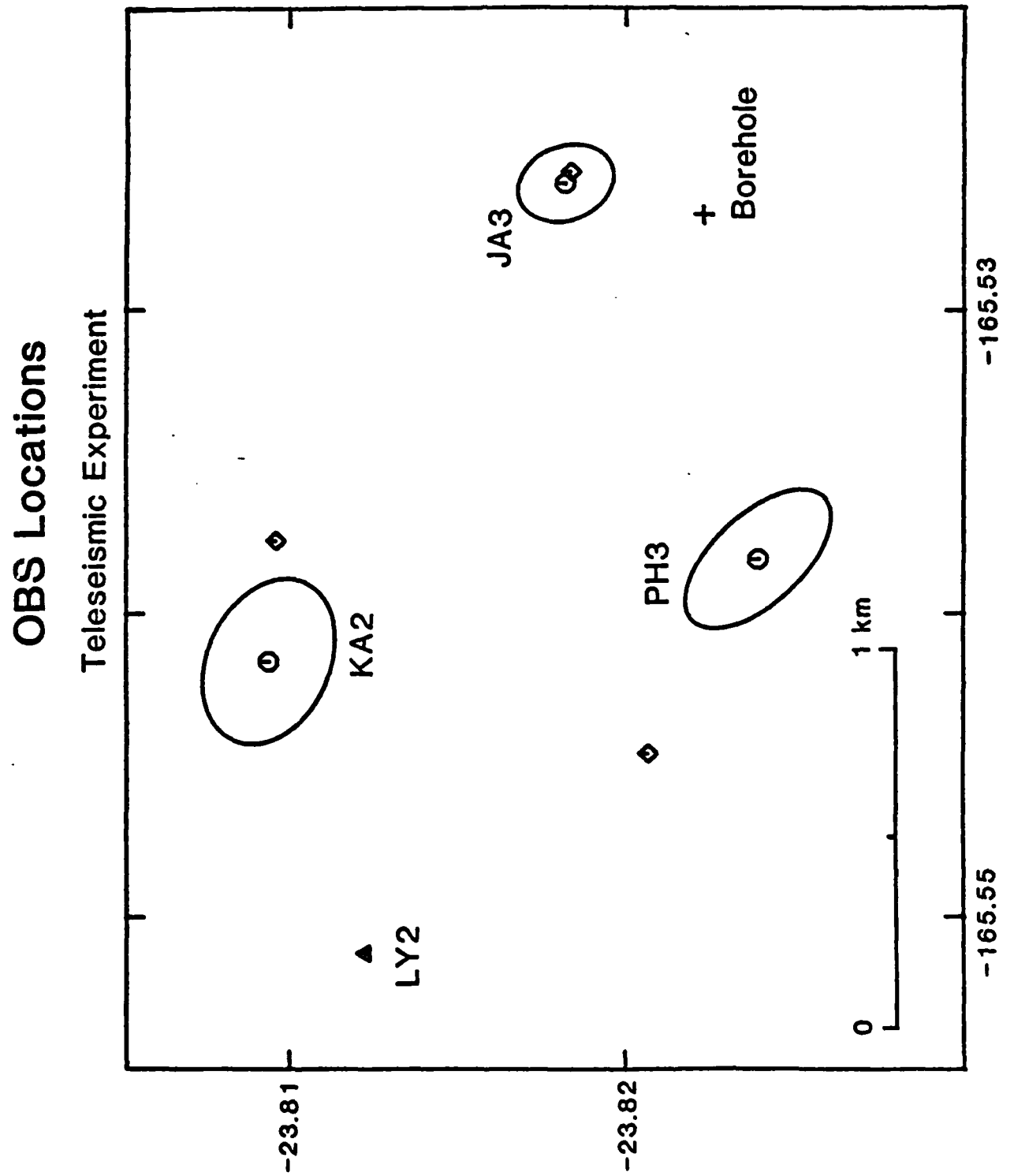
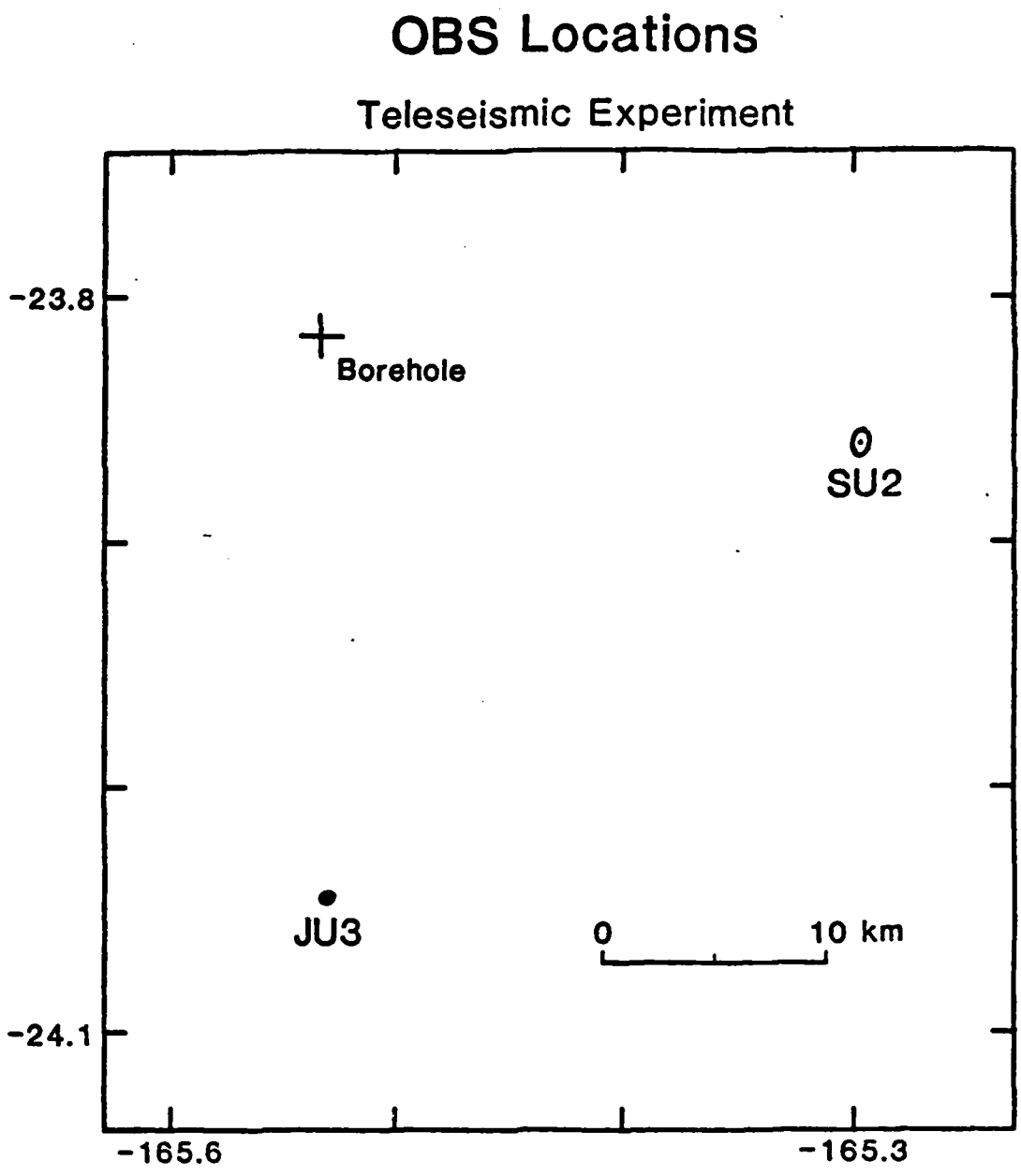


Figure 5: Absolute OBS locations away from the borehole for the 45 day teleseismic experiment. Error ellipses are 95% confidence limits.



OBS BLOCK DIAGRAM

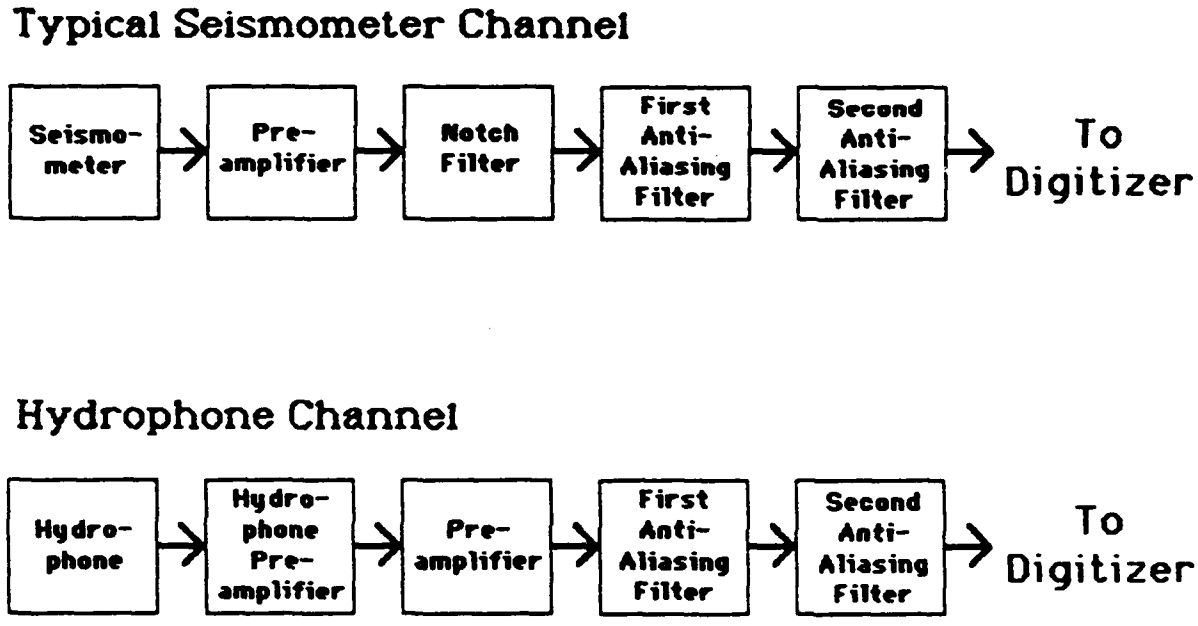


Figure 6: Data streams for OBS inertial and hydrophone channels. Notch filter for pre-whitening is used only on the inertial channels.

Figure 7: Amplitude response of notch filter used to pre-whiten seismic noise. The filter minimum is near the microseism peak while the maximum is near frequencies of interest in explosion seismology.

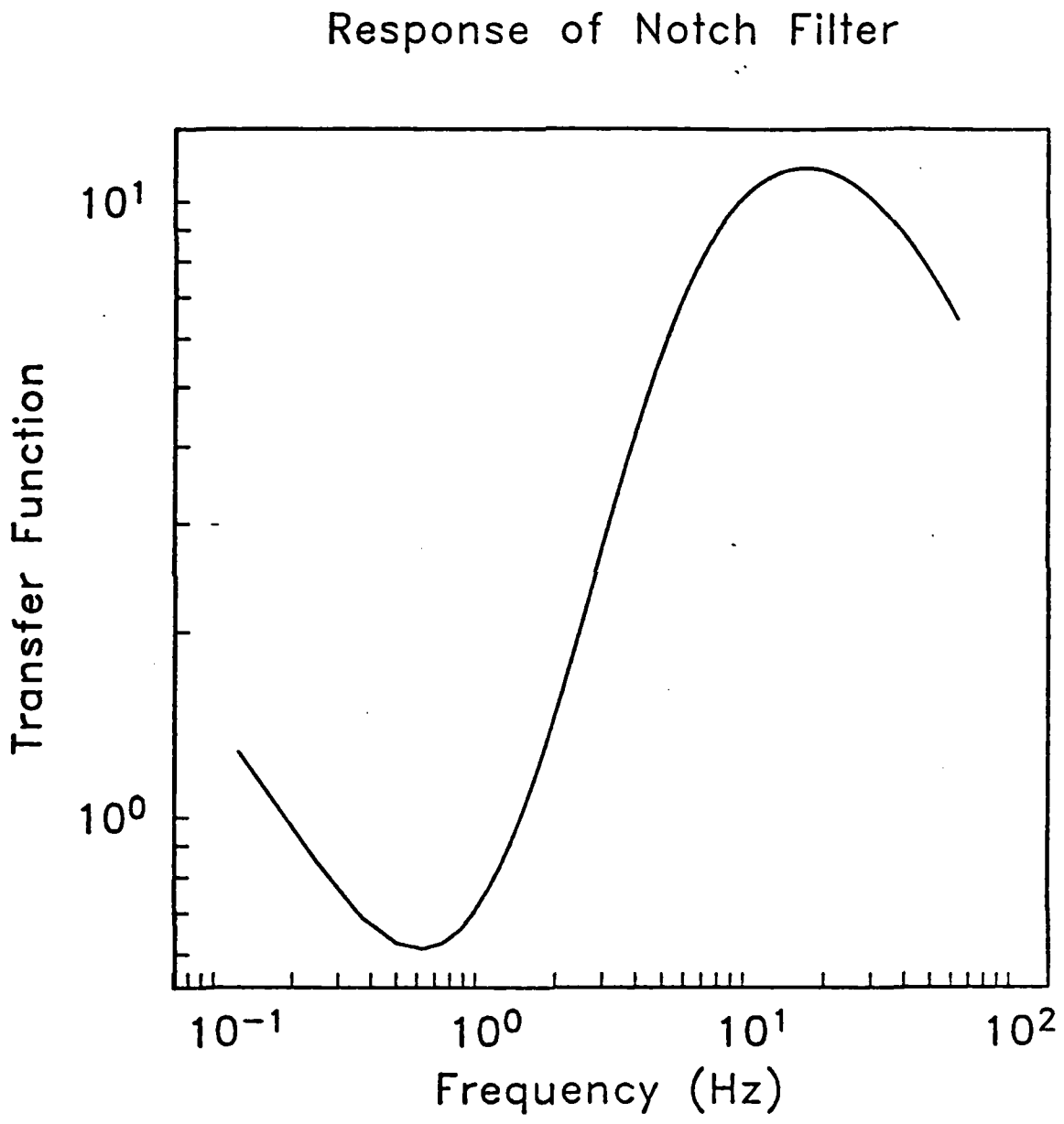


Figure 8: Amplitude of OBS response function with (Normal) and without notch filter. The removal of the notch filter emphasizes the low frequencies needed for triggering on low-frequency teleseismic arrivals.

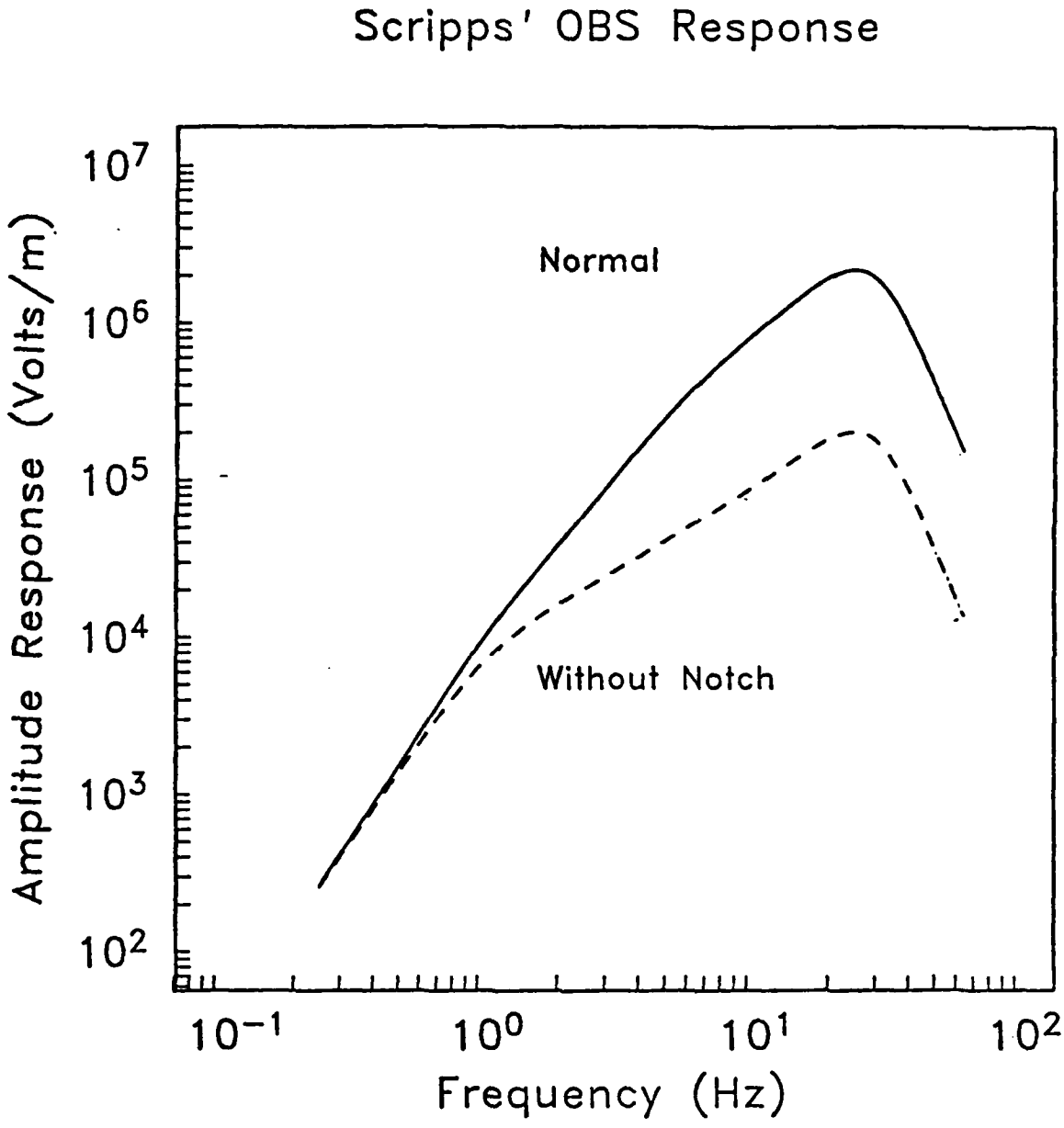
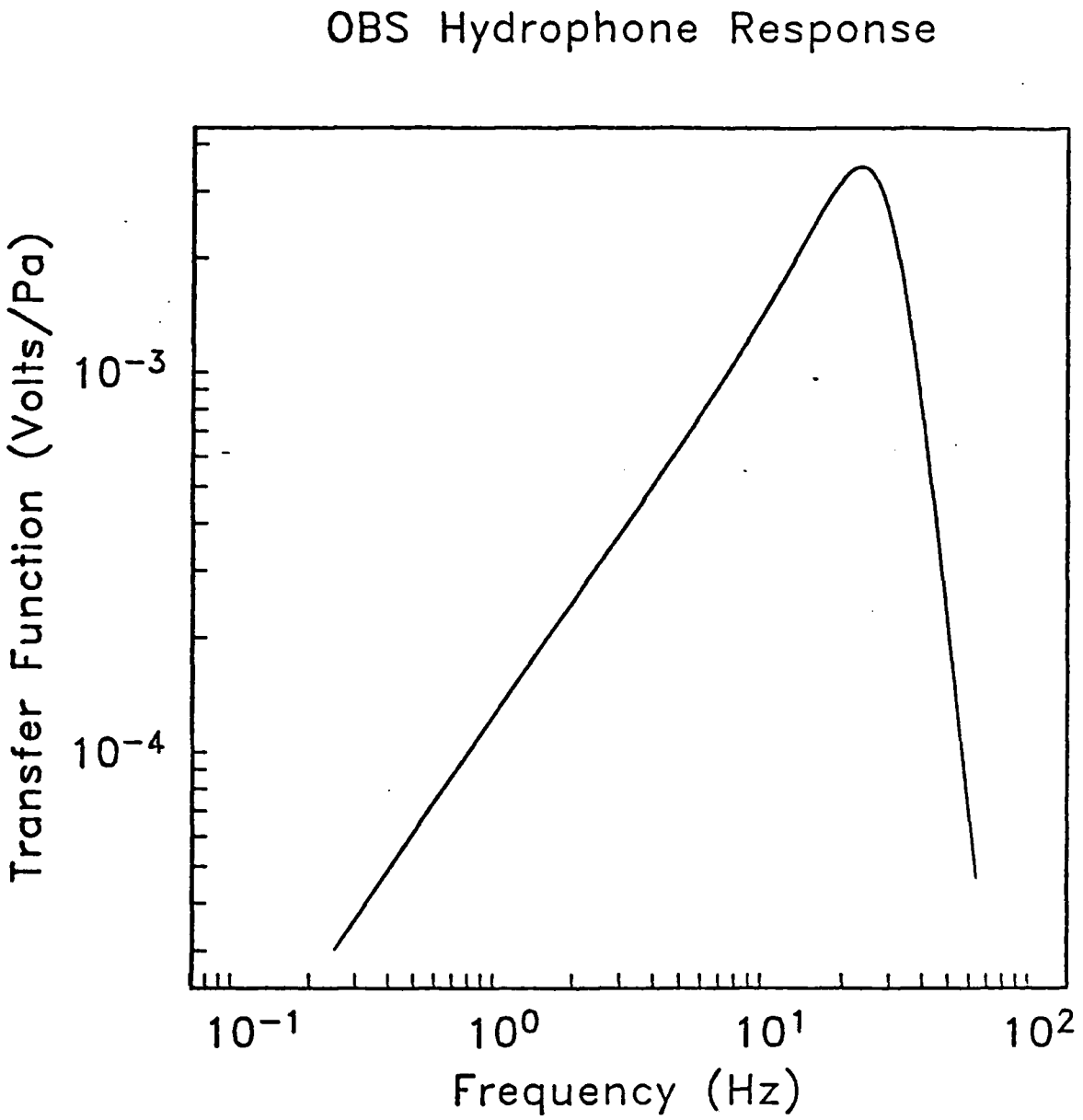


Figure 9: Response of OBS hydrophone channel. A notch filter is not used to pre-whiten the hydrophone response. The spike at 10 Hz is due to D/V Challenger thruster operation.



CHAPTER 4

PRELIMINARY ANALYSIS OF OCEAN BOTTOM AND SUB-BOTTOM AMBIENT MICROSEISMIC NOISE DURING THE NGENDEI EXPERIMENT

Richard G. Adair[1], John A. Orcutt[1], and Thomas H. Jordan[2]

1 Institute of Geophysics and Planetary Physics,
Scripps Institution of Oceanography
La Jolla, California 92093

2 Department of Earth, Atmospheric,
and Planetary Sciences
Massachusetts Institute of Technology
Cambridge, Massachusetts 02139

ABSTRACT

Simultaneous measurements of ambient microseismic noise at and below the seafloor are compared over the band 0.2-7.0 Hz using MSS and OBS data collected during the Ngendei Seismic Experiment. The MSS sensors rested unclamped at 124 m sub-bottom, 54 m within basement rock, while six 4-component OBSs were deployed at distances ranging from 0.5 to 30 km from the borehole. Noise spectra of displacement power density at both borehole and ocean- bottom sites typically displayed the microseism peak between 0.1 and 0.3 Hz. Vertical-component spectra fell off from this peak at 60-80 dB/decade with various peaks superposed. The peaks suggest a regional forcing of seismic waves trapped at the ocean bottom- seafloor interface. Vertical ocean-bottom and borehole noise levels are nearly identical at the microseism peak, on the order of 10^{8} nanometers^{2}/Hz, but OBS values exceed MSS values by 20 dB or more at frequencies between 0.5 and 7 Hz. Horizontal- component noise levels in the borehole were essentially the same as the vertical-component levels. At the ocean bottom, horizontal noise spectra were similar in shape to and 15-20 dB higher than vertical spectra between 0.4 and 7 Hz, but had comparable values at the microseism peak, which extended to approximately 0.4 Hz on the horizontal components. Ocean-bottom pressure measurements of ambient noise are comparable to other published measurements, having a value on the order of 10^{4} Pascals^{2}/Hz at the microseism peak and falling at higher frequencies at 50 - 60 dB/decade. Leg 91 vertical-component noise measurements contrast with those from the prototype MSS deployment during DSDP Leg 78B in which levels at a proximate seafloor site exceeded borehole levels by 10-30 dB over the band of valid comparisons (0.16-2.2 Hz). Between 0.3 and 2.2 Hz, Leg 78B borehole levels were greater than those of Leg 91 by 10-20 dB. Leg 78B spectra were relatively featureless. High vertical- component coherence was seen at the microseism peak between pairs of OBS's separated by 0.7 km. At the microseism peak vertical-component noise levels at the quietest land sites are between 10 and 30 dB lower than those measured in the borehole during Leg 91. At higher frequencies the noise levels measured in the borehole approached those of the quietest land sites.

INTRODUCTION

Poor sensitivity and high levels of instrumental noise plagued the earliest generation of ocean bottom seismographs (OBSs) employed during the 1960's. Most of these efforts were funded by the Advanced Research Projects Agency (ARPA) of the Air Force through Project VELA Uniform (Prentiss and Ewing, 1963; Bradner and Dodds, 1964; Latham and Sutton, 1966; Latham and Nowroozi, 1968; Schneider and Backus, 1964; and Schneider et al., 1964) to facilitate the seismic discrimination of nuclear explosions. It was hoped that ambient ocean bottom noise levels would be substantially lower that at land sites, but in fact they were

found to be comparable or higher. This result, coupled with the logistical difficulty of employing OBSs, led to the eventual abandonment of this research effort. The current revitalization of ocean bottom seismograph usage is due primarily to recent developments in semiconductor technology and hardware, particularly in digital recording techniques, and they have been used primarily to investigate seafloor structure through refraction experiments. Several problems still arise, however, from the nearly ubiquitous blanket of sediments in the world's waters. OBS's must contend with poor coupling and signal 'ringing' due to unconsolidated sediments (Sutton et al., 1981), as well as the inherent difficulty of observing important converted shear phases (Spudich and Orcutt, 1980). A final difficulty, which is the primary interest of this paper, is the high ambient noise levels at the ocean bottom, thought to be due to noise propagation as low-order Stoneley wave modes trapped near the ocean bottom-seafloor interface. This problem would be mitigated by seismometer emplacement in the more rigid material underlying the sediments. Accordingly, interest has kindled in the use of marine borehole seismographs as an alternative to OBS's. Several Deep Sea Drilling Project (DSDP) legs have been devoted to 'oblique refraction' studies employing commercially-available seismometer systems in boreholes (Stephen et al., 1980, and Stephen et al., 1983). However, these data are not suitable for ambient noise analysis, essential for optimal instrument design and siting.

Two marine borehole systems, the ocean sub-bottom seismometer (OSS) of the Hawaii Institute of Geophysics (HIG) and the DARPA (Defense Advanced Research Projects Agency)-funded Marine Seismic System (MSS) have recently been developed to answer these needs. A detailed description of the OSS and its operational use may be found in the initial reports of DSDP Leg 88 (this volume), and in Duennebier and Blackington (1983).

The feasibility of the MSS design and installation procedure was successfully tested with the deployment of a prototype borehole instrumentation package in Hole 395A during DSDP Leg 78B in late March, 1981 (Hyndman et al., 1984). Noise data and refraction signals were recorded on the prototype's two vertical-component seismometers over a 26 hour operational period. Simultaneous measurements of vertical-component noise at a nearby seafloor site were higher than the boreholes levels by at least 10 dB between 0.16 and 2.2 Hz (Adair et al., 1984). Encouraged by the Leg 78B results, a deployment of the complete MSS ensemble was attempted on DSDP Leg 88, but was thwarted by foul weather and drilling problems (Duennebier et al., in press). The MSS deployment was rescheduled for Leg 91. Originally a DSDP transit leg between Wellington, New Zealand, and Papeéte, Tahiti. The new Leg 91 was designed to specifically answer several outstanding questions regarding the generation and propagation of ambient microseismic noise in the deep ocean, and the relative characteristics of seismic signals at and below the seafloor. The experiment employed an array of six OBSs as well as the

MSS at various distances from the drill site. This paper discusses some preliminary analyses of the Leg 91 seismic data regarding the relative character and values of ambient microseismic noise at and below the seafloor.

INSTRUMENTATION AND OPERATIONS

Marine Seismic System

Only the salient features of the MSS operations and seismic instrumentation will be considered here; detailed descriptions of the system and its operational use are found elsewhere in this volume (Adair et al., 1984). When operationally deployed, the MSS comprises a borehole instrumentation package (BIP) containing the seismic sensors connected by coaxial cable to an ocean bottom recording system, the Bottom Processing Package (BPP). The BIP was developed by Teledyne Geotech, Inc., and the BPP by Gould, Inc. Following BIP emplacement, data are recorded on two shipboard consoles, each distinguished by different digitization methods and post- digitization processing (described below). One of the consoles, referred to here as the Gould system, emulates most of the BPP functions. The other, referred to as the Teledyne system, monitors the BIP and provides redundant data logging. The BIP contains separate electronics bays for communication with each of these consoles. After a satisfactory checkout of the BIP and a period of shipboard data recording, the coaxial cable link to the BIP is connected to the BPP, which is then lowered to the seafloor to record up to 45 days of data. A submerged mooring, the Installation, Recovery, and Reinstallation (IRR) system, enables BPP deployment and recovery.

A triaxial set of Teledyne Model S-750's (orthogonal horizontals, X and Y, and one vertical Z) and a backup vertical component (B) compose the MSS seismic sensors. The backup sensor B is configured 175.5 cm below the primary vertical sensor Z. During BPP deployment, output from a hydrophone mounted on the BPP replaces that of the backup sensor.

Output from each of the three primary sensors is split into a mid-period (MP) and short-period (SP) passband between approximately 0.1-2.0 Hz and 0.5-20.0 Hz, respectively, while the redundant vertical is passed through the SP band only. The resultant seven data streams, labeled MX, MY, MZ, SX, SY, SZ, and SB, are then digitized and transmitted to logging devices over the coaxial cable. Output destined for the shipboard Teledyne system is sampled, gain-ranged, and digitally- represented to yield a 21-bit dynamic range with 14-bit resolution. MP data are digitized at the rate of 4 samples/second (s/s), and SP data at 40 s/s. Either of the SP vertical channels may be sampled 80 s/s to the exclusion of the other. Data transmitted to the BPP and its shipboard counterpart are oversampled 256 times and their amplitudes represented by means of an enhanced delta modulator encoding (EDME) technique. These

encoded, oversampled streams are then sent to the recording unit, digitally convolved with a low-pass, finite-impulse response (FIR) filter, resampled at their proper rates (4 and 40 s/s for the MP and SP data, respectively), and decoded as a 24-bit integer with 24-bit resolution.

The low-ripple, zero phase-shift FIR filter is nearly flat to 75% of the Nyquist frequency, and thereafter falls 160 dB by 125% of the Nyquist frequency, a decline of approximately 720 dB/decade. Figure 1a illustrates the net MSS displacement responses for the MP and SP passbands; the dashed lines at their high frequency ends depict the augmentation due to the FIR filter. At the Nyquist frequencies and in the absence of this filter, the MP response is down 28 dB from its peak, while the SP response is down only 1.5 dB from its peak. In the case of the 80 s/s SP vertical data recorded on the Teledyne system, the response is down 11.5 dB by 40 Hz from the peak value.

OCEAN BOTTOM SEISMOGRAPHS

The six OBS's are four-component (one vertical and two horizontal seismometers, and a hydrophone), digital event recorders (Moore et al., 1981). Sensor outputs are amplified at a gain of 2^n ($0 \leq n \leq 9$), bandpassed, and digitized with a 12-bit word at 128 s/s. The gain of each channel is modified only when the long-term average of its digital output falls outside pre-defined limits of a few least significant bits. Semiconductor memory continuously accumulates four-channel data, time code, and gain information in a cyclically-overwritten buffer to avoid mechanical and electric contamination due to recorder operation. The length of this 'pre-event' buffer is normally approximately 13 seconds, but was extended to approximately 58 seconds in several of the capsules (see Tables 1 and 2 for specific OBS characteristics during the experiment). An OBS buffers an event to tape when scheduled and/or when triggered by a comparison criterion of long term and short term averages of the vertical-component's digital output. Two seismometer responses (Figure 1b) are selectable prior to capsule deployment by the exchange of a filter board. One of these, designated 'teleseismic', emphasizes lower frequencies more than the other, designated 'refraction', in order to make the OBS event-triggering algorithm more sensitive to moderate-amplitude, high-frequency depleted teleseismic signals. The hydrophone response (Figure 1b) is the same for both the 'refraction' and 'teleseismic' capsules. An acoustic transducer permits capsule ranging, release control, and exchange of diagnostic information.

OPERATIONS

Leg 91 events may be broken into three phases, a refraction experiment, a teleseismic experiment, and instrument recovery, during all of which noise measurements were made. These periods are referred to as MS1, MS2, and MS3, respectively. Figures 2 and 3 show the OBS locations during the refraction and teleseismic experiments, respectively. Reference latitudes and longitudes are given in north and east. Octagons centered on ellipses depict computed OBS locations and their 95% confidence bounds based on least-squares modeling of satellite and acoustic ranging data (Creager and Dorman, 1982). Diamonds and arrows denote OBS drop points estimated from satellite navigation and Melville radar ranging of Challenger. The borehole site is computed relative to the best satellite estimate of Challenger's location. Capsules are referred to by the first two letters of their names and a numeral denoting the deployment number. Tables 1 and 2 give identification name, location, deployment period, range and azimuth from the BIP, response type and pre-event buffer length of each capsule for the refraction and teleseismic experiments, respectively. Figure 4 summarizes events pertinent to the noise experiment.

Events which occurred during MS1 include:

1) the deployment from Melville of four OBSs within 0.7 km of the MSS site (Hole 595B) and two at approximately 30 km (Figure 2 and Table 1),

2) the aborted deployment of the primary BIP (BIP-1) and the subsequent successful deployment of the backup BIP (BIP-2),

3) commencement of recording on the Teledyne and Gould shipboard recording consoles, and

4) shooting of five distinct refraction lines.

The four OBS's nearest Hole 595B (see Fig. 2a) recorded with the 'refraction' response in scheduled mode, and the other two (see Fig. 2b) with the 'teleseismic' response in both triggered and scheduled mode. The deployment attempt of BIP-1 was aborted because of coaxial cable damage caused by its hole-lock mechanism, which was dismantled in BIP-2. BIP-2 was therefore not locked in the hole, but coupling with the basement rock was accomplished by resting it at the hole bottom. Adequate cable isolation was achieved with a length of coaxial cable coiled on the seafloor.

During MS2:

1) the six OBSs, all employing the 'teleseismic' response, were redeployed in a roughly linear array extending WNW

from Hole 595B towards the Tonga-Kermadec Trench (Figure 3 and Table 2),

2) shipboard recording on Challenger concluded with fill-in shooting of the first portion of the fourth refraction line's outbound leg, and

3) the BPP was deployed.

Finally, during MS3:

1) the BPP and all OBS's were successfully recovered,

2) the BPP was discovered to have ceased operations approximately two days after its deployment due to a water leak in one of its two power battery pressure vessels,

3) further MSS data were recorded aboard Melville on both Teledyne and Gould consoles over a 16-hour period, and

4) the BPP was replaced with a dummy load and its recovery mooring reinstalled, leaving the BIP in Hole 595B.

NOISE DATA

Figures 5-7 chart data available for noise analysis during the Ngendei Expedition prior to the teleseismic experiment for each OBS. Such data were obtained from OBSs either at specifically-scheduled times or at times when refraction shots detonated late or not at all. In particular, a refraction line abandoned on February 8, 1983, because of BIP deployment delays provided a large number of noise samples. During the teleseism experiment, all OBSs recorded daily noise samples at CUT (Coordinated Universal Time) midnight. A total of nearly 1400 noise samples are available, over half of which were recorded simultaneously with MSS data.

During the refraction experiment, improper gain-ranging of OBS Juan's hydrophone channel resulted in signal amplitudes which frequently exceeded the maximum digital amplitude, i.e. the digital data were frequently clipped. During the teleseismic experiment, Janice's vertical-channel digitizer was unable to represent certain values (i.e. suffered a 'stuck bit'), and progressive tape head misalignment in Juan rendered data recorded beyond 25 February inaccessible.

The MSS recorded continuously except during maintenance or intermittent system malfunction. A total of 119.5 hours of Teledyne data and 126.5 hours of Gould data, including that from the BPP, were recovered. The BPP shut down approximately two days after its deployment, with the last datum recorded at 1805Z, 13 February, 1983, due to a water leak. No

further borehole data were collected until shipboard recording during recovery operations. The recovered MSS data may be obtained from the DARPA-funded Center for Seismic Studies (CSS) on 9-track tape. The Teledyne data are corrected for gain-range, and both Teledyne and Gould data are represented as 32-bit integers. These tapes identify sensors X and Y as East (E) and North (N), respectively, but, in fact, their orientations are unknown. Brief gaps of approximately 15 seconds due to the establishment of playback synchronization pepper the retrieved, reformatted Teledyne data.

Certain of the MSS data channels malfunctioned or were not recorded at various times. The horizontal MSS sensor Y malfunctioned for unknown reasons throughout the experiment. An unknown source of radio frequency radiation aboard Challenger interfered with the Gould console's channel SZ, so it was disabled and only the SP vertical backup SB was recorded. As scheduled during BPP deployment, channel SZ was recorded, and channel SB replaced by hydrophone data (channel SH). The Gould electronics bay in the BIP which initiates calibrations and processes channel MZ output malfunctioned just prior to BPP deployment and never resumed operation; however, MZ data were recorded at all times on the Teledyne system. As described above, one or the other of the Teledyne short-period vertical channels was not available when SP vertical-component data were digitized at 80 s/s.

DATA QUALITY

Data quality and valid frequencies of microseismic noise measurement were assessed with both time and spectral-domain criteria. In particular, power density and coherence estimates were computed in the manner described by Welch (1971). Spectra are obtained from de-meaned, non-overlapping data segments tapered with a normalized Hanning window using a mixed-radix Fast Fourier Transform algorithm (Singleton, 1979) which doesn't require power-of-two data lengths. Stable spectral estimates are then formed from averages of cross- and auto-spectra. Spectra are normalized so that the total power per Nyquist-frequency bandwidth is equal to the time-domain variance, which essentially folds the energy of the negative frequencies into that of the positive.

Figures 8 and 9 show a typical example of multi-channel MSS data from the Teledyne and Gould systems, respectively, recorded during the shipboard recording period. (Plot scales were chosen to show background noise levels, with the result that large amplitude signals are clipped.) Y-sensor malfunction is evident from both figures. Note that Gould channel SZ (Figure 9) is disabled, as explained above. The high-frequency content of Teledyne and Gould SP signals is mostly ship-generated by Challenger.

Proper representation of the data was investigated by computing relative amplitudes and timing between the two recording systems with cross-correlations and linear regressions of corresponding channels (Figure 10). Typically, both SP and MP Gould data led Teledyne data by 15 or 16 samples and were approximately 5.5 times greater in amplitude rather than 8 times as we would expect from the difference in digital word length (24 and 21 bits, respectively), a consequent 3 dB uncertainty in spectral estimates. Comparisons of data timing with independent time code (WWV) written adjacent to Teledyne data on strip-charts indicate that Gould's timing is in error. Teledyne sensor calibrations (Figure 11) of properly-functioning channels are within their expected norms by less than 4 dB, suggesting that Gould amplitudes are skewed. However, the calibration loop excludes portions of the total seismograph circuitry so this discrepancy cannot be verified. The departure of the MY and SY calibrations from the norms further demonstrate sensor malfunction. Note that the other MP channels depart drastically from the norm below approximately 0.2 Hz.

Figure 12 compares power spectral density estimates of simultaneous vertical-component Teledyne and Gould data with instrument noise spectra; the data are not corrected for instrument response. The peaks above 8 Hz in the SB spectra (Figure 12 b, c) are ship-generated. Peaks in the SB Teledyne spectrum (Figure 12 c) which are absent in the SP Gould spectrum (Figure 12 b) are manifestations of Teledyne aliasing. However, both Gould and Teledyne spectra have comparable values near the Nyquist frequency, implying improper functioning of Gould's SB FIR-filter.

Al o shown in Figure 12 are estimates of system noise, provided by H. B. Durham of Sandia Laboratories. The system noise is not significant over the entire SP passband for either Teledyne or Gould data. The white spectrum of quantizing noise for the Teledyne data, from the uniformly-distributed round-off errors of digital representation (see e.g. Bendat and Piersol, 1975, pp 231-232), has a level near 10^{-2} counts^2/Hz, well below the Teledyne signal level. Estimates of Gould's EDME noise level are not available. Differences at frequencies greater than 4 Hz are probably due to the combined effects of aliasing and actual signal differences over the 175.5-cm sensor separation. The MZ spectra (Figure 12 a) are similarly untainted by system and sampling noise, and, furthermore, have sufficient frequency response roll-off at the high end to avoid aliasing.

Spectral coherences further delineate frequencies usable for earth noise estimates. MP coherences (Figure 13a) typically exceed 0.95 below the FIR filter knee at 1.5 Hz except at 1 Hz, where it drops sharply over a very narrow band of frequencies. The sharp drop is due to energy present in the Gould data but not the Teledyne, and may be related to the Gould digitizing scheme. Gould and Teledyne SB coherence (Figure 13b) exceeds 0.8 between approximately 0.2 and 4.0 Hz. The coherence at higher frequencies declines amidst peaks due to ship-generated signals.

The sharp drops at approximately 2 and 4 Hz are similar to that at 1 Hz in the MP coherence. The frequencies bounding the SP band of high coherence varied a great deal during the MSS deployment, but generally were those shown in Figure 13b. Coherence estimates between SB and SZ Teledyne data (Figure 13c) were similar.

Figure 14 plots typical 4-channel OBS noise data collected from a capsule employed to record refraction signals. In this figure, ship-generated noise dominates high frequency features on all channels. Since the OBSs have no redundant sensors, frequencies dominated by system and instrument noise cannot be estimated from channel coherence.

OBS's employing the refraction response are able to measure lower-amplitude ground motion at high frequencies than are those employing the teleseismic response. The refraction response was specifically designed to 'whiten' the ambient signal in the presence of typical deep-sea microseismic noise (Moore et al., 1981), while the teleseismic response was designed to low-pass it. Filtered high-frequency amplitudes are consequently less than that represented by a least significant bit as recorded with the teleseismic response. Figure 15 compares spectra measured with the different OBS responses (upper curves) and shows the corresponding spectra of least-count noise (lower curves). The spectra, corrected for instrument response, were not measured simultaneously. Although most of the data comprising the teleseismic spectrum (solid upper curve) were recorded after ship departure, their spectral levels exceed ship noise levels measured with a refraction capsule (dashed lower curve) at most frequencies. In the teleseismic spectrum, sampling noise dominates frequencies greater than 15 Hz, and is probably significant in the range 7-18 Hz.

Ship-generated noise must be estimated on a case-by-case basis because it depended on which ship was proximal to an instrument and its speed and activity. However, in general ship noise spectra were characterized by sharply distinct peaks superimposed on a broadband level. The frequency of most of the peaks were multiples of some fundamental, implying that the peaks were due to cavitation by ship propellers (e.g. Urick, 1983). Challenger generated peaks at multiples of 10 Hz while maintaining station. Two other peaks at approximately 6.5 and 7.5 Hz were generated while it was under way. Peaks due to Melville were at multiples of 6 and 9 Hz.

Figure 16(a) compares vertical-component power density spectra, corrected for gain but not instrument response, of OBS Phred data recorded before (solid curve) and after (dashed curve) both ships departed. The capsule, located 1.6 km west of the borehole, employed the teleseismic response. The measurement prior to ship departure was made at 0000Z, 12 Feb 83 as both Challenger and Melville hove to within 2 km of the OBS. In this instance, ship-generated noise clearly dominates the spectrum at all frequencies above approximately 4.5 Hz. After ship

departure, least-count noise dominated above 7 Hz, although during MS2, the lowest frequency at which it dominated varied by ± 1 Hz because its level depends on OBS gain.

Some ambiguity exists concerning ship noise in the MSS data. Because the BPP failed two days after its deployment when Challenger was 13 km away drilling Hole 596 and Melville was en route to Tahiti, MSS noise measurements in the absence of ships are not available. However, Challenger was briefly silent c 0510Z, 13 Feb, while monitoring an ocean- bottom navigational transponder, thus providing a sample of low ship noise for the MSS. The MSS spectrum of this time period is compared in Figure 16(b) with that of data observed a short time later when Challenger began using the thrusters of its dynamic positioning system. Also shown in Figure 16 (b) is an estimate of SP system noise which has been scaled to fit the 'quiet' spectrum. The good fit suggests that above 7 Hz system noise dominates the spectrum.

The abrupt change of slope in the spectra of Figure 16 due to the dominance of ship noise is diagnostic of its presence. On this basis, it is apparent from these and other spectra that ship noise may be important at frequencies as low as 3 Hz in both the OBS and MSS data.

The lowest valid frequency of OBS microseismic measurements is taken to be 0.1 Hz. At lower frequencies, least-count and system noise dominate. The latter source of noise was inferred from the lack of estimate stability over a wide range of numbers of spectra averaged to compute power density estimates.

Thus, in summary, reliable spectral estimates of ambient seismic noise are available from MSS MP data between 0.2 and 1.5 Hz; from MSS SP data between 0.2 and 7 Hz; and from OBS data between 0.1 and 7 Hz. These bands are subject to the variability described above due to ship proximity, and OBS gain range and instrument response. At frequencies greater than 7 Hz, sampling noise dominates OBS teleseismic data, so that lower bounds on ocean-bottom microseismic noise levels must be established using data recorded with the refraction response.

RESULTS AND DISCUSSION

The primary objectives of the noise analysis are the comparison of noise levels recorded by the OBS and MSS sensors, and the investigation of noise generation and propagation in the deep sea.

Given the hypothesis that high-frequency (0.1-10 Hz) microseismic noise is composed principally of interface waves trapped near the seafloor-ocean bottom boundary, substantially lower noise levels are anticipated at the MSS. This hypothesis is supported by results from the Leg 78B MSS deployment (Adair et al., 1984).

Figures 17 and 18 show typical spectral estimates, corrected for instrument response, of simultaneous MSS and OBS observations in units of nanometers^2/Hz (nm^2/Hz). The data were collected over a 70-minute period commencing 0840Z, 8 Feb 83. The estimates are averages of ten individual spectra. Each OBS spectrum was computed from 13.02 seconds of data, while each MSS spectrum is a composite of MP and SP spectra computed from, respectively, 128 and 12.8 seconds of Gould system data. The MP spectrum was used at frequencies less than 1.4 Hz to achieve high frequency resolution with a minimum of computation. The Gould spectral amplitudes have been adjusted by 3 dB to compensate the digital amplitude mismatch described above.

While the data of Figures 17 and 18 were collected, the OBS (Suzy) was 0.6 km north of the MSS site, Challenger maintained station approximately 1.5 km northwest of the borehole, and Melville was completing Refraction Line 5 more than 170 km northwest of the borehole. Ship noise for all these spectra dominated at frequencies greater than 4.5 Hz.

Differences between two spectra are significant at the 95% confidence level if they exceed 5.5 dB (-2.3 and +3.2 dB). This assumes that the spectra are derived from identically-distributed normal processes, so that each estimate is x^2-distributed with 2n degrees of freedom, where n=10, the number of spectra averaged (Bendat and Piersol, 1971). For comparison, the 90% confidence interval is 4.7 dB.

The spectra have the usual overall appearance of earth noise in this frequency band. They fall off rapidly toward higher frequencies from the microseism peak, which typically lies between 0.1 and 0.3 Hz. The ubiquitous microseism peak is generated by the nonlinear interaction of ocean surface waves having the same frequency which travel in opposite directions (Longuet-Higgins, 1950). This interaction produces ocean-bottom pressure fluctuations that oscillate at twice the frequency of the generative surface waves. While no wave spectrum data are available for the Ngendei experiment, a qualitative description may be obtained from the deck and weather logs of Challenger. Swell periods of 6, 7, 9, 10, and 12 seconds were reported during the four hours which preceded and followed the noise observations of Figures 17-18. This corresponds to a double-frequency range of 0.17-0.33 Hz, which is roughly the band of the observed microseism peak.

At the microseism peak (approximately 0.2 Hz), levels at the seafloor and in the borehole on all components were within 5 dB of each other. In the band 0.6-4.5 Hz, vertical OBS levels exceeded those on the MSS by 10-20 dB (Figure 17), and horizontal OBS levels exceeded the MSS levels by 25-30 dB (Figure 18). This contrasts with results from Leg 78B (Figure 19) in which vertical-component ocean-bottom levels observed 2 km from the MSS site exceeded borehole levels by 10 dB at the microseism peak. While the distances between the OBS and MSS were comparable for these two MSS deployments, sensor burial was much deeper (519 m with

basement rock overlain by 93 m of sediment) on Leg 78B, suggesting that the Leg 91 sensor depth was insufficient to achieve significant reduction of noise levels at the microseism peak. It was, however, apparently adequate at higher frequencies.

The irregular fall-off of the microseismic noise in Figures 17-18, at 60-80 dB/decade, is punctuated by several peaks and slope breaks. These spectral characteristics are due to the combined influences of the source spectrum and the seafloor elastic structure. The principle source of the noise in the open ocean may reasonably be assumed to be ocean-bottom pressure fluctuations acting at the seafloor (Webb, 1984; Hasselmann, 1963; Longuet-Higgins, 1950). At a given frequency, the power density would include contributions from a normal mode of the seafloor-ocean structure to the degree that the source excites it. Therefore, spectral peaks may be due to peaks in the source spectrum or to the resonant forcing of one or more seismic normal modes.

Webb (1984) predicts a fall-off of 70 dB/decade of ocean-bottom pressure noise at these frequencies when the source is due to the nonlinear interaction of wind waves in the observer's immediate vicinity. The spectrum of ocean-bottom pressure (Figure 20) measured concurrently with the displacement spectra of Figures 17-18 fell off at the lesser rate of 50-60 dB/decade, suggesting that the source was not simple local wind-wave forcing in this instance. The slope breaks at approximately 2 and 4 Hz and flattening between 6 and 15 Hz (more obvious in spectra lacking local ship noise; see Figure 21) may correspond to distant-shipping noise (Urick, 1983), as it does in the heavy traffic of the North Atlantic.

The characteristic fall-off of pressure noise from the microseism peak is reported to be on the order of 30 dB/decade (Urick, 1983), much less than was observed at the Ngendei site. This lower value may be the due to the coarse bandwidths typically employed in computing spectral measurements. Figure 21 compares three high-resolution, ocean-bottom pressure spectra, reported by Nichols (1981), to an average of 39 daily, 59-second samples of pressure observed on OBS Suzy between 12 February and 22 March, 1983. The two spectra collected by Talpey and Worley were measured in 4.3 km of water near Bermuda, and the Eleuthera spectra in 1.2 km of water. Differences between the Talpey-Worley spectra were attributed to local wind speeds. The spectra of Figure 21, in particular the OBS and Talpey-Worley spectra, have a similar shape between 0.2 and 10 Hz. The lower Eleuthera spectral levels near the microseism peak were apparently due to the shallower observation depth.

The relationships between different components of the noise at the MSS site contrasts with that at the OBS site. Vertical MSS levels uniformly exceeded the horizontal levels (Figure 22) by 4 dB whereas vertical OBS levels were 10-20 dB lower than the horizontal levels (Figure 23) at frequencies greater than the microseism peak's. Since horizontal

and vertical amplitudes, and their ratios vary differently with depth for different interface wave modes (Latham and Sutton, 1966; Latham and Nowroozi, 1968), this observation is consistent with the surface wave mode of noise propagation. For realistic models of the seafloor structure which include a sediment layer, the fundamental mode interface wave, at typical microseism peak frequencies, exhibits horizontal motion on the order of four times the amplitude of vertical motion at the seafloor, and comparable amplitudes for the two components within competent basement rock (Latham and Sutton, 1966).

Coherences between OBS capsule pairs were computed to investigate noise field propagation. To reduce possible bias due to misalignment of coincident features, the two series were aligned at the lag of their cross-correlation's maximum value after first correcting for clock drift and fiducial offsets. Figure 24 shows the coherence between Karen and Juan, which were separated by 0.7 km. The corresponding power spectrum of Juan is also shown in Figure 24 to aid identification of coherent features. Coherence is high between 0.15 and 0.31 Hz, the band of the microseism peak, as well as at those frequencies dominated by ship noise. Results for the other capsule pair (Lynn and Suzy), separated by 0.6 km, were essentially the same.

High coherence at the microseism peak persisted between the capsules throughout MS1. The alignment lags for the southwestern OBS's were consistently late (by approximately 0.5 seconds in most instances) with respect to their partner capsules to the northeast, suggesting that energy in the microseism peak was sweeping across the array towards the southwestern pair of OBS's.

The vertical-component spectra of Figure 17 are compared in Figure 25 with extrema of similar measurements from Scripps Institution of Oceanography (SIO) OBS's. Above about 1.5 Hz, the Leg 91 measurements are comparable to the lower extreme and fall-off at a similar rate. This is despite the fact that the observation sites and conditions were quite disparate. The extrema are not well defined at lower frequencies due to the short data sample lengths from which the spectra were obtained.

Figure 26 compares the Figure 17 spectra to unusually low noise observations on land. The Lajitas spectrum (Herrin, 1982) is representative of the quietest-known site, which is near the Big Bend of the Rio Grande River. At frequencies less that 2 Hz, Lajitas noise levels differ little from those measured at a quiet site in a mine shaft near Queen Creek, Arizona (Fix, 1972; Melton, 1976), so their composite delineates the lowest-known noise levels at these frequencies. The MSS levels exceed this composite by 20-35 dB below 2 Hz, but converge to within 10 dB at higher frequencies. The OBS levels similarly exceed the composite by 35-45 dB below 2 Hz, and converge to within 30 dB above 2 Hz. The 10 Hz peak in the Lajitas spectrum is not related to that in the Ngendei spectra, which is ship-generated.

CONCLUSIONS

Comparable noise levels were observed at the microseism peak on all components at both the ocean-bottom and in the borehole. However, at higher frequencies (0.3-4.5 Hz), the borehole noise levels were substantially lower than the ocean bottom levels for both vertical and horizontal components. If microseism peak noise is a trapped wave phenomenon, then the observation that the noise levels were comparable in the OBS and MSS at the microseism peak suggests that the borehole sensor was not sufficiently deep in the basaltic basement to diminish noise levels over the entire band of frequencies.

The analysis has yielded several constraints on both source character and noise propagation. The microseism peak displayed high coherence over a distance of at least 0.7 km, and low-frequency noise appeared to propagate over this distance as well. This suggests a non- local source for noise in the microseism peak range. The rate of fall-off of the OBS and MSS spectra from the microseism peak and the variety of peaks in the fall off indicate both regional and local sources for noise in this frequency range. The observed peaks are probably due to both source spectrum shape and to resonant forcing of seismic modes trapped near the seafloor-ocean bottom interface. The observed vertical- and horizontal-component noise levels in the borehole and at the ocean bottom constrain the mode of noise propagation. In the MSS vertical-component, noise was insignificantly (4 dB) higher than the noise levels measured in the horizontal components, while the OBS's had a 10-20 dB difference in the OBS horizontal and vertical component noise levels. Since changes with depth in horizontal amplitude and the ratio of horizontal to vertical amplitudes is different for different types of interface waves, detailed investigation of these differences constrain the mode of noise propagation. Near the microseism peak, these observations are consistent with propagation as a fundamental mode interface wave.

Fall-off of the pressure noise spectrum from the microseism peak was, in the instances considered here, less than that expected from local wind-wave generation, suggesting that some other source mechanism was contributing as well. The flattening of the spectrum seen at frequencies greater than 2 Hz is probably due to distant shipping noise.

The borehole noise levels observed during the Ngendei experiment are comparable to average continental sites, and approach exceptionally quiet land levels only at frequencies above 10 Hz. Deeper burial may have some effect on the noise levels, reducing levels in the microseism peak somewhat closer to levels in quiet land sites.

Modeling of the phase spectrum, relative amplitudes and coherences between different sites and components, and spectral shape should yield a better, more sophisticated characterization of the noise and source fields. These phenomena will be the subject of continuing research on the data related to seafloor noise.

References

Adair, Richard G., Orcutt, John A., and Jordan, Thomas H., 1983. Analysis of ambient seismic noise recorded downhole and ocean bottom seismometers on Deep Sea Drilling Project Leg 78B. In Hyndman, R. D., Salisbury, M. H., et al., Init. Repts. DSDP, 78: Washington (U.S. Govt. Printing Office), 767-781.

Bendat, J. S., and Piersol, G. G., 1971. Random data: Analysis and measurement procedures: New York (John Wiley)

Bradner, Hugh, and Dodds, James G., 1964. Comparative seismic noise on the ocean bottom and on land. J. Geophys. Res., 69:4339-4348.

Duennebier, F. K., and Blackington, G., 1983. The ocean subbottom seismometer, in Geophysical Exploration at Sea, R. Geyer, Editor, CRC Press, Boca Raton, Florida, 317-332.

Creager, K. C., and Dorman, L. M., 1982. Locations of instruments on the seafloor by joint adjustment of instrument and ship positions. J. Geophys. Res., 87:8379-8388.

Duennebier, F. K., Blackington, G., and Sutton, G. H., 1981. Current-generated noise recorded on ocean bottom seismometers. Mar. Geophys. Researches, 5:109-115.

Fix, J. E., 1972. Ambient earth motion in the period range from 0.1 to 2560 sec. Bull. Seism. Soc. Am., 62:1753-1760.

Herrin, Eugene, 1982. The resolution of seismic instruments used in treaty verification research. Bull. Seism. Soc. Am., 72:S61-S67.

Jenkins, Gwilyn M., and Watts, Donald G., 1968. Spectral analysis and its applications: San Francisco (Holden-Day)

Latham, Gary V., and Sutton, George H., 1966. Seismic measurements on the ocean floor, 1. Bermuda area. J. Geophys. Res. 71:2545-2572.

Latham, Gary V., and Nowroozi, Ali A., 1968. Waves, weather, and ocean bottom microseisms. J. Geophys. Res., 73:3945-3956.

Longuet-Higgins, M. S., 1950. A theory of the origin of microseisms. Phil. Trans. Roy. Soc., A., 243:1-35.

Melton, Ben S., 1976. The sensitivity and dynamic range of inertial seismographs. Rev. Geophys. Space Phys., 14:93-116.

Moore, R. D., Dorman, L., Huang, C.-Y., and Berliner, D. L., 1981. An ocean bottom, microprocessor based seismometer. Mar. Geophys. Researches, 4:451-477.

Nichols, R. H., 1981. Infrasonic ambient ocean noise measurements:

Eleuthera. J. Acoust. Soc. Am., 69:974-981.

Otnes, R. K., and Enochson, L., 1982. Digital Time Series Analysis: New York (John Wiley).

Prentiss, D. D., and Ewing, J. I., 1963. The seismic motion of the deep ocean floor. Bull. Seism. Soc. Am., 53:765-781.

Schneider, W. A., and Backus, M. M., 1964. Ocean-bottom seismic measurements off the California coast. J. Geophys. Res., 69:1135-1143.

Schneider, William A., Farrell, Patrick J., and Brannian, Ross E., 1964. Collection and analysis of Pacific ocean-bottom seismic data. Geophysics, 29:745-771.

Singleton, R. C., 1979. Mixed radix Fast Fourier Transforms In: Weinstein, Clifford, et al. (Eds), Programs for Digital Signal Processing. New York (IEEE Press), 1.4-1 - 1.4-18.

Spudich, Paul, and Orcutt, John, 1980. Petrology and porosity of an oceanic crustal site: Results from wave form modeling of seismic refraction data. J. G. R., 85:1409-1433.

Stephen, R. A., Johnson, S., and Lewis, B., 1983. The oblique seismic experiment on Deep Sea Drilling Project Leg 65. In Lewis, B. T. R., Robinson, P., et al., Init Repts. DSDP, 65: Washington (U.S. Govt. Printing Office), 675-704.

Stephen, R. A., Louden, K. E., and Matthews, D. H., 1980. The oblique seismic experiment on Deep Sea Drilling Project Leg 52. In Donnely, T. Francheteau, J., Bryan, W., Robinson, P., Flower, M., Salisbury, M., et al., Init Repts. DSDP, 51, 52, 53, Pt. 1: Washington (U.S. Govt. Printing Office), 675-704.

Sutton, G. H., Duennebier, F. K., and Iwatake, B., 1981. Coupling of ocean bottom seismometers to soft bottom. Mar. Geophys. Res., 5:35-51.

Urick, P. J., 1974. Sea-bed motion as a source of the ambient noise background of the sea. J. Acoust. Soc. Am., 56:1010-1011.

Urick, R. J., 1983. Principals of Underwater Sound. 3rd edition: New York (McGraw-Hill).

Webb, S. C., 1984. Observations of Seafloor Pressure and Electric Field Fluctuations. Ph.D. thesis, University of California, San Diego.

Welch, P. D., 1967. The use of fast Fourier transform for the estimation of power spectra: A method based on time averaging over short, modified periodograms. IEEE Trans. Audio Electro-acoust., AU-15:70-73.

Figure 1 Displacement responses of (a) Marine Seismic System (MSS) and (b) ocean-bottom seismograph (OBS) instrumentation used during the Ngendei experiment. (a) The Gould MSS mid-period (MP) and short-period (SP) responses differ from the Teledyne responses by the low-pass FIR (Finite Impulse Response) digital filter shown with dashed lines. (b) OBS seismometer and hydrophone responses. Two responses were available for the OBS's (ocean bottom seismographs).

Figure 2 Locations of the MSS and six OBS's during MS1. See text for explanation of symbols. (a) Configuration of the four capsules which recorded refraction signals (Juan, Karen, Lynn, and Suzy). (b) Configuration of the two OBS's which concurrently recorded teleseismic signals in a triggered mode (Janice and Phred).

Figure 3 (a) and (b): Locations of the OBS's during MS2. See text for explanation of symbols.

Figure 4 Chronology of events during the Ngendei experiment pertinent to the noise study. Coordinated Universal Time (CUT) data are given along the bottom axis, with a break between mid-February, 1983, and late March, 1983, when the teleseismic experiment took place and noise samples were recorded by each OBS at 24-hour intervals. See text for explanation.

Figure 5 Chart of noise data available for analysis during the early portion of MS1 prior to the start of recording by the MSS. The OBS's recorded discrete events, shown as vertical tics, while the MSS systems recorded continuously during the intervals shown with horizontal segments bounded by vertical tics. CUT date is given along the bottom axis, and capsule and MSS system names at either side.

Figure 6 Noise samples recorded MS1 near the start of MSS data recording. See caption of Figure 5 for explanation.

Figure 7 Noise samples recorded during the latter portion of MS1. See caption of Figure 5 for explanation.

Figure 8 Typical example of seven-channel data from the Teledyne system during MS1. The recording interval is listed across the top, and the time in minutes after the hour is given across the bottom. Channel identifications and amplitudes in digital counts are along the left-hand side. The event number refers to lengths of uninterrupted data present on the tapes available from the Center for Seismic Studies. (see text).

Figure 9 Typical example of seven-channel data from the Gould system during MS1. See Figure 8 for explanation.

Figure 10 Cross-correlations of various channels of the Teledyne and Gould systems. A positive lag corresponds to the second-named channel in the figure label being late with respect to the first-named channel. (a) Cross-correlation between Gould and Teledyne channels MZ. (b) Cross-correlation between Gould and Teledyne channels SB. (c) Cross-correlation of Teledyne's primary and backup SP vertical-component channels.

Figure 11 MSS sensor calibrations recorded by the Teledyne system during MS1 for (a) MP and (b) SP channels, and during MS3 for (c) MP and (d) SP channels.

Figure 12 Spectral power density estimates of typical MSS noise samples compared to system noise levels. The spectra, given in counts^2/Hz, have not been corrected for instrument response. (a) Gould Channel MZ. (b) Gould channel SB. (c) Teledyne channel SB.

Figure 13 Coherence spectra between (a) aligned Teledyne and Gould channel MZ, (b) aligned Teledyne and Gould channel SB, and (c) Teledyne channels SZ and SB.

Figure 14 Example of 4-channel OBS data recorded with the refraction instrument response. Data are from OBS Suzy. Amplitudes are given in gain-corrected counts and each channel's plot has been individually scaled. Channels are, from top to bottom, vertical, two horizontals, and hydrophone.

Figure 15 Comparison of noise spectrum obtain with the teleseismic (solid upper curve) and refraction (dashed upper curve) OBS responses. The corresponding instrumentally-corrected sampling noise spectra (lower curves) are also shown.

Figure 16 Illustration of ship noise in the OBS (a) and MSS (b) data. Solid spectra were observed when ships were nearby and operational, and the dashed spectra when ships were completely absent (OBS) or still nearby (MSS). MSS data are not available at any time when ships were completely absent.

Figure 17 Simultaneous vertical-component displacement power densities at the ocean bottom (dashed line) and in the borehole (solid line).

Figure 18 Simultaneous horizontal-component displacement power densities at the ocean bottom (dashed line) and in the borehole (solid line).

Figure 19 A comparison of vertical-component ocean-bottom and borehole noise levels observed during DSDP Leg 78B (dashed curves) and during the Ngendei experiment (solid curves).

Figure 20 Ocean-bottom pressure measurements concurrent with the displacement spectra of Figure 17.

Figure 21 Comparison of ocean-bottom pressure measurements observed on OBS Suzy during the period 12 February-22 March, 1983, with high-resolution measurements reported by Nichols (1981). The Eleuthera spectrum was observed in 1.2 km of water near Eleuthera, while the Talpey and Worley spectra were observed in 4.3 km of water near Bermuda. Also given for the Talpey-Worley spectra are the average wind speeds during data collection.

Figure 22 A comparison of simultaneous vertical (solid) and horizontal (dashed) power densities in the borehole.

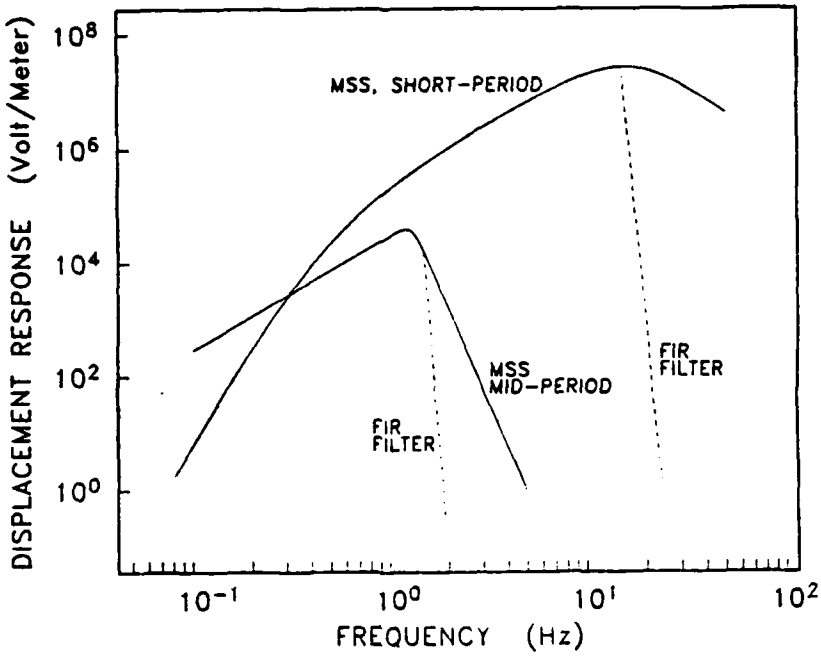
Figure 23 A comparison of simultaneous vertical (solid) and horizontal (dashed) power densities at the ocean-bottom.

Figure 24 Coherence (solid line) between measurements on OBS's Juan and Karen, separated by 0.7 km, and the corresponding instrument-corrected power densities (dashed lines) for Juan. Data were aligned by the amount corresponding to the location of their cross-correlation's peak to reduce coherence bias.

Figure 25 Comparison of vertical-component noise of Figure 17 with extrema observed on Scripps Institutions of Oceanography OBS's during their 12-year program.

Figure 26 Comparison of vertical-component noise observations from the Ngendei experiment with extremely low-level observations at land sites. The composite of the Queen Creek and Lajitas spectra may be taken as the lowest-known microseism levels at these frequencies.

(a)


DISPLACEMENT RESPONSE (Volt/Meter)
10^8
10^6
10^4
10^2
10^0
MSS, SHORT-PERIOD
MSS MID-PERIOD
FIR FILTER
FIR FILTER
10^{-1}
10^0
10^1
10^2
FREQUENCY (Hz)

(b)

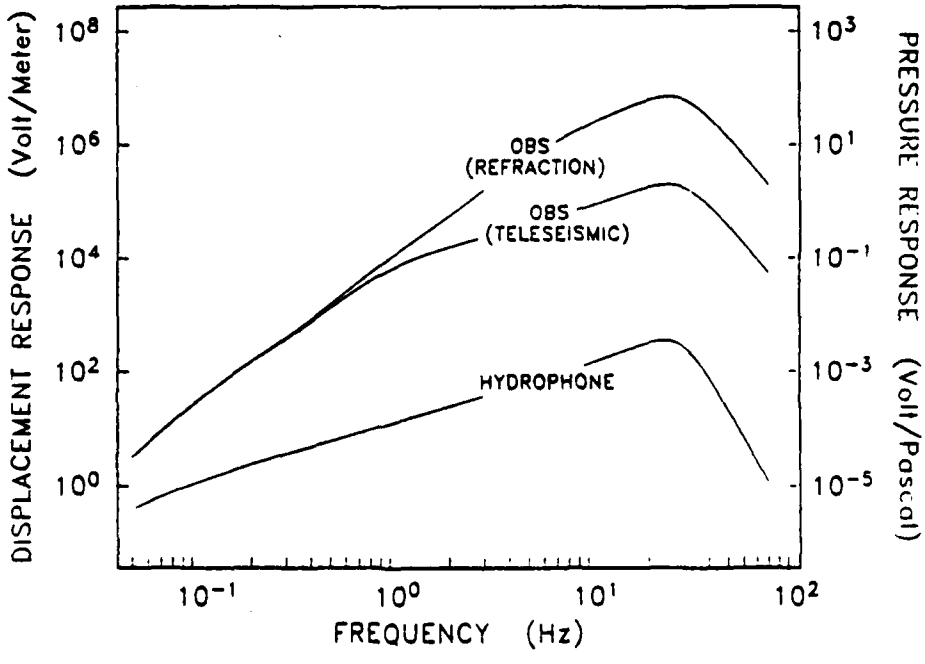

DISPLACEMENT RESPONSE (Volt/Meter)
10^8
10^6
10^4
10^2
10^0
OBS (REFRACTION)
OBS (TELESEISMIC)
HYDROPHONE
10^3
10^1
10^{-1}
10^{-3}
10^{-5}
PRESSURE RESPONSE (Volt/Pascal)
10^{-1}
10^0
10^1
10^2
FREQUENCY (Hz)

FIGURE 1

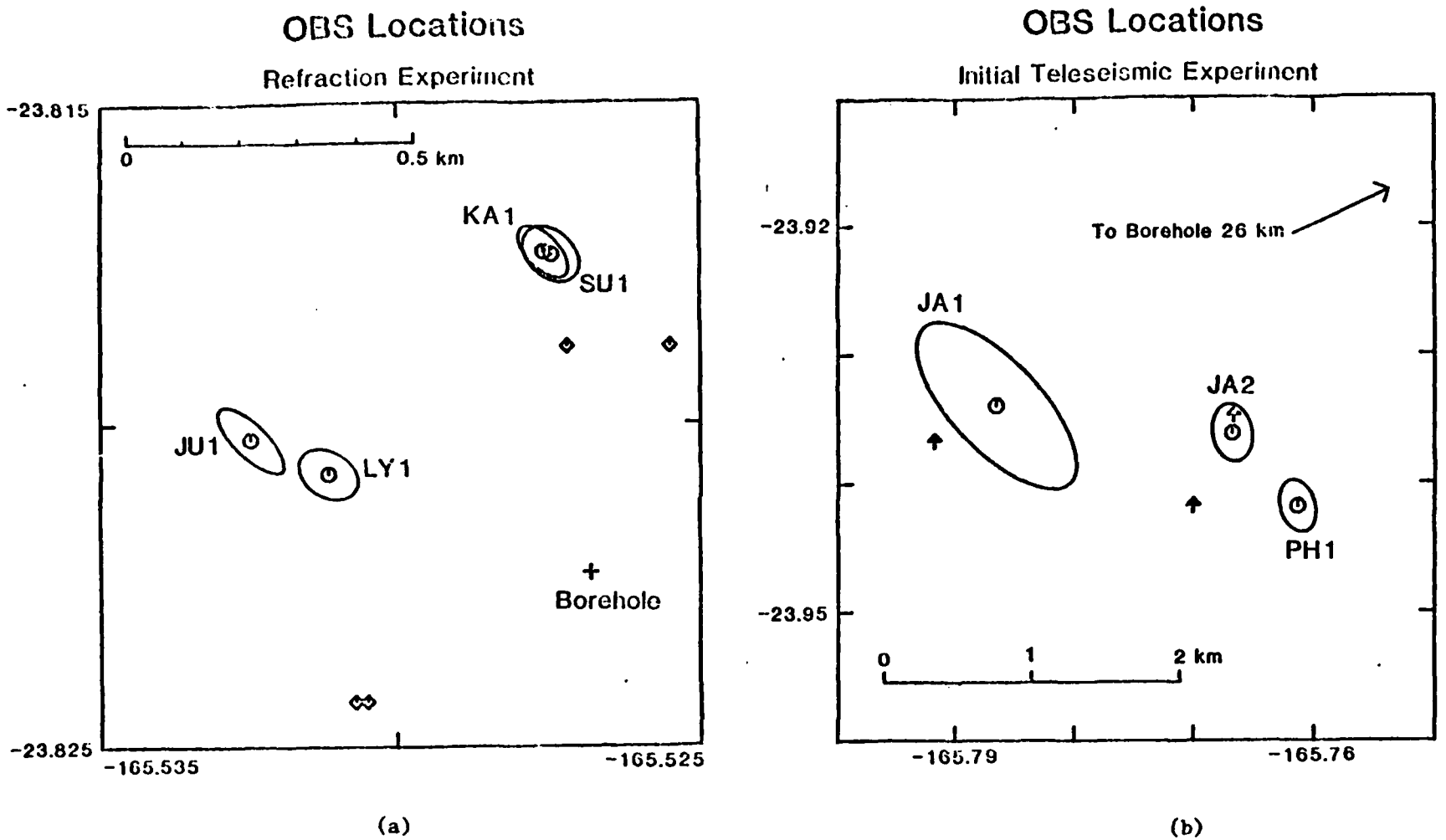
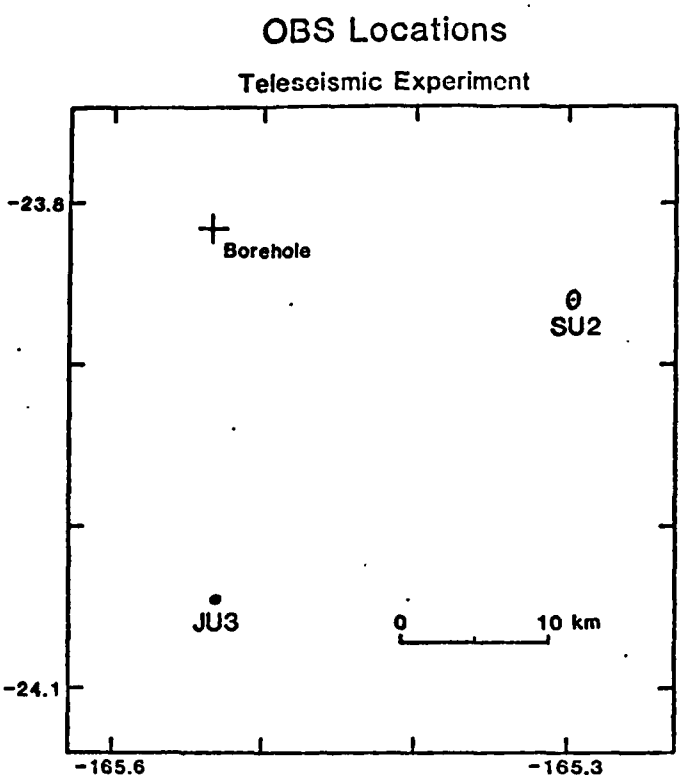
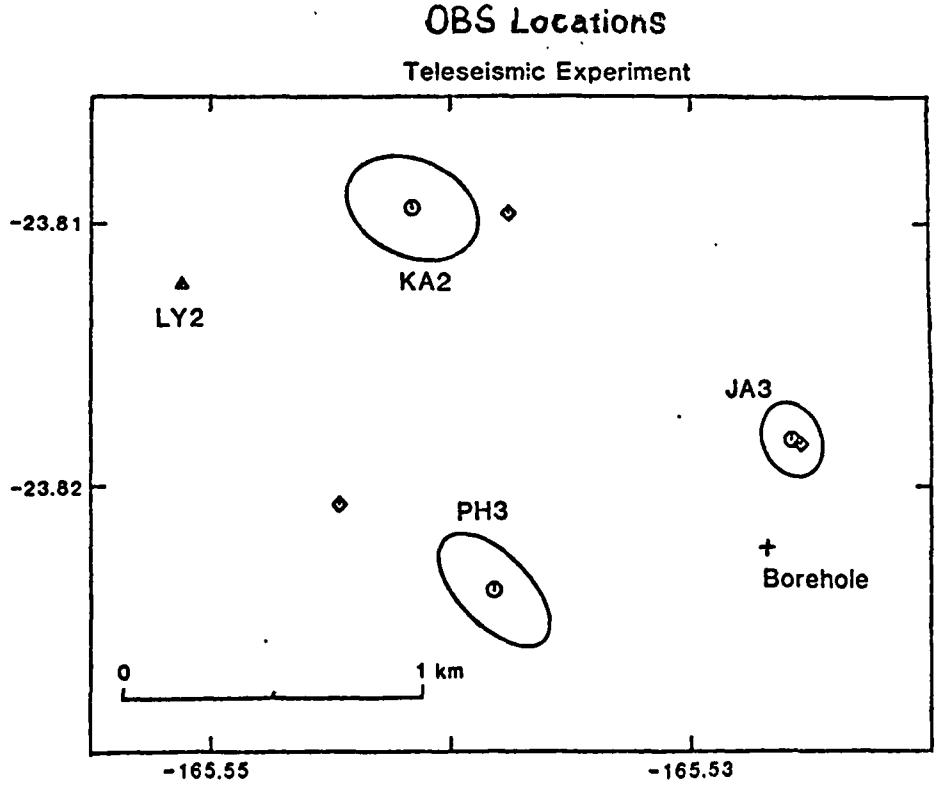

OBS Locations
Refraction Experiment
-23.815
0
0.5 km
KA1
SU1
JU1
LY1
Borehole
-23.825
-165.535
-165.525
(a)
OBS Locations
Initial Teleseismic Experiment
-23.92
To Borehole 26 km
JA1
JA2
PH1
-23.95
0
1
2 km
-165.79
-165.76
(b)

FIGURE 2


OBS Locations
Teleseismic Experiment
-23.8
-24.1
-165.6
-165.3
Borehole
SU2
JU3
0
10 km

(a)


OBS Locations
Teleseismic Experiment
-23.81
-23.82
-165.55
-165.53
KA2
LY2
JA3
PH3
Borehole
0
1 km

(b)

FIGURE 3

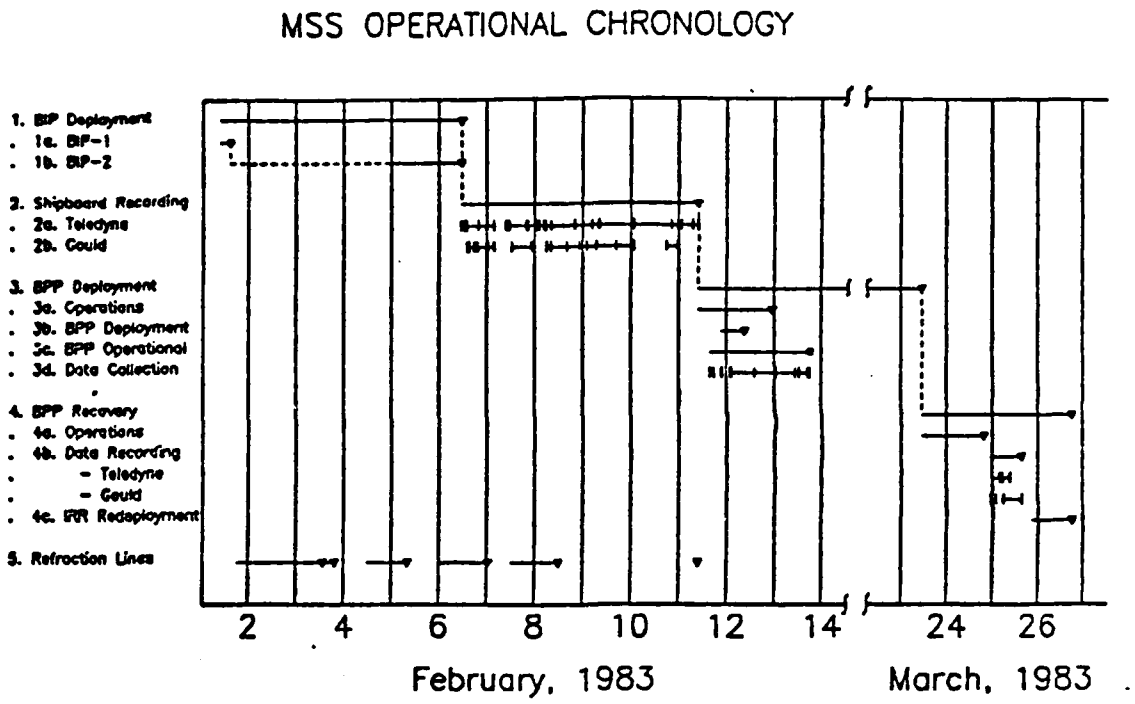


FIGURE 4

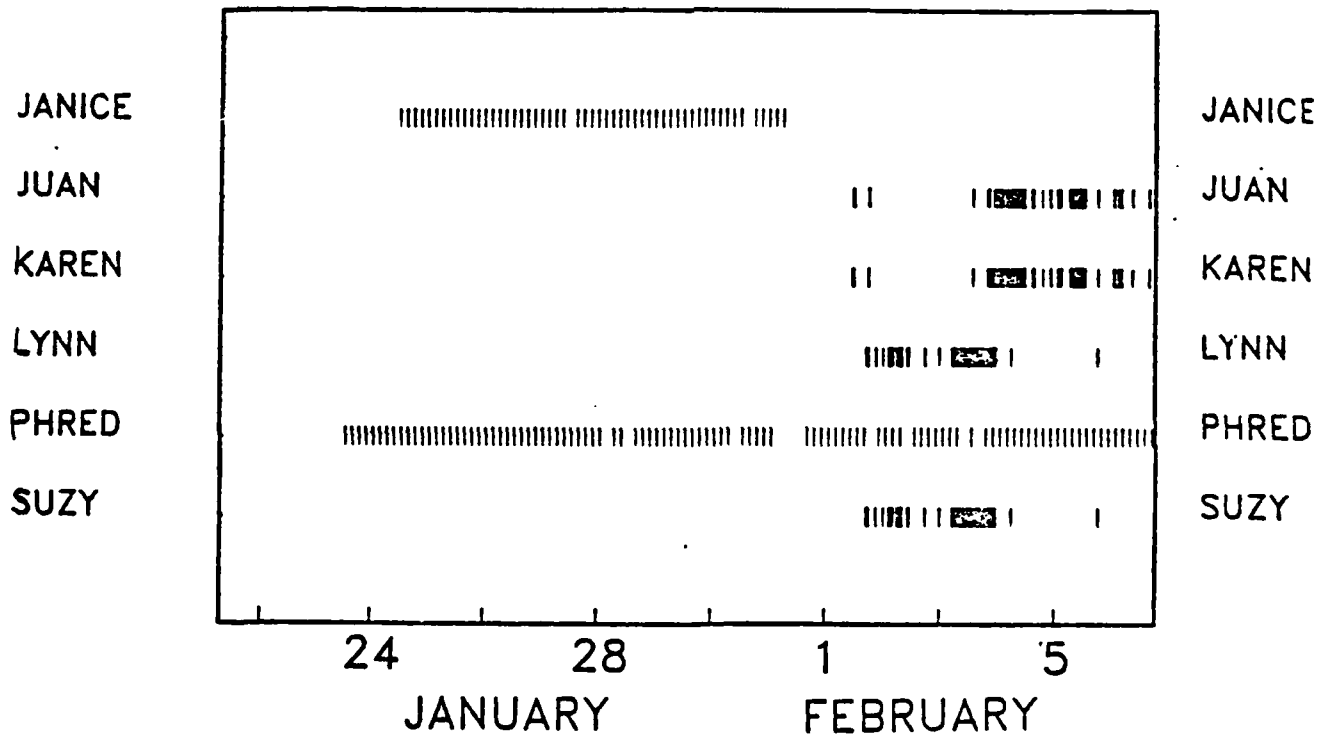


FIGURE 5

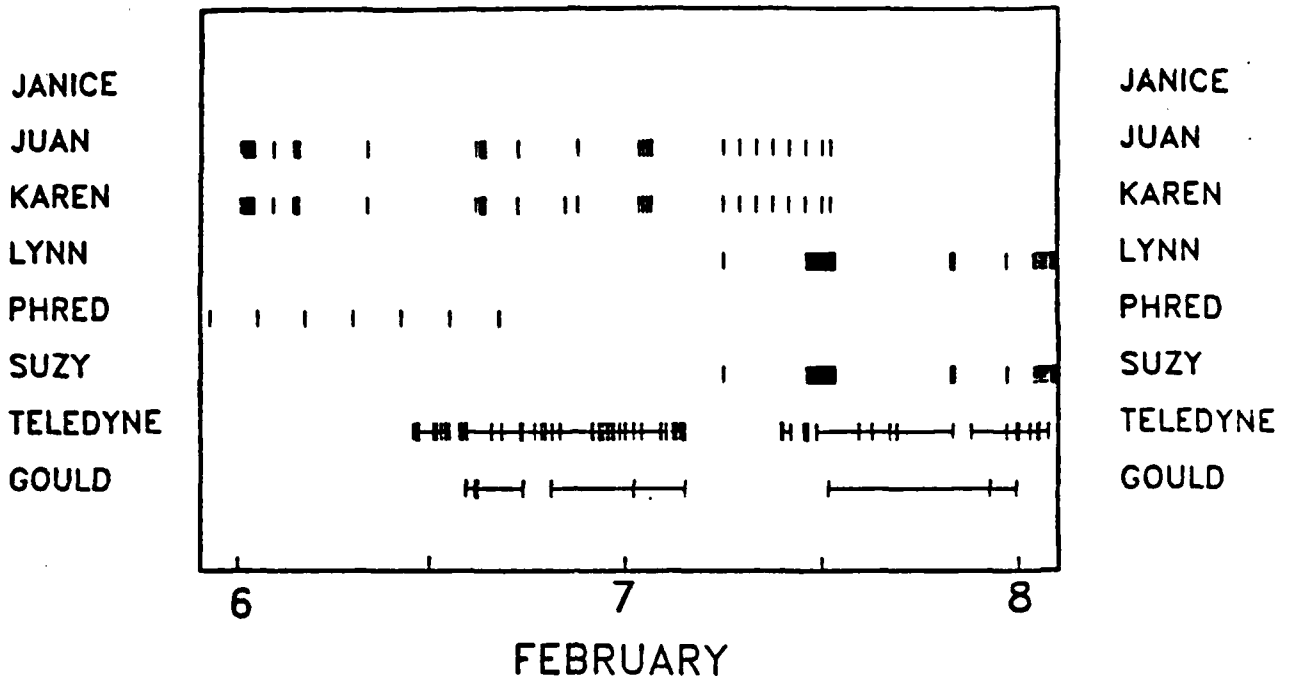


FIGURE 6

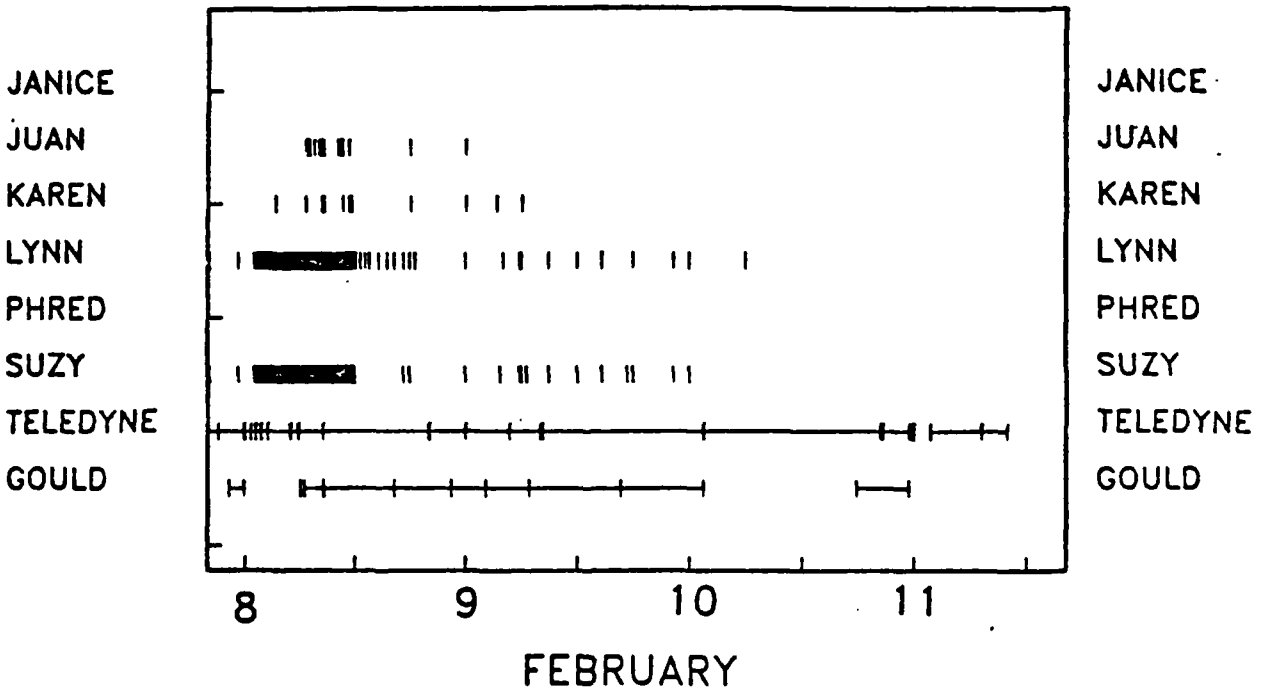


FIGURE 7

FIGURE 8

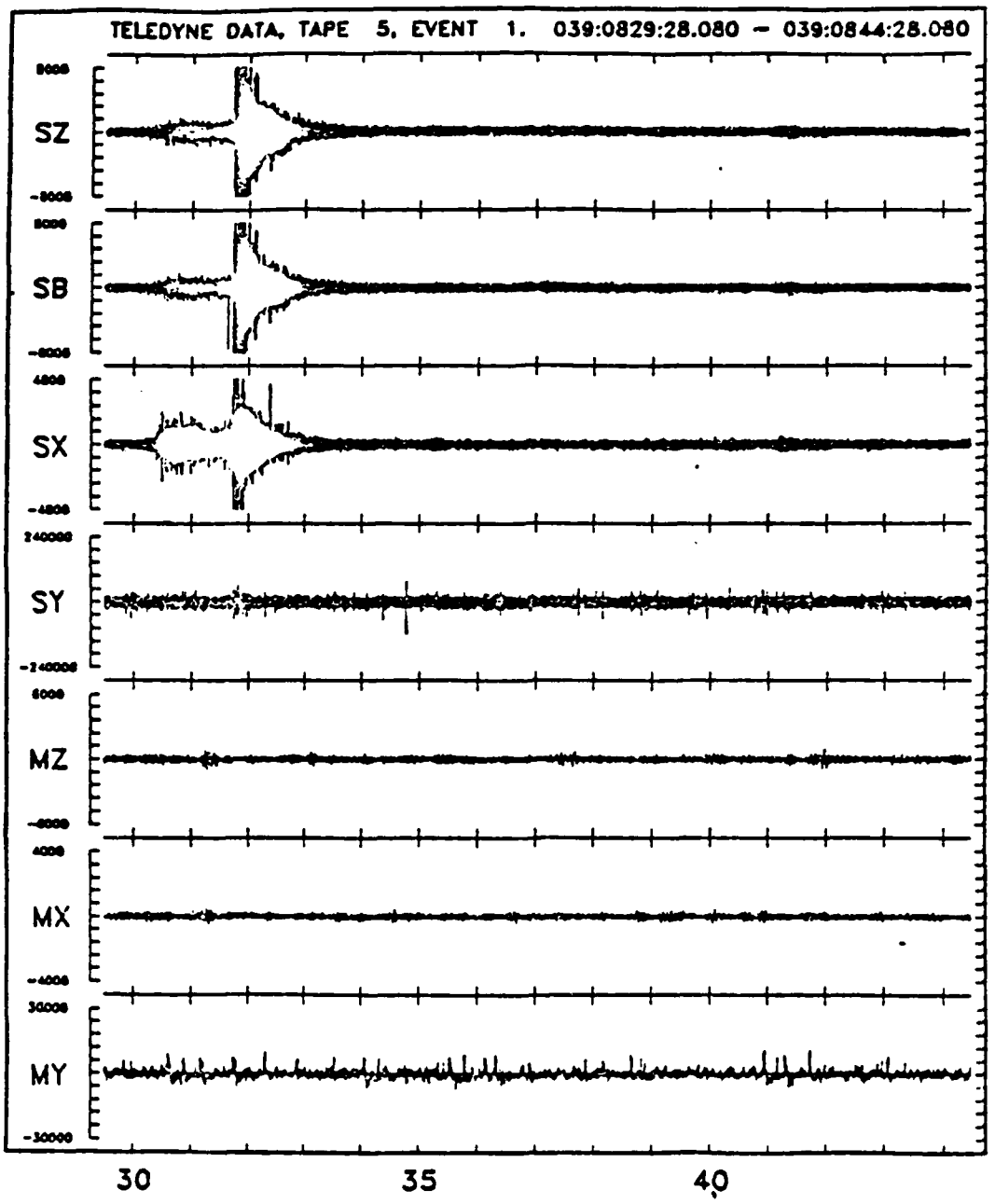
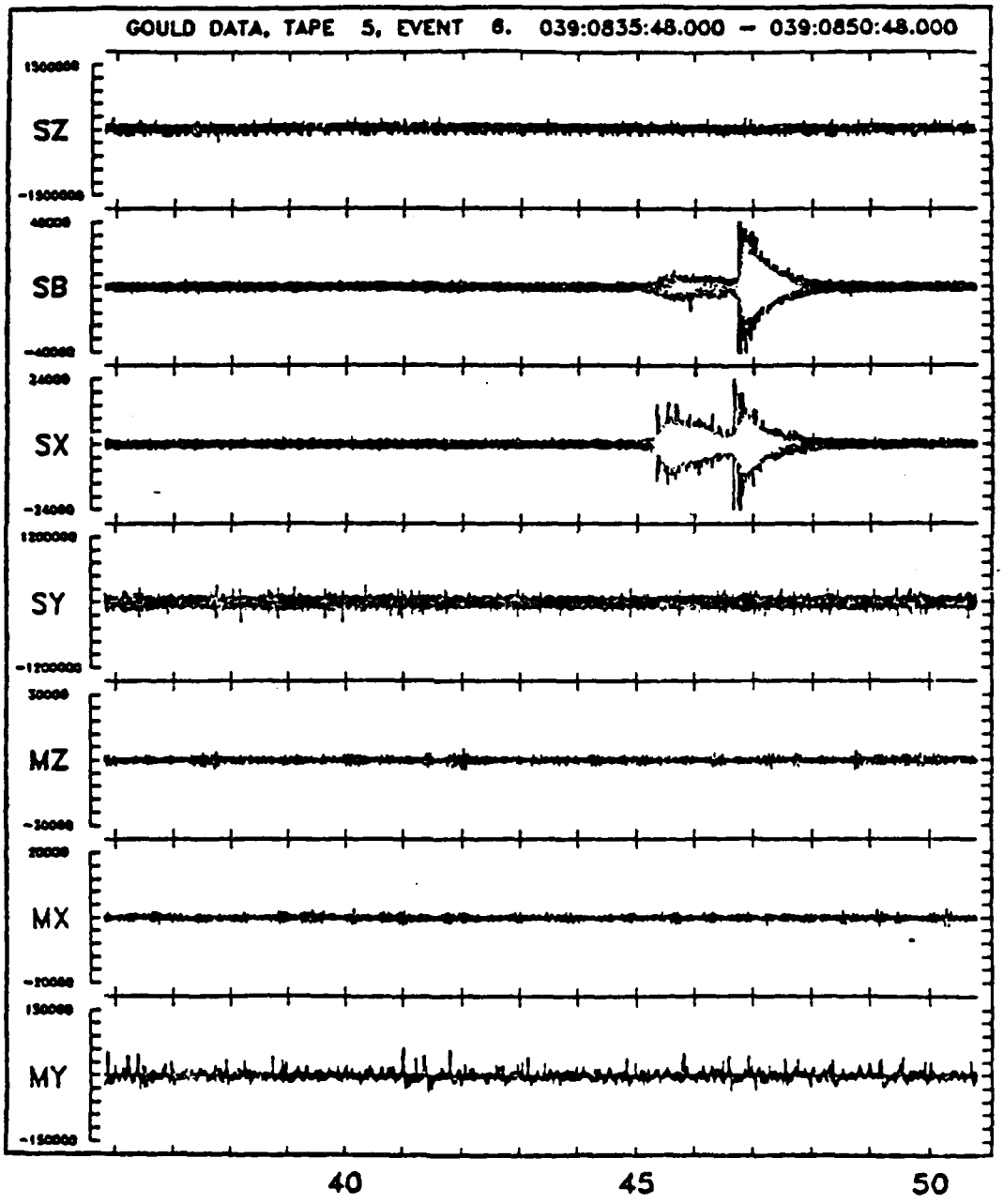

TELEDYNE DATA, TAPE 5, EVENT 1. 039:0829:28.080 – 039:0844:28.080
SZ
SB
SX
SY
MZ
MX
MY
30
35
40

FIGURE 9


GOULD DATA, TAPE 5, EVENT 6. 039:0835:48.000 – 039:0850:48.000
SZ
SB
SX
SY
MZ
MX
MY
40
45
50

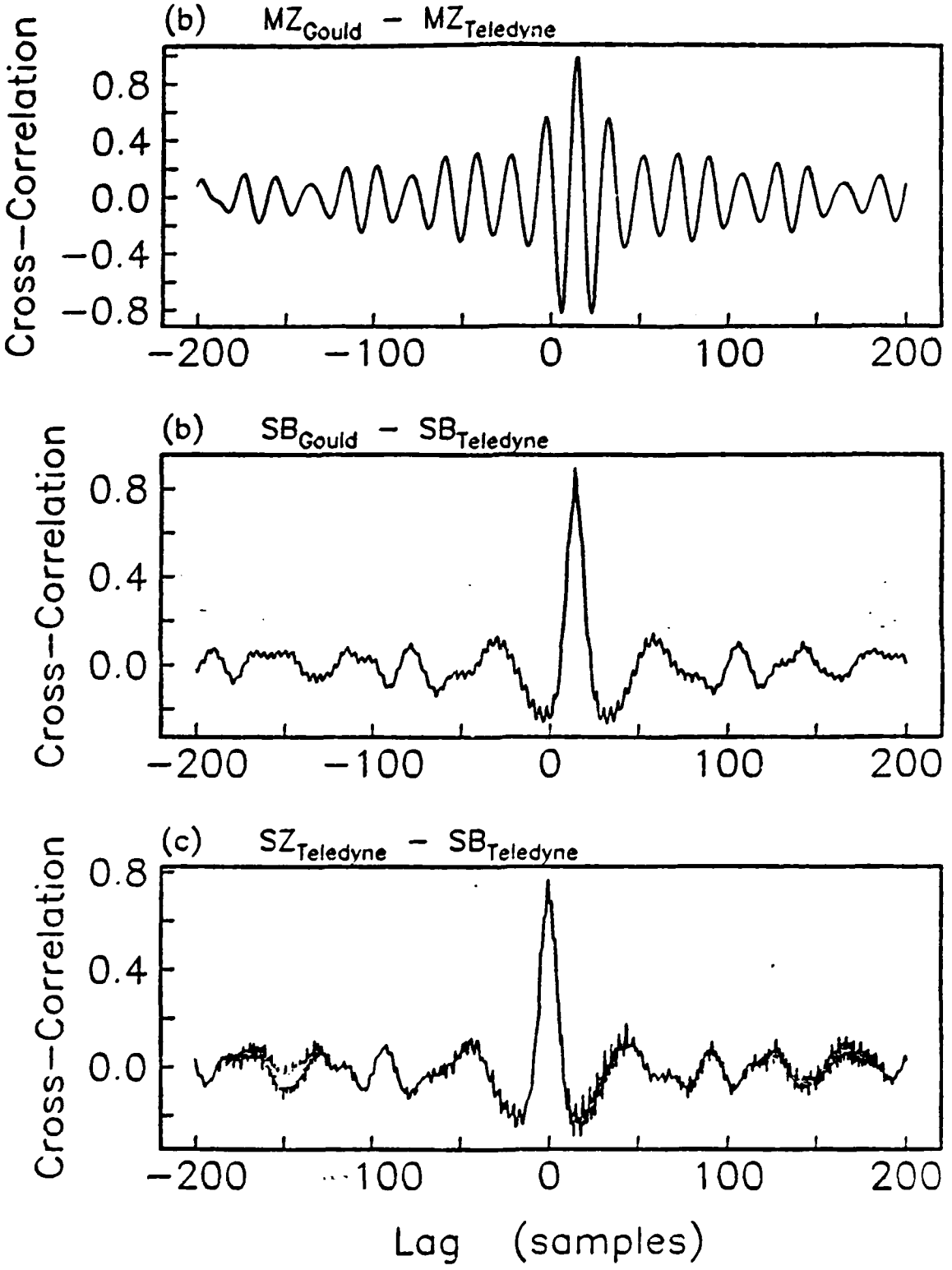

(b) MZ Gould − MZ Teledyne
Cross−Correlation
0.8
0.4
0.0
−0.4
−0.8
−200
−100
0
100
200
(b) SB Gould − SB Teledyne
Cross−Correlation
0.8
0.4
0.0
−200
−100
0
100
200
(c) SZ Teledyne − SB Teledyne
Cross−Correlation
0.8
0.4
0.0
−200
−100
0
100
200
Lag (samples)

FIGURE 10

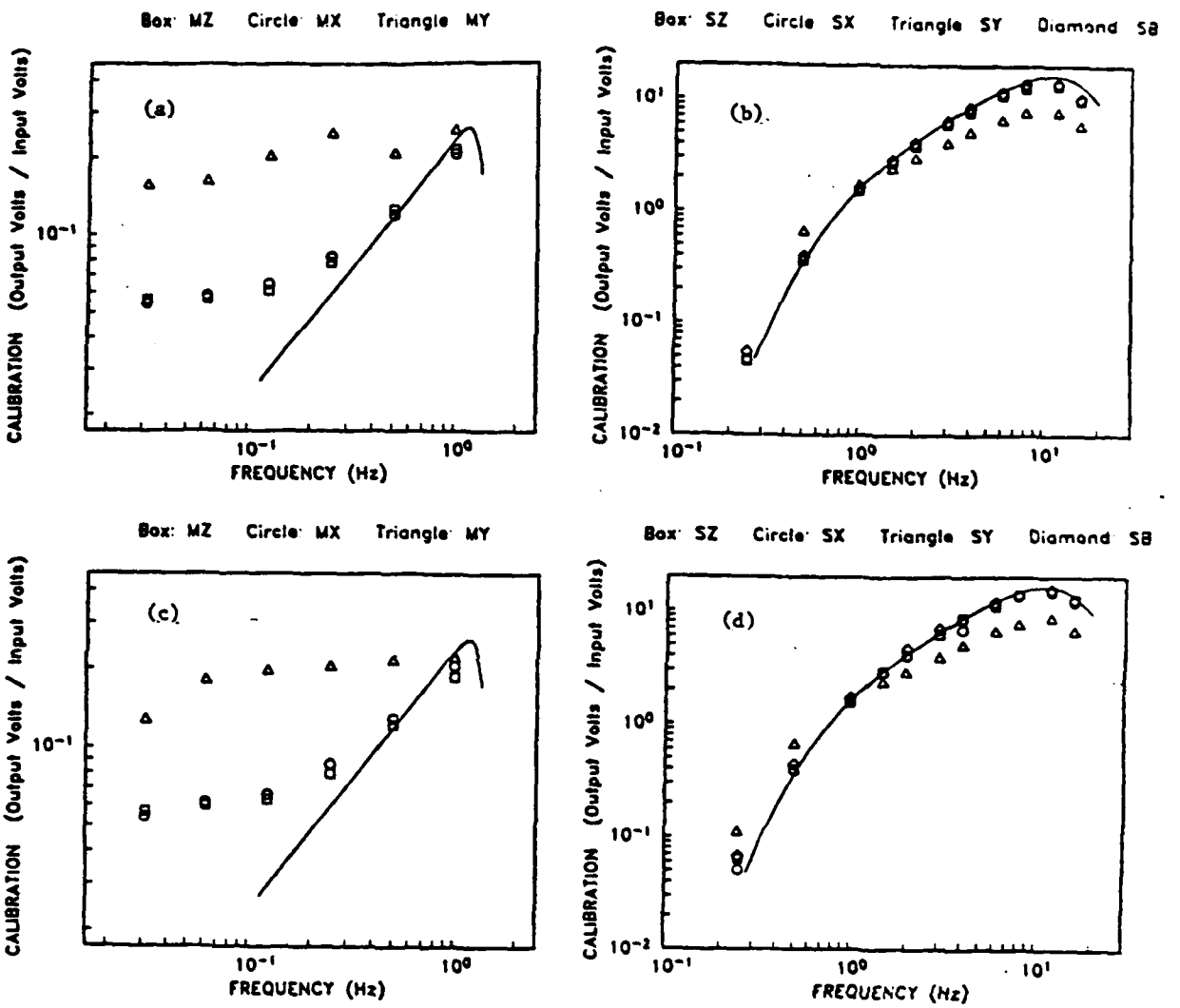

Box: MZ Circle: MX Triangle: MY
(a)
CALIBRATION (Output Volts / Input Volts)
FREQUENCY (Hz)
Box: SZ Circle: SX Triangle: SY Diamond: SB
(b)
CALIBRATION (Output Volts / Input Volts)
FREQUENCY (Hz)
Box: MZ Circle: MX Triangle: MY
(c)
CALIBRATION (Output Volts / Input Volts)
FREQUENCY (Hz)
Box: SZ Circle: SX Triangle: SY Diamond: SB
(d)
CALIBRATION (Output Volts / Input Volts)
FREQUENCY (Hz)

FIGURE 11

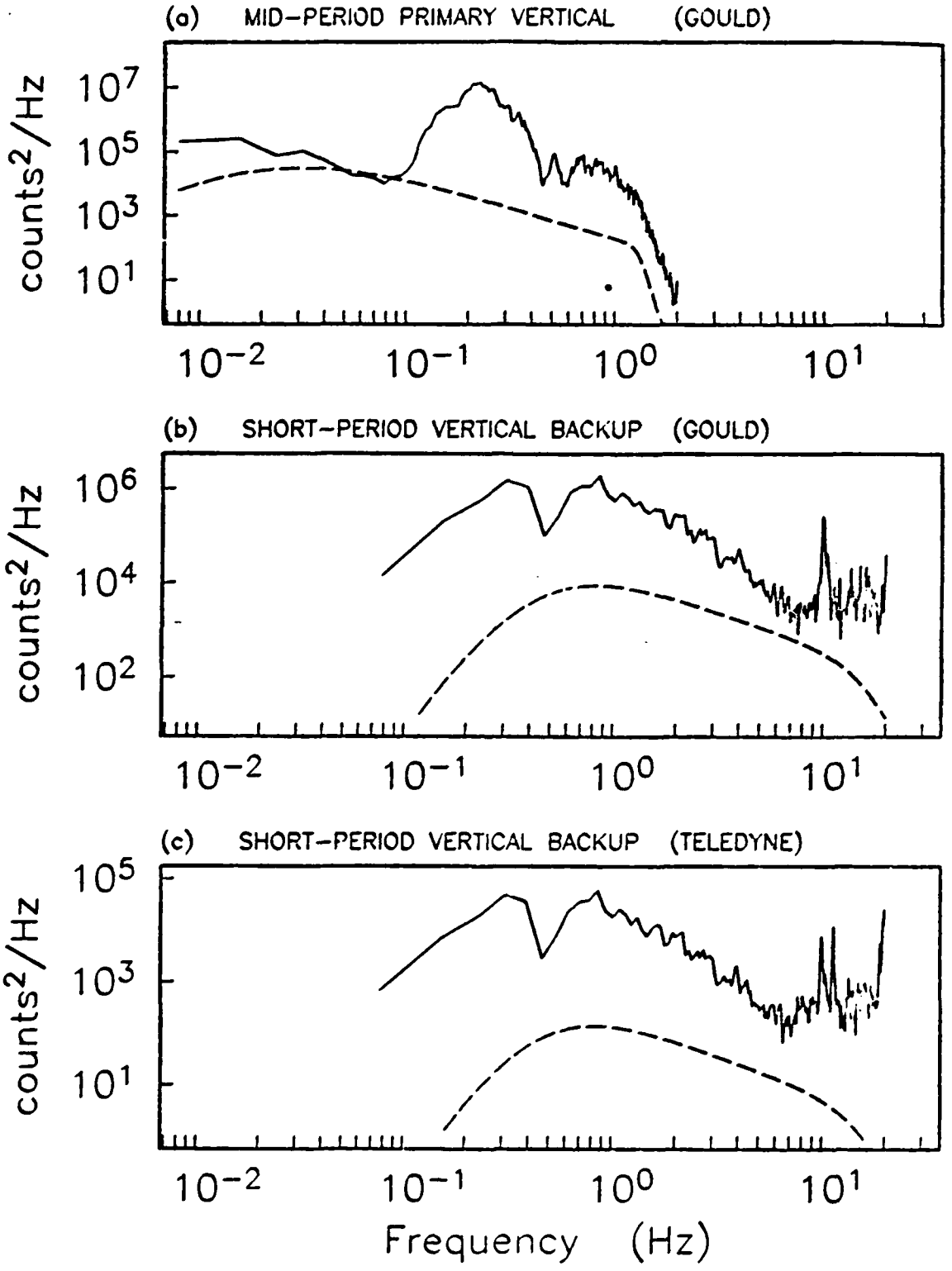

(a) MID-PERIOD PRIMARY VERTICAL (GOULD)
counts²/Hz
10⁷
10⁵
10³
10¹
10⁻²
10⁻¹
10⁰
10¹
(b) SHORT-PERIOD VERTICAL BACKUP (GOULD)
counts²/Hz
10⁶
10⁴
10²
10⁻²
10⁻¹
10⁰
10¹
(c) SHORT-PERIOD VERTICAL BACKUP (TELEDYNE)
counts²/Hz
10⁵
10³
10¹
10⁻²
10⁻¹
10⁰
10¹
Frequency (Hz)

FIGURE 12

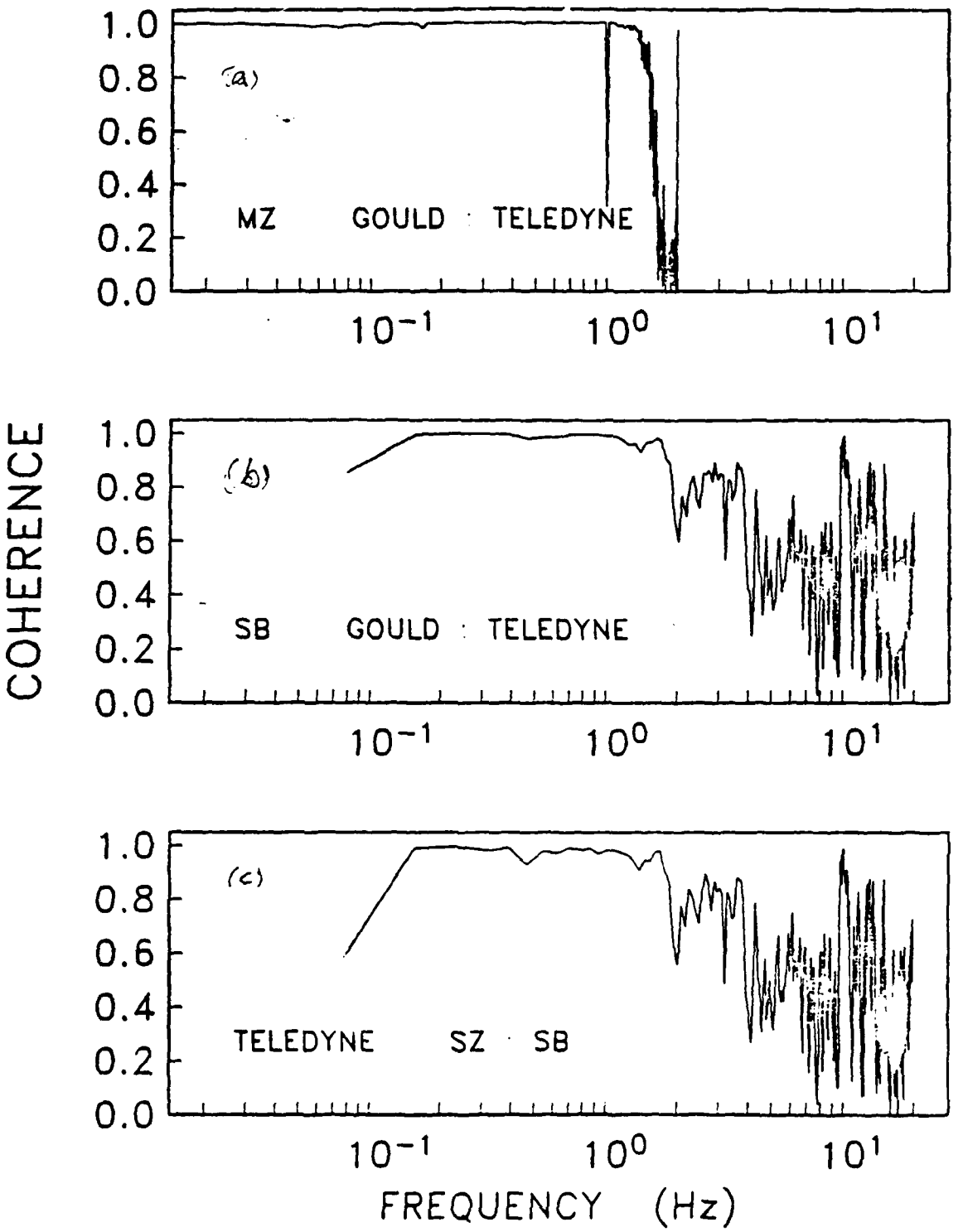

1.0
0.8
0.6
0.4
0.2
0.0
(a)
MZ GOULD · TELEDYNE
10^{-1}
10^{0}
10^{1}
COHERENCE
(b)
SB GOULD · TELEDYNE
(c)
TELEDYNE SZ · SB
FREQUENCY (Hz)

FIGURE 13

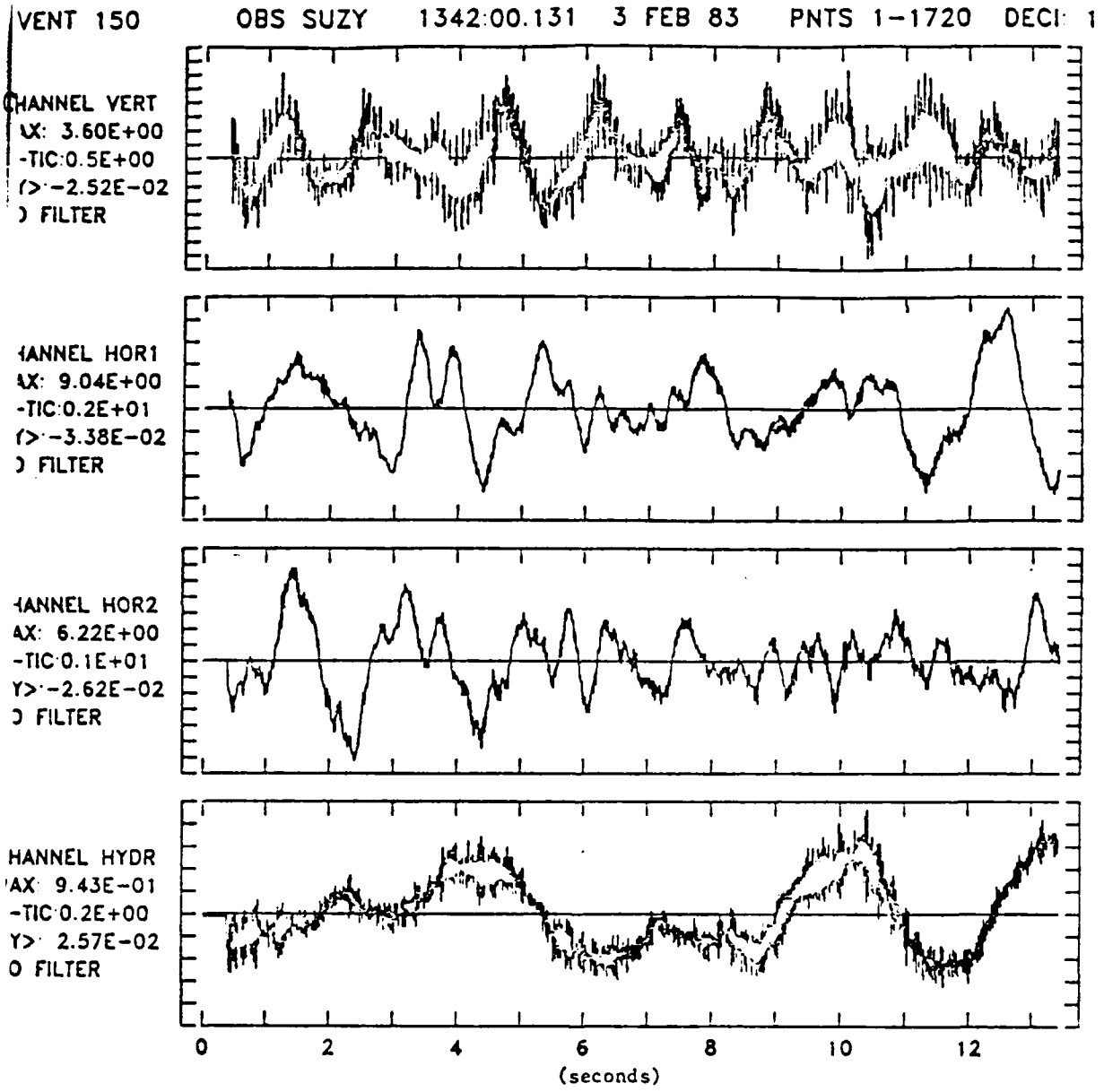

VENT 150
OBS SUZY 1342:00.131 3 FEB 83 PNTS 1-1720 DECI 1
HANNEL VERT
AX: 3.60E+00
-TIC 0.5E+00
(>-2.52E-02
) FILTER
HANNEL HOR1
AX: 9.04E+00
-TIC 0.2E+01
(>-3.38E-02
) FILTER
HANNEL HOR2
AX: 6.22E+00
-TIC 0.1E+01
Y>-2.62E-02
) FILTER
HANNEL HYDR
AX: 9.43E-01
-TIC 0.2E+00
Y> 2.57E-02
O FILTER
0
2
4
6
8
10
12
(seconds)

FIGURE 14

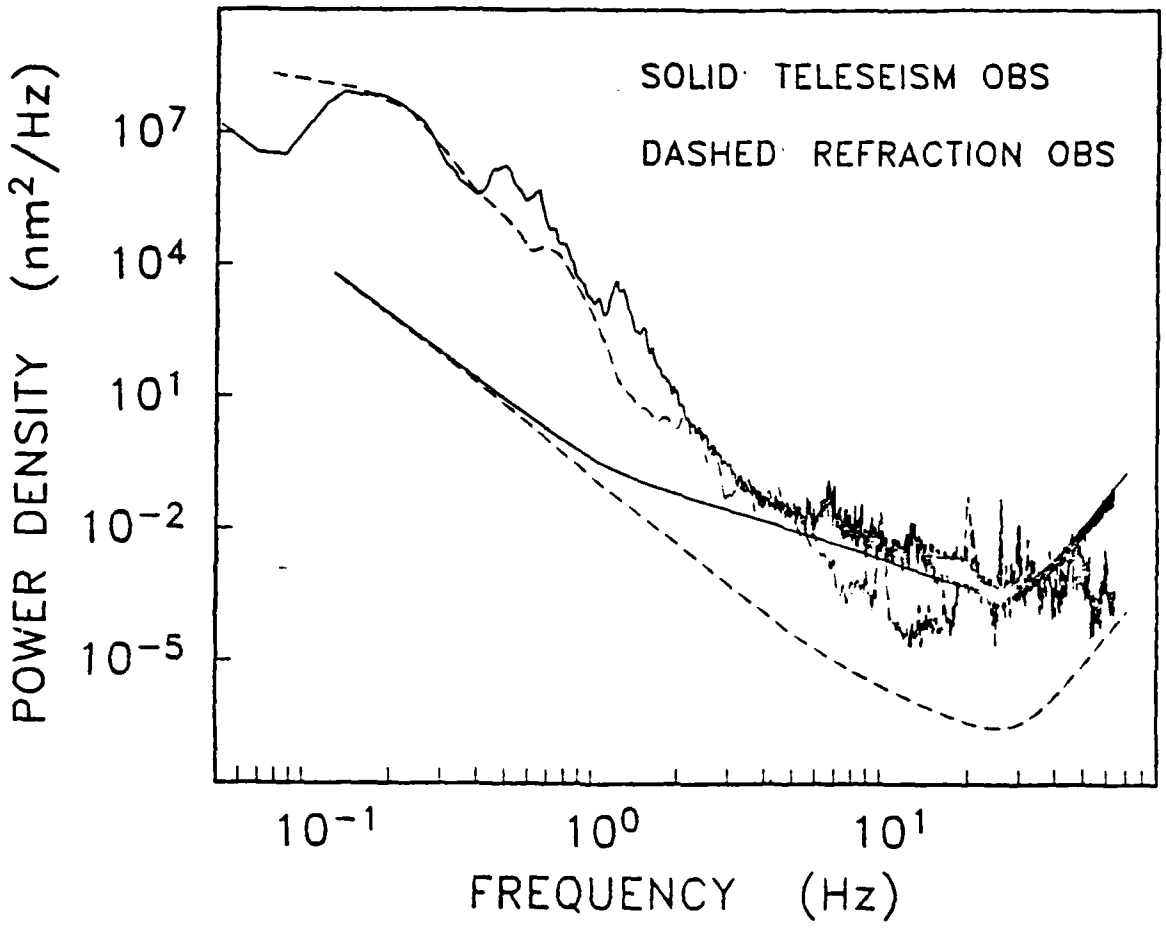

SOLID TELESEISM OBS
DASHED REFRACTION OBS
POWER DENSITY (nm²/Hz)
10⁷
10⁴
10¹
10⁻²
10⁻⁵
10⁻¹
10⁰
10¹
FREQUENCY (Hz)

FIGURE 15

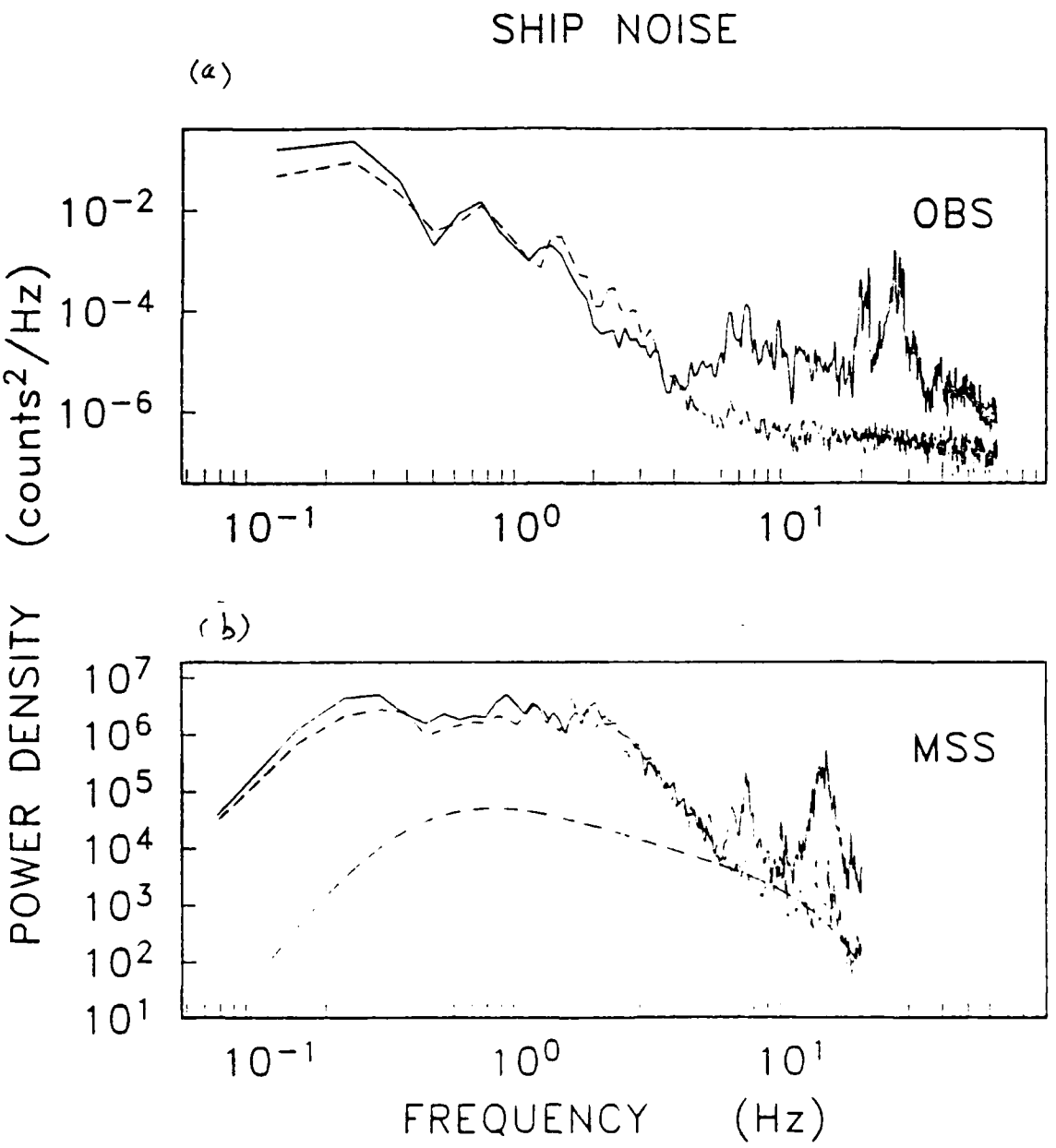

SHIP NOISE
(a)
OBS
10^{-2}
10^{-4}
10^{-6}
(counts^2/Hz)
10^{-1}
10^{0}
10^{1}
(b)
MSS
10^{7}
10^{6}
10^{5}
10^{4}
10^{3}
10^{2}
10^{1}
POWER DENSITY
10^{-1}
10^{0}
10^{1}
FREQUENCY (Hz)

FIGURE 16

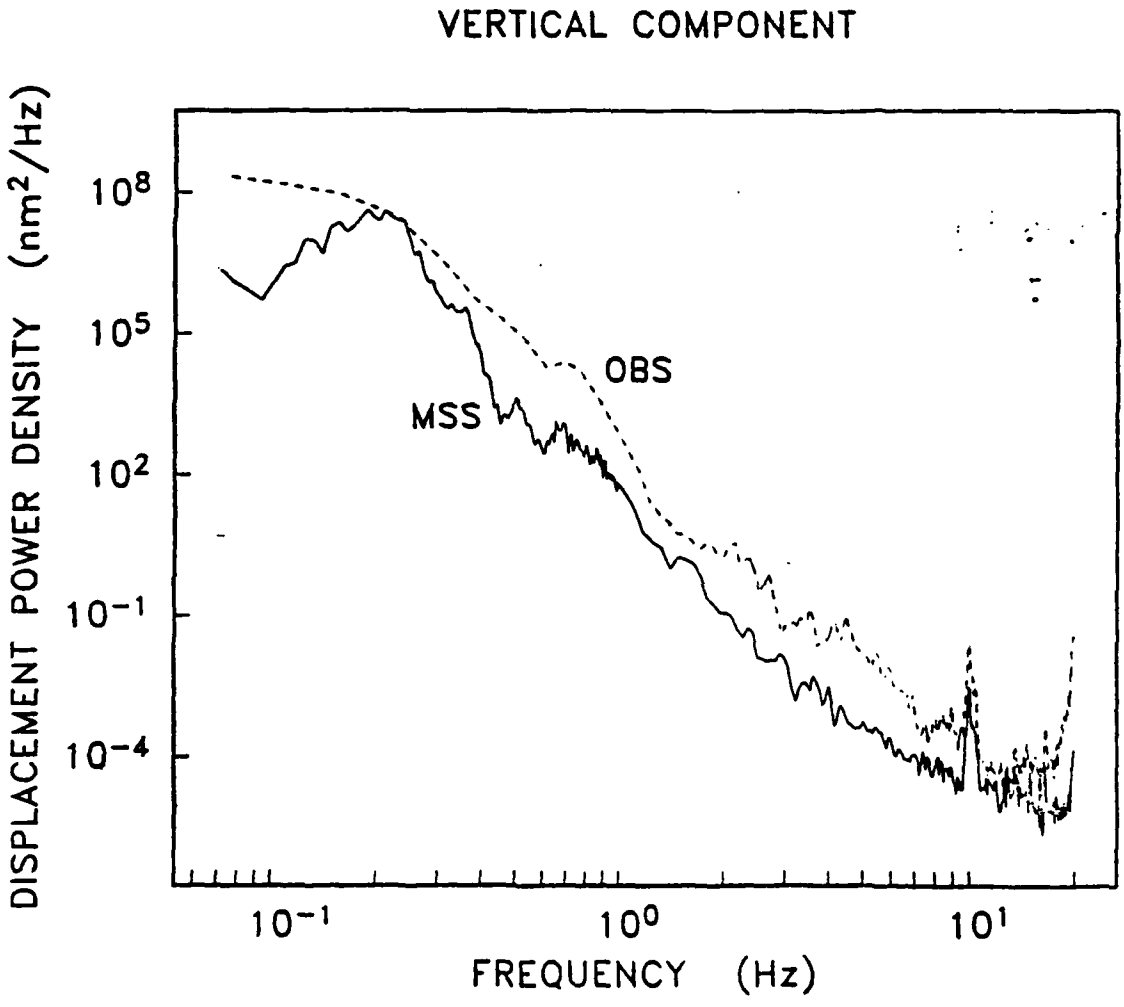

VERTICAL COMPONENT
DISPLACEMENT POWER DENSITY (nm²/Hz)
10⁸
10⁵
10²
10⁻¹
10⁻⁴
OBS
MSS
10⁻¹
10⁰
10¹
FREQUENCY (Hz)

FIGURE 17

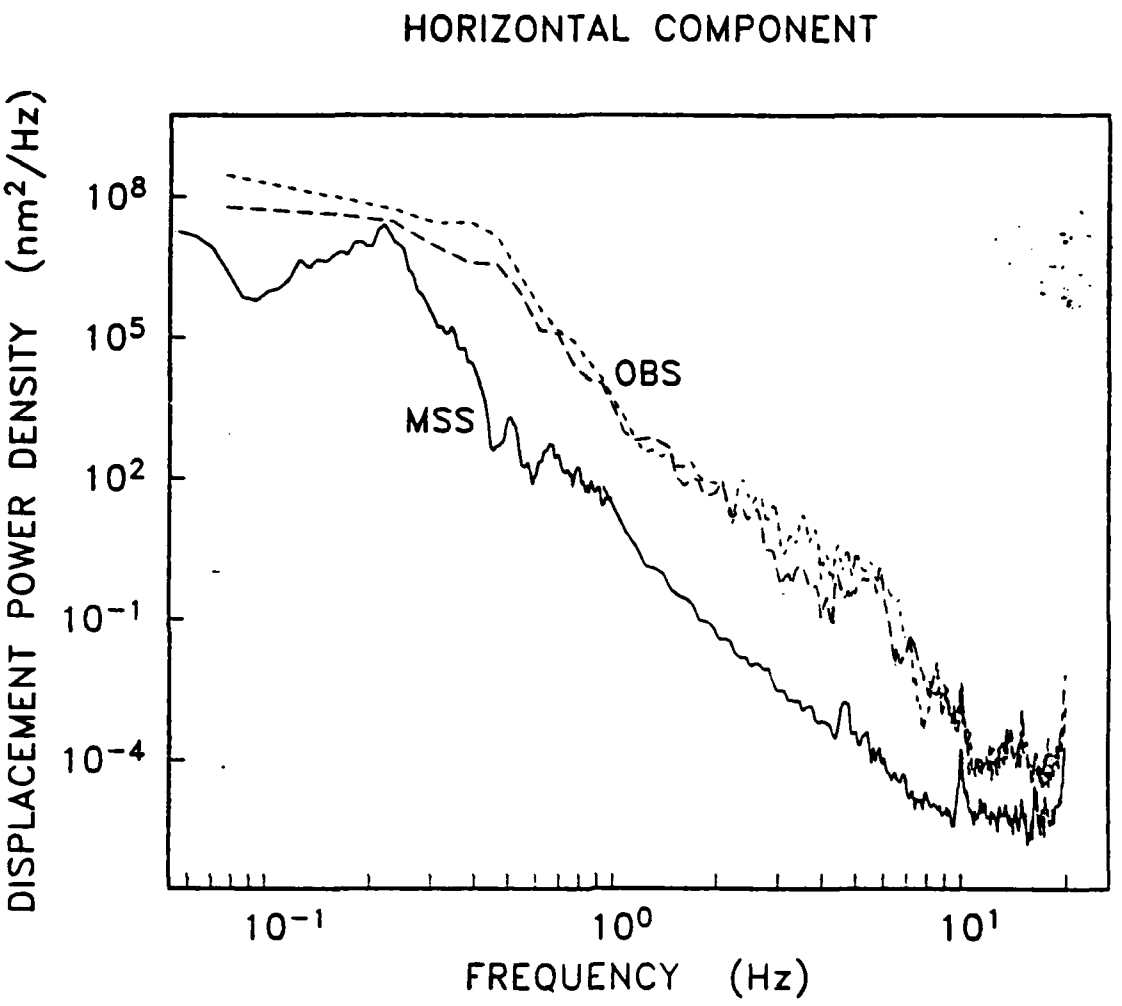

HORIZONTAL COMPONENT
DISPLACEMENT POWER DENSITY (nm²/Hz)
10⁸
10⁵
10²
10⁻¹
10⁻⁴
OBS
MSS
10⁻¹
10⁰
10¹
FREQUENCY (Hz)

FIGURE 18

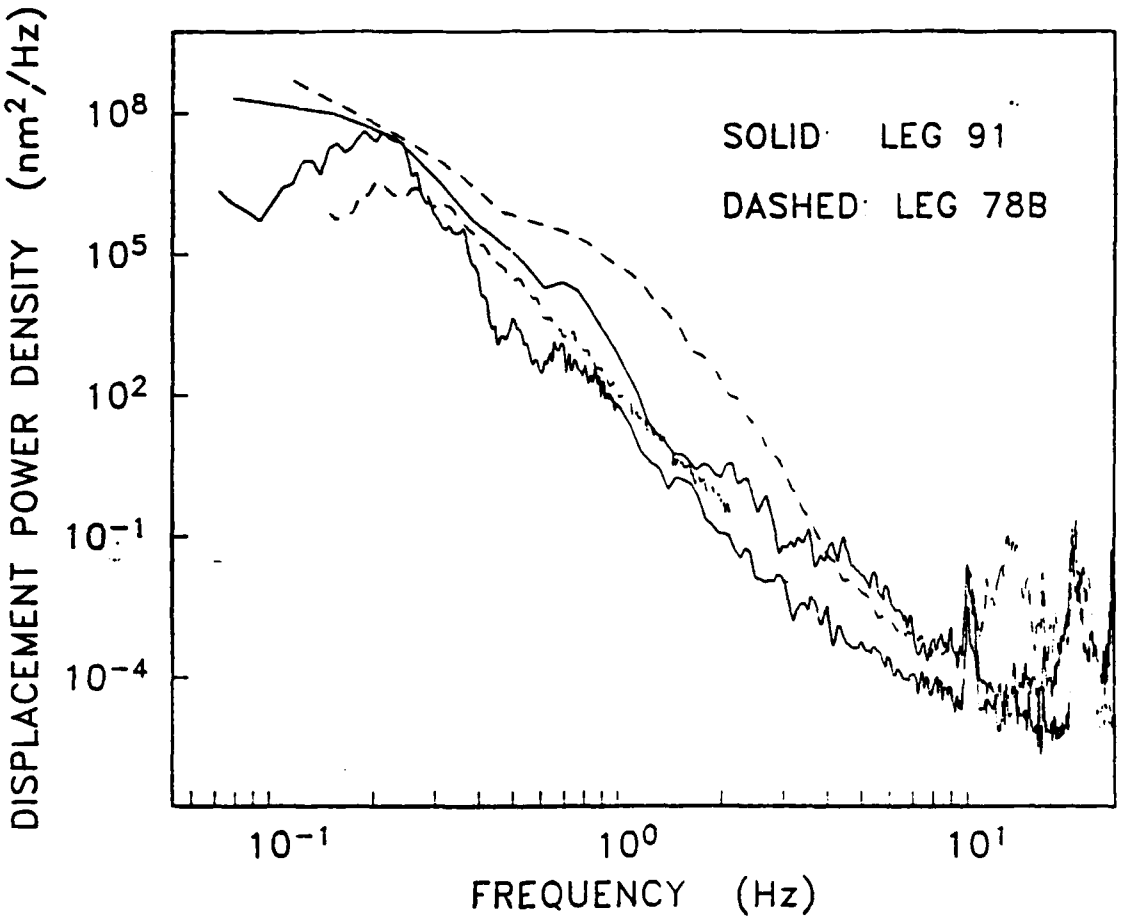

DISPLACEMENT POWER DENSITY (nm²/Hz)
10⁸
10⁵
10²
10⁻¹
10⁻⁴
SOLID LEG 91
DASHED LEG 78B
10⁻¹
10⁰
10¹
FREQUENCY (Hz)

FIGURE 19

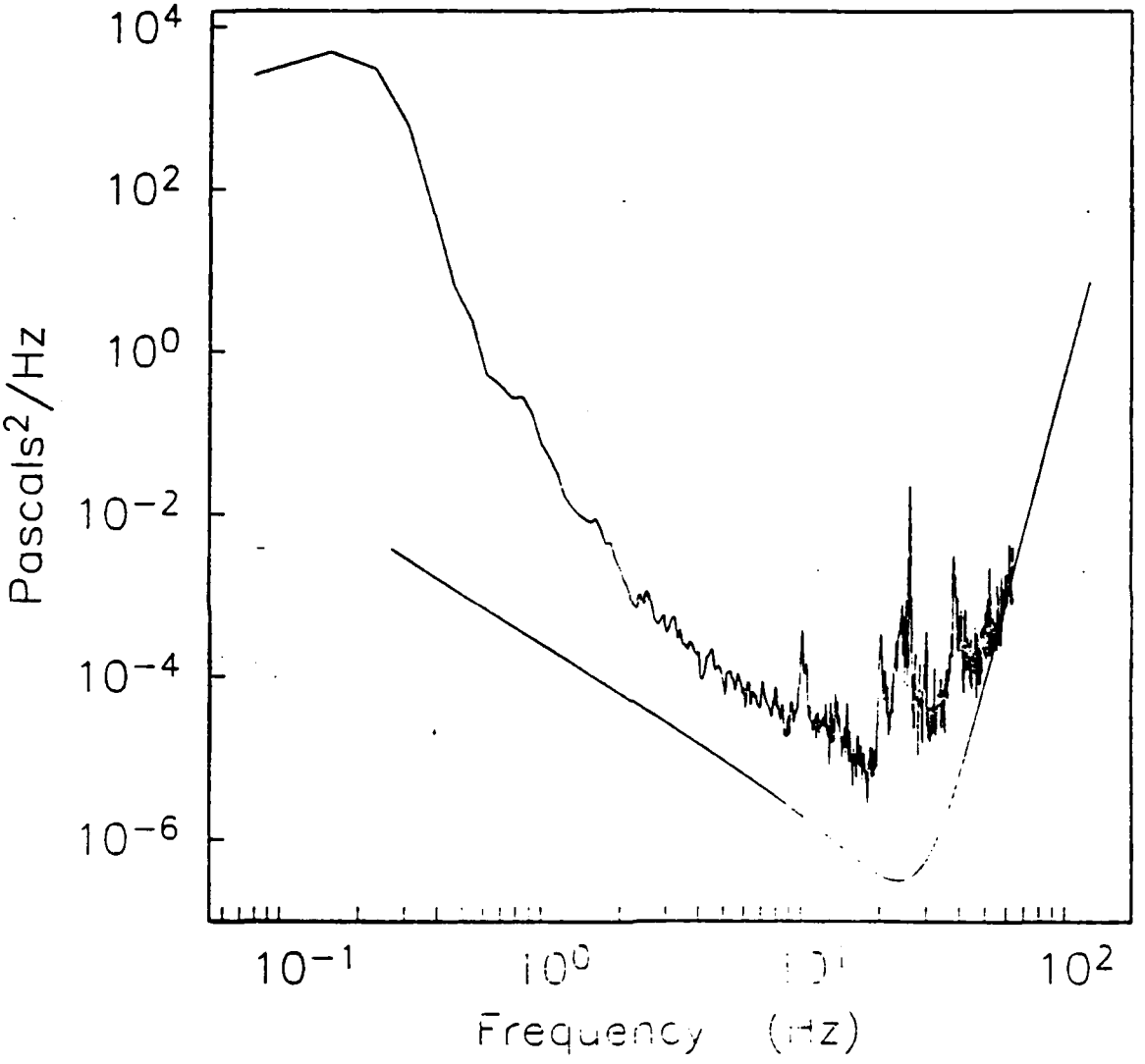


FIGURE 20

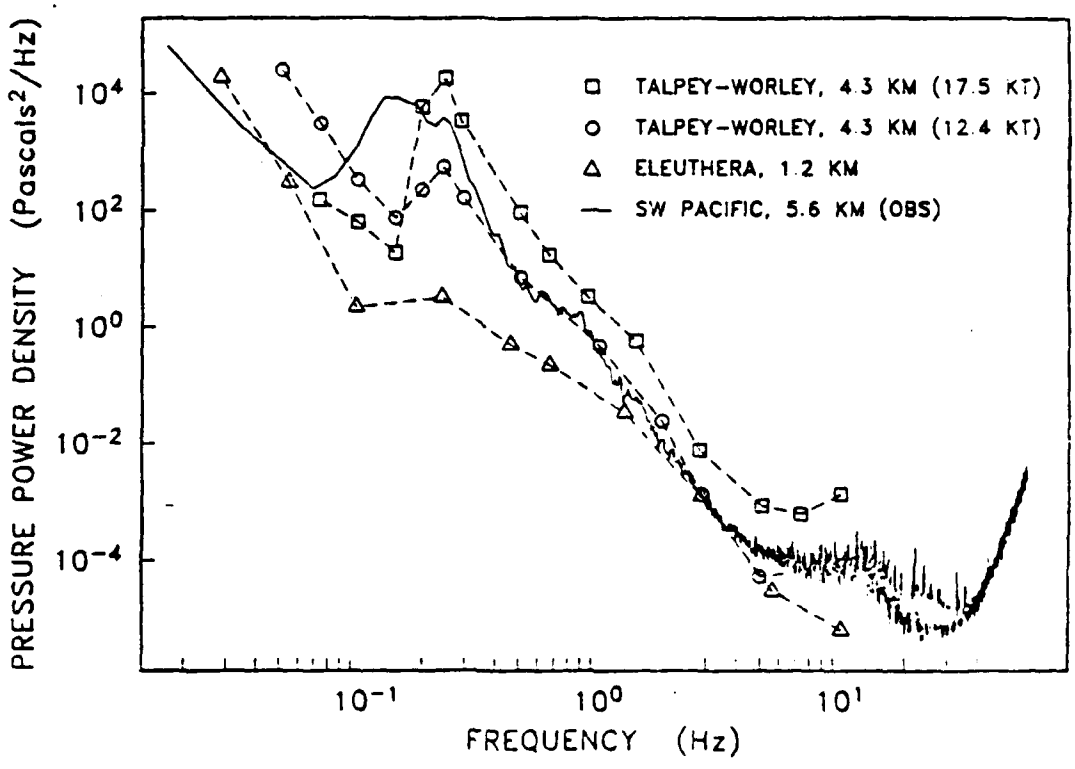

PRESSURE POWER DENSITY (Pascals²/Hz)
10⁴
10²
10⁰
10⁻²
10⁻⁴
10⁻¹
10⁰
10¹
FREQUENCY (Hz)
TALPEY-WORLEY, 4.3 KM (17.5 KT)
TALPEY-WORLEY, 4.3 KM (12.4 KT)
ELEUTHERA, 1.2 KM
SW PACIFIC, 5.6 KM (OBS)

FIGURE 21

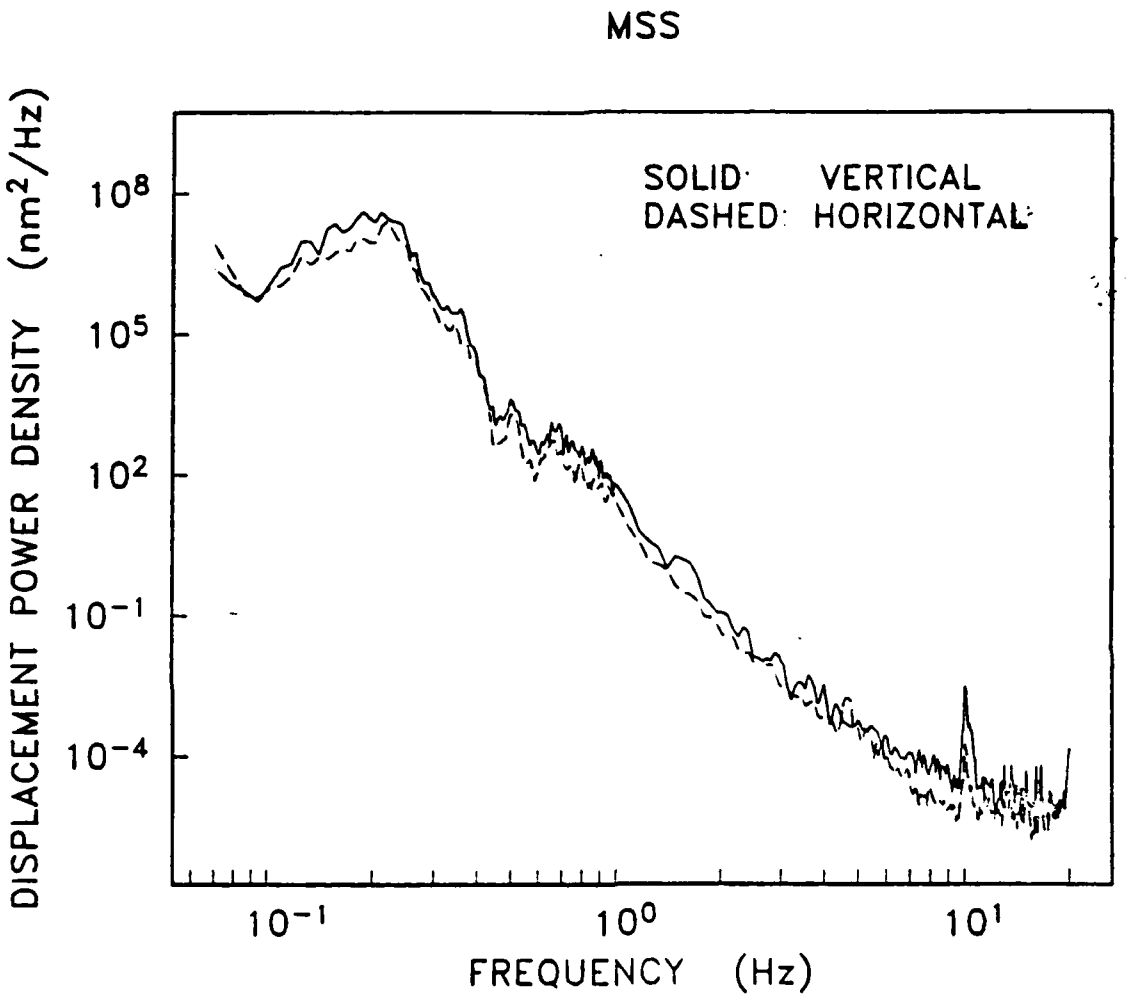

MSS
SOLID: VERTICAL
DASHED: HORIZONTAL
DISPLACEMENT POWER DENSITY (nm²/Hz)
10⁸
10⁵
10²
10⁻¹
10⁻⁴
10⁻¹
10⁰
10¹
FREQUENCY (Hz)

FIGURE 22

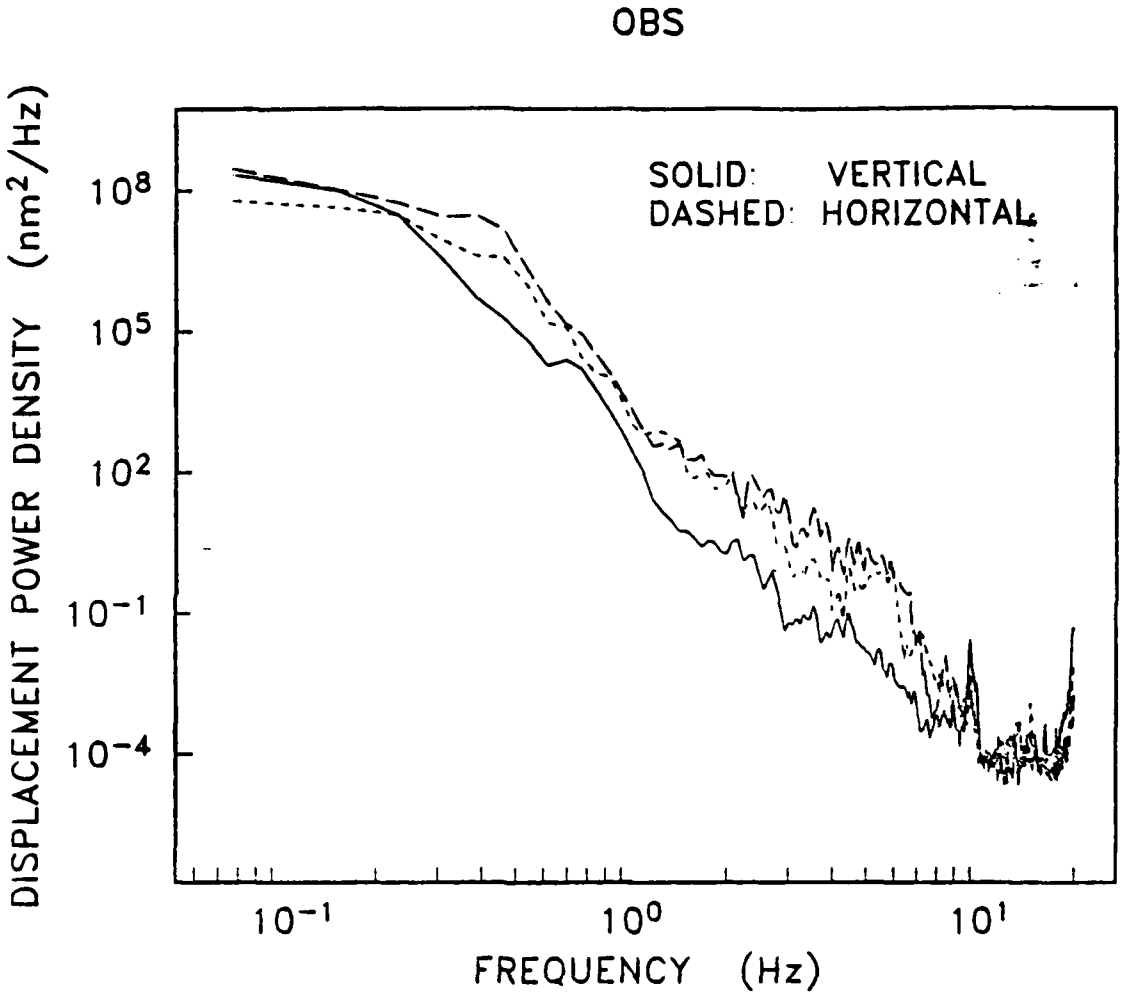

OBS
SOLID: VERTICAL
DASHED: HORIZONTAL
DISPLACEMENT POWER DENSITY (nm²/Hz)
10⁸
10⁵
10²
10⁻¹
10⁻⁴
10⁻¹
10⁰
10¹
FREQUENCY (Hz)

FIGURE 23

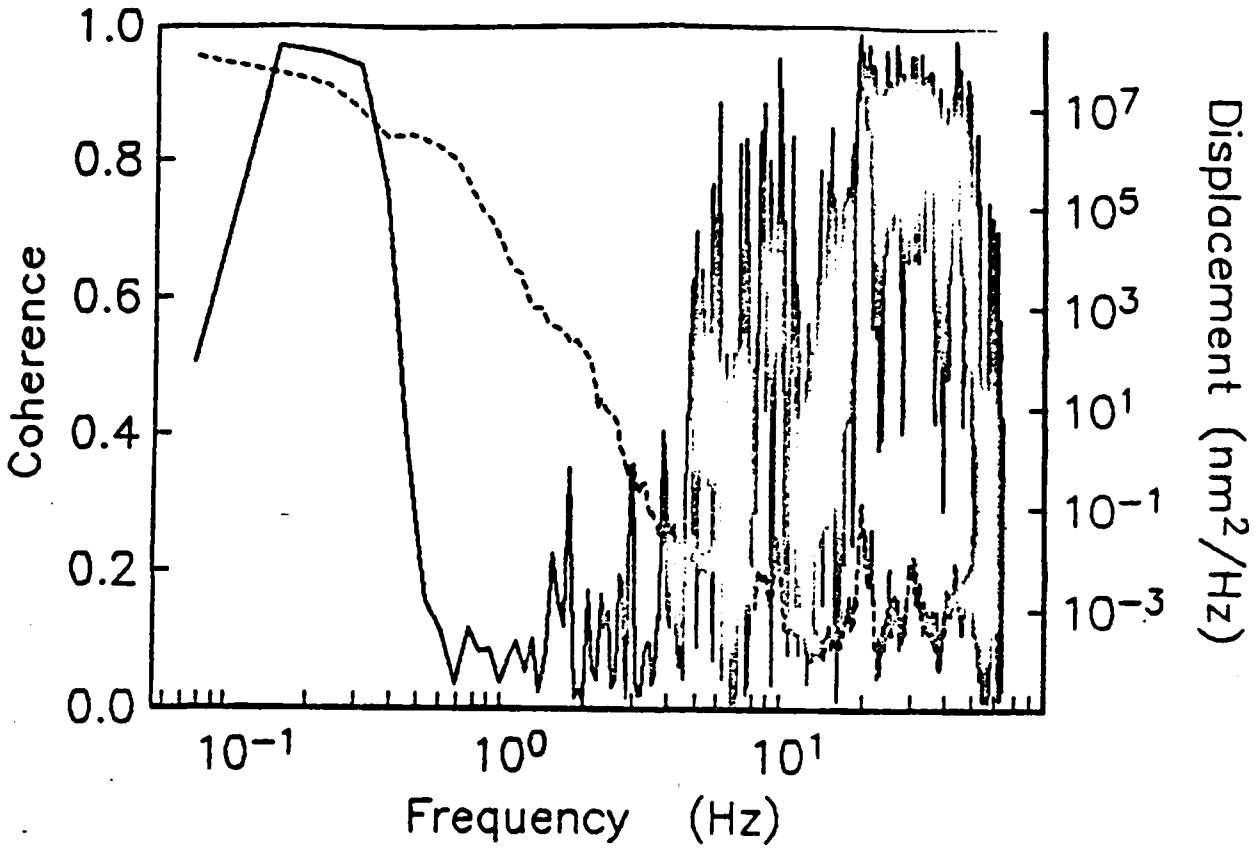

1.0
0.8
0.6
0.4
0.2
0.0
Coherence
10^{-1}
10^{0}
10^{1}
Frequency (Hz)
10^{7}
10^{5}
10^{3}
10^{1}
10^{-1}
10^{-3}
Displacement (nm^2/Hz)

FIGURE 24

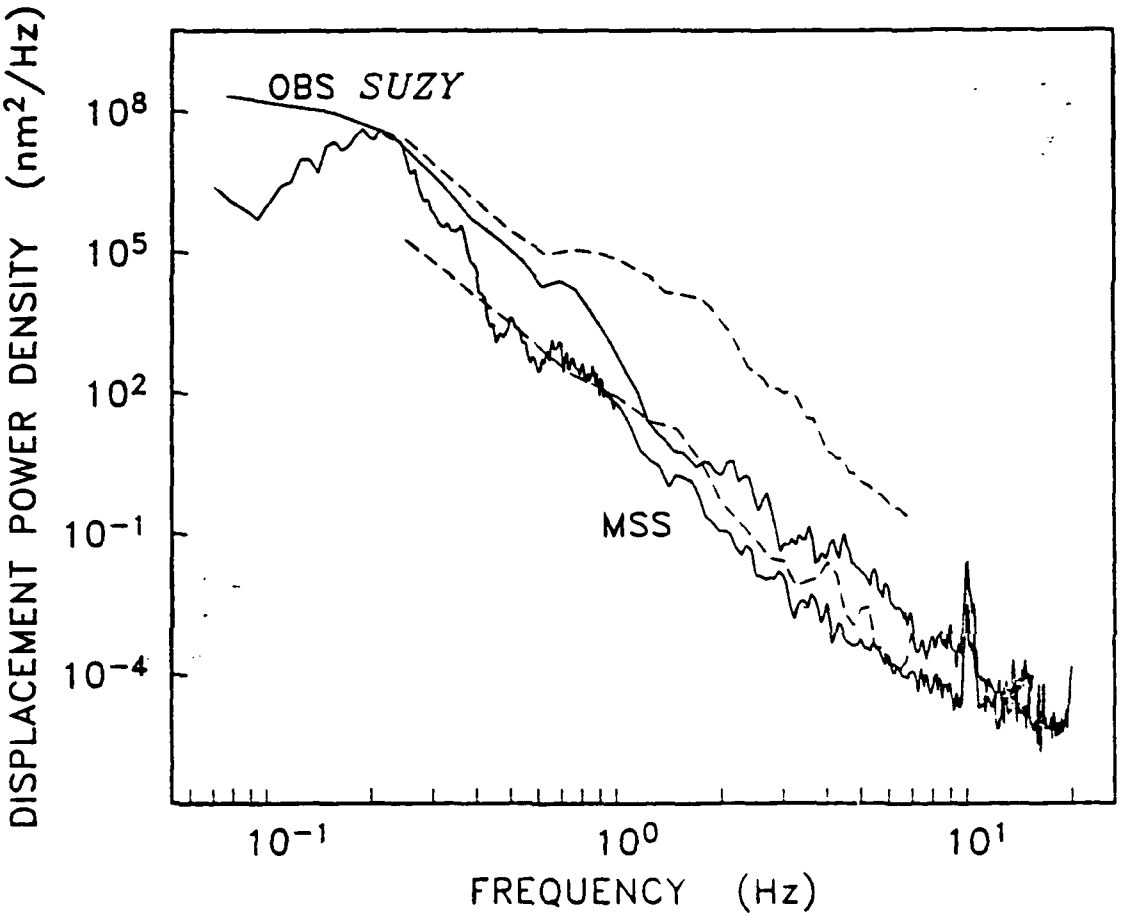

OBS SUZY
MSS
DISPLACEMENT POWER DENSITY (nm²/Hz)
10⁸
10⁵
10²
10⁻¹
10⁻⁴
10⁻¹
10⁰
10¹
FREQUENCY (Hz)

FIGURE 25

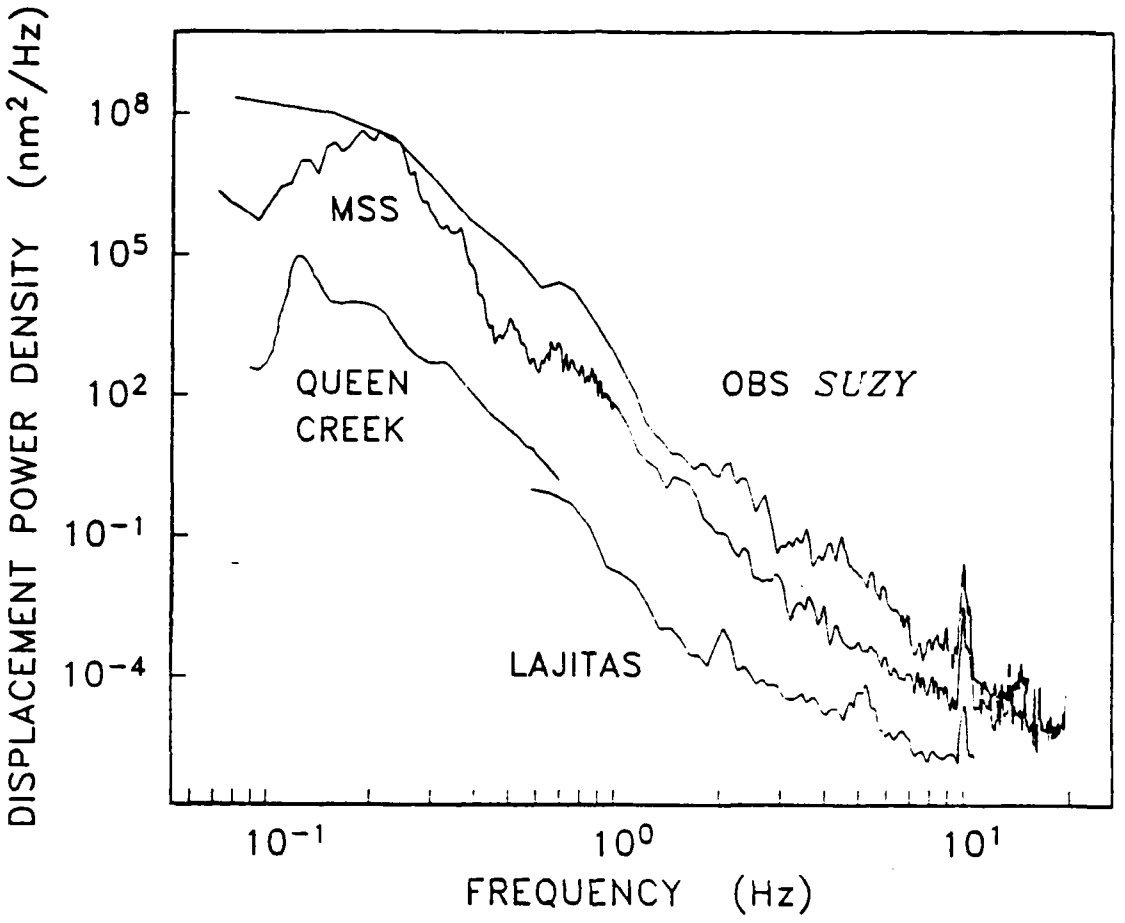

DISPLACEMENT POWER DENSITY (nm²/Hz)
10⁸
10⁵
10²
10⁻¹
10⁻⁴
MSS
QUEEN CREEK
OBS SUZY
LAJITAS
10⁻¹
10⁰
10¹
FREQUENCY (Hz)

FIGURE 26

TABLE 1

OBS LOCATIONS AND CHARACTERISTICS
DURING MSI

NAME	SITE	LOCATION LAT (S)	LOCATION LONG (W)	DEPLOYED: FROM:	DEPLOYED: TO:	RANGE, AZIMUTH* (km, degrees)	RESPONSE** TYPE	BUFFER LENGTH
JANICE	JA1	23 58.04	165 47.19	0826Z, 24 JAN 83	0715Z, 31 JAN 83	29.18 245	TEL	59 sec
JANICE	JA2	23 56.17	165 47.00	0626Z, 24 JAN 83	0715Z, 31 JAN 83	27.48 243	TEL	59 sec
JUAN	JU1	23 49.21	165 31.95	1104Z, 29 JAN 83	0535Z, 9 FEB 83	0.62 292	REF	13 sec
KAREN	KA1	23 49.04	165 31.65	0102Z, 29 JAN 83	0807Z, 9 FEB 83	0.56 352	REF	13 sec
LYNN	LY1	23 49.25	165 31.87	1123Z, 30 JAN 83	0817Z, 10 FEB 83	0.47 291	REF	13 sec
PHRED	PH1	23 56.51	165 45.68	0610Z, 30 JAN 83	0850Z, 7 FEB 83	27.29 241	TEL	59 sec
SUZY	SU1	23 49.04	165 31.65	0038Z, 30 JAN 83	0556Z, 10 FEB 83	0.56 354	REF	13 sec

* Reference site is MSS location: Lat., 23 49.34; Long., 165 31.61. Azimuth is clockwise from North.
** TEL=Teleseismic, REF=Refraction

TABLE 2

OBS LOCATIONS AND CHARACTERISTICS
DURING MS2

NAME	SITE	LOCATION LAT (S)	LOCATION LONG (W)	DEPLOYED: FROM:	DEPLOYED: TO:	RANGE, AZIMUTH* (km, degrees)		RESPONSE** TYPE	BUFFER LENGTH
JANICE	JA3	23 49.89	165 81.55	1432Z, 6 FEB 83	1520Z, 22 MAR 83	0.47	13	TEL	59 sec
JUAN	JU2	29 82.72	165 81.02	1124Z, 11 FEB 83	1100Z, 22 MAR 83	24.80	181	TEL	13 sec
KAREN	KA2	29 48.58	165 82.49	2142Z, 11 FEB 83	0600Z, 29 MAR 83	2.08	314	TEL	59 sec
LYNN***	LY2	?	?	1356Z, 9 FEB 83	1840Z, 29 MAR 83	?	?	TEL	13 sec
PHRED	PH2	23 49.44	165 82.29	2045Z, 9 FEB 83	0900Z, 23 MAR 83	1.17	261	TEL	13 sec
SUZY	SU2	23 51.64	165 17.88	2248Z, 10 FEB 83	0531Z, 22 MAR 83	23.77	100	TEL	59 sec

* Reference site is MSS location: Lat., 29 49.84; Long., 165 81.61. Azimuth is clockwise from North
** TEL=Teleseismic
*** Only drop point is available

CHAPTER 5

LEG 91 INITIAL REPORT

SIMULTANEOUS BOREHOLE AND OCEAN BOTTOM SEISMOMETER RECORDINGS OF EARTHQUAKES AND EXPLOSIONS-- RESULTS FROM THE 1983 NGENDEI EXPERIMENT AT DSDP HOLE 595B

P.M. Shearer, R.G. Adair, J.A. Orcutt, and T.H. Jordan*

Institute of Geophysics and Planetary Physics
Scripps Institution of Oceanography
La Jolla, California 92093

* now at Department of Earth, Atmospheric and Planetary Sciences, Massachusetts Institute of Technology, Cambridge, Massachusetts 02139

Introduction

Ocean bottom seismometers, or OBSs, have been used for many years to record both earthquakes and seismic refraction shots. Ocean bottom records have substantial advantages over surface hydrophone data, including improved signal-to-noise and three component capability. However, they also suffer from "noise" caused by possible sediment reverberations and unknown effects of OBS-seafloor coupling. Borehole seismometers emplaced in oceanic basement are largely free from these problems and also offer the possibility of improved signal-to-noise. Recently such borehole seismometers have been successfully deployed in DSDP drill holes (see for example Duennebier, 1984, and Stephen, 1979).

The 1983 Ngendei Experiment was designed to provide data from both OBS and borehole instruments. One of the experiment objectives was to simultaneously record earthquakes, seismic refraction shots, and background noise with both instrument types in order to compare their performance and response. The noise comparison results are detailed elsewhere in this volume (Adair et al., 1985) which also includes papers describing the seismic refraction and teleseismic experiments. This paper will compare the signals (earthquakes and explosions) recorded simultaneously by both ocean bottom and borehole seismometers and compare these results with those of the noise study.

Experiment Description

The Ngendei site is located at DSDP hole 595B in the southwest Pacific about 1500 km west-southwest of Tahiti (see Fig. 1). This site was chosen partially because of its proximity to the Tonga Trench, which provided a source of earthquakes for the teleseismic experiment described elsewhere in this volume (Jordan et al., 1985). This is a very old part of the Pacific basin with an estimated age as great as 140 m.y. (Menard, personal communication). The sediment cover at the site is 70 m thick, relatively thin considering the age of the crust. The original spreading direction at the site cannot be determined from the available magnetic and bathymetric information although upper mantle anisotropy favors a spreading direction of northeast (Shearer et al., this volume). A more detailed description of the site is available in the introductory chapter.

A borehole seismometer, the Marine Seismic System, or MSS, was emplaced at the bottom of Hole 595B at a depth 124 m below the seafloor and 56 m into layer 2. Data from a vertical and two horizontal seismometers were digitized at 40 samples/second and recorded on board the Glomar Challenger. An alternative recording system, the bottom processing package, or BPP, also recorded some data after the departure of the Challenger. The frequency response of the MSS is shown in Fig. 2. In this paper, we will use data from the MSS short-period vertical seismometer recorded by both the Gould system (includes a finite impulse

response, or FIR, anti-aliasing filter) and the Teledyne system (does not include FIR filter). The refraction shot data we will present were recorded by the Teledyne system; the earthquake and water wave data were recorded by the Gould system. Comparisons between Gould and Teledyne data have revealed that the Teledyne data are approximately a factor of 1.4 larger in amplitude than the Gould data, even after all appropriate gain adjustments have been made (Adair et al. this volume). Because the Teledyne data agreed with shipboard calibrations, we have taken the Teledyne amplitudes to be correct and have adjusted the Gould amplitudes upward by a factor of 1.4 for all analyses in this paper.

Ocean bottom seismometers (OBSs) from the Scripps Institution of Oceanography were deployed near the borehole for the seismic refraction experiment. Fig. 3 shows approximate OBS locations relative to the borehole. Although other OBS deployments were made during the Ngendei experiment, in this paper we will only examine data collected during the refraction deployments. The close proximity (0.5 km) of these OBSs to the borehole make this an ideal data set for comparisons of OBS and MSS data, since any effect of lateral variations between seismometer sites should be small. The OBSs are self-contained, digital instruments which record a vertical component, two horizontal components, and a hydrophone. Data are digitized at 128 samples/second with approximately 13 seconds of data stored in memory before tape recorder activation. The memory size was increased for the teleseismic portion of the Ngendei experiment, but was limited to 13 seconds during the refraction deployments discussed in this paper. The OBS frequency response during the refraction experiment is shown in Fig. 2.

Seismic Refraction Records

At least two OBSs recorded each of the lines shot during the refraction experiment. Unfortunately, delays in installing the borehole seismometer prevented its activation until the refraction shooting schedule was more than half completed. However, the MSS did record most of 3 refraction lines-- lines 4b, 5a, and 5b (see Fig. 5, Shearer et al., this volume) which together contain over 250 shots recorded by both the MSS and two or more OBSs.

A comparison between an MSS record section and an OBS record section for line 4b is presented in Fig. 4. Both record sections have been corrected for topography, scaled by range and shot weight, and reduced at 8 km/sec. The Moho triplication is prominent in both sections with the lower amplitude Pn arrival emerging at larger ranges. The broader frequency response of the OBS is apparent in these records as well as the improved signal-to-noise ratio of the MSS. Sediment reverberations and possible OBS-sea floor coupling oscillations show up in the OBS records as continued "ringing" following the initial P-wave and S-wave arrivals.

A comparison of MSS and OBS recordings in Fig. 5 for P-wave arrivals from shots at ranges of 22, 40, and 58 km indicates coherence between the records is excellent for the first 1 to 2 seconds following the initial arrival and then begins to break down. Again notice the greater bandwidth of the OBS and the superior signal-to-noise ratio of the MSS. Shot 4269 (58 km range) shows both a Pn and a PmP arrival. The higher frequency content of the Pn arrival relative to PmP is apparent only in the OBS seismogram.

Fig. 6 compares P-wave spectra between MSS and OBS for 9 shots at ranges from 40 to 60 km. These were calculated by selecting 2.5 second windows following the initial P-wave arrival, applying a Hanning taper, calculating spectra, correcting for instrument response, and stacking the individual spectra to achieve a degree of stability. Agreement between the absolute amplitude and shape of the MSS and OBS spectra is remarkable. Average noise spectra for the MSS and OBS (also in Fig. 6) were determined by stacking many separate simultaneous noise windows (Adair et al., this volume). Noise spectra vary somewhat between recording window time; we decided not to use windows immediately preceding the shot P-waves because the records at these times appear contaminated by reverberations from previous shots. Differences between noise spectra at different times are generally small for a given instrument, with lower frequency variations related to differences in weather conditions, and higher frequency variations related to differences in ship noise. However, regardless of the particular shape of the noise spectra, OBS noise levels are consistently 20 db higher than MSS noise levels. Fig. 6 demonstrates that noise dominates the shot P-wave spectra at frequencies lower than about 2 Hz, a frequency well below the bubble pulse frequency of the shots. At higher frequencies, the nearly identical P-wave response coupled with the much lower MSS noise levels indicates a signal-to-noise improvement of about 18 db for the MSS over the OBS.

Integrated total power between 3 and 20 Hz indicates that the OBS P-wave power is approximately a factor of 1.2 larger than the MSS P-wave power. We conducted a numerical experiment using a simple WKBJ synthetic algorithm to test this observation of near equality of the signals at the two depths. The model used was based on travel time and amplitude analyses of the Ngendei data (see Shearer et al., this volume) and physical properties measurements of the recovered sediments (see Kim at al., this volume). The sediments were taken to be 70 m thick and were characterized by a compressional velocity gradient from 1.55 km/sec at the seafloor to 1.65 km/sec at the basement interface. In the same interval the shear wave velocity increased from 100 m/sec to 150 m/sec. The basement velocity below the sediments was 4.6 km/sec and increased rapidly with depth in the upper crust.

Synthetic seismograms within the model structure were calculated for both seafloor and intracrustal receivers between ranges of 40 and 60

km. For the seafloor receiver (OBS) the upgoing P ray alone was considered, while for the crustal receiver (MSS) the upgoing P ray as well as the compressional and shear waves reflected from the overlying sediment-basement interface were included. We found that the later reflections from the water-sediment interface were much smaller and could be neglected in these calculations. For a range of 45 km, which was fairly typical, the OBS synthetic amplitude was a factor of 2.16 smaller than the synthetic amplitude for the MSS receiver. This 6 db difference contrasts somewhat with observations, but can be largely attributed to likely calibration uncertainties in the two instruments and the simplicity of the synthetic calculation. The calculation does confirm that the observed vertical amplitudes at the two levels should be comparable and that any reduction in noise level achieved by insertion in a borehole should lead to a direct increase in signal-to-noise levels.

Earthquake Records

Following the refraction shooting, the MSS and six OBSs were left on the sea floor for 45 days to record earthquakes. The OBSs operated in trigger mode and recorded dozens of regional earthquakes and teleseisms during this time period. The MSS was connected to a bottom processing package, or BPP, which was designed to record continuously for 45 days. Unfortunately, the BPP failed after less than 2 days and captured only 3 earthquakes recorded by the OBSs during their 45 day deployment. Because of the failure of the BPP, the few days of shipboard recording of the MSS have proven invaluable. Many earthquakes were recorded during and immediately after the refraction shooting. During this time, 13 earthquakes were recorded by both the MSS and at least one OBS. Many of the OBS earthquake recordings were made by OBSs deployed for the refraction experiment, but which reverted to trigger mode following the end of shooting. In many cases, the OBS earthquake records do not include the initial P-wave arrival since the OBS triggered on S or a later part of the P-wave. Thus, there are a very limited number of recordings available for MSS vs. OBS comparisons of the first arriving P-wave.

Fig. 7 compares MSS and OBS vertical component recordings of two regional earthquakes at an approximate 7 degree range. These events are not listed in the Preliminary Determination of Epicenters (National Earthquake Information Service, 1983) and we are aware of no other recordings of them. Each figure shows the MSS record of the entire seismogram, including both the P and S phases. Below this is an expanded view of the first 10 seconds of the P wavetrain as recorded by the MSS and an OBS. We do not show any more of the OBS record because it is contaminated by tape recorder noise from within the OBS capsule. As we saw in the refraction shot comparison, the broader frequency response of the OBS is apparent as well as the superior signal-to-noise ratio of the borehole instrument.

The MSS and OBS seismograms for the February 8, 1983 event are compared in detail in Fig. 8. Coherence between the traces is excellent for the first few seconds and still fairly good even up to 8 seconds following the first arrival. The lessened coherence and higher OBS amplitudes in the latter part of this record probably resulted from superior OBS sensitivity to reverberations within the sediment layer and possible resonances in the OBS-seafloor system. At roughly 8 seconds following the initial P-wave, a surface reflected phase (resulting from a bounce off the surface of the ocean) is much clearer on the OBS record than on the MSS record.

P-wave spectra for the two earthquakes are plotted in Fig. 9. We windowed 10 seconds of the P-wave with a Hanning taper, computed spectra and corrected them for instrument response. These power spectra differ from others in this paper in that stacking could not be employed to reduce the variance of the spectral estimates. The figures also show average noise spectra for the MSS vs. the OBS. The signal-to-noise advantage of the MSS is apparent in these spectra but less pronounced than in the refraction shot comparison. This reduction of the signal-to-noise ratio arises because the OBS amplitudes for the earthquakes are somewhat higher than the MSS amplitudes. Integrated power from 3 to 20 Hz is about 2.3 times larger for the OBS (2.7 for Feb. 8 quake, 2.0 for Feb. 9 quake). The signal-to-noise advantage of the MSS for these earthquakes is about 13 db. A possible cause for the higher earthquake OBS power levels relative to the refraction shots is the additional power in the sediment reverberations which were not included in the earlier analysis of refraction data.

Direct Water Waves

We also examined the direct water waves recorded during the refraction shooting in order to examine MSS and OBS differences in the decay of water arrivals with range. Fig. 10 compares MSS and OBS Suzy vertical component record sections for line 5b. Times have been reduced at 1.5 km/sec in order to isolate the water wave arrivals. The direct water wave is the first arrival shown in the sections, followed by the first water wave multiple, second multiple, etc. The OBS section is less complete because of the limited OBS recording window for each shot. In addition, most of the water waves are clipped on the OBS, and OBS tape recorder noise contaminates many of the water wave multiples.

In order to quickly examine the power level of a large number of water waves, we used a much simpler comparison method than the spectral comparisons discussed earlier in this paper. We picked arrival times for the direct water wave for both the MSS and the OBS. Using a one second window following these picks we calculated an approximate power for each water wave arrival by computing the variance. Assuming a uniform 1.5 km/sec ocean we also calculated the length of the diagonal ray path through the ocean appropriate for each shot. Fig. 11 shows the

power from the direct water wave vs. water path length for both the MSS and the OBS. The MSS did not clip on any of the water wave arrivals, but only a few unclipped water waves are available for the OBS. Direct comparison of the MSS and OBS power levels measured in this way is, of course, not meaningful because of the differences in instrument responses. In order to obtain an approximate value for the difference in MSS and OBS water wave power, we calculated displacement power spectra for a 1 second window following the water wave arrival for shot 5030 (20 km range). After correcting for instrument responses, we integrated the power between 5 and 20 Hz and obtained a ratio of 3.5 for the OBS vs. MSS water wave power, a value which we then used to constrain the relative positions of the MSS and OBS power curves in Fig. 11.

The MSS amplitudes are smaller than the amplitudes measured on the OBS. This ratio of amplitudes is expected, given that the incident waves are largely reflected at the seafloor and the MSS must be excited, for the most part, by an evanescent wave which decays exponentially in amplitude in a vertical direction. The predicted amplitude ratio could not be computed with the simple WKBJ formalism; detailed comparisons were deferred for future investigations.

At water path lengths of 17 to 25 km (the range of the OBS data) the rate of falloff is approximately the same for the MSS and the OBS. A simple model of a uniform 1.5 km/sec ocean predicts a r^{-4} falloff of power at the sea floor with path length. This results from a r^{-2} geometrical spreading term and a r^{-2} term to correct displacements along the ray path to vertical displacements. The OBS water wave power falls off slightly faster than r^{-4}. It is possible that this difference can be explained by tracing rays through a realistic ocean velocity profile. However, the steeper falloff shown in the MSS record at shorter ranges cannot be explained in this way and may reflect the evanescent behavior of the direct wave "root" (Stephen, 1984). That is, because the MSS is located 124 m below the sea floor (68 m of sediment, 56 m of rock) the direct water wave is critically reflected at the longer ranges and its amplitude below the sea floor cannot be predicted with simple geometrical ray theory. We plan further investigations of these data to see what, if anything, can be learned about the velocity of the sediment and shallow crust from water wave data of this type. One interesting feature of the data shown in Fig. 11 is the peak in power at a path length of 8 km. This is likely related to the caustic associated with the emergence of the shear wave in the basement (Burnett et al., 1984; White, 1979).

Conclusions

Ocean bottom and borehole seismometer data exhibit excellent coherence for P-waves recorded from both seismic refraction shots and regional earthquakes. The measured ratio of OBS power to MSS power is about 1.2 for explosions and 2.3 for regional earthquakes, values

comparable to those predicted by theory. Since MSS noise levels are about 20 db below OBS noise levels, this results in a signal-to-noise improvement of 18 db for the MSS over the OBS in recording explosions and a 13 db advantage in recording earthquakes. These values are more certain than the measurements of absolute power level differences, since any instrument miscalibration presumably would have an equal effect on the both the noise and signal amplitude measurements. Analysis of water wave arrivals shows that MSS direct water wave power levels fall off faster with range than would be predicted from a simple ray theory model.

References

Adair, R.G., J.A. Orcutt and T.H. Jordan, 1985. Preliminary analysis of ocean bottom and sub-bottom microseismic ambient noise during the Ngendei Experiment. Initial Rep. Deep Sea Drill. Proj., Leg 91, *this volume*.

Adair, R.G., J.A. Orcutt, T.H. Jordan, A.J. Bullard, C. Mulcahy, N. Gould and ...<more to follow>... Description and performance of the Marine Seismic System during the Ngendei Experiment. Initial Rep. Deep Sea Drill. Proj., Leg 91, this volume.

Burnett, M.S., J.A. Orcutt and J.S. McClain, 1984. Synthetic modeling of vertical component OBS water wave data. EOS, 65, p. 1013.

Duennebier, F.K., R.K. Cessaro, D. Harris and P. Anderson, 1984. The ocean sub-bottom seismometer: Results from the DSDP Leg 88 Borehole Seismic Experiment. EOS, 65, p. 1007.

Jordan, T.H. ---------- init report paper

Kim, I.I., D.K. Smith, J.A. Orcutt, T.H. Jordan and H.W. Menard, 1985. Seismic reflection site survey: Correlation with physical properties, Leg 91, Deep Sea Drilling Project. Initial Rep. Deep Sea Drill. Proj., Leg 91, submitted.

Shearer, P.M., J.A. Orcutt, T.H. Jordan, R.B. Whitmarsh, I.I. Kim, R.G. Adair and M.S. Burnett, 1985. The Ngendei Seismic Refraction Experiment at DSDP Hole 595B-- Ocean bottom seismometer data and evidence for crustal and upper mantle anisotropy. Initial Rep. Deep Sea Drill. Proj., Leg 91, submitted.

Stephen, R.A., 1979. The Oblique Seismic Experiment in oceanic crust-Experiment and technique. Mar. Geophys. Res., 4, p. 213-276.

Stephen, R.A., 1984. The direct wave root in marine seismology. EOS, 65, p. 239.

White, R.S., 1979. Oceanic upper crustal structure from variable angle seismic reflection-refraction profiles. Geophys. J. R. Astron. Soc., 57, p. 683-726.

Fig. 1. DSDP hole 595B is located in the southwest Pacific about 1000 km east of the Tonga Trench.

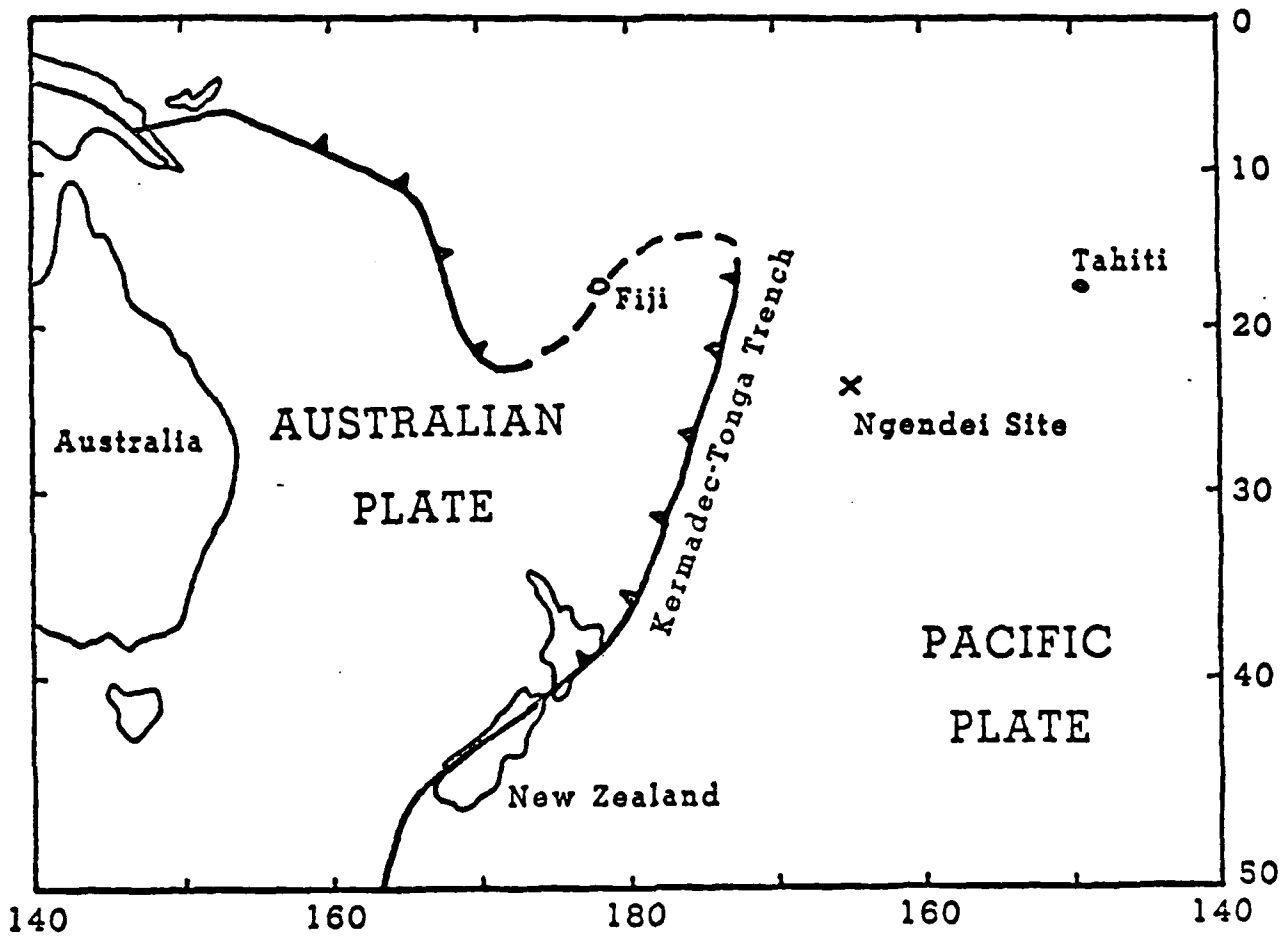


Fig. 2. The frequency response of the instruments used in the Ngendei Experiment. This paper will discuss data from the MSS short-period seismometer and the OBS refraction configuration.

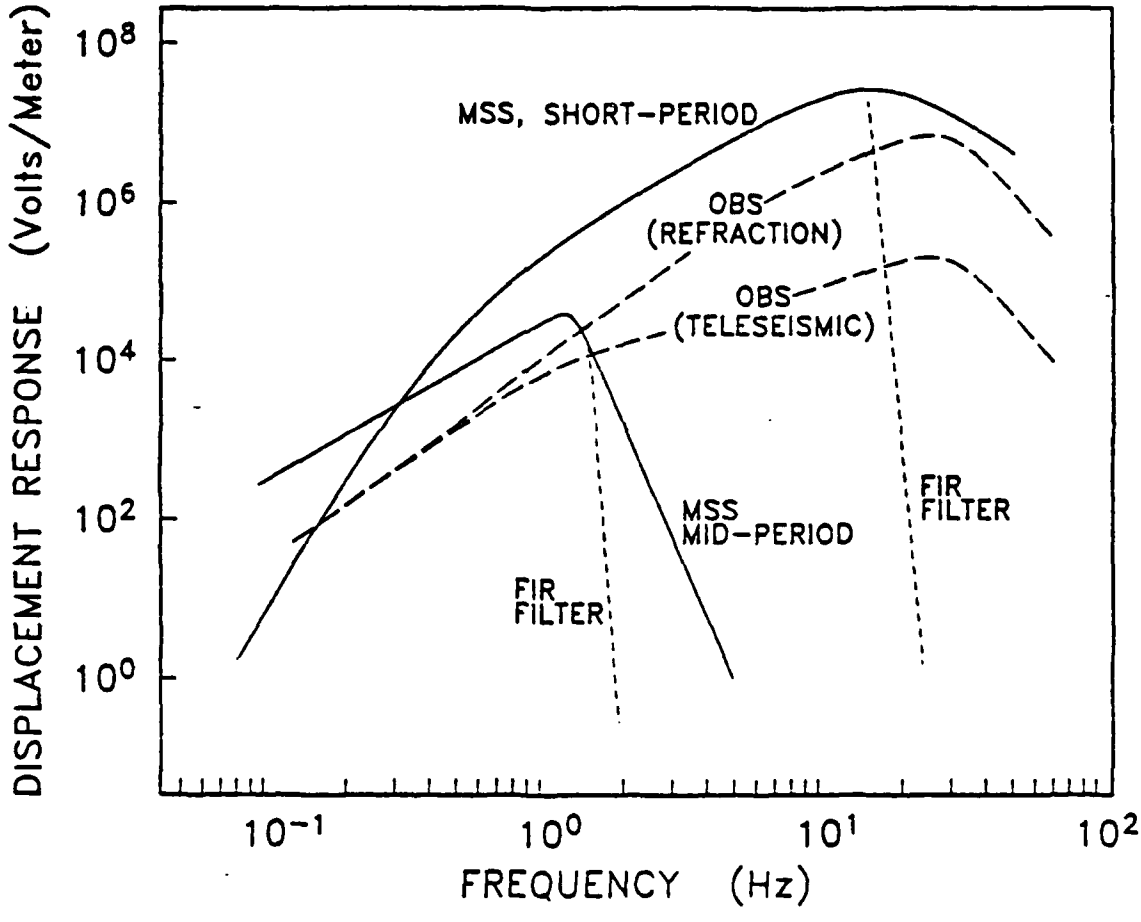


Fig. 3. The Scripps Institution of Oceanography deployed four Ocean Bottom Seismometers (OBSs) near the borehole for the seismic refraction experiment. This figure shows 95% confidence ellipses for the OBS locations relative to the borehole. Approximate drop points are shown as diamonds; OBS names are Karen, Suzy, Juan, and Lynn.

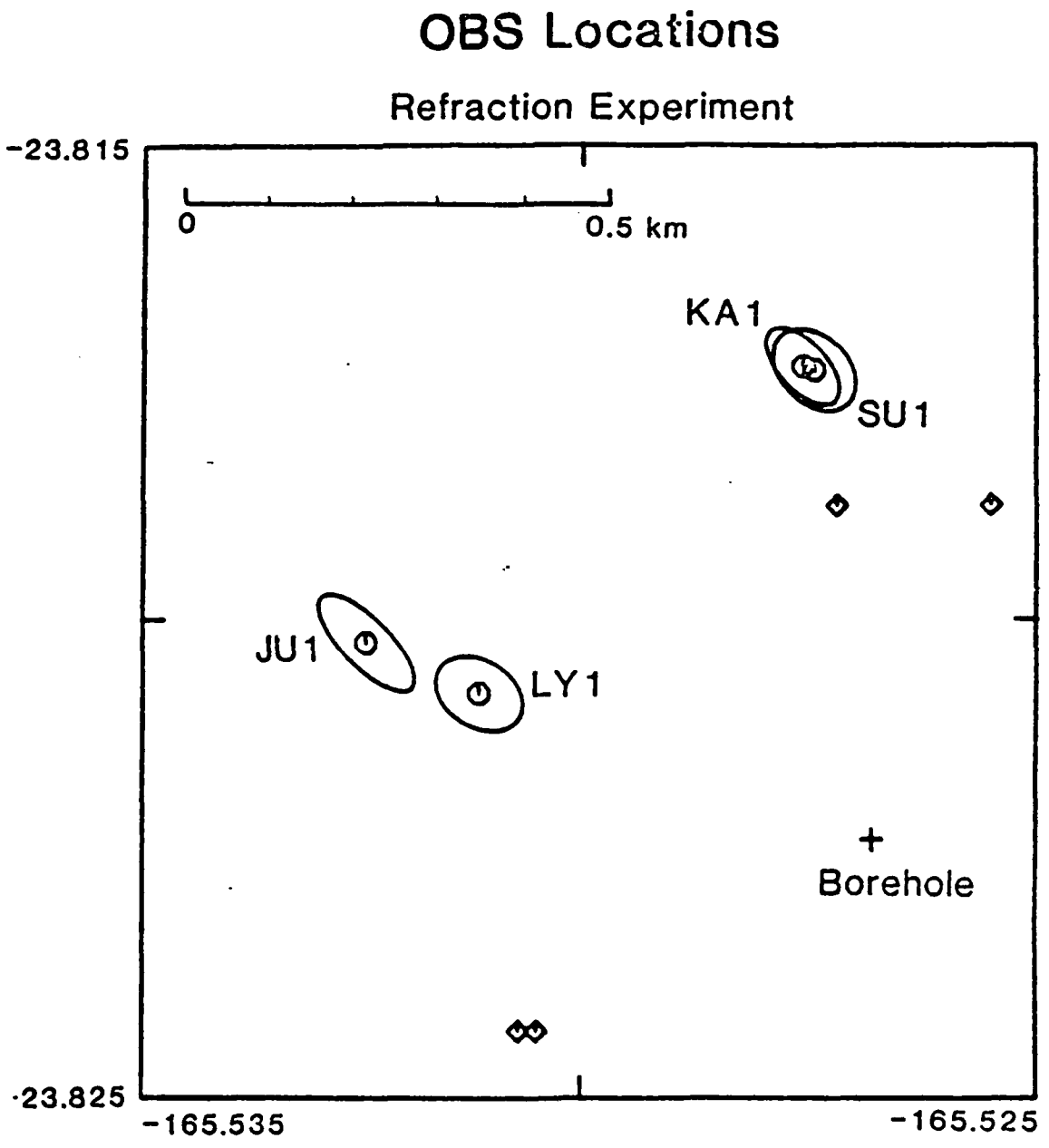
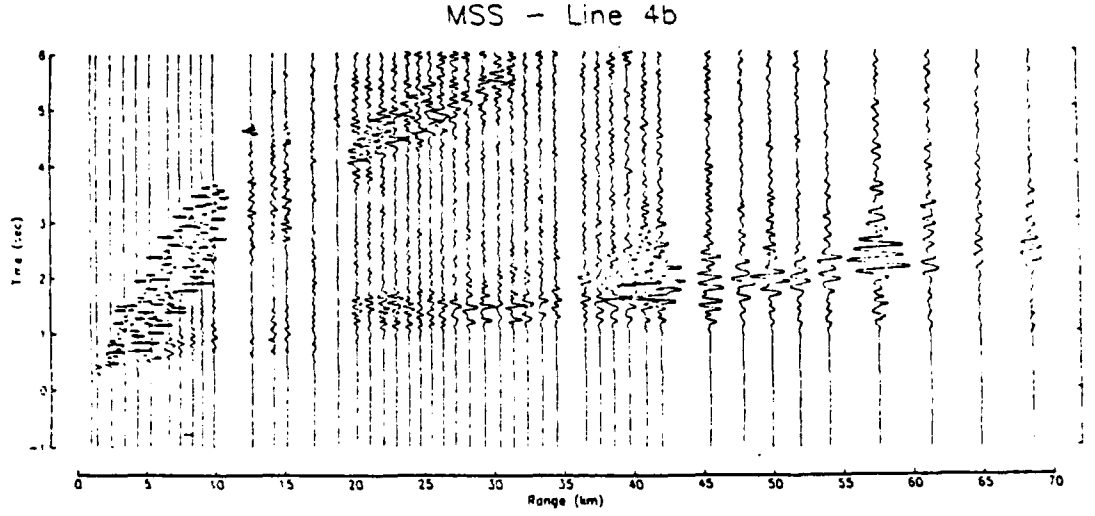


Fig. 4. A comparison of vertical component seismic record sections of refraction line 4b from the MSS borehole seismometer and OBS Karen. Times have been reduced at 8.0 km/sec. Direct water wave arrivals, prominent in the MSS record, have been removed from the OBS record. The clipped, large amplitude phases in some of the OBS records at longer ranges are the result of tape recorder noise within the OBS capsule.



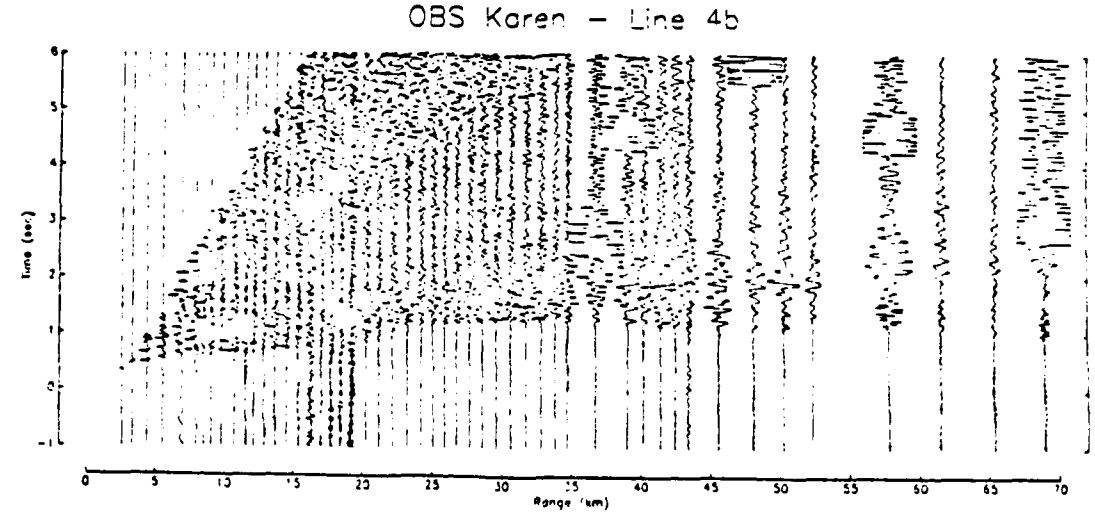


Fig. 5. Comparison of MSS and OBS recordings of P-wave arrivals from three line 4b refraction shots. Shot 4269 shows both a Pn and a PmP phase. Note that the higher frequency content of the Pn arrival shows up only on the broader band OBS record.

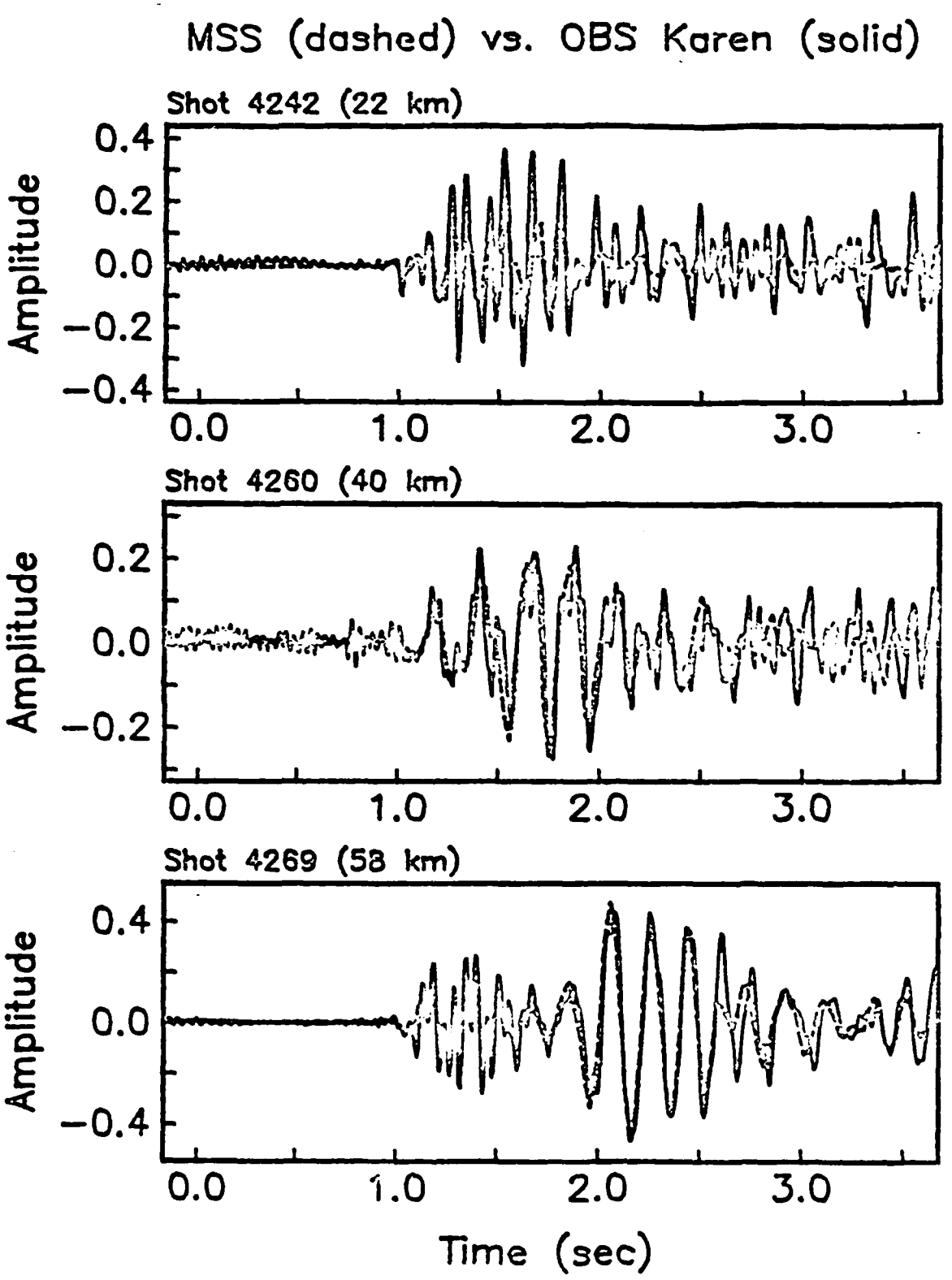


Fig. 6. Comparison of MSS and OBS spectra of 2.5 seconds of P-wave for 9 shots from line 4b at ranges of 40 to 60 km. Average noise spectra are shown below for comparison. The MSS enjoys a signal-to-noise advantage for recording these shots of about 18 db.

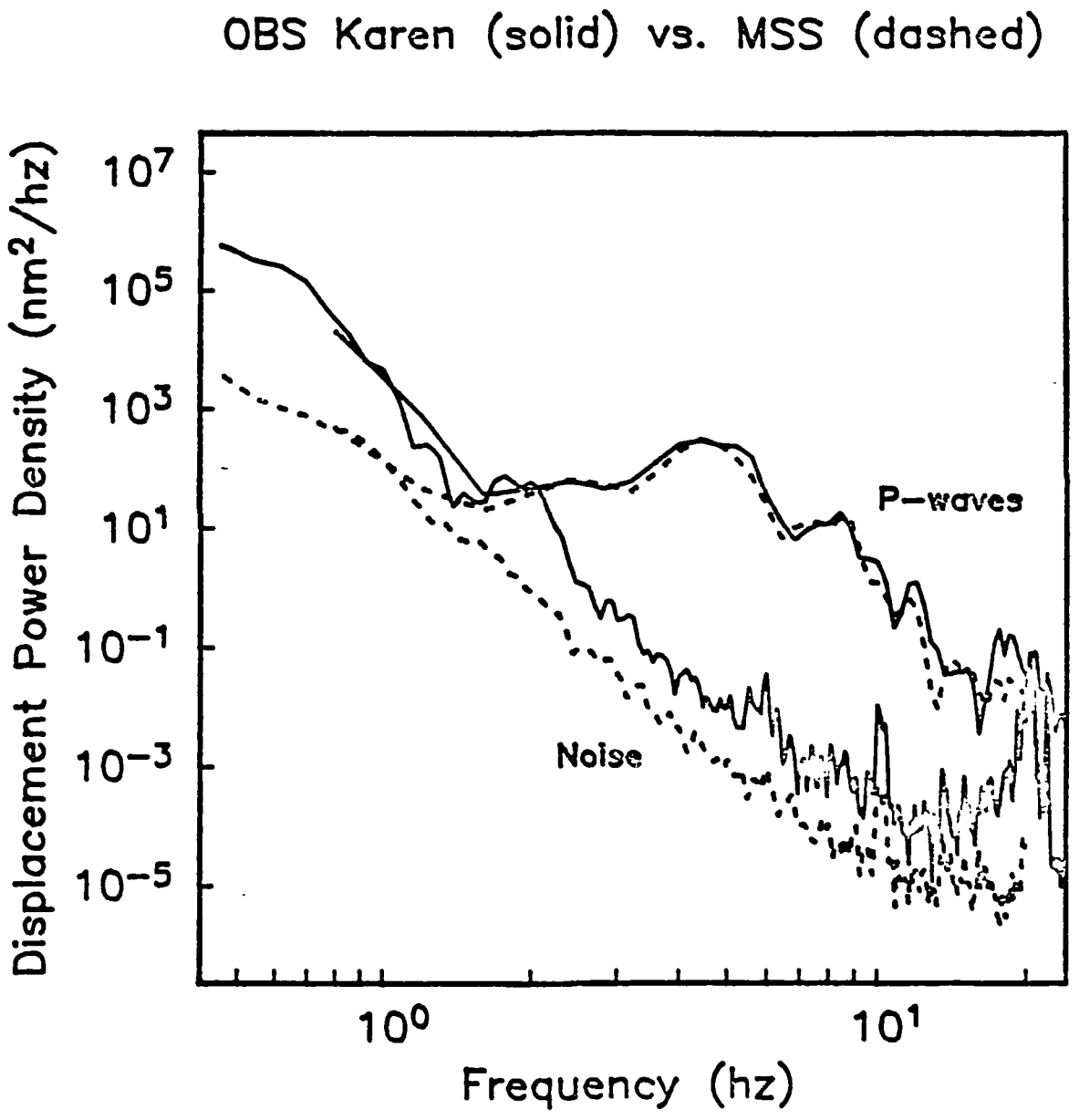


Fig. 7. **MSS and OBS vertical component recording of regional earthquakes.**

a) P-wave arrival at about 1036 UT, February 8, 1983.
b) P-wave arrival at about 1433 UT, February 9, 1983.

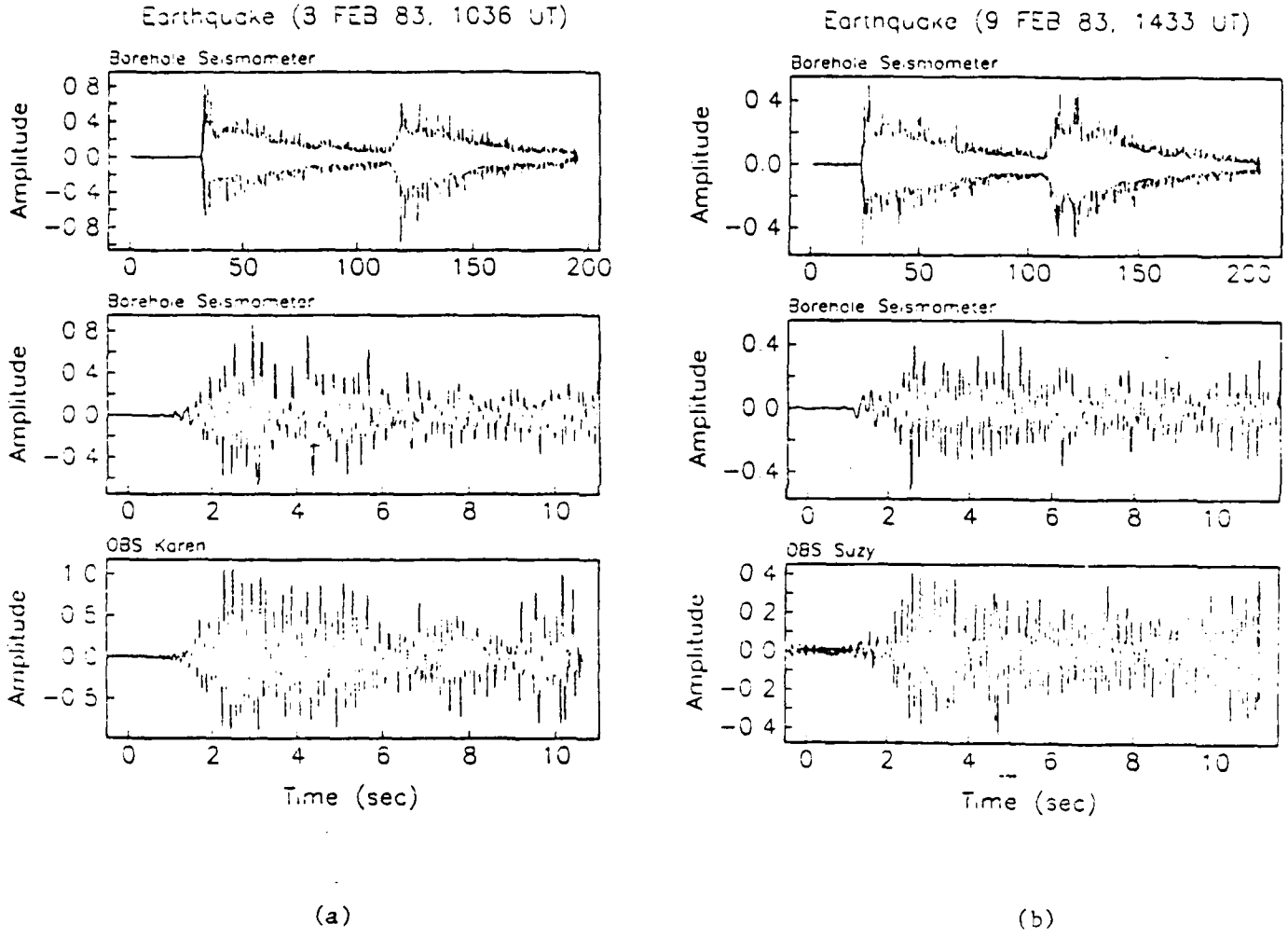


Fig. 8. Comparison of MSS and OBS recording of the February 8 earthquake. MSS record is shown as a dashed line; OBS record is shown as a solid line.

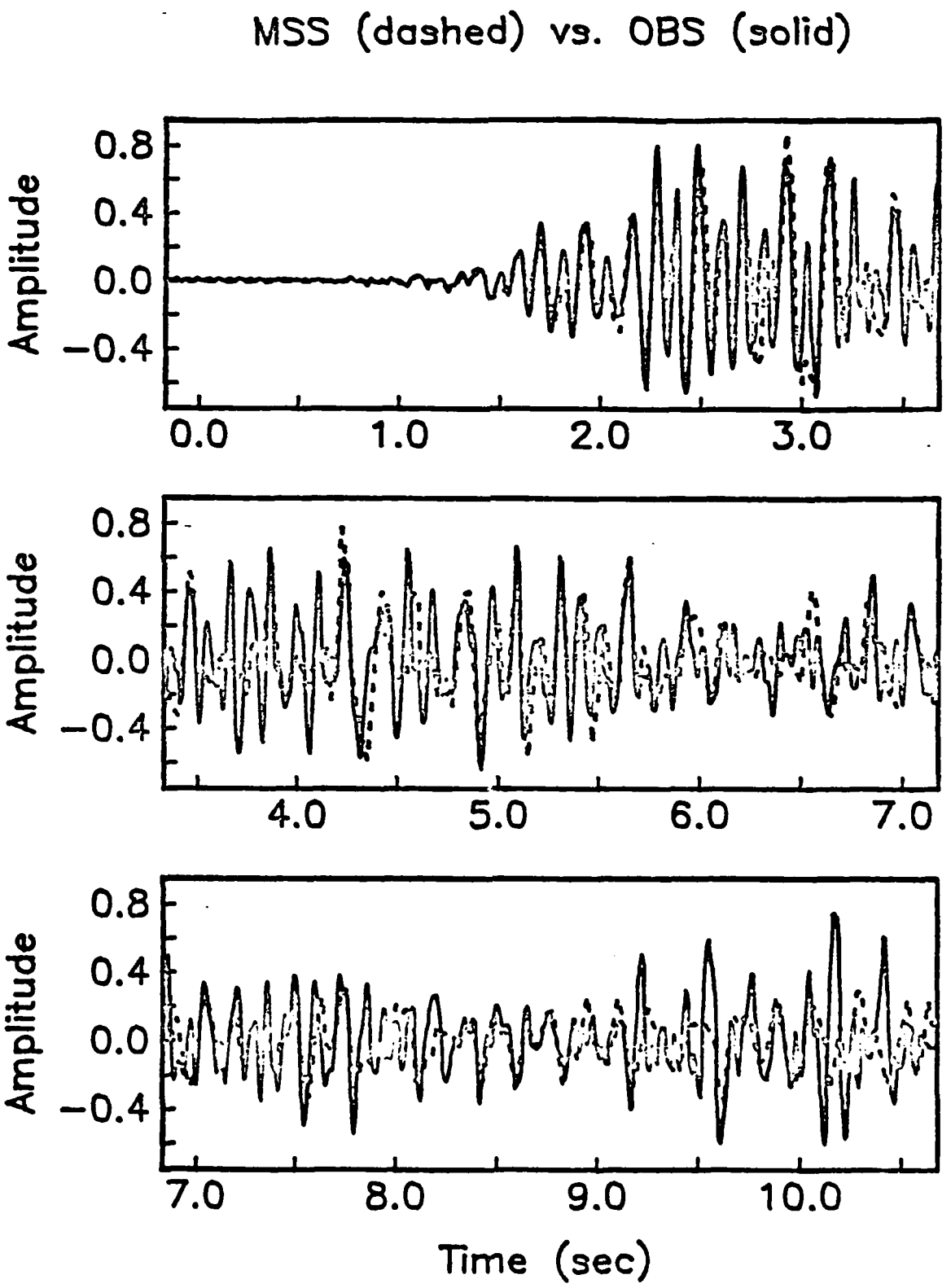
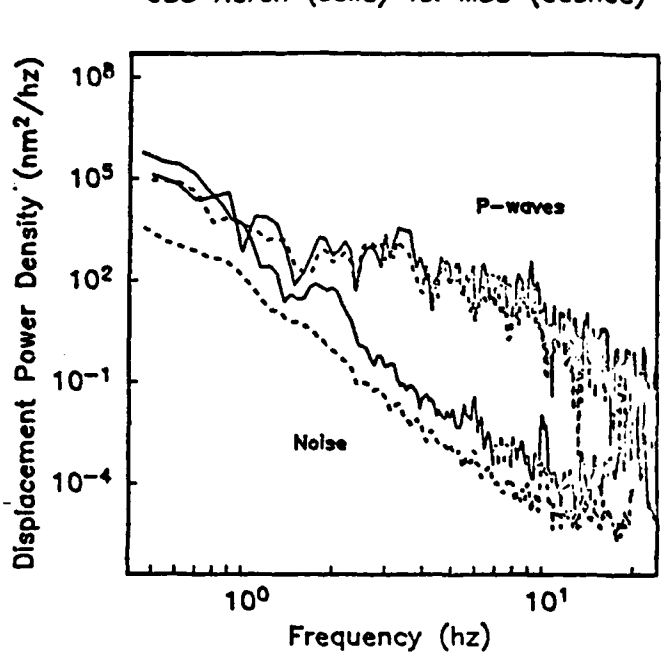
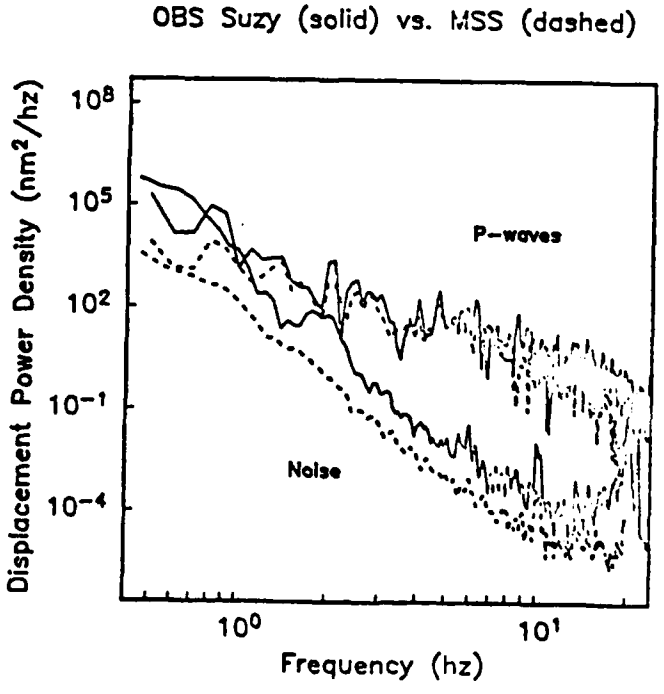


Fig. 9. Comparison of MSS and OBS spectra of 10 seconds of the initial P-wave from

a) February 8, 1983 earthquake.
b) February 9, 1983 earthquake. Average noise spectra are shown for comparison.

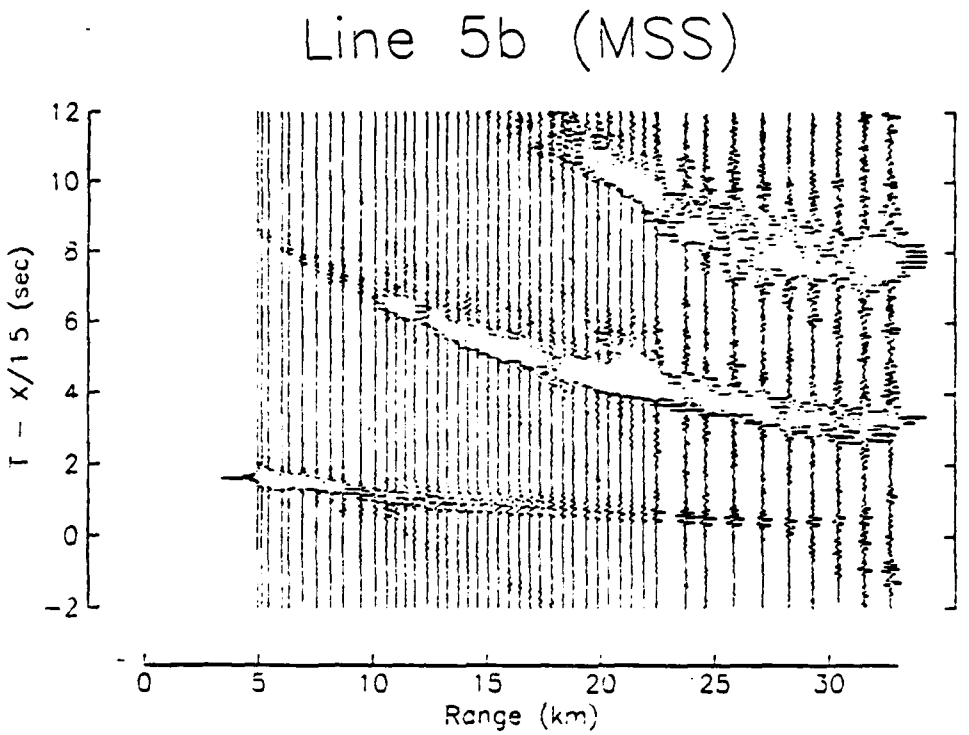


(a)

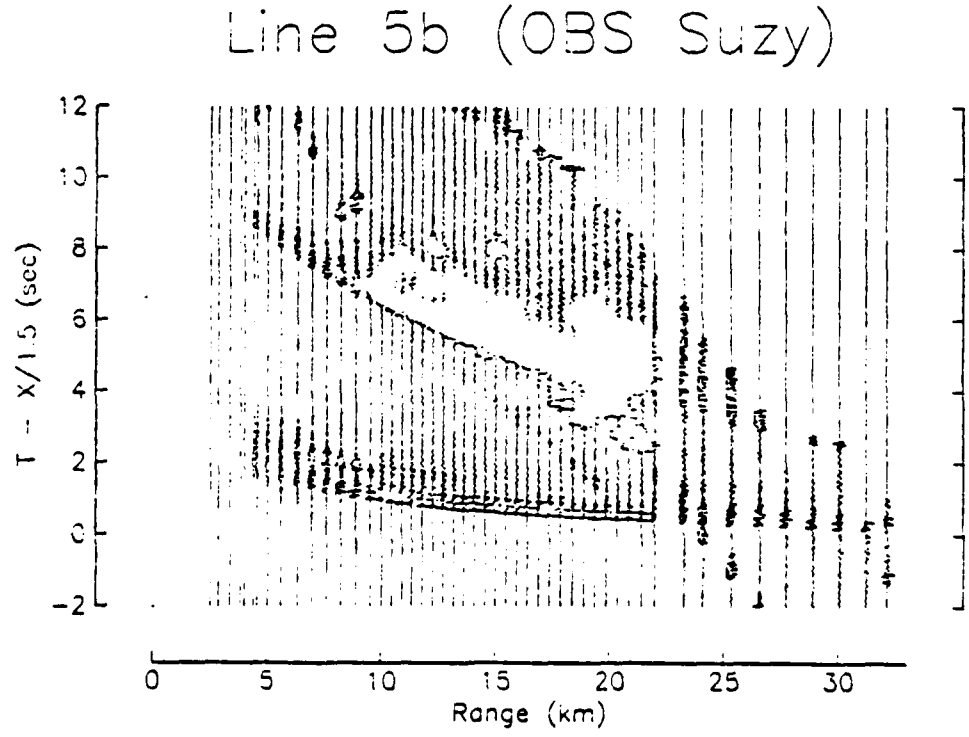


(b)

Fig. 10. Line 5b water wave arrivals as recorded by MSS and OBS Suzy vertical seismometers. Record sections are reduced at 1.5 km/sec in order to show the water waves and are scaled for range and shot weight.

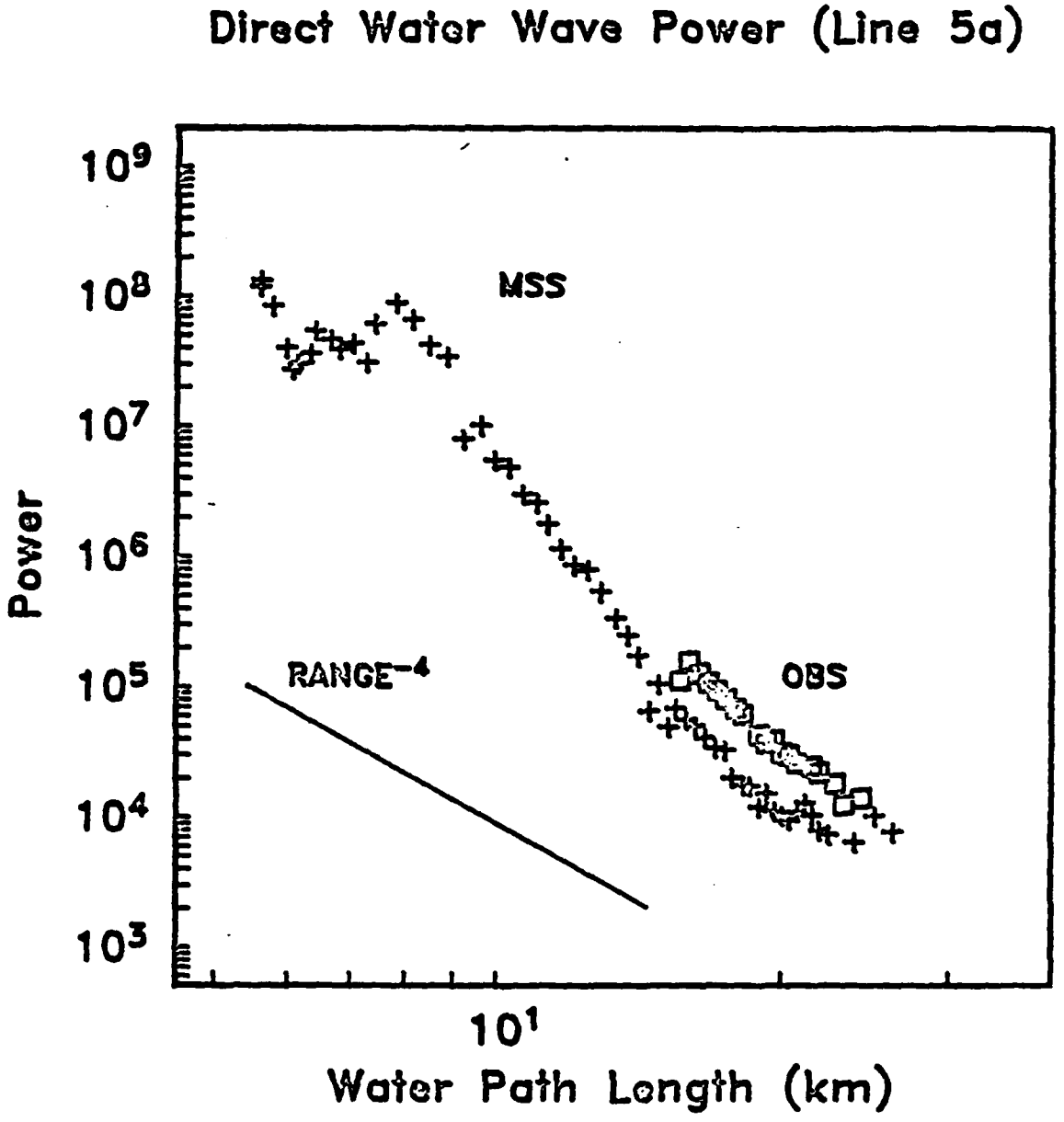


(a)



(b)

Fig. 11. Comparison of direct water wave power between the MSS and OBS S_{nzy}. Power has been scaled for shot weight by the factor $(w/w_0)^{0.65}$.



CHAPTER 6

LEG 91 INITIAL REPORT

VELOCITY BOUNDS ON THE SEISMIC STRUCTURE OF LATE JURASSIC [157 Ma old] CRUST AND UPPER MANTLE IN THE SOUTHWEST PACIFIC BASIN FROM DOWNHOLE OBSERVATIONS AT DEEP-SEA DRILLING PROJECT HOLE 595B

R.B. Whitmarsh*, J.A. Orcutt+, T.H. Jordan++, R.G., Adair+ and P.M. Shearer+

Geological Research Division,
Scripps Institution of Oceanography,
La Jolla, California 92093
United States of America

---

* On leave from the Institute of Oceanographic Sciences, Wormley, Godalming, Surrey, GU8 5UB, England.
+ Now at Institute of Geophysics and Planetary Physics, Scripps Institution of Oceanography, La Jolla, California, 92093, U.S.A.
++ Now at Department of Earth, Atmospheric and Planetary Sciences, Massachusetts Institute of Technology, Cambridge, MA, 02139, U.S.A.

INTRODUCTION

The recent advent of digitally recording ocean-bottom seismographs (OBS) has allowed data sets with high signal-to- noise and relatively broad bandwidths to be collected. However, an OBS is normally susceptible to the uncertainties of imperfect coupling via unlithified sediments of low shear strength to the solid earth (Sutton et al., 1981; Threhu, in press) and to the multiply converted and reflected phases generated at the boundaries of the sediment layer (Lewis and McClain, 1977). These problems, which can distort and complicate the signals, are largely avoided by emplacing sensors down holes drilled into igneous basement (Layer 2) beneath the sediments. Background noise is also less downhole due to the fall-off of microseismic noise with distance from the ocean-sediment interface (Adair et al., in press). Experiments using the downhole observation technique during the Deep-Sea Drilling Project have been reported by Stephen (1979, 1983), Stephen et al. (1980), Duennebier and Blackington (1983) and by Duennebier et al. (1982). This paper describes the analysis of two orthogonal unreversed refraction profiles, which exhibit an unusually good signal to noise ratio, obtained by recording signals from a set of downhole seismometers emplaced in Deep-Sea Drilling Project Hole 595B.

The experiment we describe was part of the trials of the Marine Seismic System (MSS) (Harris et al., this volume). The MSS was first emplaced in Hole 395A, Leg 78B, in the central North Atlantic Ocean in March 1981 (Hyndman, Salisbury et al., in press; Adair et al., in press). Further trials were conducted during Leg 91 in the Southwest Pacific Basin in January-February 1983 (this volume). As part of these trials, two refraction profiles were fired by R/V Melville and recorded by the MSS on board D.V. Glomar Challenger; the preliminary results of these profiles are reported here. This chapter does not take account of the more voluminous but noisier set of data recorded concurrently by four digital OBS (Moore et al., 1981) within 0.4 km of Hole 595B (Shearer et al., this volume).

REGIONAL SETTING

The experiment was conducted in the Southwest Pacific Basin about 1000 km east of the Tonga Trench and 1800 km west-south-west of Tahiti (Fig. 1, inset). This is a remote, poorly surveyed and little known region. At the time of the experiment, no clear indication of the direction of spreading centres and fracture zones was available from magnetic anomalies. From a knowledge of the regional depth (about 5600m) and of the history of adjacent portions of the Pacific Ocean, it was inferred only that the lithosphere at Site 595 had been produced at a fast-spreading ridge at high southern latitude sometime during the Mesozoic. The geoid calculated from satellite altimetry suggested that there were no substantial bathymetric or tectonic features in the immediate area (Sandwell, 1984; Dixon and Parke, 1983).

Subsequently, an analysis of magnetic anomalies and other information has suggested the existence of 050° trending seafloor spreading magnetic anomalies (H.W. Menard, personal communication). Soundings compiled within about a two-degree square enclosing the site indicate the existence of ridges and troughs with a similar trend. However, a roughly N-S to NNW arcuate high-ridge feature is also well delineated about 100 km to the east (Fig. 1).

Scant seismic reflection profiles from passage tracks of Conrad 17 and Eltanin 40, augmented by data from R.V. Melville and D.V. Glomar Challenger, indicate unusually thin sediments which are at least 0.05-0.10 seconds thick in the vicinity of Hole 595B. Sediment thicknesses are difficult to determine accurately, however, due to the ubiquitous occurrence of a very strong, presumably intra-sediment, reflector concordant with the sea bed which obscures the sediment-basement reflection. Shipboard Scientific Party (this volume) measured seismic velocities of 1.46-1.54 km s^{-1} on the cores of brown pelagic clay from Site 595.

The sediment was 70 m thick in holes 595A and 595B. Cretaceous radiolarians were found at a depth of approximately 40 m but, due to the nature of the sediments, the recovery of fossils from greater depths was poor. The sediment-basement contact was not recovered and palaeontological ages for this horizon are simply not available. An analysis of sea-floor spreading magnetic anomalies near the site indicates a crustal age considerably older than the Cretaceous quiet zone and within the Mesozoic magnetic anomaly sequence (H.W. Menard, personal communication). An earlier analysis of local magnetic anomalies placed the site at anomaly M-29 with an age of 157 Ma on the scale of Cande et al. (1978), although the interpretation is very tentative. The crust is, nevertheless, some of the oldest yet sampled in the Pacific Ocean and may be as old as late Jurassic.

THE EXPERIMENT

The objectives of the seismic refraction experiment were to investigate the crust and upper mantle structure of old lithosphere and to determine, by a pattern of radiating lines centered on the borehole, the direction and extent of upper mantle anisotropy. The experiment was constrained by the rate of progress of the MSS trials. Loss of time due to equipment malfunction allowed the shipboard recording of just two orthogonal refraction lines. The first, line 4 (including some fill-in shots of line 6) extended about 150 km SW of the hole. The second, line 5, was a split profile 50 km long to the SE and 260 km long to the NW (Fig. 1).

The shots were fired by R/V Melville. Within 30 km of the site, 1, 2 or 3 lb charges of DuPont heavy duty primers, suspended from floats at 10m depth, were used. In the immediate vicinity of Glomar Challenger the floats were dispensed with and these charges detonated at a depth of

(46 ± 2)m. These small shots were fired about every 300m. A second type of shot consisted of 13.6 to 136 kg charges of Tovex.

The seismic signals were detected by the borehole instrumentation package (BIP) of the MSS, a 10.5m long, 0.2m wide cylinder. This was emplaced at the bottom of Hole 595B which had been drilled to a depth of 124m beneath the seafloor and 56m into layer 2. Due to unforeseen technical problems, the BIP was not clamped to the wall rock. In view of the rigidity of the basalt at the bottom of the hole and the large mass (1.2 tonnes) of the BIP resting on a small area (up to $0.03m^2$) at its base, it is estimated that at frequencies of under 10 Hz the BIP followed the vertical motion of the wall-rock without distortion (Sutton et al., 1981; White, 1983). The sensors were three orthogonal broadband Teledyne Geotech Inc. S750 accelerometers with one sensor vertical. There was no device to orientate the horizontal sensors.

After band-pass filtering (Fig. 2) the signals were digitised and passed up an electromechanical cable to Glomar Challenger where they were recorded at 40 samples/sec/channel. Due to the appearance of strong instrumental noise on one of the horizontal seismometers shortly after emplacement, data from only the vertical and from one horizontal seismometer were available for analysis (data from just the vertical seismometer are presented here).

A near-surface hydrophone was also deployed from Glomar Challenger at a depth of 10m to record the relatively high-frequency water- waves from the explosions. This was necessary for the accurate determination of shot-to- receiver ranges.

Timing was with respect to a local clock on each ship which was checked regularly against radio time-signals from station WWVH.

DATA REDUCTION

A sound-velocity/depth profile (Table 1) was constructed on the basis of temperature and salinity observations, made during the experiment down to 1000m and from observations made 500 km away by Stommel et al. (1973) to 5400m in June-July 1967, using the equation of Clay and Medwin (1977). This profile was used to calculate shot-to-borehole ranges from the water-wave travel times of mainly bottom reflected phases detected by the near surface hydrophone. These ranges included a correction for the offset of Glomar Challenger from the borehole using the precise (± 15m) measurements provided by the ship's dynamic positioning system. Ranges calculated by this method were consistent within ± 80m with ranges based on water-waves detected by the OBS hydrophones. At ranges in excess of about 90 km the signals at the surface hydrophone were too weak. Instead, the arrival-time on the vertical seismometer of a probable tube-wave, generated by the arrival of the water-wave at the top of the hole, was used after correction for an estimated downhole propagation time of 0.09s.

To minimise the scatter in arrival times of several tenths of a

second caused by the varying water-depth under the shots (Fig. 3) the water-path correction used by Spudich and Orcutt (1980), and described in detail by Purdy (1982), was applied. This modifies travel-times and ranges to those applicable to a source situated at the point of entry into the sea-bed of the ray setting off from each actual shot. A horizontal phase-velocity/range function must be known or assumed with this method and this was determined from a cubic spline fitted to all the time/distance data for each line segment. The tightness of fit of the spline was chosen subjectively to the smoothest which seemed to fit the general trends in the data. Most time and distance corrections were about 3.9s and 1.3 km respectively. The appreciable decrease in travel-time scatter achievable by this technique is shown in Figure 3.

Nevertheless, even after applying the water-path correction a systematic correlation between travel-times and the depths of the ray-entry point is apparent. For each line the depth residual with respect to the mean along-profile depth and the residual of the water-path- corrected travel-times, from a second spline fitted to the time-distance data, were plotted. Least-squares linear regression on a compilation of all such depth and time residuals gave highly-significant (more than 99%) correlation coefficients of -0.41 and -0.47 for crustal and mantle arrivals respectively. The associated regression coefficients, which we shall call dt/dh, were -0.11 and -0.18s km^{-1} respectively. These values fall within the ranges of -0.09 to -0.11 and -0.15 to -0.19s km^{-1} found by White and Purdy (1983) for a larger data set of lower crustal and upper mantle arrivals, respectively. White and Whitmarsh (in press) determined dt/dh values of -0.10 and -0.14s km^{-1} for the upper and lower crust respectively.

The significance of our correlation coefficients and the consistency between dt/dh values from three different data sets indicates a genuine systematic relationship. White and Purdy (1983), on the basis of ray-tracing experiments, believed the relationship was caused by deeper and deeper isovelocity surfaces becoming approximately planar. Therefore, we applied a second correction, equivalent to our appropriate regression coefficient, to the travel-times to remove the linear correlation between time and bathymetry so as to obtain the smoothest possible set of time/distance data prior to the application of tau-p analysis. This correction involved no adjustment of distance since it is assumed, over a given distance range, that the regression coefficient is independent of distance. The datum chosen to apply the dt/dh correction was 5740 m, the depth of the BIP. It was further assumed that 75m of 1.5 km s^{-1} sediment lay under all shot points (there were no reflection profiles along the shooting tracks) and a small time correction was applied to remove the effect of this layer.

Finally, record sections of the three profile segments were plotted using ranges and time adjusted by the above procedures (Fig. 4). There are differences and similarities between the three observed record-sections. The profile 4 section has an excellent signal:noise ratio and many first arrival onsets can be picked to within $\pm$ 0.05s or better even

beyond 100 km. Weak lower crust arrivals between 20 and 30 km are followed by strong Moho reflections. At greater ranges there are unusual strong low-frequency secondary arrivals to just beyond 130 km which crudely fall on a 6.8 km s^{-1} slope but in detail segments with phase velocities as high as 7.2 km s^{-1} can be distinguished. The mantle first arrivals maintain a fairly constant amplitude but exhibit quite marked variations in high-frequency content (compare 40-65 km with 68-84 km).

Profile 5 was shot over a rougher sea-floor than Profile 4 and the effects of focussing and defocussing near sea-floor elevations manifest themselves as rapid trace-to-trace amplitude changes (e.g. on Section 5A, 7-13 km and beyond 24 km; on Section 5B 19-27 km, 110-111 km). The signal:noise ratio is again excellent out to about 150 km. Most arrivals could be picked to $\pm$ 0.04s or better. Between 150 and 260 km the Section 5B first arrivals become increasingly hard to pick and for the last 70 km of the profile cannot be picked with any confidence. This was due in part to an increased noise level caused by a series of earthquakes probably originating in the Tonga- Kermadec Trench region. Again, weak lower crustal first arrivals are evident. Unlike Profile 4, strong low-frequency secondary arrivals are not seen between 40 and 130 km. The crust-mantle triplication is also less clear on Sections 5A and 5B. The mantle first arrivals exhibit trace-to-trace variations in high-frequency content similar to Section 4 but they seem to be less systematic.

The above features will be accounted for eventually when full wave-form modelling of the observed record-sections has been completed.

A compilation of the corrected first-arrival travel-times from both profiles (Fig. 5) shows that all times out to 28 km fall within a narrow $\pm$ 0.07s band suggesting only limited lateral variation in structure in all but the lowermost crust. Conversely, the upper mantle intercept time of Profile 4 is about 0.4s smaller than that of Profile 5; such a large difference suggests a thinner crust. Lastly, the increasingly earlier mantle arrivals seen as range increases along Profile 4 suggest higher velocity uppermost mantle material under that profile.

For the initial analysis of our data, we chose to carry out a joint (x-p and tau-p) linear extremal inversion, based on travel-times, in order to obtain bounds outside which no velocity/depth model should lie (Orcutt, 1980). This procedure assumes a laterally homogeneous earth. Spudich and Orcutt (1980) discussed the disproportionately large effect of a small number of bad observations on the calculated bounds. As explained earlier, we took considerable care to correct the observed (X,T) points not only for the varying water-path but also for the well-established correlation of travel-time residuals and depth residuals. Application of the dt/dh correction, where dh is relative to a horizontal datum has the effect of "flattening" the sea-bed. Any remaining scatter in arrival times must represent the effect of non-horizontal (undulating) isovelocity surfaces, real lateral velocity variations or observational errors (including poorly-known bathymetry and sediment thickness under the shots).

Stephen and Harding (1983) have noted that borehole observations give rise to an inflexion in the travel-time curve the inverse slope of which corresponds to the velocity at the receiver. However, this inflexion point is expected to occur at ranges of less than 3 km (about 1 km corrected range) for the MSS observations. The few points apparently affected by this phenomenon were excluded from the inversion. Our shot spacing was not sufficiently small to accurately predict the velocity at the BIP. Most measurements during Leg 91 on basalt cores gave velocities in the range 4.4 to 5.2 km s^{-1} (Shipboard Scientific Party, this volume).

The joint extremal inversion proceeded in steps. The first stage was to assign an uncertainty (typically in the range $\pm$ 0.01 to $\pm$ 0.04 seconds) to each arrival-time pick. Upper and lower bounds to the arrival times were then picked in time, distance (T,X) space by selecting a small number of straight lines arranged to form the smallest possible envelope enclosing all the data (the x-p functions). The corresponding tau-p points (one for each straight line in (T,X) space) then formed the input to the initial joint extremal inversion. This inversion disregarded clear evidence for triplications and therefore gave bounds which varied smoothly with depth (Fig. 6a). In reality, there is a clear triplication in the record-sections due to the crust-mantle transition. The existence of such a triplication was introduced as a further constraint in the inversion procedure, firstly, by estimating the (T,X) bounds on the lower-crust/mantle cross-over point and then by introducing, in addition, estimated bounds on the location of the Moho reflection/upper mantle refraction cusp. The appropriate critical distance cannot be easily identified on record sections (Cerveny *et al.*, 1977) and an overestimate by several kilometres was probably made. Smaller errors in the location of triplication cusps will also exist on record sections where the water-path correction has been applied to the traces. These errors (typically 0.24 km, 0.05 secs for the mantle critical point) are due to using a ray-parameter appropriate not to the cusp but to the nearby first arrivals. Thus the introduction of the cross-over constraint tightened the extremal bounds substantially (Fig. 6b); only a slight improvement was achieved by also using the cusp constraint due to the uncertainties in locating it (Fig. 6c).

The combined results of the extremal inversions are given in Figure 7. The bounds provide only quite broad constraints on possible velocity/depth models in spite of the carefully corrected travel-times due to the scatter in these times. Inspection of Figure 3 reveals that the most scattered travel-times along Profile 5 are associated with highs in the bathymetric profiles. The combination of the shooting track not being always directed precisely away from the MSS and rapid unknown depth changes normal to this track probably made a significant contribution to this scatter. It is notable that the velocity bounds for the main crustal layer of Profile 4, which experienced a total relief of only about 250 m, are significantly narrower than those of Profile 5 which experienced over four times as much relief.

In summary, Figure 7 indicates a normal oceanic crustal structure at Site 595; a 5.5 to 9 km thick crust overlies upper mantle material with a velocity of at least 8.0 km s^{-1}. Greater resolution of the structure will only be achieved when synthetic seismogram modelling has been completed.

REFERENCES

Adair, R.G., Orcutt, J.A. and Jordan, T.H., in press. Analysis of ambient seismic noise recorded by downhole and ocean-bottom seismometers on Deep Sea Drilling Project Leg 78B. Init. Repts. DSDP, Leg 78, U.S. Govt. Printing Office, Washington, D.C.

Cande, S.C., Larson, R.L. and La Brecque, J.L., 1978. Magnetic lineations in the Pacific Jurassic quiet zone. Earth Planet. Sci. Letts., 41, 434-440.

Cerveny, V., Molotov, I.A. and Psencik, I., 1977. Ray method in seismology. Univerzita Karlova, Praha, 214 pp.

Clay, C.S. and Medwin, H., 1977. Acoustical oceanography: principles and applications. New York, John Wiley and Sons, 544 pp.

Dixon, T.H. and Parke, M.E., 1983. Bathymetry estimates in the southern oceans from Seasat altimetry. Nature, 304, 406-411.

Duennebier, F., Stephen, R., Gettrust, J., Harris, D., Avedik, F., Pascal, G., Inderbitzen, A., Bibee, D., Fehler, M., Ballard, J.A. and Jacobsen, R., 1982. OSS IV: the results of the downhole seismometer experiment, DSDP Leg 88 (abstract). EOS, 63, 1025.

Duennebier, F.K. and Blackington, G., 1983. The ocean sub-bottom seismometer. CRC Handbook of geophysical exploration at sea. CRC Press Inc., Boca Raton, Florida, 317-332.

Harris, M. et al., this volume. MSS technical report.

Hyndman, R., Salisbury, M., et al., in press. Initial Reports of the Deep Sea Drilling Project, Leg 78B. U.S. Government Printing Office, Washington, D.C.

Jordan, T.H., Orcutt, J.A. et al., this volume. OBS results. Initial Reports of the Deep Sea Drilling Project, Leg 91. U.S. Government Printing Office, Washington, D.C.

Lewis, B.T.R. and McClain, J., 1977. Converted shear waves as seen by ocean-bottom seismometers and surface buoys. Bull. Seismol. Soc. Amer., 67, 1291-1302.

Moore, R.D., Dorman, L.M., Chin-Yen, H. and Berliner, D.L., 1981. An ocean-bottom microprocessor-based seismometer. Mar. Geophys. Res., 4, 451-477.

Orcutt, J.A., 1980. Joint linear, extremal inversion of seismic kinematic data. J. Geophys. Res., 85, 2649-2660.

Purdy, G.M., 1982. The correction for the travel time effects of sea-floor topography in the interpretation of marine seismic data. J. Geophys. Res., 87, 8389-8396.

Sandwell, D.T., 1984. A detailed view of the South Pacific geoid from satellite altimetry. J. Geophys. Res., 89, 1089-1104.

Spudich, P. and Orcutt, J., 1980. Petrology and porosity of an oceanic crustal site: results from wave-form modelling of seismic refraction data. J. Geophys. Res., 85, 1409-1433.

Stephen, R.A., 1979. The oblique seismic experiment in oceanic crust, equipment and technique. Mar. Geophys. Res., 4, 213-226.

Stephen, R.A., 1983. The oblique seismic experiment on DSDP, Leg 70.

Int. Rept. Deep Sea Drilling Project, U.S. Govt. Printing Office, 69, 301-308.

Stephen, R.A., Louden, K.E. and Matthews, D.H., 1980. The oblique seismic experiment on DSDP, Leg 52. Geophys. J. Roy. astr. Soc., 60, 289-300.

Stephen, R.A. and Harding, A.J., 1983. Travel-time analysis of borehole seismic data. J. Geophys. Res., 88, 8289-8298.

Stommel, H., Stroup, E.D., Reid, J.L. and Warren, B.A., 1973. Transpacific hydrographic sections at Lats. 43°S and 28°S: the SCORPIO Expedition - I: Preface. Deep Sea Res., 20, 1-7.

Sutton, G.H., Duennebier, F.K. and Iwatake, B., 1981. Coupling of ocean-bottom seismometers to soft bottom. Mar. Geophys. Res., 5, 35-51.

Trehu, A.M., 1984. On the use of observed incident angles and azimuths to infer lateral velocity variations in the Orozco Transform Fault. Geophys. J. Roy. astr. Soc., in press.

White, J.E., 1983. Underground sound-application of seismic waves. Elsevier.

White, R.S. and Purdy, G.M., 1983. Crustal velocity structure on the flanks of the Mid-Atlantic Ridge at 24°N. Geophys. J. Roy. astr. Soc., 74.

White, R.S. and Whitmarsh, R.B., in press. An investigation of seismic anisotropy due to cracks in the upper crust at 45°N, Mid-Atlantic Ridge. Geophys. J. Roy. astr. Soc.

FIGURE CAPTIONS

Figure 1. Bathymetry and locations of Profiles 4 and 5 around Site 595 in the Southwest Pacific Basin (see inset). Fine lines denote available sounding tracks; tracks were too dense to be shown clearly within the box. Contour interval 400 m (solid lines) or 200 m (dashed lines).

Figure 2. Displacement response of the short-period channels of the MSS.

Figure 3. First arrival picks (reduced to 8 km s^{-1}) before and after application of the water-path and dt/dh corrections (upper and lower curves, respectively) plotted above bathymetry along each profile (a, Line 4; b, Line 5a; c, Line 5b).

Figure 4. Unfiltered record-sections (reduced to 8 km s^{-1}) after application of water-path and dt/dh corrections. Selected traces are from a short-period vertical seismometer. (a) Line 4; (b) Line 5a; (c) Line 5b.

Figure 5. Combined corrected first arrival picks (reduced to 8 km s^{-1}) from Lines 4 and 5 to illustrate the differences in upper mantle arrival times.

Figure 6. Extremal bounds obtained from Line 4 based on: (a) first arrival times alone (dotted line); (b) first arrival times plus an estimate of the lower crust/upper mantle cross-over point (dashed line, only shown where different from (c)); (c) as (b) plus an estimate of the mantle reflection/refraction cusp (solid line).

Figure 7. The results of joint linear extremal tau-p analysis on Lines 4 (dashed line), 5a and 5b (continuous line).

TABLE 1

Sound speed/depth model

Depth (m)	Sound speed ($m\ s^{-1}$)
0	1535.5
380	1513.0
630	1488.7
1000	1484.3
1500	1484.3
3910	1519.6
6000	1553.1

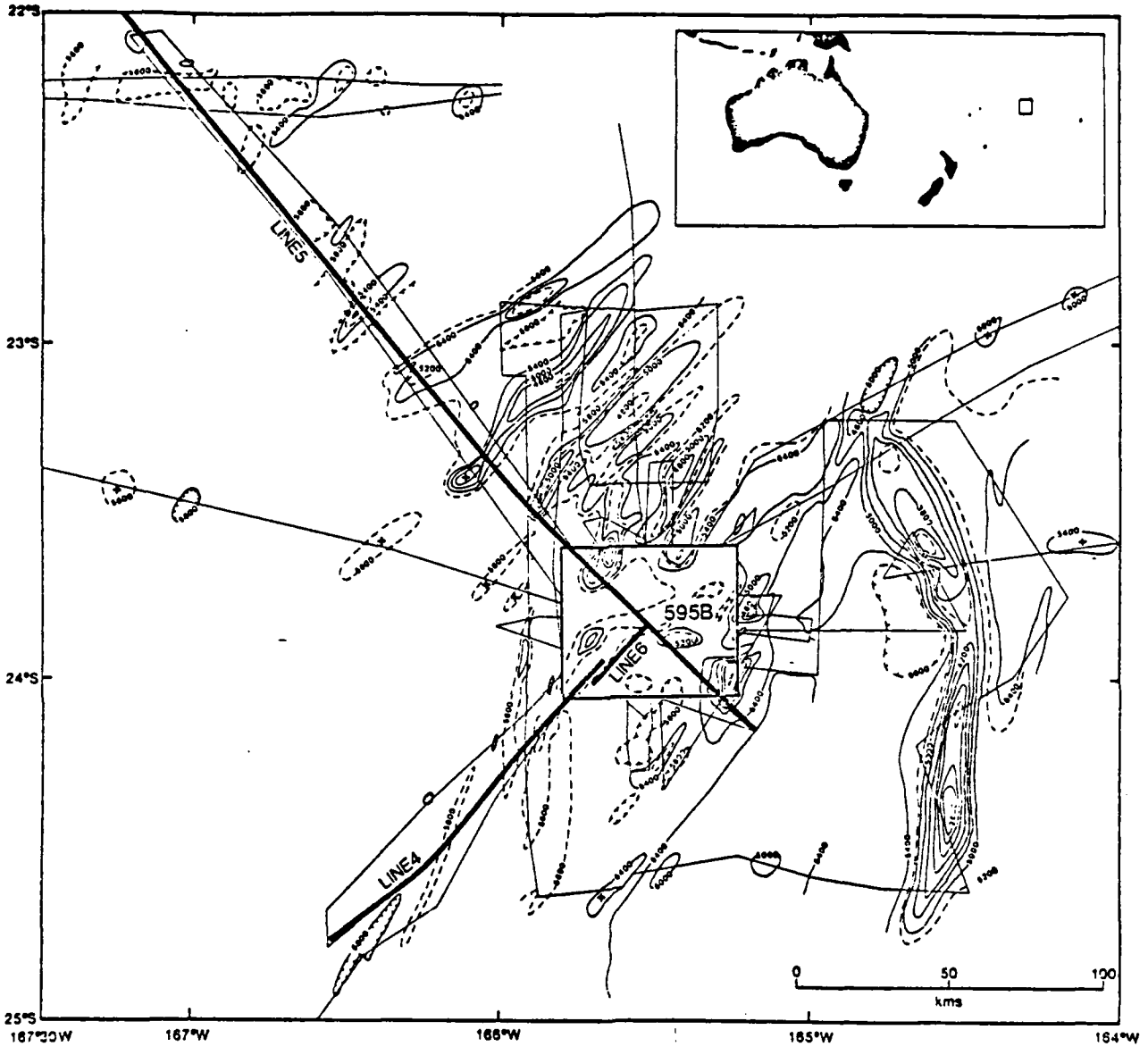

22°S
23°S
24°S
25°S
167°30W
167°W
166°W
165°W
164°W
LINE5
LINE6
LINE4
595B
0
50
100
kms

Figure 1

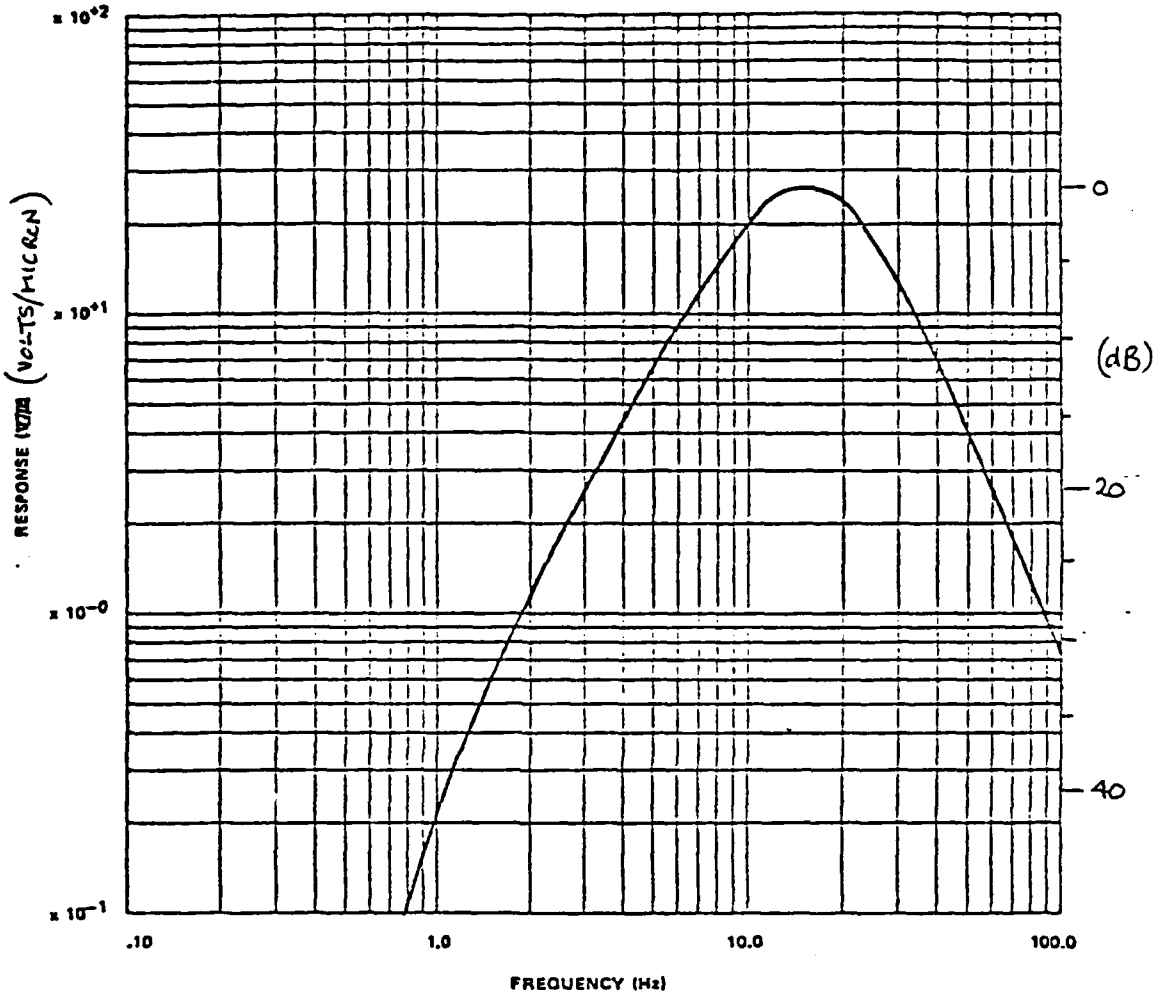
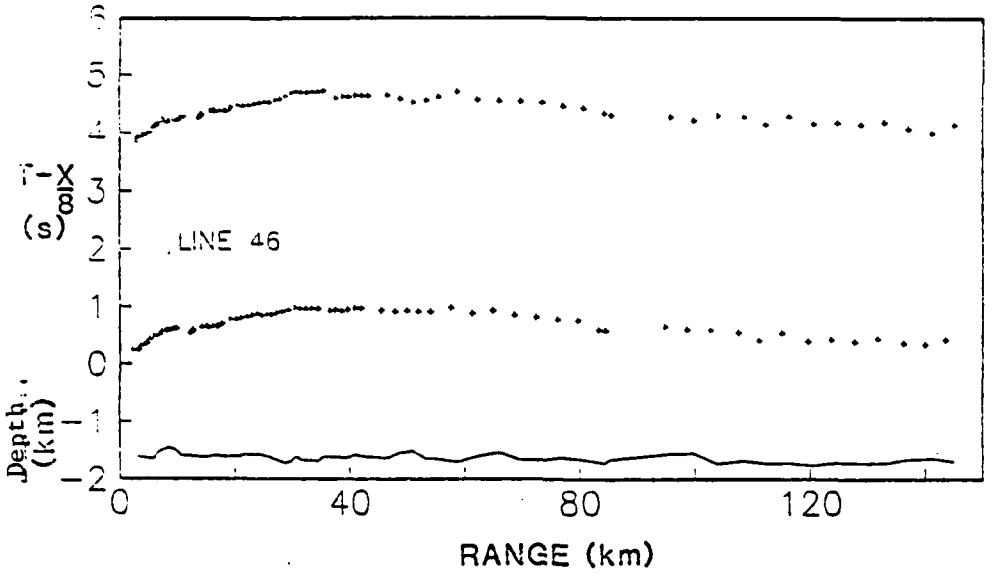
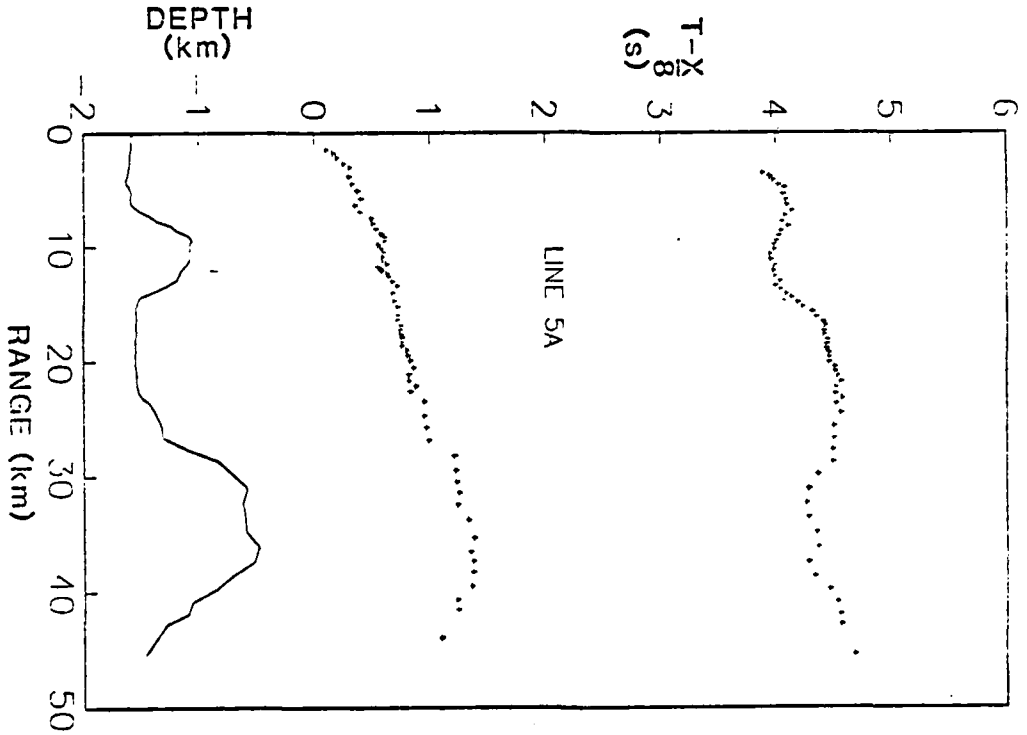

x 10^+2
x 10^+1
x 10^-0
x 10^-1
RESPONSE (VOLTS/MICRON)
0
(dB)
20
40
.10
1.0
10.0
100.0
FREQUENCY (Hz)

Figure 2

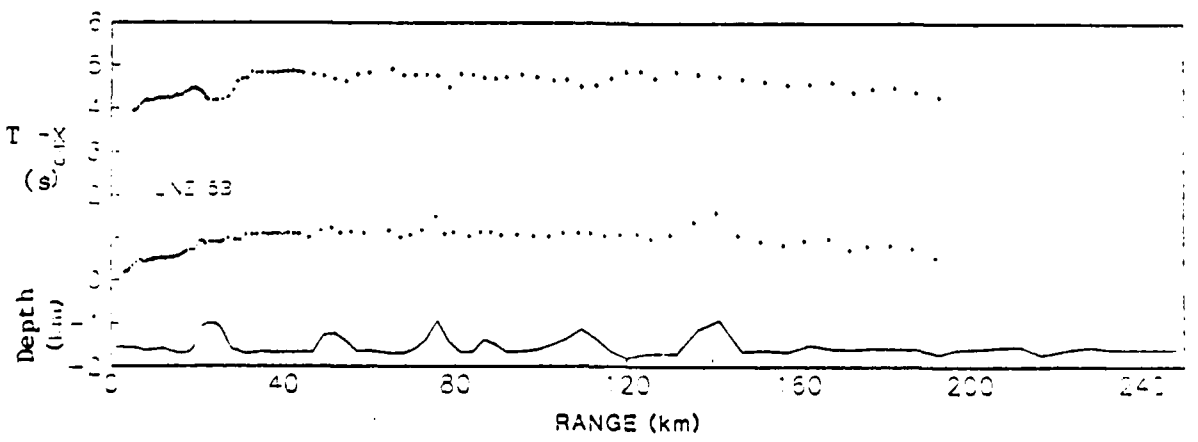


3-a



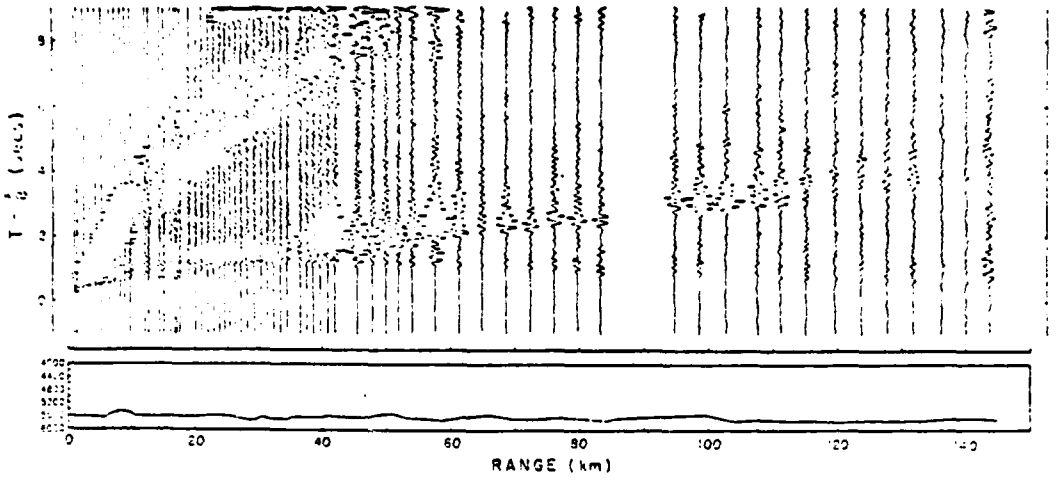
3-b

FIGURE 3

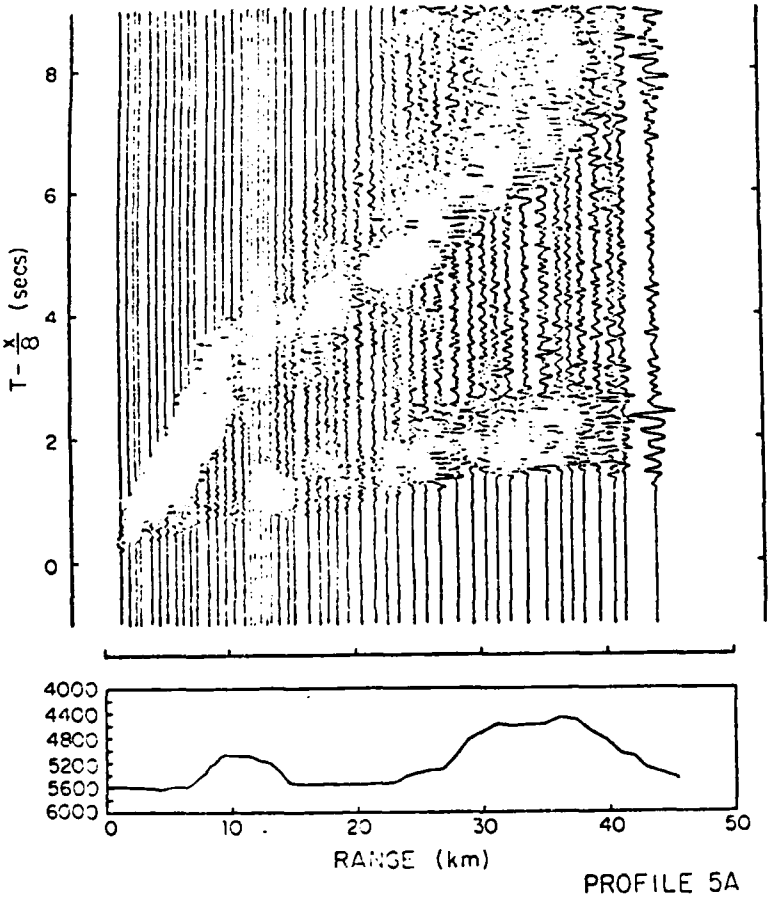


3-c

PROFILE 4



4-a

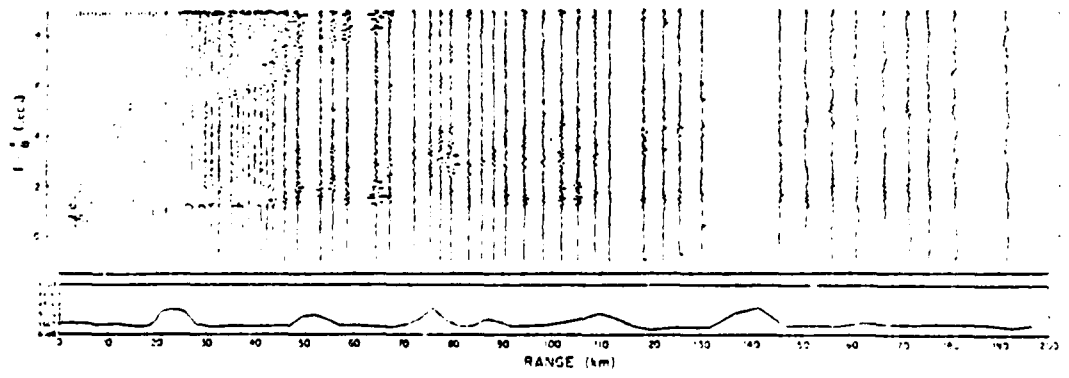


PROFILE 5A

4-b

FIGURE 4

PROFILE 5B



4-c

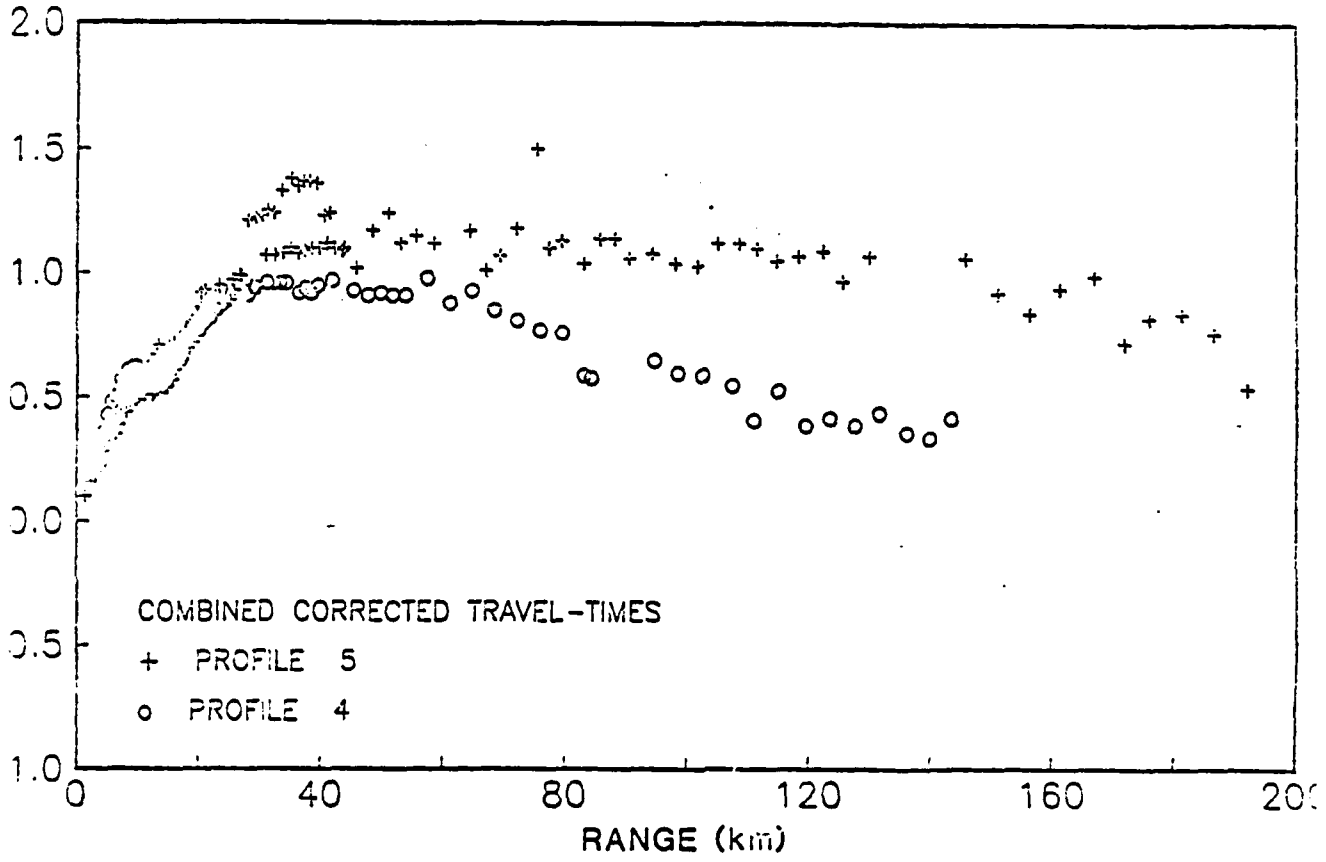

2.0
1.5
1.0
0.5
0.0
0.5
1.0
0
40
80
120
160
RANGE (km)
COMBINED CORRECTED TRAVEL-TIMES
+ PROFILE 5
o PROFILE 4

Figure 5

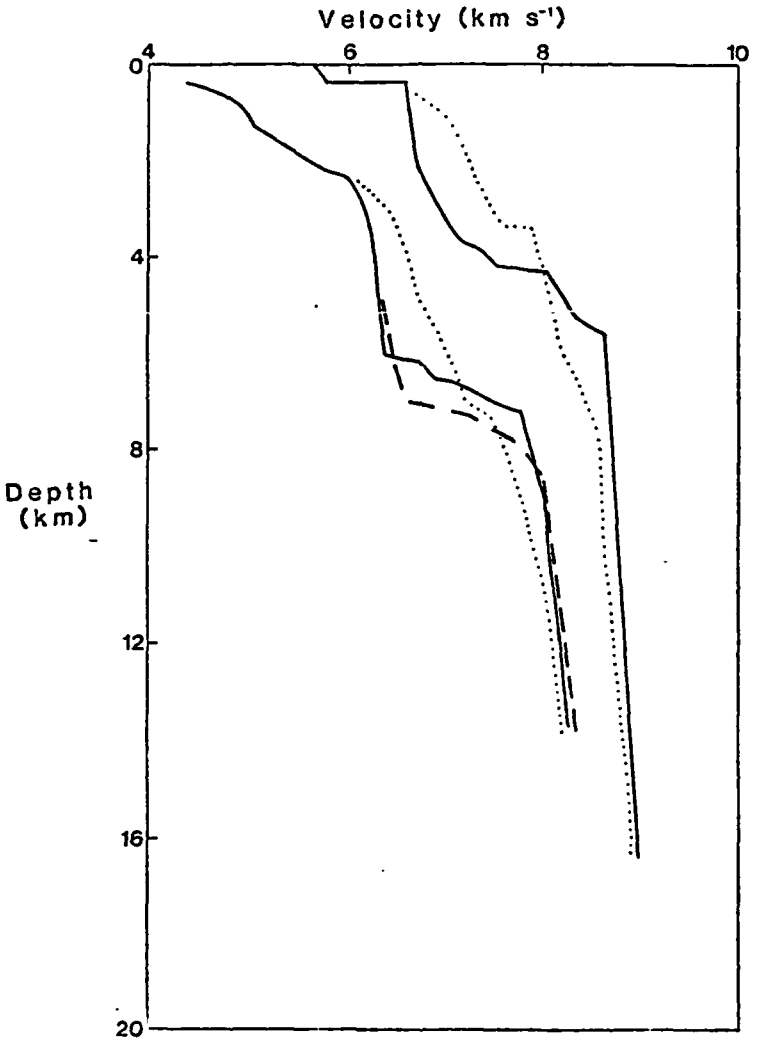


Figure 6

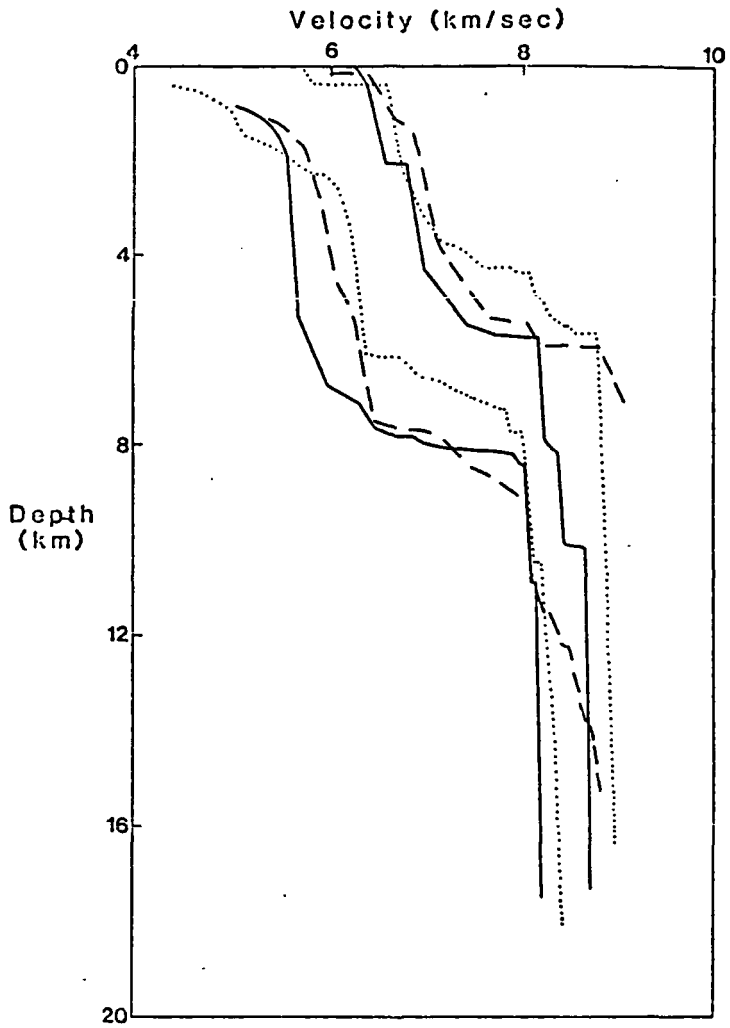


Figure 7

CHAPTER 7

LEG 91 INITIAL REPORT

THE NGENDEI SEISMIC REFRACTION EXPERIMENT AT DSDP HOLE 595B -- OCEAN BOTTOM SEISMOMETER DATA AND EVIDENCE FOR CRUSTAL AND UPPER MANTLE ANISOTROPY

P.M. Shearer, J.A. Orcutt, T.H. Jordan*,
R.B. Whitmarsh**, I.I. Kim,
R.G. Adair, and M.S. Burnett

Institute of Geophysics and Planetary Physics (A-025) Scripps Institution of Oceanography La Jolla, California 92093

* now at Department of Earth, Atmospheric and Planetary Sciences, Massachusetts Institute of Technology, Cambridge, Massachusetts 02139

** on leave from the Institute of Oceanographic Sciences, Wormley, Goldalming, Surrey, GU8 5UB, England

Introduction

Seismic refraction is the primary technique for gathering information about the structure of the oceanic lithosphere because of its high resolution for elastic parameters. In the preceding decades, marine scientists have used data from refraction experiments to constrain the seismic velocities of the crust and upper mantle. The successful deployment of Ocean Bottom Seismometers (OBSs) in the 1970's led to great improvements in the quality and resolution of these data sets. More recent refraction experiments using borehole seismometers promise a further improvement in data quality.

The 1983 Ngendei Seismic Refraction Experiment was designed to provide data from both OBS and borehole instruments from a relatively unexplored region of the southwest Pacific. The closely spaced shots and multiple receivers allowed for comparisons of ocean bottom and borehole seismometer responses as well as a detailed look at the seismic velocity structure at the Ngendei site.

This paper is a description of the OBS refraction data set- the borehole seismometer data are described elsewhere in this volume (Whitmarsh et al., 1984). We will describe the refraction experiment and the techniques used in reducing the data. Preliminary analysis of P-wave travel times indicates anisotropy both within a crustal layer and within the upper mantle at the Ngendei site. We will discuss the implications of these observations for theories concerning the tectonics and evolution of the oceanic lithosphere.

Experiment Description

The Ngendei site is located at DSDP hole 595B in the southwest Pacific about 1500 km west-southwest of Tahiti (see Fig. 1). This site was chosen partially because of its proximity to the Tonga Trench, which provided a source of earthquakes for the teleseismic experiment described elsewhere in this volume (Jordan et al., 1984). This is a very old part of the Pacific basin with an estimated age of 140 to 160 m.y. (Menard, personal communication). The sediment cover at the site is 70 m thick, relatively thin considering the age of the crust. The original spreading direction at the site cannot be determined from the available magnetic and bathymetric information. A more detailed description of the site is available in the introductory chapter.

Ocean bottom seismometers (OBSs) from the Scripps Institution of Oceanography were deployed near the borehole for the seismic refraction experiment. These are self-contained, digital instruments which record a vertical component (Channel 1), two orthogonal horizontal components (Channels 2 and 3), and a hydrophone (Channel 4). Data are digitized at 128 samples/second with approximately 13 seconds of data stored in

memory before tape recorder activation. The OBS frequency response during the refraction experiment is shown in Fig. 2 (Moore et al., 1981). Two way acoustic communication between ship and OBS allows monitoring of OBS functions and is also useful for calculating OBS locations.

During the Ngendei refraction experiment, the OBSs were programmed to record data in 20 second windows at pre-selected times which corresponded to a refraction shooting schedule. Four OBSs were used for the refraction experiment- OBS Suzy, OBS Lynn, OBS Juan, and OBS Karen. They were deployed in two pairs- OBS Suzy and OBS Karen were located approximately 0.5 km north of the borehole, while OBS Lynn and OBS Juan were located about 0.5 km west of the borehole (see Fig. 3). As a hedge against the possibility of instrument failure, as well as to facilitate comparisons between OBS recordings, each refraction line was recorded by two OBSs. OBS Suzy and OBS Lynn recorded lines 1, 2, and 5, while OBS Juan and OBS Karen recorded lines 3 and 4. All of the OBSs performed well during the experiment and thus each shot was recorded by at least two OBSs.

The OBS locations shown in Fig. 3 were determined from two-way ship to OBS acoustic travel times, satellite ship locations, and Melville to Challenger bearings and ranges. The OBS and ship locations were then jointly determined, using an iterative inversion procedure (Creager and Dorman, 1982). The error ellipses on Fig. 3 show the estimated 95% uncertainty in the OBS locations relative to a common center of mass. For reference, the borehole location and the shipboard OBS drop points are shown also.

During the experiment the drift of a shipboard lab clock was monitored relative to WWVH. Shot instant times were measured with the lab clock and the OBS clocks were synchronized to the lab clock prior to launch. Upon recovery, the OBS clock drift rate was noted and all OBS times were corrected to lab clock times, assuming a linear drift rate. Finally, to ensure correct coordination with the borehole seismometer data, all times were corrected to WWVH.

The refraction shooting schedule is shown in Fig. 4. Shots of 1 to 3 lbs were used at close ranges, while shots of 60 to 240 lbs were used at more distant ranges. On each radial line the shooting ship, the R.V. Melville, doubled back so that at some ranges (typically 20 to 25 km) both small and large shots were recorded. The locations of the shots are shown in Fig. 5. The refraction shooting included 4 split refraction lines at 45 degree increments (lines 1, 3, 4, 5) and a circular line at an approximate 10 km radius (line 2c). Line 2, which was shot entirely with 10 lbs charges, also included a short split refraction profile (line 2a, 2b) parallel to line 1. Over 1000 shots were detonated during the 6 days of shooting, consuming approximately 20 tons of explosives.

Unfortunately, delays in installing the borehole seismometer prevented its activation until the shooting schedule was more than half completed. The MSS recorded only parts of lines 4b, 5a, and 5b. To make up for some of the gaps in the MSS records, an additional line (line 6) was shot. This line was approximately parallel to line 4b, and was not recorded by the OBSs.

The large shots were composed of TOVEX (DuPont) "sausages" ignited with primer cord and fuses. Most of the shots were recorded on ship with a calibrated hydrophone connected to a Nicolet digital oscilloscope. Both the shot instant and bubble pulse period were read with this instrument. For each shot we calculated a shot depth, based on the empirical formula (Helmberger, 1967):

$$d = \left| \frac{CW^{\frac{1}{3}}}{T} \right|^{1.2} - 33$$

where d = shot depth in feet
C = constant for type of explosive used
= 4.36 for HDP
= 5.06 for Tovex
W = shot weight in lbs
T = bubble pulse period (sec)

Calculated shot depths for the large shots (30 to 360 lbs) ranged from 40 to 120 m. This variation reflects differences in the rate that the charges sink in the ocean. Since the TOVEX sausages are packaged in cardboard boxes which can contain air pockets of varying size, it is difficult to control shot buoyancy. Different shot depths and irregularities in shot burns led to variations in source functions. In order to consider these differences in eventual data processing, we used the digital oscilloscope to record the source function of most of the large shots. Fig. 6 shows the source function for some typical shots, and demonstrates the varying bubble pulse periods (related to differences in shot depth) for the large shots. Fig. 7 shows close-ups of the first pulse for the same shots and again demonstrates the differences in the source functions for the large shots.

For the smaller shots of 1 to 3 lbs (HDP boosters) we were able to largely eliminate differences in shot depth by suspending the charges from floats. We used 10 m of nylon kite string to connect each shot to a balloon. The constant shot depth and consistency of the HDP explosions led to very repeatable source functions (see 2 and 3 lbs shots in Fig. 6 and Fig. 7). In the immediate vicinity of the drilling ship, the Glomar Challenger, it was considered dangerous to suspend the shots, so floats were not used, and the charges sank to depths of 40 to 50 m

before detonation.

The shot instant recorded on ship is not identical to the true shot instant due to the travel time through the water between the shot and the ship. This distance can be estimated from the speed of the ship and the time the shot enters the water; the travel time is determined by dividing by the oceanic sound speed (1.5 km/sec). This modification is termed the time of firing or TF correction. Although this correction is small (0.05 to 0.3 sec), it is probably the leading source of error in shot-receiver timing, given the lack of precision that the ship speed is known relative to the ocean. Ship speeds used were determined by adjusting shipboard dead reckoning positions to agree with satellite navigation fixes. We estimate the uncertainty in the ship speed relative to the ocean to be about 1 knot. This leads to TF uncertainties of about 0.02 second for the small shots and 0.04 second for the large shots.

In summary, for each shot the shot instant, bubble pulse period, burn time, and water depth were recorded. The bubble pulse period was used to calculate the shot depth. The burn time was used together with the ship speed to calculate a TF correction for the shot instant. The water depth was used to determine the sea floor topographic profile along the refraction line- information later used in making topographic corrections.

Data Reduction

The OBS data tapes were played back, timing corrections made, and the data stored in the standard ROSE format (LaTraille et al., 1982). Shot information (e.g. shot time, explosion size, bubble pulse period, TF correction) was then added to the event headers. The next processing step involved picking direct water wave arrivals in order to calculate epicentral ranges. Using interactive picking software, we picked the direct water wave arrivals (from the OBS hydrophone channel) for each of some 2000 seismograms. The water wave arrivals are sufficiently impulsive that we estimate the pick uncertainty to be the digitizing rate (1/128 = 0.008 sec).

Using a sound velocity vs. depth profile (Fig. 8, see also Whitmarsh et al., this volume, for more discussion), the shot depths, the OBS depths, and the water wave travel times, we calculated the epicentral ranges with a ray tracing technique. Calculated ranges are consistent ($\pm$80 m) with independent ranges obtained using water wave arrivals recorded at the surface by the Glomar Challenger. This consistency is encouraging given that the ray paths are completely different. Calculated ranges to different OBSs are consistent to within $\pm$20 m which is about what might be expected from the digitizing rate alone.

The direct water waves cannot be picked at ranges greater than about 30 km because the arrival times fall outside the short 20 second OBS recording window. In other isolated cases, an irregular shot time led to a similar problem. Whenever possible we used the Challenger ranges to estimate OBS ranges for these cases. If this was not possible, we interpolated between known water wave determined ranges, or (in the worst case) extrapolated the distant ranges using the ship speed and shipboard radar ranges to the Challenger.

We used a water path topographic correction technique (Spudich and Orcutt, 1980; Purdy, 1982) in order to adjust the initial P-wave arrivals down to the sea floor. The first step in this procedure was to pick P-wave arrivals for all the seismograms by examining the OBS vertical channel with an interactive picking program. Next, we fitted a smoothing spline curve to the P-wave travel times for each refraction line. In some cases, first arrivals were ambiguous- these picks were excluded from the spline fitting procedure, but topographic time and range corrections were calculated for these seismograms so that they could be displayed in the final record sections. Parameters of the spline were adjusted subjectively until a satisfactory fit was obtained. We used the slope of the spline curve at each shot range in order to calculate the approximate ray parameter for the P-wave ray leaving each shot. Since the topography is known along each refraction line, we then calculated the point (range and depth) at which the ray entered the sea floor. For the circular line (line 2c) we assumed that the depth at this point was the same as the water depth at the shot. However, recognizing the inaccuracies in this assumption, we did not include circular line data in the $\frac{dt}{dh}$ calculations discussed in the next paragraph. All of these rays are sufficiently steep that a simple uniform 1.5 km/sec ocean model is adequate and the ray paths can be approximated as straight lines. The topographic time correction is the travel time along this ray path through the water; the range correction is the horizontal projection of this ray path.

The effect of these corrections is to produce P-wave travel times appropriate for a shot on the sea floor, thus removing the gross timing differences associated with different length water paths. However, these corrections do not completely remove topographic effects from the data unless all deeper layers in the velocity profile mimic the surface profile. For the Ngendei data set, a negative correlation existed between depth and travel time. That is, at shallower depths, associated with seamounts or ridges, the P-wave travel times typically were larger than travel times over flat, deeper terrain. In order to correct for this effect, we calculated P-wave travel time residuals by fitting a smoothing spline curve to the topographically adjusted travel times. Topography at the Ngendei site is typically flat (5600 m depth) with isolated seamounts and ridges rising as much as 1000 m above the surrounding sea floor. We deemed sea surface depths less than 5200 m to be anomalous and did not include them in the spline fits at this stage

(more about this later). We subtracted the travel time predicted by the spline fit from the topographically corrected travel time at the appropriate (topographically corrected) range in order to calculate P-wave travel-time residuals.

Fig. 9 shows a plot of these residuals vs. depth for the entire Ngendei data set (1178 points), which demonstrates the strong negative correlation between residuals and depth (correlation coefficient = -0.83). Most of the points cluster around 5600 m and zero residual, reflecting the predominate depth of 5600 m at the Ngendei site. The near zero residuals are to be expected at this depth since the spline used to calculate the residuals was fit through these points. At shallower depths the residuals become positive, reflecting the delayed travel times over seamounts and ridges. The line drawn in Fig. 9 is the least squares fit and has a slope ($\frac{dt}{dh}$) of -0.23 sec km^{-1}.

We used this slope to make an empirical correction to the travel times and remove any correlation between travel times and bathymetry. However, as can be seen in Fig. 9, there is more scatter in the travel times at shallower depths, and this scatter will remain even after this correction. The increased scatter reflects the uncertainties in choosing ray parameters at the initial stage of topographic corrections and the unknown effects of topography to the sides of the refraction line. These uncertainties are larger when the depth is changing rapidly, as it typically does at the shallower depths at the Ngendei site.

Fig. 10 shows an example of this topographic correction procedure for OBS Suzy and refraction line 5a. Fig. 10a shows the raw P-wave travel time picks and illustrates the strong positive correlation between travel time and depth. The curve shown is the spline which we used to calculate the ray parameters needed to correct the travel times down to the sea floor. Fig. 10b shows the resulting corrected travel times. As can be seen, the correction is too large, and shallow bathymetry is now correlated with travel time delays. We next calculated travel time residuals based on the spline fit shown in Fig. 10b. Points at depths shallower than 5.2 km were excluded from the spline fitting procedure. As noted above, we used travel time residuals for the entire Ngendei data set to calculate a $\frac{dt}{dh}$ value of -0.23 sec km^{-1}. The result of the application of the $\frac{dt}{dh}$ corrections is shown in Fig. 10c. Most of the correlation between travel time and bathymetry has been removed, but the travel times, not surprisingly, show increased scatter near zones of steep bathymetry.

We noted a slight difference in the behavior of travel-time residuals at crustal ranges (less than 30 km) and those at mantle ranges (greater than 30 km). We calculated a $\frac{dt}{dh}$ value of -0.20 sec km^{-1} for crustal ranges (987 points, correlation coefficient = -0.67) and a value of -0.23 sec km^{-1} for mantle ranges (191 points, correlation coefficient = -0.90). In another paper in this volume (Whitmarsh et al., 1984), a

$\frac{dt}{dh}$ value of -0.11 sec km^{-1} was calculated for crustal arrivals, and -0.18 sec km^{-1} for mantle arrivals. These values are substantially different from the values calculated from the OBS data.

Some of this discrepancy can be attributed to the much smaller MSS data set. However, most of it probably resulted from a difference in the way that the travel time residuals were calculated. For the MSS data, all of the travel times were used in fitting the spline curve used to calculate the travel time residuals, while for the OBS data, the travel time points at anomalous depths were excluded from the spline fitting procedure. In the MSS procedure, the spline curve tends to bend slightly to compensate for the delayed travel times associated with the seamounts and ridges. Thus, smaller residuals are calculated and smaller magnitude $\frac{dt}{dh}$ values result. This effect is exaggerated at crustal ranges at the Ngendei site since the relief is generally less and the spline can better mimic the travel times than at mantle ranges. We believe that the procedure used for the OBS data is more appropriate for the Ngendei site, since the region is characterized by generally flat topography with relatively isolated seamounts and ridges. The larger magnitude $\frac{dt}{dh}$ value more accurately corrects the travel times to what they would be in the absence of topographic variations.

The $\frac{dt}{dh}$ value at the Ngendei site contains information about the P-wave velocity in the seamounts and ridges. If we assume that the oceanic lithosphere is laterally homogeneous below 5600 m (that is, the subsurface layers are flat and do not mimic the surface) we can calculate an appropriate velocity for an overlying material of constant velocity. In this case

$$\frac{dt}{dh} = -(u^2 - p^2)^{\frac{1}{2}}$$

where u = slowness of overlying material
p = ray parameter

A seamount and ridge velocity of 3.85 km/sec ($u = 0.26$ sec/km) fits our data accurately. At mantle ranges ($p = 0.12$ sec/km), we calculate $\frac{dt}{dh} = -0.23$ sec/km, while at crustal ranges ($p = 0.15$ sec/km) we calculate $\frac{dt}{dh} = -0.21$ sec/km.

Fig. 11 shows the raw P-wave travel time picks for the entire Ngendei data set and the corresponding topographically corrected travel times. Note that much of the scatter in the travel times has been removed. We next used these topographic corrections in order to produce record sections for each line (Appendix 1).

All record sections are reduced at 8 km/sec and show 6 seconds of data. Traces have been truncated at the onset of the direct water wave

in order to avoid overwriting adjacent traces. Amplitudes have been scaled for range and shot weight according to the formula

$$A = \left|\frac{r}{r_0}\right|^2 \left|\frac{w_0}{w}\right|^{.65} A_{raw}$$

where r = range
w = shot weight

No seismograms are shown at epicentral distances greater than 50 km because of the poor signal to noise ratio at long ranges. Also, seismograms from small shots are not shown at ranges greater than the closest large shot, again because of poor signal to noise. Three defective channels are not shown (OBS Juan, Channels 3 and 4; OBS Lynn, Channel 2). The data presented have not been filtered in any way except for the modifications imposed by the instruments (see Fig. 2).

The overall quality of the data is excellent. The close shot spacing, repeatable sources, multiple receivers, and complete azimuthal coverage make this one of the finest data sets ever collected in a marine refraction experiment. In addition to the P-wave arrivals, many of the lines have excellent shear wave arrivals, which we plan to analyze later.

Data Analysis

Following an extremal inversion technique discussed by Garmany et al. (1979),we used the P-wave travel times to infer bounds in the τ-p plane. We then calculated the appropriate bounds on the velocity-depth function outside of which solutions cannot exist. At this stage, we did not use X-p or triplication constraints (Orcutt, 1980) although we plan to add these later; these constraints were used in the analysis of the MSS data (Whitmarsh et al., this volume). Fig. 12 shows the result for all of the refraction lines. Unfortunately, scatter in the data, presumably related to lateral heterogeneities at the Ngendei site, causes the calculated velocity-depth bounds to be quite broad, and thus not very useful in calculating a precise velocity-depth function. However, the velocity bounds are consistent with velocity models of the oceanic lithosphere involving a surface layer with a steep velocity gradient (layer 2) above a deeper layer with a shallow velocity gradient (layer 3). These inversions provide an approximate starting model for eventual synthetic seismogram calculations.

In order to investigate the possibility of azimuthal differences in travel times, we plotted travel times vs. range for the different refraction line azimuths. Fig 13a shows a comparison of travel times for shots along N-S azimuths vs. shots along E-W azimuths. Although there is considerable scatter in the data, some trends are apparent.

Between about 5 and 15 km, the E-W arrivals come in before the N-S arrivals, while at ranges greater than 35 km, the N-S arrivals are first. Fig. 13b shows a similar comparison of NE-SW arrivals vs. NW-SE arrivals. In this case the NW-SE arrivals are early at ranges of about 6 to 17 km, while the NE-SW arrivals are early at ranges greater than 35 km. These differences in P-wave travel times are indicative of anisotropy at two levels in the oceanic lithosphere. The fast direction in the upper mantle anisotropy appears to be about N-NE while the fast direction in the crustal anisotropy is about N-NW.

The upper mantle anisotropy is consistent with the MSS travel times, which, because of better signal to noise, extend to much larger ranges than the OBS data (see Whitmarsh et al., this volume). At mantle ranges the SW arrivals at the MSS consistently come in ahead of the NW-SE arrivals.

Fig. 14 is a closeup of the OBS arrivals at close ranges. Out to about 4 km the N-S, NE-SW arrivals are roughly coincident with the E-W, NW-SE arrivals. Between about 4 and 6 km, the E-W, NW-SE arrivals come in increasingly early, and then maintain an approximately constant offset at ranges greater than 6 km. Since the slope of the travel time curve is approximately flat at these ranges, the data can be reduced for a constant velocity in order to make a travel time vs. azimuth plot. Fig. 15 shows such a plot for travel time picks between 7 and 11 km, reduced at 6.6 km/sec. The vertical alignments in the plot represent individual refraction lines, which were shot at approximately constant azimuth. Points between these alignments represent data from the circular line. The data show considerable scatter, presumably representing lateral heterogeneities. However, some systematic azimuthal trends are apparent. Arrivals at azimuths of 0 to 45 degrees (N-NE) and 180 to 225 degrees (S-SW) are generally late, while arrivals at azimuths of 90 to 135 degrees (E-SE) and 270 to 315 degrees (W-NW) are generally early.

We fit this data with a curve of the form

$$t = a_1 + a_2\cos 2\theta + a_3\sin 2\theta + a_4\cos 4\theta + a_5\sin 4\theta$$

where t = travel time
θ = azimuth of shot

The least squares fit for this curve is shown in Fig. 15. The magnitude of the azimuthal travel time differences is about 0.05 second and the fast direction for the crustal anisotropy is about N120°E.

Fig. 16 shows a similar plot for P-wave arrivals at mantle ranges, reduced at 8 km/sec. Although less data are available at these ranges, the anisotropy is quite clear. The curve shown is a least squares fit for a function of the form

$$t = a_1 + a_2\cos 2\theta + a_3\sin 2\theta$$

We did not include 4θ terms, because of the limited azimuthal distribution of our data at these ranges. The magnitude of the travel time differences is about 0.3 second while the inferred fast direction for the anisotropy is N30°E.

Discussion

The travel time data support anisotropy with a 2θ P-wave velocity dependence on azimuth at two levels in the oceanic lithosphere at DSDP hole 594B. The fast direction of the crustal anisotropy, N120°E, is orthogonal to the fast direction of upper mantle anisotropy, N30°E (see Fig. 17). Previous studies of Pacific upper mantle anisotropy have found that the fast direction in the upper mantle is parallel to the original spreading direction (see for example Raitt et al., 1969). Assuming that this is true at the Ngendei site, then the inferred fossil spreading direction is N30°E and the fast direction in the crustal anisotropy is perpendicular to this spreading direction.

The area surrounding the Ngendei site is a relatively unexplored region in the Pacific Plate. Available bathymetric and magnetic data are inconclusive in constraining the original spreading direction. For example, roughly parallel ridges to the north of the borehole (see Fig. 17) suggest that the fossil spreading direction was north-northwest. However, the largest bathymetric feature in the area, the arc shaped ridge to the east of the borehole, is inconsistent with a simple model of spreading in any direction. Available magnetic data are similarly confusing (Menard, personal communication). Thus, the direction of the observed upper mantle anisotropy is the only reliable constraint available concerning the orientation of the fossil spreading at the Ngendei site, assuming, of course, the validity of the association of upper mantle anisotropy with aligned olivine crystals parallel to the original spreading direction. This suggests that in some cases seimic refraction experiments similar to the Ngendei experiment may prove invaluable in reconstructing fossil tectonics in areas where other data are unavailable or ambiguous.

To our knowledge this is the first observation of both crustal and upper mantle anisotropy in the same seismic refraction experiment. Thus, the Ngendei data set will provide important constraints on the direction and magnitude of anisotropy in the ocean lithosphere. In future analyses, we plan to use synthetic seismogram modeling for both P and S waves in order to develop as complete a picture as possible of the distribution of elastic parameters at the Ngendei site, information which should help in understanding the structure and mechanisms of formation of the oceanic crust and upper mantle.

References

Creager, K.C., and Dorman, L.M., 1982. Location of instruments on the seafloor by joint adjustment of instrument and ship positions. J. Geophys. Res., 87:8379-8388.

Garmany, J., Orcutt, J.A., and Parker, R.L., 1979. Travel time inversion: a geometrical approach. J. Geophys. Res., 84:3615-3622.

Garmany, J., 1984. The recovery of true particle motion from three component ocean bottom seismometer data. J. Geophys. Res., in press.

Helmberger, D.V., 1967. Head waves from the oceanic Mohorovicic discontinuity. Phd thesis, Univ. Calif. San Diego.

LaTraille, S.L., Gettrust, J.F., and Simpson, M.E., 1982. The ROSE seismic data storage and exchange facility. J. Geophys. Res., 87:8359-8363.

Moore, D.M., Dorman, L.M., Huang, C.Y., and Berliner, D.L., 1981. An ocean bottom, microprocessor based seismometer. Mar. Geophys. Res., 4:451-477.

Orcutt, J.A., 1980. Joint linear, extremal inversion of seismic kinematic data. J. Geophys. Res., 85:2649-2660.

Purdy, G.M., 1982. The correction for the travel time effects of seafloor topography in the interpretation of marine seismic data. J. Geophys. Res., 87:8389-8396.

Raitt, R.W., Shor, G.G., Francis, T.J.G., and Morris, G.B., 1969. Anisotropy of the Pacific upper mantle. J. Geophys. Res., 74:3095-3109.

Spudich, P., and Orcutt, J., 1980. Petrology and porosity of an oceanic crustal site: results from wave form modeling of seismic refraction data. J. Geophys. Res., 85:1409-1433.

Whitmarsh, R.B., Orcutt, J.A., Jordan, T.H., Adair, R.G., and Shearer, P.M., 1984. Velocity bounds on the seismic structure of late Jurassic [157 ma old] crust and upper mantle in the southwest Pacific basin from downhole observations at Deep-sea Drilling Project hole 595B. Initial Rep. Deep Sea Drill. Proj, Leg 91.

Appendix 1

This section contains 73 record sections which show the highlights of the OBS refraction data set. They are arranged by OBS, refraction line, and channel number (in that order). All seismograms are scaled by range and shot weight (see text). Some record sections do not indicate a channel number-- these are always channel 1. Channel 1 is vertical; channels 2 and 3 are horizontals; channel 4 is a hydrophone. Horizontal gains and hydrophone gains are the same for all record sections; vertical traces are amplified by a factor of two relative to the horizontals. Lines 2a, 2b, and 2c are scaled differently than the other lines.

Because of the large amplitude of the direct water wave, the seismograms were truncated beyond this arrival to avoid overwriting adjacent traces. The water wave phase can be seen sloping up to the right at the close ranges of each record section. The digital OBSs store approximately 13 seconds of data in internal memory and after 13 seconds the tape recorder must be activated in order to store more data. Tape recorder noise contaminates the records at this point and its effect is quite distinctive in these seismograms; a typical example is the large amplitude signal which begins about 5 seconds into the last seismogram in Line 3a, OBS Juan, Channel 1.

Some of the arrivals are clipped; a typical example of this is shown in the large shots recorded in Line 3a, OBS Juan, Channel 2. The peculiar appearance of these seismograms (one-sided spikes) is a consequence of wraparound of the 12-bit word used in the OBS microcomputer. Another problem was noise in the poorly isolated preamp for the hydrophone channel-- this is the cause of the spikes in Line 1a, OBS Lynn, Channel 4. The OBS design has been changed to eliminate this problem in future experiments.

Frequently the horizontal component data are contaminated by resonant modes, presumably related to oscillations of the OBS on the sea floor. These resonances typically appear about 0.5 second after the initial P-wave and S-wave arrivals and can be remarkably coherent over many seismograms (e.g. see Line 4b, OBS Karen, Channel 3). The general problem of OBS to sea floor coupling, and a procedure for recovering true ground motion from OBS data have recently been investigated by Jan Garmany (Garmany, 1984). A preliminary analysis of some of the Ngendei OBS horizontal component data by Garmany achieved some success in removing these resonances.

Despite the problems mentioned above, the overall quality of the data is excellent, characterized by close shot spacing, good signal to noise ratios, and four channels of data per OBS. A particularly striking example of the quality of the data is the circular line, Line 2c, as

recorded by OBS Suzy. Both P and S waves are very distinct. Seismograms at similar azimuths are coherent but vary dramatically in character and amplitude at azimuth differences of 45 degrees or more. For example, note the 2θ pattern in the P-wave arrivals as recorded by the horizontal channel 3. This pattern is expected if the P-wave particle motion points away from the shots. However, other patterns, such as those visible on the vertical channel, cannot be so easily explained and presumably are related to lateral heterogeneity and/or anisotropy at the site. Many other lines exhibit well defined S-wave arrivals (for example, Line 4a, OBS Karen) although a comprehensive study of the shear wave structure at the Ngendei site has only begun.

Fig. 1

DSDP hole 595B is located in the southwest Pacific about 1000 km east of the Tonga Trench.

Fig. 2

The frequency response of the Ocean Bottom Seismometers from the Scripps Institution of Oceanography which were used in the refraction experiment.

Fig. 3

Relative locations of the OBSs and the borehole. Ellipses are 95% confidence limits for the OBS locations relative to a common center of mass. The shipboard OBS drop points are shown as diamonds.

Fig. 4

The refraction shooting schedule is shown in this plot of shot range (km from OBS Karen and OBS Suzy) vs. time (days). All of the shots except those in line 6 (not shown) were recorded by at least two OBSs. The borehole seismometer (MSS) recorded most of lines 4b, 5a, 5b, and 6. The gaps between shots at long ranges (large shots) and those at close ranges (small shots) represent times when the ship doubled back and repeated part of the refraction line. The range is not constant for line 2c, the circular line, because of the small offset between the OBSs and the borehole at the center of the circle.

Fig. 5

Map of the area around DSDP hole 595B showing the orientations of the refraction lines. The circular line (line 2c) is of 10 km radius.

Fig. 6

Examples of source functions for shots recorded on the R/V Melville for

a) 2 pound shots (shot numbers 5038-5044, no 5043).
b) 3 pound shots (shot numbers 5615,5635,5655,5675,5690,5710).
c) 30 pound shots (shot numbers 4240-4245).
d) 60 pound shots (shot numbers 4246-4251).
e) 120 pound shots (shot numbers 4259-4264).
f) 180 pound shots (shot numbers 4268-4273).

The 2 and 3 pound shots were suspended from balloons and exploded at a constant depth of 10 m. This is reflected in the nearly identical bubble pulse period (the time between the first and second pulses) for these shots. In contrast, the 30 to 180 pound shots sank freely in the water and exploded at varying depths, indicated by the irregular bubble pulse periods for these shots.

Fig. 7

Close-ups of the first pulse of the source functions shown in Fig. 6. Notice the nearly identical pulse characteristics for the 2 and 3 pound

shots compared to the more irregular pulse shapes for the 30 to 180 pound shots.

Fig. 8
Sound velocity vs. depth profile used to calculate water wave ray paths.

Fig. 9
Travel time residual vs. depth for the entire OBS data set. Line is least squares fit and corresponds to a $\frac{dt}{dh}$ value of -0.23 sec/km.

Fig. 10
P-wave travel times vs. range for refraction line 5b. Times are reduced at 8 km/sec.

a) Raw travel times show strong positive correlation with depth. Curve is spline used to estimate ray parameter appropriate for each shot.

b) Travel times corrected (by time and range) down to the sea floor. Note the negative correlation with depth. Curve is spline used to determine residuals for $\frac{dt}{dh}$ calculation. Points with X's indicate depths shallower than 5.2 km- these points were not included in the spline fit.

c) Travel time points corrected for a $\frac{dt}{dh}$ value of -0.23 sec/km.

Fig. 11
P-wave travel times for the entire OBS data set.

a) Raw travel times.

b) Topographically corrected (including $\frac{dt}{dh}$ correction) travel times.

Fig. 12
Velocity-depth bounds as determined from extremal inversion of τ-p bounds. The bounds were determined separately for each line. Upper bounds are shown as solid lines, lower bounds as dotted lines.

Fig. 13
a) P-wave travel times for shots at azimuths along a N-S line (shown as vertical bars) compared to shots at azimuths along an E-W line (shown as horizontal bars). Between about 5 and 15 km the E-W arrivals are early, while at ranges greater than 35 km the N-S arrivals are early.

b) NE-SW shots (shown as diagonals to upper right) vs. NW-SE shots (shown as diagonals to lower right). NW-SE arrivals are early between about 6 and 17 km, while NE-SW arrivals are early at ranges greater than 35 km.

Fig. 14
A comparison of N-S, NE-SW arrivals (circles) with E-W, NW-SE arrivals (crosses) at ranges of 1 to 12 km. Arrivals from rays entering the sea floor at depths shallower than 5400 m have been eliminated

because of scatter in the data and uncertainties in applying topographic corrections.

Fig. 15

Travel times vs. shot azimuth for shots at ranges of 7 to 11 km. All times have been reduced at 6.6 km/sec. Arrivals from rays entering the sea floor at depths shallower than 5400 m have been eliminated. Curve is least squares fit for a function of the form

$$t = a_1 + a_2\cos 2\theta + a_3\sin 2\theta + a_4\cos 4\theta + a_5\sin 4\theta$$

Fig. 16

Travel time vs. shot azimuth for shots at ranges between 35 and 50 km. Times have been reduced at 8 km/sec. Arrivals from rays entering the sea floor at depths shallower than 5200 m have been eliminated. Curve is least squares fit for function of form $t = a_1 + a_2\cos 2\theta + a_3\sin 2\theta$.

Fig. 17

The fast direction in the upper mantle is at about N30°E, while the fast crustal direction is at N120°E.

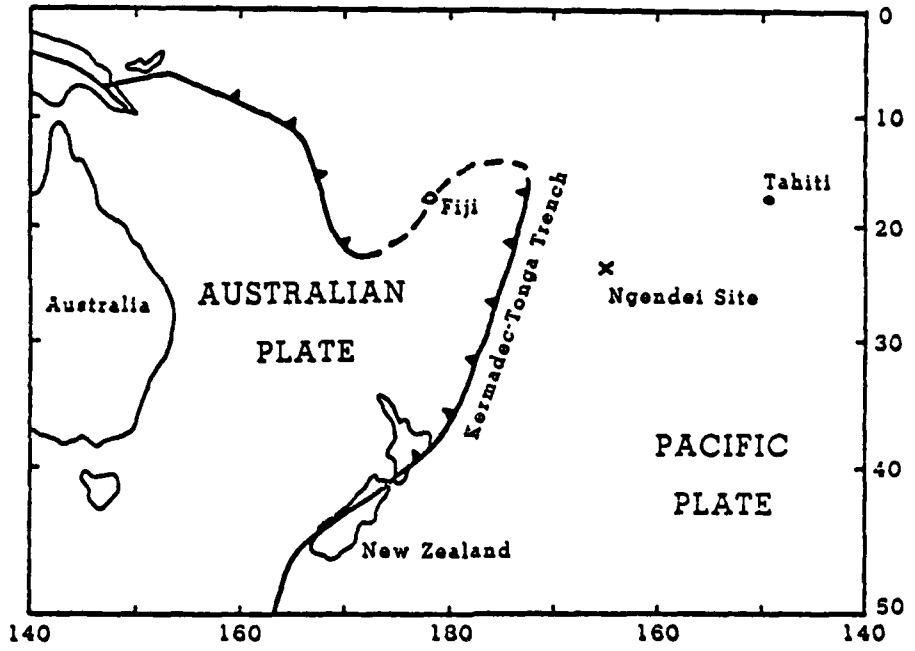


FIGURE 1

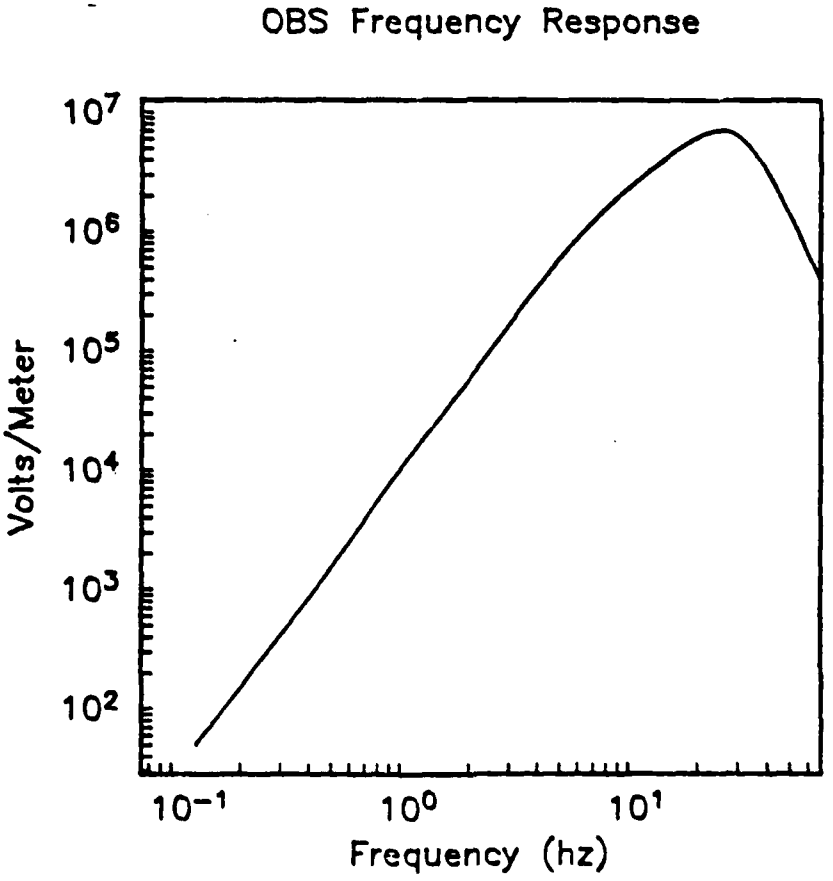


FIGURE 2

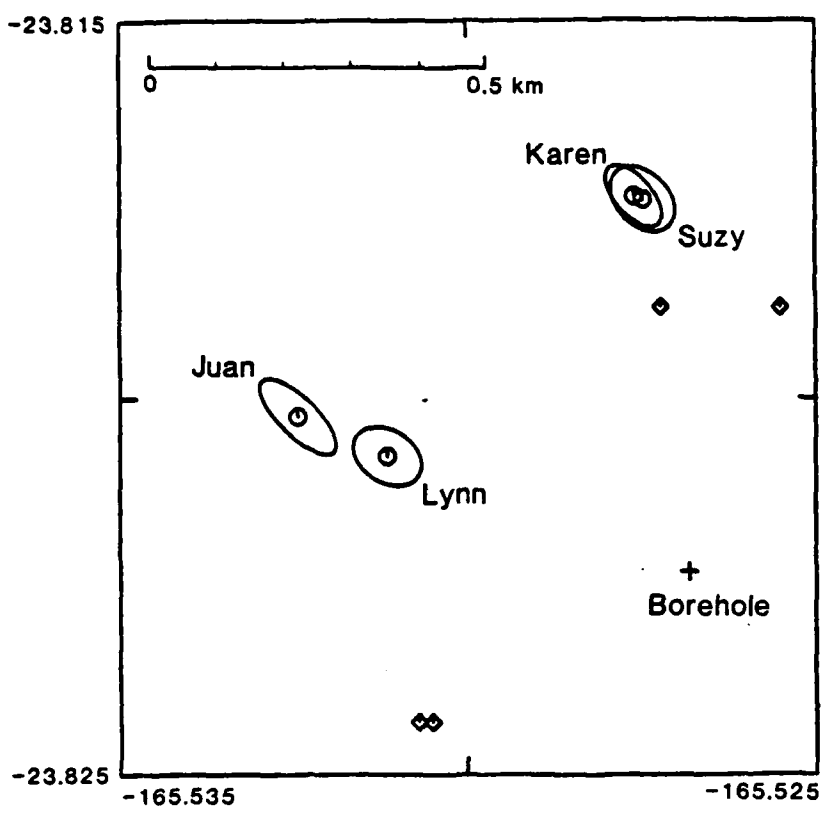


FIGURE 3

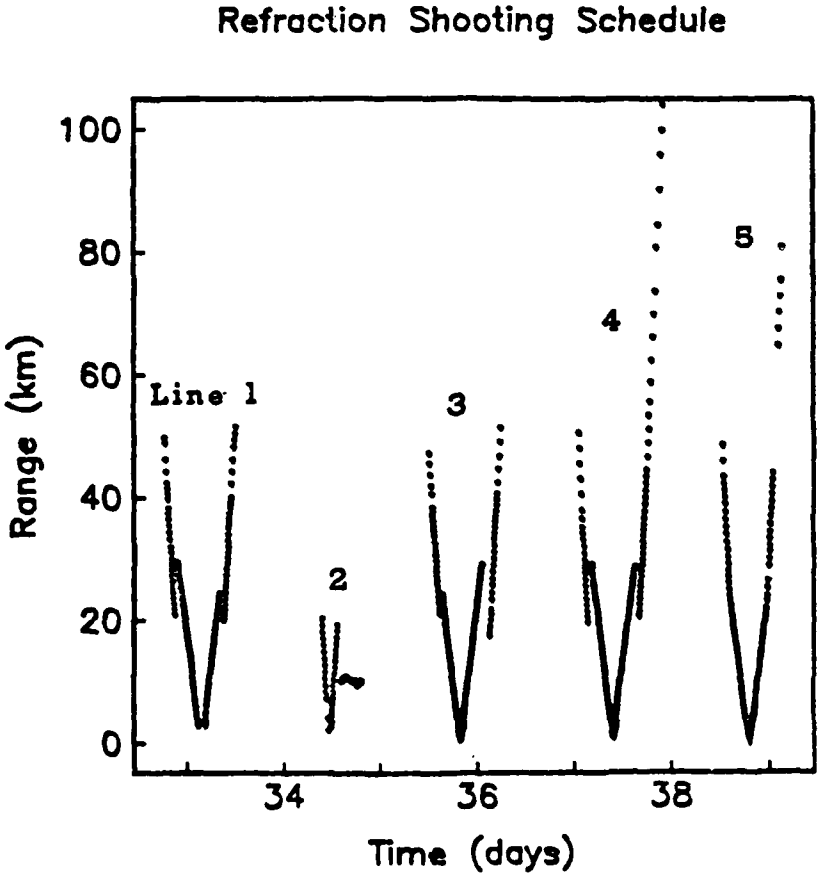


FIGURE 4

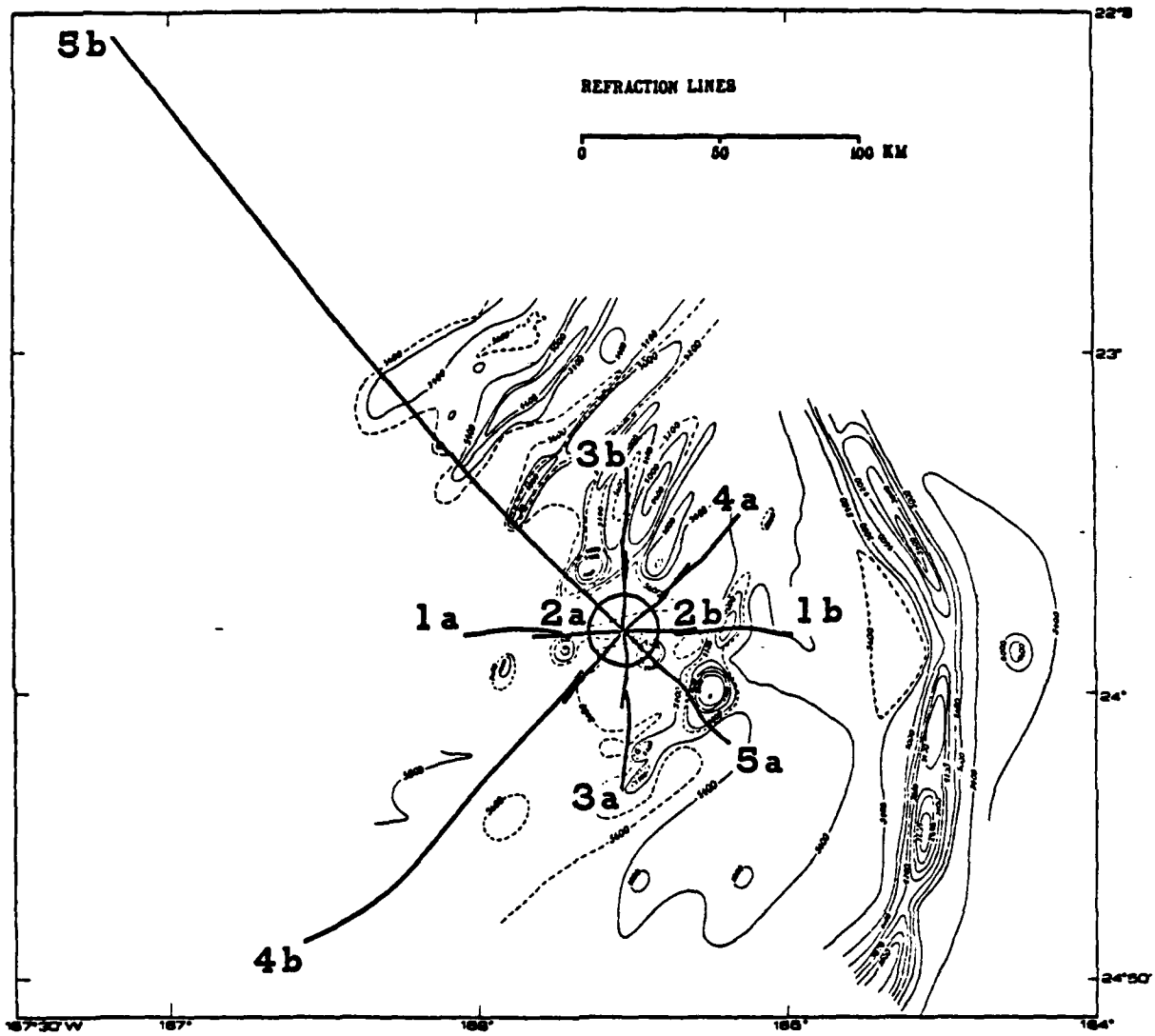

REFRACTION LINES
0
50
100 KM
5b
4a
3b
1a
2a
2b
1b
5a
3a
4b
22°8
23°
24°
24°50'
167°30'W
167°
166°
165°
164°

FIGURE 5

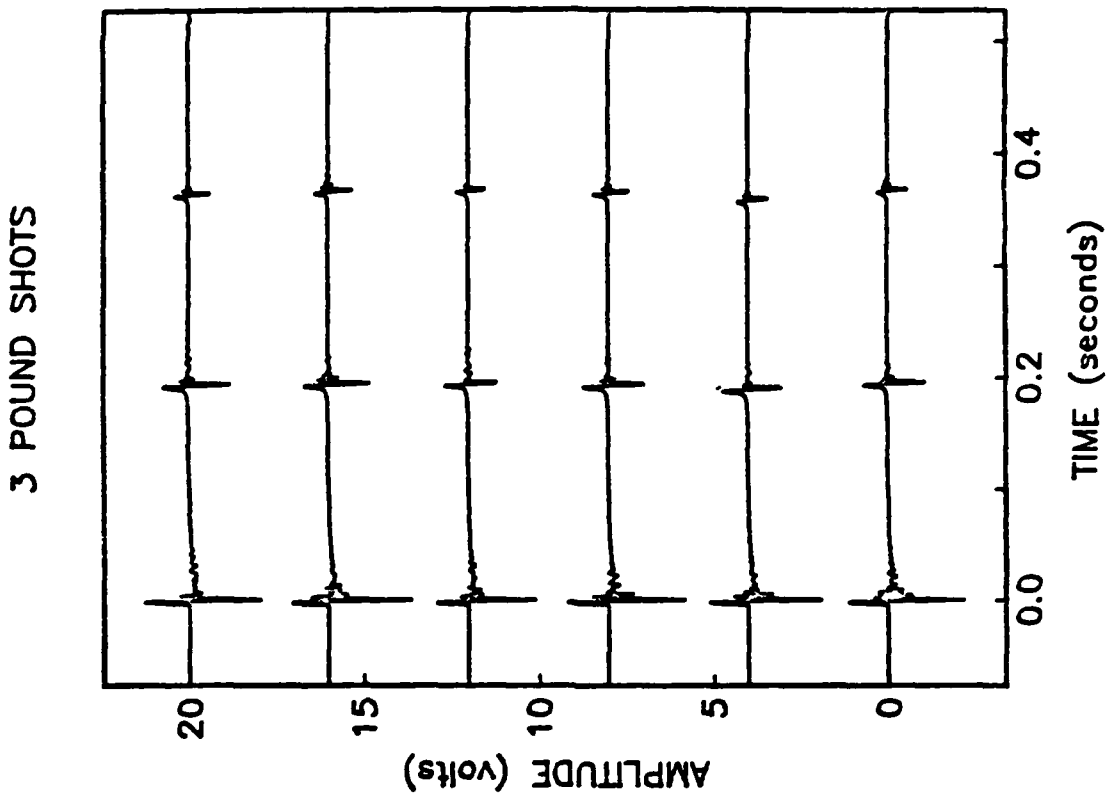


FIGURE 6a

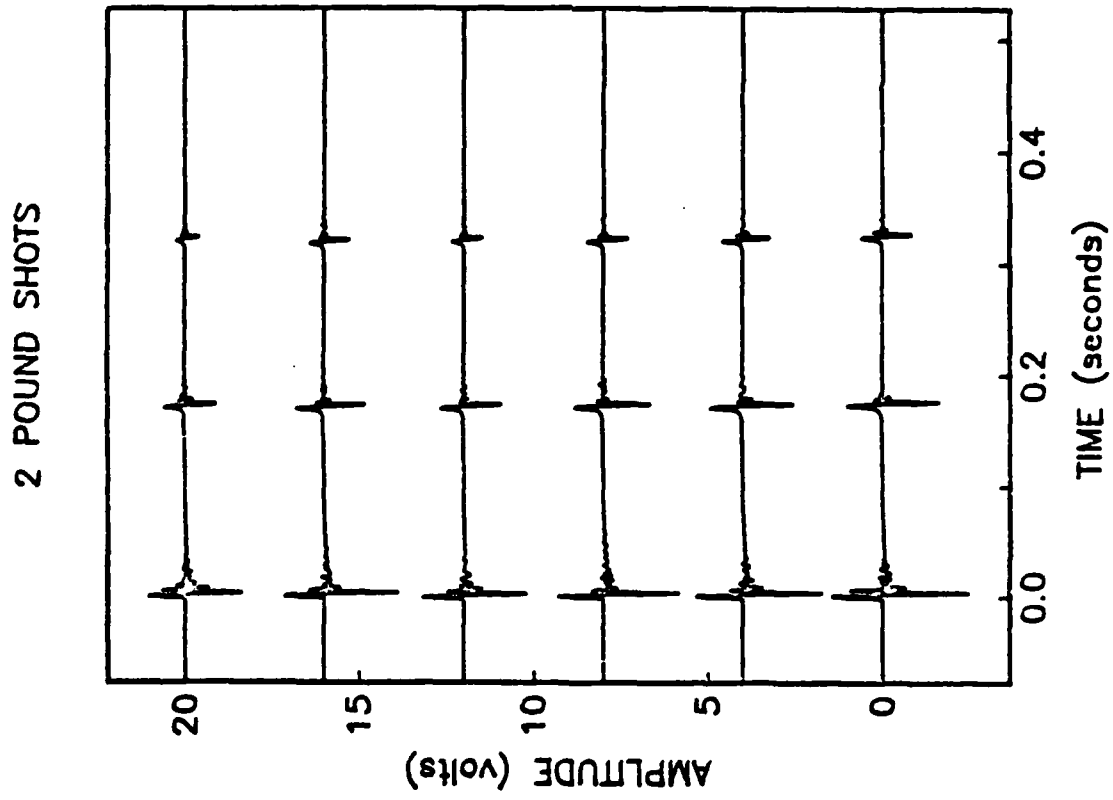


FIGURE 6b

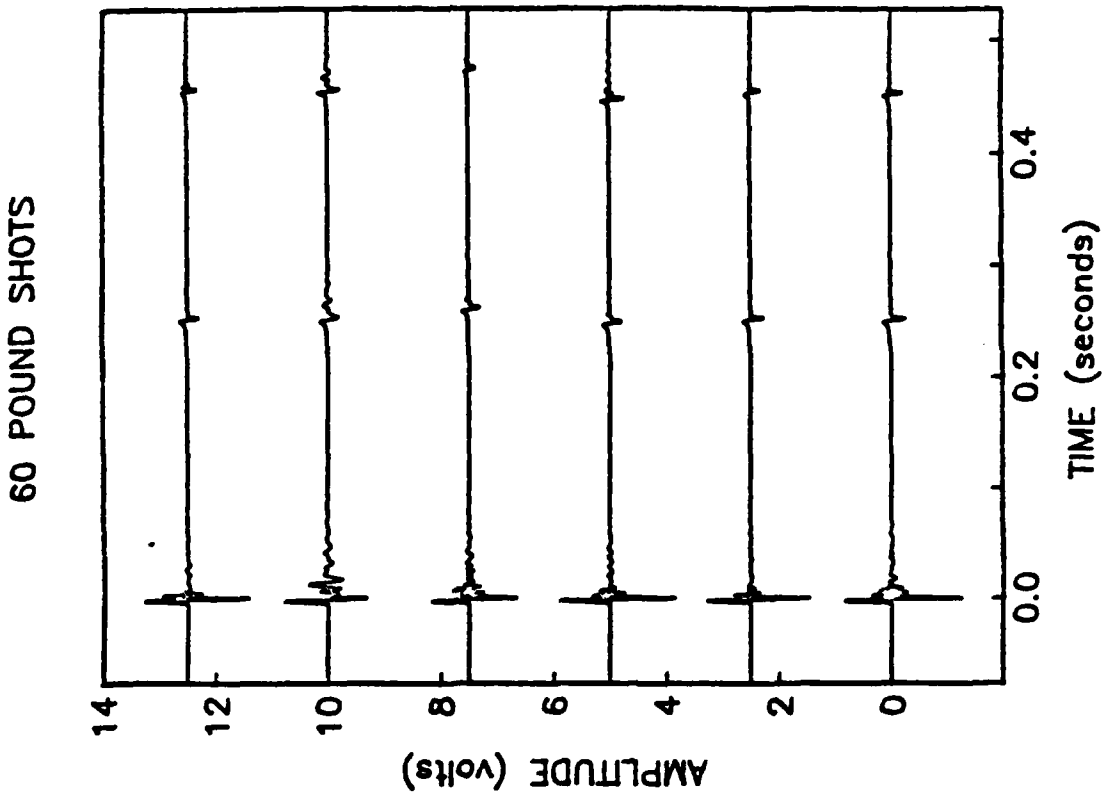


FIGURE 6c

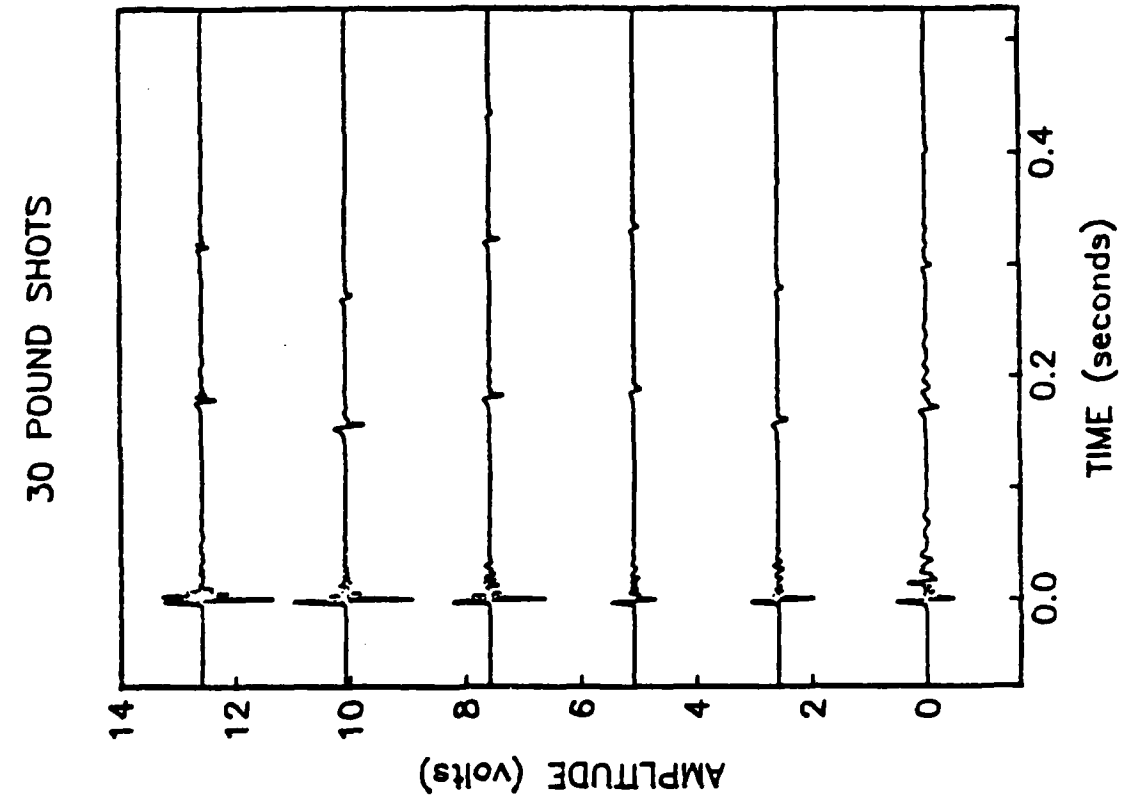


FIGURE 6d

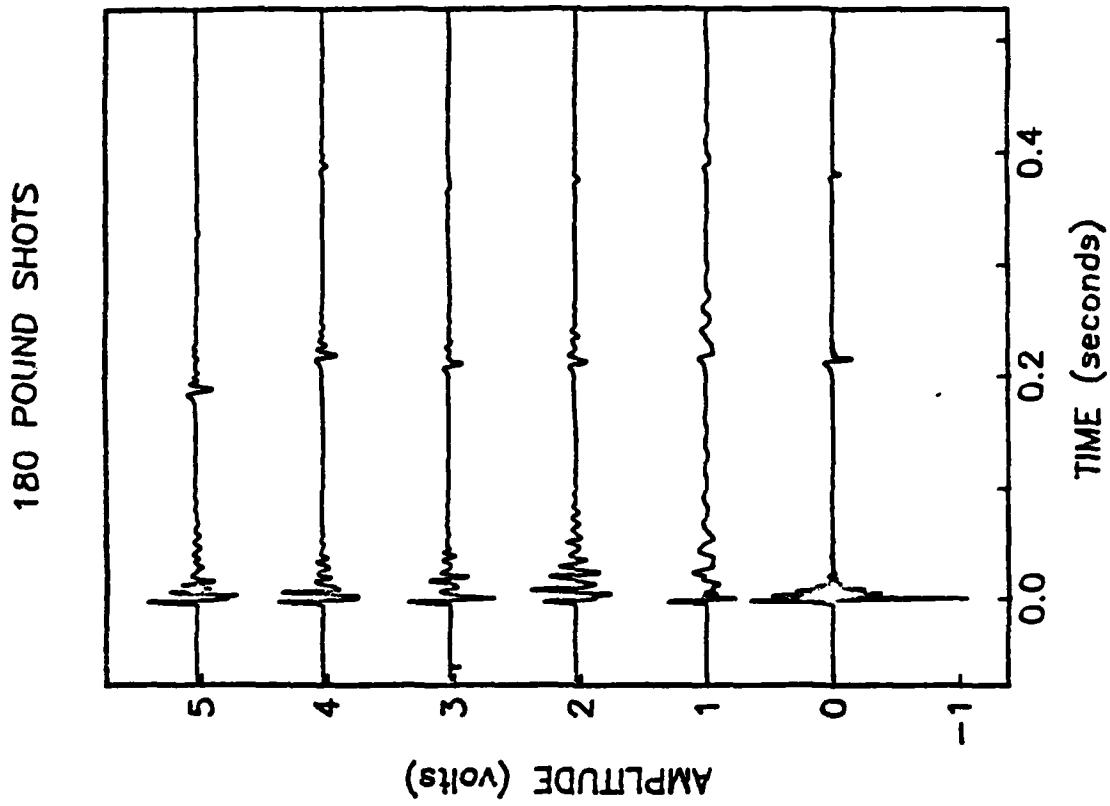


FIGURE 6e

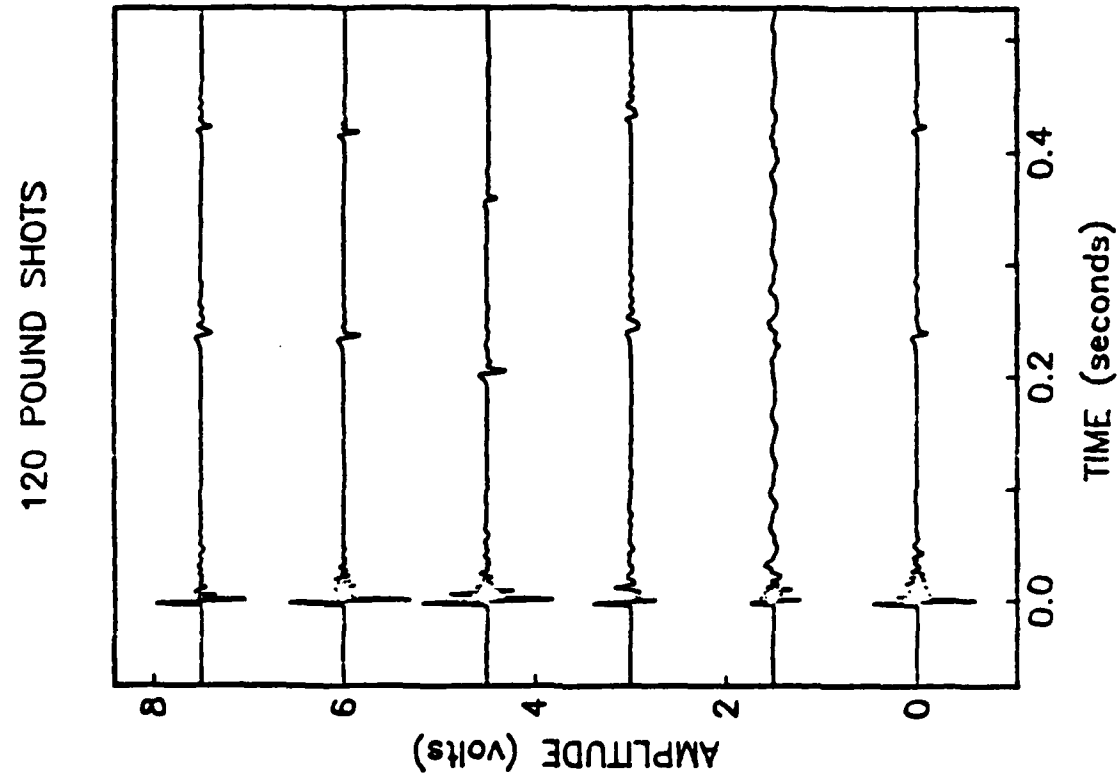


FIGURE 6d

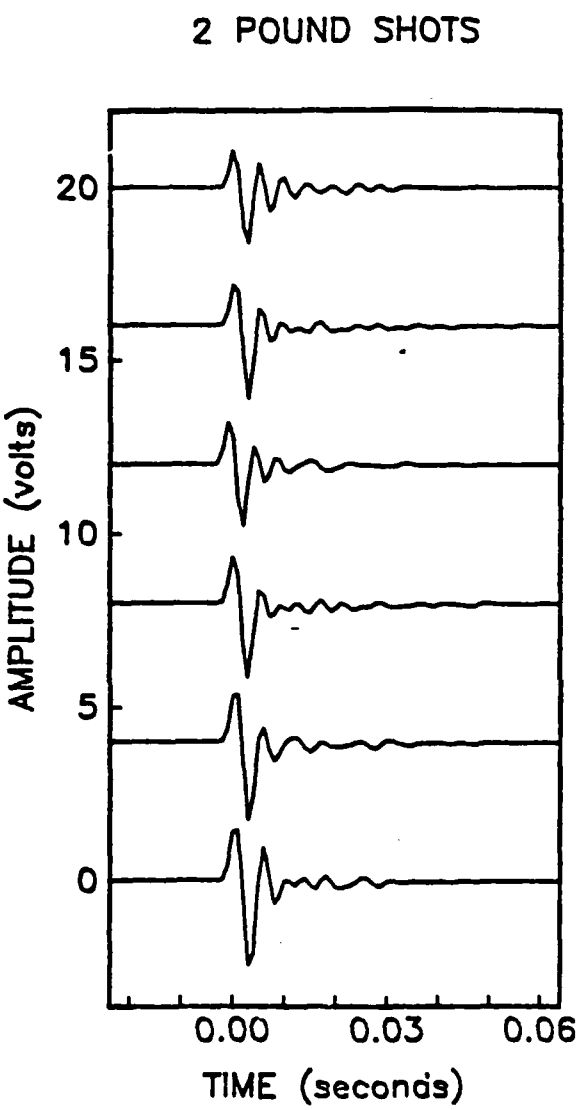


FIGURE 7a

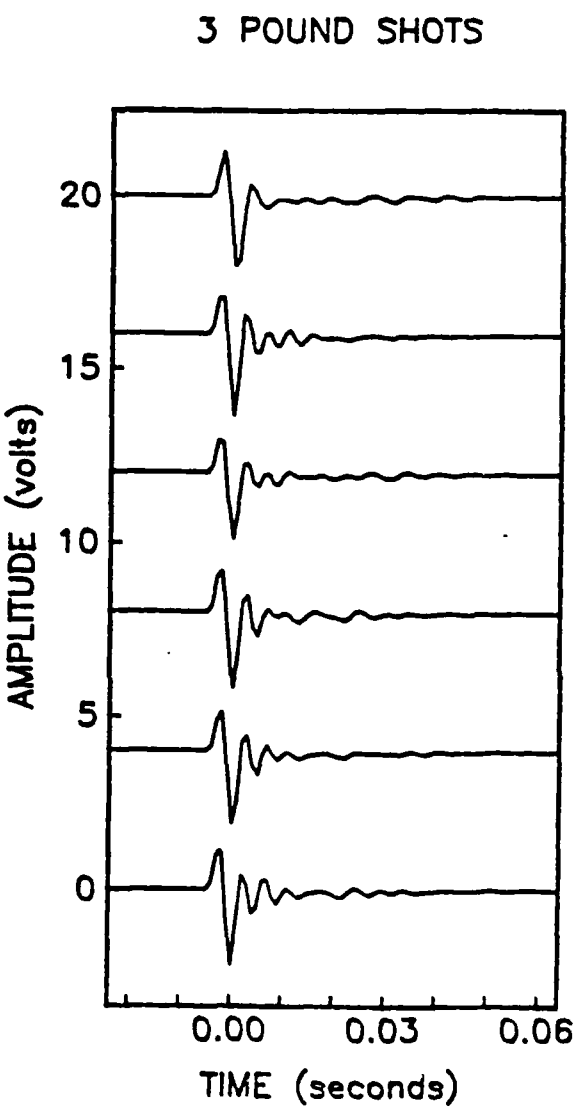


FIGURE 7b

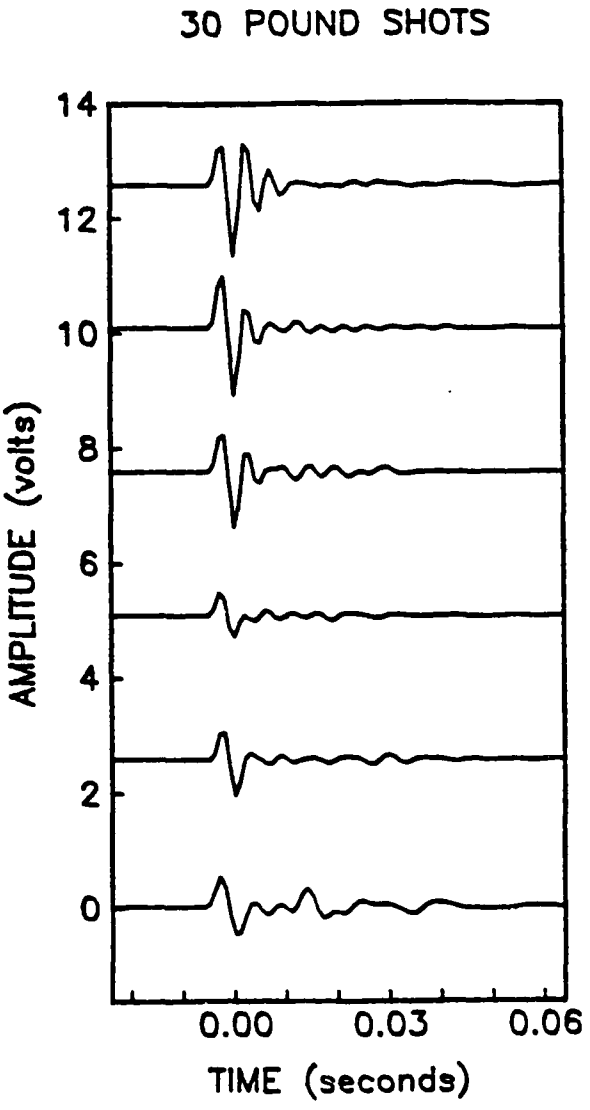


FIGURE 7c

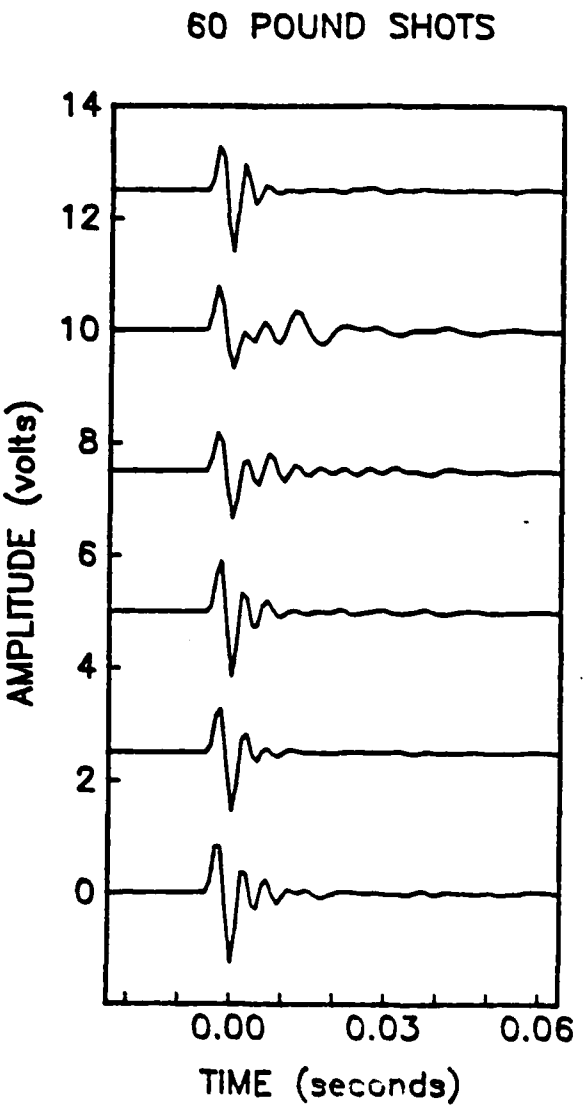


FIGURE 7d

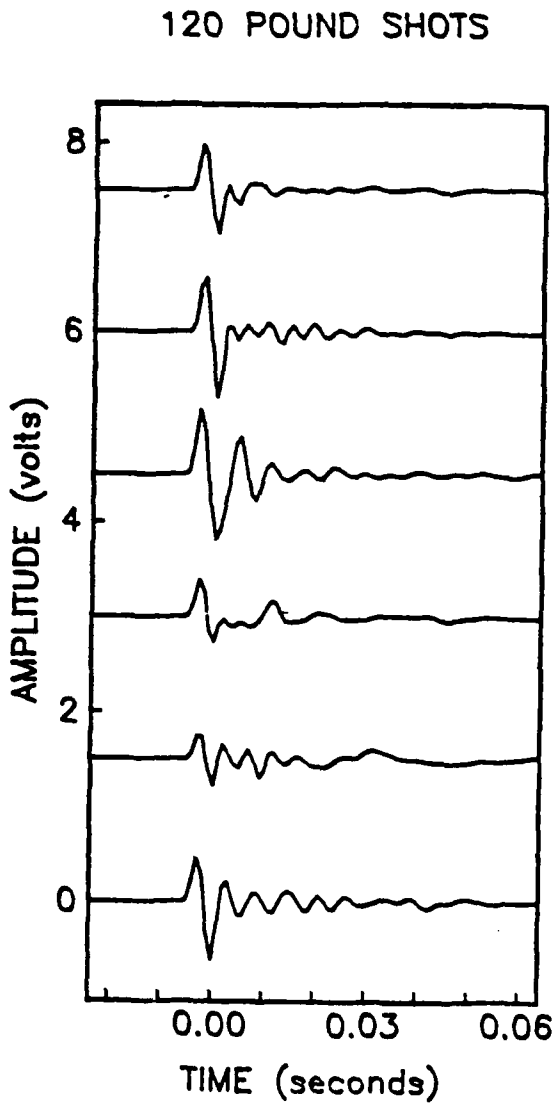


FIGURE 7e

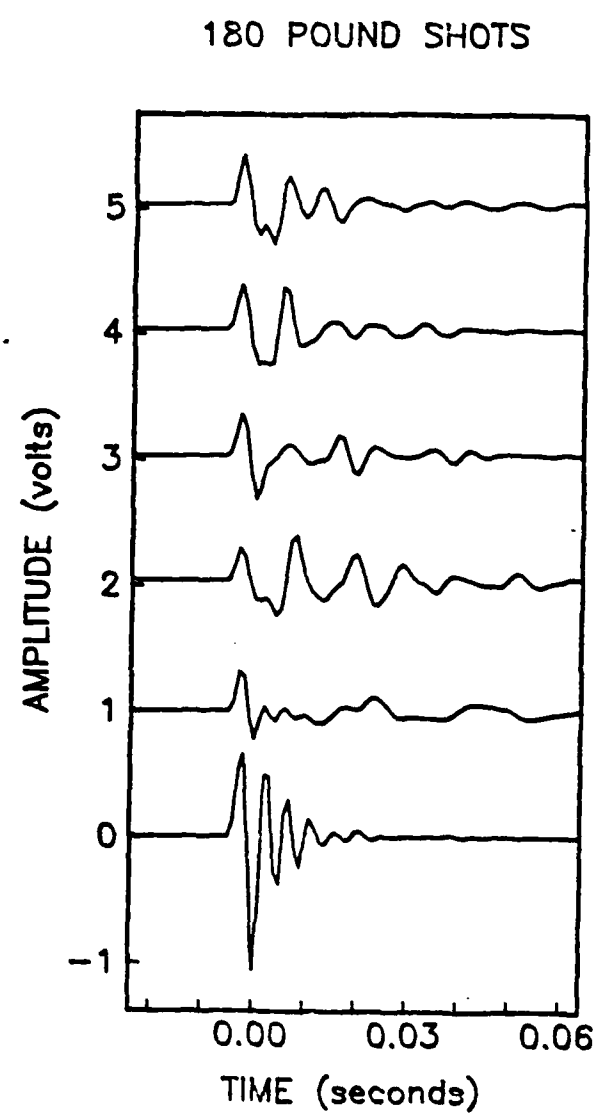


FIGURE 7f

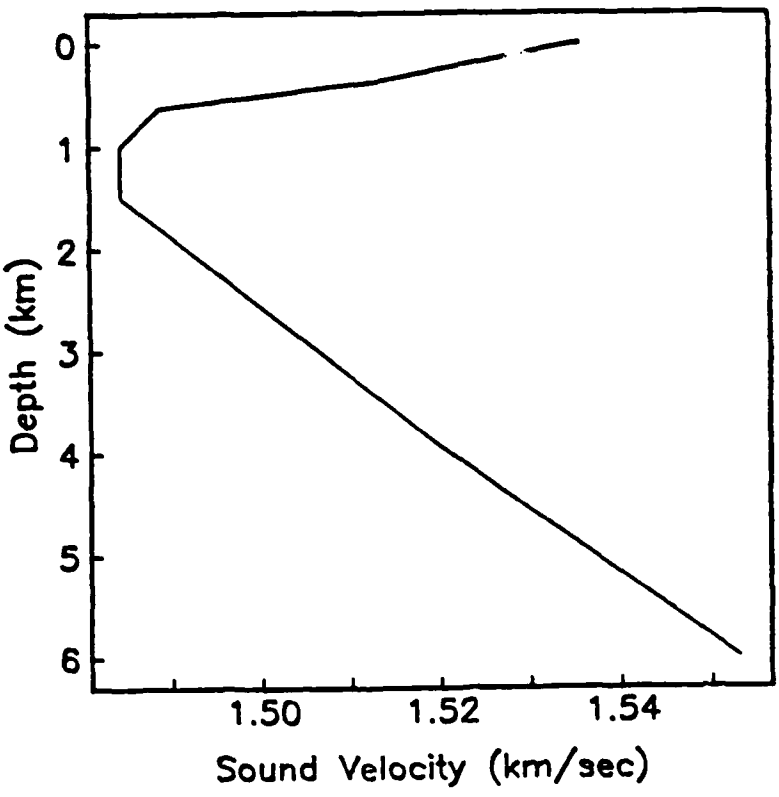


FIGURE 8

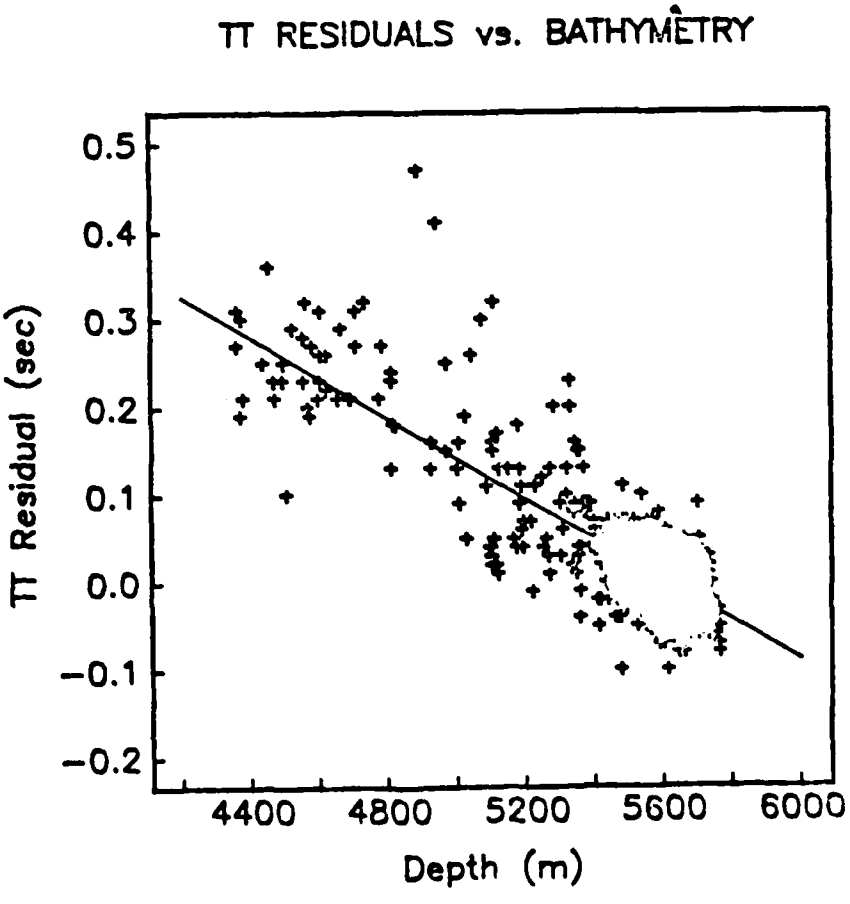


FIGURE 9

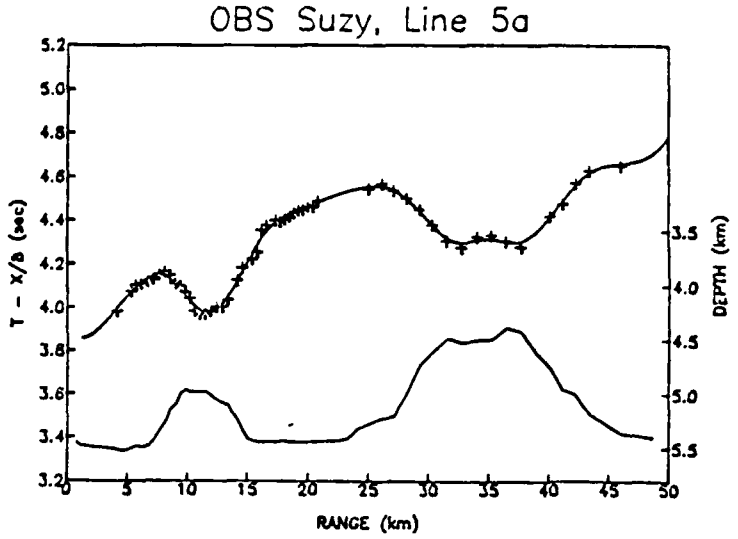


FIGURE 10a

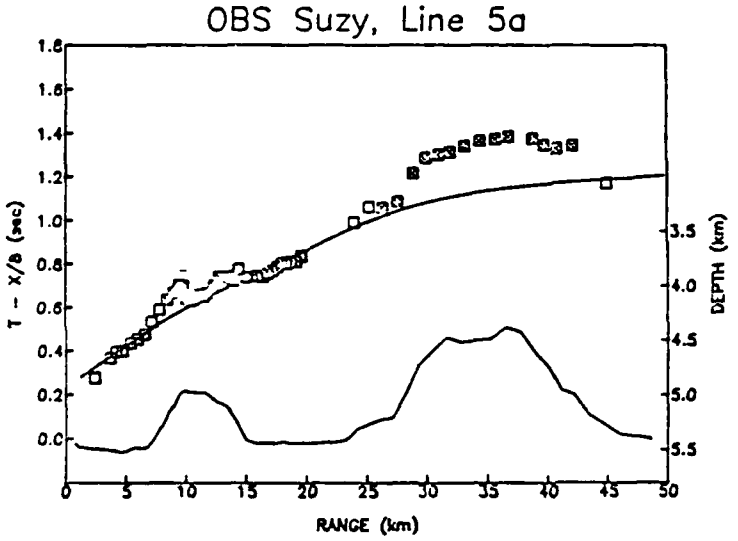


FIGURE 10b

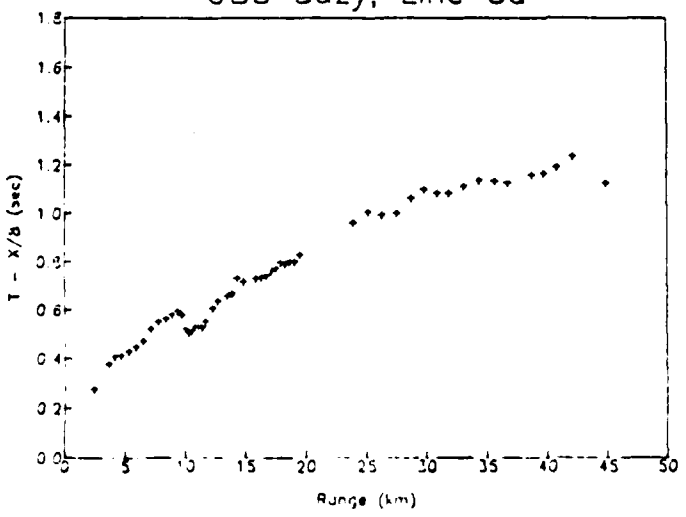


FIGURE 10c

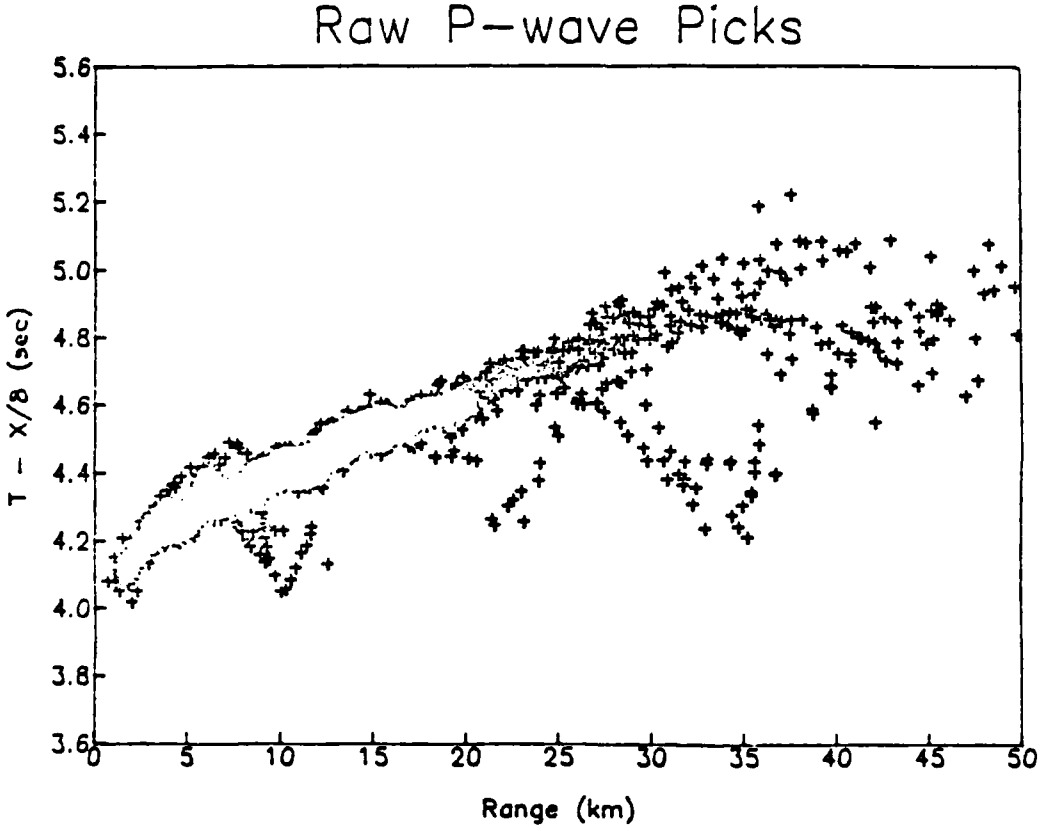


FIGURE 11a

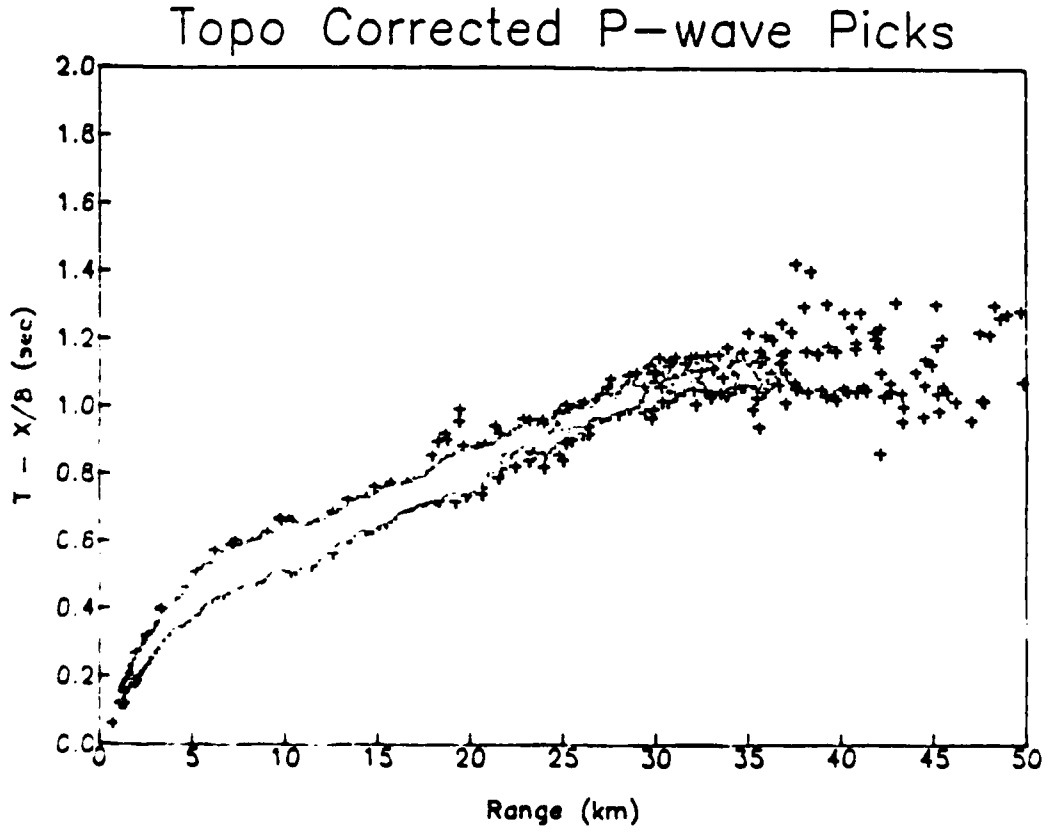


FIGURE 11b

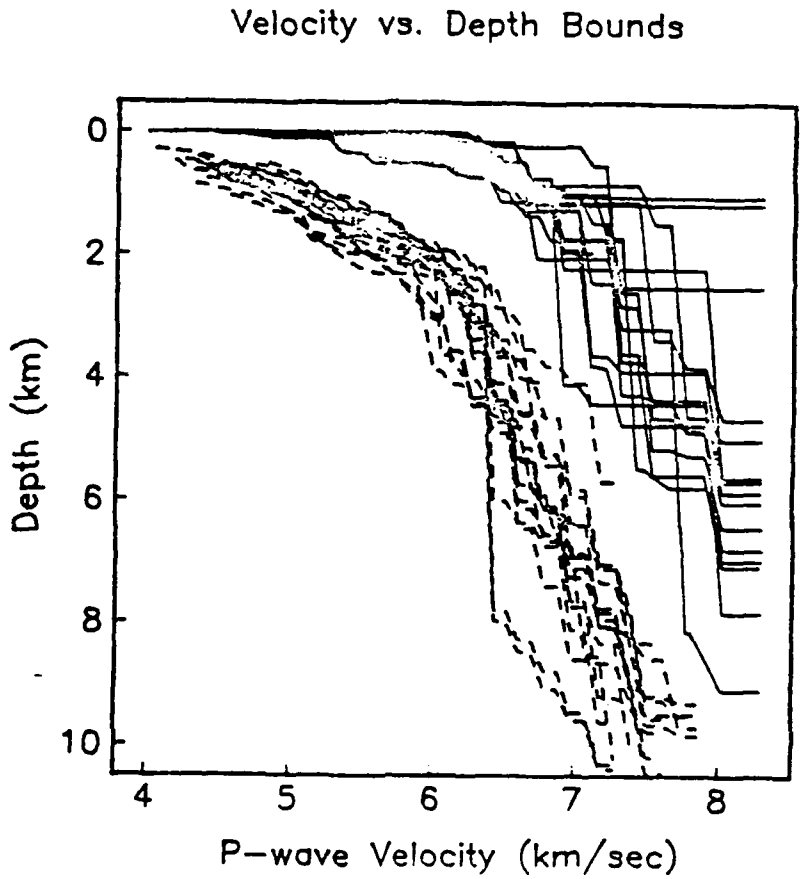

Velocity vs. Depth Bounds
Depth (km)
0
2
4
6
8
10
4
5
6
7
8
P—wave Velocity (km/sec)

FIGURE 12

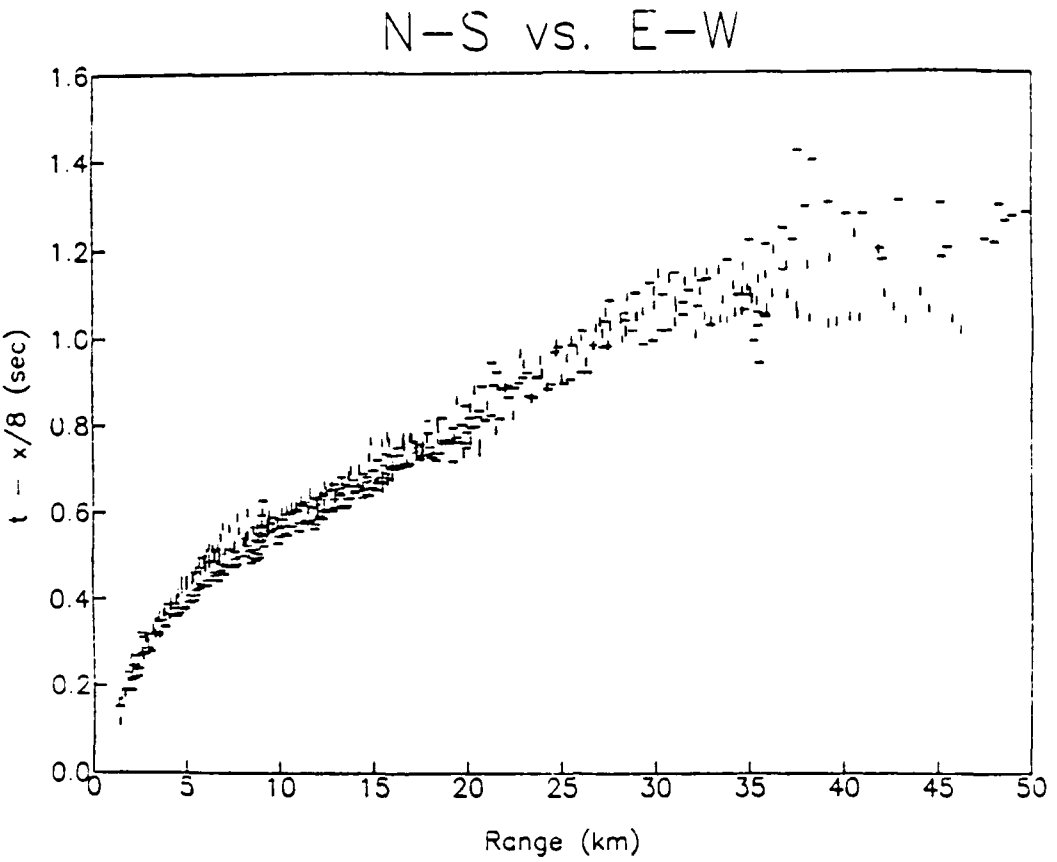


FIGURE 13a

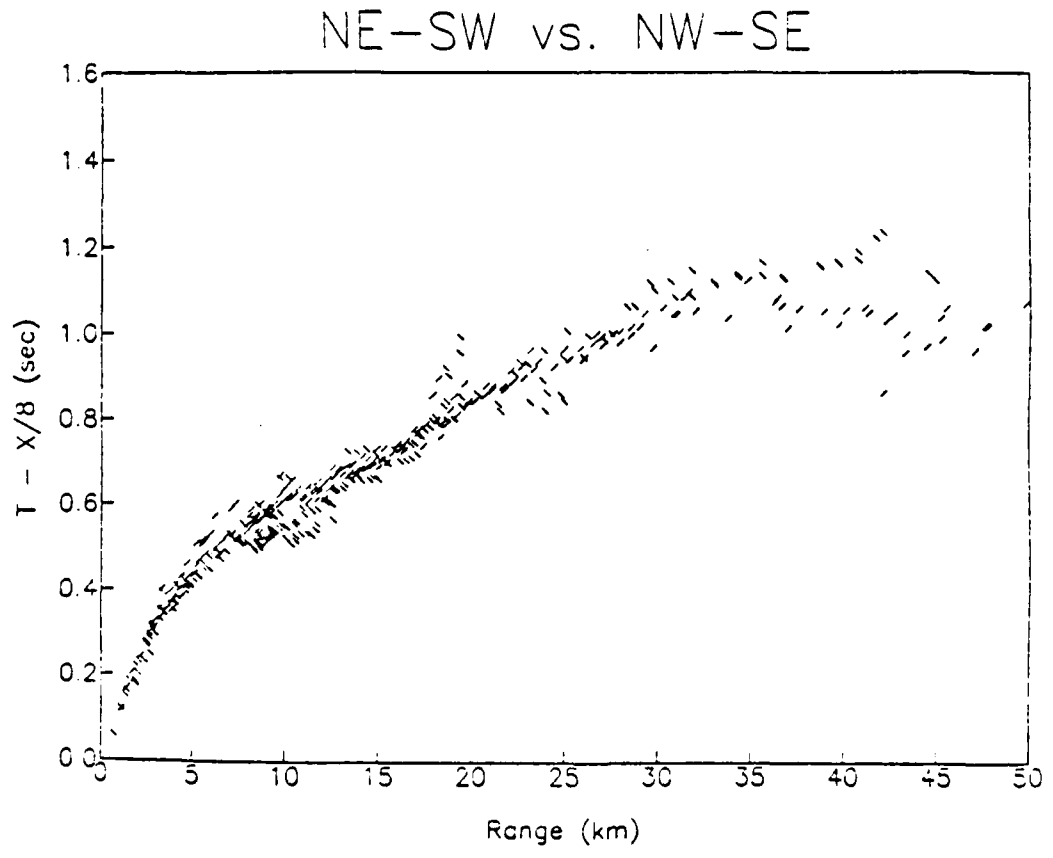


FIGURE 13b

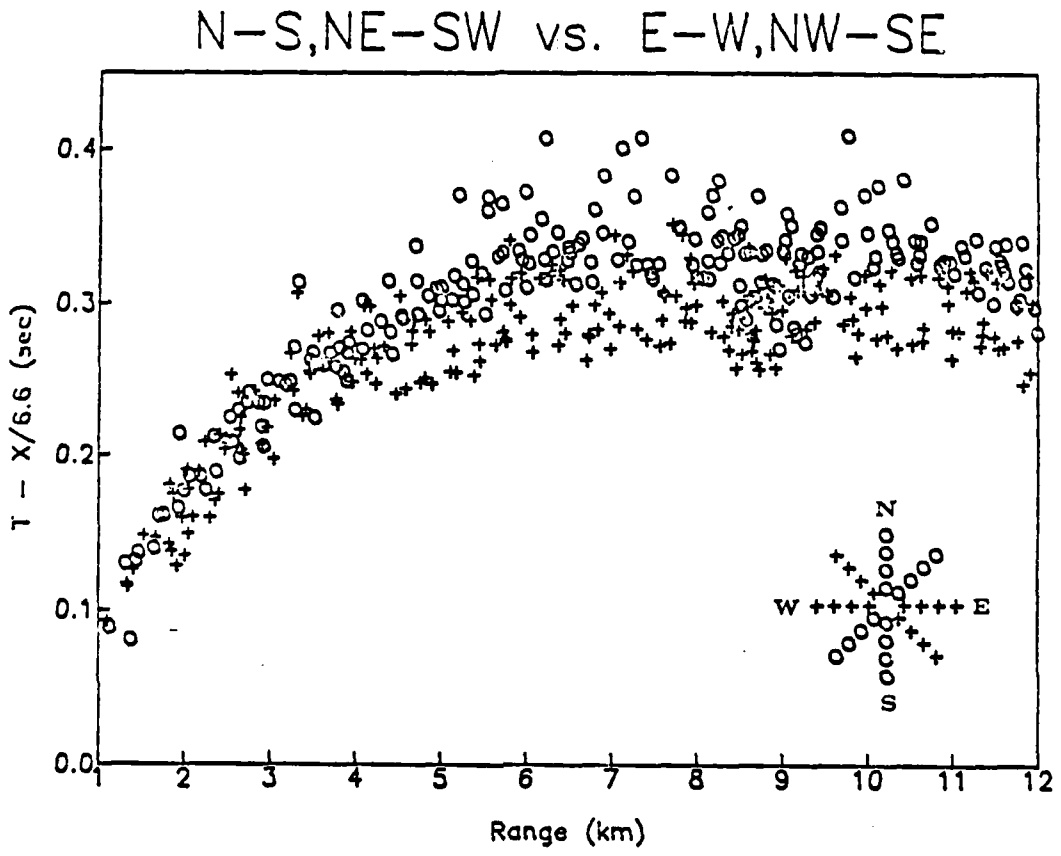

N–S,NE–SW vs. E–W,NW–SE
T – X/6.6 (sec)
0.0
0.1
0.2
0.3
0.4
1
2
3
4
5
6
7
8
9
10
11
12
Range (km)
N
W
E
S

FIGURE 14

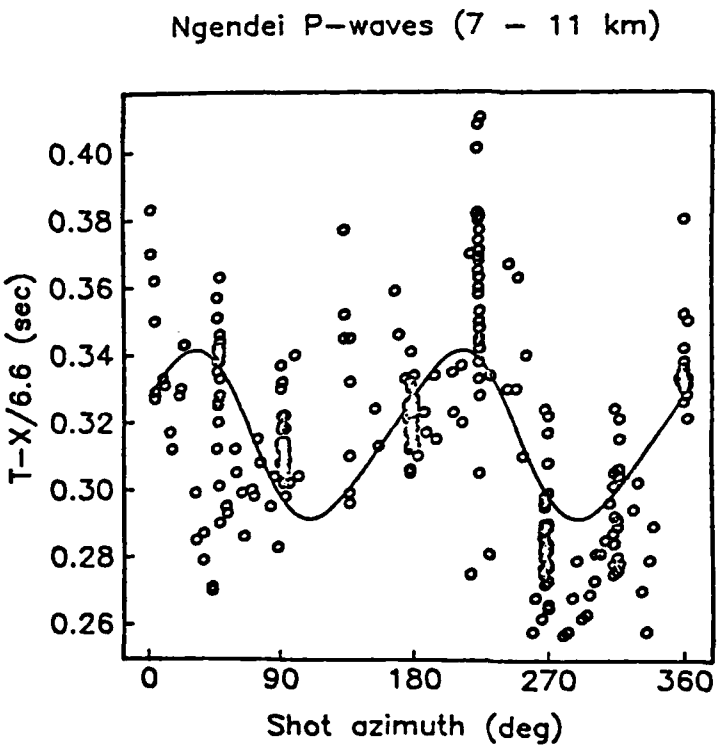


FIGURE 15

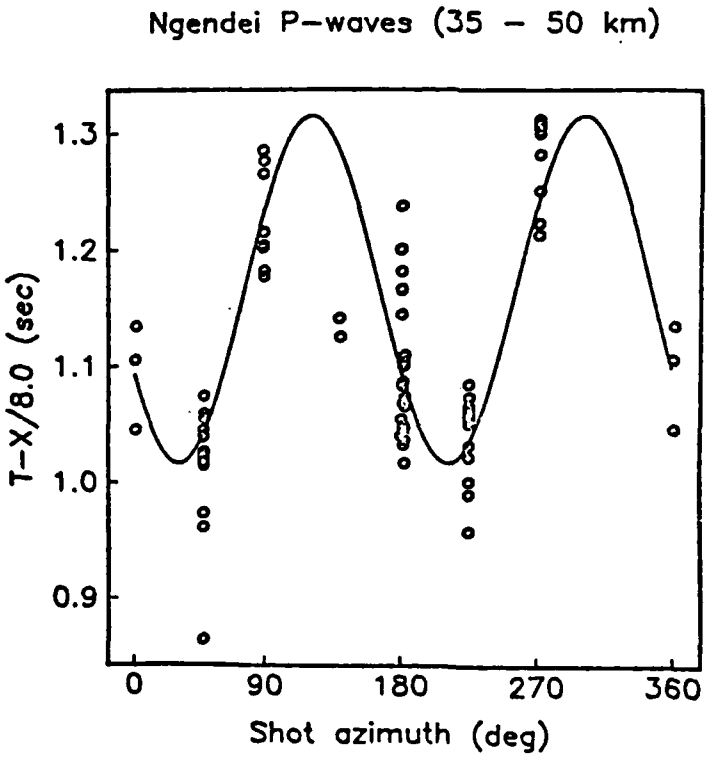


FIGURE 16

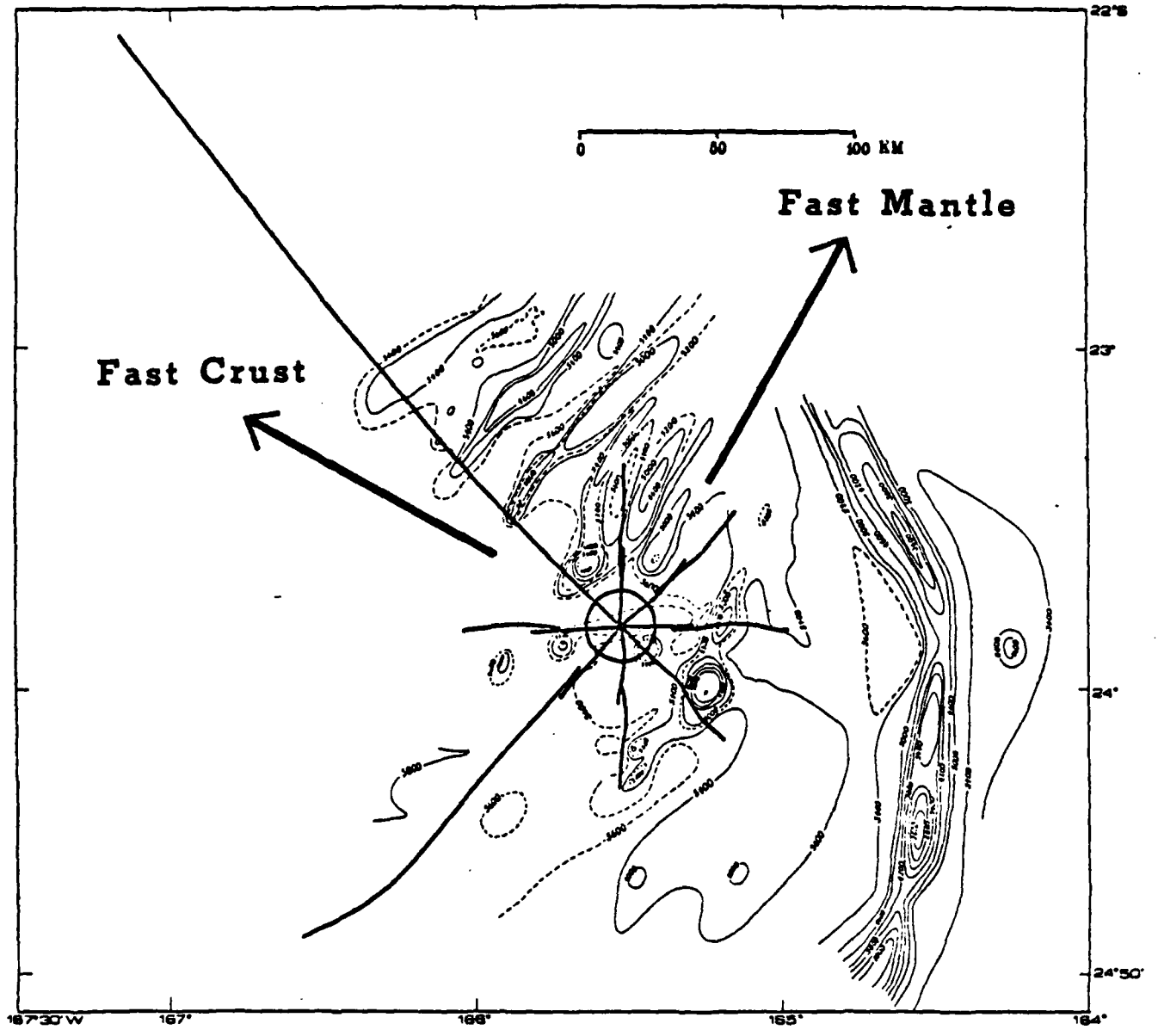

0
50
100 KM
Fast Mantle
Fast Crust
22°S
23°
24°
24°50'
167°30'W
167°
166°
165°
164°

FIGURE 17

CHAPTER 8

ANISOTROPY IN THE OCEANIC LITHOSPHERE— THEORY AND OBSERVATIONS FROM THE NGENDEI SEISMIC REFRACTION EXPERIMENT IN THE SOUTHWEST PACIFIC

P. Shearer and J. Orcutt

Geological Research Division
Scripps Institution of Oceanography
La Jolla, California 92093
RUNNING TITLE: Ngendei Anisotropy

Geophys. J. R. astr. Soc. (1985) vol. 80, 493-526

Summary

P-wave travel time data from a seismic refraction experiment on the 1983 Ngendei expedition to the south Pacific indicate anisotropy at two levels in the oceanic lithosphere. In the upper mantle, P-wave velocities vary between 8.0 and 8.5 km/sec with the fast direction at N30°E. Crustal anisotropy within layer 2 is characterized by azimuthal P-wave velocity differences of about 0.2 to 0.4 km/sec, with the fast direction at N120°E, orthogonal to the upper mantle anisotropy. The observed anisotropy is consistent with a model in which aligned olivine crystals cause anisotropy in the upper mantle and aligned cracks within layer 2 cause anisotropy in the crust.

We examine a model of P-wave propagation from a point source in an isotropic layer above an anisotropic half-space and show that under these conditions anisotropy can cause seismic ray paths to deviate from the vertical plane connecting source and receiver. This deviation has a negligible effect on seismic travel times but must be taken into account in modeling P-wave polarization anomalies. P-wave polarization anomalies within the anisotropic half-space are the sum of the particle motion deviation from the ray path, and the ray path deviation from the source receiver azimuth, and are typically range dependent. P-wave polarization anomalies will also occur in the overlying isotropic layer, purely as a result of the ray path deviation, with greater deviations at long ranges. A simple model of upper mantle anisotropy (6 km/sec crust above 8.0 to 8.6 km/sec anisotropic mantle) produces surface polarization anomalies of 1.5 to 3.5 degrees. In practice, P-wave polarization anomalies are difficult to observe because they are small compared to observed scatter in polarization data and are sensitive to differences in horizontal seismometer gain levels. We examine the implications of anisotropic ray path deviations on travel times and P-wave polarizations for the Ngendei data as well as some previous marine seismic refraction experiments.

Introduction

The physics of wave propagation in general anisotropic media has been understood for some time. Recently seismologists have been considering the added complexities of anisotropy and many theoretical studies have been done (see for example Geophys. J. R. astr. Soc. 49, 76). Most of these studies deal with the forward problem; that is, given a complete set of elastic constants for a medium, these studies describe analytical and numerical methods for computing the seismic waves which can travel in the medium. Many exotic types of possible anisotropy have been investigated (see, for example, Crampin 1982) and interesting complications in wave propagation have been discussed.

Unfortunately, actual, reliable observations of seismic anisotropy are found much less frequently in the literature. Anisotropy, unless quite strong, is easily hidden by inadequate source-receiver distributions and lateral heterogeneities in the earth. Allowing general anisotropy in the earth introduces so many additional free parameters that inverting for these parameters is difficult.

Refraction seismology is one area in which successful observations of anisotropy have been made. Hess, Raitt, Shor, and others in the 1960's used travel-time data to establish P-wave anisotropy of the upper mantle in the Pacific (for example, Raitt et al. 1969). Travel-time data have also been used to measure upper mantle anisotropy on continents (Bamford 1977, 1979). More recently, studies of travel-times, P-wave polarizations, and shear wave splitting have led to hypotheses of marine crustal anisotropy (Stephen 1981; White and Whitmarsh, in press). These have been primarily observational studies which have not dealt with theoretical detail about the nature of anisotropic wave propagation.

This paper will present some results from the 1983 Ngendei expedition to the South Pacific. We find evidence for P-wave anisotropy at two distinct levels in the oceanic lithosphere. The observed anisotropy is consistent with models in which sheeted dike complexes are related to anisotropy in an upper crustal layer and aligned olivine crystals cause anisotropy in the upper mantle. The suggested original spreading direction for the Ngendei site (23.82°S, 165.53°W) is N30°E.

In addition, we examine the general problem of extracting anisotropic parameters from seismic refraction data. In particular, we will look at P-wave travel times and polarizations resulting from a point source within an isotropic layer above an anisotropic half-space, a model which is typical of that used for many seismic refraction experiments. We will show that under these conditions, anisotropy can cause seismic ray paths to deviate from the vertical plane connecting source and receiver. We will show that this deviation has a negligible effect on P-wave travel times, but a significant effect on P-wave polarizations. Finally, we will show some examples of possible anisotropy induced P-wave polarizations which might be observable by receivers either within the anisotropic material or on the isotropic layer above.

Heuristic Review of Anisotropic Wave Propagation

There are three important directions in the propagation of a seismic wave. The group velocity direction is the direction along which energy moves and corresponds to a seismic ray path. The phase velocity direction is perpendicular to the advancing wavefront. The particle motion direction is the direction that particles actually move as the wave passes.

In a homogeneous, isotropic medium the group velocity and phase velocity directions coincide. For P-waves the particle motion is also along this direction and for s-waves the particle motion is orthogonal to this direction. The geometry for P-waves emanating from a point source is almost trivial. The wavefronts will be spheres centered about the source. Energy travels radially out from the source in a direction normal to the wavefronts.

For a homogeneous, anisotropic medium the situation is more complicated. In general, the group velocity, phase velocity, and particle motion directions will each be distinct, even for P-waves. In an anisotropic medium, the P-wave group velocity will vary with direction. Thus, wavefronts from a point source will not form spheres (see Fig. 1), and directions normal to these wavefronts (the phase velocity direction) will not generally coincide with the line joining the source and the wavefront (the group velocity direction). Further, the P-wave particle motion direction will not generally coincide with either the group velocity or phase velocity directions.

This suggests a way to observe P-wave anisotropy by measuring differences between the source-receiver and particle motion directions. Crampin et al. (1982) examined this idea and found that the difference between the group velocity direction and particle motion direction is generally much smaller than the difference between the group velocity direction and phase velocity direction, and thus may be difficult to observe.

Following Crampin (1981) we may define the P-wave polarization anomaly as the difference between the observed P-wave particle motion and that which we would expect for purely isotropic media. In our example, the anomaly would be the angular difference between the source-receiver path (the expected particle motion direction for isotropic material) and the observed particle motion at the receiver.

Before leaving this example it will be helpful to make several other observations. We are not allowed an arbitrary dependence of group velocity with direction since this angular dependence is a function of the elastic constants of the medium. There is no easy way to predict what the particle motion directions will be from the group velocities; in general we must derive both from the elastic constants. The ray paths define directions of energy transport which must obey Fermat's Principle; that is, the ray is a path in the group velocity field along which the travel time is stationary. This means that we could predict ray paths in any medium if we knew the group velocity throughout the medium as a function of position and direction.

Now consider a plane interface between an anisotropic medium and an isotropic medium. A source in the isotropic medium and a receiver in the anisotropic medium lie within a plane perpendicular to the interface

(Fig. 2). If both media were isotropic the ray path between the source and receiver would be a straight line lying in this plane. However, in our example the ray path will skew to one side as required by Fermat's Principle. The ray will want to "take advantage" of faster directions in the anisotropic medium in order to minimize its travel time. The ray path which is stationary with respect to travel time will in general not be a straight line between source and receiver.

In this case the P-wave polarization anomaly will be the sum of the deviation of the ray path from the source-receiver line and the deviation of the particle motion direction from the ray direction. Notice that now the polarization anomaly is not only a function of the anisotropic properties of the receiver medium and the ray azimuth, but also of the relative positions of the source and receiver and the velocity of the isotropic material. Also, if we imagine switching the positions of the source and receiver we see that we could observe a polarization anomaly with a receiver in an isotropic medium, provided that the ray path goes at least partially through an anisotropic medium. We will consider this reciprocity later in the paper.

Finally, let us extend this example by considering head-waves propagating on an anisotropic half-space generated by a point source in a slower isotropic layer above (Fig. 3). We see that the ray path will generally skew to the side, out of the vertical plane connecting source and receiver, and will arrive at the receiver at an angle to the source-receiver azimuth. In this case we see that the group velocity direction within the anisotropic half-space is not generally the same as the shot-receiver azimuth.

Again the observed P-wave polarization anomaly at the receiver will be the sum of the ray path deviation from the source-receiver azimuth and the particle motion deviation from the ray direction (we will only concern ourselves with the horizontal polarization anomaly). This polarization anomaly will be a function not only of the anisotropic half-space, but also of the velocity and thickness of the isotropic layer and the source-receiver range. In addition, the travel-time between source and receiver is not solely related to the group velocity of the anisotropic half-space along the source-receiver azimuth, but is also a function of the above mentioned parameters.

Anisotropic Ray Tracing

Wave propagation in an anisotropic medium can be completely described if the 21 independent elements of the elastic tensor C_{ijkl} are known. If we consider a plane wave with unit direction $\hat{s}$ of slowness, we may write the eigenvalue equation (Aki and Richards 1980):

$$M_{ip} u_p = \frac{\rho}{|s|^2} u_i$$

where $M_{ik} = C_{ijkl}\hat{s}_j\hat{s}_l$
$|s|$ = magnitude of s (slowness surface $s = |s|\hat{s}$)
u = polarization vector (particle motion direction)
ρ = density

In general there will be 3 values of $|s|$ which will satisfy the equation and 3 orthogonal eigenvectors u . In the case of an isotropic medium there will be one eigenvalue for the P-wave and two coincident eigenvalues for s-waves. By solving this eigenvalue problem we can obtain phase velocities and polarization directions for any direction in slowness space that we require. In the general anisotropic case we will have 3 sheets in slowness space although we will consider only the P-wave surface in our analysis.

The ray direction (group velocity) is normal to the slowness surface. As we discussed earlier for the general anisotropic case, the group velocity direction, phase velocity direction (slowness direction), and particle motion direction are all distinct, even for P-waves.

Now imagine a horizontal interface between an isotropic layer and an anisotropic layer with a planar P-wave traveling down from the top layer into the bottom layer. If we rotate the coordinate system such that the x_2 component of the phase velocity is zero, we can construct a diagram such as Fig. 4. The generalization of Snell's law for anisotropic media is that the horizontal phase velocity s_1 is conserved (Aki and Richards 1980). For any point S_i on the upper slowness surface for the incident wave we can find the appropriate point S_t on the lower slowness surface for the transmitted P-wave. Notice that in general the group velocity directions (rays) are not in the plane of the diagram (although the phase velocity directions must be) since they are perpendicular to the slowness surfaces.

If we wish to find the head wave which will travel in the s_1 direction, we simply find the point H_t on the lower slowness surface for which the group velocity vector (the perpendicular to the slowness surface) points in the x_1 direction. For general anisotropy this point will not lie on the s_1 axis. However, in all the examples we will deal with in this paper the anisotropy will be symmetric about horizontal planes and thus will lie on the s_1 axis. The incident wave which will generate this head wave is given by H_i .

This is all the machinery we need in order to proceed with our forward modeling. We assume an isotropic layer velocity and values of C_{ijkl}/ρ for the anisotropic half-space and we specify an azimuth for the ray leaving the source. This provides the horizontal phase direction which we use to find the appropriate point on the lower slowness surface for a head wave. We can now find the phase velocity direction in the upper layer and the group velocity direction and particle motion direction in the half-space. The phase velocity direction in the upper layer

defines the ray parameter and azimuth of the ray in the isotropic layer, while the group velocity direction in the lower layer defines the ray azimuth in the anisotropic half-space.

In order to compute polarization anomalies for a given source and receiver, we specify a thickness for the isotropic layer and a source-receiver range. This allows us to calculate the source-receiver azimuth, which can then be compared to the ray azimuth and particle motion azimuth in the anisotropic medium.

Examples

Based on particle motion anomalies and s-wave splitting in a borehole seismic refraction experiment, Stephen (1981) modeled the oceanic crust as a highly anisotropic half-space with P-wave velocities varying from 4.0 to 5.5 km/sec with a 2θ dependence. He predicted particle motion deviations of up to 6 degrees with this model.

Using Stephen's values for $\Gamma_{ijkl} = C_{ijkl}/\rho$ for an anisotropic half-space with hexagonal symmetry ($\Gamma_{1111} = 30.25$, $\Gamma_{2222} = 16.00$, $\Gamma_{1212} = 8.50$, $\Gamma_{1122} = 10.00$, $\Gamma_{1313} = 5.00$ km^2 sec^{-2}), a water thickness of 5.5 km, and water sound velocity of 1.5 km/sec, we modeled the appropriate ray paths and particle motions. The results are shown schematically in Fig. 5; these diagrams demonstrate many of the features that we have discussed. At the interface, the rays turn toward the fast direction in the anisotropic medium. The difference between ray azimuths and shot-receiver azimuths will be maximized at short ranges and will approach zero at long ranges.

Stephen calculated the particle motion deviation from the ray path (group velocity direction) for his model. In comparing these deviations directly with his data, Stephen made the implicit assumption that the ray path deviations from the source-receiver plane are small. However, we will show in this paper that the ray path deviation is significant and must be taken into account at these nearby ranges of 3 to 12 km. Fig. 6 summarizes the expected polarization anomalies at these ranges. The ray path deviations are opposite in sign to the particle motion deviations and are larger in magnitude at ranges closer than about 8 km. Summing the ray path deviations and the particle motion deviations, we see that the expected polarization anomalies are very range dependent with maximum anomalies of -8 degrees at 3 km to +2.5 degrees at 12 km. Along lines of constant azimuth the polarization anomalies change sign -- at about 8 km they essentially vanish.

It is difficult to reconcile these predicted values with the data, which show maximum anomalies of +15 to +20 degrees (although with large error bars). The large magnitude of the polarization anomalies in the data and their apparent lack of range dependence suggest that is will be

difficult to fit the anomalies with any reasonable anisotropy model. One possible alternative explanation is miscalibrated gains in the two horizontal channels of the seismometer, which would cause an apparent 2θ dependence in polarization anomalies. This is an effect which White and Whitmarsh (in press) noticed in their data. Nevertheless, the S-wave splitting that Stephen observes cannot be explained in this way and remains evidence for anisotropy.

The procedure we have described gives us the ray path for rays leaving the source at specified angles. An iterative scheme can be used to find the appropriate ray path to a specified receiver position and to then calculate the source-receiver travel time. We used this procedure to calculate travel time curves for lines running radially away from the source. Fig. 7 shows the results for the Stephen anisotropy model. As one would expect, the slopes of the travel time curves asymptotically approach the group velocity in the direction of the line. However, even at close ranges, the travel time curves deviate only slightly from straight lines. This is remarkable, considering how large the anisotropy is in the Stephen model (4 to 5.5 km/sec), and indicates that the travel-time perturbations due to ray perturbations are truly a second order effect. This is a result of Fermat's principle -- to first order, travel times are unaffected by ray path deviations.

Using realistic data, it is difficult enough to observe differences in velocity with direction (i.e. noting the different slopes and positions of the lines in Fig. 7); it would be almost impossible to distinguish the slight curvature of the travel time curves associated with the ray path deviations.

The classical travel-time studies of upper mantle anisotropy in the Pacific (for example Raitt et al. 1969) assumed the group velocity was associated with a straight path between source and receiver. In this upper mantle case the anisotropy (8 to 8.6 km/sec) is smaller than the Stephen model anisotropy and the ranges (40 to 100 km) are greater which argues that this assumption was entirely justified.

In an OBS seismic refraction experiment in the Atlantic, White and Whitmarsh (in press) found particle motion deviations from the shot-receiver azimuth of 5 to 8 degrees and velocity variations of up to 0.4 km/sec, both with a 4θ dependence. They compare these results with model predictions for velocity and polarization anomalies as a function of azimuth for distributions of thin parallel cracks in an isotropic solid (Crampin 1978; Crampin et al. 1982). These modeled polarizations are the particle motion deviations from the ray azimuth, which, as Crampin et al. (1982) correctly note, are applicable for an anisotropic half-space containing both source and receiver.

However, in this case the source is not within an anisotropic half-space, but is in an overlying isotropic layer (the ocean). Thus,

as we have seen, it is incorrect to assume that the ray direction is equivalent to the source-receiver azimuth. For the simple example of an isotropic layer over an anisotropic half-space, the observed polarization anomaly will be the sum of the particle motion deviation from the ray direction and the ray deviation from the source-receiver azimuth. In order to test the size of the ray deviation effect, we studied a specific anisotropy model hypothesized to explain the travel time and polarization observations (White and Whitmarsh, personal communication). Using the White and Whitmarsh values of C_{ijkl}/ρ ($\Gamma_{1111} = 26.30$, $\Gamma_{2222} = 26.30$, $\Gamma_{1212} = 16.5$, $\Gamma_{1122} = -11.8$, $\Gamma_{1313} = -5.5$ km^2 sec^{-2}) for an anisotropic half-space with hexagonal symmetry, a water thickness of 2 km, and water sound velocity of 1.5 km/sec, we modeled the ray path and particle motion deviations from the source receiver azimuth. Unlike the Stephen anisotropy model, the particle motion deviations and ray deviations are in the same direction, so that the total deviation is greater than either part. At the ranges of the White and Whitmarsh data (4 to 10 km) we can predict maximum deviations of the ray path from the shot-receiver azimuth of 0.25 to 1.0 degree. Summing this with the maximum particle motion versus ray deviations (4 degrees) will give a slightly better fit to the data than the particle motion to ray deviations alone.

The ray path deviations from the shot-reciever azimuth are much smaller for this anisotropy model than for the Stephen anisotropy model because the group velocity has a much smaller variation with azimuth (4.88 to 5.13 km/sec for White and Whitmarsh versus 4.0 to 5.5 km/sec for Stephen). Thus, the error caused by neglecting the ray path deviation from the shot-receiver azimuth is much smaller for the White and Whitmarsh model than for the Stephen model.

One apparent limitation to P-wave polarization studies of anisotropy is that the deviation of the particle motion from the ray path can only be measured by a seismometer within the anisotropic medium. In most places in the earth (i.e. inside!) such a direct measurement will be impossible. However, the anisotropy induced deviation of the ray path from the source-receiver azimuth can be measured by receivers in an overlying isotropic layer (see Fig. 8). In this case we see that the deviation will be opposite in direction to the deviation within the anisotropic layer. Our procedure for calculating head wave ray paths in an anisotropic layer can easily be modified to account for this situation by noting the symmetry between the ray entering the anisotropic layer and the ray leaving the anisotropic layer. In this case we need not bother calculating particle motion directions, since they are not measurable in the anisotropic layer and are coincident with the ray path in the isotropic layer.

P-wave anisotropy in the upper mantle has been widely observed. We chose to model P-wave polarization anomalies that might be observable on the surface of the crust for two simple cases -- oceanic and

continental. We used a 2θ model of P-wave anisotropy with velocities varying from 8.0 to 8.6 km/sec. The exact shape of the group velocity versus azimuth curve will determine how large the ray path deviations will be, so we approached this problem in two ways.

First, as an example, we scaled the Stephen anisotropy model discussed earlier (but leaving out the 4θ part) so that it would produce the appropriate group velocity maxima and minima. This gave us values for Γ_{ijkl} ($\Gamma_{1111} = 73.96$, $\Gamma_{2222} = 64.00$, $\Gamma_{1212} = 21.716$, $\Gamma_{1122} = 23.53$, $\Gamma_{1313} = 13.57$ km^2 sec^{-2}) which we could directly use to calculate ray paths. Second, we approximated the group velocity function as

$$U^2 = 68.98 + 4.98\cos 2\theta$$

following Backus (1965) and again not including 4θ terms. Using this function for the group velocity we used an iterative procedure to find the least time ray path between source and receiver.

Fig. 9 shows a comparison between the group velocity function determined by the exact model and the approximation. The curves are slightly different and thus we should not expect identical results for our calculated polarization anomalies.

Fig. 10a shows the polarization anomalies expected for a typical continental situation with source and receiver atop a 30 km thick layer of 6 km/sec crust. The anomalies are range dependent with larger anomalies at longer ranges. Note that this range dependence is opposite to that predicted for ray path deviations within the anisotropic halfspace. The anomalies range from 1.5 degrees at 100 km to 3.5 degrees at 500 km. The angular deviation is away from the fast direction of anisotropy, again opposite to the ray path deviations within the anisotropic medium, which are toward the fast direction. Note also that the least time algorithm gives nearly the same result as the exact calculation based on the Stephen type model. This is encouraging since the methods used to calculate the anomalies were completely different.

Fig. 10b shows the polarization anomalies expected for a typical oceanic situation, with 6 km of 1.5 km/sec water above 6 km of 6 km/sec crust above an anisotropic upper mantle. The source is assumed to be on the surface of the water; the receiver on the surface of the crust. The polarization anomalies range from 2 degrees at 30 km to 3.8 degrees at 240 km. As we saw in the continental example, the two methods used to compute the anomalies give nearly the same answer.

Thus we see that upper mantle P-wave anisotropy should cause small, but perhaps still observable, P-wave polarization anomalies on the surface of the crust. The amount of the polarization is a function of the range, crustal thickness and velocity, as well as the magnitude of the

upper mantle anisotropy.

If we model the earth as a series of flat, homogeneous (but possibly anisotropic) layers, we see that an observation of a polarization anomaly on the surface does not necessarily indicate anisotropy in the surface layer, but simply that anisotropy must be present in at least one of the layers through which the ray passes. Since travel time variations and shear wave splitting also do not require surface anisotropy, the data presented by Stephen (1981) and by White and Whitmarsh (in press) do not directly require anisotropy within a surface layer.

In many cases the ray path deviation from the source-receiver azimuth will be greater in an overlying isotropic layer than it will be in the underlying anisotropic layer. For example, if we add a 1 km thick, 3 km/sec isotropic layer to the top of the crust in the Stephen model discussed earlier, we would generate the polarization anomalies shown in Fig. 11. These anomalies range from 5 degrees at 5 km to 14 degrees at 12 km. They are all at angles bending away from the fast direction of anisotropy.

In such a model, other evidence for anisotropy, such as travel time dependence upon azimuth and S-wave splitting would still be present. We do not mean to suggest that this model is the correct one, but only that models of this type should be considered. Large polarization anomalies (10 to 20 degrees) can be fit with models involving an isotropic layer above an anisotropic half-space with less anisotropy than would be necessary to generate the polarization anomalies with the anisotropic half-space alone. However, as in other ray theoretical approaches to seismic problems, we must be careful not to exceed the limits of the ray approach; our resolution will always be limited by the wavelengths involved. For example, it is clearly incorrect to generate huge polarization anomalies by adding a 10 m thick surface isotropic layer to our models, because seismic wavelengths in seismic refraction experiments are, at best, 150 m long (20 hz at 3 km/sec).

Summary of Ray Deviation Effects

We have calculated the ray path deviation from the vertical source-receiver plane for a few simple examples involving a source on an isotropic layer above an anisotropic half-space. We found that in some cases this deviation is significant and should be taken into account when modeling polarization anomalies.

For a receiver on the anisotropic half-space the polarization anomaly will be the sum of the ray path deviation from the source-receiver azimuth and the particle motion deviation from the ray path. The ray path deviation will be in a direction toward the fast direction in the anisotropic medium, and will be range dependent, with the largest

deviations at close ranges and deviations decreasing asymptotically to zero at infinite range.

For a receiver on the isotropic layer above the anisotropic half-space, the polarization anomaly will be the deviation of the ray path from the source-receiver azimuth and will be away from the fast direction in the anisotropic medium. The ray path deviation will increase with source-receiver range and asymptotically approach a finite limit at infinite range.

The polarization anomalies in both of these cases are, of course, dependent on the source-receiver azimuth and decrease to zero at azimuths aligned with either the fast or slow axes in the anisotropic medium. The deviation of the ray path from the vertical source-receiver plane also affects travel time calculations, but this is a second order effect which can be ignored in typical seismic refraction experiments.

The Ngendei Seismic Refraction Experiment

The 1983 Ngendei expedition to the southwest Pacific (Jordan et al. 1983; Orcutt et al. 1983) was at a site (23.82°S, 165.53°W) approximately 1000 km east of the Tonga Trench and 1500 km west-southwest of Tahiti (see Fig. 12). The name is derived from Polynesian mythology -- Ngendei was the deity responsible for earthquakes and volcanos. The oceanic lithosphere is estimated to be about 140 m.y. old at the site (Menard et al. 1983), one of the oldest areas in the Pacific. The Scripps Institution of Oceanography ship R/V Melville shot 4 split refraction profiles with azimuth spacing of 45 degrees and a circular line of 10 km radius (see Fig. 13). All of the lines were recorded by at least two Scripps ocean bottom seismometers (OBSs) and two of the lines were recorded by a borehole seismometer, the Marine Seismic System (MSS). The MSS was emplaced 124 m in DSDP Hole 595B by the Glomar Challenger on DSDP Leg 91. All of the OBSs were within 500 m of this hole.

Ranges were calculated and topographic corrections applied with standard techniques (Spudich and Orcutt 1980; White and Whitmarsh, in press). All of the P-wave travel time data in this paper have been corrected for topography. Fig. 14 shows the reduced P-wave travel times for the entire OBS data set. The data are consistent with typical models of oceanic crustal velocity structure involving a steep velocity gradient in layer 2, a shallow velocity gradient in layer 3, and mantle velocities below the moho.

In an earth consisting of horizontal isotropic layers we would expect no systematic variations of travel time with azimuth. Fig. 15a shows a comparison of travel times for shots along N-S azimuths vs. shots along E-W azimuths. Although there is considerable scatter in the data, some trends are apparent. Between about 5 and 15 km, the E-W

arrivals come in before the N-S arrivals, while at ranges greater than 35 km, the N-S arrivals are first. Fig. 15b shows a similar comparison of NE-SW arrivals vs. NW-SE arrivals. In this case the NW-SE arrivals are early at ranges of about 6 to 17 km, while the NE-SW arrivals are early at ranges greater than 35 km. These differences in P-wave travel times are indicative of anisotropy at two levels in the oceanic lithosphere. We can already see that the fast direction in the upper mantle anisotropy will be about N-NE while the fast direction in the crustal anisotropy will be about N-NW.

The borehole seismometer had much lower noise levels than the OBSs. Thus, it was possible to pick P-wave arrivals out to greater ranges. Fig. 16 shows a comparison of MSS travel times for NW-SE vs. SW azimuths (the only lines the MSS recorded). At mantle ranges, the SW arrivals consistently come in ahead of the NW-SE arrivals, agreeing with the OBS data.

Fig. 17 is a closeup of the OBS arrivals at close ranges. Out to about 4 km the N-S, NE-SW arrivals are roughly coincident with the E-W, NW-SE arrivals. Between about 4 and 6 km, the E-W, NW-SE arrivals come in increasingly early, and then maintain an approximately constant offset at ranges greater than 6 km. Since the slope of the travel time curve is approximately flat at these ranges, the data can be reduced for a constant velocity in order to make a travel time vs. azimuth plot. Fig. 18 shows such a plot for travel time picks between 7 and 11 km, reduced at 6.6 km/sec. The vertical alignments in the plot represent individual refraction lines, which were shot at approximately constant azimuth. Points between these alignments represent data from the circular line. The data show considerable scatter, presumably representing lateral heterogeneities. However, some systematic azimuthal trends are apparent. Arrivals at azimuths of 0 to 45 degrees (N-NE) and 180 to 225 degrees (S-SW) are generally late, while arrivals at azimuths of 90 to 135 degrees (E-SE) and 270 to 315 degrees (W-NW) are generally early.

Backus (1965) derived an approximate expression for the velocity of P-waves traveling in a general weakly anisotropic medium

$$v^2 = a_1 + a_2\cos 2\theta + a_3\sin 2\theta + a_4\cos 4\theta + a_5\sin 4\theta$$

where v = phase or group velocity of wave
θ = azimuth of wave propagation

As previously discussed, P-wave travel times are very insensitive to anisotropic ray deviation effects; thus, travel times at a particular azimuth are directly related to seismic group velocities at the same azimuth. To first order in the anisotropy, P-wave travel times which represent waves turning at approximately equal depths can be represented by a function of the form

$$t = a_1 + a_2\cos 2\theta + a_3\sin 2\theta + a_4\cos 4\theta + a_5\sin 4\theta$$

A curve of this type was fitted in a least squares sense to the travel time data (see Fig. 18), reducing the variance of the data residuals (vs. residuals from the mean) by about 33%. The magnitude of the azimuthal travel time differences is about 0.05 second and the fast direction for the crustal anisotropy is N120°E.

It is difficult to assign confidence limits to a curve of this type since the leading alternative (non-anisotropic) explanation for the observed azimuthal variations is lateral heterogeneity. Because a hypothetical slow "blob" of crust will systematically affect many travel times, statistical confidence tests such as the f-test, which assume independence of the data, are not appropriate and would return unrealistically high confidence levels for the curve shown in Fig. 18. We will simply say that anisotropy seems a simpler and less contrived explanation for the gross azimuthal trends in the data than lateral heterogeneity.

As an additional check, we fit the travel time data with a Fourier series which included θ, 2θ, 3θ, 4θ, and 5θ terms. The variance reduction achieved with 2θ terms alone (32%) was far greater than for any other terms (3θ was second best with a 13% variance reduction). The dominance of the 2θ terms is an argument in favor of anisotropy, since we would not a priori expect lateral heterogeneity to be organized in a 2θ sense.

Fig. 19 shows a similar plot for P-wave arrivals at mantle ranges, reduced at 8 km/sec. Although less data are available at these ranges, the anisotropy is quite clear. The curve shown is the least squares fit for a function of the form

$$t = a_1 + a_2\cos 2\theta + a_3\sin 2\theta$$

We did not include 4θ terms, which lead to wildly oscillatory fits (this is because the data are only present at approximate 45 degree increments, which can coincide with zero crossings in the 4θ terms). The curve reduced the variance of the data residuals by about 70%. The magnitude of the travel time differences is about 0.3 second while the inferred fast direction for the anisotropy is N30°E.

The travel time data support anisotropy with a 2θ P-wave velocity dependence on azimuth at two levels in the oceanic lithosphere at the Ngendei site. The fast direction of the crustal anisotropy (N120°E) is orthogonal to the fast direction of upper mantle anisotropy (N30°E). The crustal anisotropy appears to occur at depths just above layer 3 of the oceanic crust.

Fig. 20 shows a P-wave velocity profile of the oceanic lithosphere which satisfies the travel time data. Such a model, while clearly not unique, demonstrates the features which are necessary to explain the azimuthal variations in travel times. A separate velocity profile is shown for each of two orthogonal azimuths. N30°E is approximately appropriate for the N-S and NE-SW lines, while N120°E is about right for the E-W and NW-SE lines. These azimuths were determined from the curves shown in Fig. 18 and Fig. 19. Fig. 21 shows the travel time curves for each model superimposed on the data for the associated refraction lines.

As can be seen in Fig. 20, the two velocity models are identical in the uppermost crust, with velocities increasing from 4.3 km/sec at the surface to 5.2 km/sec at 0.75 km depth. This reflects the approximate agreement at all azimuths in the travel time data at the closest ranges (see Fig. 17).

We model the crust between 0.75 km and 1.4 km with a velocity gradient also, but with a 0.4 km/sec offset between the two azimuths. The N30°E azimuth is slower, with velocities increasing from 5.4 km/sec at 0.75 km to 6.0 km/sec at 1.4 km. The N120°E azimuth is faster, with velocities increasing from 5.8 km/sec to 6.4 km/sec. The azimuthal differences in the velocity model reflect the azimuthal differences in slopes in the travel time data between about 3 and 6 km (see Fig. 17).

The models are again identical between 1.4 and 7.4 km with velocities increasing from 6.6 to 7.5 km/sec. This shallow velocity gradient represents the relatively flat part of the travel time data between about 7 and 30 km. The models again diverge at 7.4 km. The N30°E azimuth is faster with an upper mantle velocity of 8.5 km/sec. The N120°E azimuth is slower with an upper mantle velocity of 8.0 km/sec. This difference reflects the azimuthal difference in the travel times at mantle ranges.

The travel time curves based on this model (shown in Fig. 21) were calculated using a ray tracing program appropriate for an isotropic earth. In particular, it is assumed that the velocity at a given depth is not a function of ray parameter. This is not generally true within an anisotropic medium. However, for hexagonally symmetric anisotropy with a horizontal symmetry axis (which we will later claim is the most likely anisotropy model for both the crustal and upper mantle anisotropy) this type of ray tracing is approximately correct for rays near their turning points. We do not believe that using an anisotropic ray tracing program would result in significant changes to our model.

Because of scatter in the data, the depth of the crustal anisotropy is not well constrained. In particular, we cannot exclude the possibility that anisotropy is present throughout layer 2. A velocity model with a 0.2 km/sec azimuthal velocity difference throughout layer 2 fits the travel time data almost as well as the model discussed above, and

has the advantages of requiring less anisotropy and agreeing with previous observations of surface anisotropy in the oceanic crust (Stephen 1981; White and Whitmarsh 1984). However, it is not possible to fit the Ngendei travel time data without at least some anisotropy in layer 2c.

The gross shape of this velocity model agrees with previous models of the oceanic crust involving a steep velocity gradient in oceanic layer 2 and a shallow velocity gradient in layer 3 (Spudich and Orcutt 1980). The non-uniqueness of inverting real travel time data is well known, and we do not wish to place undue emphasis on this particular model, which was generated subjectively without the benefits of triplication constraints, amplitude modeling, or waveform analysis. However, we do think the model is useful because it demonstrates that a very simple velocity structure can explain the travel time data. More sophisticated future models will differ from this model in detail, but presumably will share the more general characteristics.

These features include a velocity gradient in a layer 2 with anisotropy in layer 2c and possibly above, an isotropic layer corresponding to layer 3, and an anisotropic upper mantle. The upper mantle anisotropy is about 8.5 km/sec in the fast direction (N30°E) and about 8.0 km/sec in the slow direction. The absolute upper mantle anisotropic velocities are much better constrained (from the MSS data) than the crustal anisotropic velocities. The anisotropic velocity difference in the crustal layer is about 0.2 to 0.4 km/sec, with the fast direction approximately N120°E.

Ngendei Polarization Analysis

Only one of the two horizontal components of the MSS borehole seismometer was recorded, so unfortunately the MSS data are unsuitable for polarization studies. In addition, OBS Lynn and OBS Juan horizontal data are unusable. However, OBS Karen and OBS Suzy both recorded good horizontal data and all of the refraction shots were recorded by one of these two instruments. The OBS Pn arrivals are too weak for polarization analysis, so we will restrict our attention to the OBS crustal P-wave arrivals.

In order to obtain an idea of the size of the P-wave polarization anomalies that might occur at the Ngendei site, we simplified our crustal anisotropy model and considered a 0.75 km thick, 4.8 km/sec isotropic layer above a 5.7 to 6.1 km/sec anisotropic layer. We modeled the anisotropy as hexagonally symmetric with a 2Θ azimuthal dependence ($\Gamma_{1111} = 37.21$, $\Gamma_{2222} = 32.49$, $\Gamma_{1212} = 10.97$, $\Gamma_{1122} = 12.91$, $\Gamma_{1313} = 6.86$ km^2 sec^{-2}). Fig. 22 shows the resulting P-wave polarization anomalies for a receiver on the isotropic layer at ranges of 4 to 7 km (these ranges are not corrected to the sea floor). The polarization anomalies are purely a result of the ray path deviations discussed

earlier and increase with range from the source. The maximum expected polarization anomaly at these ranges is about 2 degrees. We did not calculate polarization anomalies at ranges greater than 7 km because the initial P-wave arrivals at longer ranges represent rays turning beneath our anisotropic layer. These arrivals will also exhibit polarization anomalies, but a more sophisticated ray tracing program is needed to calculate them.

In order to compute P-wave polarization anomalies for the Ngendei OBS data we need to know the shot azimuth from the OBS, the absolute orientation of the OBS horizontal components, and the particle motion direction recorded by the OBS. The shot azimuths are the most easily computed. The Challenger drill ship provided a fixed reference point to which sightings were made from the shooting ship. Since the OBS location was known relative to the Challenger, these sightings, together with the OBS to shot ranges, allow the direct calculation of the OBS to shot azimuths. This approach is identical to the azimuth estimations used for the travel time analysis and we estimate the uncertainty in the shot azimuths to be ± 2 degrees.

No direct measurement of the azimuths of the OBS horizontal components is possible since the OBS settles to the bottom at a random orientation. However, the orientation can be estimated from polarization analysis of the direct water waves recorded by the OBS. Since sound speed in the ocean is usually assumed to vary only in the vertical direction, the particle motion direction of the direct water wave at the OBS will be aligned with the shot azimuth. Thus, knowing the shot azimuth and the water wave polarization relative to the OBS horizontal components, we can calculate the absolute OBS horizontal orientation.

We used a method of polarization analysis from Kanasewich (1973) in which we form the covariance matrix between the horizontal channels. We assume that this matrix can be modeled as the sum of a directional signal and incoherent noise, and thus has the form

$$\begin{bmatrix} s^2\cos^2\theta + n^2 & s^2\sin\theta\cos\theta \\ s^2\sin\theta\cos\theta & s^2\sin^2\theta + n^2 \end{bmatrix}$$

where θ = angle from OBS channel 2 to shot azimuth
s = amplitude of signal
n = amplitude of noise

This matrix has eigenvalues

$$\omega_1 = s^2 + n^2$$

$$\omega_2 = n^2$$

and eigenvectors

$$(\cos\theta,\ \sin\theta)^T$$

$$(-\sin\theta,\ \cos\theta)^T$$

We may also define a "rectilinearity" function

$$F(\omega_1,\omega_2) = 1 - \frac{\omega_2}{\omega_1}$$

which provides a measure of the degree of directionality of the signal. F varies between 0 and 1 with the endpoints respectively representing random noise and complete directionality.

In our water wave polarization analysis of the Ngendei OBS data, we windowed the horizontal time series for 0.1 second after the initial water wave arrival. Many of the water wave arrivals were clipped and thus could not be used; however, the unclipped arrivals typically were very directional. Fig. 23 shows the estimated channel 2 orientations for OBS Suzy and OBS Karen, based on unclipped water wave polarizations with $F \geq 0.95$.

The 182 water wave polarizations from OBS Karen (Fig. 23a) show considerable scatter, but there appear to be systematic variations of polarization direction as a function of shot azimuth. In P-wave polarization data, such variations might lead to hypotheses of anisotropy. However, in the case of water wave data, it is clear that there must be errors in either the calculated shot azimuths or the OBS horizontal response.

One possibility is that the horizontal gains of the OBS are slightly miscalibrated. This can lead to an apparent 2θ dependence in polarization anomalies (White and Whitmarsh, in press). In such a case we can express the relationship between the true channel 2 azimuth and the apparent channel 2 azimuth as

$$\tan(\phi' - \theta) = k\tan(\phi - \theta)$$

where θ = shot azimuth
ϕ = channel 2 orientation
ϕ' = apparent channel 2 orientation
k = (channel 3 amplitude) / (channel 2 amplitude) for equal inputs

We solved for the unknowns k and ϕ using a non-linear least squares procedure. The curve shown in Fig. 23a is the best fit for the OBS

Karen water wave data (ϕ = 130.5 degrees, k = 1.10) -- it reduces the variance of the data residuals (vs. residuals from the mean) by about 30%. However, systematic variations of a few degrees remain which are not explained by the differences in the horizontal gains.

These variations are also apparent in the 97 water wave polarizations from OBS Suzy (Fig. 23b). Since these polarization data are only available at shot azimuths separated by 180 degrees, we were unable to constrain the ratio of the horizontal gains. The mean channel 2 azimuth is 173.6 degrees, but there exists a slight difference between the polarizations at shot azimuths of 90 and 270 degrees.

The systematic polarization differences with shot azimuth for both OBS Suzy and OBS Karen are disturbing, since, ultimately, we want to use P-wave polarization data to look for anisotropic polarization anomalies. As we have seen, these anomalies are usually quite small -- on the order of a few degrees. The water wave arrivals provide a null test of our ability to detect P-wave polarization anomalies, because direct water wave arrivals should not produce polarization anomalies. Since we do not have data in common between OBS Suzy and OBS Karen, we cannot determine if the polarization differences that we observe are the result of inaccurate shot azimuths or variations in the OBS horizontal response.

The OBS P-wave arrivals were less directional than the water wave arrivals. We used the covariance matrix technique discussed earlier to determine polarizations for the first 0.2 second of the P-wave arrival, including only those polarization directions with a F value greater than 0.80. We then calculated polarization anomalies based on the shot azimuths, channel 2 orientations, and the ratio of horizontal gains (we assumed k = 1.0 for OBS Suzy). These anomalies did not exhibit significant range dependence -- anomalies for ranges between 1 and 12 km (ranges corrected to sea floor) are shown in Fig. 24. The polarization anomalies are very scattered, with variations of roughly $\pm$30 degrees.

The OBS Karen polarization anomalies appear randomly scattered while those from OBS Suzy have an apparent $\sin\theta$ azimuthal dependence. White and Whitmarsh (in press) noted a strong $\sin\theta$ term in their polarization data, which they ascribed to tilted horizontal seismometer components and/or dipping structures beneath the OBS. In our example, the lack of a similar variation in the OBS Karen data argues for the former explanation. The problem is complicated by the apparent difference between the OBS response to the direct water waves and the response to the P-waves. In addition, lateral heterogeneities in the crust can cause ray path deviations that will contribute scatter to the polarization data.

In any case, it is clear that anisotropic P-wave polarization anomalies of the magnitude predicted by the travel time data (about 2 degrees) will be very difficult to observe with Ngendei OBS polarization

data. We are studying this problem further to see what, if anything, can be learned about OBS response from P-wave and water wave polarization data but we are not optimistic about use of OBS P-wave polarization data for observing anisotropy.

Interpretation of Ngendei Anisotropy

Magnetic and bathymetric data at the Ngendei site are currently insufficient to determine the original spreading direction (Menard, personal communication). Previous studies of Pacific upper mantle anisotropy have found that the fast direction in the upper mantle is parallel to the original spreading direction (see for example Raitt et al. 1969). Assuming that this is true at the Ngendei site, then the inferred fossil spreading direction is N30°E (of course with a 180 degree ambiguity). The fast direction in the crustal anisotropy is then perpendicular to this spreading direction.

Upper mantle anisotropy is usually explained by aligned olivine crystals (see, for example, Christensen 1984) which cause hexagonally symmetric anisotropy with a horizontal symmetry axis. Our observed upper mantle anisotropy (8.0 to 8.5 km/sec with a 2θ azimuthal dependence) is consistent with previous observations and undoubtedly results from the same cause.

The interpretation of our observed crustal anisotropy is not so straightforward. To our knowledge, while anisotropy has been hypothesized at the surface of the oceanic crust (Stephen 1981; White and Whitmarsh, in press) and in layer 3 (Christensen 1972; Christensen and Salisbury 1975) this is the first observation of layer 2c anisotropy.

Ophiolite models of the oceanic crust as well as recent drilling results (Anderson et al. 1982) indicate that layer 2c is composed of a sheeting dike complex. The dikes are approximately vertical and oriented normal to the original spreading direction. Individual dikes are typically 0.5 to 2 m thick with a single chilled margin which is fine grained and glassy compared to the central part of the dikes. Laboratory velocity measurements of oriented cores 1.2 to 2.5 cm in diameter from ophiolite sheeted dike complexes have not indicated any velocity anisotropy (Salisbury and Christensen 1978; Christensen and Smewing 1981).

We wish to explain our observed layer 2c anisotropy in terms of a physical model based on what is known about the oceanic crust. For simplicity of calculation we model the anisotropic crustal layer as a homogeneous section in which the P-wave velocity varys with azimuth from 5.7 to 6.1 km/sec. Thus we seek to explain an anisotropic velocity variation of 5.9 ± 0.2 km/sec (about a 7% total difference) in which the fast

direction is parallel to the sheeted dikes in layer 2c. Clearly these figures are approximate but anisotropy of roughly this magnitude will be necessary to fit the travel time data. One possible source for anisotropy is preferred crystal orientation in a material. However, if this was present in oceanic sheeted dikes, it seems probable that it would be observable in ophiolites. The lack of observed crystal alignments or velocity anisotropy in samples from ophiolite sheeted dikes (Salisbury and Christensen 1978; Christensen and Smewing 1981) suggests that preferred crystal orientation is not responsible for our observed layer 2c anisotropy.

Another possible type of anisotropy is thin alternating layers of isotropic material of different velocities. At wavelengths long compared to the layer spacing, this results in effective anisotropy with an axis of hexagonal symmetry perpendicular to the layers. This is called periodic thin-layered (PTL) anisotropy and relationships between layer parameters and the effective anisotropic elastics constants have been theoretically derived (see, for example, Backus 1962) and experimentally tested (Melia and Carlson 1984). If the isotropic layers are vertical, then P-waves travelling within a horizontal plane will typically exhibit a 2θ azimuthal velocity dependence, with the fast direction parallel to the layers.

Since our observed anisotropy is 2θ dependent with the fast direction parallel to the sheeted dikes within layer 2c, PTL anisotropy would seem to be a good candidate to explain our observations. Certainly the dikes are much thinner than typical wavelengths in seismic refraction experiments. The difficulty with this explanation is that although the observed anisotropy and that predicted from modeling a sheeted dike complex agree very well in phase, they don't agree in amplitude. With PTL anisotropy, very large velocity differences in the isotropic velocities between layers are necessary to generate even small azimuthal velocity variations at large wavelengths. Realistic models of oceanic sheeted dike complexes do not include such large velocity variations.

For example, we might generously assume that chilled dike margins impose 10% of the volume of the sheeted dikes, and have a P-wave velocity 0.3 km/sec slower than the central part of the dikes (Salisbury, personal communication). Modeling the sheeted dike complex as alternating layers of 1 unit thick, 5.7 km/sec chilled margin material and 9 unit thick, 6.0 km/sec central dike material, and assuming a Poisson's ratio of 0.29 (P-wave result is very insensitive to choice of Poisson's ratio) we calculate an anisotropic P-wave velocity variation of 5.970 to 5.968 km/sec, or about 0.03%. This is over 200 times smaller than the 7% velocity anisotropy that we are trying to explain. Clearly, velocity variations related to chilled dike margins do not contribute significantly to anisotropy.

PTL anisotropy is largest when the alternating layers have equal thickness (Backus 1962); thus, we can generate more anisotropy than in the chilled margin example if we consider the possibility of velocity differences between individual dikes of equal thickness. Velocity measurements of sheeted dike complexes in ophiolites typically show scatter of about 0.2 km/sec. If we assume that these variations are largely the result of velocity differences between dikes, and create a model of a sheeted dike complex consisting of alternating layers of 5.7 km/sec and 6.1 km/sec material, we calculate anisotropic P-wave velocity variations of 5.901 to 5.890 km/sec. This velocity anisotropy of about 0.19% is over 35 times smaller than our observed 7% anisotropy. Clearly, isotropic velocity variations within the sheeted dike complex itself are inadequate to account for the observed anisotropy.

Another possibility is PTL anisotropy in a transition zone between layers 2b and 2c. In this region individual dikes might intrude into the lower velocity overlying basalt. This could provide a greater velocity difference between layers than the previous examples. If we assume that this transition zone consists of alternating vertical layers of 4.7 km/sec and 5.9 km/sec material, we could generate P-wave anisotropy of 5.20 to 5.31 km/sec (about 2%). This is still too small to explain our observed 7% anisotropy. Further, this transition zone would be restricted to the top of layer 2c and would be relatively thin. A borehole section into layer 2c near the Costa Rica Rift indicated a transition zone of about 200 m thickness (Anderson et al. 1982). Thus, anisotropy within the transition zone alone would need to be much greater than the 7% anisotropy previously discussed (based on modeling anisotropy throughout layer 2c) in order to explain the offset in the travel times.

Thus, we must conclude that PTL anisotropy is not a viable explanation for our observed layer 2c anisotropy. The probable velocity contrasts between layers within the sheeted dike complex are simply too small to generate anisotropy of the required magnitude.

Another possible cause for anisotropy is preferred crack orientation, which some authors (Stephen 1981; White and Whitmarsh, in press) have suggested is responsible for generating marine crustal anisotropy. Randomly placed cracks of similar orientation can generate hexagonally symmetric anisotropy in an otherwise isotropic medium. Large porosities are not required to generate substantial anisotropy. Anderson et al. (1974) studied oriented, disc shaped, ellipsoidal, fluid filled zones within an isotropic matrix, and, using a method developed by Eshelby (1957), calculated anisotropic seismic velocities as a function of the velocities and porosity of the matrix, the parameters of the ellipsoids, and the bulk modulus of the fluid. These calculations indicated substantial P-wave anisotropy even for porosities as low as 1%.

For example, granite containing aligned ellipsoidal cracks (aspect ratio of 20) filled with sea water (bulk modulus of 20 kbar) with a

crack density corresponding to 1% porosity will have a P-wave velocity anisotropy of 5.85 to 6.50 km/sec, or about 10% (Fig. 1, Anderson et al. 1974). The velocities have a 2θ dependence upon direction with the slow direction along the symmetry axis of the ellipsoidal disks. If the cracks are dry, the amplitude of the anisotropy is slightly greater. Porosities within layer 2c have been measured at 1 to 3% with very little fracture porosity (Becker et al. 1982). These porosities, although quite low, do not exclude the possibility of crack anisotropy of this type.

Garbin and Knopoff (1973, 1975) examined the case of oriented circular cracks of effectively zero thickness. This can be considered as the limit of the Anderson et al. calculations for ellipsoids of infinite aspect ratio. Anisotropy based on cracks of this type does not require any porosity at all in the host matrix. Garbin and Knopoff considered two different boundary conditions at the cracks. In one, corresponding to the fluid filled case, they assumed that the normal compressional component of stress is continuous and the normal shear component of stress vanishes at the crack boundary. In the other, corresponding to the dry crack case, all components of the normal stress vanish at the boundary.

Crampin (1978) used the Garbin and Knopoff results to calculate seismic velocities as a function of direction for materials with various crack densities. Again, P-wave velocity anisotropy can be substantial. For example, an isotropic matrix with P-wave velocity of 5.8 km/sec and a crack density $\varepsilon = 0.1$ ($\varepsilon = Na^3/V$, number N of cracks of radius a in volume V) will have P-wave velocities varying from about 4.6 to 5.8 km/sec for dry cracks and from about 5.6 to 5.8 km/sec for saturated cracks (Fig. 1a, 2a, Crampin 1978). For the dry crack example, the P-wave velocities are 2θ dependent with fast directions aligned with the cracks and the slow direction normal to the cracks. For saturated cracks the velocities are 4θ dependent with fast directions both normal to and aligned with the cracks, and slow directions at 45 degrees to the crack normal.

This 4θ velocity dependence seems surprising, at least to the authors, but is a necessary consequence of the Garbin and Knopoff boundary conditions for saturated cracks of effectively zero thickness. Since normal stresses and displacements are continuous across the liquid filled cracks, the cracks can only make their presense felt when there is shear across them. Compressional waves traveling both orthogonal and parallel to the cracks will not generate any shear stress across the cracks and will be unaffected by them. This is why the P-wave velocities are identical for these waves. However, P-waves traveling at angles between 0 and 90 degrees from the crack normal will generate shear across the cracks and will be slowed down. These unusual boundary conditions give rise to the 4θ velocity dependence with velocity maxima both normal to and aligned with the cracks.

Our observed layer 2c P-wave anisotropy has a 2θ velocity dependence, so we can eliminate the possibility of saturated cracks of the Garbin and Knopoff type. It seems probable that any cracks in layer 2c will be wet. This conclusion is supported by the good agreement of in situ porosity measurements in layer 2c from DSDP Hole 504B and the shipboard measurements of porosity (Becker et al. 1982). The in situ measurements are based on electrical resistivity within the rock and assume a sea water pore fluid, while the shipboard observations directly measure the fluid content of the rock. These measurements do not exclude the possibility of additional dry porosity, but the measured porosity must be wet. Assuming that all the porosity is fluid filled, we can eliminate the dry crack models from further consideration.

The Anderson et al. (1974) model of fluid filled cracks is the most reasonable model which can explain our observed crustal anisotropy. It requires the presence of cracks throughout layer 2c, oriented parallel to the sheeted dikes. Such cracks could have formed from tensional stress associated with the initial cooling of the dikes. The lack of observable anisotropy in oriented cores from ophiolite sheeted dikes indicates that these cracks may be cemented during ophiolite emplacement, or that they may be on too large a scale to affect velocities within a small core sample.

As discussed earlier, the Ngendei crustal anisotropy may extend throughout layer 2. In this case, aligned cracks remain the most likely cause for the anisotropy, provided that they also are present throughout layer 2. Some evidence that aligned cracks are present at the surface of the oceanic crust is available from direct observations of the sea floor (Stephen 1981), although it is difficult to prove that they are of sufficient density to cause seismic anisotropy. In the 140 m.y. old crust at the Ngendei site such surface cracks might have become cemented.

Observing Anisotropy with Seismic Refraction Experiments

We have discussed two ways in which P-wave anisotropy might be observed in typical seismic refraction experiments. These methods involve the measurement of azimuthal differences in travel times and P-wave polarization anomalies. In most situations, we believe that travel time analysis provides a more robust, less ambiguous, and more convenient way of measuring anisotropy than P-wave polarization analysis.

Seismic ray paths can be perturbed both by anisotropy and by lateral heterogeneities. To first order, P-wave travel times are insensitive to these ray path perturbations, but P-wave polarization anomalies are directly affected. Travel times can be measured with a single seismometer, while polarization measurements require either a small array of seismometers or horizontal components. In practice, this

has limited marine polarization measurements to the sea floor, using either an OBS or borehole seismometer. In these circumstances, orienting the horizontal channels and calibrating gains is difficult. While approximate horizontal orientation and calibration can be derived from direct water wave arrivals at an OBS, no such procedure is available for borehole seismometers. This is a significant problem, since even a small difference in gain between the horizontal channels will lead to large apparent 2θ polarization anomalies. OBS polarization observations also suffer from unknown effects of OBS to sea floor coupling, which can lead to strange results in horizontal observations (Shearer and Orcutt 1982; Sutton et al. 1984). Taking all this into consideration, it is not surprising that the Ngendei P-wave polarization observations were unable to confirm the crustal anisotropy which was clearly resolved in the travel time data. We believe that this will generally be true -- seismic travel times will measure anisotropy more clearly than P-wave polarization analysis. However, we do not mean to condemn all of polarization analysis, since shear wave splitting is an important indicator of anisotropy.

Adequate azimuthal coverage is very important for both travel time and polarization analysis. At a minimum, data should be available at increments of 45 degrees (even closer if 4θ anisotropy is suspected) and lines should be reversed in order to minimize the effects of dipping structures. For example, the 2θ dependent, 4.0 to 5.5 km/sec anisotropy hypothesized by Stephen (1981) for the upper oceanic crust should easily be observable in seismic travel times. Unfortunately, the two orthogonal lines which were shot at this site are 45 degrees from the symmetry axis of the anisotropy, and thus cannot help constrain the magnitude of the anisotropy (each line indicated surface P-wave velocities of 5.0 ± 0.25 km/sec). Closer azimuthal spacing of refraction lines would eliminate problems of this type.

Summary

Observations of anisotropy are becoming increasingly important in seismology because of the directional information that they provide. Deep anisotropy is probably related to processes of mantle convection, while shallow anisotropy likely results from surface tectonics. Oceanic observations are particularly significant because they can be directly compared with plate tectonics models.

The 1983 Ngendei expedition to the South Pacific detected anisotropy both in the upper mantle and within an upper crustal layer. The upper mantle anisotropy agrees with previous observations and suggests that the original spreading direction at the Ngendei site was N30°E. The crustal anisotropy appears to be within layer 2c and possibly above, and is most likely caused by oriented cracks.

These observations are based on P-wave travel time analysis, which can be used directly to measure anisotropy. P-wave polarization analysis has the potential to detect anisotropy, but care should be used in interpreting polarization anomalies. Anisotropic ray path deviations contribute significantly to polarization anomalies within anisotropic media, and can also cause polarization anomalies on overlying isotropic media. Polarization anomalies are typically range dependent, and the nature of this range dependence can provide constraints on the depth and magnitude of anisotropy.

Acknowledgements

This research was supported by DARPA contract AFOSR-84-0043. The authors thank the officers and crew of the R/V Melville and D/V Glomar Challenger for making the Ngendei experiment possible and also thank Stuart Crampin, Ralph Stephen, Bob White, and Bob Whitmarsh for their helpful comments and reviews. We also wish to acknowledge the splendid performance of the MSS which had been developed by the Naval Oceanographic Research and Development Agency (NORDA) and the excellent work of the ocean bottom seismometer crew (Bob Moore, Dave Willoughby, Dave Weeks) at Scripps. Tom Jordan provided valuable advice in this work and shot many of the explosives while Judy Lancaster, through her tireless assistance, made the logistical problems more bearable.

References

Aki, K. and Richards, P., 1980. Quantitative seismology, theory and methods, W. H. Freeman.

Anderson, R.N., Honnorez, J., Becker, K., Adamson, A.C., Alt, J.C., Emmermann, R., Kempton, P.D., Kinoshita, H., Laverne, C., Mottl, M.J. and Newmark, R.L., 1982. DSDP Hole 504B, the first reference section over 1 km through Layer 2 of the oceanic crust, Nature, 300, 589-594.

Anderson, D.L., Minster, B. and Cole, D., 1974. The effect of oriented cracks on seismic velocities, J. geophys. Res., 79, 4011-4015.

Backus, G.E., 1962. Long-wave elastic anisotropy produced by horizontal layering, J. geophys. Res., 67, 4427-4440.

Backus, G.E., 1965. Possible forms of seismic anisotropy of the uppermost mantle under oceans, J. geophys. Res., 70, 3429-3439.

Bamford, D., 1977. Pn velocity anisotropy in a continental upper mantle, Geophys. J. R. astr. Soc., 49, 29-48.

Bamford, D., Jentsch, M. and Prodehl, C., 1979. Pn anisotropy studies in northern Britain, and in the eastern and western United States, Geophys. J. R. astr. Soc., 57, 397-429.

Becker, K., Von Herzen, R.P., Francis, T.J.G., Anderson, R.N., Honnorez, J., Adamson, A.C., Alt, J.C., Emmermann, R., Kempton, P.D., Kinoshita, H., Laverne, C., Mottl, M.J. and Newark, R.L, 1982. In situ electrical resistivity and bulk porosity of the oceanic crust Costa Rica Rift, Nature, 300, 594-598.

Christensen, N.I., 1972. Seismic anisotropy in the lower oceanic crust, Nature, 237, 450-451.

Christensen, N.I., 1984. The magnitude, symmetry and origin of upper mantle anisotropy based on fabric analysis of ultramafic tectonites, Geophys. J. R. astr. Soc., 76, 89-111.

Christensen, N.I. and Salisbury, M.H., 1975. Structure and constitution of the lower oceanic crust, R. Geophy. Space Phys., 13, 57-86.

Christensen, N.I. and Smewing, J.D., 1981. Geology and seismic structure of the northern section of the Oman Ophiolite, J. geophys. Res., 86, 2545-2555.

Crampin, S., 1978. Seismic-wave propagation through a cracked solid: polarization as a possible dilatancy diagnostic, Geophys. J. R. astr. Soc., 53, 467-496.

Crampin, S., 1981. A review of wave motion in anisotropic and cracked elastic-media, Wave Motion , 3, 343-391.

Crampin, S., 1982. Comments on 'possible forms of anisotropy of the uppermost mantle under oceans' by George E. Backus, J. geophys. Res., 87, 4636-4640.

Crampin, S., Stephen, R.A. and McGonigle, R., 1982. The polarization of P-waves in anisotropic media, Geophys. J. R. astr. Soc., 68, 477-485.

Eshelby, J.D., 1957. The determination of the elastic field of an ellipsoidal inclusion and related problems, Proc. Roy. Soc. Ser. A, 241, 376-396.

Garbin, H.D. and Knopoff, L., 1973. The compressional modulus of a material permeated by a random distribution of circular cracks, Q. appl. Math., 30, 453-464.

Garbin, H.D. and Knopoff, L., 1975. The shear modulus of a material permeated by a random distribution of circular cracks, Q. appl. Math., 33, 296-300.

Garbin, H.D. and Knopoff, L., 1975. Elastic moduli of a medium with liquid filled cracks, Q. appl. Math., 33, 301-303.

Jordan, T.H., Orcutt, J.A., Menard, H.W. and Natland, J., 1983. Ngendei seismic experiment: teleseismic and noise studies, EOS, 64, 269.

Kanasewich, E.R., 1973. Time series analysis in geophysics, University of Alberta Press, pp 364.

Melia, P.J. and Carlson, R.L., 1984. An experimental test of P-wave anisotropy in stratified media, Geophysics, 49, 374-378.

Menard, H.W., Jordan, T.H., Natland, J.H. and Orcutt, J.A., 1983. Tectonic evolution of the southwestern tropical Pacific basin, EOS, 64, 315.

Orcutt, J.A., Jordan, T.H., Menard, H.W. and J. Natland, 1983. Ngendei seismic experiment: refraction and reflection studies, EOS, 64,

269.

Pallister, J.S., 1981. Structure of the sheeted dike complex of the Samail Ophiolite near Ibra, Oman, J. geophys. Res., 86, 2661-2672.

Raitt, R.W., Shor, G.G., Francis, T.J.G. and Morris, G.B., 1969. Anisotropy of the Pacific upper mantle, J. geophys. Res., 74, 3095-3109.

Salisbury, M.H. and Christensen, N.I., 1978. The seismic velocity structure of a traverse through the Bay of Islands Ophiolite complex, Newfoundland, an exposure of oceanic crust and upper mantle, J. geophys. Res., 83, 805-817.

Shearer, P. and Orcutt, J., 1982. Use of horizontal component data from ocean bottom seismographs, EOS, 63, 1025.

Spudich, P. and Orcutt, J., 1980. A new look at the seismic velocity structure of the oceanic crust, Rev. Geophys. Space Phys., 18, 627-645.

Spudich, P. and Orcutt, J., 1980. Petrology and porosity of an oceanic crustal site: Results from wave form modeling of seismic refraction data, J. geophys. Res., 85, 1409-1433.

Stephen, R., 1981. Seismic anisotropy observed in upper oceanic crust, Geophys. Res. Lett., 8, 865-868.

Sutton, G.H., Duennebier, F.K., Iwatake, B., Tuthill, J.D., Lewis, B.T.R. and J. Ewing, 1984. An overview and general results of the Lopez Island Experiment, Mar. geophys. Res., 5, 3-34.

White, R.S. and R.B. Whitmarsh, in press. An investigation of seismic anisotropy due to cracks in the upper oceanic crust at 45N, Mid-Atlantic Ridge, Geophys. J. R. astr. Soc., in press.

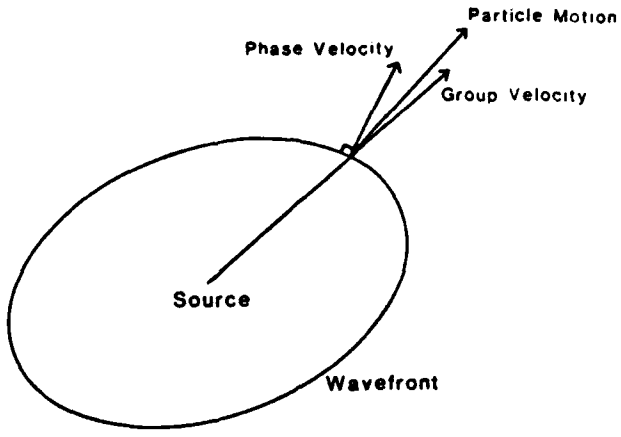


Figure 1. Wavefront from point source in a homogeneous, anisotropic medium. At a point on the wavefront, the group velocity vector, phase velocity vector, and particle motion vector all point in different directions.

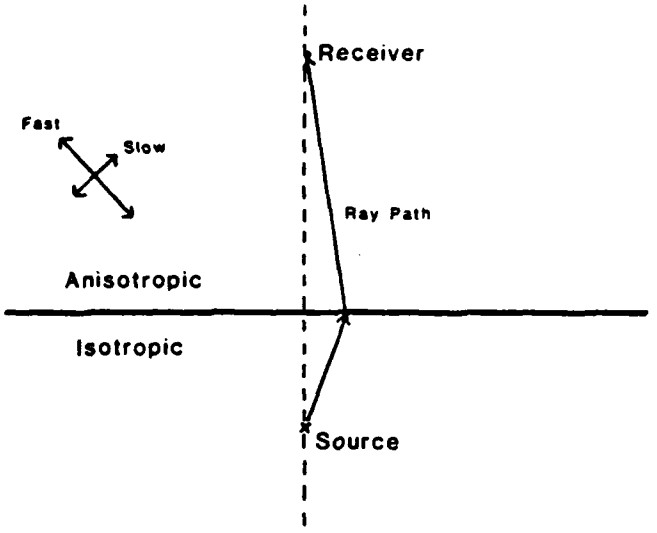


Figure 2. Ray-path between a source in an isotropic medium and a receiver in an anisotropic medium. Both source and receiver are along a line perpendicular to the interface. The ray-path skews to the side, so that the ray-path within the anisotropic medium is rotated towards the fast direction.

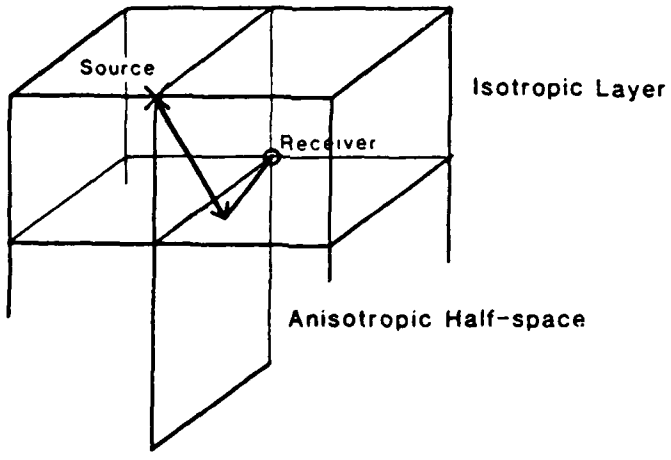


Figure 3. Ray-path for a head-wave travelling on an anisotropic half-space generated by a point source in an overlying isotropic layer. The ray-path skews to the side, out of the vertical plane connecting source and receiver. The azimuth of the ray at the receiver will differ from the source–receiver azimuth.

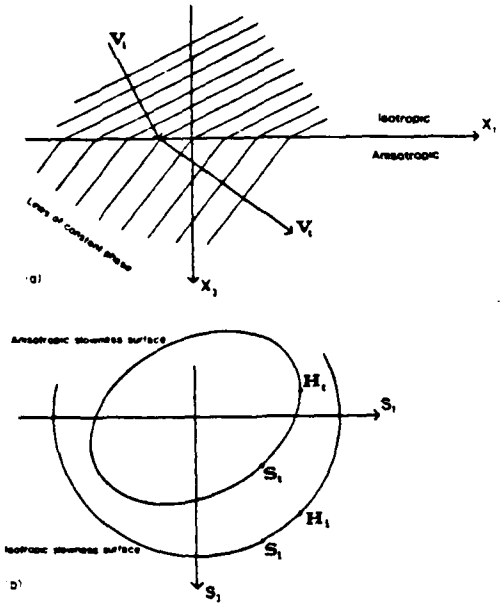


Figure 4. (a) Plane *P*-wave striking an interface between an isotropic layer and an anisotropic layer. Vectors V_i and V_t do not represent rays, but are phase velocity vectors. (b) Slowness surface representation for *P*-waves of the isotropic and anisotropic layers. The outer, spherical slowness surface represents the isotropic layer. The inner slowness surface represents the anisotropic layer. Notice that in this example the anisotropic medium has smaller slowness in every direction, or in other words, is faster in every direction. S_i represents the downgoing incident *P*-wave. S_t represents the downgoing transmitted *P*-wave. The horizontal slowness s_1 is conserved. The head-wave which would propagate in the s_1 direction is given by H_t. H_i corresponds to the incident wave which would generate the head-wave.

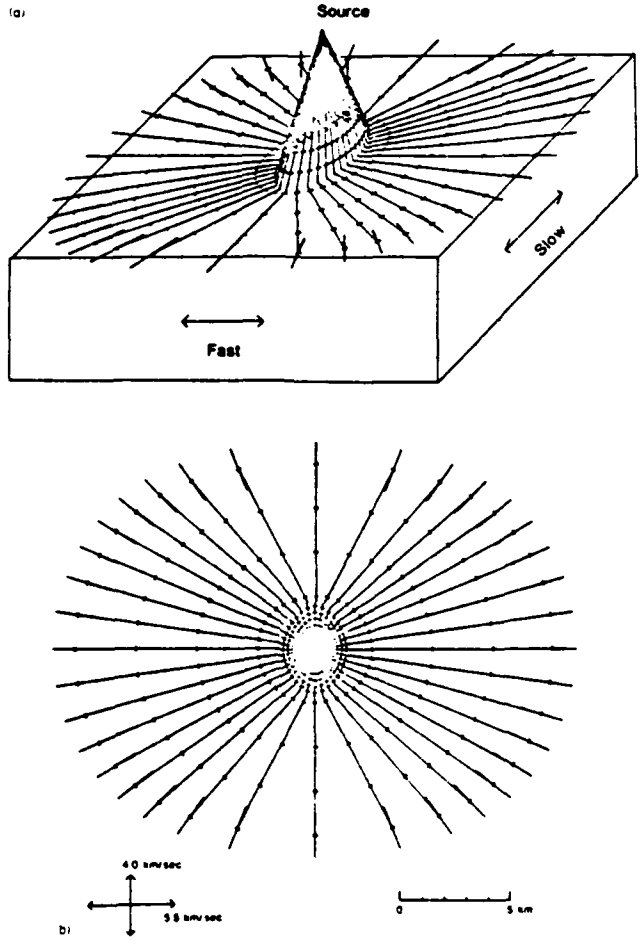


Figure 5. (a) Schematic representation of ray-paths for the Stephen anisotropy model. Near vertical lines leaving the source correspond to ray-paths within the ocean. Horizontal lines correspond to head-wave ray-paths on the surface of the anisotropic half-space. The rays shown are at increments of 10° in azimuth leaving the source. Tic marks on the rays occur at intervals of 0.5 s. Black lines at the end of the rays represent particle motion directions for each ray-path shown in the anisotropic half-space. (b) Map view of (a) as seen from a point directly above the source. Ray-paths turn toward the fast direction in the anisotropic half-space.

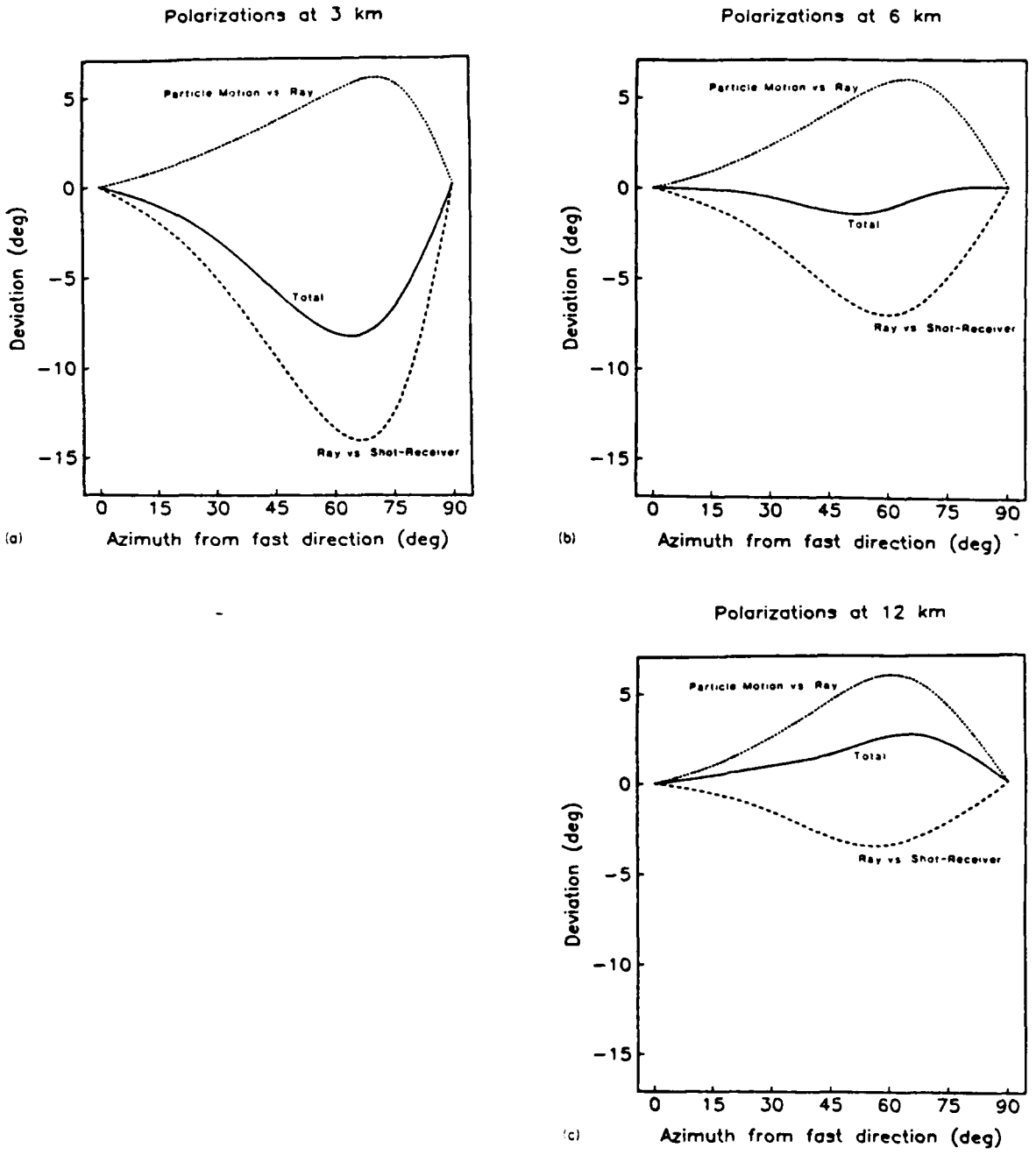


Figure 6. Polarization anomalies for the Stephen model at shot receiver ranges of (a) 3 km, (b) 6 km and (c) 12 km. These show the ray deviation from the shot–receiver azimuth, the particle motion deviation from the ray, and the total (observable) deviation – the particle motion deviation from the shot–receiver azimuth. Positive deviations represent deviations away from the fast direction in the anisotropic half-space.

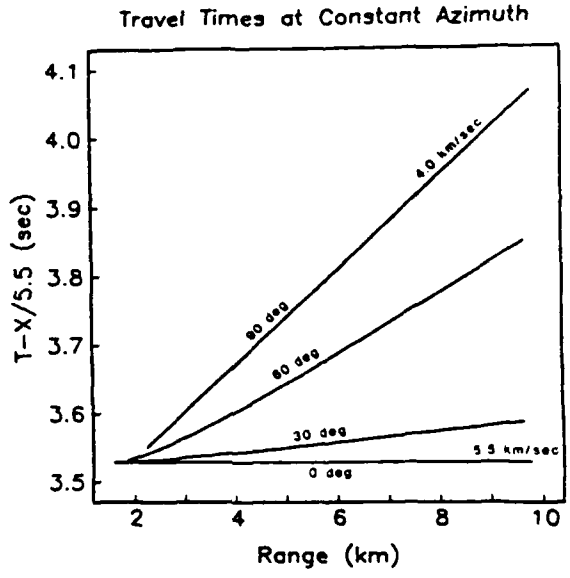


Figure 7. Travel-time curves for the Stephen anisotropy model along lines at various angles from the fast direction in the anisotropy. Curves start at the closest range at which head waves are generated. Travel times have been reduced at 5.5 km s^{-1}, the velocity of the fast direction in the anisotropic medium. Travel-time curves at azimuths of 30 and 60° are slightly curved, while travel-time curves at 0 and 90° (corresponding to anisotropic symmetry axes) are straight.

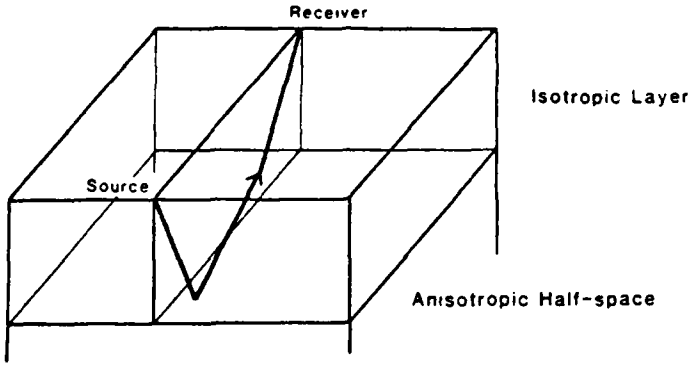


Figure 8. Ray-path for a source and receiver on an isotropic layer above an anisotropic half-space. The ray-path is skewed, and the ray at the receiver will be at an angle to the vertical plane connecting source and receiver.

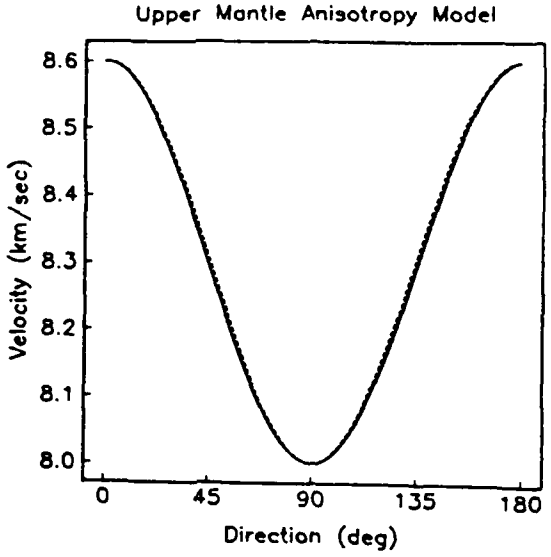


Figure 9. The solid line is the group velocity function for a specific model of upper mantle anisotropy ($\Gamma_{1111} = 73.96$, $\Gamma_{2222} = 64.00$, $\Gamma_{1212} = 21.716$, $\Gamma_{1122} = 25.55$, $\Gamma_{1313} = 13.57\,km^2s^{-2}$). The dashed line is the calculated group velocity curve using the Backus approximation applied to this model ($v^2 = 68.98 + 4.98 \cos 2\theta$).

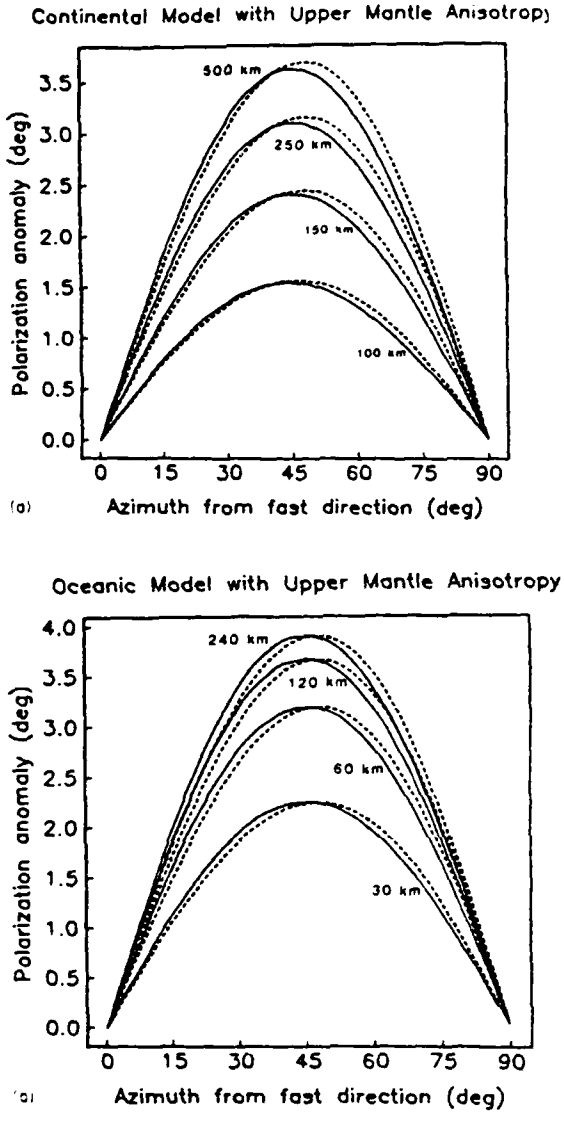


Figure 10. (a) Calculated polarization anomalies for a continental model with 30 km of 6 km s^{-1} crust above an anisotropic upper mantle with a 2θ velocity variation from 8.0 to 8.6 km s^{-1}. Solid lines were calculated from the slowness surfaces for the exact model. Dashed lines were calculated using a least time algorithm on an approximate group velocity function. (b) Calculated polarization anomalies for an oceanic model with 6 km of 1.5 km s^{-1} water above 6 km of 6 km s^{-1} crust above an anisotropic upper mantle. The source was assumed to be at surface of water; the receiver was assumed to be at the surface of the crust. Anisotropy model calculations were done as in (a).

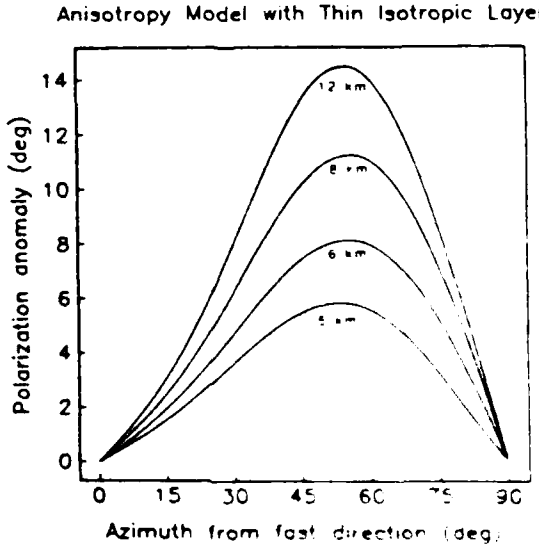


Figure 11. Calculated polarization anomalies for a model consisting of a 3 km thick, 3 km s^{-1} isotropic layer above the Stephen model. The layer thickness is the same as in the Fig. 6 example. Anomalies are shown for layer thicknesses of 5, 6, 8 and 12 km. Positive anomalies represents deviations away from the fast direction in the isotropic half-space.

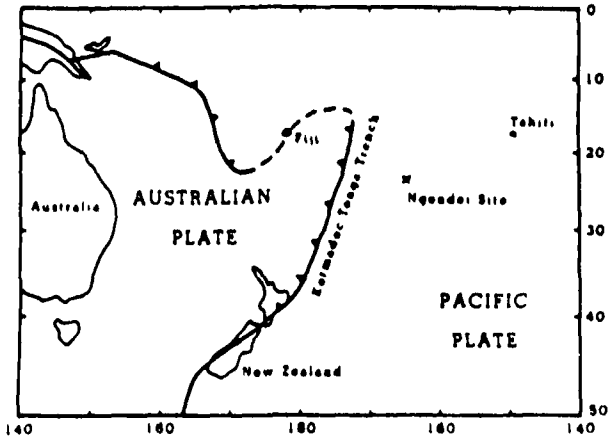


Figure 12. The Ngendei site (DSDP Hole 596) shown on a map of the South Pacific

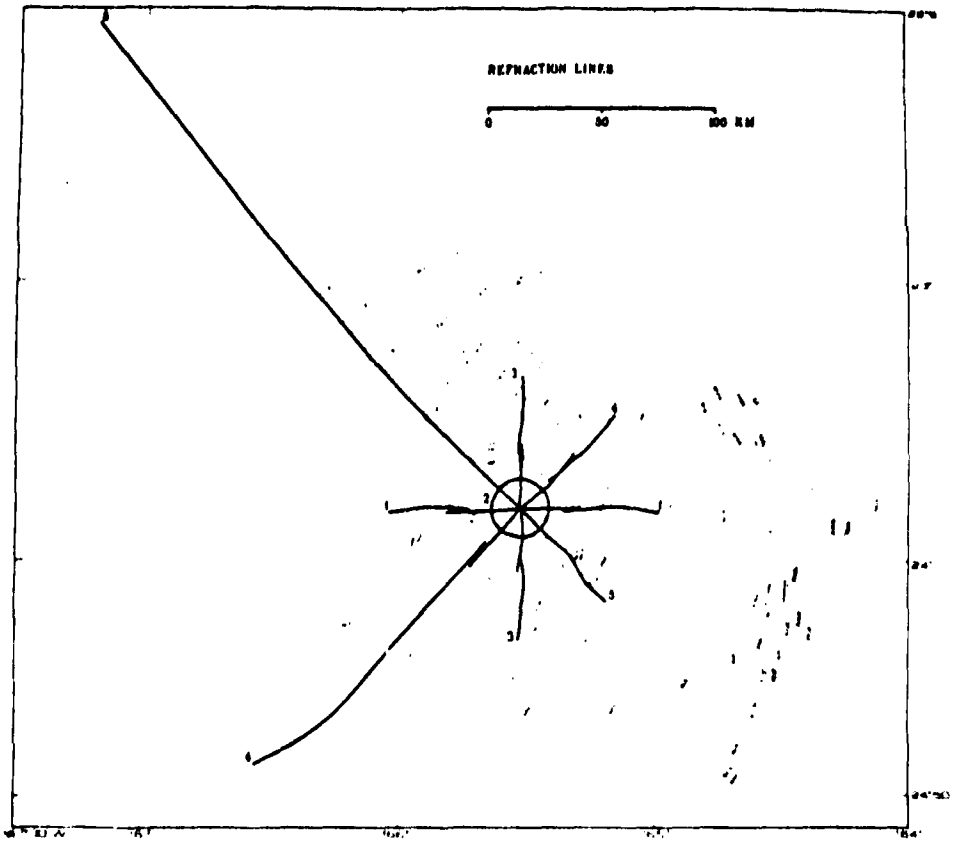


Figure 13. Four split refraction lines and a circular line of 10 km radius were shot at the Ngendei site. Water depth at the site is 5600 m.

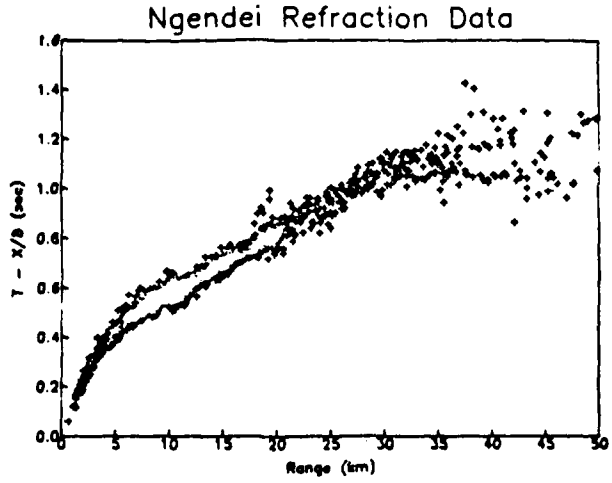


Figure 14. One thousand and five *P*-wave picks from the Ngendei refraction shooting. Topographic time and range corrections have been made and the travel times reduced at 8 km s^{-1}.

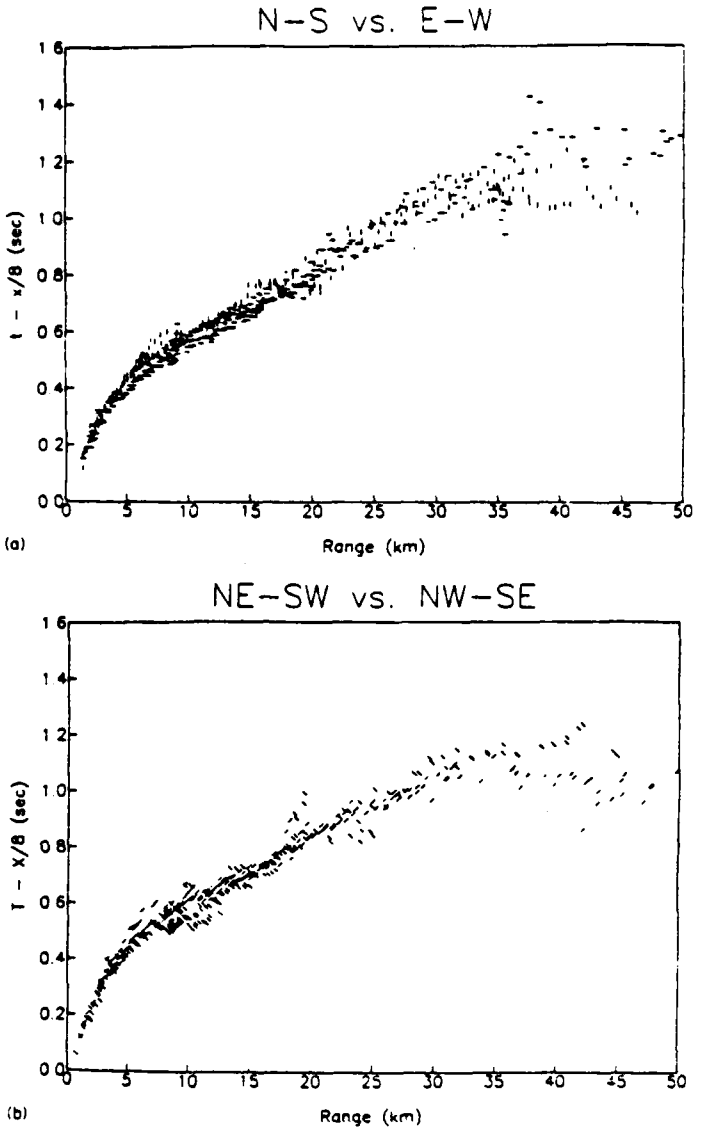


Figure 15. (a) *P*-wave travel times for shots at azimuths along a N–S line (shown as vertical bars) compared to shots at azimuths along an E–W line (shown as horizontal bars). Between about 5 and 15 km the E–W arrivals are early, while at ranges greater than 35 km the N–S arrivals are early. (b) NE–SW shots (shown as diagonals to upper right) versus NW–SE shots (shown as diagonals to lower right). NW–SE arrivals are early between about 6 and 17 km, while NE–SW arrivals are early at ranges greater than 35 km.

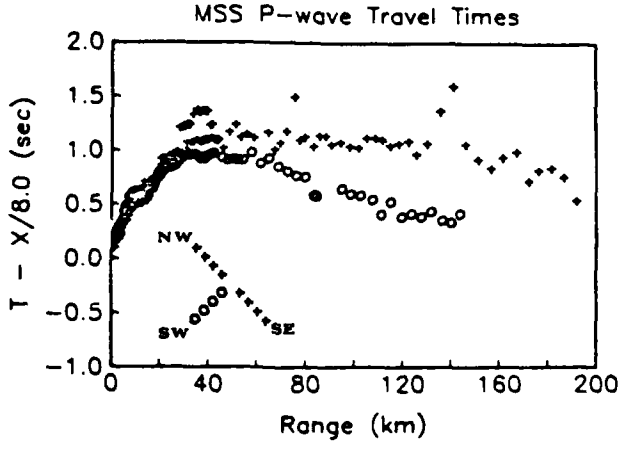


Figure 16. *P*-wave travel times as recorded by the MSS. Circles represent shots along a SW line, while crosses represent shots along a NW–SE line. Note the difference in upper mantle velocity.

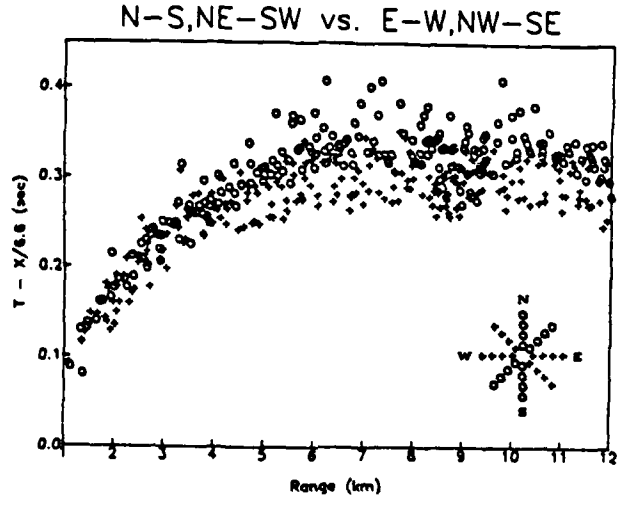


Figure 17. A comparison of N–S, NE–SW arrivals (circles) with E–W, NW–SE arrivals (crosses) at ranges of 1–12 km. Arrivals from rays entering the seafloor at depths less than 5400 m have been eliminated because of scatter in the data and uncertainties in applying topographic corrections.

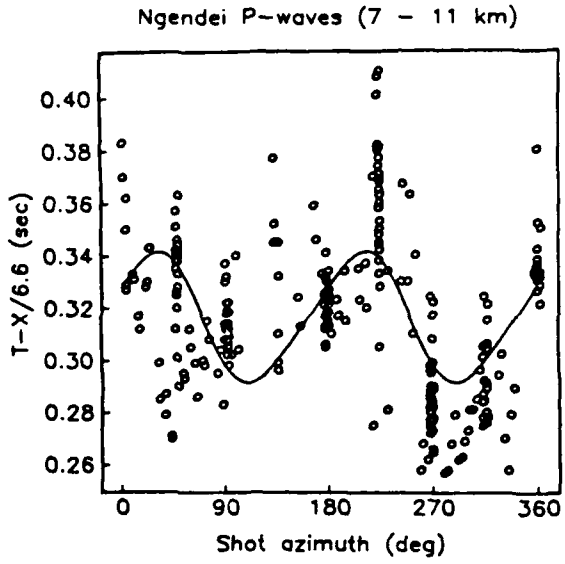


Figure 18. Travel times versus shot azimuth for shots at ranges of 7–11 km. All times have been reduced at 6.6 km s^{-1}. Arrivals from rays entering the seafloor at depths shallower than 5400 m have been eliminated. The curve is least squares fitted for a function of the form $t = a_1 + a_2 \cos 2\theta + a_3 \sin 2\theta + a_4 \cos 4\theta + a_5 \sin 4\theta$.

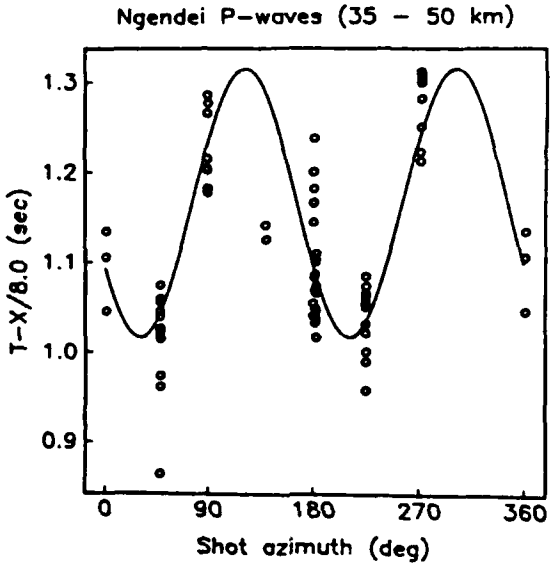


Figure 19. Travel time versus shot azimuth for shots at ranges between 35 and 50 km. Times have been reduced at 8 km s^{-1}. Arrivals from rays entering the seafloor at depths shallower than 5200 m have been eliminated. The curve is least squares fitted for a function of the form $t = a_1 + a_2 \cos 2\theta + a_3 \sin 2\theta$.

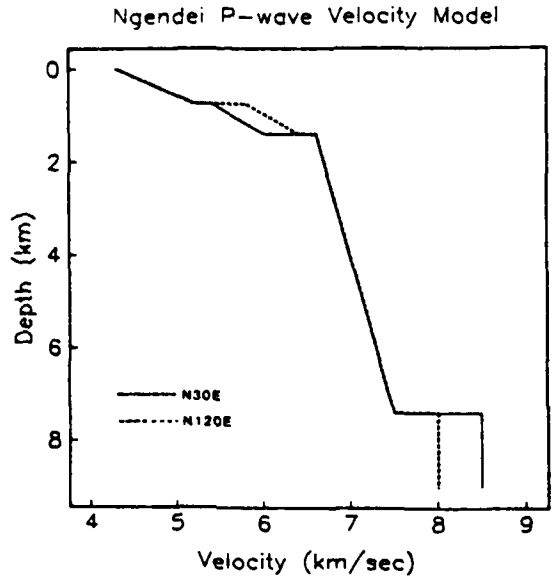


Figure 20. Anisotropic velocity versus depth model which satisfies the Ngendei travel-time data. The solid line is a velocity model at N30°E azimuth; the dashed line is at N120°E azimuth.

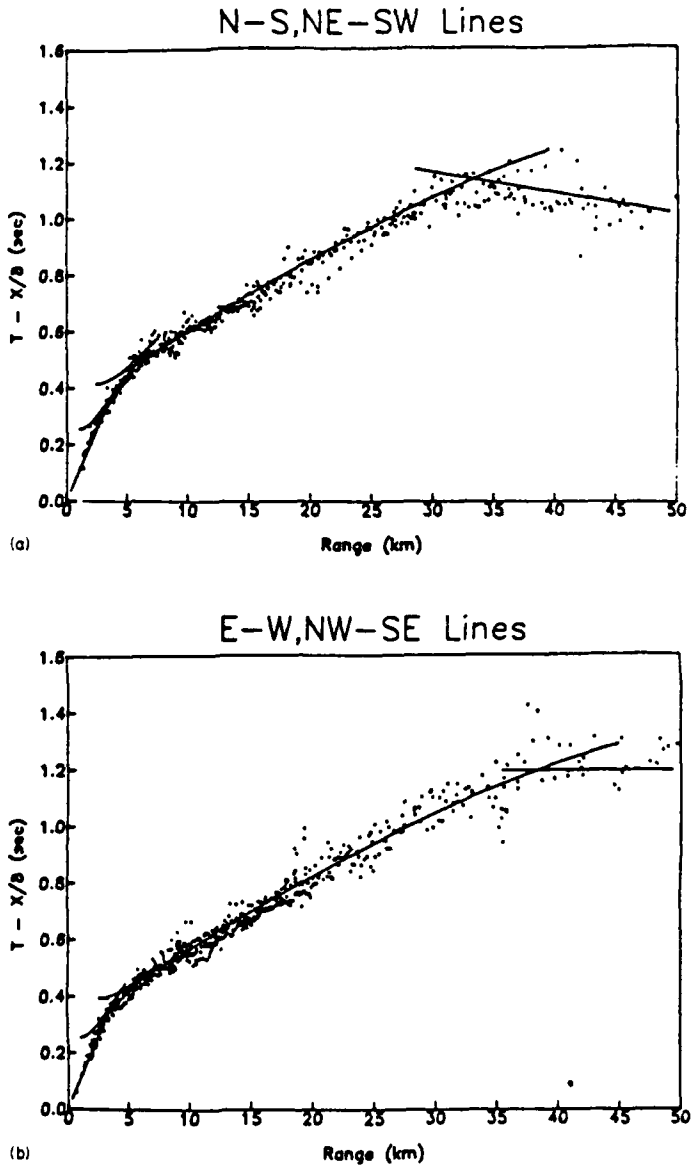


Figure 21. Travel-time curves calculated from the model shown in Fig. 20 superimposed on the data for: (a) N–S, NE–SW azimuths, (b) E–W, NW–SE azimuths.

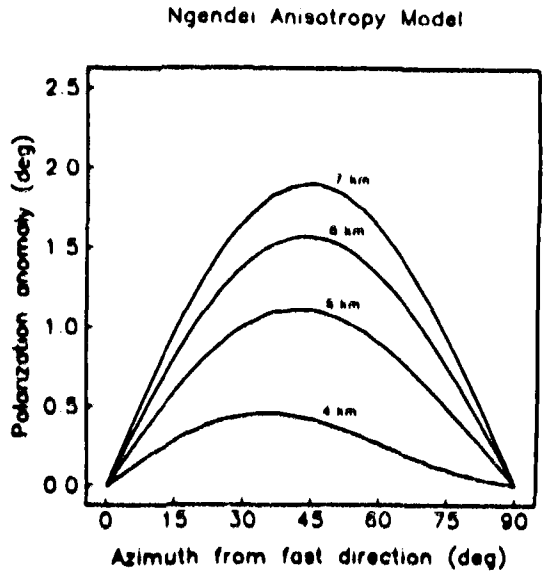


Figure 22. Predicted *P*-wave polarization anomalies for a simplified Ngendei model. Ranges are from the source to the receiver, equivalent ranges corrected to the seafloor are about 1.5 km closer. Positive anomalies represent deviations away from the fast direction in the anisotropy.

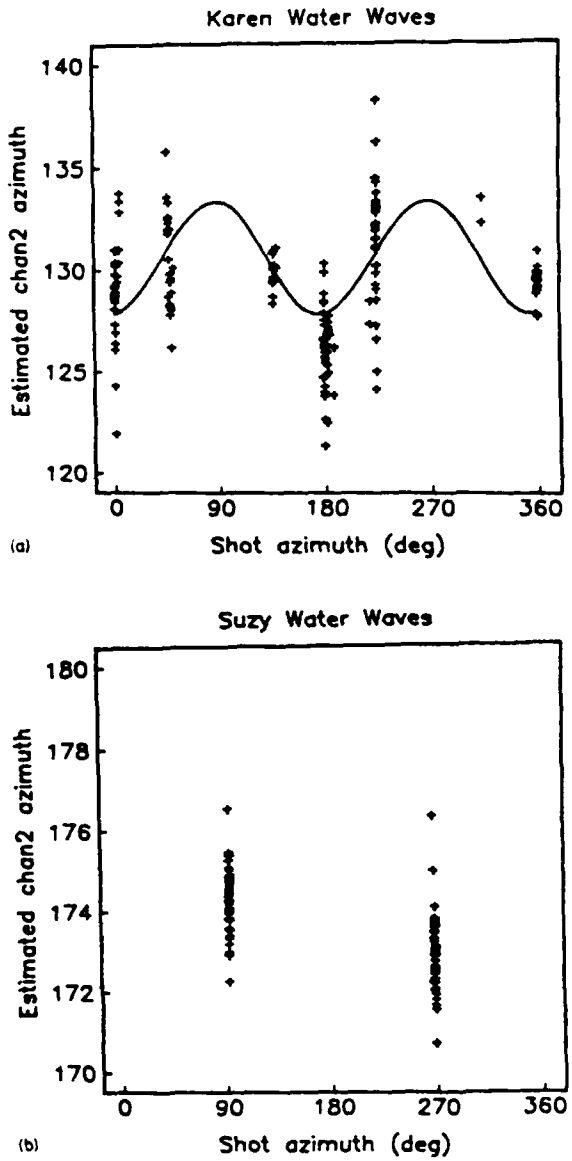


Figure 23. (a) Estimated azimuth of channel 2 (first horizontal) for OBS Karen based on polarization analysis of unclipped direct water waves. The curve shown is the best least squares fit resulting from allowing the ratio of the gains of the two OBS horizontal components to vary. For the curve shown, the true channel 2 azimuth is 130.5° and channel 3 (second horizontal) is 10 per cent more sensitive than channel 2. (b) Estimated azimuth of channel 2 for OBS Suzy.

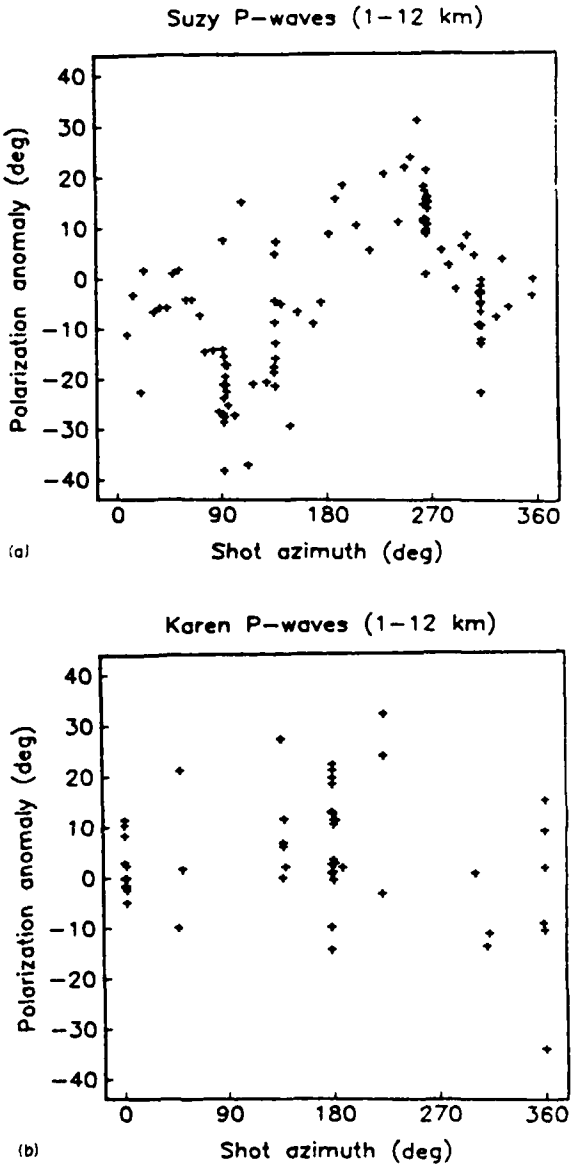


Figure 24. *P*-wave polarization anomalies for OBS (a) Suzy and (b) Karen at ranges (corrected to seafloor) of 1–12 km. Note the large scatter in the data.

CHAPTER 9

SYNTHETIC SEISMOGRAM MODELING OF THE OCEANIC P_n PHASE

T. J. Sereno and J. A. Orcutt

Institute of Geophysics and Planetary Physics,
Scripps Institution of Oceanography
La Jolla, California 92093

The seismic oceanic P_n phase is characterized by low spatial attenuation, a high-frequency wavetrain of extremely long duration and an onset velocity near 8.0 km/s. Models proposed for the mode of propagation of this phase include energy entrapment within a low velocity channel[1,2], propagation within an extremely low attenuation lithosphere waveguide[3,4] and forward-scattering from local heterogeneity within the oceanic crust[5,6]. Through synthetic seismogram modeling, we have generated realistic oceanic P_n phases for an oceanic lithosphere model that did not contain any of these intrinsic properties. It is found that the synthetic P_n phase can be explained rather simply as a set of refractions from the lower lithosphere with subsequent reverberations within the oceanic water column and sediment layer. Many of the spectral properties associated with layer reverberation observed in the synthetic P_n phase are revealed in data collected in the southwest Pacific. Complicated oceanic lithosphere models are not required to explain the gross characteristics of P_n propagation.

The synthesis of realistic oceanic P_n phases was accomplished using wavenumber integration[7]. The technique involves a quadrature over wavenumber at fixed frequency points with the result then Fourier transformed into the time domain. The resulting seismograms contain all reverberations, including those off the free surface, as well as all P to S and S to P mode conversions. While the algorithm is similar to the widely used reflectivity method[8], it differs in several important respects. The inability of reflectivity to incorporate reverberations and mode conversions outside of a "reflection zone" that cannot contain the free surface renders the method inadequate for the study of P_n propagation. It will be shown that near-receiver sediment and water reverberations are quite important in the synthesis of oceanic P_n wavetrains and therefore wavenumber integration is well suited for the study of this phase.

The most serious limitation of wavenumber integration is the restriction to models consisting of a stack of laterally homogeneous layers. We have chosen a model representative of normal oceanic lithosphere consisting of a vertically inhomogeneous oceanic crust and upper mantle overlain by a 4 km thick water layer and a 500 m thick sediment layer. The values of the quality factor, Q, chosen in agreement with seismic refraction studies[9], were less than 500 for compressional waves in the crust and upper mantle and 50,000 in the oceanic water column. A low velocity channel was not included and the seismic velocity was a monotonically increasing function of depth.

Figure 1 is an example of complete synthetic seismograms generated for a sub-MOHO thrust fault at an epicentral range of 1000 km. The vertical component is illustrated in figure 1a and the horizontal component in 1b. The division of these seismograms into two groups facilitates the schematic identification with the oceanic P_n and S_n phases. The group with an onset velocity near 4.7 km/s (figure 1b) is grossly identified

as the oceanic S_n phase. The first arriving energy within this group is entirely comprised of horizontally polarized shear waves and is absent from the vertical component. The first arriving group has an o et velocity of 8.1 km/s, a duration on the order of 100 seconds and extends into the onset of S_n. This group is characteristic of the oceanic P_n phase.

To illustrate the presence of both water and sediment reverberations in the synthetic P_n phase consider the schematic representation of a seismogram comprised of a wavelet reverberating in the two layers. The seismogram, x(t), can be expressed as

$$x(t)=w(t)*\left[\mathrm{III}\left(\frac{t}{T_s}\right)e^{-\alpha_s t}e^{-i\pi t/T_s}\right]*\left[\mathrm{III}\left(\frac{t}{T_w}\right)e^{-\alpha_w t}e^{-i\pi t/T_w}\right] \qquad (1)$$

which is a convolution of the wavelet, w(t), with terms associated with sediment and water reverberations respectively. In (1) the subscript 's' refers to sediment reverberations while 'w' refers to water reverberations. The shah functions[10] in (1) serve to equally space the reverberations with interval T and attenuation is modeled as an exponential decay with parameter α. The last term in each reverberation function is due to a π-phase shift between multiples[11]. The power spectrum of (1) can thus be written as

$$|X(f)|^2 = |W(f)|^2\left[T_s^2\,\mathrm{III}\left(\frac{f}{df_s}+\frac{1}{2}\right)*\left[\frac{2\alpha_s}{(\alpha_s^2+4\pi^2f^2)}\right]^2\right]^2 x$$

$$\left[T_w^2\,\mathrm{III}\left(\frac{f}{df_w}+\frac{1}{2}\right)*\left[\frac{2\alpha_w}{(\alpha_w^2+4\pi^2f^2)}\right]^2\right]^2 \qquad (2)$$

where $df_s = \frac{1}{T_s}$ and $df_w = \frac{1}{T_w}$. The shah functions in (2) produce spectral peaks associated with reverberation at frequencies given by $f_n=(2n+1)\frac{df}{2}$, (n=0,1,2,...). In order to penetrate the mantle layers the rays must be quite steep at the receiver thus the time between multiples can be approximated by the two-way travel time in the layer. This implies that the spacing of the sediment reverberation peaks, df_s, is much greater than the corresponding spacing for water reverberation peaks, df_w. The presence of attenuation widens the spectral peaks and the extremely high value of Q in the water column relative to that in the sediments implies that $\alpha_w \ll \alpha_s$. Thus the power spectrum of a wavelet

reverberating in the oceanic water column and sediment layer consists of widely spaced spectral "humps" due to sediment reverberation superimposed on finely spaced spectral "peaks" associated with water reverberation.

Figure 2 illustrates this behavior in the synthetic P_n power spectrum. Figure 2a is the synthetic P_n wavetrain of figure 1a. The horizontal component power spectrum is shown in figure 2c with vertical lines indicating predicted positions of spectral "humps" associated with S-wave sediment reverberation. Figure 2b is the first 3.0 Hz of the vertical component spectrum with lines at the predicted frequencies of water reverberation peaks. Comparison with the schematic representation, (2), quite clearly illustrates the presence of these reverberations in the synthetic P_n wavetrain.

Data were collected during the 1983 Ngendei Seismic Experiment by an ocean bottom seismometer (OBS) array in the southwest Pacific (23° 49'S, 165° 32'W), approximately 900 km east of the Tonga trench[12]. Each OBS contained one vertical and two horizontal seismometers and a hydrophone. Figure 3 is an example of these data along with their corresponding power spectra.

A clear feature of the P_n phase in figure 3c, also seen in the synthetic P_n phase of figure 2a, is a predominance of low frequencies late in the wavetrain. This is in direct contrast to models of forward-scattered coda[6] which predict the fall-off rate to be a decreasing function of frequency. This feature can, however, be explained as the superposition of different modes of reverberation.

The hydrophone is a more narrow band instrument than the OBS vertical component seismometer and was better able to isolate the water reverberations and their corresponding spectral peaks as depicted in figure 3b. The vertical component seismometer, on the other hand, was able to record the dominant frequency associated with sediment reverberation and clearly exhibits the corresponding spectral "humps" in figure 3d. The predicted frequencies of spectral peaks in both figures 3b and 3d were calculated using values of the sediment and water layer velocities and thicknesses obtained in an independent study[13].

The amplitude of the synthetic P_n phase was within a factor of 2 or 3 of the data amplitudes. An event located by the National Earthquake Information Service (NEIS) with a published magnitude of 5.8 and moment of 2.6×10^{24} dyne-cm was recorded by three of the OBS's at the Ngendei site. The event was a thrust fault source with an azimuth relative to the receiver of 90° at an approximate epicentral range of 920 km. The absolute amplitudes in the first 20 seconds recorded for this event ranged from 0.76 to 1.44 volts. To obtain the maximum amplitude of the synthetic P_n phase we used a thrust fault source with an azimuth relative to the receiver of 90° at an epicentral range of 900 km. The moment

determined by NEIS was used and, after convolving with the instrument response, the resulting maximum amplitude was 0.420 volts. Differences of this order can be easily explained in terms of differences in model parameters, fault orientation and focal depth. Thus the low spatial attenuation observed for P_n propagation does not require an intrinsically high Q lithosphere waveguide but rather can be explained by the extremely low attenuation within the oceanic water column.

In summary, the oceanic P_n phase can be explained simply as a set of refractions from the lower lithosphere with subsequent water and sediment reverberations. The impulsive character of these reverberations can explain the high frequency content of the wavetrain. Synthetic P_n wavetrains with durations on the order of 100 seconds were generated in the absence of scattering. Thus the propagation of the oceanic P_n phase does not require features of the oceanic lithosphere such as low velocity channels, anomalously high Q values or thin high velocity lenses but rather can be explained in terms of simple models with monotonically increasing velocity-depth profiles containing no lateral heterogeneity.

REFERENCES

1. Fuchs, K. and Schulz, K. J. Geophys., 42, 175-190 (1976).
2. Talandier, J. and Bouchon, M. J. of Geophys. Res., 84, 5613-5619 (1979).
3. Sutton, G., McCreery, C., Duennebier, F. and Walker, D. Geophys. Res. Lett., 5, 745-747 (1978).
4. Walker, D., McCreery, C., Sutton, G. and Duennebier, F. Science, 199, 1333-1335 (1978).
5. Menke, W. and Richards, P. J. of Geophys. Res., 85, 5416-5422 (1980).
6. Menke, W. and Chen, R. Bull. Seism. Soc. Am., 74, 1605-1621 (1984).
7. Apsel, R. Ph.D. thesis, University of California, San Diego, La Jolla, 349 pp. (1979).
8. Fuchs, K. and Müller, G. Geophys. J. R. Astr. Soc., 23, 417-433 (1971).
9. Spudich, P. and Orcutt, J. J. of Geophys. Res., 85, 1409-1433 (1980).
10. Bracewell, R., McGraw Hill, Inc., New York (1978).
11. Luco, E. and Apsel, R. Bull. Seism. Soc. Am., 73, 909-929 (1983).
12. Adair, R., Orcutt, J. and Jordan, T. Initial Rep. Deep Sea Drill. Proj., Leg 91 (1985).
13. Kim, I., Smith, D., Orcutt, J., Jordan, T. and Menard, H. Initial Rep. Deep Sea Drill. Proj., Leg 91 (1985).

FIGURE CAPTIONS

FIGURE 1. Complete synthetic seismograms at an epicentral range of 1000 km for a thrust fault source at 14.0 km depth. The fault had a dip of 45°, a rake of 270° and an azimuth relative to the receiver of 60°. (a) Vertical component and (b) horizontal component rotated 25° clockwise from the radial direction. Group velocities of 8.1, 4.7, 2.6 and 1.6 km/s are indicated. Phase velocities between 3.85 and 25.0 km/s were included in the calculation.

FIGURE 2. Power spectrum of the synthetic P_n wavetrain. (a) Synthetic P_n wavetrain in figure 1a. (b) First 3.0 Hz of the vertical component power spectrum with vertical lines at frequencies associated with water reverberation. (c) Horizontal component spectrum with vertical lines indicating predicted positions of spectral "humps" associated with S-wave sediment reverberation. The synthetics were limited to a Nyquist frequency of 6.4 Hz due to the high computational costs involved.

FIGURE 3. Data collected in the Southwest Pacific during the Ngendei Seismic Experiment. (a) Hydrophone recording and (b) the first 3.0 Hz of its corresponding power spectrum with vertical lines at predicted frequencies of water reverberation peaks. (c) OBS vertical component seismometer data and (d) its corresponding power spectrum. Vertical lines indicate predicted positions of spectral "humps" associated with P-wave sediment reverberation.

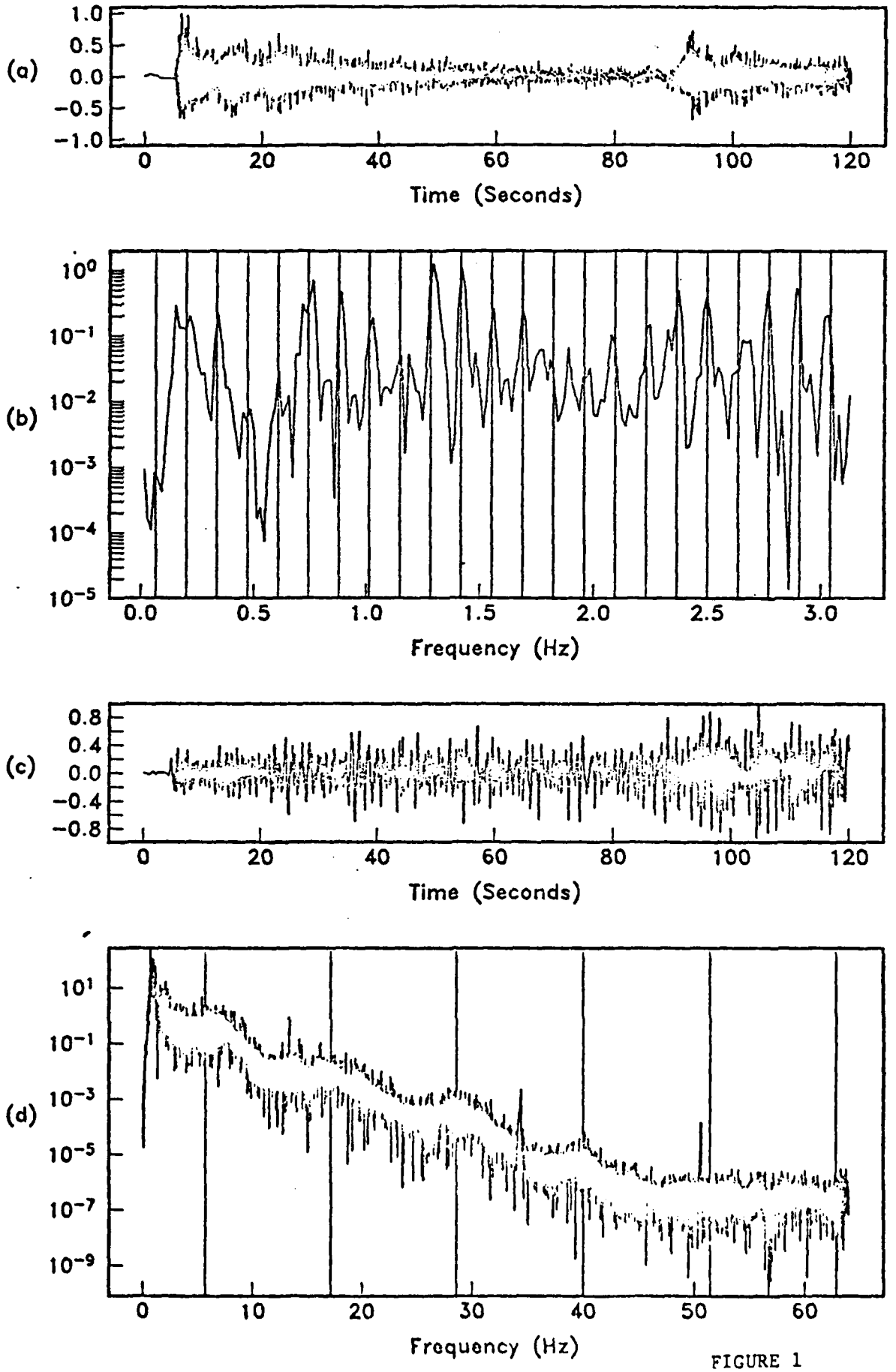

(a)
1.0
0.5
0.0
−0.5
−1.0
0
20
40
60
80
100
120
Time (Seconds)
(b)
10^{0}
10^{-1}
10^{-2}
10^{-3}
10^{-4}
10^{-5}
0.0
0.5
1.0
1.5
2.0
2.5
3.0
Frequency (Hz)
(c)
0.8
0.4
0.0
−0.4
−0.8
0
20
40
60
80
100
120
Time (Seconds)
(d)
10^{1}
10^{-1}
10^{-3}
10^{-5}
10^{-7}
10^{-9}
0
10
20
30
40
50
60
Frequency (Hz)

FIGURE 1

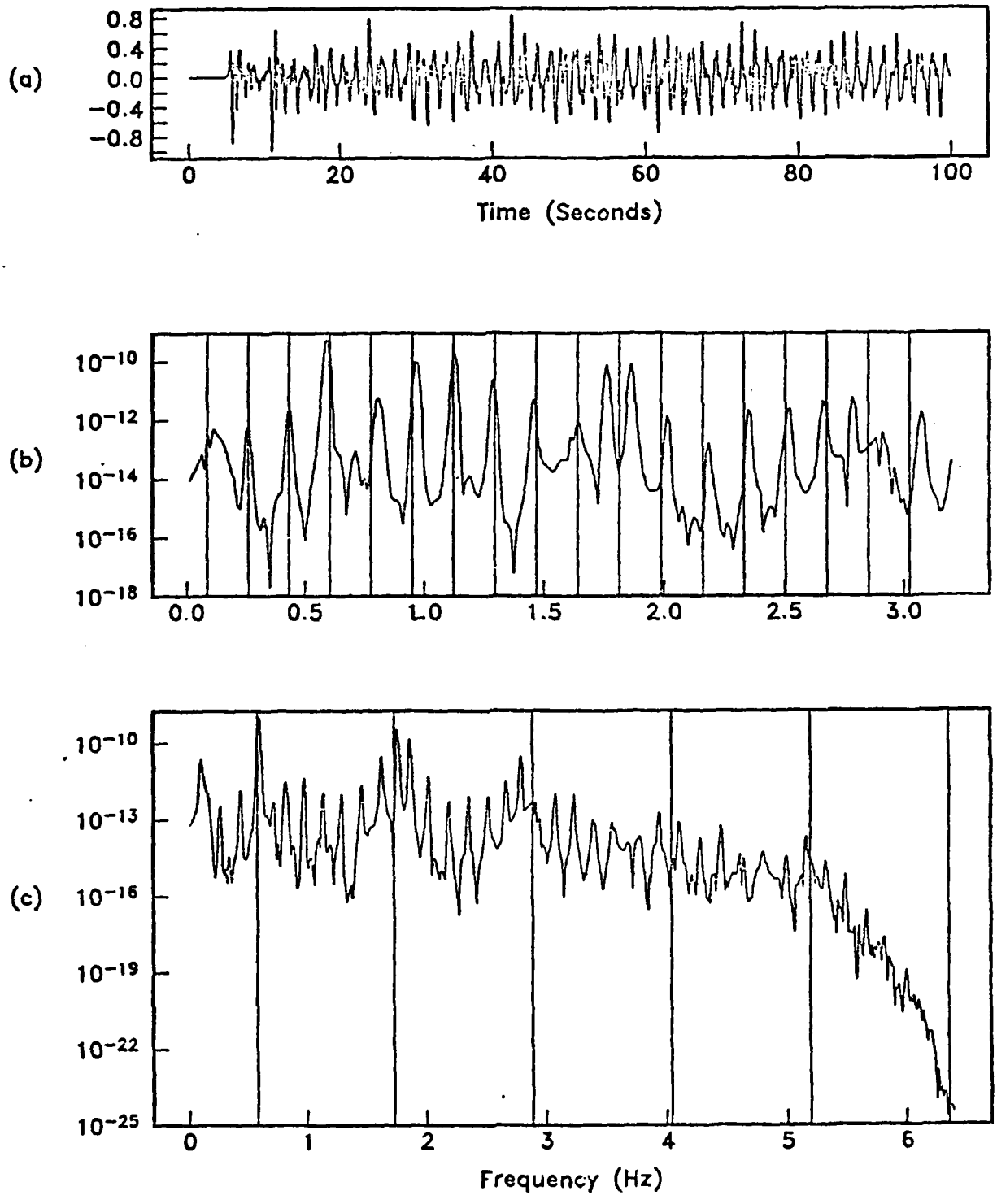

(a)
0.8
0.4
0.0
−0.4
−0.8
0
20
40
60
80
100
Time (Seconds)
(b)
10^{-10}
10^{-12}
10^{-14}
10^{-16}
10^{-18}
0.0
0.5
1.0
1.5
2.0
2.5
3.0
(c)
10^{-10}
10^{-13}
10^{-16}
10^{-19}
10^{-22}
10^{-25}
0
1
2
3
4
5
6
Frequency (Hz)

FIGURE 2

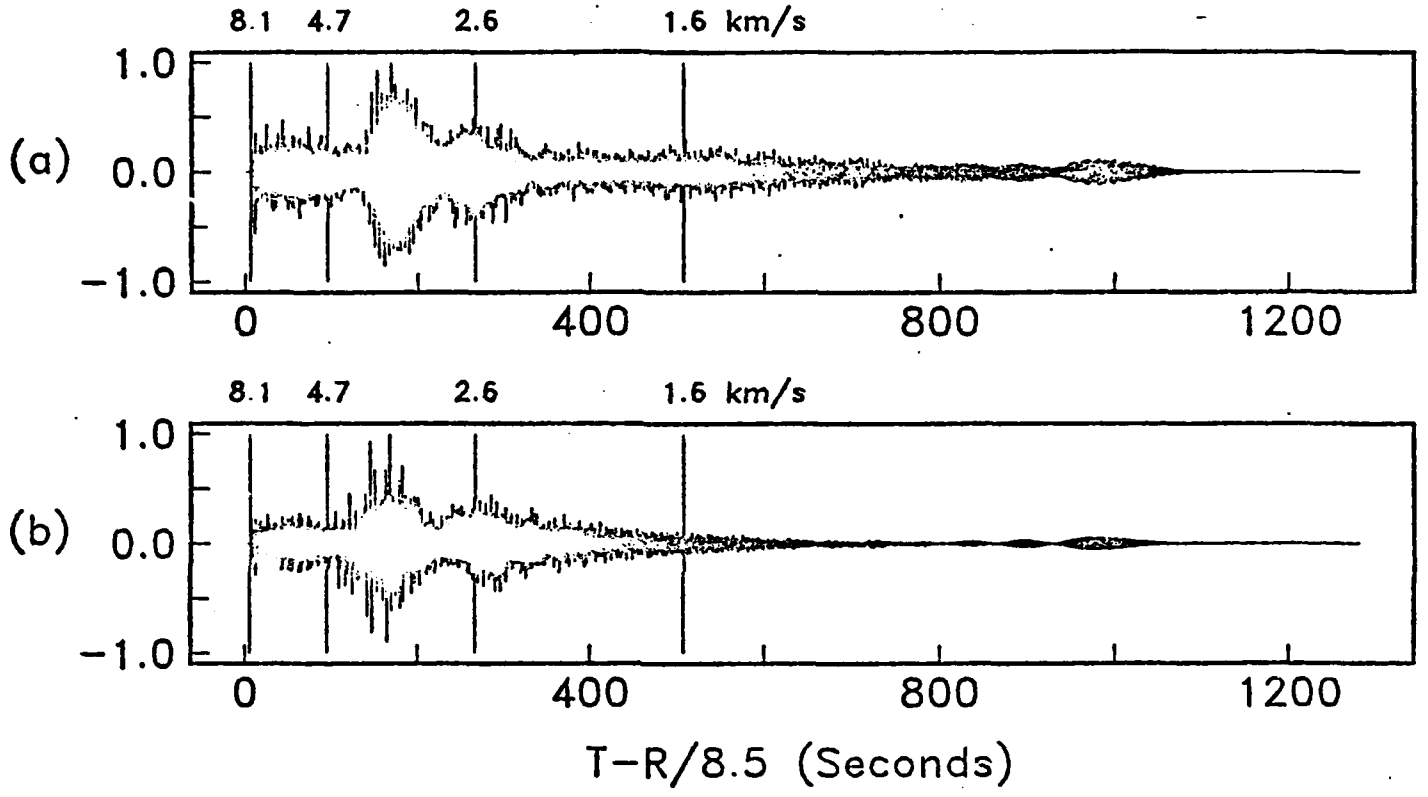

8.1 4.7 2.6 1.6 km/s
(a)
1.0
0.0
-1.0
0
400
800
1200
8.1 4.7 2.6 1.6 km/s
(b)
1.0
0.0
-1.0
0
400
800
1200
T-R/8.5 (Seconds)

FIGURE 3

CHAPTER 10

THE SYNTHESIS OF REALISTIC OCEANIC P_n WAVETRAINS

T. J. Sereno and J. A. Orcutt

Institute of Geophysics and Planetary Physics,
Scripps Institution of Oceanography
La Jolla, California 92093

ABSTRACT

The synthesis of realistic oceanic P_n phases was accomplished using wavenumber integration. Wavetrains with durations on the order of 100 seconds following the initial compressional wave arrival were generated for a laterally homogeneous, vertically inhomogeneous oceanic lithosphere model. The excitation of these long wavetrains is primarily a result of near-receiver water and sediment reverberations and does not involve scattering. A late arriving wavetrain with a group velocity of 1.6 km/s having an emergent onset and substantial duration, characteristic of oceanic T-phases, was also generated even with phase velocities restricted to be greater than 5.5 km/s. The synthetic P_n wavetrain was compared to data collected in the Southwest Pacific during the Ngendei Seismic Experiment. A comparison of absolute amplitudes indicates that the low spatial attenuation observed for P_n propagation is associated with the presence of a high Q water column and does not require an intrinsically high Q lithosphere waveguide. Many of the spectral characteristics associated with sediment and water reverberation observed in the synthetics were also observed in the data. First, it was found that the amplitude fall-off rate of the P_n wavetrain is a strongly increasing function of frequency, in direct contrast to results predicted for forward-scattered coda. This leads to a predominance of low frequencies late in the wavetrain which is easily interpreted in terms of the constructive interference of different modes of reverberation. Second, the presence of spectral peaks at frequencies associated with both sediment and water reverberations were observed. The predicted frequencies were computed using values of the water depth, sediment thickness and sediment velocity obtained in an independent study. Strong alignment of the spectral peaks with the predicted frequencies was achieved thereby illustrating the reverberating nature of the P_n wavetrain. The confinement of energy to a narrow frequency band of 6 to 10 Hz, as asserted in other studies, was not observed in the Ngendei data and the presence of substantial power in excess of 15 Hz can be attributed to the impulsive character of reverberations. The P_n wavetrain can be characterized as a refraction from the lower lithosphere with multiple reverberations in the oceanic water column and sediment layer acting to extend the wavetrain. Complicated oceanic lithosphere models are not needed to explain the gross characteristics of P_n propagation.

INTRODUCTION

The oceanic P_n phase is characterized by an onset velocity of approximately 8.0 km/s, a high-frequency wavetrain of extremely long duration and low spatial attenuation. Reported apparent onset velocities range between 8.33 km/s in the Northwest Pacific (Walker, 1977b) and 7.34-7.4 km/s at the Cocos plate (McCreery, 1981). A value of 7.95 km/s for the Central and South-Central Pacific was determined by Talandier and Bouchon (1979). The suggestion that P_n velocity increases with

increasing age of the oceanic lithosphere was made by McCreery (1981). A similar velocity dependence on lithosphere age for the oceanic S_n phase in the North Atlantic was reported by Hart (1973). In nearly all areas of the Pacific the value of the apparent velocity of the oceanic P_n phase is less than that of the mantle refracted compressional arrival which has a maximum velocity near 8.4 km/s.

Efficient high-frequency P_n propagation to teleseismic distances ($\Delta \simeq 30^o$) indicates the phase travels a low attenuation path. The P_n wavetrain contains substantial power at frequencies in excess of 15 Hz and estimates of the effective quality factor, Q, were made by Walker, et al. (1978) for two separate earthquakes in the Western Pacific. The resulting high Q's of 3700 $\pm$ 200 and 8400 $\pm$ 1300 were attributed to propagation within a high Q lithosphere waveguide.

Wavetrains associated with the oceanic P_n phase can last several minutes and generally extend to the onset of S_n (Walker et al., 1978 and McCreery, 1981). Several explanations of the long duration of the P_n wavetrain have been presented. Menke, et al. (1984) suggest the P_n wavetrain consists predominantly of forward-scattered coda while Gettrust and Frazer (1981) explain it as a combination of free surface reflections and multiple bounces within the crust. In this paper we will present evidence that the oceanic P_n wavetrain is comprised predominantly of water and sediment reverberations and while scattering does contribute to the complexity of the wavetrain, it is of secondary importance.

WAVENUMBER INTEGRATION

In order to investigate the nature of the oceanic P_n phase, synthetic seismograms were generated for a realistic oceanic lithosphere model using wavenumber integration. A complete description of the integration method is given by Apsel (1979) in his Ph.D. thesis and only a brief outline is presented here.

The technique involves an integration over wavenumber at fixed frequency points of the form

$$I(\omega; Z_0, Z_0^s, r_0) = \int_0^\infty F(K, \omega; Z_0, Z_0^s) J_n(Kr_0)\, dK \; ; \; n=0,1,2. \qquad (1)$$

Table 1 identifies the variables and the order of the Bessel function, n, is determined by the source geometry. The time domain response can be obtained by applying a Fourier transform to the complex spectrum represented in (1). The resulting seismograms contain all reverberations, including those off the free surface, as well as all P to S and S

to P mode conversions. The most serious limitations in the technique are the restriction to models consisting of laterally homogeneous layers and the substantial computational cost involved for models with more than 10 to 15 layers.

The introduction of realistic attenuation is accomplished by allowing the material velocities to be complex. This has the desired effect of moving the poles of the F integrands in (1) off the real K axis thus avoiding the need for principle values or contour integration. The F integrands can be computed at a particular frequency and wavenumber without approximation using factorizations of the upgoing and downgoing wave amplitudes in terms of the generalized reflection and transmission coefficient matrices (Kennett, 1974). These matrices are formed recursively from one layer to the next thereby including all types of waves. At large values of wavenumber, low frequency expansions of the F integrands are incorporated to avoid the confusion of P and SV wave propagation. These expansions do not alter the form of (1) but merely the way in which the F integrands are calculated.

The wavenumber quadrature is performed, using Filon's method (Filon, 1928; Frazer and Gettrust, 1984), by sampling the F integrands in such a way as to allow a quartic polynomial to be used to interpolate the amplitudes of the F integrands between integration points. The numerical integration over the Bessel functions can then be determined analytically over each integration interval thus avoiding the problem of the severe oscillatory nature of the Bessel functions at large wavenumbers and ranges. For each five point interval, K_j (j=1,5), the interpolation is represented as

$$F(K,Z_0,Z_0^s) = \sum_{m=1}^{5} A_m(Z_0,Z_0^s)\left[\frac{K-K_2}{\Delta K}\right]^{m-1} \quad ; \; (K_1 \le K \le K_5) \tag{2}$$

where $\Delta K = K_4 - K_2$. The coefficients $A_m(Z_0,Z_0^s)$ (m=1,5) are determined by imposing (2) at the five integration points on the interval. Using the expansion (2), the integral equation (1) can be approximated by

$$I(\omega;Z_0,Z_0^s,r_0) = \sum_{n=1}^{N}\left[\sum_{j=1}^{5} F_j \sum_{m=1}^{5} C_{mj} \int_{K_2}^{K_4}\left[\frac{K-K_2}{\Delta K}\right]^{m-1} J_n(Kr_0)\,dK\right] = \sum_{n=1}^{N} \Delta I_n \tag{3}$$

where $F_j = F(K_j,Z_0,Z_0^s)$. The elements of the coefficient matrix, C_{mj}, are dependent upon the spacing of the sampling points and N is the total number of five point integration intervals. The error in passing a quartic polynomial through each of the F integrands at the five K points is estimated by examining a high order curvature and is restricted to be

smaller than a user-defined tolerance level. If this condition is not met a new K point is inserted midway between the widest spacing on the five point interval and the relative error is resampled. To determine the tolerance level the integration is performed for a few frequencies spanning the band of interest. By employing an iterative scheme in which the tolerance level is decreased between iterations until convergence is achieved, the maximum acceptable tolerance level is obtained.

Two methods were used to evaluate the integrals appearing in (3) depending upon the value of the argument of the Bessel function, Kr_0. For large arguments the Bessel functions are replaced with Hankel's asymptotic expansions (Abramowitz and Stegun, 1964; p.364) and the coefficients of these expansions are included in the interpolation of the F integrands. The integrals in (3) are thereby reduced to a form

$$\int_{K_2}^{K_4} \left[\frac{K-K_2}{\Delta K}\right]^{m-1} \begin{bmatrix}\cos\\ \sin\end{bmatrix}(Kr_0)\,dk \tag{4}$$

which can be integrated analytically. The second method is valid for small values of Kr_0 with the restriction that ΔK be small enough that the Bessel functions oscillate slowly on the five point interval and can be interpolated with the F integrands. In this case the integrals in (3) reduce to the simple form

$$\Delta I_n = \sum_{j=1}^{5} F_j J_n(K_j r_0) \sum_{m=1}^{5} C_{mj} \int_{K_2}^{K_4} \left[\frac{K-K_2}{\Delta K}\right]^{m-1} dk$$

$$= \sum_{j=1}^{5} F_j J_n(K_j r_0) \sum_{m=1}^{5} \frac{C_{mj}\Delta K}{m} \tag{5}$$

where once again analytic evaluation of the integrals was possible. The variable step size employed accommodates the change in the F integrands as a function of wavenumber for each frequency.

In order to reduce computational costs an option has been added to the algorithm to limit the integration to a user-specified phase velocity window. An undesirable effect of restricting the range of integration is the introduction of cut-off phases. By artificially setting the upper and lower limits of integration a pulse in the integrand is introduced for all frequencies at phase velocities corresponding to the upper and lower limits of the chosen window. When integrated, these finite

bandwidth functions yield non-dispersed cut-off phases at plus and minus the limiting phase velocities. This effect is easily reduced by including a cosine-squared taper to both ends of the desired phase velocity range prior to integration.

The displacement due to an arbitrarily oriented double couple source can be easily obtained from the elements of the stress tensor due to vertical and horizontal point forces through application of the representation theorem (Shaw and Orcutt, 1984). The Green's functions are computed using wavenumber integration and through the appropriate linear combination the response due to a first seismic moment tensor source can be obtained.

The wavenumber integration algorithm employed is similar to the widely used reflectivity method (Fuchs and Müller, 1971) but differs in several important respects. First, reflectivity correctly computes all reverberations only within a "reflection zone" which cannot contain the free surface. Second, both the source and the receiver must lie outside this "reflection zone". This implies that near-source or near-receiver reverberations and mode conversions are not included whereas they are automatically incorporated in the present method. Wavenumber integration can, as a result, include all surface wave and leaky mode phenomena whereas reflectivity cannot. Ray theoretical methods are also inappropriate when a large number of reverberations are important. For example, the number of separate ray calculations needed to describe paths with seven reflection points in a ten layer model, not including mode conversion, was shown in table 1 of Müller (1970) to be 760,804. It will be shown that near-receiver reverberations are very important in the generation of synthetic P_n wavetrains and therefore we believe the present method to be the most appropriate for the study of the oceanic P_n phase.

SYNTHETIC SEISMOGRAMS

The model used in the generation of the synthetic seismograms consists of a vertically inhomogeneous oceanic crust and upper mantle overlain by a 4 km thick water layer and a 500 m thick sediment layer (table 2). The velocity and density profile, shown in figure 1, was adopted from Gettrust and Frazer (1981) and is representative of realistic oceanic lithosphere. No low velocity channel was included and the restriction to models consisting of a stack of homogeneous, elastic layers precludes any lateral heterogeneity.

The values of the quality factors, Q_p for compressional waves and Q_s for shear waves, were chosen in agreement with seismic refraction studies (Spudich and Orcutt, 1980) and are shown in table 3.

Source depths corresponding to the top of the crust, the base of the crust and 4.0 km below the MOHO were used and are indicated by asterisks in figure 1. The receivers were located at the water-sediment interface at epicentral ranges from 500 to 1500 km.

The modulus of the F integrand of equation (1) corresponding to the horizontal normal stress $\sigma_{221}(K,\omega;Z_0,Z_0^s)$ is plotted as a function of ray parameter and frequency in figure 2 for the three source depths used in the calculation. For ray parameters greater than the reciprocal of the shear wave velocity at the source, indicated by arrows in figure 2, only inhomogeneous waves are generated. Beyond this ray parameter there is essentially no contribution to the integrands at high frequencies. The vertical extent of the exponential tail of these waves decreases with increasing frequency. Therefore, as indicated in figure 2, only low frequency contributions can be observed for inhomogeneous waves generated at the two deeper sources. The phase velocity window used in the calculation was chosen to enclose the range 3.85 to 25.0 km/s corresponding to a ray parameter range of 0.04 to 0.26 s/km. Comparison with figure 2 shows that at least for the two deeper sources this includes almost the entire response, except at quite low frequencies.

Each of the Green's functions contain 8193 complex frequency points which extend to a Nyquist frequency of 6.4 Hz. The number of K points required in the integration at a single frequency is typically on the order of 950. Fine frequency sampling was necessary to avoid time series wraparound and, while the method is not strictly limited in frequency, the computational costs of extending the calculation to higher frequencies are formidable.

Figure 3 is an example of complete synthetic seismograms generated for a sub-MOHO thrust fault at an epicentral range of 1000 km. The fault used had a dip of 45°, a rake of 270°, an azimuth relative to the receiver of 60° and was at a depth of 14.0 km. The horizontal component shown in figure 3b was rotated 25° clockwise from the radial direction. Group velocities of 8.1, 4.7, 2.6 and 1.6 km/s are indicated in the figure. The division of these seismograms into three distinct groups facilitates the schematic identification with the high frequency oceanic P_n, S_n and T-phases. The late arriving energy in figure 3a with apparent velocity of 1.6 km/s is emergent in nature and has a substantial duration characteristic of oceanic T-phases. Several points of interest can be made in reference to this arrival. First, the model is laterally homogeneous and therefore a sloping bottom topography, a condition asserted in other studies as necessary for the excitation of T-phases within the SOFAR channel (Northrop, 1972 and Johnson, et al., 1970), is not included. Walker (1982) suggested that the T-phase may be the result of P_n and/or S_n coupling into the SOFAR channel which acts as an acoustical waveguide. The water layer in the velocity model used to generate the synthetics did not, however, contain heterogeneity, vertical or lateral, and therefore did not feature a SOFAR channel. It is for these

reasons that we believe a far simpler explanation for the generation of T-phases is warranted. In a previous calculation the same velocity model was used but phase velocities were restricted to the range 5.5 to 8.5 km/s. T-phases were generated even within this narrow window and the lower limit of 5.5 km/s indicates the phase cannot be trapped in the water column but rather samples well into the oceanic crust. In fact, by comparing the $F(\omega,p)$ integrands of (1) for Green's functions that contain T-phases to those for Green's functions that do not, it is observed that the phase velocity range comprising the synthetic T-phase corresponds to that of post-critical P wave reflections off the MOHO. The restriction to high phase velocities imposes the constraint that the rays comprising the T-phase are steep at the receiver and, because it appears much stronger on the vertical component than on the horizontal component, the T-phase is predominantly compressional energy. Thus it appears the oceanic T-phase is confined between the free surface and structure as deep as the MOHO with the duration of the wavetrain being due to a significant number of water, as well as crustal, reverberations.

The group of energy arriving with an onset velocity of 4.7 km/s, seen most clearly in figure 3b, and extending to the onset of the T-phase is grossly identified as the oceanic S_n phase. The first arriving energy of this group is almost entirely comprised of horizontally polarized S waves and is essentially absent from the vertical component, figure 3a. The absence of a strong, high group velocity S_n signal on the vertical component suggests that conversion of SH waves to SV or P through either instrument coupling or scattering from local heterogeneity may be important. The general trend of decreased phase velocity with increased travel time has been observed in the synthetics which causes the rays to be less steep at the receiver in the S_n wavetrain than in the P_n wavetrain. The travel time for reverberations in the water column for rays comprising the S_n wavetrain is therefore greater than that for rays comprising the P_n wavetrain. With the extremely high value of the quality factor, Q, of the water, this could account for the observation (Walker, 1982) that the effective Q of the oceanic S_n phase is greater than that of the oceanic P_n phase. Work is continuing on both oceanic S_n and T- phases in an effort to quantify these preliminary findings and detailed results will be presented in future papers.

The first arriving energy in figure 3 has an onset velocity of 8.1 km/s, a duration of over 100 seconds, is propagated to 1500 km with appreciable amplitude and extends into the onset of S_n. This group is characteristic of the oceanic P_n phase and will be the subject of the remaining portion of this paper.

SYNTHETIC Pn WAVETRAIN

The synthetic P_n wavetrain of figure 3 is expanded in figure 4 by plotting the first 100 seconds of the records. Examination of the various Green's functions necessary to represent an arbitrary source indicate that the overall characteristics of the synthetic P_n wavetrain are not strongly dependent upon the source mechanism.

An interesting feature of the P_n wavetrain is the narrow range of phase velocities comprising the entire group. This is illustrated in figure 5 which is a record section of the vertical normal stress σ_{zz0} at a depth of 14.0 km. The low frequency forerunner in figure 5 at ranges greater than 1200 km is due to a slight time series wraparound. Parallel lines are drawn across the record with an inverse slope of 8.17 km/s and are separated by the two-way travel time in the water column, 5.33 seconds. The actual phase velocity range within the P_n wavetrain is bounded by the sub-MOHO compressional wave velocity and that of the underlying halfspace, corresponding to near-critical P wave reflections in the lower lithosphere. With the shallow compressional wave velocity gradient of .00032 s^{-1} in the mantle (table 2) this corresponds to a range of only 8.1654 to 8.2038 km/s. Rays with phase velocities greater than 8.2038 km/s are pre-critical in the mantle and transmit most of their energy into the halfspace below (figure 6) while compressional waves with phase velocities less than 8.1654 km/s have "geometrical turning points" in the crust.

To illustrate the reverberating nature of the synthetic P_n wavetrain consider a seismogram comprised of a wavelet reverberating in a single layer. The seismogram, x(t), can be represented as

$$x(t) = w(t) * \left[III\left(\frac{t}{T}\right) e^{-\alpha t} e^{-i\pi t/T} \right] \tag{6}$$

which is a convolution of a single wavelet, w(t), with a shah function of period T (Bracewell, 1978). Attenuation is modeled as an exponential decay with parameter α and the last term in (6) represents a π-phase shift between multiples due to reflection off the free surface (Luco and Apsel, 1983a). Through multiple applications of the convolution theorem, the power spectrum of equation (6) can be written in the form

$$\left|X(f)\right|^2 = \left|W(f)\right|^2 \left[T^2 III\left(\frac{f}{df} + \frac{1}{2}\right) * \left[\frac{2\alpha}{(\alpha^2 + 4\pi^2 f^2)} \right]^2 \right] \tag{7}$$

where $df = \frac{1}{T}$ and $\left|W(f)\right|^2$ is the power spectrum of the wavelet, w(t). Figure 7a is an example of a wavetrain generated using (6) with T = 0.46

seconds and $\alpha = 1.0$ for an arbitrary wavelet, w(t). The power spectrum of the wavetrain is shown in figure 7b. The dashed curve is the spectrum of a single wavelet, $|W(f)|^2$, while the solid curve is the spectrum of the entire wavetrain. The wavetrain spectrum is therefore a discrete sampling of the wavelet spectrum at equally spaced frequency points given by

$$f_n = (2n+1)\frac{df}{2} \; ; \; (n=0,1,2,\ldots) \tag{8}$$

where $df = \frac{1}{T}$ and T is the time between multiples. For near-vertical incidence this is essentially the two-way travel time in the layer. The offset of the spectral peaks in (8) by an amount $\frac{df}{2}$ is due to the π-phase shift between multiples. The presence of attenuation merely serves to widen the spectral peaks.

The previous discussion can be easily extended to include the case of reverberation within two layers. A schematic representation of a wavetrain comprised of reverberations within the oceanic water column and sediment layer follows. The wavetrain, x(t), can be expressed as

$$x(t)=w(t)*\left[\mathrm{III}(\tfrac{t}{T_s})e^{-\alpha_s t}e^{-i\pi t/T_s}\right]*\left[\mathrm{III}(\tfrac{t}{T_w})e^{-\alpha_w t}e^{-i\pi t/T_w}\right] \tag{9}$$

where the subscript 'w' refers to properties of the water reverberations while the subscript 's' refers to those of the sediment reverberations. The power spectrum of (9) is

$$|X(f)|^2 = |W(f)|^2\left[T_s^2\,\mathrm{III}(\tfrac{f}{df_s}+\tfrac{1}{2})*\left[\frac{2\alpha_s}{(\alpha_s^2+4\pi^2f^2)}\right]^2\right]x$$

$$\left[T_w^2\,\mathrm{III}(\tfrac{f}{df_w}+\tfrac{1}{2})*\left[\frac{2\alpha_w}{(\alpha_w^2+4\pi^2f^2)}\right]^2\right] \tag{10}$$

where $df_s = \frac{1}{T_s}$ is the spacing of the spectral peaks due to sediment reverberation and $df_w = \frac{1}{T_w}$ is the spacing due to water reverberation. It should be noted that while the surface of the sediment layer is not a free surface, the phase shift between multiples is nevertheless equal to

π. For example, figures 8a and 8b are the upward reflection coefficients at the ocean-sediment boundary (Luco and Apsel, 1983a) and figures 8c and 8d are the downward reflection coefficients at the sediment-crust boundary (Aki and Richards, 1980, p.150-151) for the model in figure 1. For compressional waves with phase velocities near 8.1 km/s reverberating in the sediments the downward reflection coefficient at the sediment-crust interface has a phase of zero (figure 8c) while the upward reflection coefficient at the ocean-sediment interface has a phase of π (figure 8a). Conversely, for shear waves with high phase velocities reverberating in the sediments the downward reflection coefficient at the sediment-crust interface (figure 8d) has a phase of π while at the ocean-sediment interface (figure 8b) it has a phase of zero. In either case the phase shift between multiples for sediment reverberation is π.

The thickness of the water layer is substantially greater than that of the sediments so the time between multiples due to water reverberation, T_w, is substantially larger than the corresponding time due to sediment reverberation, T_s. In addition, the attenuation in the sediments is far greater than in the water. As a result, the spectral peaks associated with sediment reverberation have a much wider spacing and a substantially larger characteristic width than those associated with water reverberation. Figure 9 illustrates this for a specific case in which we have chosen $T_w = 8.0$ seconds, $T_s = 0.086$ seconds, $\alpha_w = 0.05$ and $\alpha_s = 3.0$. Figure 9a is the wavelet, w(t), and figure 9b is the corresponding power spectrum. The wavelet was chosen to have a simple spectrum to allow the spectral characteristics of the wavetrain due to the two layer reverberations to be easily isolated. The second term in (9), due to sediment reverberation, and its corresponding power spectrum are plotted in figures 9c and 9d. Similarly, the third term of (9), due to water reverberation, and the first 4.0 Hz of its power spectrum are plotted in figures 9e and 9f. The full wavetrain, shown in figure 9g, is a result of the convolution of the functions represented in figures 9a, 9c and 9e (equation(9)). The power spectrum of the full wavetrain, figure 9h, is thereby a result of the multiplication of the spectra in figures 9b, 9d and 9f (equation(10)). The spectrum of the full wavetrain is plotted again in figure 10. The complete spectrum is shown in figure 10b with the position of the spectral peaks associated with sediment reverberation, as defined by (8) with $df_s = \frac{1}{T_s} = 11.63$ Hz, indicated by dashed vertical lines. Figure 10a is a plot of the first 3.0 Hz of this spectrum with dashed lines at frequencies given by (8) for water reverberation with $df_w = \frac{1}{T_w} = 0.125$ Hz.

The seismic spectrum of a simple wavelet reverberating in the oceanic water column and sediment layer therefore consists of widely spaced spectral "humps" due to sediment reverberation superimposed on finely spaced spectral "peaks" associated with water reverberation.

The power spectra of the synthetic P_n wavetrains of figure 4 are presented in figure 11. A Hanning window was applied to each of the time series prior to computing the spectral estimates. The vertical component spectrum is shown in figures 11a-11c while the horizontal component spectrum is shown in figures 11d-11f. The rapid roll-off at frequencies greater than 5.0 Hz is due to a cosine-squared taper applied to the spectrum before Fourier transforming. The complete spectrum, figures 11c for the vertical component and 11f for the horizontal component, illustrate the equally spaced spectral peaks associated with layer reverberation. The reverberation period represented by these peaks is not solely a water reverberation, but rather a reverberation between the free surface and the base of the sediments. This is to be expected because the velocity and density contrast across the ocean-sediment interface for compressional waves is much smaller than that across the sediment-crust interface. Figures 11a and 11d contain the first 3.0 Hz of the spectra with dashed vertical lines at frequencies given by (8) with

$$df = \frac{\bar{V}_p}{2(h_s+h_w)} \tag{11}$$

where $\bar{V}_p$, the average compressional velocity along the path, is defined as

$$\bar{V}_p = \frac{h_s V_p^s + h_w V_p^w}{h_s+h_w} \tag{12}$$

In equations (11) and (12) we have defined h_s and h_w as the sediment and water layer thicknesses respectively, V_p^s as the compressional velocity of the sediments and V_p^w as the acoustic velocity of the water layer. For the velocity model used, figure 1, V_p = 1.5556 km/s and df=0.1728 Hz. The alignment of the peaks in figures 11a and 11d is quite good except near frequencies associated with sediment reverberation.

The two-way travel time for shear waves in the sediments is 0.866 seconds and for compressional waves it is 0.5 seconds. With the high phase velocities comprising the P_n wavetrain (figure 5) the rays are quite steep at the receiver and the two-way travel time in the layer can be taken as the time between multiples. This yields a spacing of spectral peaks for compressional waves reverberating in the sediments of df=2.0 Hz and for shear waves, df=1.1548 Hz. Figures 11b and 11e were obtained by applying a 41-point running mean filter to the complete spectra in figures 11c and 11f. This was done to remove the sharp water reverberation peaks allowing the spectral "humps" associated with sediment reverberation to be isolated. In figure 11b, the vertical

component spectrum, the dashed lines with long bars are at frequencies given by (8) for shear wave reverberation in the sediments and the lines with short bars indicate the predicted frequencies associated with compressional wave reverberation in the sediments. The horizontal component spectrum, figure 11e, contains dashed lines only at the predicted frequencies of shear wave sediment reverberation peaks. The alignment of the peaks with frequencies predicted by (8) is quite good with the exception that the first two peaks are slightly offset to higher frequencies. The pronounced shear wave reverberation peaks on the horizontal component are due to the steep incidence of the rays. In figure 11b the spectral signature of both compressional and shear wave reverberations are evident although the alignment with the predicted frequencies is not as good.

In figure 11 the strongest misalignment of the spectral peaks with respect to the frequencies predicted by (8) occurs where the frequencies for different layer reverberations nearly coincide. In this case coupling between the different modes of oscillation can occur thus shifting the eigenfrequencies to higher values. This is analogous to the shift of spectral peaks due to mode coupling encountered in low frequency seismology. In figure 11b the first two peaks associated with shear wave reverberation and the first peak associated with compressional wave reverberation in the sediments are all at frequencies higher than those predicted by (8) indicating coupling between these modes of reverberation is occurring. Similarly the shift in the first two peaks in figure 11e can also be attributed to mode coupling between P and S wave reverberation in the sediments. Physically, this coupling can take the form of P to S or S to P mode conversion at either the ocean-sediment or sediment-crust boundary.

To further illustrate the presence of sediment reverberation within the P_n wavetrain we have examined the F integrands of (1) for several Green's functions. The moduli of the F integrands corresponding to the vertical normal stress $\sigma_{220}(\omega,p)$ and the horizontal normal stress $\sigma_{221}(\omega,p)$ are plotted in figure 12 for the ray parameter range comprising the P_n wavetrain.

Figure 12a is an F integrand corresponding, given the source representations (Shaw and Orcutt, 1984), to vertical displacement. The three dominant ridges at 1.0, 3.0 and 5.0 Hz are associated with compressional wave reverberation in the sediments (equation (8)). Similarly, figure 12b corresponds to horizontal displacement and the ridges at 0.6, 1.7, 2.9, 4.0, 5.2 and 6.4 Hz are associated with shear wave reverberation in the sediments. These ridges are also quite clearly seen in figure 2c for ray parameters less than 0.13 s/km. To verify our interpretation of these ridges we reduced the sediment thickness by a factor of two and recomputed the integrands. The effect of this was to increase the spacing of the ridges by a factor of two thereby validating the interpretation that these ridges are the result of sediment

reverberation.

The narrow spikes separated by less than 0.2 Hz in both figures 12a and 12b are a result of the reverberation between the free surface and the base of the sediments. The extremely spiked nature of these peaks is due to the high value of Q in the water layer whereas the highly attenuating sediments have much broader spectral peaks (table 3).

Through computation of the Fourier transform of the $F(\omega,p)$ integrands, delay time wavefields, $F(\tau,p)$, can be generated. Figure 13 is an example of a delay time wavefield for the vertical normal stress, σ_{220}. The large, relatively straight, ridges at ray parameters less than 0.12 s/km are the first and second water reverberations. These ridges curve sharply inward at a ray parameter of 0.122 s/km corresponding to the reciprocal of the compressional wave velocity at the source. The ridges delineate the delay time curves for the direct ray plus one water bounce and the direct ray plus two water bounces. Figure 13 thus illustrates the shingling effect or harmonic nature of delay time curves for paths differing by a single layer reverberation (McMechan and Ottolini, 1980).

The depletion of high frequency energy late in the wavetrain relative to the early part is another feature of layer reverberation (figure 4a). The first arrivals are impulsive mantle reflected body waves that have undergone only a small number of layer reverberations. These arrivals are most easily interpreted in terms of geometrical rays which have traveled discrete paths between source and receiver. In the case where several different layer reverberations are involved the number of possible ray paths for fixed source and receiver locations is a strongly increasing function of travel time. This implies that late in the wavetrain the decomposition of arrivals into separate rays is inappropriate. Thus the latter part of the wavetrain is the result of the constructive interference of multiply reflected P and SV body waves and is more suitably thought of in terms of a modal description (Brune, 1964).

The constructive interference late in the wavetrain is manifested in the frequency domain as the isolation of peaks at frequencies common to all layer reverberations as well as the wavelet spectrum. Figure 14 is a schematic representation of this effect. Figure 14a is an idealized wavelet spectrum and 14b and 14c represent the spectra associated with compressional and shear wave reverberation in the sediments respectively (equation (10)). Figure 14d results from the multiplication of 14a-14c and represents the spectrum of a wavetrain comprised of P and S wave reverberations in the sediments. The conspicuous peak at 0.8 Hz has been isolated due to constructive interference of the two modes of reverberation and constitutes the dominant frequency contained in the latter part of the wavetrain. In the case of the synthetic P_n wavetrain this isolation occurs predominantly near 0.6 Hz but more generally between 0.6 and

1.7 Hz (figures 11c and 11f). As can be seen in figure 14, the constructive interference phenomenon can also have the effect of shifting the spectral peaks. This shift, however, is not in the same direction for all the peaks. Note, for example, that the first two S wave sediment reverberation peaks are on opposite flanks of the first P wave sediment reverberation peak and therefore will necessarily be shifted in opposite directions. It is for this reason that we have attributed the shift in the spectral peaks of figures 11b and 11e to mode coupling.

COMPARISON WITH DATA

Data were collected during the 1983 Ngendei Seismic Experiment by an ocean bottom seismometer (OBS) array in the Southwest Pacific (23° 49'S, 165° 32'W), approximately 900 km east of the Tonga trench. Each OBS contained one vertical and two horizontal seismometers and a hydrophone. A complete description of the OBS array at the Ngendei site is given by Adair, et al. (1985).

Examples of vertical component seismograms collected during the experiment are shown in figure 15 and seismograms recorded by the hydrophones are shown in figure 16. Note that figures 15b-15e correspond to the same events, recorded by the vertical component instrument, as figures 16b-16e which were recorded by the hydrophone. In figures 15 and 16 the first arriving group of energy is the P_n wavetrain while the second arriving group is the beginning of the S_n wavetrain. The durations of the P_n wavetrains are on the order of 80 seconds and extend into the onset of S_n. Figure 17 is a comparison of the synthetic P_n wavetrain, after including the instrument response, to data from the Ngendei site. The model used in the generation of the synthetic seismograms is quite different from the Ngendei site so a direct comparison of the synthetics to the data is not intended. The general characteristics of the P_n wavetrain can, however, be explained in terms of properties observed in the synthetics. Figure 17a is the synthetic P_n wavetrain of figure 4a before including the instrument response and 17b includes the OBS vertical component response. Figure 17c is the vertical component seismogram of figure 15d. Strong water reverberations are quite evident in both the synthetics and the data as well as the predominance of low frequencies late in the wavetrain. Figure 17d was obtained by approximating the pressure response through differentiation in the frequency domain of the synthetic P_n wavetrain in figure 17a and then convolving with the hydrophone response. Figure 17e is the hydrophone data depicted in figure 16d. A significant portion of the difference between the synthetics and the data is due to the limitation of the computation of the synthetics to frequencies less than 6.4 Hz. The non-decaying nature of the synthetic wavetrain could be partially explained in this manner; however, comparison with figures 15b, 15c, 15e and 16b indicates that this feature is also clearly seen in data.

The amplitudes of the synthetic P_n wavetrains, after including the instrument response, are well within an order of magnitude of the data amplitudes. This suggests that the high value of Q observed for P_n propagation does not require an anomalously high Q lithosphere waveguide and that the model proposed for P_n propagation is appropriate. The synthetics were computed up to a Nyquist frequency of only 6.4 Hz therefore, prior to computing the amplitudes, the data were bandpassed between 0.0 and 6.4 Hz. Table 4 lists the maximum amplitudes in the first 20 seconds of three separate recordings of the same event. The event was located by the National Earthquake Information Service (NEIS) and had an epicenter of (21.592° S, 174.179° W), near the Tonga Islands. This yields an epicentral range of 920 km and, assuming a fault strike parallel to the Tonga trench, an azimuth relative to the receiver of nearly 90°. The magnitude of the event was estimated at 5.8 with a focal depth of 32 km. The best fit double couple source, published by NEIS, had a moment of 2.6×10^{24} dyne-cm. To obtain the maximum amplitude in the synthetic P_n wavetrain we used a thrust fault source with an azimuth relative to the receiver of 90° at an epicentral range of 900 km. The moment determined by NEIS was used and the remaining fault parameters are the same as those described for figure 3. The resulting maximum amplitude for the vertical component P_n wavetrain is 0.420 volts. Although direct comparison with table 4 is inappropriate due to differences in fault orientation, focal depth and model parameters, the amplitudes of the synthetics are within a factor of 3 of the data amplitudes.

As discussed in the previous section the dominance of lower frequencies late in the wavetrain can be accounted for in terms of the constructive interference between different layer reverberations (figure 14). Figures 15b-15e quite clearly exhibit this feature and the subdued nature of this behavior on the hydrophone records (figure 16) is due to the response of the instrument. The hydrophone is a more narrow band instrument than the vertical component seismometer as illustrated by the instrument response curves in figure 18. The hydrophone thus acts essentially as a high pass filter thereby selectively attenuating the latter part of the wavetrain. The more rapid decay of the P_n wavetrains recorded by the hydrophone than those recorded by the OBS vertical component seismometer is clearly demonstrated in the data. Comparison of figures 15b-15e to figures 16b-16e indicates that the water reverberations are more clearly shown on the hydrophone recordings while the low frequencies late in the wavetrain, indicative of sediment reverberations, are better recorded by the OBS vertical component instrument.

To quantify the result that the latter part of the wavetrain is dominated by lower frequencies, figure 19 presents the seismogram pictured in figure 15c bandpassed into three separate frequency bands, each two octaves wide. Figure 19a is the full seismogram and the pass bands used for 16b-16d are 0.25 to 1.0 Hz, 1.0 to 4.0 Hz and 4.0 to 16.0 Hz respectively. This figure clearly demonstrates that the decay rate of

the P_n wavetrain is an increasing function of frequency with the two lower frequency bands exhibiting almost no amplitude decay. This is in direct contrast to the results of Menke, et al. (1984) who show for a one-dimensional, randomly layered acoustic medium, the fall-off rate of forward-scattered coda decreases with increasing frequency. The forward-scattering model thus does not fit these data accurately while the gross characteristics of the P_n wavetrain can be explained simply as near-receiver layer reverberations.

The spectral characteristics of layer reverberation presented in the previous section can be examined in the data. The Ngendei site was also the location of Hole 595B of Deep Sea Drilling Project (DSDP) leg 91. The depth of the oceanic water column at the site is 5.5 km and, from core sample measurements, the sediment thickness is 70 meters with a compressional velocity of 1.6 km/s (Kim, et al., 1985). To calculate the predicted positions of spectral peaks associated with water reverberation we have used a layer depth of 5.55 km and a velocity of 1.5 km/s yielding a spacing of $df_w = 0.1351$Hz. The layer depth needed to fit the spectral peaks indicates, as was the case in the synthetics, that the reverberation is taking place between the free surface and the base of the sediments. For compressional wave reverberation in the sediments the predicted frequencies of spectral peaks can be calculated from (8) where df_s is the reciprocal of the two-way travel time in the layer. For the Ngendei site the spectral peak spacing is $df_s = 11.43$Hz.

As was mentioned previously, the hydrophone was better able to record water reverberations while the OBS vertical component was more sensitive to sediment reverberations. This was also evident in the power spectra of seismograms recorded by the two instruments. Figure 20 is the power spectrum of the P_n wavetrain pictured in figure 15b. Figure 20a was obtained by applying a 41-point running mean filter to the complete spectrum shown in figure 20b. In both figures, dashed lines indicate the frequencies predicted by (8) of spectral peaks associated with P wave reverberation in the sediments. Comparison with the schematic spectral representation of sediment reverberation in figure 10b reveals the predominance of this feature in the P_n wavetrain. The wide spacing and large characteristic width, due to the low value of Q in the sediments, of the spectral peaks is quite apparent. The isolated peaks in figure 20 at 34.3 and 50.7 Hz are due to instrument noise.

Figure 21 is the power spectrum of the P_n wavetrain shown in figure 16e. Figure 21b is the complete spectrum and in 21a the first 3.0 Hz are plotted with vertical lines at frequencies predicted by (8) for water reverberation. Comparison with figures 11a, 11d and 10a illustrates that the spectral signature of the water reverberations is quite pronounced in the data.

While in figures 20 and 21 we have chosen examples which best illustrate the layer reverberations, these features were present to a

lesser degree in nearly all of the data. Figure 22 is the power spectrum of the seismogram in figure 15a. This was recorded on the OBS vertical component and does exhibit features common to both sediment and water reverberations. Figures 23a and 23b are the first 3.0 Hz of spectra of the hydrophone recordings in figures 16a and 16c and also exhibit a fairly high degree of alignment with frequencies predicted by (8) for water reverberations. The P_n wavetrain in figure 16a has a relatively short duration in comparison with the other data. Therefore fewer time points were used in the construction of the power spectrum (figure 23a) yielding a poorer frequency resolution.

It should be noted that in none of the P_n spectra we have analyzed was there a confinement of energy to a small frequency range between 6 and 10 Hz as asserted by Ouchi (1981). The solid curve in figure 24b is the power spectrum, after correcting for the instrument response, of the P_n wavetrain in figure 24a which was recorded by the borehole seismometer at Hole 595B. The noise spectrum is depicted in this figure as a dashed curve. We have chosen to use data recorded by the borehole seismometer in this figure because of the enhancement of the signal to noise ratio for this instrument relative to the sea floor seismometers (Shearer, et al., 1985). The spectra are somewhat unreliable at frequencies less than 0.1 Hz, however, the data spectrum is well above the noise spectrum at frequencies between 1.0 and 5.0 Hz. The lack of power at low frequencies observed by Ouchi may be due to a combination of the instrument response and sediment reverberation peaks. For the data we have collected the first P wave sediment reverberation peak is at 5.7 Hz and when combined with the instrument response could produce a broad peak in power between 5 and 10 Hz.

The observation that the apparent velocity of P_n is generally higher at epicentral ranges less than approximately 30° than at ranges in excess of 30° (Walker, 1981) can be explained qualitatively in terms of the curvature of the earth. As a simple example, the grazing ray on the lithosphere-asthenosphere boundary for a uniform, 100 km thick lithosphere arrives at an epicentral range of approximately 20°. At distances greater than this the first arriving ray that remains in the lithosphere must include one free surface reflection and would thus have a correspondingly lower group velocity. The first arriving P wave at large distances is a normal refracted arrival that penetrates the low Q asthenosphere constituting the commonly observed low frequency forerunner of the P_n wavetrain (Latham, et al., 1966). In this case the first arrival of the high-frequency P_n phase would be analogous to the seismic phase PP, which has remained in the lithosphere. The group velocity of this high-frequency phase is thus slower at large epicentral distances. A similar interpretation was made by Menke, et al. (1980) in terms of whispering gallery phases (WGP's). At distances in excess of 20° to 30° the first ray of the whispering gallery group (WG1) is shadowed by their low velocity asthenosphere and the first arrival of the oceanic P_n phase is the second whispering gallery phase (WG2) which

includes an additional upward reflection at the MOHO. This ray does not penetrate as deep into the lithosphere and thus has a correspondingly lower group velocity than WG1.

A more data intensive investigation of the characteristics of P_n wavetrains will be the subject of a future paper. This will include a comparison of P_n wavetrains recorded on the sea floor to those recorded by a borehole seismometer at the same site.

CONCLUSION

The synthesis of realistic oceanic P_n phases was accomplished using wavenumber integration with a model that contained no lateral inhomogeneity. Wavetrains with durations in excess of 80 seconds were generated without the need to include scattering. While it is not our intent to assert that the oceanic lithosphere contains no lateral heterogeneity and that all the features of the oceanic P_n wavetrain can be accounted for in terms of the model in figure 1, we have shown that the duration and many characteristics of the oceanic P_n phase can be explained in the absence scattering.

The spectral characteristics of the P_n wavetrain can be explained rather simply in terms of near-receiver oceanic and sediment reverberations. In terms of a ray path description, the onset of P_n can be thought of as a refraction from the lower lithosphere with multiple near-receiver reverberations within the oceanic water column and sediment layer. The latter part of the P_n wavetrain is more suitably characterized as the constructive interference of the different layer reverberations which could, in part, occur at any point along the propagation path.

The low spatial attenuation observed for P_n propagation is associated with the presence of the high Q water column and does not require an intrinsicly high Q lithosphere. Certainly the value of Q in the lithosphere is greater than that in the highly attenuating underlying asthenosphere; however, relatively low values in agreement with seismic refraction studies are sufficient to propagate this phase to teleseismic distances.

The observation of frequencies in excess of 15 Hz in the P_n wavetrain is due to the impulsive character of reverberations and the extremely high value of Q in the water column. In the data we have examined there is no strong confinement of energy between 6 and 10 Hz as asserted by Ouchi (1981) and the need for a lithosphere model that accommodates this feature seems unwarranted. The excitation of the oceanic P_n phase does not require features of the oceanic lithosphere such as low velocity channels, anomalously high Q values or thin high velocity lenses but rather can be explained in terms of simple models with

monotonically increasing velocity-depth profiles containing no lateral heterogeneity.

REFERENCES

Abramowitz, M. and I. A. Stegun, (1964). Handbook of Mathematical Functions, U.S. National Bureau of Standards.

Adair, R. G., J. A. Orcutt, T. H. Jordan, (1985). Preliminary analysis of ocean bottom and sub-bottom microseismic ambient noise during the Ngendei Experiment, Initial Rep. Deep Sea Drill. Proj., Leg 91.

Aki, K., (1972). Scaling law of earthquake source-time function, Geophys. J. R. Astr. Soc., 31, 3-25.

Aki, K. and P. G. Richards, (1980). Quantitative Seismology: Theory and Methods, W. H. Freeman, San Francisco, Calif.

Apsel, R. J., (1979). Dynamic Green's functions for layered media and applications to boundary-value problems, Ph.D. thesis, 349 pp., University of California, San Diego, La Jolla.

Bracewell, R. N., (1978). The Fourier Transform and its Applications, McGraw-Hill, Inc., New York.

Brune, J., (1964). Travel times, body waves, and normal modes of the earth, Bull. Seism. Soc. Am., 54, 2099-2128.

Brune, J., (1966). P and S wave travel times and spheroidal normal modes of a homogeneous sphere, J. of Geophys. Res., 71, 2959-2965.

Filon, L. N. G., (1928). On a quadrature method for trigonometric integrals, Proc. R. Soc. Edinb., 49, 38-47.

Frazer, L. N. and J. F. Gettrust, (1984). On a generalization of Filon's method and the computation of the oscillatory integrals of seismology, Geophys. J. R. Astr. Soc., 76, 461-481.

Fuchs, K. and G. Müller, (1971). Computation of synthetic seismograms with the reflectivity method and comparison with observations, Geophys. J. R. Astr. Soc., 23, 417-433.

Fuchs, K. and K. Schulz, (1976). Tunneling of low-frequency waves through the subcrustal lithosphere, J. Geophys., 42, 175-190.

Gettrust, J. F. and L. N. Frazer, (1981). A computer model study of the propagation of the long-range PN phase, Geophys. Res. Lett., 8, 749-752.

Hart, R. and F. Press, (1973). S_n velocities and the composition of the lithosphere in the regionalized Atlantic, J. of Geophys. Res., 78, 407-411.

Isacks, B. and M. Barazangi, (1973). High frequency shear waves guided by a continuous lithosphere descending beneath western South America, Geophys. J. R. Astr. Soc., 33, 129-139.

Johnson, R. and R. Norris, (1970). T-wave generation mechanisms, Hawaii Institute of Geophysics Rept. HIG-70-7, 16 pp.

Kennett, B., (1974). Reflections, rays and reverberations, Bull. Seism.

Soc. Am., 64, 1685-1696.

Kim, I. I., D. K. Smith, J. A. Orcutt, T. H. Jordan and H. W. Menard, (1985). Seismic reflection site survey: correlation with physical properties, leg 91, Deep Sea Drilling Project, Initial Rep. Deep Sea Drill. Proj., Leg 91.

Kind, R., (1974). Long range propagation of seismic energy in the lower lithosphere, J. Geophys., 40, 189-202.

Latham, G. V. and G. H. Sutton, (1966). Seismic measurements of the ocean floor, J. of Geophys. Res., 71, 2545-2573.

Luco, J. E. and R. J. Apsel, (1983a). On the Green's functions for a layered half-space. Part I, Bull. Seism. Soc. Am., 73, 909-929.

Luco, J. E. and R. J. Apsel, (1983b). On the Green's functions for a layered half-space. Part II, Bull. Seism. Soc. Am., 73, 931-951.

McCreery, C., (1981). High-frequency PN, SN phases recorded by ocean bottom seismometers on the Cocos plate, Geophys. Res. Lett., 8, 489-492.

McMechan, G. and R. Ottolini, (1980). Direct observation of a $p-\tau$ curve in a slant stacked wave field, Bull. Seism. Soc. Am., 70, 775-789.

Menke, W. H. and P. G. Richards, (1980). Crust-mantle whispering gallery phases: a deterministic model of teleseismic P_n wave propagation, J. of Geophys. Res., 85, 5416-5422.

Menke, W. and R. Chen, (1984). Numerical studies of the coda falloff rate of multiply scattered waves in randomly layered media, Bull. Seism. Soc. Am., 74, 1605-1621.

Müller, G., (1970). Exact ray theory and its application to the reflection of elastic from vertically inhomogeneous media, Geophys. J. R. Astr. Soc., 21, 261-281.

Northrop, J., (1972). National Academy of Sciences report: The Great Alaska Earthquake of 1964: Oceanography and Coastal Engineering; T-phases, National Academy of Sciences, Washington D.C.

Ouchi, T., (1981). Spectral structure of high frequency P and S phases observed by OBS's in the Mariana Basin, J. Phys. Earth, 29, 305-326.

Ouchi, T., (1983). Separation of high-frequency P_N phases and mantle refracted P phases at distances between 6° and 18° in the western Pacific by ocean bottom seismograph array, Geophys. Res. Lett., 10, 1069-1072.

Shaw, P. and J. A. Orcutt, (1984). Propagation of PL and implications for the structure of Tibet, J. of Geophys. Res., 89, 3135-3152.

Shearer, P. M., R. G. Adair, J. A. Orcutt and T. H. Jordan, (1985). Simultaneous borehole and ocean bottom seismometer recordings of earthquakes and explosions--results from the 1983 Ngendei Experiment at DSDP Hole 595B, Initial Rep. Deep Sea Drill. Proj., Leg 91.

Spudich, P. and J. A. Orcutt, (1980). Petrology and porosity of an oceanic crustal site: results from wave form modeling of seismic refraction data, J. of Geophys. Res., 85, 1409-1433.

Sutton, G., C. McCreery, F. Duennebier and D. Walker, (1978). Spectral analysis of high-frequency PN, SN phases recorded on ocean bottom

seismographs, Geophys. Res. Lett., 5, 745-747.

Talandier, J. and M. Bouchon, (1979). Propagation of high frequency P_n waves at great distances in the Central and South Pacific and its implications for the structure of the lower lithosphere, J. of Geophys. Res., 84, 5613-5619.

Walker, D., (1977a). High-frequency P_n phases observed in the Pacific at great distances, Science, 19, 257-259.

Walker, D., (1977b). High-frequency P_n and S_n phases recorded in the Western Pacific, J. of Geophys. Res., 82, 3350-3360.

Walker, D., C. McCreery, G. Sutton and F. Duennebier, (1978). Spectral analyses of high-frequency P_n and S_n phases observed at great distances in the Western Pacific, Science, 199, 1333-1335.

Walker, D., (1981). High-frequency PN, SN velocities: some comparisons for the Western, Central and South Pacific, Geophys. Res. Lett., 8, 207-209.

Walker, D., (1982). Oceanic PN/SN phases: a qualitative explanation and reinterpretation of the T-phase, Hawaii Institute of Geophysics Rept. HIG-82-6, 19 pp.

$\bar{\beta}$	Shear wave velocity of the reference layer
p	Ray parameter
ω	Angular frequency
Z	Receiver depth
Z^s	Source depth
r	Epicentral range
K	Dimensionless wavenumber = $\bar{\beta}p$
Z_0	Normalized receiver depth = $\frac{\omega Z}{\bar{\beta}}$
Z_0^s	Normalized source depth = $\frac{\omega Z^s}{\bar{\beta}}$
r_0	Normalized epicentral range = $\frac{\omega r}{\bar{\beta}}$

TABLE 1. Variable definition.

LAYER NUMBER	V_p (km/s)	V_s (km/s)	DENSITY (Mg/m^3)	THICKNESS (km)
1	1.5000	0.0000	1.0000	4.0
2	2.0000	1.1548	1.0096	0.5
3	5.5000	3.1760	2.3350	1.0
4	6.4018	3.6962	2.6756	0.5
5	6.8032	3.9279	2.8265	2.0
6	7.4058	4.2759	3.0527	2.0
7	8.1654	4.7144	3.3232	31.6
8	8.1807	4.7233	3.2975	31.6
9	8.1961	4.7322	3.2717	31.6
10	8.2038	4.7366	3.2588	∞

TABLE 2. Model representation.

LAYER	DEPTH	Q_p	Q_s
Water	0-4 km	50,000	----
Sediments	4-4.5 km	200	100
Crust/Upper Mantle	>4.5 km	450	225

TABLE 3. Quality factors Q_p and Q_s used in the synthetic seismogram calculation.

OBS	EVENT	MAX. AMPLITUDE (Volts)
Janice	41	0.76
Karen	24	1.44
Suzy	25	1.38

TABLE 4. Gain corrected maximum amplitudes in volts for a magnitude 5.8 earthquake at an epicentral range of 920 km.

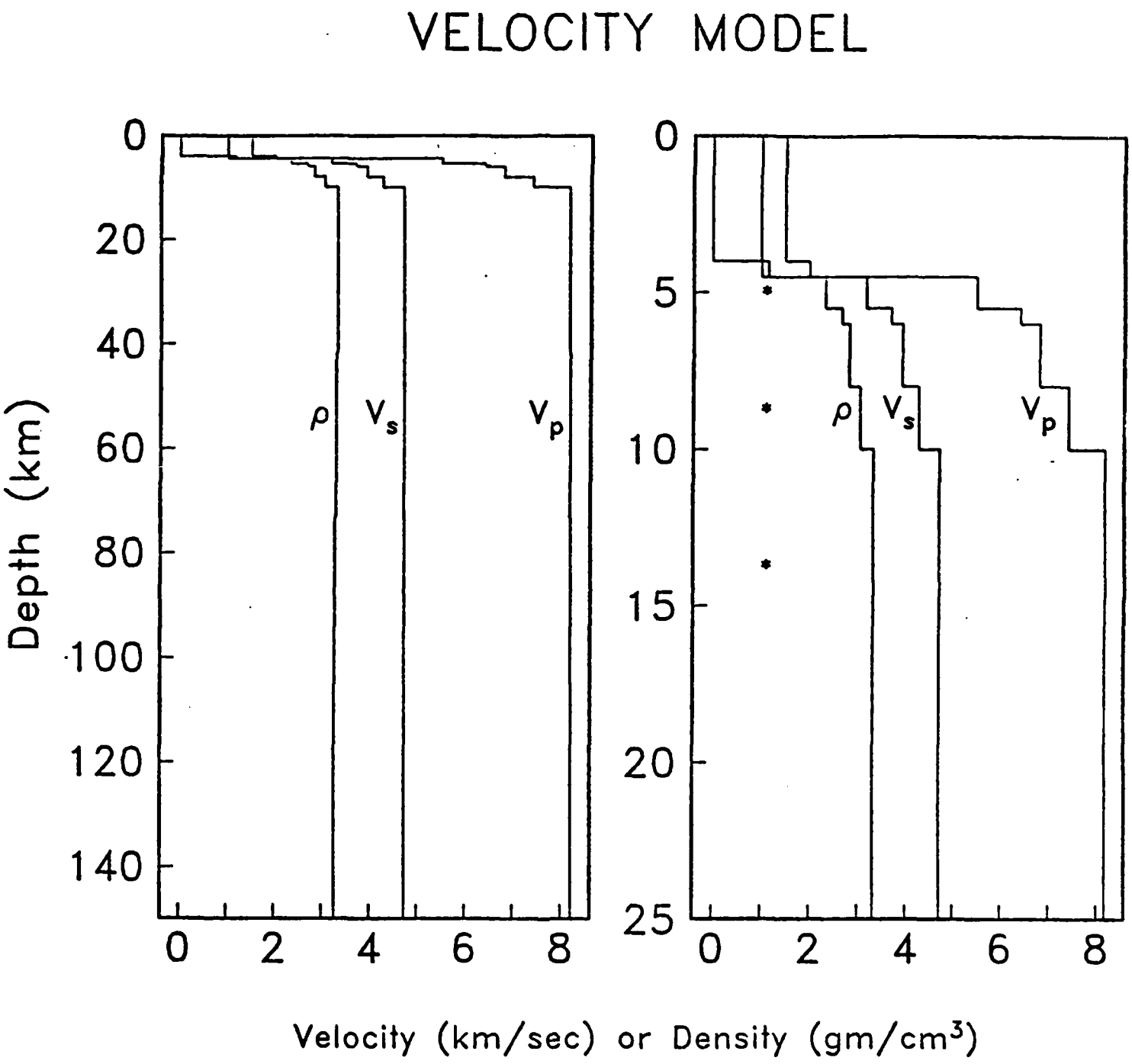


FIGURE 1. Velocity and density model. The left side shows the entire model while on the right the depth scale is expanded to show detail in the crust. Asterisks indicate source depths. The model is from Gettrust and Frazer (1981).

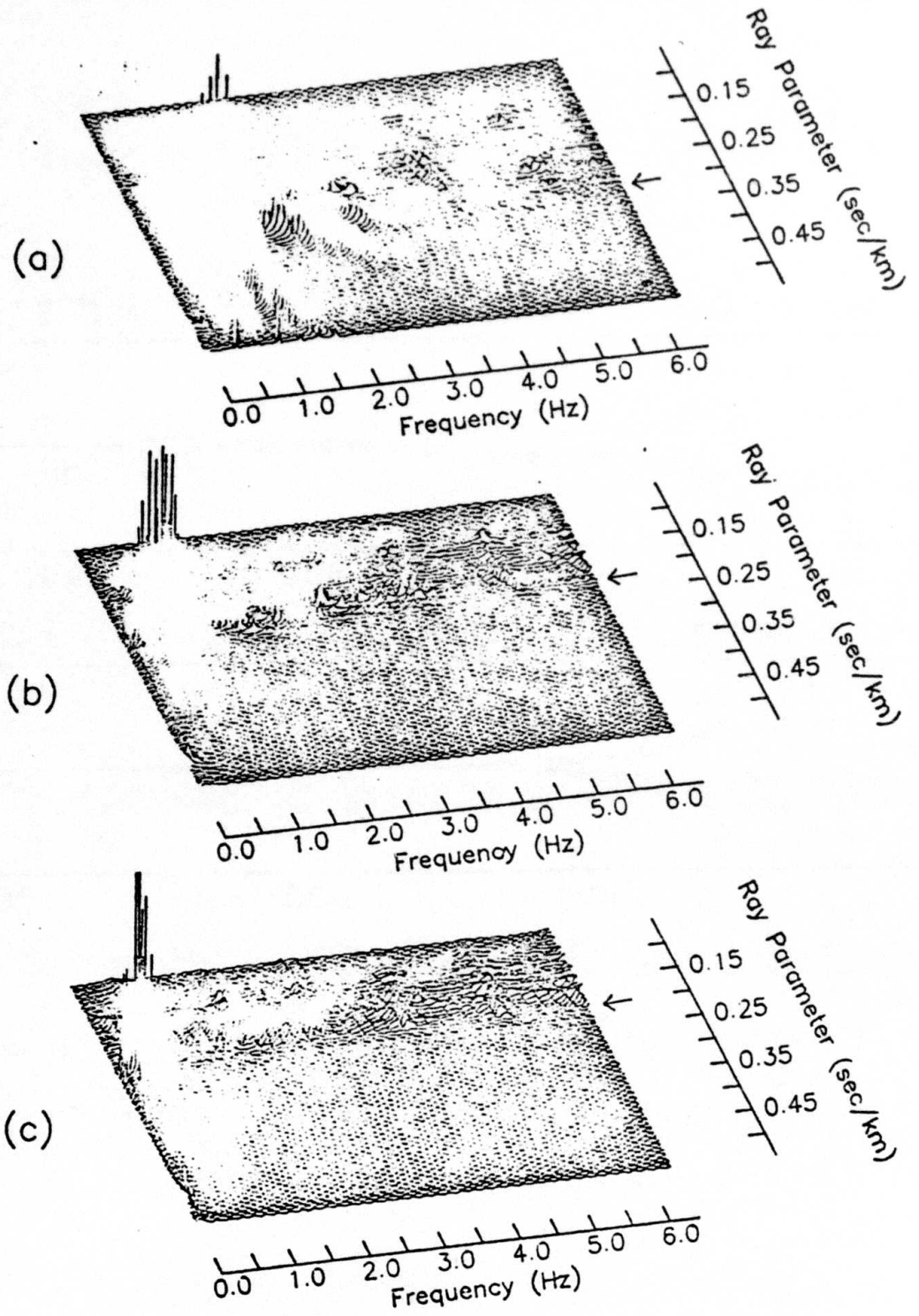


FIGURE 2. Modulus of the horizontal normal stress, $\sigma_{221}(\omega,k)$ at source depths of a) 5.25 km, b) 9.0 km and c) 14.0 km. Arrows indicate V_s^{-1} of the layer containing the source.

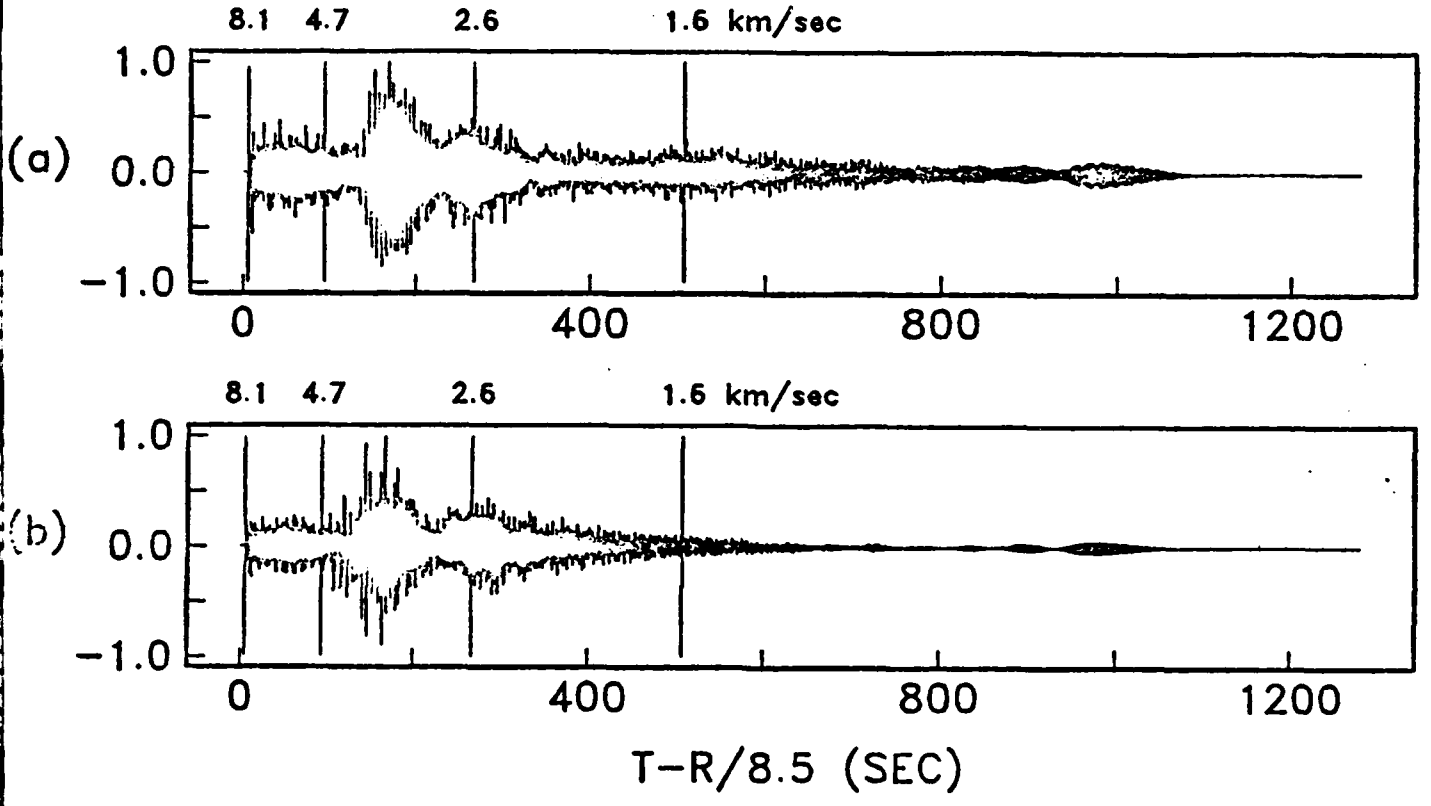


FIGURE 3. Complete synthetic seismograms for a thrust fault source at 14.0 km depth at an epicentral range of 1000 km. a) Vertical component, b) horizontal component rotated 25 degrees clockwise from the radial direction. Velocities of 8.1, 4.7, 2.6 and 1.6 km/sec are indicated.

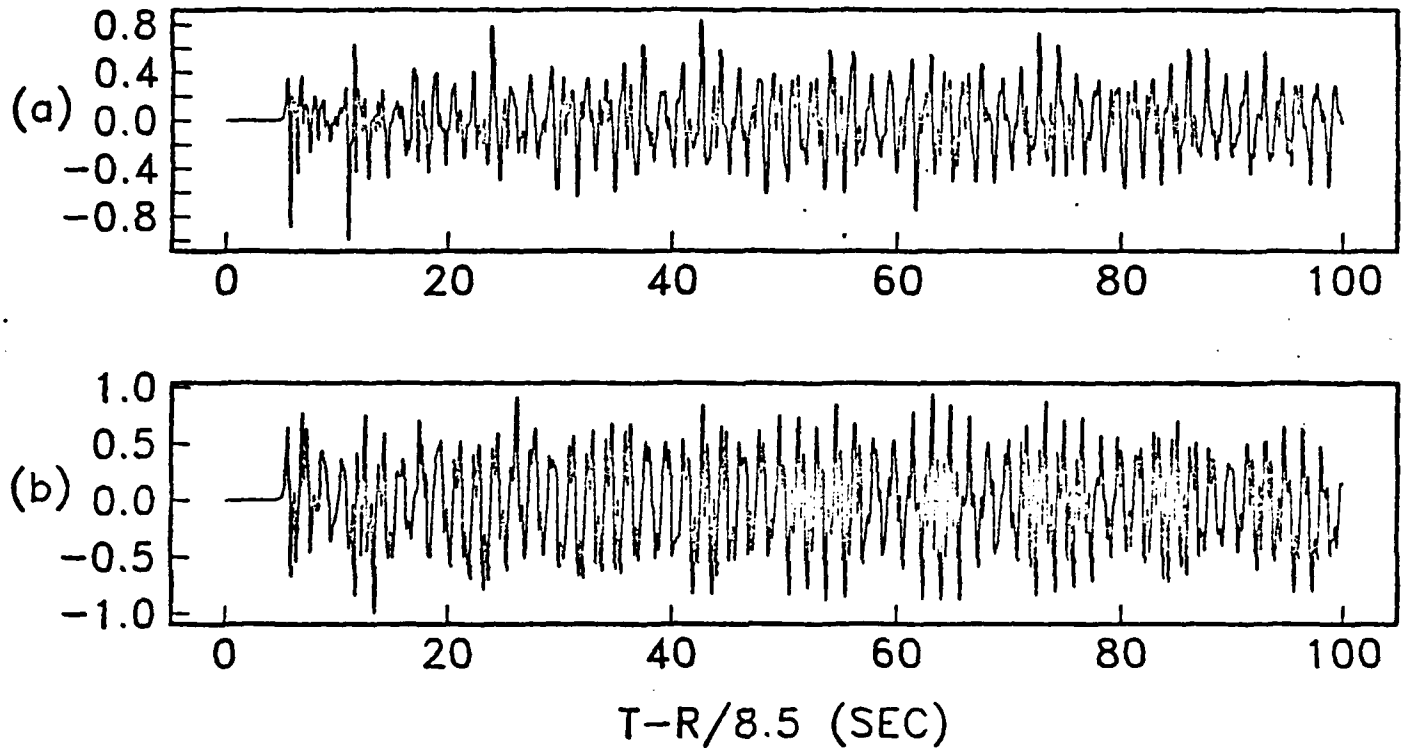


FIGURE 4. Synthetic P_n wavetrain. Contains the first 100 seconds of the records in figure 3. a) Vertical component and b) horizontal component.

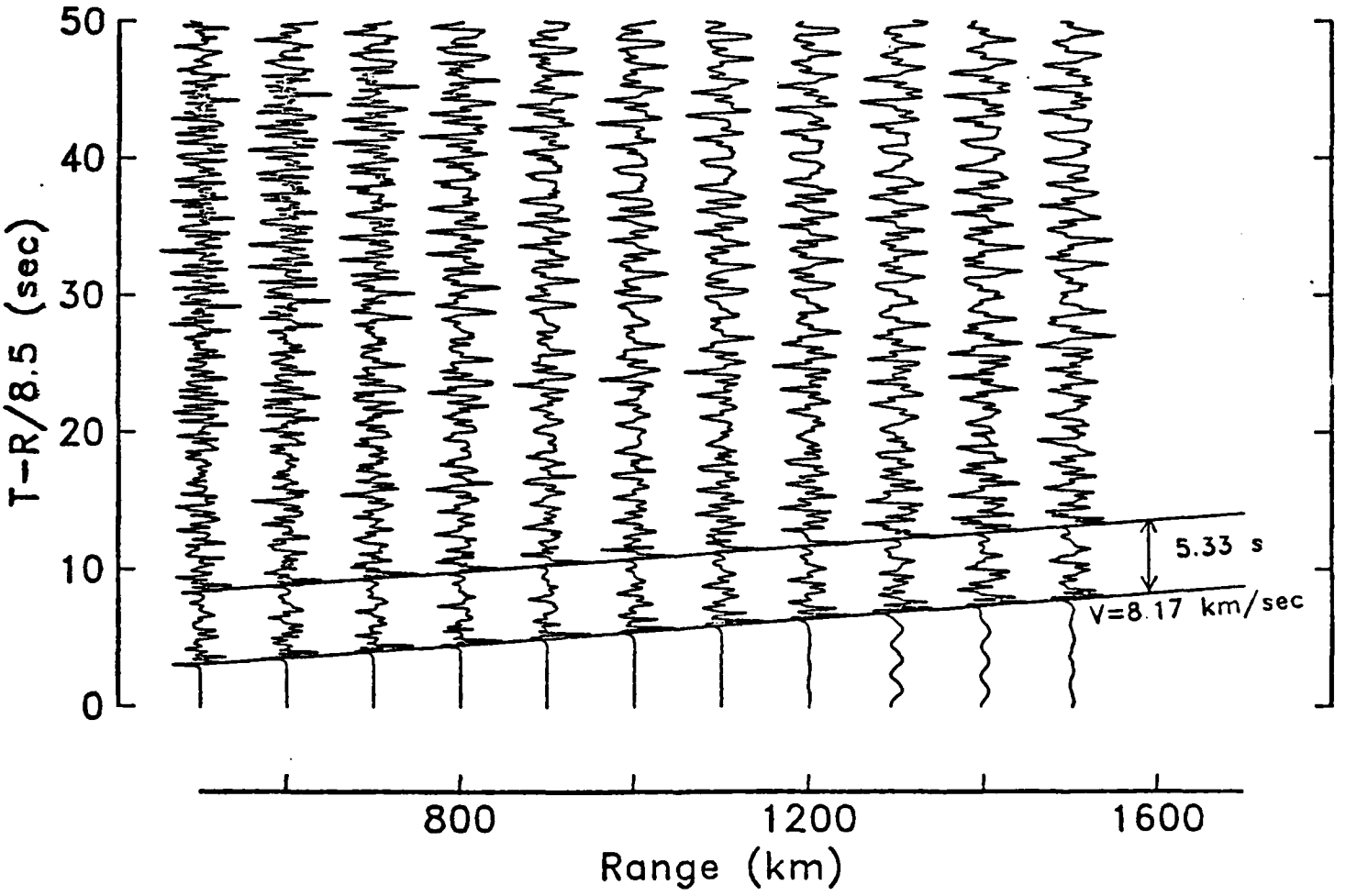


FIGURE 5. Record section of the vertical normal stress, σ_{zz0}, at 14.0 km depth. Lines are drawn with an inverse slope of 8.17 km/sec separated by the two-way travel time in the water column, 5.33 sec.

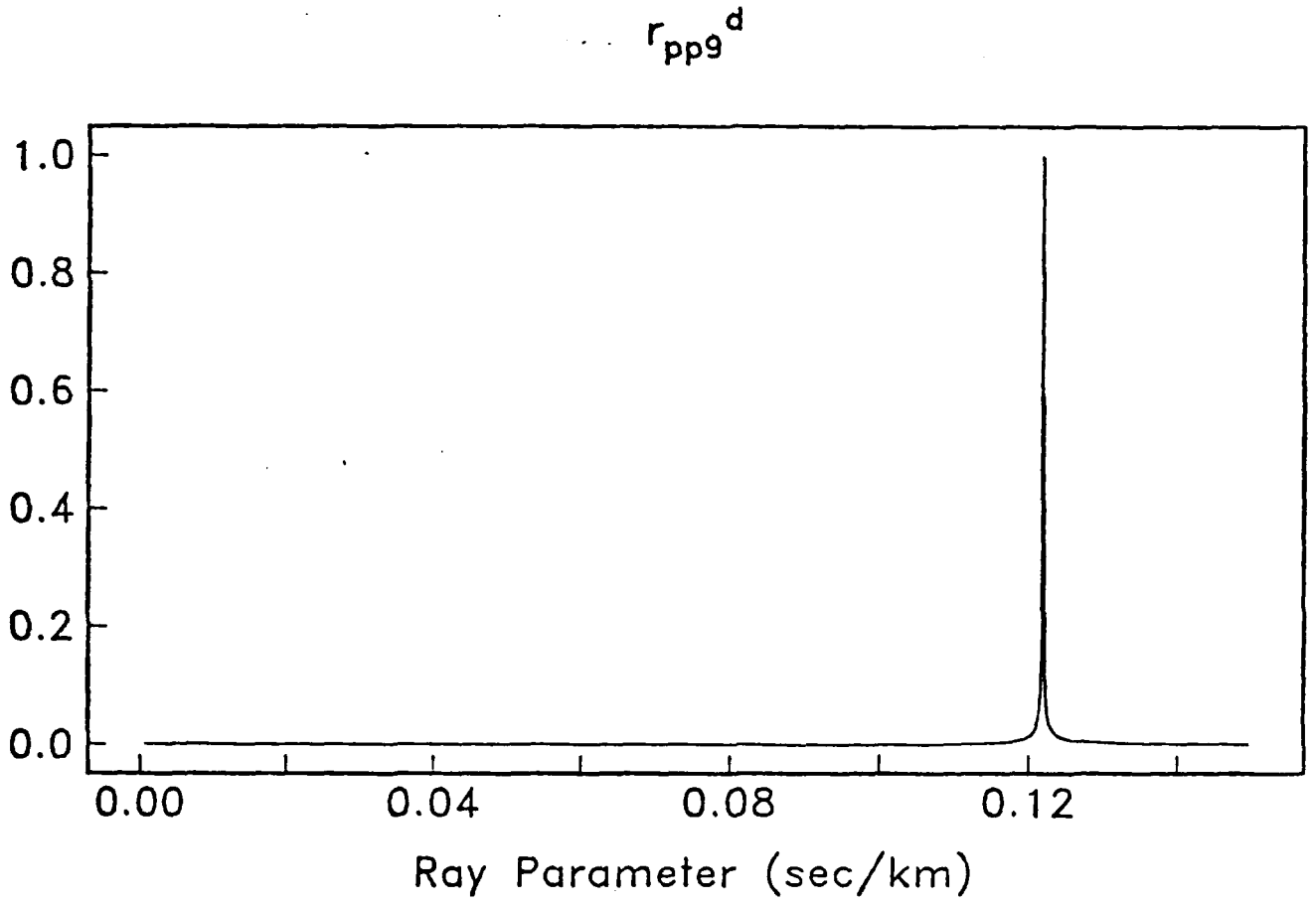


FIGURE 6. Modulus of the downward reflection coefficient, $r_{pp}{}^{d}$, at the interface between the reflection stack and the infinite halfspace (interface 9). For pre-critical rays ($p < 0.1219$ sec/km) this boundary is an extremely poor reflector.

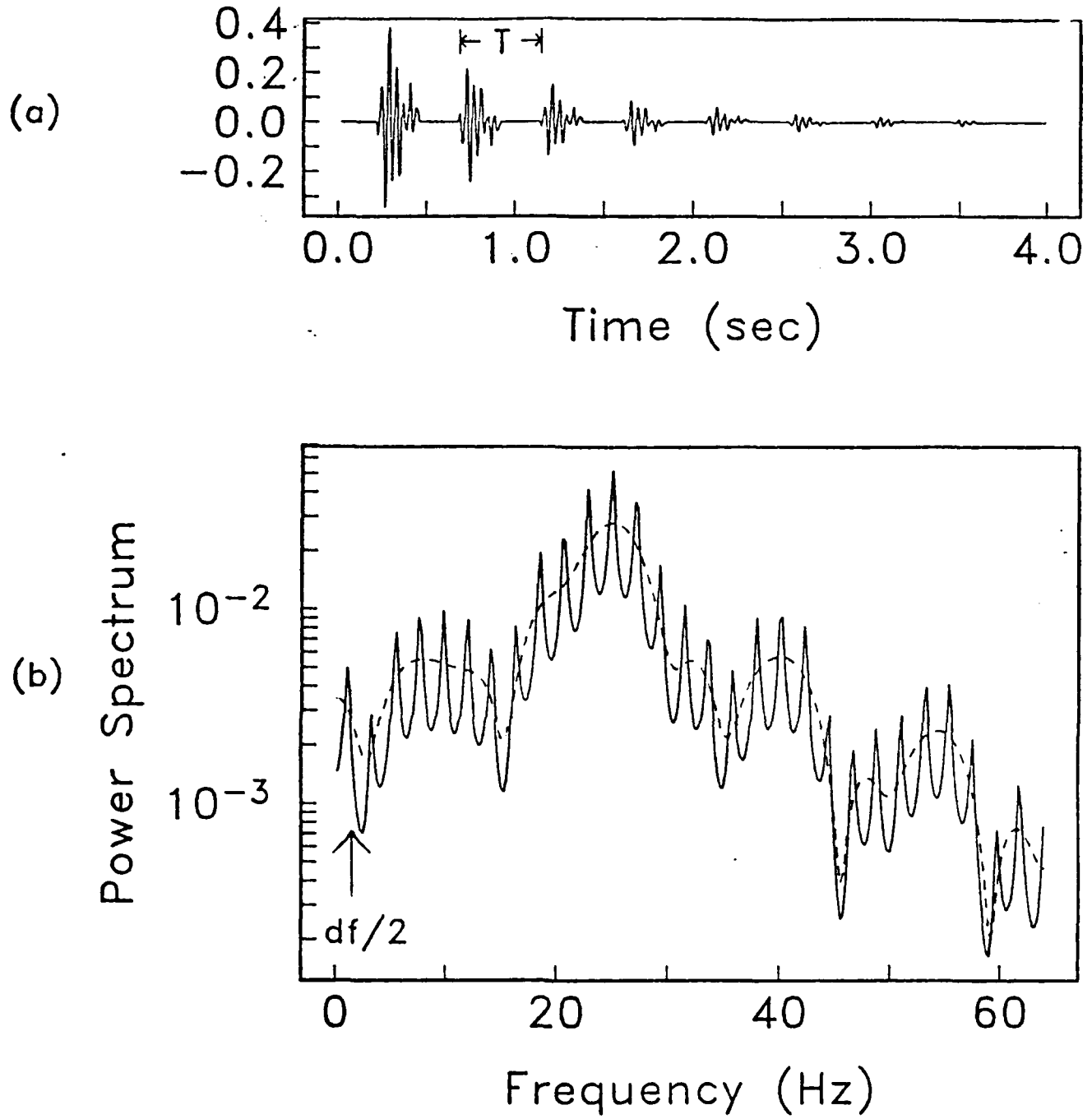


FIGURE 7. Power spectrum of a reverberating wavelet. a) Wavetrain comprised of a reverberating wavelet with a spacing between multiples of T=0.46 seconds and attenuation factor, α=1.0. b) Power spectrum of the wavetrain in (a) superimposed on the spectrum of a single wavelet (dashed). The peaks are equally spaced with df=1/T=2.17 hz and are offset by an amount df/2.

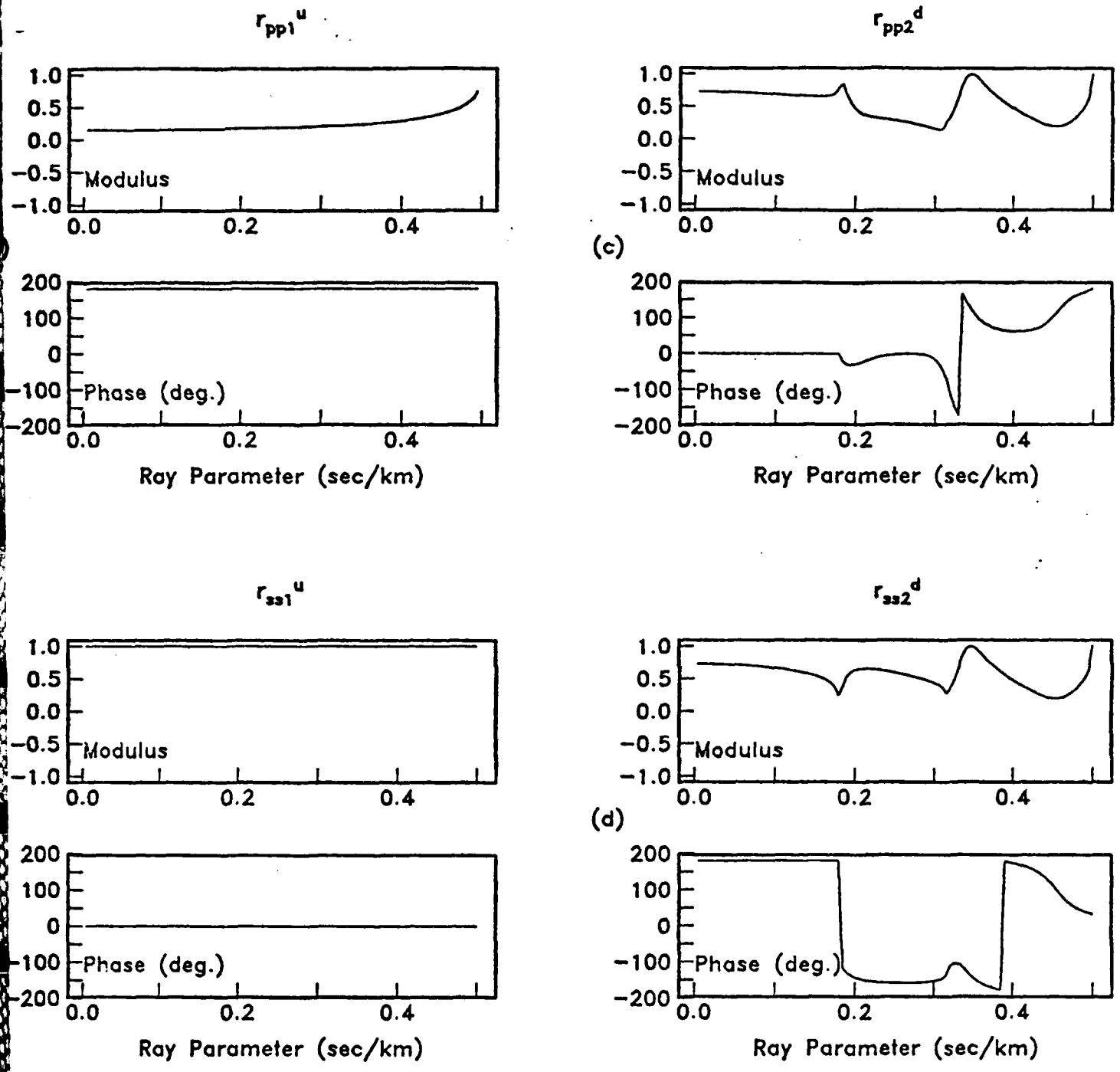


FIGURE 8. Reflection coefficients for the model in figure 1. Superscript 'u' designates an upward coefficient while 'd' designates a downward coefficient. Subscript '1' refers to the ocean–sediment boundary while '2' refers to the sediment–crust boundary. The modulus and phase for each coefficient are plotted.

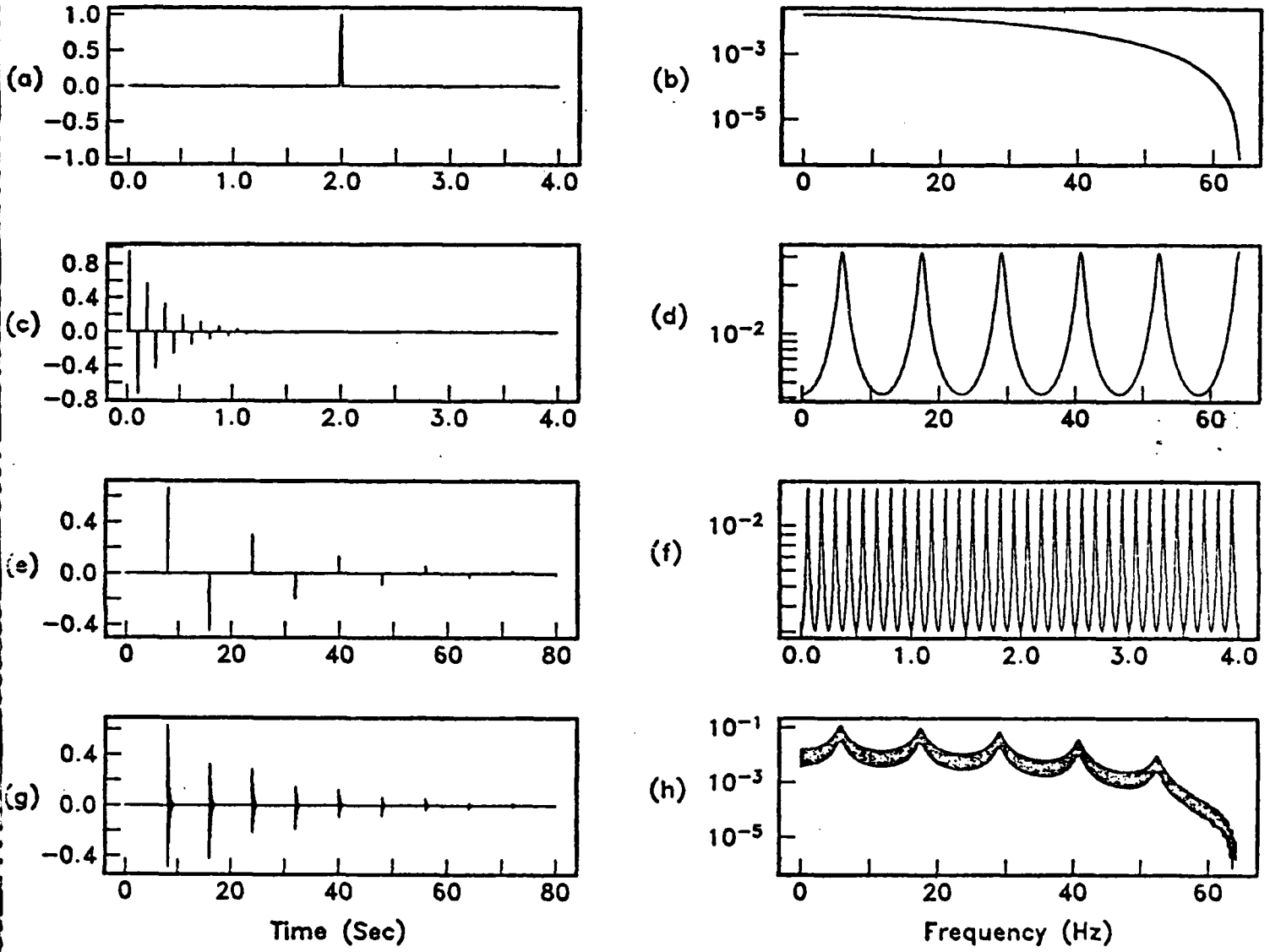


FIGURE 9. Spectral characteristics of sediment and water reverberations. a) Wavelet, w(t); b) wavelet spectrum, $|W(f)|^2$. c) Sediment reverberation with α_s=3.0 and T_s=0.086 sec; d) sediment reverberation spectrum. e) Water reverberation with α_w=0.05 and T_w=8.0 sec; f) first 4.0 hz of the water reverberation spectrum. g) Full wavetrain, x(t); h) wavetrain spectrum, $|X(f)|^2$.

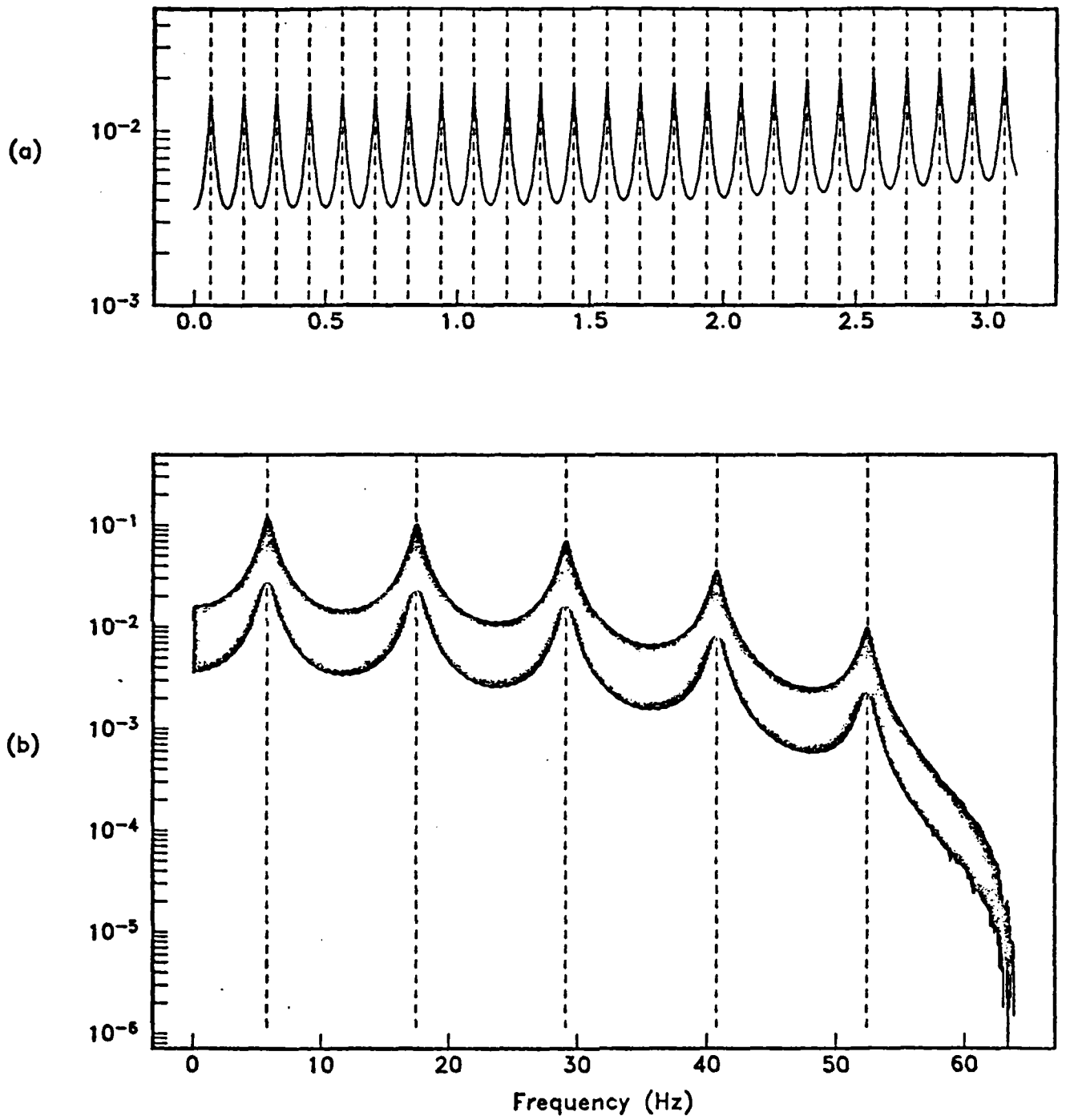


FIGURE 10. Full wavetrain spectrum, $|X(f)|^2$. a) First 3.0 hz of the spectrum with vertical lines at $f_n=(2n+1)df_w/2$, $(n=0,1,2,\ldots)$. b) Complete spectrum with vertical lines at $f_n=(2n+1)df_s/2$, $(n=0,1,2,\ldots)$.

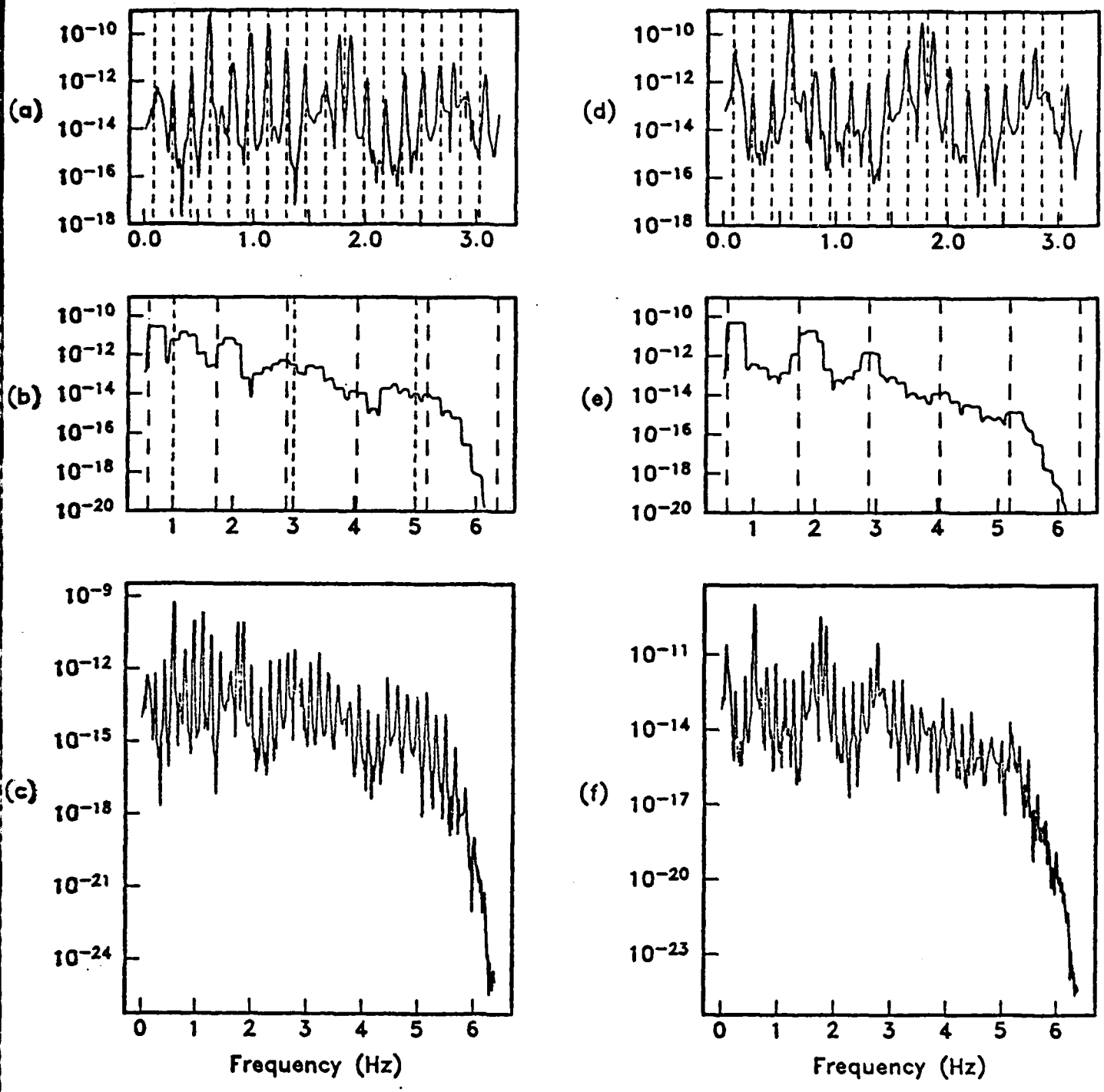
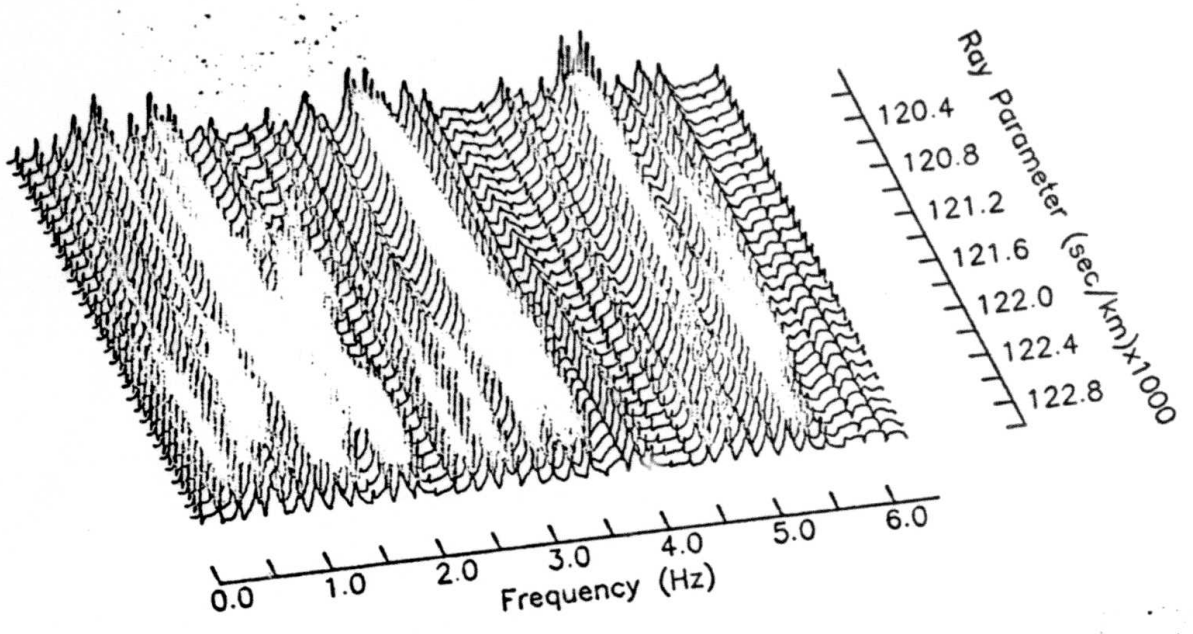
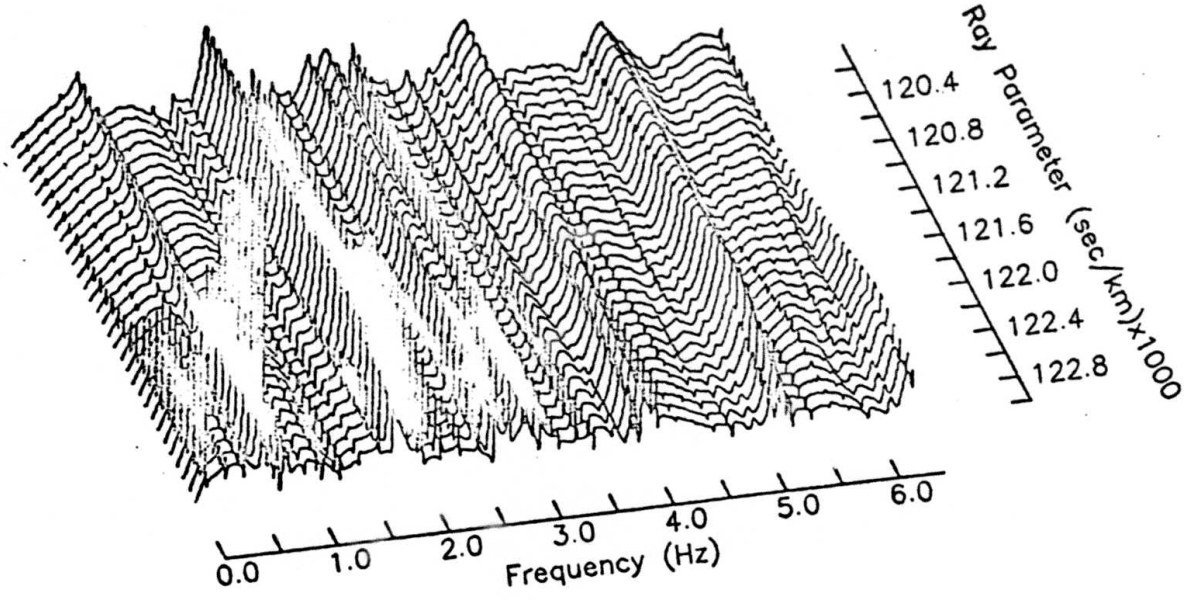


FIGURE 11. Power spectra of the synthetic P_n wavetrains in figure 4. The vertical component spectrum is shown in (a)–(c) and the horizontal component spectrum in (d)–(f). Figures (c) and (f) are the complete spectra. Figures (b) and (e) were obtained by application of a running mean filter to the complete spectra. Dashed lines indicate the predicted frequencies associated with sediment reverberation, long bars for S–waves and short bars f P–waves. Figures (a) and (d) are the first 3.0 hz of the spectr with dashed lines at $f_n=(2n+1)df/2$ $(n=0,1,2,\ldots)$ where df is defined by equation (11).

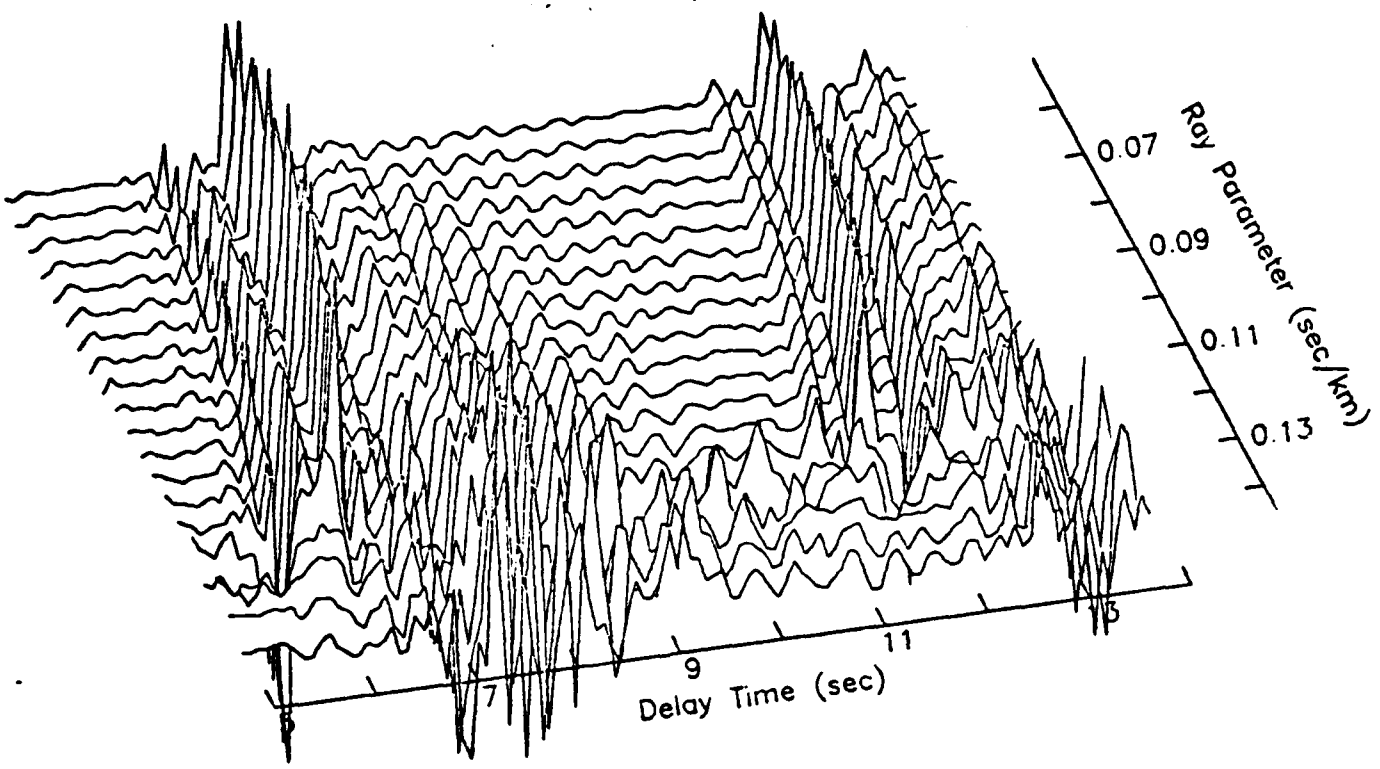


(a) $|\sigma_{220}|$, Z=14.0 km



(b) $|\sigma_{221}|$, Z=14.0 km

FIGURE 12. Moduli of F–integrands corresponding to a) vertical normal stress and b) horizontal normal stress for a source depth of 14.0 km.



σ_{220}, Z=14.0 km

FIGURE 13. Delay time wavefield of the vertical normal stress σ_{220} for a source depth of 14.0 km.

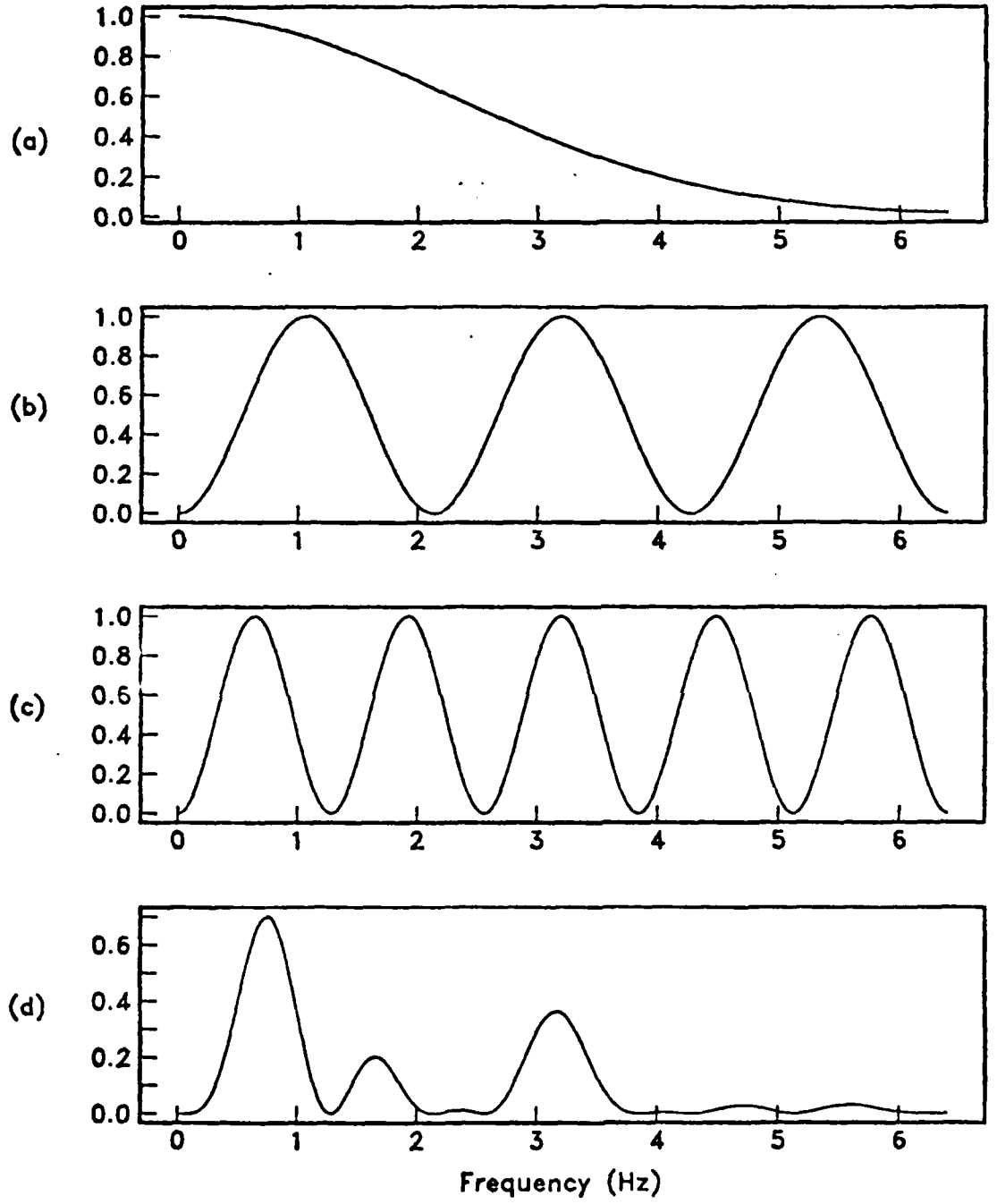


FIGURE 14. Schematic representation of the isolation of a low frequency spectral peak through the constructive interference of different layer reverberations. The figures represent idealized spectra. a) Wavelet spectrum, b) P-wave sediment reverberation spectrum, c) S-wave sediment reverberation spectrum and d) wavetrain spectrum.

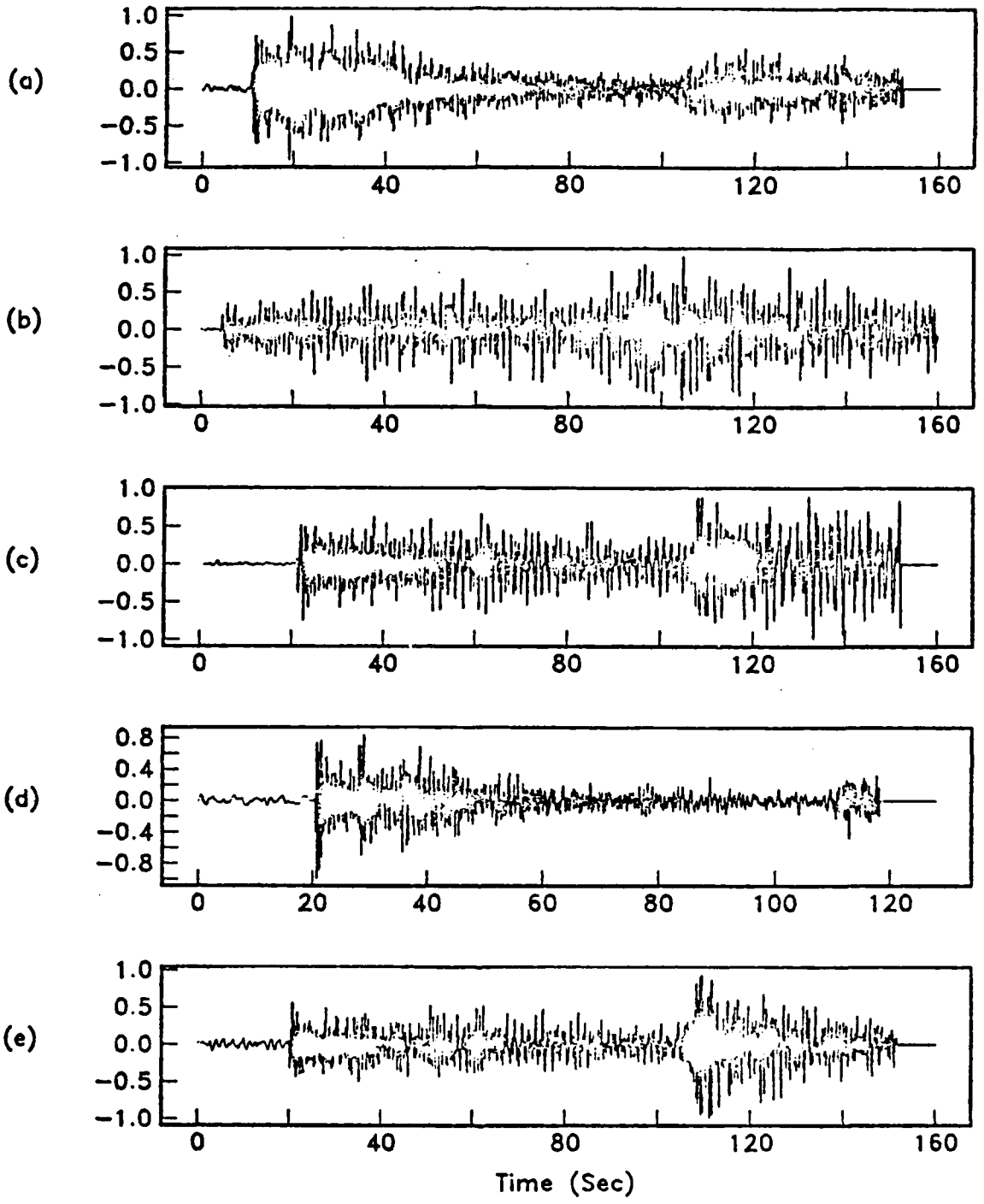


FIGURE 15. OBS data, vertical component. a) OBS Juan, event 14, b) OBS Karen, event 24, c) OBS Suzy, event 25, d) OBS Suzy, event 100 and e) OBS Suzy, event 130.

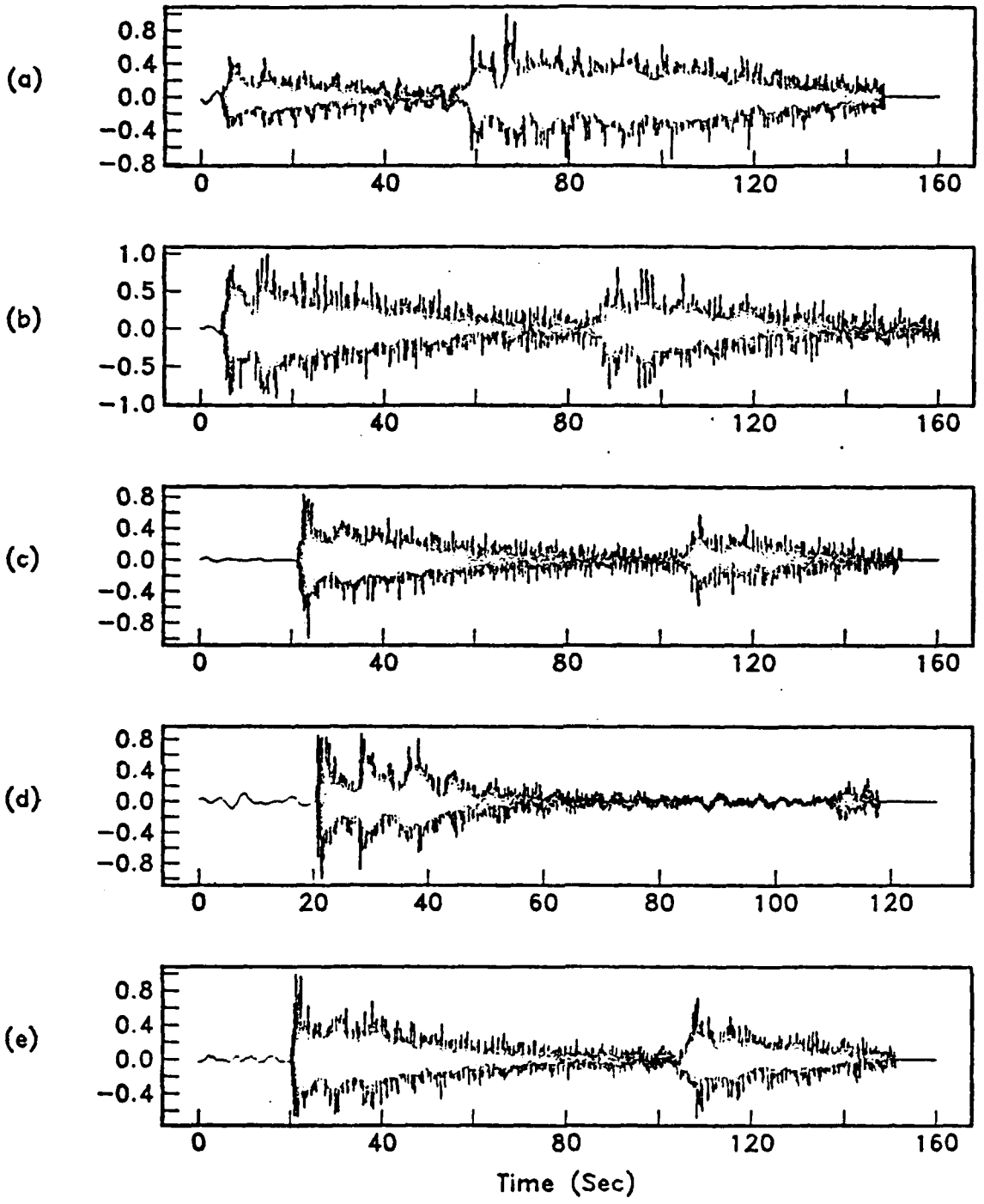


FIGURE 16. OBS data, hydrophone. a) OBS Suzy, event 35, b) OBS Karen, event 24, c) OBS Suzy, event 25, d) OBS Suzy, event 100 and e) OBS Suzy, event 130.

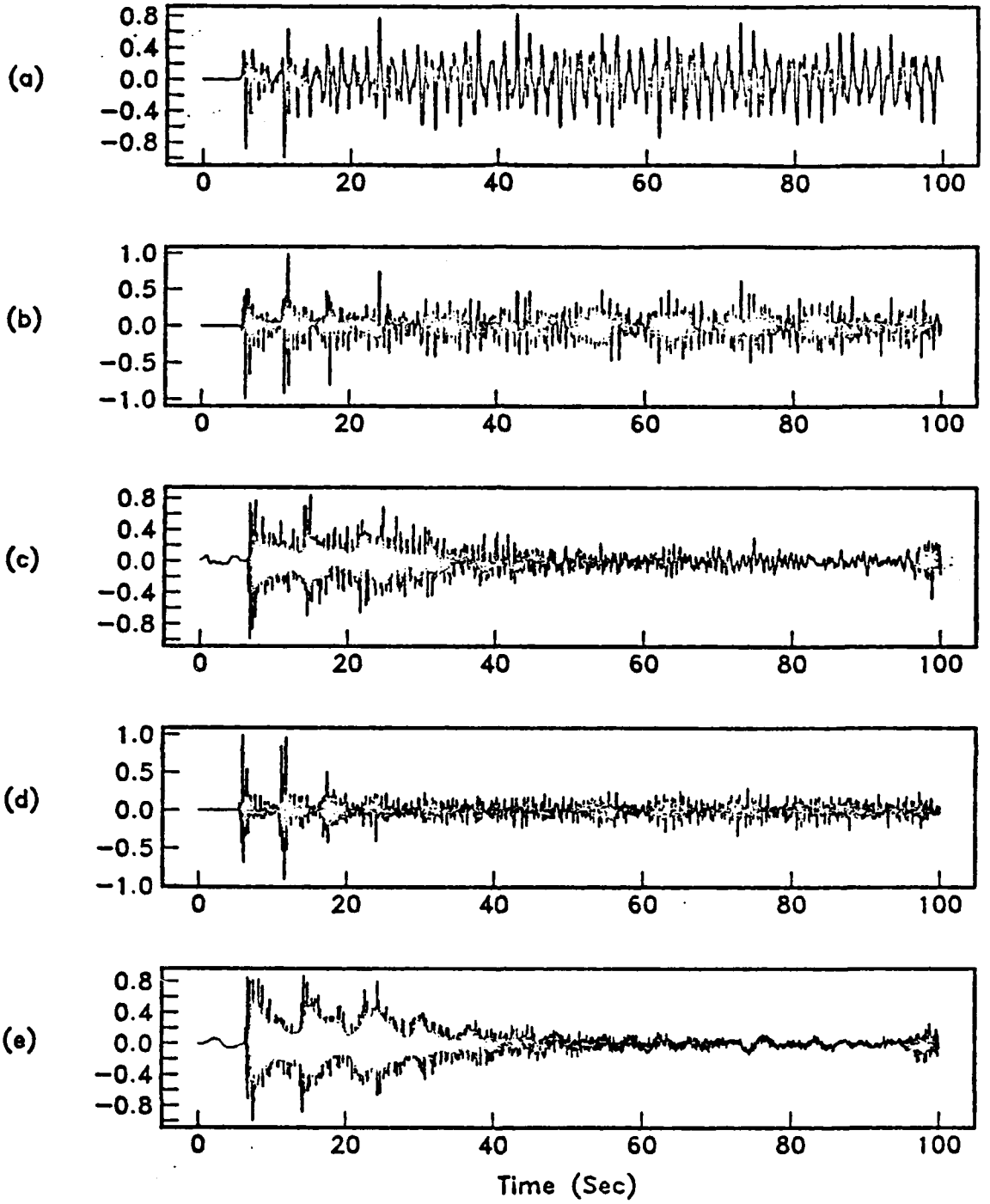


FIGURE 17. The effect of the instrument on the synthetic P_n wavetrain. (a) Synthetic P_n wavetrain of figure 4a with no instrument and (b) with the vertical component OBS response included. (c) OBS Suzy, event 100; vertical component, (d) synthetic P_n wavetrain with hydrophone response included and (e) OBS Suzy, event 100; hydrophone.

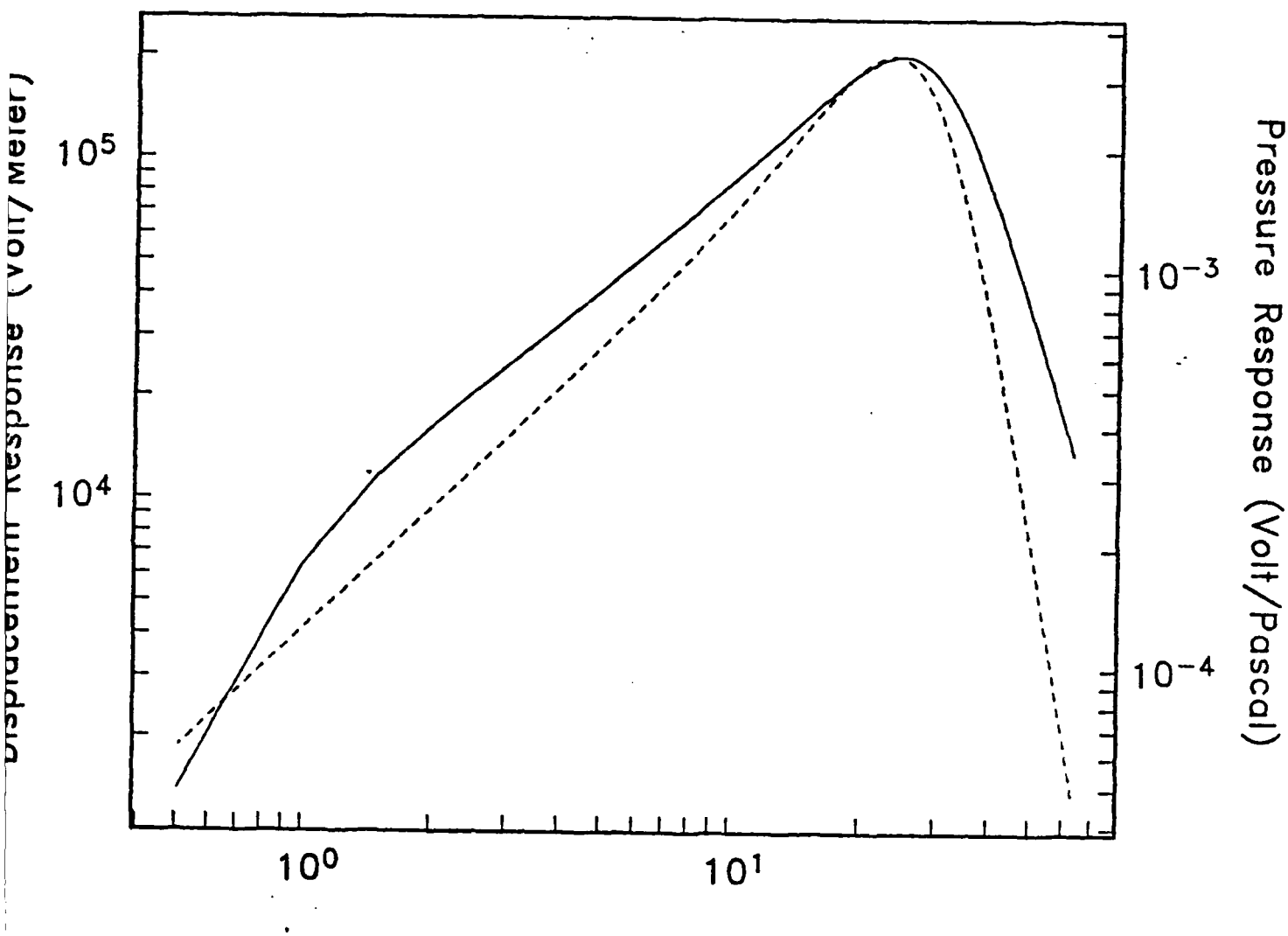


FIGURE 18. Instrument response curves for the OBS vertical component (solid) and hydrophone (dashed).

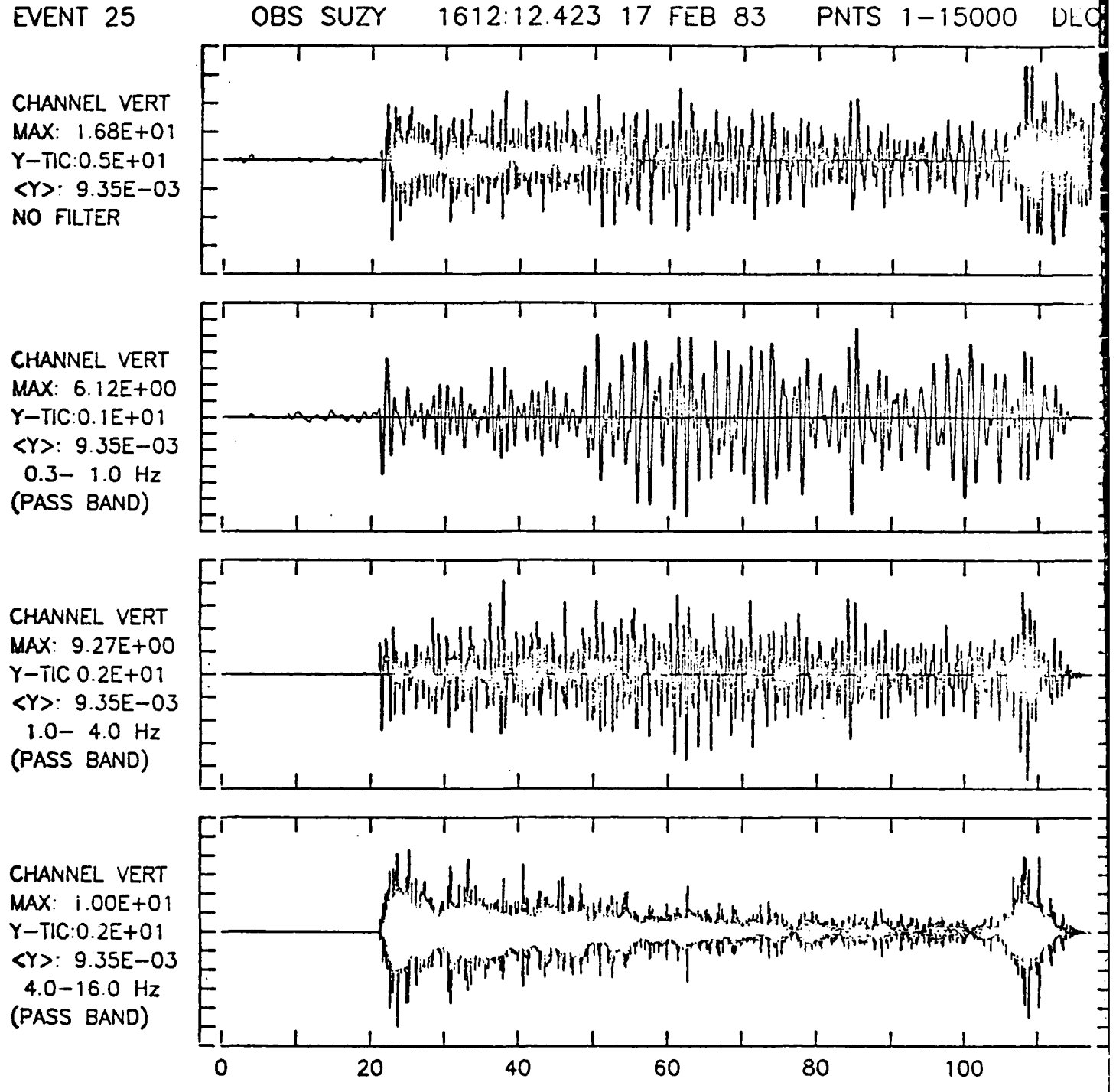


FIGURE 19. Bandpassed versions of the seismogram in figure 15c. The seismogram in (a) is unfiltered and the pass bands in (b)-(d) are 0.25 to 1.0 hz, 1.0 to 4.0 hz and 4.0 to 16.0 hz respectively.

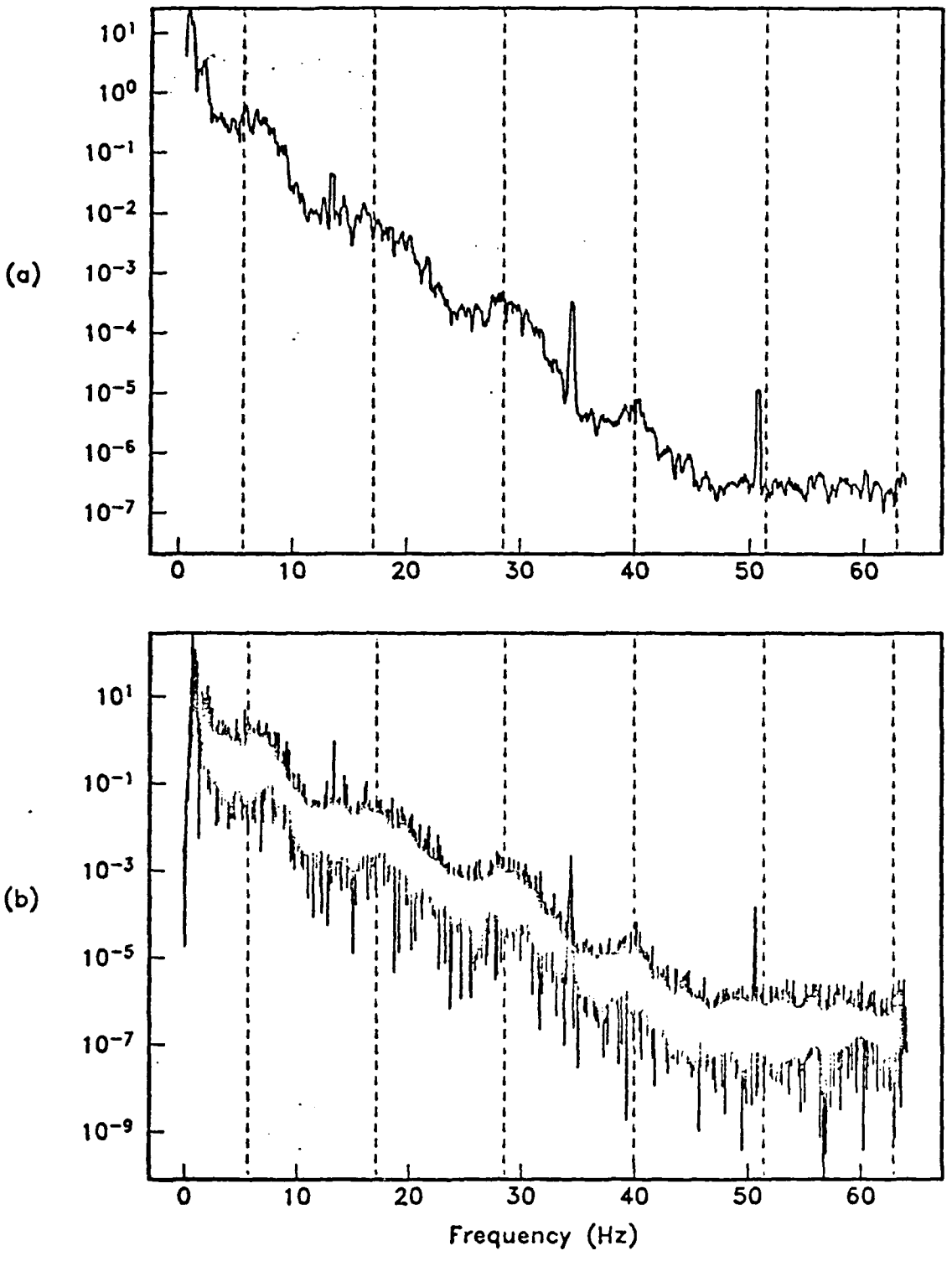


FIGURE 20. Power spectrum of the seismogram in figure 15b. Dashed lines indicate predicted frequencies of the spectral peaks associated with P-wave reverberations in the sediments. (a) Smoothed version of the spectrum in (b).

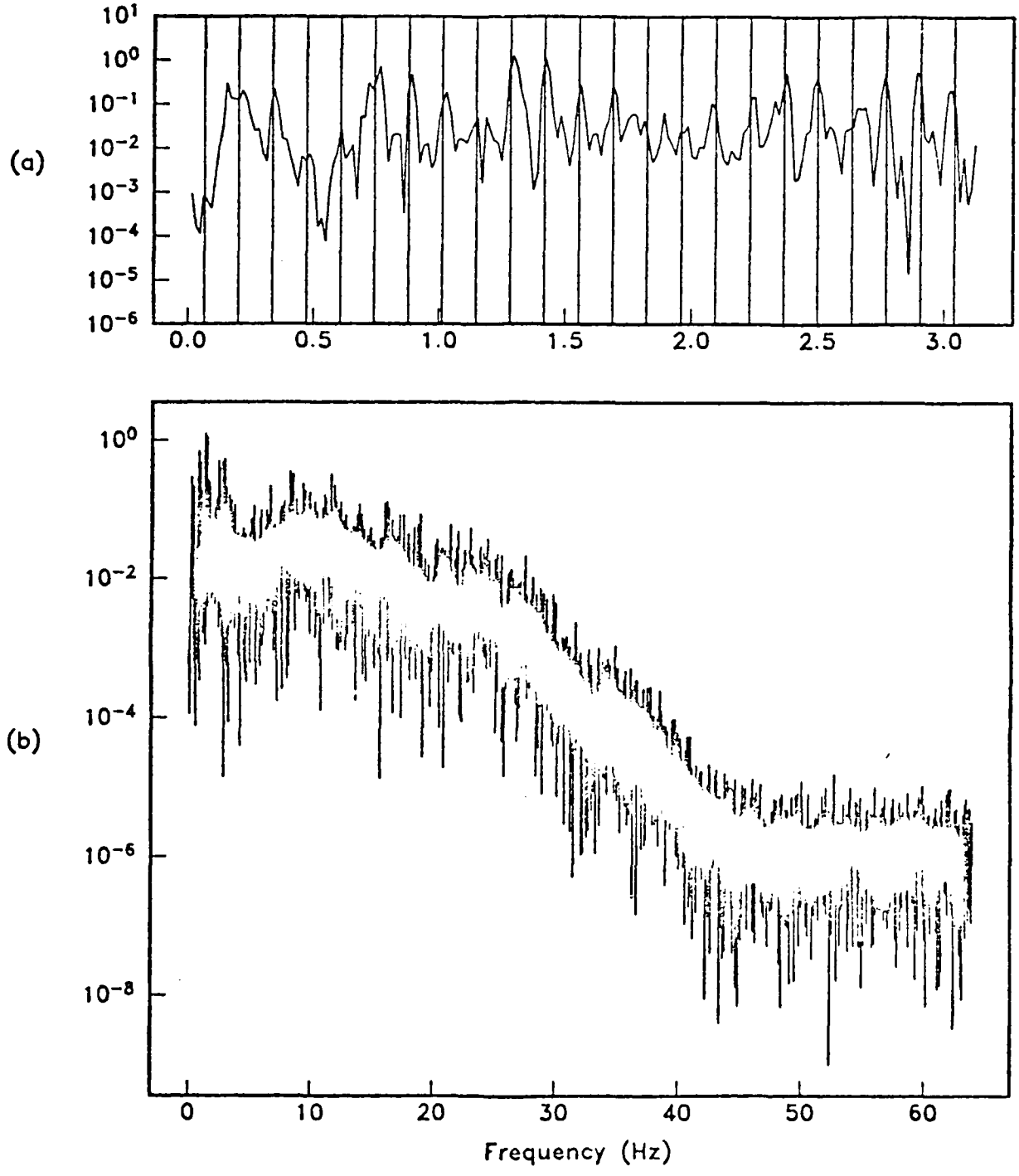
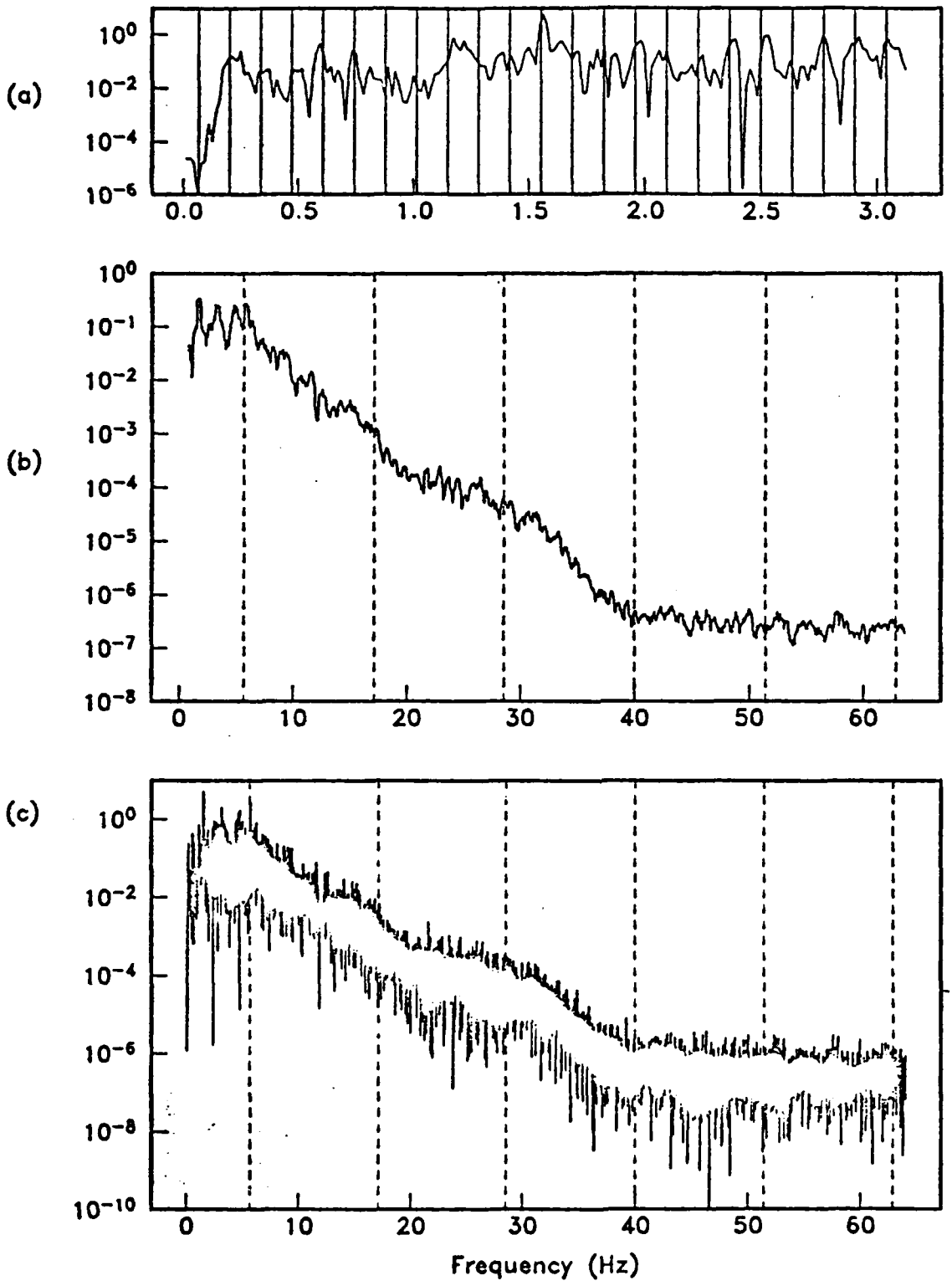


FIGURE 21. Power spectrum of the seismogram in figure 16e. (a) First 3.0 hz of the spectrum with vertical lines at predicted frequencies of the spectral peaks associated with water reverberation. (b) Complete spectrum.



IGURE 22. Power spectrum of the seismogram in figure 15a. The complete spectrum is shown in (c). Figure (b) is a smoothed version of the complete spectrum with dashed lines at the predicted frequencies associated with P-wave sediment reverberation. (a) First 3.0 hz of the spectrum with vertical lines indicating the predicted positions of peaks associated with water reverberation

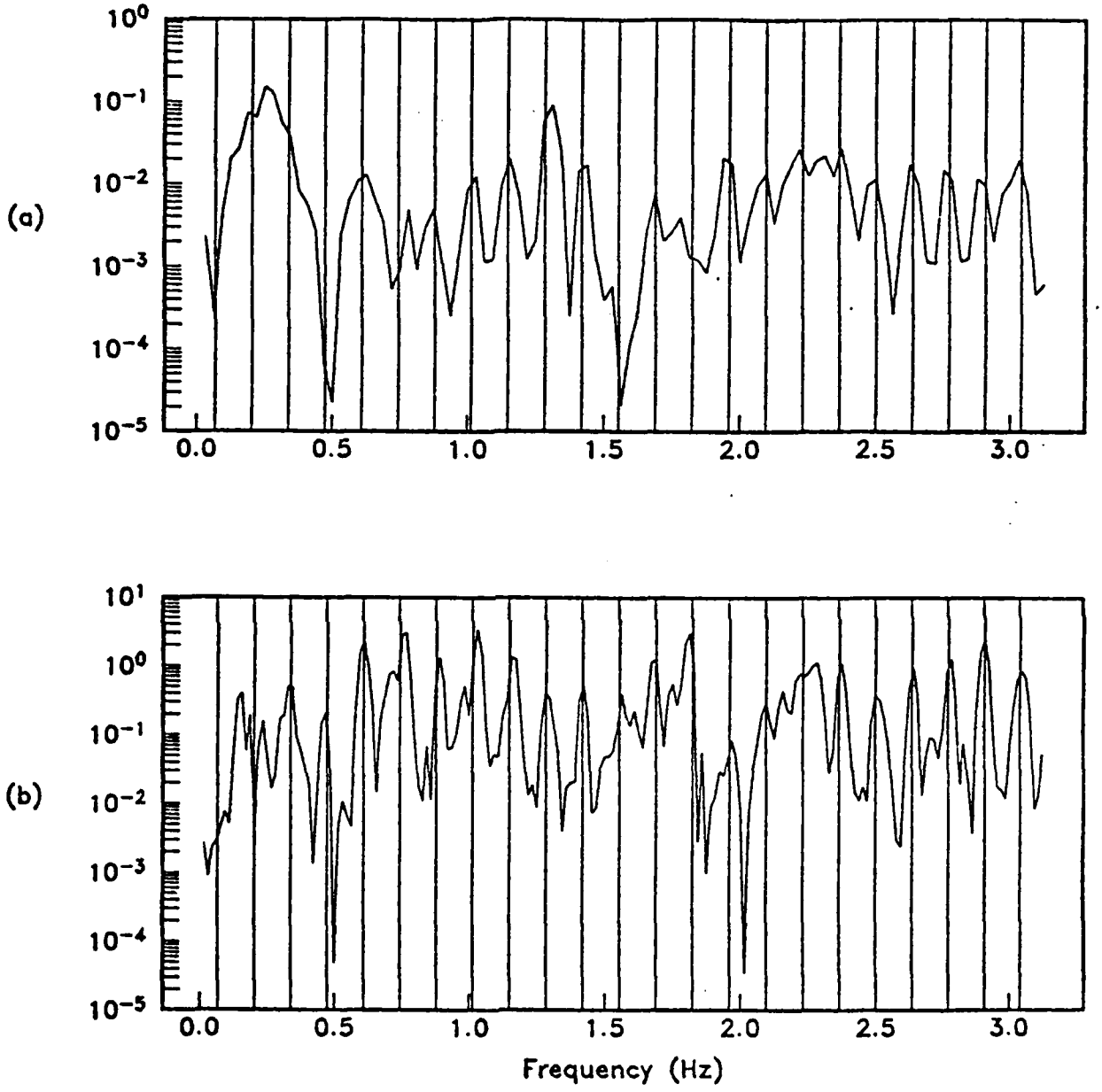


FIGURE 23. First 3.0 hz of the spectra of the seismograms in (a) figure 16a and (b) figure 16c. Vertical lines indicate the predicted frequencies of water reverberation peaks.

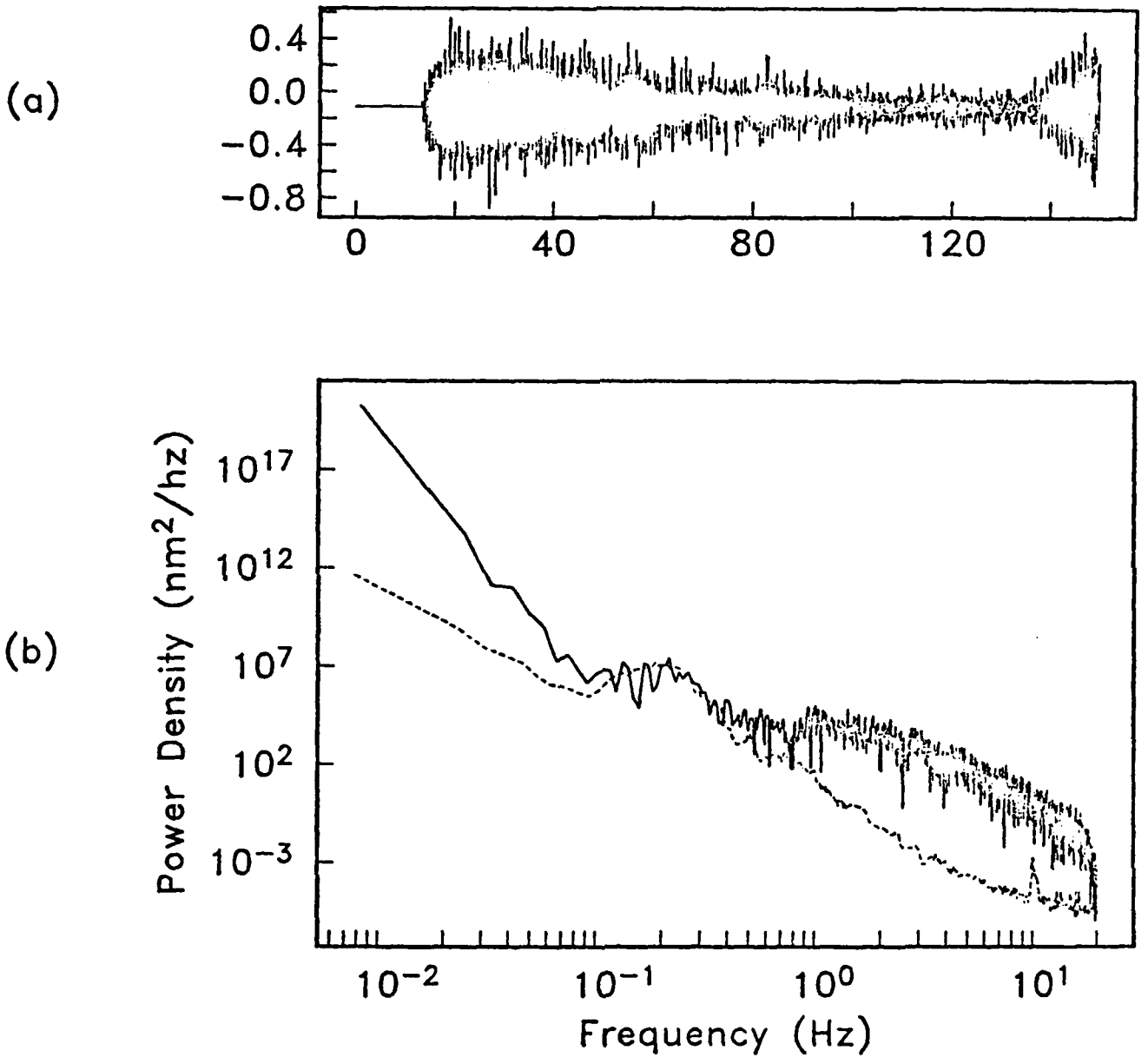


FIGURE 24. Power spectrum of borehole seismometer data. (a) Seismogram recorded by the borehole seismometer at Hole 595B of Deep Sea Drilling Project, leg 91. (b) The solid curve is the power spectrum of the data in (a) and the dashed curve is the noise spectrum.

CHAPTER 11

THE PROPAGATION OF P_n

T. J. Sereno and J. A. Orcutt

Institute of Geophysics and Planetary Physics,
Scripps Institution of Oceanography
La Jolla, California 92093

THE PROPAGATION OF P_n

Thomas Sereno and John Orcutt

Institute of Geophysics and Planetary Physics
Scripps Institution of Oceanography, A-025
La Jolla, California 92093

ABSTRACT

A propagation model for the oceanic P_n phase is presented in which the onset consists of a refraction from the lower oceanic lithosphere while the subsequent coda is a result of near-receiver sediment and water reverberation. The first arrival of the oceanic P_n phase remains entirely within the lithosphere and for epicentral ranges in excess of 25° to 30° contains a free surface reflection, similar to the seismic phase PP. At large epicentral distances, or similarly for deep events, the P_n wavetrain is preceded by a low frequency forerunner which has traversed the low Q asthenosphere. The coda of the P_n phase was analyzed through the computation of synthetic seismograms using wavenumber integration. Spectral characteristics associated with both sediment and water reverberation are clearly observed in both the synthetics and data collected in the southwest Pacific during the 1983 Ngendei Seismic Experiment.

INTRODUCTION

The oceanic P_n phase is characterized by low spatial attenuation, a high frequency wavetrain of extremely long duration and an onset velocity near 8.0 km/s[1]. Through the computation of synthetic seismograms in a laterally homogeneous, vertically stratified medium we will show that these properties can be achieved in the absence of scattering, low velocity channels or high Q waveguides.

SYNTHETIC SEISMOGRAMS

Wavenumber integration, in which a quadrature over wavenumber is performed at fixed frequency points, was used to generate the synthetic seismograms[2]. The time domain response was obtained by applying a Fourier transform to the resulting complex spectrum. The seismograms contain all reverberations, including those off the free surface, as well as all P to S and S to P mode conversions. Attenuation is included by allowing the material velocities to be complex thereby allowing the integration to be performed along the real wavenumber axis. The most serious limitations of the method include the restriction to models consisting of a stack of

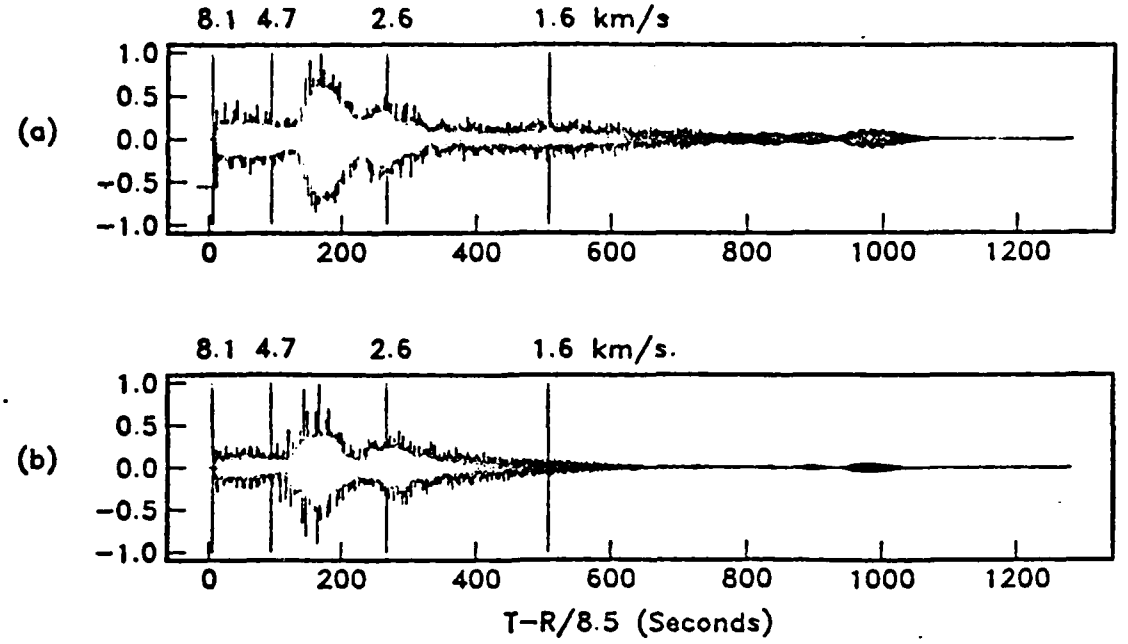


Figure 1. Complete synthetic seismograms at an epicentral range of 1000 km for a thrust fault source at 14.0 km depth. The fault had a dip of 45°, a rake of 270° and an azimuth relative to the receiver of 60°. (a) Vertical component and (b) horizontal component rotated 25° clockwise from the radial direction. Group velocities of 8.1, 4.7 2.6 and 1.6 km/s are indicated. Phase velocities between 3.85 and 25.0 km/s were included in the calculation.

homogeneous layers and the high computational costs involved for models with more than 10 to 15 layers.

As an exploratory model we have adopted that of Gettrust and Frazer[3] which includes a 4 km thick water layer and a 500 m thick sediment layer overlying a vertically inhomogeneous oceanic crust and upper mantle. Compressional and shear wave velocities are monotonically increasing functions of depth. The values of the quality factor, Q, were less than 500 in the crust and upper mantle and 50,000 in the oceanic water column.

Figure 1 is an example of complete synthetic seismograms generated for a sub-MOHO thrust fault at an epicentral range of 1000 km. The late arriving energy on the vertical component (figure 1a) with a group velocity of 1.6 km/s is emergent in nature and has a substantial duration characteristic of oceanic abyssal T-phases[4]. Through a comparison of delay time wavefields between Green's functions that contain this late arriving energy and Green's functions that do not, it was observed that the ray parameter range comprising this group corresponds to that of post-critical reflections off the MOHO. The synthetic T-phase is thus explained as a reverberation between the free surface and the MOHO with a substantial number of water and crustal reverberations acting to extend the wavetrain. The 4.7 km/s arrival on the horizontal component (figure 1b) is grossly identified as the oceanic S_n phase. The first arrivals of this group are horizontally polarized shear waves and are thus absent from the vertical component. Work is continuing in an effort to synthesize more realistic S_n phases.

The synthetic P_n wavetrain has an onset velocity of 8.1 km/s, a duration of over 100 seconds and extends into the onset of S_n. The amplitude

of the synthetic P_n wavetrain was within a factor of 2 or 3 of data amplitudes obtained during the 1983 Ngendei Seismic Experiment in the southwest Pacific (23° 49' S, 165° 32' W). An event located near the Tonga Islands by the National Earthquake Information Service (NEIS) with a magnitude of 5.8 and a moment of 2.6×10^{-4} dyne-cm was recorded by three ocean bottom seismometers (OBS's) at the Ngendei site. The maximum amplitudes of these recordings ranged between 0.76 and 1.44 volts. Convolution of the synthetic P_n phase with the OBS instrument response and scaling by the NEIS published moment yielded a maximum amplitude of 0.42 volts. Differences of this order can be explained simply in terms of differences in model parameters, fault orientation and focal depth.

REVERBERATIONS

The importance of reverberations within the oceanic water column and sediment layer is most effectively demonstrated in the frequency domain. It is simple to show that the power spectrum of a wavelet reverberating in a single layer has eigenfrequencies given by

$$f_n = (2n+1)\frac{df}{2} \; ; \; (n=0,1,2,\ldots) \qquad (1)$$

where $df = \frac{1}{T}$ and T is the time between multiples. In the case of near-vertical incidence T can be approximated by the two-way travel time in the layer and (1) represents the eigenfrequencies for an organ-pipe mode[5]. Arrivals within the P_n wavetrain must penetrate the mantle in order to have group velocities between 6 and 8 km/s and must therefore have phase velocities greater than 8 km/s. A result of this is that the rays are quite steep at the receiver, justifying the use of the two-way travel time in equation (1). The $\frac{df}{2}$ offset of the spectral peaks is due to a π-phase shift between multiples. The width of the spectral peaks at frequencies given by (1) is governed by the impedance contrast at the boundaries of the layer. Thus leaky modes, which suffer a continuous loss of energy along the propagation path due to leakage into the surrounding medium, will attenuate more rapidly than locked modes and will thus have substantially wider spectral peaks. The decay of the reverberation peaks with increasing mode number, n, is a function of Q in the layer.

The computation of the full synthetic seismograms pictured in figure 1 required extremely fine frequency sampling to avoid time series wrap-around. The calculation extended to a Nyquist frequency of only 6.4 Hz which involved obtaining the response at 8193 frequency points. While the wavenumber integration algorithm is not strictly bandlimited, the costs of extending the calculation to higher frequencies are formidable. Synthetic power spectra do not, however, require this fine frequency sampling and can be computed rather efficiently up to a Nyquist frequency of 64.0 Hz. Thus direct comparison between data collected at the Ngendei site and synthetics is easily achieved in the frequency domain.

The Ngendei site was the location of hole 595B of Deep Sea Drilling Project (DSDP), Leg 91. The depth of the oceanic water column at the site is 5.5 km and, from core sample measurements, the sediment thickness is 70 m with a compressional velocity of 1.6 km/s[6]. For compressional wave sediment reverberation the two-way travel time in the layer is 0.0875 s yielding an eigenfrequency spacing of df=11.43 Hz. The impedance contrast at the ocean/sediment interface is quite small for compressional waves. Thus the sediment layer acts as an extremely leaky waveguide for compressional wave propagation and the peaks associated with sediment reverberation have a large characteristic width. The reverberations within the water column actually include the sediment layer and take place between the free surface and the base of the sediments. The resulting eigenfrequency spacing

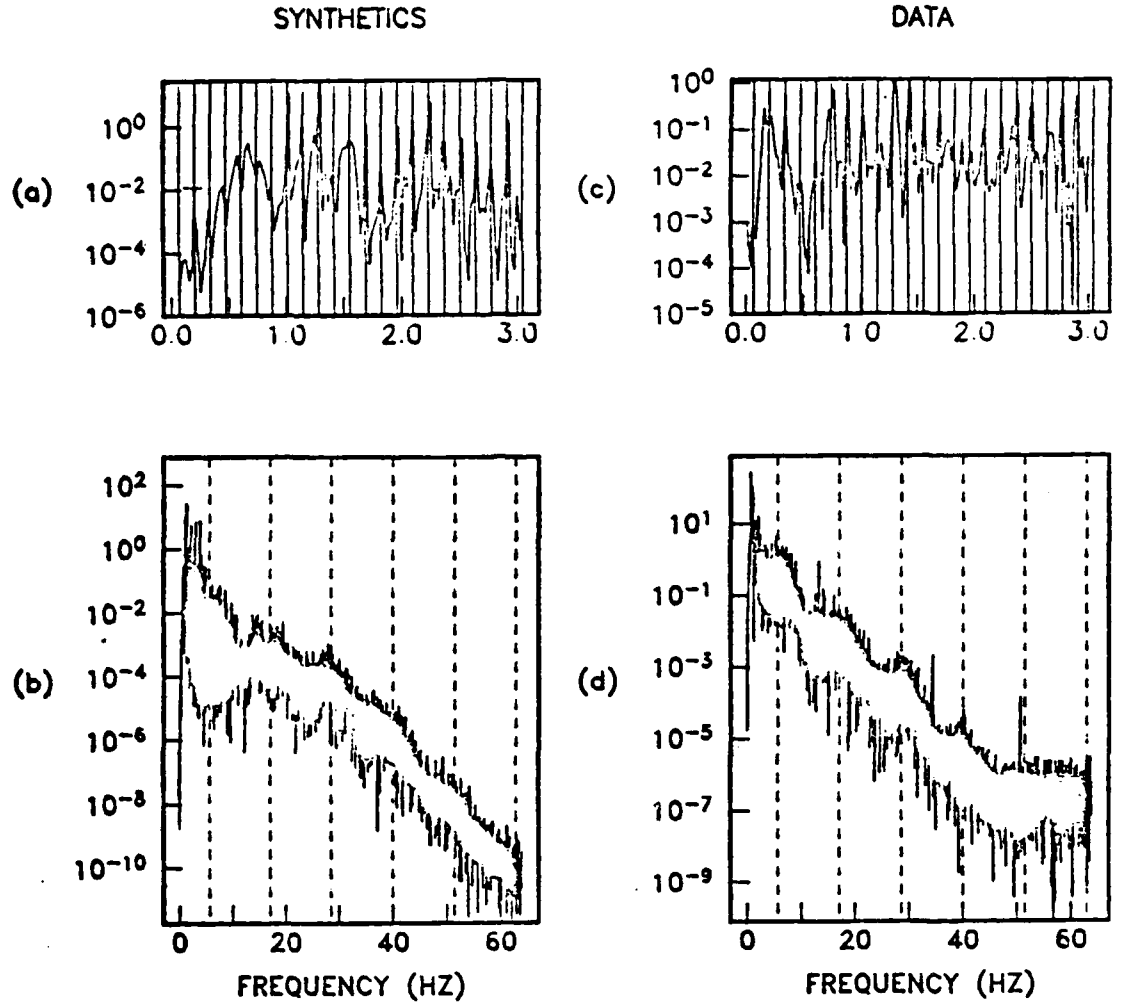


Figure 2. Power spectra illustrating the presence of reverberation within the P_n coda. (a) First 3.0 Hz of the synthetic vertical component spectrum depicted in (b). (c) First 3.0 Hz of a hydrophone spectrum and (d) a complete OBS vertical component spectrum. In figures (a) and (c) vertical lines indicate predicted eigenfrequencies associated with water reverberation (equation (1)). In figures (b) and (d) vertical lines indicate predicted eigenfrequencies for P-wave sediment reverberation.

for water reverberations is therefore df=.1375 Hz. Both interfaces in this case have very strong impedance contrasts and the associated spectral peaks are quite narrow. Thus the power spectrum of a wavelet reverberating in the oceanic water column and sediment layer consists of widely spaced spectral "humps" due to P-wave sediment reverberation superimposed on finely spaced spectral "peaks" due to water reverberation.

Figure 2 is an illustration of this behavior. Figure 2b is a synthetic power spectrum computed using wavenumber integration in which we have used the sediment and water properties of the Ngendei site. In an effort to reduce computational costs we have included only phase velocities between 6.9 and 25.0 km/s. Figure 2a depicts the first 3.0 Hz of the spectrum with vertical lines indicating the eigenfrequencies of water reverberation computed using equation (1). Figure 2b contains the full spectrum[5] after correcting for the OBS instrument response and a source spectrum of the form

$$|S(f)|^2 = S(0)^2\left[1+\frac{f}{f_c}\right]^{-4} \qquad (2)$$

where f_c is the corner frequency and was given a value of 0.6 Hz. In this case the vertical lines indicate positions of spectral "humps" associated with P-wave sediment reverberation. To verify our interpretation of these features we doubled the layer thicknesses and recomputed the spectra. The effect was to decrease the spacing of the spectral peaks by a factor of 2 thereby validating the interpretation.

Figures 2c and 2d contain power spectra of data collected at the Ngendei site. Figure 2c is the first 3.0 Hz of a hydrophone spectrum illustrating the presence of water reverberations and figure 2d is an OBS vertical component spectrum illustrating the presence of sediment reverberation. These spectral features were quite common in the data and were independent of the source characteristics.

The presence of S-wave sediment reverberation is most easily detected in horizontal component spectra due to the steep incidence of the rays. For shear waves the impedance contrasts at both the ocean/sediment and sediment/crust interfaces are quite large yielding relatively narrow spectral peaks. The low quality factor for shear waves in the sediments, however, results in a rapid decay of the spectral peaks with increasing mode

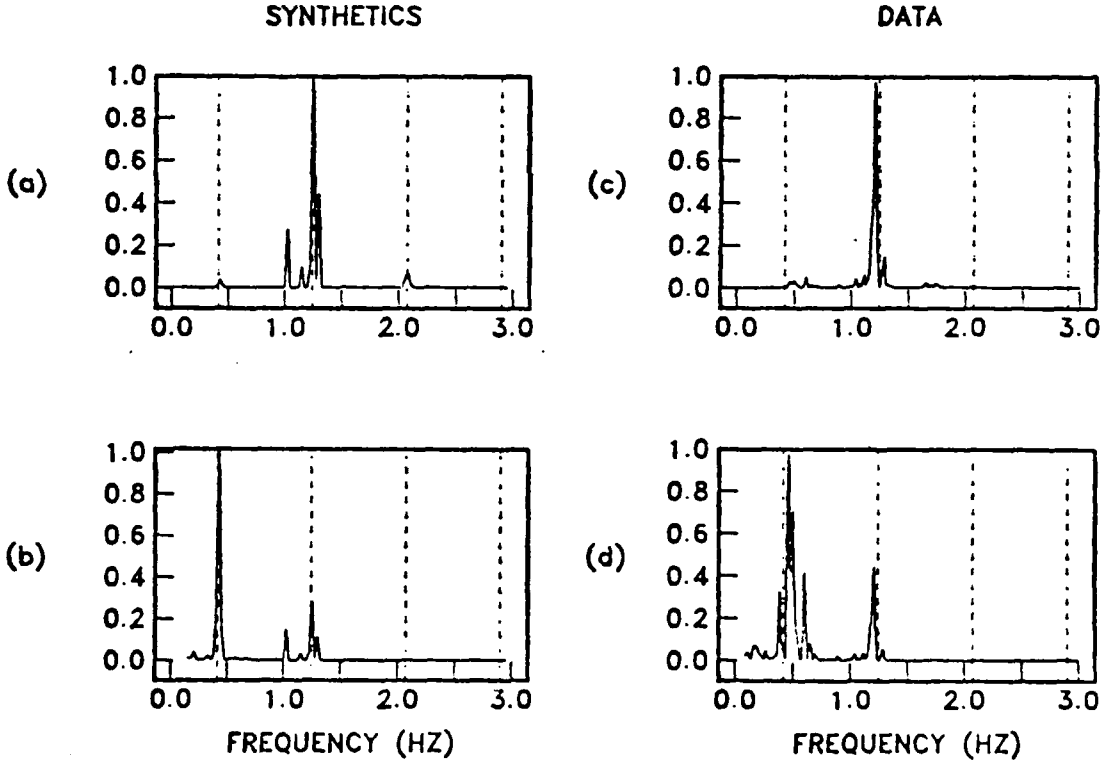


Figure 3. Power spectra illustrating shear wave sediment reverberations within the P_n coda. (a) First 3.0 Hz of the synthetic horizontal spectrum after including the instrument response and source spectrum. (b) Synthetic spectrum of (a) without including the instrument response. Power spectra of horizontal component data taken at the Ngendei site (c) before removing the instrument response and (d) after removing the instrument response. In (a)-(d), dashed vertical lines indicate predicted eigenfrequencies of S-wave sediment reverberation. The peak amplitudes in each figure were scaled to a value of one.

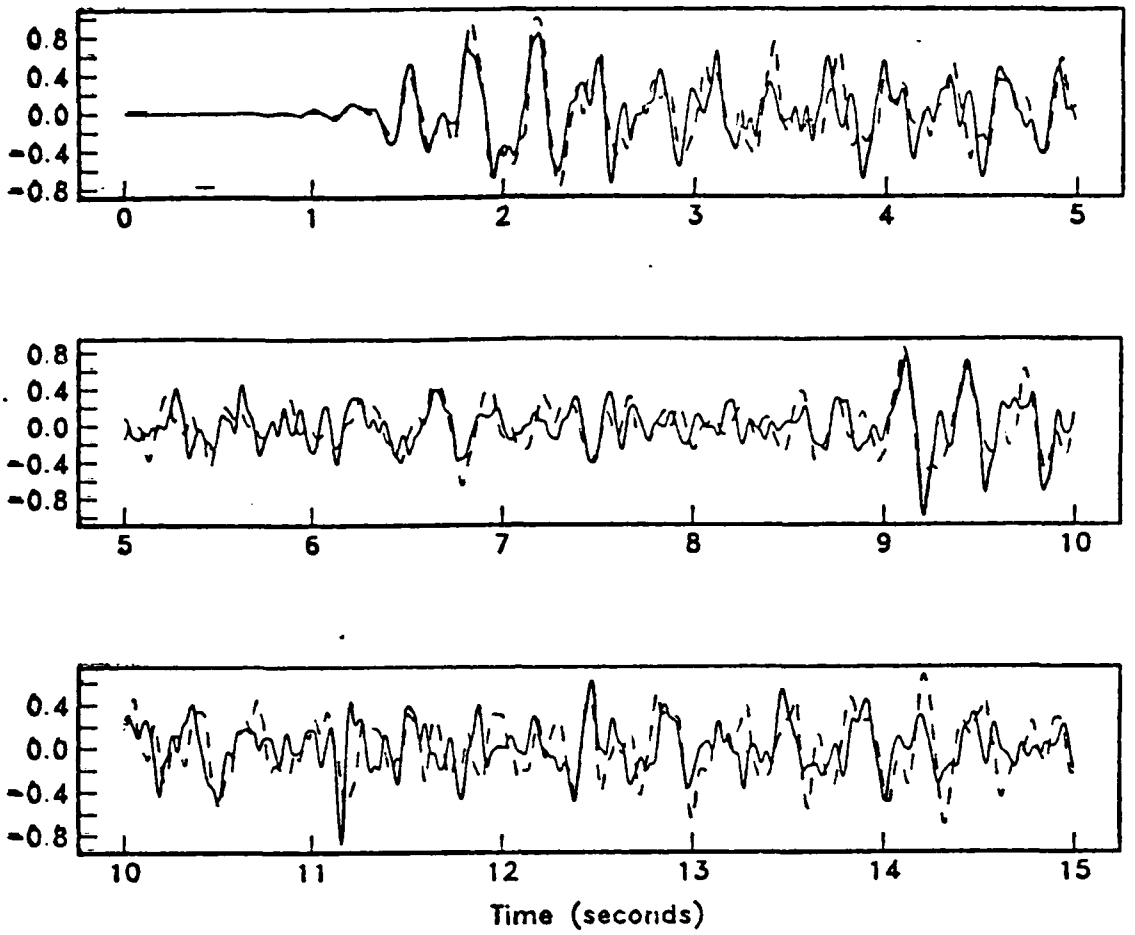


Figure 4. Coherence of the oceanic P_n phase. Comparison of recordings of the same event taken by OBS's separated by a distance of 1.9 km. OBS Karen (solid) vs. OBS Janice (dashed). The records were bandpassed between 2.0 and 25.0 Hz prior to comparison.

number. Figure 3a depicts the first 3.0 Hz of the synthetic horizontal component power spectrum after including the OBS instrument response and source spectrum given by (2). The shear wave sediment velocity used in the computation of the synthetic spectrum was 116 m/s yielding an eigenfrequency spacing of 0.83 Hz. Figure 3b is the synthetic spectrum without including the instrument response. Figure 3c is the first 3.0 Hz of the power spectrum of horizontal component data taken at the Ngendei site and 3d was obtained after removing the instrument response. In figures 3a-3d, dashed vertical lines indicate predicted frequencies (equation (1)) of spectral peaks associated with S-wave sediment reverberation. The positions, widths and spectral decay rates of these peaks all agree with predictions for shear wave sediment reverberation. Once again we altered the sediment thickness and recomputed the spectra to verify our interpretation of the peaks in the synthetic spectra.

COHERENCE

Strong coherence of the P_n wavetrain between OBS's separated by large distances is not expected unless the water and sediment properties at the two sites are nearly equal. It was found in the Ngendei data that far greater coherence could be achieved by bandpassing the data between 2.0 and 25.0 Hz prior to comparison. The result of even a small change in either S-wave sediment velocity or sediment thickness would result in a

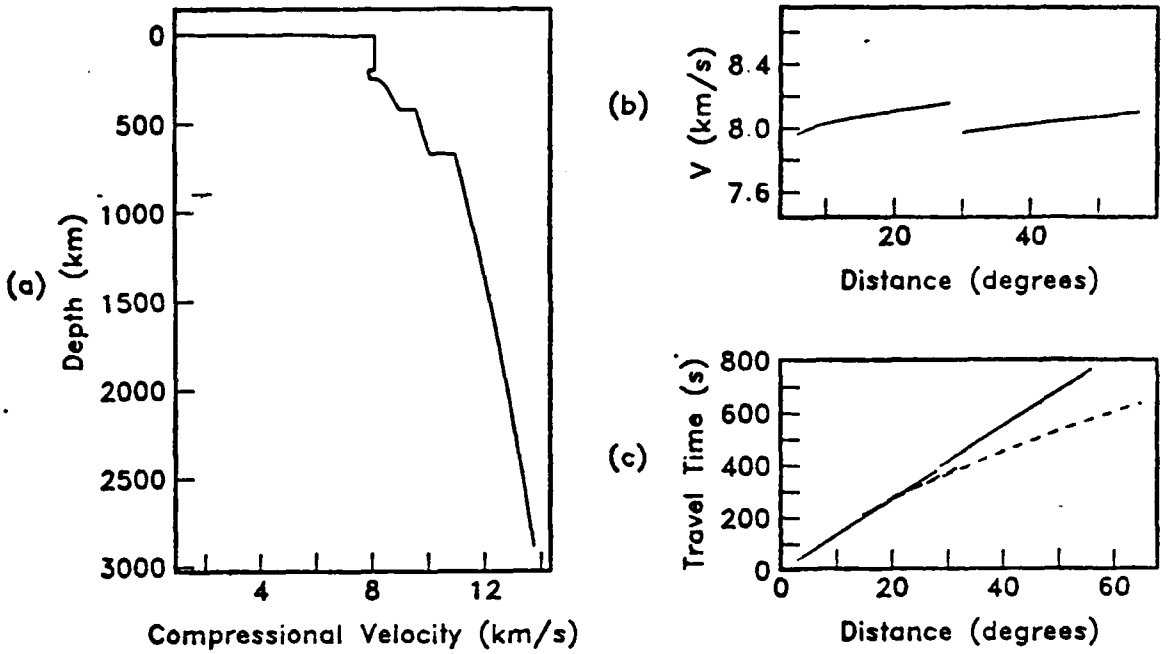


Figure 5. (a) Velocity model used to compute group velocities and travel times of P_n and normally refracted P. The results are shown for a surface source and receiver. (b) Group velocity of P_n as a function of epicentral distance for the model in (a). Group velocity has been defined as epicentral distance divided by total travel time. The discontinuous break at 30° represents the crossover between a ray normally refracted in the lithosphere and one that contains a free surface reflection. (c) Travel time curve of P_n (solid) verses normal refracted P with turning points below the base of the lithosphere (dashed) for the model in (a).

measurable shift in the dominant frequency of the wavetrain (figure 3). The frequency band between 0.0 and 2.0 Hz is the most sensitive to these changes resulting in a reduction of coherence at these lower frequencies. Figure 4 is a comparison of data collected by two different OBS's separated by a distance of 1.9 km for the same event after bandpassing between 2.0 and 25.0 Hz. The first water reverberation is evident at about 9 seconds and the excellent coherence well into the P_n wavetrain is evidence for reverberation, as opposed to scattering, as the dominant mechanism of P_n coda generation. Work is continuing on the problem of coherence as well as that of polarization within the P_n coda.

PROPAGATION PATH

The observation that the group velocity of P_n is generally higher at epicentral ranges between 12° and 30° than at distances outside this range can be explained by the confinement of P_n to the oceanic lithosphere. At ranges less than 30° the onset of P_n is associated with a normal refracted P-wave remaining in the lithosphere, however at distances in excess of 30° the first arrival that remains in the lithosphere contains a free surface reflection, similar to the seismic phase PP, thereby decreasing the group velocity. This is demonstrated in figure 5b which displays the group velocity of P_n as a function of epicentral distance for the velocity model shown in figure 5a. In order to achieve a crossover distance of 30°, a lithosphere thickness of nearly 200 km is required. The decrease in group velocity at ranges less than 12° is the result of

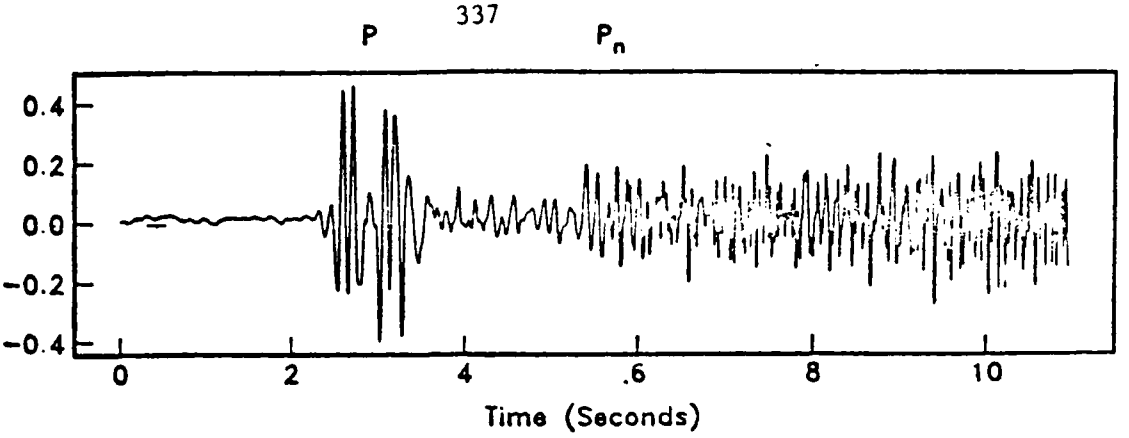


Figure 6. Vertical component seismogram recorded by a borehole seismometer at the Ngendei site. The focal depth of the event was 293 km in the Kermadec trench (m_b=5.0, Δ=12.91°). The complex P waveform between 2 and 4 seconds is a triplication from the 400 km discontinuity. Arrivals following 5.5 seconds constitute the P_n arrival. The enrichment in high frequency content of P_n relative to P is indicative of the low Q of the sub-lithosphere mantle.

shallower turning points in the lithosphere. A similar interpretation was presented by Menke and Richards[8] in terms of whispering gallery modes at the MOHO.

Figure 5c is a travel time curve illustrating the arrival times of normal refracted P verses P_n for the model in figure 5a. The curves diverge at an approximate range of 25° where the normal refracted arrival is a ray that has crossed the low Q asthenosphere constituting the commonly observed low frequency forerunner of the P_n wavetrain[9]. Figure 6 is an example illustrating the normal refracted P forerunner of oceanic P_n. For deep events the separation of normal refracted P and P_n occurs for smaller ranges as P_n must propagate up and around the corner of the descending slab. During the Ngendei Experiment the deployment of a continuously recording borehole seismometer enabled the recording of strong P_n phases for events with focal depths in excess of 450 km. The suggestion that a descending slab can act as a waveguide to propagate the high frequency oceanic S_n phase was made by Isacks and Barazangi[10]. Their model consists of a transformation of the basaltic oceanic crust to a thin, high velocity, eclogite layer as the slab descends to greater depths. Thus the upper flank of the slab provides an effective reflecting surface and, in combination with a velocity gradient within the slab, could provide an efficient waveguide for the propagation of high frequency seismic energy.

SUMMARY

The model of the propagation of P_n presented consists of an arrival confined to the oceanic lithosphere with subsequent water and sediment reverberations comprising the ensuing wavetrain. The low spatial attenuation observed for P_n does not require an intrinsically high Q lithosphere waveguide but rather can be explained in terms of the extremely high Q in the oceanic water column. The depletion of high frequencies in the normal refracted arrival relative to P_n is due to propagation through the low Q asthenosphere.

Acknowledgements. The data used for this study were collected with the support of DARPA Grant No. AFOSR-84-0043 while the synthetic calculations were supported by ONR Contract No. N00014-80-C-0440.

REFERENCES –

1. D. Walker, High-frequency P_n and S_n phases recorded in the western Pacific, J. of Geophys. Res. 82:3350 (1977).
2. R. Apsel, Ph. D. thesis, University of California, San Diego, La Jolla, 349 pp. (1979).
3. J. F. Gettrust and L. N. Frazer, A computer model study of the propagation of the long-range PN phase, Geophys. Res. Lett. 8:749 (1981).
4. R. H. Johnson and R. A. Norris, T-wave generation mechanisms, Hawaii Institute of Geophysics Rept. HIG-70-7, 16 pp. (1970).
5. K. Aki and P. G. Richards, "Quantitative Seismology: Theory and Methods," W. H. Freeman, San Francisco (1980).
6. I. I. Kim, D. K. Smith, J. A. Orcutt, T. H. Jordan and H. W. Menard, Seismic reflection site survey: correlation with physical properties, leg 91, Deep Sea Drilling Project, Initial Rep. Deep Sea Drill. Proj., Leg 91 (1985).
7. D. Walker, High-frequency PN, SN velocities: some comparisons for the western, central and south Pacific, Geophys. Res. Lett. 8:207 (1981).
8. W. H. Menke and P. G. Richards, Crust-mantle whispering gallery phases: a deterministic model of teleseismic P_n wave propagation, J. of Geophys. Res. 85:5416 (1980).
9. G. V. Latham and G. H. Sutton, Seismic measurements of the ocean floor, J. of Goophys. Res. 71:2545 (1966).
10. B. L. Isacks and M. Barazangi, High frequency shear waves guided by a continuous lithosphere descending beneath western South America, Geophys. J. R. astr. Soc. 33:129 (1973).

CHAPTER 12

COMPRESSIONAL AND SHEAR WAVE ANISOTROPY IN THE OCEANIC LITHOSPHERE - THE NGENDEI SEISMIC REFRACTION EXPERIMENT

P. M. Shearer and J. A. Orcutt

Institute of Geophysics and Planetary Physics,
Scripps Institution of Oceanography
La Jolla, California 92093

Submitted to Geophys. J. R. Astron. January 1986

Abstract

Synthetic seismogram modeling of seismic refraction data from the 1983 Ngendei expedition to the south Pacific indicates seismic anisotropy both within the top kilometer of oceanic crust and in the uppermost mantle. We calculate average P and S-wave velocity versus depth functions for two orthogonal azimuths: N30°E, approximately aligned with the fast mantle direction, and N120°E, close to the fast crustal direction. Probable lateral heterogeneities at the Ngendei site prevent perfect matching of data and synthetic waveforms. Crustal anisotropy is indicated by a 2θ pattern of both P and S-wave travel times as a function of azimuth, and is consistent with an approximate 0.2 km/s difference in P-wave velocities and 0.1 km/s difference in S-wave velocities. Upper mantle anisotropy is characterized by P_n velocity differences of 7.95 to 8.4 km/s and a nearly uniform S_n velocity of 4.65 km/s. We use these velocity profiles and travel time data to calculate bounds on the properties of the elastic constants of the crust and upper mantle. The crustal anisotropy can be explained by a model involving aligned cracks parallel to the original spreading ridge, resulting in a fast direction perpendicular to the fossil spreading direction. The upper mantle anisotropy is consistent with aligned olivine crystal models, in which the fast direction is parallel to the fossil spreading direction. For both of these models, we use bounds from the Ngendei data to place constraints on the physical properties of the lithosphere.

Introduction

Traditionally, seismologists have assumed that the earth is isotropic and laterally homogeneous, not simply because this is a good first order approximation or to make calculations easier, but also because of limitations in the avail-

able data. However, as the quantity and quality of seismic data have improved, seismologists have been increasingly able to address the difficult problems of anisotropy and lateral heterogeneity. Early anisotropy studies made the assumption of transverse anisotropy (hexagonal with vertical symmetry axis), in which velocity varies only with ray parameter and not with direction. More recent work has emphasized the importance of azimuthal anisotropy, in which velocity varies with azimuth.

Azimuthal anisotropy of the oceanic upper mantle was recognized in the 1960's by Hess, Raitt, Shor and others (see, for example, Raitt 1969). More recent studies have found evidence for azimuthal anisotropy within the upper oceanic crust (Stephen 1981, 1985; White and Whitmarsh 1984). Upper mantle anisotropy appears to result from aligned olivine crystals, while crustal anisotropy is probably caused by aligned cracks. Both are related to the tectonics of the oceanic lithosphere at the spreading center where the crust and upper mantle material was originally formed.

The 1983 Ngendei Seismic Refraction Experiment provided a unique opportunity to study both oceanic crustal and upper mantle anisotropy at a single location. In an earlier paper (Shearer and Orcutt 1985), we examined P-wave travel times from the Ngendei data set and found azimuthal patterns related to anisotropy within the crust and upper mantle. We now continue this work by examining the S-wave arrivals at the Ngendei site, and by using synthetic seismogram modeling to fit amplitude as well as travel time information. We will show that crustal S-wave travel times show an azimuthal pattern similar to that observed for P-waves. In contrast, limited S_n data do not show an azimuthal dependence of upper mantle shear wave velocities.

We will derive expressions and approximate error bounds for the anisotropic elastic constants for both the Ngendei crust and uppermost mantle and then

compare these results with aligned crack models appropriate for the crustal anisotropy and aligned olivine models for the upper mantle. Finally, we look for possible S-wave splitting in the Ngendei data, but fail to find it in the noisy horizontal component data available at the Ngendei site.

The Ngendei Seismic Refraction Experiment

The 1983 Ngendei expedition to the southwest Pacific was located at DSDP hole 595B (23.82°S, 165.53°W) approximately 1000 km east of the Tonga Trench and 1500 km west of Tahiti (see Fig. 1). This is a very old part of the Pacific basin with an estimated age of 140 m.y. (Menard, personal communication). The sediment cover at the site is 70 m thick (Kim, 1986), relatively thin considering the age of the crust. The original spreading direction at the site cannot be determined from the available magnetic and bathymetric information although upper mantle anisotropy observations favor a spreading direction of northeast (Shearer and Orcutt 1985). A more detailed description of the site is available in the Initial Reports of DSDP, Leg 91.

The Scripps Institution of Oceanography ship R/V Melville shot four split refraction profiles with azimuth spacing of 45° and a circular line of 10 km radius (see Fig. 2). All of the lines were recorded by at least two Scripps ocean bottom seismometers (OBSs) and two of the lines (4b, 5a, 5b) were recorded by a borehole seismometer, the Marine Seismic System (MSS). The MSS was emplaced 124 m in DSDP Hole 595B at an ocean depth of 5600 m by the Glomar Challenger on DSDP Leg 91. During the refraction experiment, all of the OBSs were within 500m of this hole (see Fig. 3).

The close shot spacing (typically 200 shots per line), complete azimuthal coverage, and multiple receivers combine to make this perhaps the largest seismic refraction data set yet collected at a single site. The 4 channel OBSs recorded

about 8000 individual seismograms: the MSS recorded an additional 600 seismograms. Procedures used to process these data (calculate shot ranges, make topographic corrections, etc.) are described for both the OBS and MSS data sets in the Initial Reports of DSDP, Leg 91 (Shearer et al. 1986a: Whitmarsh et al. 1986). These papers also show record sections for each seismic line and receiver

A previous paper (Shearer and Orcutt 1985) examined P-wave travel times from these data and found evidence for anisotropy both within the upper mantle and in the upper crust. The fast direction in the upper mantle is about N30°E, approximately orthogonal to the fast crustal direction. This paper is a continuation of this work and extends the analysis to include synthetic seismogram modeling of both the P and S-wave velocity structure at the Ngendei site.

Upper Crustal P-wave Velocity Structure

The P-wave velocity structure of the upper crust has its greatest influence on seismic arrivals at ranges out to about 20 km. The Ngendei OBS data, while noisier than the MSS data (Adair et al. 1986), are more complete than those of the MSS and thus better suited for upper crustal P-wave analysis. We thus used only the OBS data at nearby ranges (0 to 20 km), reserving the MSS data for more distant ranges (20 to 100 km) where the advantage of lower noise levels becomes more important than the disadvantage of the sparse azimuthal coverage of the MSS. A previous analysis of P-wave travel times for the OBS data at nearby ranges led to a preliminary P-wave velocity structure which included azimuthal differences in velocity related to upper crustal anisotropy at the Ngendei site (Shearer and Orcutt 1985). This analysis did not use any of the amplitude or waveform content of the data, information employed in this paper in synthetic seismogram modeling to better constrain the velocity structure.

As a first step in this modeling procedure, we reduced each seismogram to just two numbers, the P-wave travel time and amplitude. The P-wave travel times were picked by hand using an interactive picking program. Amplitudes were determined by finding the maximum value in a 0.4 second window following the P-wave pick. The 0.4 second window was chosen to be long enough to include the first bubble pulse (usually the largest amplitude in the P-wave) but short enough to exclude the $P_m P$ arrivals of the Moho triplication.

P-wave amplitudes tend to scatter widely within individual refraction lines, probably due to lateral heterogeneities causing focusing and defocusing of seismic energy. Source irregularities were minimized for the shots at these nearby ranges by suspending the shots from balloons so that they exploded at a constant depth of 10 m. In order to remove the gross scatter in the amplitude data we averaged amplitudes within 1 km sections for each refraction line. For a typical line, each 1 km section contained about 6 P-wave arrivals (3 shots per km and 2 OBS receivers). Fig. 4 shows P-wave travel times and amplitudes (including one standard deviation error bars) for refraction lines 1a, 1b, 3a, 3b, 4a, and 5b. Travel times have been reduced at 6.8 km/s and amplitudes have been scaled for range and shot weight by the empirical formula

$$A = \left\{\frac{r}{r_0}\right\}^2 \left\{\frac{w_0}{w}\right\}^{0.65} A_{raw}$$

where r = range

w = shot weight

Although topographic corrections can remove the gross effects of bathymetric differences on P-wave travel times, such corrected travel times tend to exhibit more scatter in regions containing significant seafloor topography (Shearer et al. 1986a). Not surprisingly, we noticed similar increased scatter in

the observed P-wave amplitudes for shots near the seamounts and ridges at the Ngendei site. Fig. 5 shows P-wave arrival times and amplitudes compared to the ocean depth along refraction lines 4b and 5a. Both the travel times and amplitudes show significant anomalies related to the irregularities in the sea floor. P-wave travel times are reduced for shots above topographic highs (although note the slight range offset), reflecting the decreased travel time in the relatively slow ocean. Amplitude behavior is less predictable but certainly exhibits more scatter in these lines than in the lines shown in Fig. 4, which were along relatively smooth parts of the sea floor.

Because of these large topographic effects, our analysis excluded data from those lines which contained significant sea floor relief. The lines shown in Fig. 4 all contain less than 150 m of relief at the ranges shown, although it was necessary to truncate line 3b at 18 km, line 4a at 17 km, and line 5b at 18 km in order to meet this criterion. To account for the slight remaining variations in water depth, topographic corrections based on the ray path through the water were applied (Shearer et al. 1986a, for a full discussion). We did not use lines 2a and 2b in our amplitude analysis because those lines used larger shots which cannot be easily compared to the shots used in the other lines, and also because 2a and 2b duplicate data already available from lines 1a and 1b (see Fig. 2).

Although there are significant variations between the range versus amplitude behavior of the different refraction lines shown in Fig. 4, some gross trends are apparent. Amplitudes tend to increase rapidly from very small values at 3 km to an amplitude peak at about 5 or 6 km, then decrease to a local minimum at about 10 km. Some of the lines contain another amplitude peak at about 15 km but this is highly variable between lines. The P-wave travel times for these lines show an azimuthal variation which indicates that upper crustal P-wave velocities are faster in the direction N120°E and slower in the direction N30°E

(Shearer and Orcutt, 1985). Because of this systematic difference in P-wave travel times, which we believe is caused by anisotropy in the upper crust, we divided the data into what we will call the NNE lines (lines 3a, 3b, and 4a) and the ESE lines (lines 1a, 1b, and 5b). Fortunately, this division based on travel time differences also appears to make sense in terms of the P-wave amplitudes. The amplitude peak at about 15 km is more prominent in the ESE lines than in the NNE lines.

Although such a division of the data set into two orthogonal azimuths is necessarily approximate (individual lines are 15 to 30 degrees off from the group azimuth) it has the advantage of allowing us to compute separate average velocity versus depth profiles for the fast crustal direction (ESE) and the slow crustal direction (NNE). Since the crustal anisotropy appears to exhibit a 2θ variation of velocity with azimuth (Shearer and Orcutt 1985) this will be sufficient to define the azimuthal P-wave velocity anisotropy. The averaging of adjacent azimuths will simply have the effect of slightly underestimating the total magnitude of the anisotropy at a given depth.

Considering the scatter in the data, we tried to chose a modeling strategy for the Ngendei data set that would be as simple and robust as possible. We used the WKBJ technique (Chapman 1978) for calculating synthetic seismograms, which, because of its relatively low cost, permitted us to try dozens of different models. The WKBJ method is an asymptotic solution which in some situations can differ significantly from more exact solutions (Chapman and Orcutt 1985). However, we found that in practice the misfit between the synthetics and the data was dominated by probable effects of lateral heterogeneity, and thus we saw no reason to use a more accurate synthetic technique. For a check on our final crustal P-wave models, we calculated synthetic seismograms with the more accurate reflectivity method (Fuchs and Müller 1971) and found

no significant differences from the WKBJ synthetic seismograms. We recognize that the WKBJ method is not strictly valid for anisotropic materials, but believe that this will not cause serious problems in analyzing the rather noisy Ngendei waveform data, provided we use different velocity versus depth profiles for different azimuths.

One approach to analyzing this data set would be to determine a velocity versus depth profile for each individual refraction line (8 separate azimuths) and then to compare the results for evidence of lateral heterogeneity and/or anisotropy. We rejected this approach because of the difficulty of accurately fitting the individual lines. Most of the lines exhibit travel time and amplitude behavior inconsistent with a laterally homogeneous model. That is, travel times might not agree with a travel time curve of ever decreasing slope, or a few seismograms might display large amplitude anomalies where the amplitude change is too abrupt for a one-dimensional model to predict. This behavior is true even of the lines which do not cross any of the numerous ridges and seamounts at the Ngendei site, and is evidence for substantial heterogeneity not strictly related to topographic focusing.

Recognizing these difficulties, we decided to attempt to "average out" the lateral heterogeneities within individual lines and then use synthetic seismogram modeling to determine a single "best" velocity versus depth structure for the entire data set. Fig. 6a shows the results of combining data from the NNE lines and the ESE lines. The P-wave travel times show a distinct difference between the two azimuths with the ESE arrivals coming in ahead of the NNE arrivals. The P-wave amplitudes also appear different with the ESE amplitudes exhibiting sharper peaks at 5 and 15 km and a sharper minimum at 10 km than the more smooth behavior of the NNE amplitudes. Note also the greatly increased scatter in the OBS P-wave picks at 20 to 30 km range.

We attempted to fit the P-wave travel times and amplitudes at these two azimuths by forward modeling. We assumed a velocity versus depth profile, calculated WKBJ synthetic seismograms, convolved with the appropriate source and instrument response and then compared the calculated travel times and maximum amplitudes with those of the data. Our technique is similar to that of Bratt and Purdy (1984), except that we used maximum amplitude rather than integrated power as a basis for comparison. We made no attempt to compare absolute amplitudes of data and synthetics, trying only to obtain agreement in the relative shape of the amplitude curves. There is a tradeoff between fitting the travel time and the amplitude data, in that either alone can be fit better than both together. This is largely because the amplitude peak at 15 km occurs at what appears to be a relatively flat part of the travel time curve. Normally, higher amplitudes are expected at sharply curved portions of the travel time curve, indicative of a large number of rays arriving at nearly the same range. However, through a laborious trial and error procedure we were eventually able to obtain velocity versus depth profiles which fit both the travel time and amplitude data reasonably well.

These velocity versus depth models are shown in Fig. 7 and Table 1; the resulting fit to the travel time and amplitude data is shown in Fig. 6b. Both models are characterized by a relatively high velocity gradient in the top kilometer of the crust, a lower velocity gradient between 1 and 2 km depth, and a constant lower crustal velocity of 6.8 km/s. This lower crustal velocity was a constraint we imposed on our modeling based on our preliminary analysis of the longer borehole seismometer refraction lines (more about this later in the paper). A linear velocity versus depth gradient will generally lead to an amplitude peak caused by the increased focusing of rays turning at the bottom of the gradient. The steep velocity gradient down to 1 km depth is the cause of the amplitude

peak at about 5 km range. The amplitude minimum at about 10 km is related to rays turning in the top of the shallow gradient between 1 and 2 km depth, with the bottom part of this gradient related to the amplitude peak at about 15 km range. As an illustration of how these amplitude peaks relate to the velocity model, Fig. 8 shows a cross-section of the ESE model with ray paths in the shallow part of the crust. The bunching of rays at 5 and 15 km range is related to the amplitude peaks in the WKBJ synthetics (see Fig. 6b).

Amplitude peaks can also be caused by localized sharp velocity gradients or velocity discontinuities, and we cannot exclude the possibility of their presence near the bends in our velocity versus depth function at 1 and 2 km depth. However, they are not required by the data and, if present, are likely to involve relatively small differences in velocity (less than 0.3 km/s). Velocity gradients must be present in the upper 2 km of crust; no simple "layer cake" model involving a small number of constant velocity layers can adequately explain both the amplitude and travel time data.

Using data from the Rivera Ocean Seismic Experiment (ROSE) on the East Pacific Rise, Bratt and Purdy (1984) noticed sharp power peaks at ranges of 6 to 10 km. Since the ocean is deeper at the Ngendei site (5.6 km vs. 2.9 km), we would expect amplitude peaks to occur at a somewhat greater range, but this effect is not large enough to reconcile the peaks at 15 km in the Ngendei data with the ROSE data peaks. However, in both the Bratt and Purdy velocity model and our Ngendei velocity model, the amplitude peaks are related to a velocity gradient near the bottom of layer 2, and thus we believe that they are caused by similar structures. The difference in the position of the peaks results from overall differences in the velocity models, in particular from the much slower upper crustal velocities at the younger ROSE site. Bratt and Purdy related the range variations in their observed peak positions to differences in

layer 2 thickness: our observed amplitude peaks exhibit a similar range variation (see Fig. 4) and support this conclusion. The Ngendei and ROSE data sets are also similar in that some lines do not show strong amplitude peaks.

P-wave anisotropy in the top 1 to 1.5 km of the crust at the Ngendei site is indicated by the approximate 0.2 km/s offset between the NNE and ESE velocity profiles. The travel time data alone indicate that NNE velocities must be faster than ESE velocities in the upper crust (Shearer and Orcutt 1985). However, the amplitude information which we are now considering give us much better constraints on the depth and magnitude of this velocity difference. In particular, we believe that P-wave anisotropy is confined to the top 1 to 1.5 km of the crust, and that it is probably present at the surface of the crust. The overall similarity of the NNE and ESE amplitude versus range curves indicates that there can be no large differences in the shape of the velocity profiles. The slower near surface velocities for our NNE model are consistent with the broad nature of the data amplitude peak at 5 km range. Differences in the transition at 1 to 1.5 km depth from the higher to the lower velocity gradient lessen the severity of both the amplitude minimum at 10 km and the amplitude peak at 15 km for the NNE model.

The resolution of our model is difficult to assess quantitatively, particularly because we have attempted to produce a model which in some sense averages the differences between individual refraction lines related to lateral heterogeneities. It is interesting to note that the amplitude peak near 15 km range is generally sharper for the individual lines (Fig. 4) than on the azimuthally averaged lines (Fig. 6a). This is because the range at which the amplitude peak occurs varies between the lines so that the averaged peak becomes shortened and broadened. This suggests that the transition to the constant velocity layer at 2 km depth may be sharper (causing a higher, narrower amplitude peak) than in our model

but that the depth to this transition may vary between lines (changing the range at which the peak occurs). If this is the case, our model is still approximately correct for a laterally averaged earth since averaging different velocity profiles would have a similar effect.

As a final check, we compared synthetic seismograms to data for line 5b, using the ESE velocity model. Fig. 9 shows a comparison of selected seismograms, scaled for range and shot weight. Although this model is an average for all lines of similar azimuth, the fit to line 5b is still reasonably good. In particular, note the reproduction of the large amplitudes at ranges of 6 and 16 km. The two distinct pulses in the data and synthetics are the initial source and first bubble pulses, often not separated with less broadband instruments than the Scripps OBS.

P-wave Velocity Structure Near The Moho

At ranges greater than 20 km, noise severely limited the quality of the OBS data. Much of this noise was associated with operations of the drilling ship, the Glomar Challenger, during the refraction shooting. However, even under quiet conditions OBS noise levels were about 10 to 15 db higher than MSS (borehole) noise levels (Adair et al. 1986). Since signal levels as recorded by the OBSs and the MSS were approximately the same (Shearer et al. 1986b) this resulted in a considerable signal-to-noise improvement for the MSS recordings. This proved particularly important for examining the relatively weak P_n arrivals at the Ngendei site. P_n arrivals on the OBS seismograms could only be picked out to ranges of about 50 km. Although these picks proved adequate to constrain the direction and magnitude of upper mantle anisotropy at the Ngendei site (Shearer and Orcutt, 1985) the poor quality of the P_n arrivals precluded the possibility of any amplitude or waveform analysis.

Thus, we decided to use only MSS data from the two orthogonal lines 4b and 5b (see Fig. 2) for modeling with synthetic seismograms. Fortunately, these lines are approximately aligned with the fast and slow axes of the upper mantle anisotropy, so the lack of complete azimuthal coverage is not a severe problem. OBS P-wave travel time data from all azimuths indicate that lower crustal velocities do not vary with azimuth and that the upper mantle anisotropy can be described with a simple 2θ function of azimuth (Shearer and Orcutt 1985). We assumed the upper crustal P-wave model discussed in the previous section for all subsequent modeling.

Fig. 10 shows MSS record sections for lines 4b and 5b and our best fitting WKBJ P-wave models, based on the velocity models shown in Fig. 7. Both data and synthetics have been reduced at 8 km/s and scaled for range and shot weight. Topographic time corrections have been made to account for differences in sea floor bathymetry along the lines in a similar way to the OBS corrections discussed earlier; however times and ranges have not been corrected to the sea floor. The data have been multiplied in the frequency domain with a $sinc^4$ function in order to make a direct comparison with the WKBJ synthetics, which have undergone a similar smoothing operation (Chapman and Orcutt 1985). Alternatively, the WKBJ synthetics could have been calculated at a much higher sampling rate than the data, but this seemed unnecessary considering the generally low frequency nature of the MSS data which are little affected by the smoothing operation. We checked our final models by calculating synthetic seismograms with the reflectivity method (Fuchs and Müller 1971), and found no significant differences from the WKBJ results.

The most striking difference between the lines is in the P_n arrivals, which for line 4b are both weaker and faster than those of line 5b. Our synthetic seismogram modeling suggests that the upper mantle P-wave velocity in the

direction of line 4b is 8.4 km s with a relatively weak velocity gradient of 0.007 (km s) km compared to a velocity of 7.95 km s and a somewhat stronger gradient of 0.026 (km s) km for the line 5b direction. The velocities are based on matching the P_n arrival times: the amplitudes are based on matching the relative amplitudes of the P_n arrivals with the $P_m P$ arrivals. This observation of a stronger P-wave gradient in the upper mantle in the slow P-wave direction is opposite to observations discussed by Garmany (1981), and is probably inconsistent with his model of a gradient in anisotropy in the uppermost mantle.

The large velocity increase at the Moho in the model for line 4b is required by the significant $P_m P$ reflections at large ranges, the low amplitude of the P_n arrivals compared to $P_m P$, and the observed phase velocity of the mantle arrivals. The smaller jump in velocity for the model corresponding to line 5b serves to increase the size of P_n and concentrates the larger $P_m P$ amplitudes closer to the near caustic. Note in Fig. 10b that the ratio of P_n to $P_m P$ amplitudes is substantially smaller for the line 5b synthetics than for the 4b synthetics. The weak crustal P-waves at ranges of 20 to 30 km are indicative of a very low velocity gradient in the lower crust. For both lines we found that a constant lower crustal velocity of 6.8 km/s provided the best fit to the position and amplitude of the crustal P phase.

Significant differences remain between the synthetic record sections and the data. For example, the line 4b data contain an amplitude peak on the retrograde $P_m P$ branch at 40 to 50 km range. The amplitude peak in the synthetics is at a closer range of 20 to 40 km and is associated with the caustic at the end of the retrograde branch. After much adjusting of our models we came to realize that no one-dimensional model can explain the line 4b data, since for such models large amplitudes cannot occur in the middle of retrograde branches, only near the endpoints. An additional problem is that $P_m P$ amplitudes at long ranges are

much greater in the line 4b data than in the line 5b data. a difference which cannot easily be accounted for in the synthetics. Thus. we believe that any fit to the data which does not include lateral heterogeneity will only be approximate. In particular, it seems likely that undulations in the Moho surface are distorting the amplitude behavior of the $P_m P$ branch.

The P-wave velocity model we are now proposing for the Ngendei site differs from that which we proposed earlier based only upon P-wave travel times (Shearer and Orcutt 1985). The earlier model included a substantial velocity gradient throughout layer 3. The amplitude data which we have discussed preclude such a high gradient, and our new model with a constant velocity layer 3 still fits the crustal P-wave travel times quite well. The crustal P-wave anisotropy in the earlier model is large in magnitude (0.4 km/s difference between azimuths) and is confined to a layer between 0.75 and 1.4 km depth. We now believe that the anisotropy is smaller in magnitude ($\approx$ 0.2 km/s) and is present throughout the top 1.4 km of crust. P-wave travel times alone cannot distinguish between these two models; there is a tradeoff between the magnitude of the anisotropy and the thickness of the anisotropic layer. However, the P-wave amplitude data are inconsistent with the sharp velocity discontinuities of the earlier model, and thus favor the smoother velocity profiles of the new model.

Upper Crustal S-wave Velocity Structure

The quality of the shear waves observed in the Ngendei refraction lines is highly variable. Many of the lines have well defined shear wave arrivals, while in other lines shear waves are not observed. However, enough data are present to form constraints on the shear wave structure at the Ngendei site. As in the case of the P-wave analysis, we decided to use the OBS data to examine upper crustal P-wave structure, reserving the MSS data at longer ranges for the lower crustal

and upper mantle structure.

Using interactive picking software, we picked shear wave arrivals at ranges out to 20 km. Two shear wave arrivals could usually be identified. Arriving first was the wave which converted to a P-wave at the crust-sediment interface. This arrival was most prominent on the OBS vertical component. Arriving about 0.55 seconds later was the direct S-wave through the sediments, which appeared most prominently on the OBS horizontal channels. Since we know that the sediments are 70 m thick with a P-wave velocity of about 1.6 km/s, this allowed us to calculate a sediment shear wave velocity of about 120 m/s. This value is in agreement with that obtained by modeling eigenfrequencies associated with sediment reverberations in Ngendei earthquake data (Sereno and Orcutt 1985).

Since many of the shear wave arrivals were very weak and contaminated by noise from the earlier arriving P-waves, it was difficult to accurately pick the travel times. In particular, picking traces individually without reference to those at similar ranges along the same line proved impossible. However, by displaying an entire reduced record section on the computer screen at once, and switching between the horizontal and vertical channels, it often became possible to identify phases which otherwise would be missed. In this way, 415 shear wave arrivals were identified, including at least some for all lines except lines 4b and 5a.

The sediment converted P-wave arrival proved to be the easiest to pick and was used for all of the shear wave travel time analysis. Fig. 11 shows OBS P-wave, S-wave and water wave picks at ranges from 4 to 20 km. Travel times have been reduced at 6.6 km/s. No topographic corrections have been applied but all arrivals from shots in ocean depths less than 5400 m have been eliminated. Note that the scatter in the S-wave arrival times is not significantly worse than that in the P-wave travel times. The direct water wave arrivals show no scatter because shot to OBS ranges were calculated based on water wave

travel times.

Fig. 12 shows a close up of the shear wave arrivals (now corrected for topography), reduced at 3.75 km/s. Plus signs represent arrivals from within 45 ° of a ESE azimuth; circles represent arrivals within 45 ° of a NNE azimuth. The cluster of data at about 10 km range is from the circular line (line 2c). In general, the travel times are approximately flat from 9 to 20 km, indicating a shear wave velocity of 3.75 km/s. At closer ranges, the slope of the travel time curve indicates slower velocities. Although there is considerable scatter in the data, the ESE arrivals come in slightly before the NNE arrivals at ranges from 6 to 11 km. Beyond 11 km, the arrivals appear randomly scattered with respect to azimuth.

This pattern is similar to that which can be seen with greater clarity in the P-wave travel time data (Shearer and Orcutt 1985). The azimuthal S-wave travel time difference seems clearest at ranges between 9 and 11 km. Since the slope of the travel time curve is approximately flat at these ranges, the data can be reduced for a constant velocity in order to make a travel time versus azimuth plot. Fig. 13 shows such a plot for S-wave travel time picks between 9 and 11 km, reduced at 3.75 km/s. Topographic time and range corrections have adjusted the arrivals to the sea floor. The vertical alignments in the plot represent individual refraction lines, which were shot at approximately constant azimuth. Points between these alignments represent data from the circular line. The data show considerable scatter, presumably representing lateral heterogeneities. However, some systematic azimuthal trends are apparent. Arrivals at azimuths of 0-45 ° (NNE) and 180-225 ° (SSW) are generally late, while arrivals at azimuths of 90-135 ° (ESE) and 270-315 ° (WNW) are generally early.

The crustal shear wave phase relevant to these picks is vertically polarized since only SV waves would convert to P-waves in the sediment. Following Backus (1965) and Crampin (1977) we may express the velocity of a quasi-SV

wave (approximately vertically polarized) traveling within a horizontal plane in a general weakly anisotropic medium as

$$V^2 = a_1 + a_2\cos 2\theta + a_3\sin 2\theta$$

where V = qSV phase or group velocity

θ = azimuth of wave propagation

To first order in the anisotropy, qSV-wave travel times which represent waves turning at approximately equal depths can be represented by a function of the form

$$T = a'_1 + a'_2\cos 2\theta + a'_3\sin 2\theta$$

A curve of this type was fitted in a least squares sense to the travel time data (see Fig. 13), reducing the variance of the data residuals (versus residuals from the mean) by 21%. The magnitude of the azimuthal travel time differences is about 0.08 s and the inferred fast direction for the qSV crustal anisotropy is N119°E. This compares to an azimuthal travel time difference of 0.05 seconds and fast direction of N120°E for compressional arrivals (Shearer and Orcutt 1985). We also fit the travel time data shown in Fig. 13 with a Fourier series which included θ, 2θ, 3θ, 4θ, and 5θ terms. The variance reduction achieved with 2θ terms alone was far greater than for any other terms (4θ was second best with an 10% variance reduction).

We obtained these results by applying topographic time and range corrections for both P and S-waves. These corrections are based on finding the intersection of the ray path with the appropriate point on the sea floor. The P-wave topographic corrections are described in detail in Shearer et al. (1986a). We determined the S-wave corrections in a similar manner, except that we used a constant phase velocity of 3.75 km/s in calculating the water path and did not apply a dt/dh correction. Although all data discussed in this paper have been

corrected for topography, we wish to emphasize that our results are not very sensitive to these corrections. Even if we had applied no corrections at all, we would have obtained similar results regarding the orientation and magnitude of anisotropy.

The similarity of the azimuthal pattern of the Ngendei S-wave travel times to the P-wave pattern is not additional evidence for anisotropy at the Ngendei site since the leading alternative (non-anisotropic) explanation for the observed azimuthal variations in travel times is lateral heterogeneity. A hypothetical slow "blob" of crust would slow both P and S-waves and lead to similar travel time patterns. Thus, it is not surprising that we observe an azimuthal dependence of S-wave travel times. However, we believe that anisotropy is a more likely explanation for the gross azimuthal trends in the data, since we would not *a priori* expect lateral heterogeneity to be organized in a 2θ sense. Furthermore, if we accept that these travel time patterns are caused by anisotropy, then the shear wave data place additional constraints on the anisotropic elastic constants in the upper crust. We will discuss these constraints in more detail later in this paper.

The noisy and irregular nature of the S-wave arrivals precluded any amplitude or waveform analysis of the data. In addition, S-wave amplitudes are at least partially dependent on P-to-S conversion efficiency, which depends on properties at the sediment/basement interface and not on the velocity structure at depth. Thus, we formulated velocity versus depth models based only on the S-wave travel times. Fig. 7 illustrates a simple S-wave velocity profile of the upper crust which is consistent with the travel time data, although more complicated models are certainly not excluded. The P and S-wave velocity models are generally consistent but with the difference that the S-wave profile reaches the constant layer 3 velocities at about 1.7 km depth versus 2 km for the P-wave velocity profile. This difference appears required by the travel time data and pro-

duces a slight dip in the Poisson's ratio of the model at a depth of 1.7 km in the crust. Spudich and Orcutt made a similar observation in synthetic modeling of refraction data in the eastern Pacific (Spudich and Orcutt 1980a).

S-wave Velocity Structure Near The Moho

As in our P-wave analysis, we used MSS data from the two orthogonal lines 4b and 5b (see Fig. 2) at ranges of 20 to 100 km in order to constrain the shear wave structure of the lower crust and upper mantle. Fig. 14 shows MSS vertical component record sections for lines 4b and 5b and our best fitting WKBJ S-wave models, based on the velocity model shown in Fig. 7 and Table 1. Both data and synthetics have been reduced at 4.65 km/s and scaled for range and shot weight. Topographic time corrections appropriate for S-wave phase velocities have been made to account for differences in sea floor bathymetry along the lines; however times and ranges have not been corrected to the sea floor. The data have been multiplied in the frequency domain with a $sinc^4$ function in order to make a direct comparison with the WKBJ synthetics.

A very weak S_n arrival is apparent in these record sections with an apparent phase velocity of about 4.65 km/s in both lines. S_n observations are rare in seismic refraction experiments; our success here was due in part to the low noise levels of the MSS borehole seismometer. In many cases, S_n is obscured by the second arriving P-wave which results from a single multiple in the water column, but the relatively deep ocean at the Ngendei site (5600 m) delays this phase sufficiently to prevent an overlap with S_n except at ranges greater than 80 km.

An S_n velocity of 4.65 km/s is in general agreement with other studies. A previous refraction experiment in the northeast Pacific observed isotropic S_n

velocities of 4.5 to 4.6 km s (Clowes and Au 1982). Earthquake studies have found S_n velocities of 4.66 km s in the Caribbean (Molnar and Oliver 1969), 4.58 to 4.71 km/s in the Atlantic (Hart and Press, 1973), and 4.70 to 4.88 km/s in the western Pacific (Walker and Sutton, 1971; Walker 1977; Shimamura et al. 1977).

We found that we could fit the S-wave travel time data from both lines with a nearly identical shear wave velocity model. The constant lower crustal velocity of 3.75 km/s in the model is constrained by the weak crustal S-waves at ranges of 20 to 30 km. We found that the Moho depths obtained from the P-wave modeling also fit the S-wave data. Our modeled S-wave upper mantle velocity gradients of 0.013 (km/s)/km for line 4b and 0.026 (km/s)/km for line 5b are poorly constrained by the amplitudes of the weak S_n arrivals and represent very approximate estimates.

Obtaining Elastic Constants from Travel Time Data

In general, it is impossible to completely recover the elastic constants of a medium from velocity measurements within a single plane. However, such recovery is possible under certain simplifying assumptions which we believe are realistic for the Ngendei crustal and upper mantle anisotropy. Using relationships first derived by Backus (1965) and discussed extensively by Crampin (1977) we can approximate the azimuthal velocity dependence of P and SV waves in a general, weakly anisotropic medium with a known horizontal symmetry axis as

$$\begin{aligned} V^2_P &= A + B\cos 2\theta + C\cos 4\theta \\ V^2_{SV} &= D + E\cos 2\theta \end{aligned} \tag{1}$$

θ is the angle from the symmetry axis and A, B, C, D, and E are constants. These constants are related to components of the anisotropic elastic tensor by

$$\begin{aligned} \Gamma_{1111} &= A + B + C \\ \Gamma_{2222} &= A - B + C \end{aligned} \tag{2}$$

$$\Gamma_{1313} = D + E$$
$$\Gamma_{2323} = D - E$$
$$\Gamma_{1122} + 2\Gamma_{1212} = A - 3C$$

where Γ is the anisotropic elastic tensor (normalized by density) and we have assumed that the symmetry axis has a (100) orientation and the vertical axis is (001).

We believe that the assumptions of weak anisotropy and a horizontal symmetry axis are appropriate for the Ngendei data. Azimuthal crustal velocity variations are about ± 2%: upper mantle variations are about ± 3%. Small velocity variations alone do not establish the accuracy of these equations (see Crampin 1982: Backus 1982) but they are suggestive of weak anisotropy. As a further check, we calculated the parameter a_E, a measure of the size of the deviation of an elastic tensor from an isotropic tensor (Backus 1982), and found that $a_E < 0.2$ for all models which we will consider in fitting both the Ngendei crustal and upper mantle anisotropy. Since the above approximations are valid for $a_E << 1$, we consider the weak anisotropy assumption to be appropriate for the Ngendei anisotropy. The additional assumption of a horizontal symmetry axis is difficult to justify purely from the observations, but is appropriate for any type of anisotropy based upon a single preferred orientation of cracks or crystals.

Under these assumptions we can recover some but not all of the components of Γ from azimuthal velocity measurements of P and SV. If we further restrict the form of the anisotropy to hexagonal with symmetry axis (100), then knowledge of A, B, C, D, and E is sufficient to obtain all components of Γ. As we will discuss later, such hexagonal models are appropriate for upper crustal anisotropy resulting from vertical aligned cracks and upper mantle anisotropy resulting from preferred crystal alignment with a horizontal symmetry axis. For such a hexagonal material, we have the symmetry relationships (Musgrave 1970)

$$\Gamma_{3333} = \Gamma_{2222}$$
$$\Gamma_{1212} = \Gamma_{1313}$$
$$\Gamma_{1122} = \Gamma_{1133}$$
$$\Gamma_{2323} = \frac{1}{2}(\Gamma_{3333} - \Gamma_{2233})$$

Thus we have the additional relationships

$$\begin{aligned} \Gamma_{3333} &= \Gamma_{2222} = A - B + C \\ \Gamma_{1212} &= \Gamma_{1313} = D + E \\ \Gamma_{1122} &= \Gamma_{1133} = A - 3C - 2(D + E) \\ \Gamma_{2233} &= A - B + C - 2(D - E) \end{aligned} \tag{3}$$

The remaining 12 independent components of Γ are zero.

From our Ngendei velocity model we can obtain approximate values for A, B, C, D, and E for the crustal and upper mantle anisotropy which the model predicts. Assuming hexagonal symmetry we can use the above relationships to derive approximate values for the anisotropic elastic constants. However, there is a remaining ambiguity (discussed by Crosson and Christensen 1969) in that we must specify if the symmetry axis (100) represents the slow or the fast velocity direction. Essentially this is equivalent to deciding if the vertical velocity in our hexagonal model corresponds to the fast or the slow horizontal velocity. We will decide between these two possibilities by examining the physical models which we believe are most appropriate to explain our observed anisotropy. The aligned crack models which seem appropriate for the upper crustal anisotropy contain a slow hexagonal symmetry axis. In contrast, the aligned olivine models considered likely for the upper mantle contain a fast hexagonal symmetry axis.

Previous sections of this paper have concentrated on obtaining P and S-wave velocity vs. depth sections for two orthogonal azimuths. These profiles could be used to estimate the constants A, B, D, and E in the above equations. However, in order to make estimates of C (the 4θ P-wave term) and to

constrain possible errors, it is helpful to examine reduced travel time data vs. azimuth. As a first order approximation, assume that velocity perturbations at a particular depth are linear functions of travel time perturbations. We thus have

$$T = T_0 + \Delta T$$
$$V = V_0 + \Delta V = V_0 + k\,\Delta T$$

Now assume that travel time perturbations ΔT are related to azimuthal anisotropy such that (in the P-wave case)

$$T = A' + B'\cos 2\theta + C'\cos 4\theta$$
$$V = V_0 + k\,(B'\cos 2\theta + C'\cos 4\theta)$$

If the velocity is known at angles of 0 and 90 degrees from the symmetry axis, we have

$$V(0) = V_0 + k\,(B' + C')$$
$$V(90) = V_0 + k\,(-B' + C')$$

Solving for k and v_0, we have

$$k = \frac{V(0) - V(90)}{2B'} \qquad (4)$$
$$V_0 = V(0) - k\,(B' + C')$$

Notice that k is the scaling factor that relates travel time variations to velocity variations. We will estimate $V(0)$ and $V(90)$ from the velocity models previously discussed. These velocity models are not independent of the travel time data, because they were chosen at least partially so that travel time points calculated from the models would approximately lie on the best fitting curves for the reduced travel time data.

If we assume the anisotropy is weak ($\Delta V << V_0$), then to first order

$$V^2 = V_0^2 + 2V_0kB'\cos 2\theta + 2V_0kC'\cos 4\theta$$

Thus, we see that the constants A, B, and C in Eqn. (1) are related to the

equivalent constants for reduced travel times by

$$\begin{aligned} A &= V_0^2 \\ B &= 2V_0 kB' \\ C &= 2V_0 kC' \end{aligned} \tag{5}$$

Expressions for the SV constants D and E are similar.

Thus, if we know $V(0)$ and $V(90)$ for both P and S-waves at a particular depth and the constants A', B', C', D', and E' for the appropriate reduced travel time plot, we can calculate the anisotropic azimuthal velocity coefficients A, B, C, D, and E. Assuming hexagonal symmetry, we can then calculate all of the components of the elastic tensor at that depth. This is the procedure which we used to analyze the Ngendei anisotropy.

In addition to a single best fitting model, it is helpful to obtain error bounds on the fit in order to estimate the resolution of the model. We attempted to do this for the Ngendei data by calculating bounds on parameters for the curves which we fit to the travel time data. If we assume that the errors in the travel time data are statistically independent, there are formal procedures for calculating such bounds. Unfortunately, the misfits in the data clearly are *not* statistically independent, and any parameter bounds calculated under such an assumption will be unrealistically narrow. This statistical dependence of the data arises because the leading non-anisotropic explanation for variations in travel times at the Ngendei site is lateral heterogeneity, which will systematically affect many travel time points simultaneously.

It is difficult to objectively estimate the statistics of contamination from lateral heterogeneity at the Ngendei site. Our *ad hoc* procedure for estimating parameter error bounds was to allow a parameter value to change until the variance of the fit to the travel time data increased by more than 10% (versus the best fitting model). The resulting bounds are much more conservative than those

which would be obtained by assuming statistical independence. The 10% variance increase criterion is subjective: it is close to the point at which the visual fit between the the curve and the data begins to deteriorate noticeably. We applied this procedure to the Ngendei travel time data for crustal and upper mantle anisotropy; results are shown in Table 2.

We believe that approximately the top 1 km of crust at the Ngendei site is anisotropic, with velocity increasing strongly with depth (see Fig. 7). As an example, we chose to calculate anisotropic parameters at an arbitrary depth of 0.5 km. At this depth, V_P varies from 5.18 to 5.40 km/s and V_S varies from 2.81 to 2.90 km/s based on our velocity model. The crustal P-wave travel time data best show an azimuthal dependence at ranges between 7 and 11 km. We fit these data (reduced at 6.6 km/s) with a curve of the form

$$T = A' + B'\cos 2(\theta - \phi) + C'\cos 4(\theta - \phi)$$

where θ = azimuth of shot

ϕ = azimuth of fast velocity direction

This equation is nonlinear in ϕ; we used an iterative least squares procedure to find a solution. In a similar way, we fit S-wave travel time data between 9 and 11 km (reduced at 3.75 km/s) with a curve of the form

$$T = D' + E'\cos 2(\theta - \phi)$$

For the crustal P-wave data, the best fit was at ϕ = N117°E with upper and lower bounds of 101 to 129° (based on the 10% greater variance criterion), while for the S-wave data the best fit was at ϕ = 119° with bounds of 97 to 134°. The close agreement between the azimuths of the fast P-wave direction and the fast S-wave direction (117° vs. 119°) suggests a symmetry axis in an anisotropic material. For consistency we used ϕ = 118° for subsequent analysis of both the P and S-wave data. We took the intersection of the P and S-wave

bounds on o to be the true bounds on o (101 to 129°).

Using o = 118°, we calculated the best fitting values for A', B', C', D', and E'. We then forced each parameter to higher and lower values (solving for the best fit for the remaining parameters) until the variance of the solution was 10% more than the original variance. Table 2 contains the best fitting values with upper and lower bounds. Note that the limits on the parameters represent extremal bounds for one parameter at a time: in general, a curve using two or more of these bounds together would exceed the 10% criterion for allowed increase in misfit variance.

Next, we used our values for V_P and V_S at 0 and 90° (from the fast direction) and the relationships in Eqn. (4) and (5) to calculate the velocity anisotropy coefficients A, B, C, D, and E. We switched the signs of B and E so that the horizontal symmetry axis would correspond to the slow direction, a relationship appropriate for the crack models which we will consider later. Bounds on B, C, and E were calculated from the equivalent bounds on B', C', and E'. We assumed that A, related to the absolute P-wave velocity, was precisely known. Clearly this is unrealistic at an exact depth of 0.5 km, but since velocities are increasing rapidly with depth, it is apparent that an appropriate value could be found close to the 0.5 km depth. The bounds shown on D in Table 2 were estimated subjectively, and represent the uncertainty in the absolute S-wave velocity relative to the P-wave velocity (equivalent to uncertainty in the azimuthally averaged Poisson's ratio), an uncertainty we assumed to be ± 0.1 km/s.

Finally, using the relationships in Eqn. (2) and (3), we calculated the best fitting values for the elastic constants for a hexagonally symmetric anisotropic material with a (slow) horizontal symmetry axis. We also calculated bounds on the elastic constants by using the appropriate extremal values of A, B, C, D, and E, but, because we used extremal values of more than one parameter at a

time, these bounds are looser than the bounds on A, B, C, D, and E. In fact, they are so loose that they are of little practical use for comparison with physical models. These bounds could be tightened by directly searching for limits on the linear combinations of A, B, C, D, and E which are contained in Eqn. (2) and (3). However, it is easier to simply calculate model values for A, B, C, D, and E and compare these parameters to the data, rather than comparing the elastic constants.

We used a similar procedure for analyzing the Ngendei upper mantle anisotropy, but were limited by less complete data. Since S_n was observed at only two azimuths, we were unable to fit a curve to the S-wave upper mantle data. Because of the limited azimuthal coverage of the OBS P-wave travel time data for the upper mantle (see Fig. 19, Shearer and Orcutt 1985), we excluded 4θ terms from the travel time fit. In order to estimate C', the 4θ travel time coefficient, we examined other studies of P-wave upper mantle anisotropy in the Pacific which used much larger data sets (Raitt et al. 1969; Morris et al. 1969). These studies found that the 4θ terms were small compared to the 2θ terms, with magnitudes generally less than 20% of the 2θ term magnitude. Thus, assuming that the Ngendei upper mantle anisotropy is similar to that observed elsewhere, we assigned a "best" value for C' of zero, with lower and upper bounds defined by 20% of the maximum value of B'.

The best P-wave fit for ϕ, the fast direction, was N30°E, with lower and upper bounds of 25 and 35°. Values and bounds for A', B', and C' are shown in Table 2. It is interesting to note that the calculated fast direction of the upper mantle anisotropy (N30°E) is very close to 90° away from the fast direction in the upper crust (N118°E). From our two orthogonal velocity models we obtained values for $V_P(0)$ and $V_P(90)$ of 8.4 and 7.95 km/s respectively, and a single velocity of 4.65 km/s for $V_S(0)$ and $V_S(90)$. We then calculated best

values for the velocity parameters A, B, C, D, and E (including bounds on B and C). In order to obtain the remaining bounds, we needed a measure of the uncertainty in our estimates of the upper mantle P and S-wave velocities. Based on the synthetic seismogram modeling, we estimated this uncertainty in upper mantle velocities to be $\pm$ 0.1 km/s, and we used this value to infer bounds on A, D, and E. Notice that for the upper mantle we assumed that the horizontal symmetry axis corresponded to the fast direction, and thus it was not necessary to switch the signs of B and E as we did for the crustal anisotropy. We would expect anisotropy of this type if the upper mantle anisotropy is caused by aligned olivine crystals.

Anisotropy from Aligned Cracks

Several candidate physical models might explain the anisotropy which we observe at the Ngendei site. In a previous paper (Shearer and Orcutt 1985), we discussed possible causes of the observed Ngendei crustal P-wave anisotropy and concluded that aligned cracks within the upper crust was the most likely cause. We have now refined our estimates of the depth and extent of the upper crustal anisotropy, and believe that aligned cracks within approximately the top 1 to 1.5 km of crust are responsible for the observed P and S-wave anisotropy. The presence of such aligned cracks is not unexpected since systems of oriented cracks have been directly observed on the surface of the oceanic crust (see for example Ballard and van Andel 1977; Luyendyk and Macdonald 1977; Ballard et al. 1982), and cracks have been hypothesized to explain other crustal marine anisotropy observations (Stephen 1981, 1985; White and Whitmarsh 1984). Furthermore, since it is widely believed that the sharp velocity gradients at the top of the crust are a direct result of decreasing porosity in the crust (Spudich and Orcutt 1980b; Bratt and Purdy 1984), it seems likely that cracks could cause a

directional velocity dependence as well.

Many theoretical studies of the effects of aligned cracks on elastic parameters have been done (Anderson et al. 1974; Garbin and Knopoff 1973, 1975a, 1975b; Crampin 1980). For the purposes of this paper, the most useful treatment is presented by Hudson (1981, 1982), as explained and illustrated by Crampin (1984). The Hudson equations provide approximate expressions for the components of the anisotropic elastic tensor in the long wave-length limit for a weak distribution of parallel penny-shaped cracks, in terms of the Lamé parameters of the host solid and the material within the cracks, the crack density and the crack aspect ratio. The crack density $\epsilon = \frac{Na^3}{v}$ where N is the number of cracks of radius a in volume v, and the aspect ratio $d = \frac{c}{a}$ where c is the crack thickness. The theory is valid for low crack densities ($\epsilon << 1$) and small aspect ratios ($d << 1$).

The examples which Crampin discusses in his paper suggest a difference between dry and wet crack models in which dry crack models are defined by 2θ P-wave velocity variations and wet crack models are defined by 4θ variations. This presents a problem since the observed Ngendei P-wave crustal anisotropy is 2θ dominant, but cracks near the top of old oceanic crust are almost certainly saturated. However, wet crack models need not be 4θ dominant; their characteristics are a strong function of the aspect ratio d. At aspect ratios appropriate for very thin cracks ($d < 0.001$), such as those used in the Crampin paper, P-wave velocity variations are almost entirely 4θ, but at larger aspect ratios appropriate for thicker cracks ($d = 0.1$ tc 0.01), velocity variations are largely 2θ. At an aspect ratio of 0.005, 2θ and 4θ terms are approximately equal. This aspect ratio dependence explains the difference in the theoretical wet crack studies of Anderson et al. (1974), who found 2θ P-wave velocity variations for

fluid-filled cracks with aspect ratios of 0.01 to 0.80, with those of Garbin and Knopoff (1973) who found 4θ velocity variations for infinitely thin cracks.

Thus, if we know the relative contributions of the 2θ and 4θ terms in the P-wave velocity anisotropy we can place constraints on the aspect ratio of aligned cracks which we assume are causing the anisotropy. For the Ngendei crustal anisotropy, we also have constraints on the magnitude of the S-wave anisotropy. In order to evaluate the effect of different crack densities and aspect ratios, we used the Hudson formalism to calculate the velocity parameters B, C, and E for a variety of values of ϵ and d, using appropriate values for the host solid. These results are shown contoured in Fig. 15, with bounds on B, C, and E for the Ngendei crustal anisotropy shown as shaded regions. For this comparison, we have assumed that the cracks are vertical and oriented parallel to the fast direction of the crustal anisotropy (N118°E). Fig. 15d shows the intersection of the bounded regions and defines the aspect ratios and crack densities for which this model can explain the Ngendei crustal anisotropy. Clearly the bounds on B and E are the most useful; the bounds on C are so broad as to be useless in constraining the model. The limits of the bounded region at large aspect ratios ($d > 0.1$) are unclear because the Hudson theory is only valid at small aspect ratios.

The product $\pi \epsilon d$ is the effective porosity (ratio of crack material volume to total volume) of the host rock. The limits on d and ϵ implied by this analysis ($d \approx 0.01$ to 0.1, $\epsilon \approx 0.01$ to 0.05) require a porosity of 0.03 to 1.6%, but higher porosities, consisting of pores or other voids in the host solid not related to the aligned cracks in this model, are not excluded. Measurements from DSDP Hole 504B in the eastern Pacific indicated that porosity decreased from 12 to 14% at the surface of the crust to less than 3% at 1 km depth (Becker et al. 1982). If only a fraction of this porosity represents aligned cracks, this could

explain the observed upper crustal anisotropy at the Ngendei site.

The Hudson penny-shaped crack model can only approximate what is undoubtedly a complex pattern of holes, fractures, and cracks in the upper oceanic crust. It would be wrong to infer too much from theoretical models of this type, since cracks probably vary in size, shape, and degree of alignment. The sides of the thinner cracks are likely to touch at points across the face of the crack, reducing the effect of the cracks on the elastic parameters of the material. Nevertheless, the Hudson crack model can explain the Ngendei observations, and provides some insight about the type and degree of cracking which is necessary to cause the upper crustal anisotropy.

The predicted orientation of the upper crustal cracks at the Ngendei site corresponds to the fast crustal direction of approximately N118° E. As previously discussed, this is nearly orthogonal to the fast upper mantle direction. Since the fast direction in the upper mantle has been found to correlate with the fossil spreading direction (Shor et al. 1971; Bibee and Shor 1976) we can infer that the aligned cracks at the Ngendei site are perpendicular to the fossil spreading direction, or parallel to the original ridge axis. This is consistent with observations of aligned faults, fissures, and cracks in crust at modern spreading ridges in both the Atlantic and Pacific (Ballard and van Andel 1977; Luyendyk and Macdonald 1977; Ballard et al. 1982).

Upper Mantle Anisotropy

Azimuthal P-wave anisotropy in the upper mantle is now well established by seismic refraction experiments (Raitt et al. 1969; Morris et al. 1969; Au and Clowes 1982; Shimamura et al. 1983) and also suggested by surface wave studies (Forsyth 1975; Mitchell and Yu 1980; Kawasaki and Kon'no 1984). The velocity anisotropy can be described by a $\cos 2\theta$ function of azimuth with the fast

direction generally perpendicular to the local magnitude anomaly pattern and thus parallel to the original spreading direction. Anisotropy similar in magnitude and orientation has been observed in ophiolite upper mantle material (Peselnick and Nicolas 1978; Christensen and Salisbury 1979; Christensen and Smewing 1981; Christensen 1984) and is largely a result of preferred orientation of olivine crystals. Thus, the original observation and interpretation of upper mantle anisotropy by Hess (1964) seems confirmed.

For these reasons, the observation of azimuthal upper mantle P-wave anisotropy at the Ngendei site is not surprising. It seems likely that all oceanic upper mantle anisotropy is of similar origin, and thus the Ngendei anisotropy probably results from a preferred alignment of olivine crystals along a fossil spreading direction of N30° E. Individual olivine crystals are orthorhombic and highly anisotropic with an a-axis P-wave velocity of 9.89 km/s, b-axis velocity of 7.73 km/s, and c-axis velocity of 8.43 km/s (Kumazawa and Anderson 1969). The ophiolite studies have shown that the a-axis tends to align parallel to the original spreading direction with the b and c-axes confined to a vertical plane perpendicular to this direction. Within this plane, observations suggest that the b and c-axes have little or no preferred orientation. The resulting anisotropy is approximately hexagonally symmetric with a horizontal symmetry axis corresponding to the fast P-wave direction. This is the justification for the assumptions which we made in solving for the elastic constants for the upper mantle.

Although the Ngendei S_n arrivals were very weak, we believe that they do constrain the upper mantle SV velocity to be 4.65± 0.1 km/s at two azimuths, approximately corresponding to the slow and fast P-wave directions. If we assume that one SV velocity is high by 0.1 km/s and the other low by 0.1 km/s, this still limits the upper mantle SV-wave anisotropy at the Ngendei site to be less than ± 2% compared with observed P-wave anisotropy of ± 3%. These

results are similar to refraction results of Clowes and Au (1982), who found upper mantle S-wave anisotropy of ± 1% and P-wave anisotropy of ± 5%. The smaller SV-wave velocity differences compared to the P-wave differences is consistent with ophiolite studies. For example, Peselnick and Nicolas (1978) calculated velocity differences for a harzburgite sample (at 5 kbar and 250 ° C) from the Antalya ophiolite in Turkey and found P-wave velocity differences of ± 5% and corresponding SV velocity differences of ± 2.5%. Fig. 16, reproduced from Christensen and Smewing (1981), shows average velocities for samples from the Oman ophiolite. The slower shear wave velocity corresponds to SV in an oceanic refraction experiment, and the faster shear wave velocity to SH. The approximately hexagonal nature of the anisotropy is clear, as well as the smaller directional variations of SV-waves compared to P-waves.

These properties can also be seen directly in the anisotropy of olivine crystals. We calculated the elastic constants for an aggregate of olivine crystals with fixed a-axis orientation and random b and c-axes orientations within a vertical plane, by averaging the elastic tensor for olivine over the possible orientations. This is equivalent to the Voight averaging scheme for determining aggregate elastic properties from single crystal data (see Crosson and Lin [1971] for a discussion). We used values for elastic constants of olivine from Kumazawa and Anderson (1969), uncorrected for pressure and temperature. Table 3 contains values for the resulting hexagonally symmetric elastic tensor, and, for comparison, the Ngendei upper mantle results. The hexagonal olivine model has azimuthal P-wave velocity anisotropy of ± 10% and SV-wave anisotropy of ± 3.5%. We also show the approximate velocity coefficients A, B, C, D, and E, but these are not very accurate for off-axis velocities because of the large anisotropy of the hexagonal olivine model (a_E = 0.62).

A more realistic upper mantle model will contain other crystals in addition to the aligned olivine crystals. Using the Voight averaging scheme, we created a composite upper mantle model which consists of the weighted average of aligned olivine crystals and a purely isotropic distribution of crystals. This isotropic part could contain unaligned olivine crystals (randomly distributed) in addition to other mineral components. We constrained this model to fit the Ngendei P_n velocities of 7.95 to 8.4 km/s and average SV velocity of 4.65 km/s, and obtained the model shown in Table 3. The composite upper mantle model consists of 22% aligned olivine crystals and 78% unaligned crystals (isotropic when averaged over all orientations), and fits within all appropriate bounds for the Ngendei travel time data. In particular, the SV-wave velocity anisotropy is less than 1%. Using a similar method, Crampin and Bamford (1977) used P-wave data from Raitt et al. (1969) in the eastern Pacific to produce an upper mantle model consisting of 12% hexagonal olivine and 88% isotropic material. The smaller percentage of aligned olivine in the Crampin model is a direct result of the relatively small P_n anisotropy found in the Raitt et al. study ($\pm$ 0.15 km/s).

Clearly this composite model for the Ngendei site is a simplification of a complicated situation in the oceanic upper mantle. The model considers only perfectly aligned olivine crystals or unaligned crystals; it does not allow for variations in olivine crystal alignment, non-hexagonal olivine alignments, non-horizontal symmetry axes, or non-olivine mineral alignments (orthopyroxene, for example). It is unrealistic to expect all of the olivine in the upper mantle to be perfectly aligned; thus 22% represents a lower bound for the upper mantle olivine percentage in models of this type. However, it does contain the main features of upper mantle anisotropy of the type seen in ophiolites (dominated by olivine a-axis alignment) and is consistent with Ngendei travel time data. More refined models are certainly possible, but will be difficult to resolve with available

seismic refraction data.

For comparison, Table 3 also contains a model proposed by Kawasaki and Kon'no (1984), who attempted to estimate values for the elastic constants of the uppermost mantle beneath the Pacific, based on seismic refraction experiments, surface wave studies, and ophiolite measurements. This model does not fit within the bounds for the Ngendei site, primarily because it was designed to fit larger P_n anisotropy (7.9 to 8.6 km/s) and higher S_n velocities (4.8 km/s). If these velocities are scaled downward in order to match the velocities observed at the Ngendei site, the model would agree reasonably well with our Ngendei composite model. No single model can be expected to fit the upper mantle precisely throughout the Pacific since there are observed variations in P_n and S_n velocities and the size of P_n anisotropy (see for example Bibee and Shor, 1976).

Anisotropic S-wave Splitting

Much of the analysis in this paper has been based on azimuthal travel variations at the Ngendei site. Another important way in which anisotropy might be observed involves studying the polarization of arriving phases. In a previous paper (Shearer and Orcutt 1985), we discussed the nature of P-wave polarization anomalies, and concluded that observed crustal P-wave polarizations at the Ngendei site were too scattered to be useful in constraining the anisotropy. Another type of anisotropic polarization anomaly involves S-wave splitting (discussed extensively by Crampin 1985) in which an S-wave of one polarization might arrive ahead of an S-wave of different polarization. Observational evidence for such anomalies has been claimed for the oceanic crust (Stephen 1981, 1985), and for the upper mantle (Ando 1984).

Ideally, shear-wave polarizations at the Ngendei site would be observed with the borehole seismometer, because ocean bottom recordings suffer from problems of converted sediment phases, free surface reflections, and unknown OBS to seafloor coupling effects. Unfortunately, only one of the two horizontal components of the borehole seismometer at the Ngendei site functioned properly, so we were forced to use OBS data in order to examine particle motions.

We examined crustal shear-wave polarizations recorded by OBS Suzy for the circular line (2c). The first arriving shear phase, most prominent on the vertical component, was the converted P-wave in the sediment. We would not expect to see splitting in this phase, because only the SV wave in the crust will convert to a P-wave in the sediment. Arriving about 0.55 s later is the S-wave in the sediment, which we might expect to show S-wave splitting, since the crack models which we have considered for the upper crust at the Ngendei site predict a difference between SV and SH arrival times at certain azimuths. Unfortunately, particle motion analysis of this phase revealed a chaos of different polarizations, largely unrelated even to the shot azimuth. While individual shots occasionally exhibit particle motions consistent with S-wave splitting, this appears to be a random occurrence, since there is no consistent relationship between observed polarizations and azimuth. This large scatter in shear-wave polarizations is similar to the randomness observed in the P-wave polarizations (Shearer and Orcutt 1985), and might be caused by lateral heterogeneities at the Ngendei site, sediment reverberations, and/or problems of OBS to seafloor coupling.

Similarly, upper mantle models predict that SH waves should arrive ahead of SV waves at certain azimuths. OBS data at mantle ranges are too noisy to even identify the S_n phase, so the borehole seismometer (MSS) data provided our only hope of seeing upper mantle shear-wave splitting. As previously dis-

cussed, we identified a weak upper mantle SV phase on the vertical component of the MSS, and calculated its velocity at approximately 4.65 km/s for both line 4b and line 5b. We examined the single horizontal component of the MSS (unknown orientation) but were unable to identify a phase which might correspond to SH (see Fig. 17). We do not consider this evidence against upper mantle anisotropy, because a weak SH phase could easily be lost in the noise. In addition, significant SH-wave energy is not always efficiently generated in marine refraction experiments, because it requires scattering of seismic energy out of the sagital plane by lateral heterogeneities and/or off-axis anisotropy.

Conclusions

The 1983 Ngendei expedition to the south Pacific detected anisotropy both within the upper crust and the uppermost mantle. Shear-wave travel times indicate azimuthal S-wave anisotropy in the crust, which, together with the P-wave anisotropy previously observed, is sufficient to calculate anisotropic elastic constants (under an assumption of hexagonal symmetry). The upper crustal anisotropy is probably caused by aligned cracks parallel to the original ridge axis at the Ngendei site. Constraints on anisotropic parameters in the upper crust are consistent with a penny-shaped crack model involving crack aspect ratios of 0.01 to 0.1.

Despite Ngende P_n anisotropy of 7.95 to 8.4 km/s, S_n velocities are close to constant at 4.65 km/s. The observed upper mantle anisotropy agrees with previous seismic experiments and ophiolite studies, and suggests that the fossil spreading direction at the Ngendei site was N30°E. Calculated expressions for the anisotropic elastic constants are consistent with a simple model of the upper mantle consisting of 22% aligned olivine crystals. The character of the velocity profiles derived from synthetic seismogram modeling is in general agreement with

other refraction studies.

Acknowledgements

This research was supported by DARPA contract AFOSR-84-0043. We thank the scientists and crew on the R/V Melville and D/V Glomar Challenger for making the Ngendei experiment a success. Steven Bratt provided a helpful review of this paper.

References

Adair. R.G., J.A. Orcutt, and T.H. Jordan. 1986. Preliminary analysis of ocean bottom and sub-bottom microseismic ambient noise during the Ngendei Experiment, Initial Rep. Deep Sea Drill. Proj., Leg 91, in press.

Anderson. D.L., B. Minster, and D. Cole, 1974. The effect of oriented cracks on seismic velocities, J. geophys. Res., 79, 4011-4015.

Ando, M., 1984. ScS polarization anisotropy around the Pacific Ocean. J. Phys. Earth, 32. 179-195.

Au. C.Y.D. and R.M. Clowes, 1982. Crustal structure from an ocean bottom seismometer survey in the Nootka fault zone off western Canada, Geophys. J. R. astr. Soc., 68, 27-47.

Backus, G.E., 1965. Possible forms of seismic anisotropy of the uppermost mantle under oceans, J. geophys. Res., 70, 3429-3439.

Backus, G.E., 1982. Reply: limits of validity of first-order perturbation theory for quasi-P velocity in weakly anisotropic media, J. geophys. Res., 87, 4641-4644.

Ballard, R.D. and T.H. van Andel. 1977. Morphology and tectonics of the inner rift valley at lat 36 ° 50'N on the Mid-Atlantic Ridge, Geol. Soc. Am. Bull., 88, 507-530.

Ballard, R.D., T.H. van Andel, and R.T. Holcomb, 1982. The Galapagos Rift at 86 ° W: variations in volcanism, structure, and hydrothermal activity along a 30-kilometer segment of the rift valley, J. geophys. Res., 87, 1149-1161.

Becker, K., R.P. von Herzen, T.J.G. Francis, R.N. Anderson, J. Honnorez,

A.C. Adamson. J.C. Alt. R. Emmermann. P.D. Kempton. H. Kinoshita. C. Laverne. M.J. Mottl. and R.L. Newmark. 1982. In situ electrical resistivity and bulk porosity of the oceanic crust Costa Rica Rift, Nature. 300. 594-598.

Bibee, L.D. and G.G. Shor. 1976. Compressional wave anisotropy in the crust and upper mantle, Geophys. Res. Lett., 3, 639-642.

Bratt. S.R. and G.M. Purdy. 1984. Structure and variability of oceanic crust on the flanks of the East Pacific Rise between 11 ° and 13 ° N, J. geophys. Res., 89, 6111-6125.

Chapman, C.H., 1978. A new method for computing synthetic seismograms, Geophys. J. R. astr. Soc., 54, 481-518.

Chapman, C.H. and J.A. Orcutt, 1985. The computation of body-wave synthetic seismograms in laterally homogeneous media, Rev. Geophys. Space Phys., 23, 105-163.

Christensen, N.I. and M.H. Salisbury, 1975. Structure and constitution of the lower oceanic crust, Rev. Geophys. Space Phys., 13, 57-86.

Christensen, N.I. and J.D. Smewing, 1981. Geology and seismic structure of the northern section of the Oman Ophiolite, J. geophys. Res., 86, 2545-2555.

Christensen, N.I., 1984. The magnitude, symmetry and origin of upper mantle anisotropy based on fabric analyses of ultramafic tectonites, Geophys. J. R. astr. Soc., 76, 89-111.

Clowes, R.M. and D. Au, 1982. In-situ evidence for a low degree of S-wave anisotropy in the oceanic upper mantle, Geophys. Res. Lett., 9, 13-16.

Crampin, S., 1977. A review of the effects of anisotropic layering on the propagation of seismic waves, Geophys. J. R. astr. Soc., 49, 9-27.

Crampin, S., 1982. Comments on 'Possible forms of anisotropy of the

uppermost mantle under oceans' by George E. Backus. J. geophys. Res., 87, 4636-4640.

Crampin, S., 1984. Effective anisotropic elastic constants for wave propagation through cracked solids. Geophys. J. R. astr. Soc., 76, 135-145.

Crampin, S., 1985. Evaluation of anisotropy by shear-wave splitting. Geophysics, 50, 142-152.

Crampin, S. and D. Bamford, 1977. Inversion of P-wave velocity anisotropy. Geophys. J. R. astr. Soc., 49, 123-132.

Crosson, R.S. and N.I. Christensen, 1969. Transverse isotropy of the upper mantle in the vicinity of Pacific fracture zones. Bull. seismol. Soc. Am., 59, 59-72.

Crosson, R.S. and J.W. Lin, 1971. Voight and Reuss prediction of anisotropic elasticity of Dunite, J. geophys. Res., 76, 570-578.

Forsyth, D.W., 1975. The early structural evolution and anisotropy of the oceanic upper mantle, Geophys. J. R. astr. Soc., 43, 103-162.

Fuchs, K. and G. Müller, 1971. Computation of synthetic seismograms with the reflectivity method and comparison with observations. Geophys. J. R. astr. Soc., 23, 417-433.

Garbin, H.D. and L. Knopoff, 1973. The compressional modulus of a material permeated by a random distribution of circular cracks, Q. appl. Math., 30, 453-464.

Garbin, H.D. and L. Knopoff, 1975a. The shear modulus of a material permeated by a random distribution of circular cracks, Q. appl. Math., 33, 296-300.

Garbin, H.D. and L. Knopoff, 1975b. Elastic moduli of a medium with liquid filled cracks, Q. appl. Math., 33, 301-303.

Garmany, J., 1981. Anisotropic gradients in the upper mantle, Geophys.

Res. Lett., 8, 955-957.

Hart, R.S. and F. Press, 1973. S_n velocities and the composition of the lithosphere in the regionalized Atlantic, J. geophys. Res., 78, 407-411.

Hess, H.H., 1964. Seismic anisotropy of the uppermost mantle under oceans, Nature, 203, 629-631.

Hudson, J.A., 1981. Wave speeds and attenuation of elastic waves in material containing cracks. Geophys. J. R. astr. Soc., 64, 133-150.

Hudson, J.A., 1982. Overall properties of a cracked solid, Math. Proc. Camb. phil. Soc., 88, 371-384.

Kawasaki, I. and F. Kon'no, 1984. Azimuthal anisotropy of surface waves and the possible type of the seismic anisotropy due to preferred orientation of olivine in the uppermost mantle beneath the Pacific Ocean, J. Phys. Earth, 32, 229-244.

Kim, I.I., D.K. Smith, H.W. Menard, J.A. Orcutt, T.H. Jordan, 1986. Seismic reflection site survey: Correlation with physical properties, Leg 91, Deep Sea Drilling Project, Initial Rep. Deep Sea Drill Proj., Leg 91, in press.

Luyendyk, B.P. and K.C. Macdonald, 1977. Physiography and structure of the inner floor of the FAMOUS rift valley: observations with a deep-towed instrument package, Geol. Soc. Am. Bull., 88, 648-663.

Mitchell, B.J. and G.-K. Yu, 1980. Surface wave dispersion, regionalized velocity models, and anisotropy of the Pacific crust and upper mantle, Geophys. J. R. astr. Soc., 63, 497-514.

Molnar, P. and J. Oliver, 1969. Lateral variations of attenuation in the upper mantle and discontinuities in the lithosphere, J. geophys. Res., 74, 2648-2682.

Morris, G.B., R.W. Raitt, and G.G. Shor, 1969. Velocity anisotropy and

delay-time maps of the mantle near Hawaii. J. geophys. Res., 74. 4300-4316.

Musgrave. M.J.P.. 1970. Crystal Acoustics. Holden-Day.

Peselnick. L. and A. Nicolas. 1978. Seismic anisotropy in an ophiolite peridotite: application to oceanic upper mantle. J. geophys. Res., 83. 1227-1235.

Raitt. R.W.. G.G. Shor, T.J.G. Francis. G.B. Morris, 1969. Anisotropy of the Pacific upper mantle, J. geophys. Res., 74. 3095-3109.

Sereno. T.J. and J.A. Orcutt. 1985. The synthesis of realistic oceanic P_n wave trains, J. geophys. Res. 90, 12755-12776.

Shearer, P. and J. Orcutt, 1985. Anisotropy in the oceanic lithosphere– theory and observations from the Ngendei seismic refraction experiment in the southwest Pacific. Geophys. J. R. astr. Soc., 80, 493-526.

Shearer, P.M., J.A. Orcutt, T.H. Jordan, R.B. Whitmarsh, I.I. Kim, R.G. Adair, M.S. Burnett, 1986a. The Ngendei seismic refraction experiment at DSDP Hole 595B– ocean bottom seismometer data and evidence for crustal and upper mantle anisotropy. Initial Rep. Deep Sea Drill. Proj., Leg 91. in press.

Shearer, P.M., R.G. Adair, J.A. Orcutt, and T.H. Jordan, 1986b. Simultaneous borehole and ocean bottom seismometer recordings of earthquakes and explosions– results from the 1983 Ngendei Experiment at DSDP Hole 595B, Initial Rep. Deep Sea Drill. Proj., Leg 91, in press.

Shimamura, H., T. Asada, and M. Kumazawa, 1977. High shear wave velocity layer in the upper mantle of the western Pacific, Nature, 269, 680-682.

Shimamura, H., T. Asada, K. Suychiro, T. Yamada, and H. Inatani, 1983. Longshot experiments to study velocity anisotropy in the oceanic

lithosphere of the northwestern Pacific. Phys. Earth planet. Inter., 31, 348-362.

Shor, G.G., H.W. Menard, R.W. Raitt, 1971. Structure of the Pacific basin. The Sea, v. 4, part II, p. 3-27, John Wiley and Sons.

Spudich, P. and J. Orcutt, 1980a. Petrology and porosity of an oceanic crustal site: results from wave form modeling of seismic refraction data, J. geophys. Res., 85, 1409-1433.

Spudich, P., and J. Orcutt, 1980b. A new look at the seismic velocity structure of the oceanic crust, Rev. Geophys. Space Phys., 18, 627-645.

Stephen, R.A., 1981. Seismic anisotropy observed in upper oceanic crust, Geophys. Res. Lett., 8, 865-868.

Stephen, R.A., 1985. Seismic anisotropy in the upper oceanic crust, J. geophys. Res., 90, 11383-11396.

Walker, D.A. and G.H. Sutton, 1971. Oceanic mantle phases recorded on hydrophones in the northwestern Pacific at distances between 9° and 40°, Bull. seismol. Soc. Am., 61, 65-78.

Walker, D.A., 1977. High-frequency P_n and S_n phases recorded in the western Pacific, J. geophys. Res., 82, 3350-3360.

White, R.S. and R.B. Whitmarsh, 1984. An investigation of seismic anisotropy due to cracks in the upper oceanic crust at 45°N, Mid-Atlantic Ridge, Geophys. J. R. astr. Soc., 79, 439-467.

Whitmarsh, R.B., J.A. Orcutt, T.H. Jordan, R.G. Adair, and P.M. Shearer, 1986. Velocity bounds on the seismic structure of late Jurassic crust and upper mantle in the southwest Pacific basin from downhole observations at Deep Sea Drilling Project Hole 595B, Initial Rep. Deep Sea Drill. Proj., Leg 91, in press.

Table 1

Ngendei P-wave and S-wave velocity vs. depth model for NNE and ESE azimuths. Equivalent Poisson's ratio σ is also shown.

Table 2

Best fitting anisotropic parameters and bounds for the Ngendei upper crustal (0.5 km depth) and upper mantle anisotropy. Elastic tensor values have been normalized by density. Azimuth ϕ is the direction of the fast anisotropic symmetry axis.

Table 3

Anisotropic parameters for the Ngendei upper mantle data compared with an olivine based model and a model proposed by Kawasaki and Kon'no (1984). Units are as in Table 2.

Fig. 1

The Ngendei site (DSDP Hole 595B) is located in the south Pacific about 1000 km east of the Tonga Trench.

Fig. 2

Four split refraction lines and a circular line of 10 km radius were shot at the Ngendei site. Water depth at the site is 5600 m.

Fig. 3

95% confidence limits for the OBS locations. All OBSs were within 500 m of the borehole.

Fig. 4

P-wave travel times and amplitudes for refraction lines 1a, 1b. 3a. 3b, 4a, and 5b. Travel times have been corrected for topography and are reduced at 6.8 km/s. Amplitudes represent the maximum value in the seismogram within 0.4 s following the P-wave arrival. Amplitudes have been averaged within 1 km increments; error bars represent one standard deviation. Note the non-random scatter in the travel times, a probable result of contamination from lateral heterogeneity at the Ngendei site.

Fig. 5

P-wave travel times and amplitudes for refraction lines 4b and 5a, compared to bathymetry. Topographic perturbations have a strong effect on both travel times and amplitudes.

Fig. 6

a) Averaged P-wave travel times and amplitudes for the NNE lines (3a, 3b, and 4a) and the ESE lines (1a, 1b, and 5b).

b) Synthetic travel times and amplitudes calculated with the WKBJ method. based on the velocity models shown in Table 1 and Fig. 7.

Fig. 7

Anisotropic velocity vs. depth model which satisfies the Ngendei data. The solid line is the NNE velocity model: the dashed line is the ESE model.

Fig. 8

Ray trace diagram for the ESE model, showing rays turning in the shallow crust. For comparison. the velocity depth function for the model is shown in the inset to the left.

Fig. 9

Data vs. synthetic comparison of selected seismograms for line 5b. WKBJ synthetic seismograms were calculated using the ESE velocity model. Both data and synthetics have been scaled for range and shot weight.

Fig. 10

a) Borehole seismometer (MSS) data for lines 4b and 5b. Seismograms have been corrected for topography, reduced at 8.0 km/s, and scaled by range and shot weight. Notice the difference in upper mantle (P_n) velocities between the two lines.

b) P-wave synthetic seismograms for lines 4b and 5b.

Fig. 11

Crustal travel times for P-waves (lower), S-waves (middle), and direct water waves (upper). Travel times have been reduced at 6.6

km s and arrivals from shots in ocean depths less than 5400 m have been removed.

Fig. 12

Close-up of S-wave arrivals, reduced at 3.75 km/s. Plus signs are arrivals from within 45° of a ESE azimuth: circles represent arrivals within 45° of a NNE azimuth. S-wave travel times have been corrected for topographic variations.

Fig. 13

S-wave travel times vs. azimuth for shots at ranges of 9 to 11 km, reduced at 3.75 km/s. All times have been corrected for topography, and arrivals from rays entering the seafloor at depths less than 5400 m have been eliminated. The curve is a least squares fit for a function of the form $T = a'_1 + a'_2\cos 2\theta + a'_3\sin 2\theta$.

Fig. 14

a) Borehole seismometer (MSS) data for lines 4b and 5b. Seismograms have been corrected for topography, reduced at 4.65 km/s, and scaled for range and shot weight.

b) S-wave synthetic seismograms for lines 4b and 5b.

Fig. 15

Values of the velocity parameters B, the 2θ P-wave coefficient, C, the 4θ P-wave coefficient, and E, the 2θ S-wave coefficient, are contoured for different values of the crack density ϵ and crack aspect ratio d in a theoretical model of parallel, penny-shaped cracks by Hudson (1982). The shaded regions indicate the appropriate bounds on B, C, and E from the observed Ngendei crustal anisotropy. The

final shaded region is the intersection of these bounds.

Fig. 16

Equal-area projections of averaged velocities from samples of the Oman ophiolite (from Christensen and Smewing, 1981). Velocities are in km/s. The cross in the V_P diagram indicates the position of the normal to the sheeted dikes within the complex. the inferred direction of fossil spreading.

Fig. 17

Borehole seismometer (MSS) horizontal component data for lines 4b and 5b. Seismograms have been corrected for topography, reduced at 4.65 km/s. and scaled for range and shot weight. The 4.65 km/s SV-wave arrival (also visible on vertical component data, see Fig. 14) is indicated by the solid line. Note that a faster phase, corresponding to SH. cannot be identified in these data.

NGENDEI VELOCITY versus DEPTH MODEL

Depths		NNE asimuth			ESE asimuth			Comments
Ocean km	Crust km	P km/s	S km/s	σ	P km/s	S km/s	σ	
0.0	−5.65	1.52	—	—	1.52	—	—	ocean surface
5.58	−0.07	1.52	—	—	1.52	—	—	OBS depth
5.58	−0.07	1.6	0.12	.50	1.6	0.12	.50	sediment surface
5.65	0.0	1.6	0.12	.50	1.6	0.12	.50	
5.65	0.0	4.22	2.33	.28	4.38	2.42	.28	crustal surface
5.704	0.054	4.32	2.38	.28	4.49	2.47	.28	MSS depth
6.50	0.85	5.85	3.15	.30	6.11	3.24	.30	
6.66	1.015	6.16	3.30	.30	6.29	3.34	.30	
6.90	1.25	6.41	3.44	.30	6.55	3.48	.30	
7.05	1.40	6.57	3.52	.30	6.57	3.52	.30	
7.36	1.71	6.64	3.75	.27	6.64	3.75	.27	
7.67	2.02	6.80	3.75	.28	6.80	3.75	.28	
12.00	6.35	6.80	3.75	.28	6.80	3.75	.28	Moho
12.35	6.70	8.40	4.65	.28	7.95	4.65	.24	
20.00	14.35	8.45	4.75	.27	8.15	4.85	.23	

Table 1

NGENDEI ANISOTROPY MODEL

		Crust (0.5 km depth)			Upper Mantle		
	Units	Best	Min	Max	Best	Min	Max
ϕ	deg	118	101	129	30	25	35
A'	s	0.315	0.308	0.323	1.165	1.144	1.186
B'	s	−0.0251	−0.0363	−0.0137	−0.149	−0.181	−0.117
C'	s	0.0032	−0.0114	0.0178	0.000	−0.036	0.036
D'	s	0.622	0.604	0.636	—	—	—
E'	s	−0.0395	−0.0638	−0.0151	—	—	—
V_P (0)	km s^{-1}	5.40	—	—	8.40	8.30	8.50
V_P (90)	km s^{-1}	5.18	—	—	7.95	7.85	8.05
V_{SV} (0)	km s^{-1}	2.90	—	—	4.65	4.55	4.75
V_{SV} (90)	km s^{-1}	2.81	—	—	4.65	4.55	4.75
A	km^2 s^{-2}	28.13	—	—	66.83	65.26	68.53
B	km^2 s^{-2}	−1.17	−1.69	−0.64	3.68	2.89	4.47
C	km^2 s^{-2}	−0.15	−0.83	0.53	0.0	−0.89	0.89
D	km^2 s^{-2}	8.15	7.59	8.73	21.62	20.70	22.56
E	km^2 s^{-2}	−0.26	−0.42	−0.10	0.0	−0.93	0.93
Γ_{1111}	km^2 s^{-2}	26.81	25.62	28.02	70.51	67.26	73.89
Γ_{2222}	km^2 s^{-2}	29.15	27.94	30.35	63.15	59.90	66.53
Γ_{1313}	km^2 s^{-2}	7.89	7.17	8.63	21.62	19.77	23.49
Γ_{2323}	km^2 s^{-2}	8.41	7.69	9.15	21.62	19.77	23.49
Γ_{1122}	km^2 s^{-2}	12.79	9.27	16.26	23.59	15.61	31.66

Table 2

UPPER MANTLE MODELS

	Ngendei Model			Crystal Aggregate Model			Kawasaki
	Best	Min	Max	Olivine	Host	Both	& Kon'no
Γ_{1111}	70.51	67.26	73.89	97.77	62.82	70.51	73.94
Γ_{2222}	63.15	59.90	66.53	64.48	62.82	63.18	62.12
Γ_{1313}	21.62	19.77	23.49	23.72	21.50	21.99	22.73
Γ_{2323}	21.62	19.77	23.49	20.39	21.50	21.26	20.91
Γ_{1122}	23.59	15.61	31.66	20.83	19.82	20.04	21.82
A	66.83	65.26	68.53	77.91	62.82	66.14	67.84
B	3.68	2.89	4.47	16.65	0.0	3.66	5.91
C	0.00	−0.89	0.89	3.21	0.0	0.71	0.19
D	21.62	20.70	22.56	22.05	21.50	21.62	21.82
E	0.0	−0.93	0.93	1.67	0.0	0.37	0.91
V_P (0)	8.40	8.30	8.50	9.89	7.93	8.40	8.60
V_P (90)	7.95	7.85	8.05	8.03	7.93	7.95	7.88
V_{SV} (0)	4.65	4.55	4.75	4.87	4.64	4.69	4.77
V_{SV} (90)	4.65	4.55	4.75	4.52	4.64	4.61	4.57

Table 3

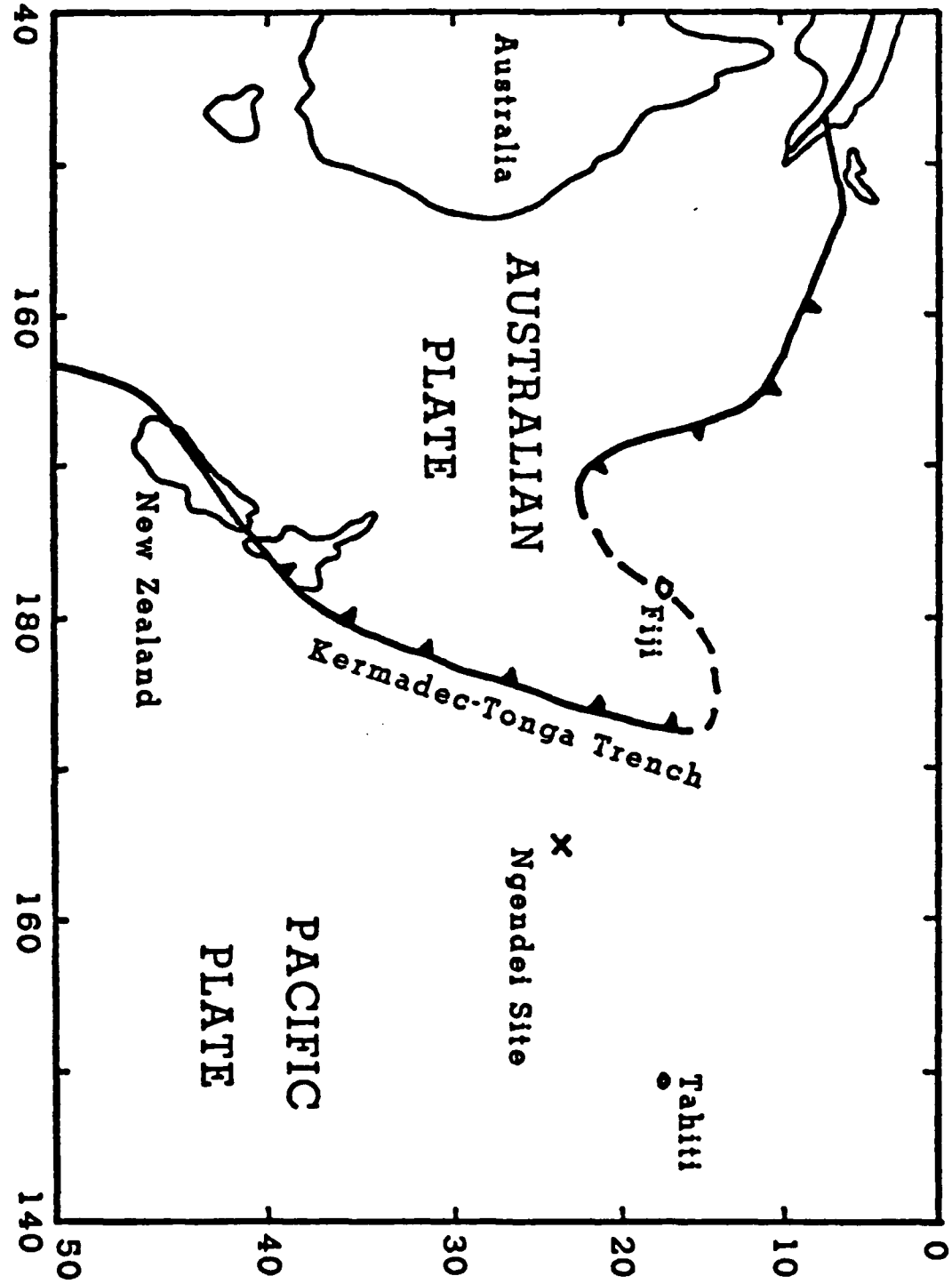

140
160
180
160
140
0
10
20
30
40
50
Australia
AUSTRALIAN
PLATE
Fiji
Kermadec-Tonga Trench
New Zealand
Ngendei Site
Tahiti
PACIFIC
PLATE

Fig. 1

22°S
23'
24'
24°30'
184°
185°
186°
187°
187°30'W
REFRACTION LINES
0
50
100 KM
1a
1b
2a
2b
3a
3b
4a
4b
5a
5b

Fig. 2

Fig. 2

OBS Locations

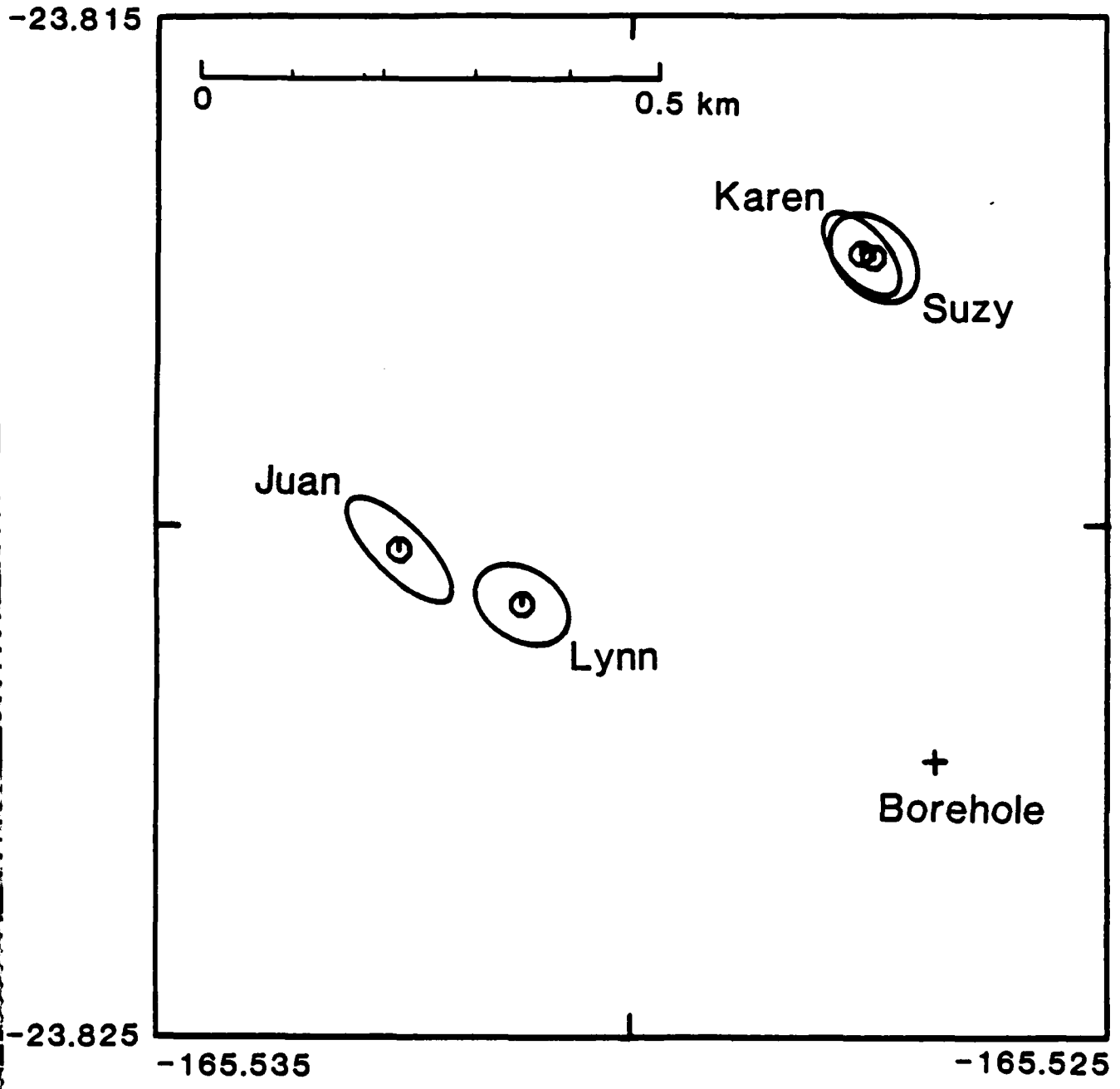


Fig. 3

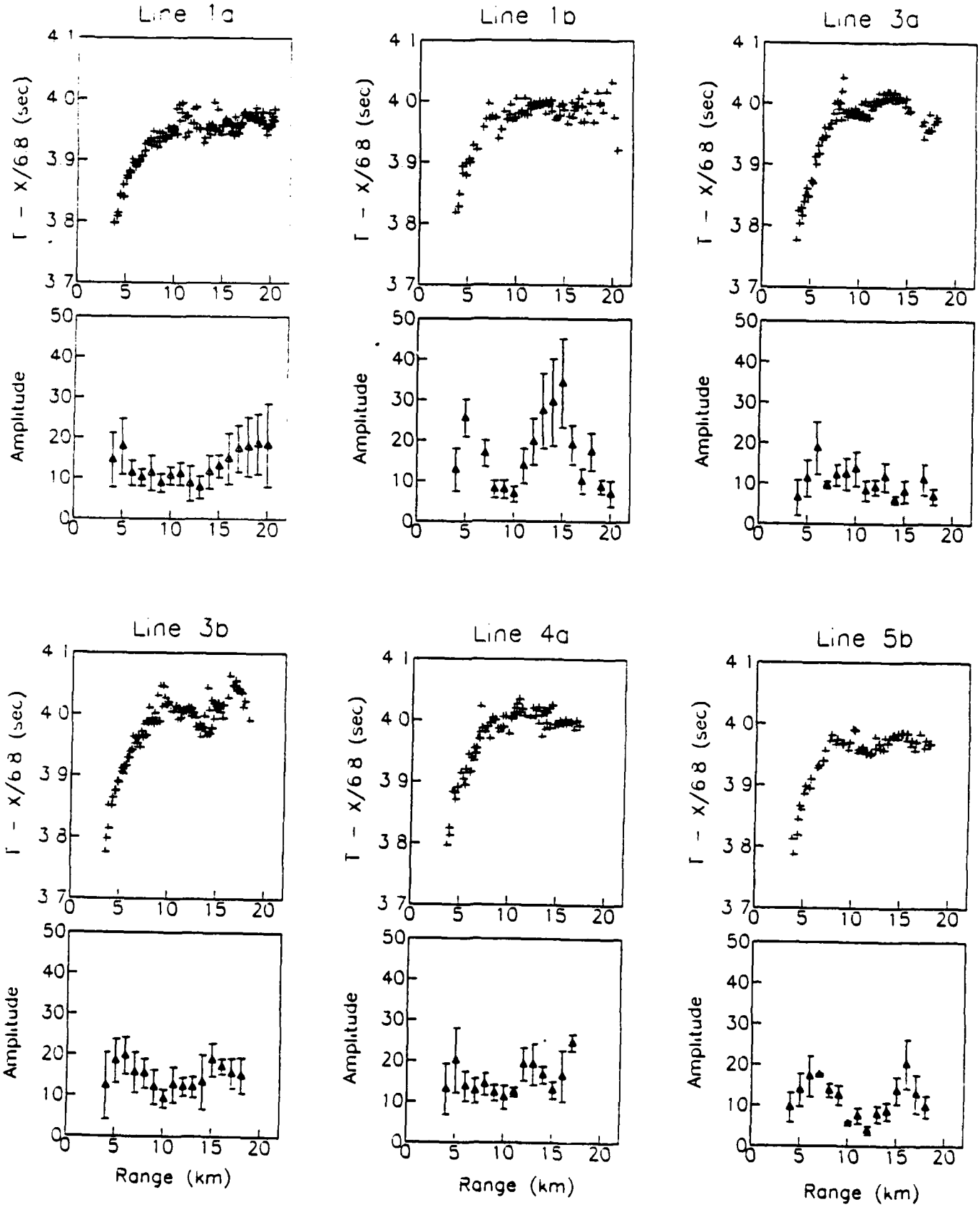

Line 1a
Line 1b
Line 3a
Line 3b
Line 4a
Line 5b
T - X/6.8 (sec)
Amplitude
Range (km)

Fig. 4

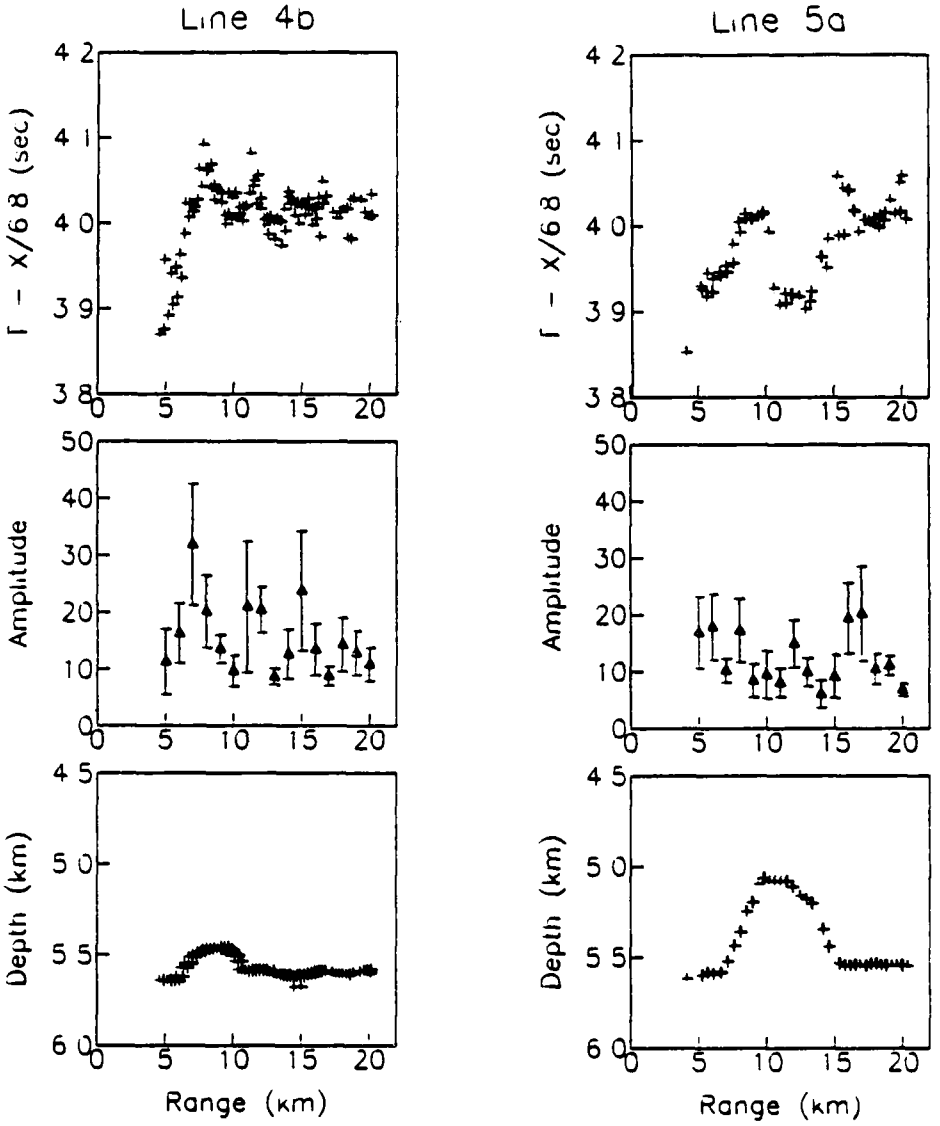


Fig. 5

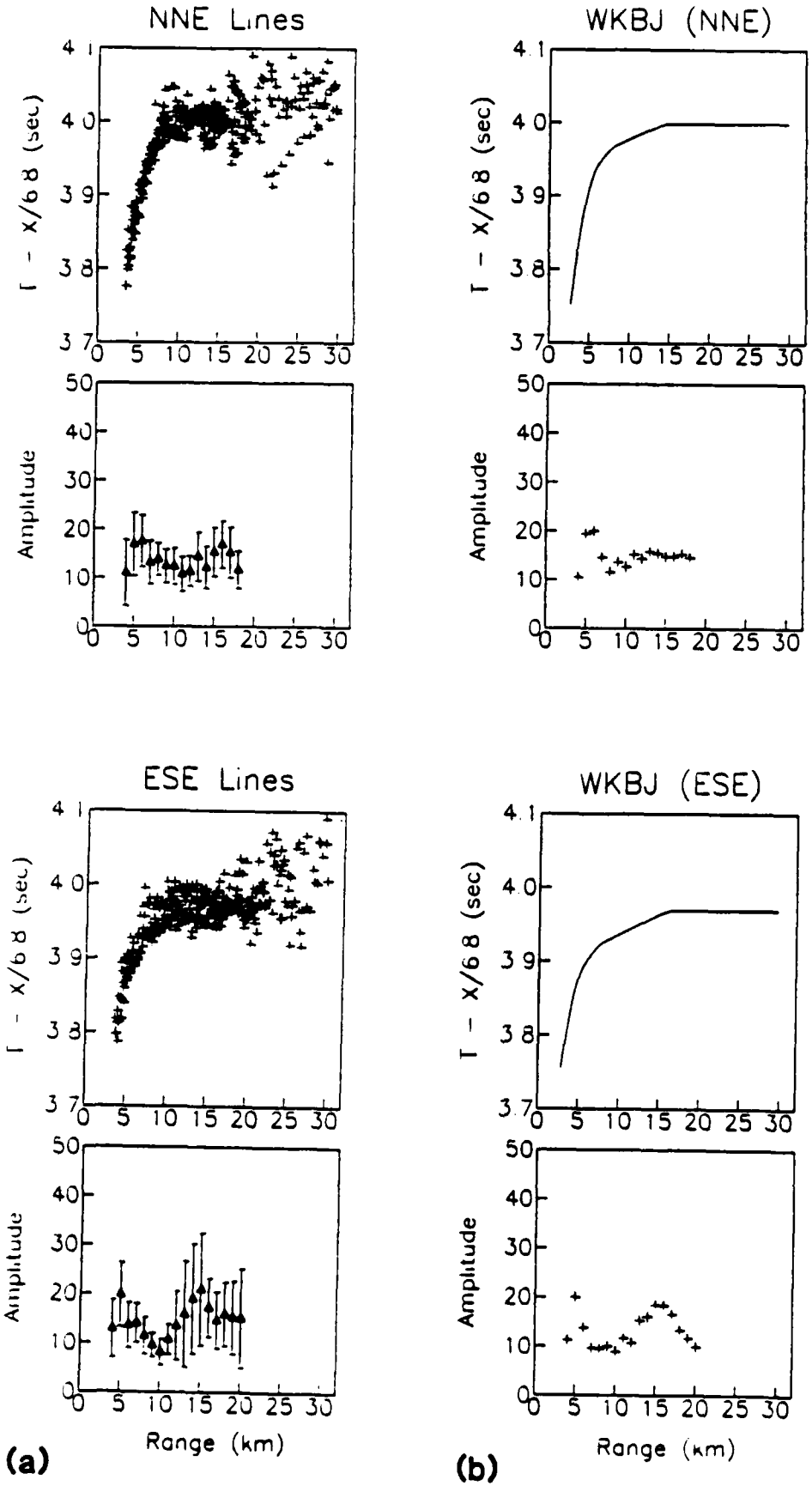

NNE Lines
WKBJ (NNE)
ESE Lines
WKBJ (ESE)
Γ - X/6.8 (sec)
Amplitude
Range (km)
(a)
(b)

Fig. 6

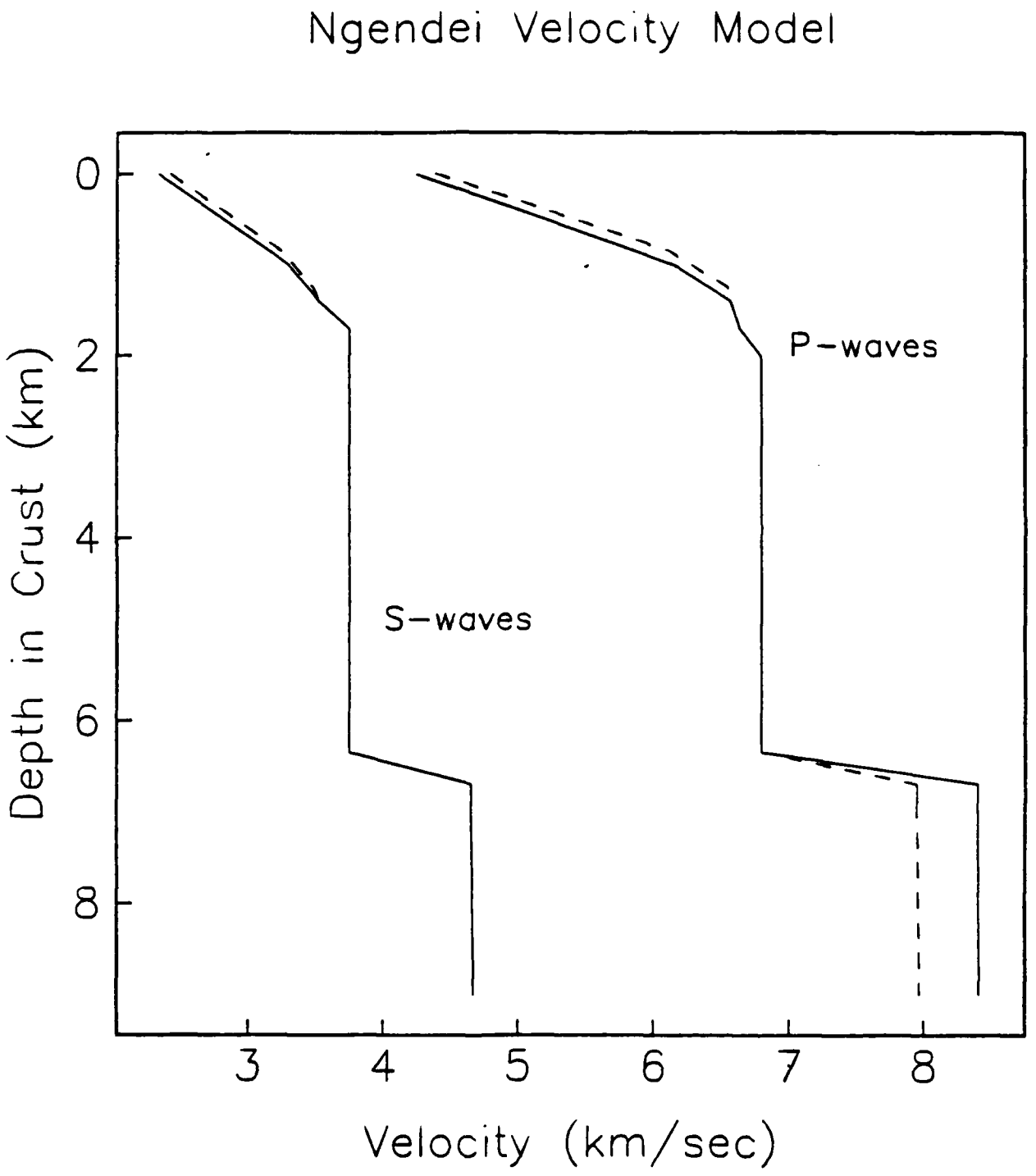
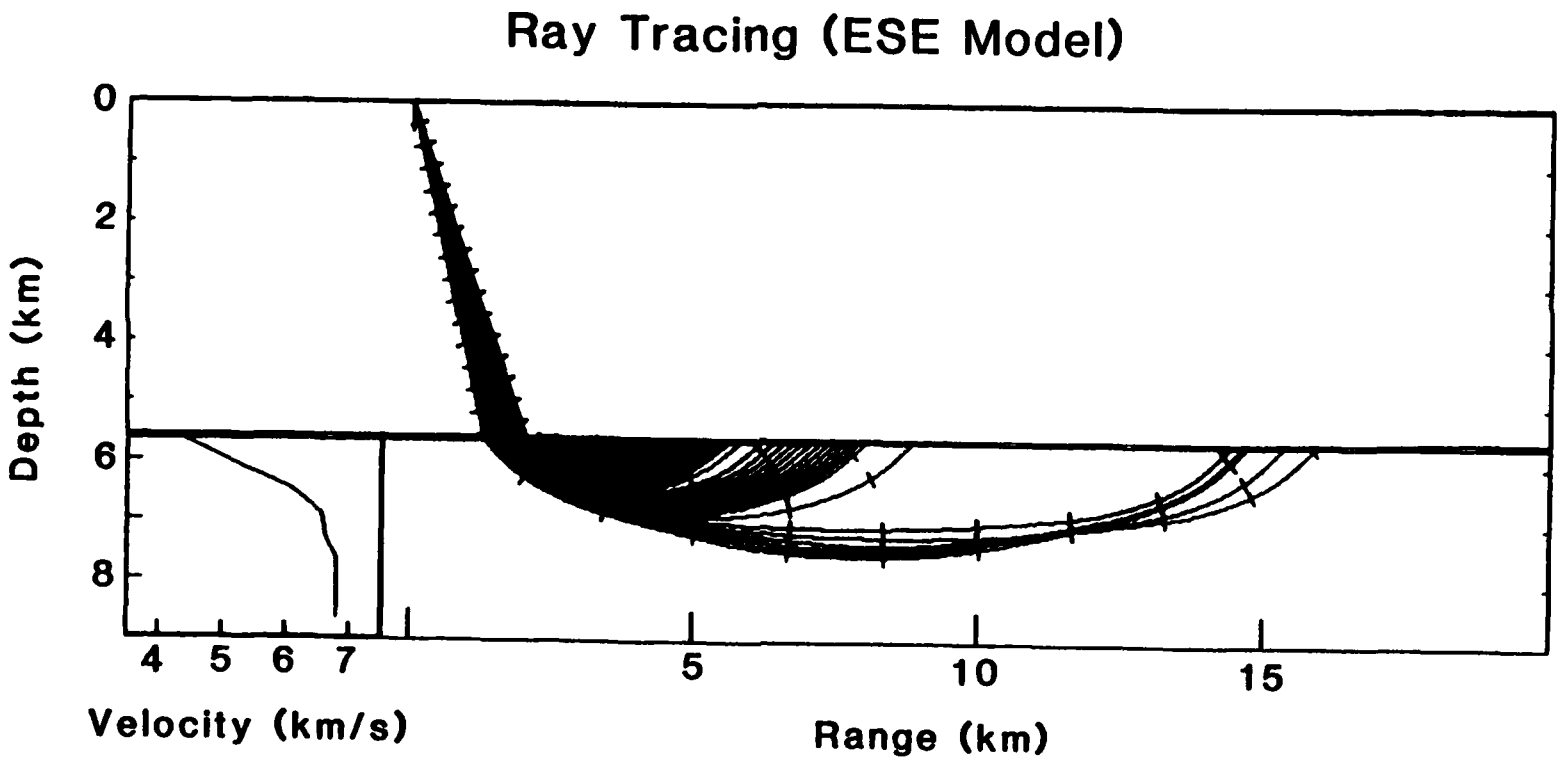

Ngendei Velocity Model
Depth in Crust (km)
0
2
4
6
8
P-waves
S-waves
3
4
5
6
7
8
Velocity (km/sec)

Fig. 7

Fig. 8


Ray Tracing (ESE Model)
Depth (km)
0
2
4
6
8
4
5
6
7
Velocity (km/s)
5
10
15
Range (km)

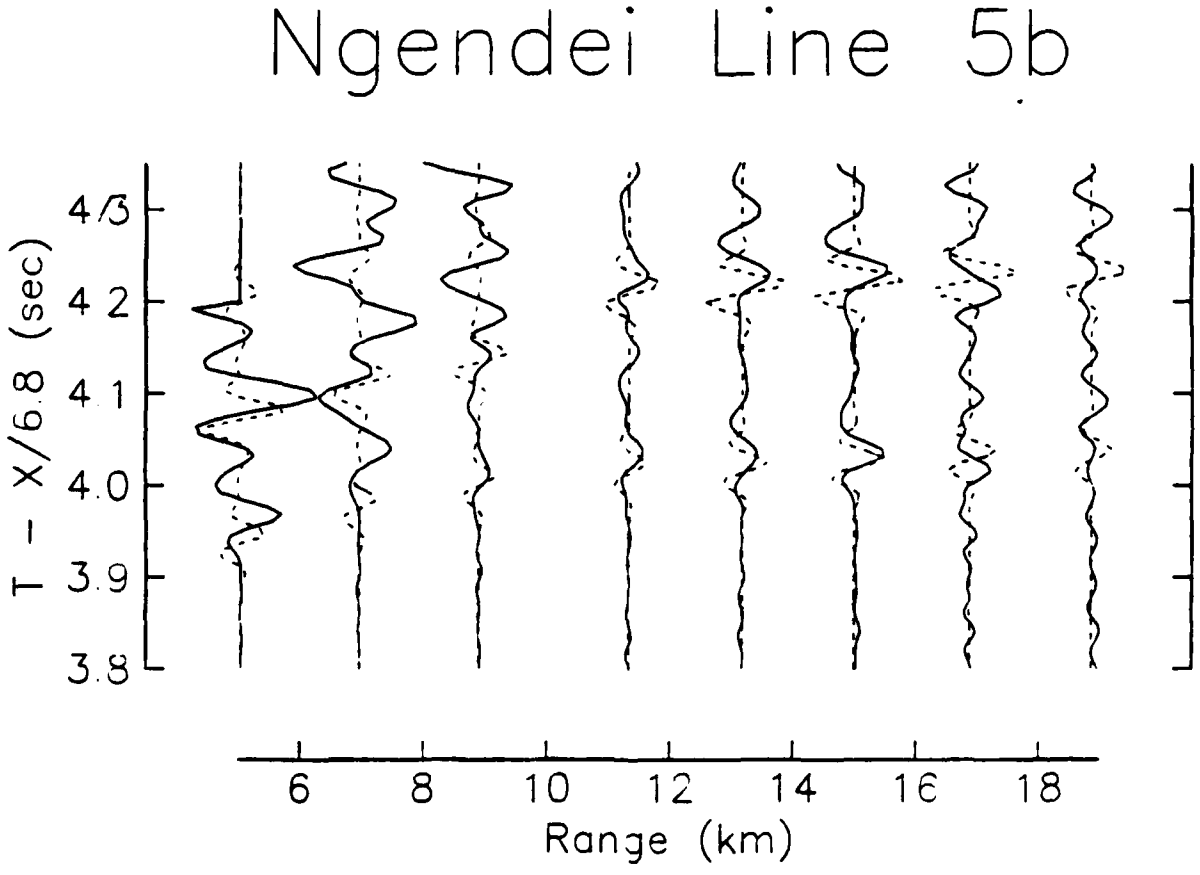
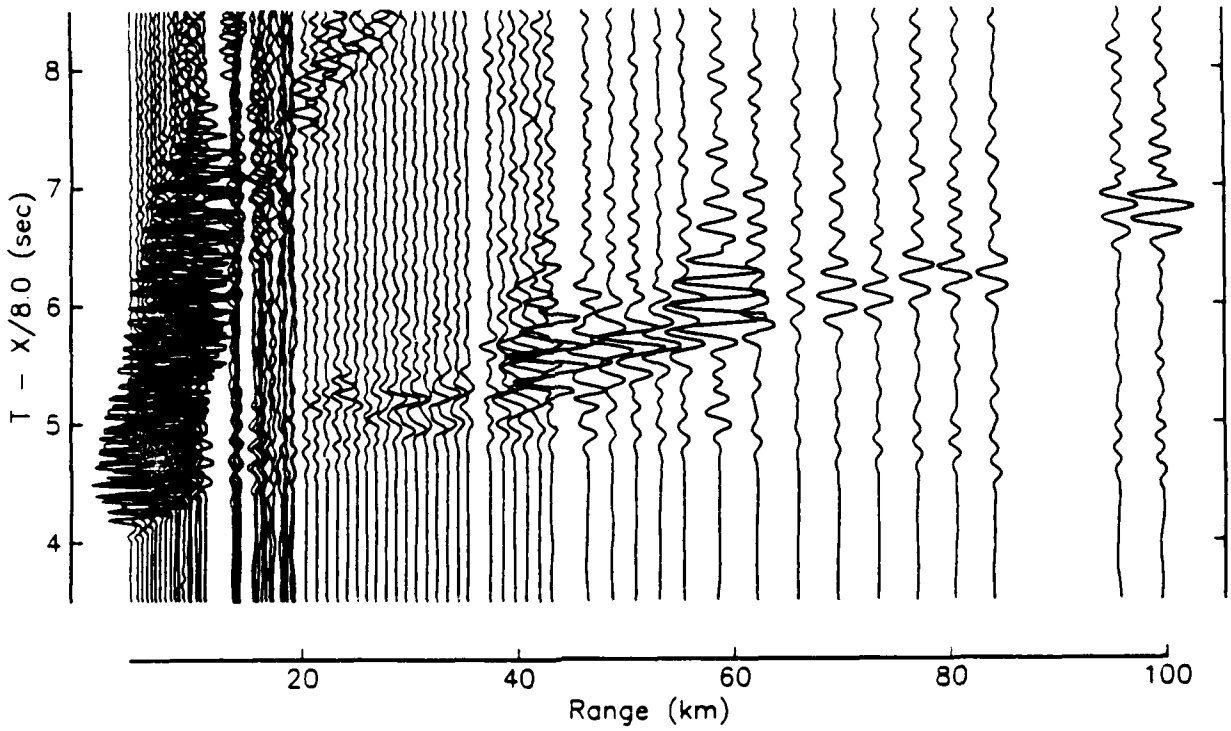

Ngendei Line 5b
T - X/6.8 (sec)
4.3
4.2
4.1
4.0
3.9
3.8
6
8
10
12
14
16
18
Range (km)

Fig. 9

Line 4b (MSS)



Line 5b (MSS)

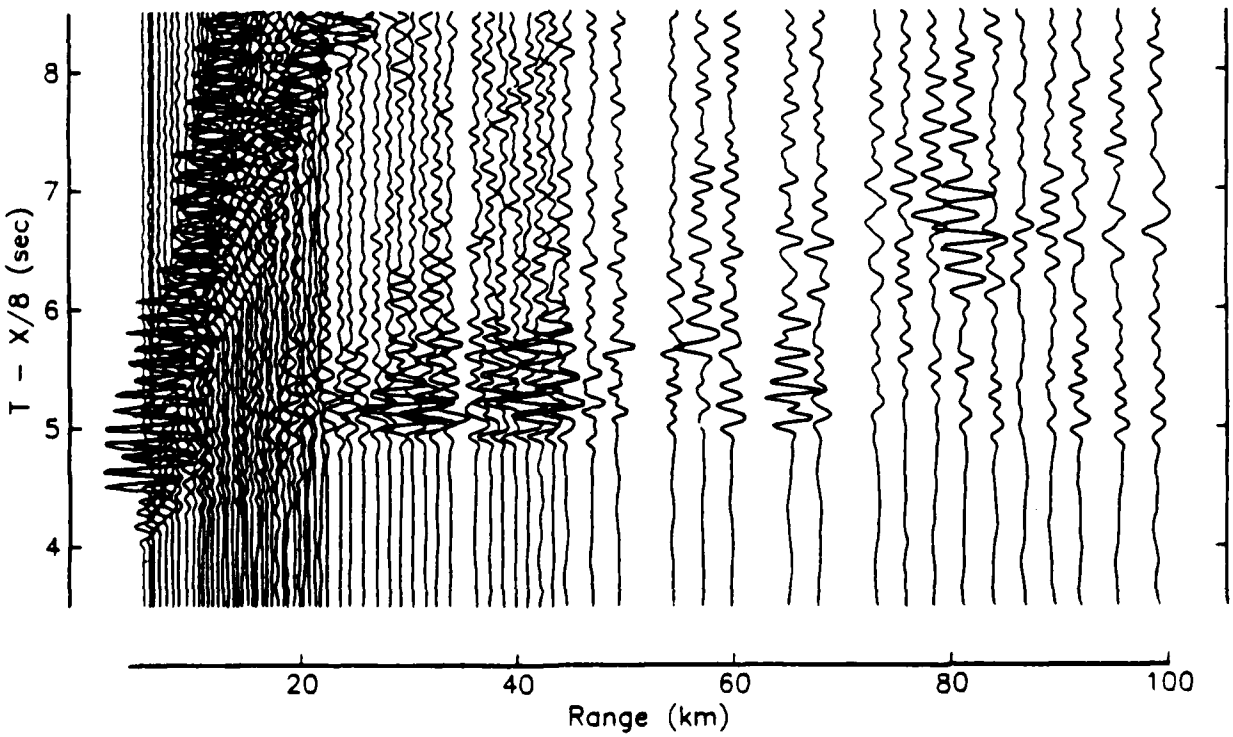
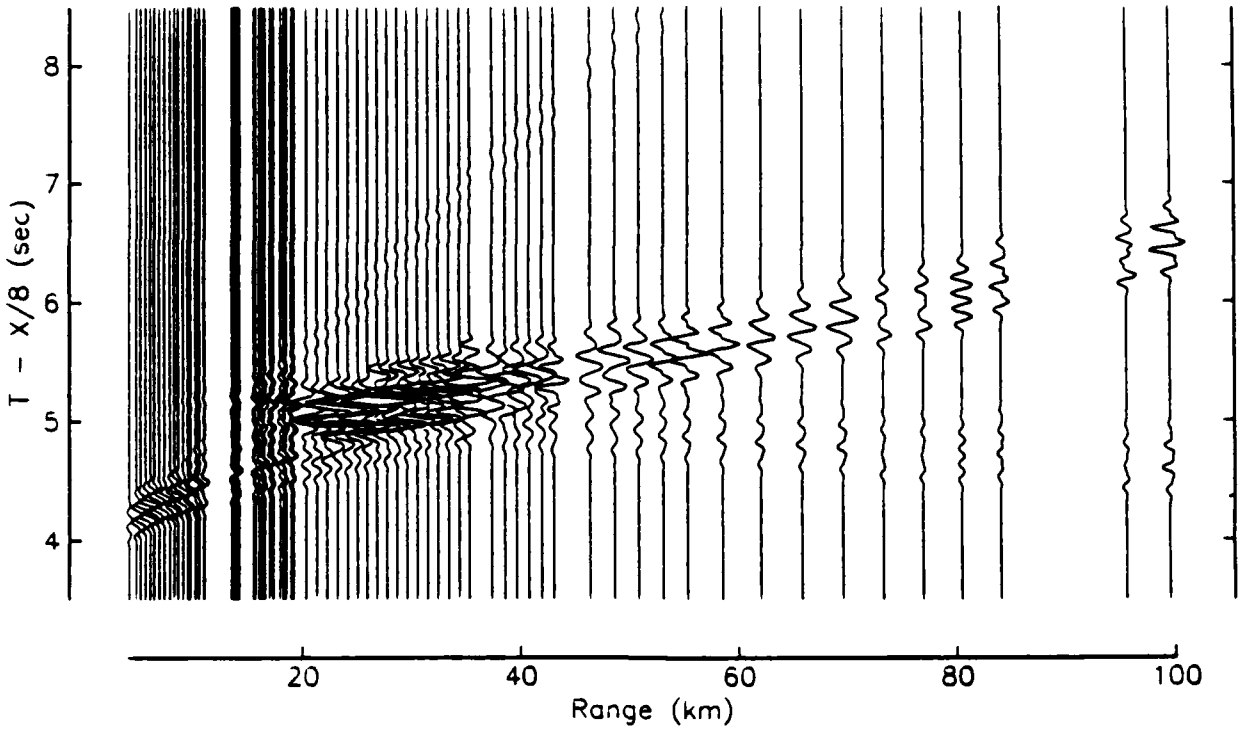


Fig. 10a

Line 4b (WKBJ Synthetics)



Line 5b (WKBJ Synthetics)

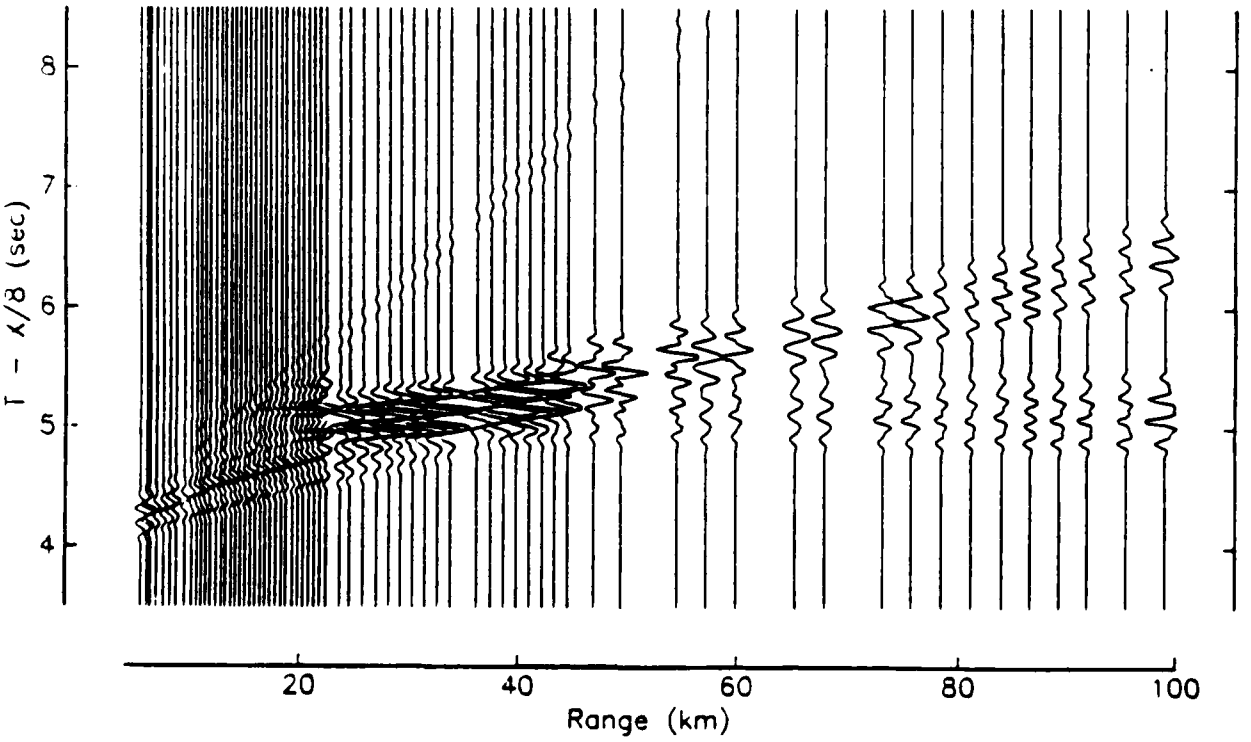


Fig 10

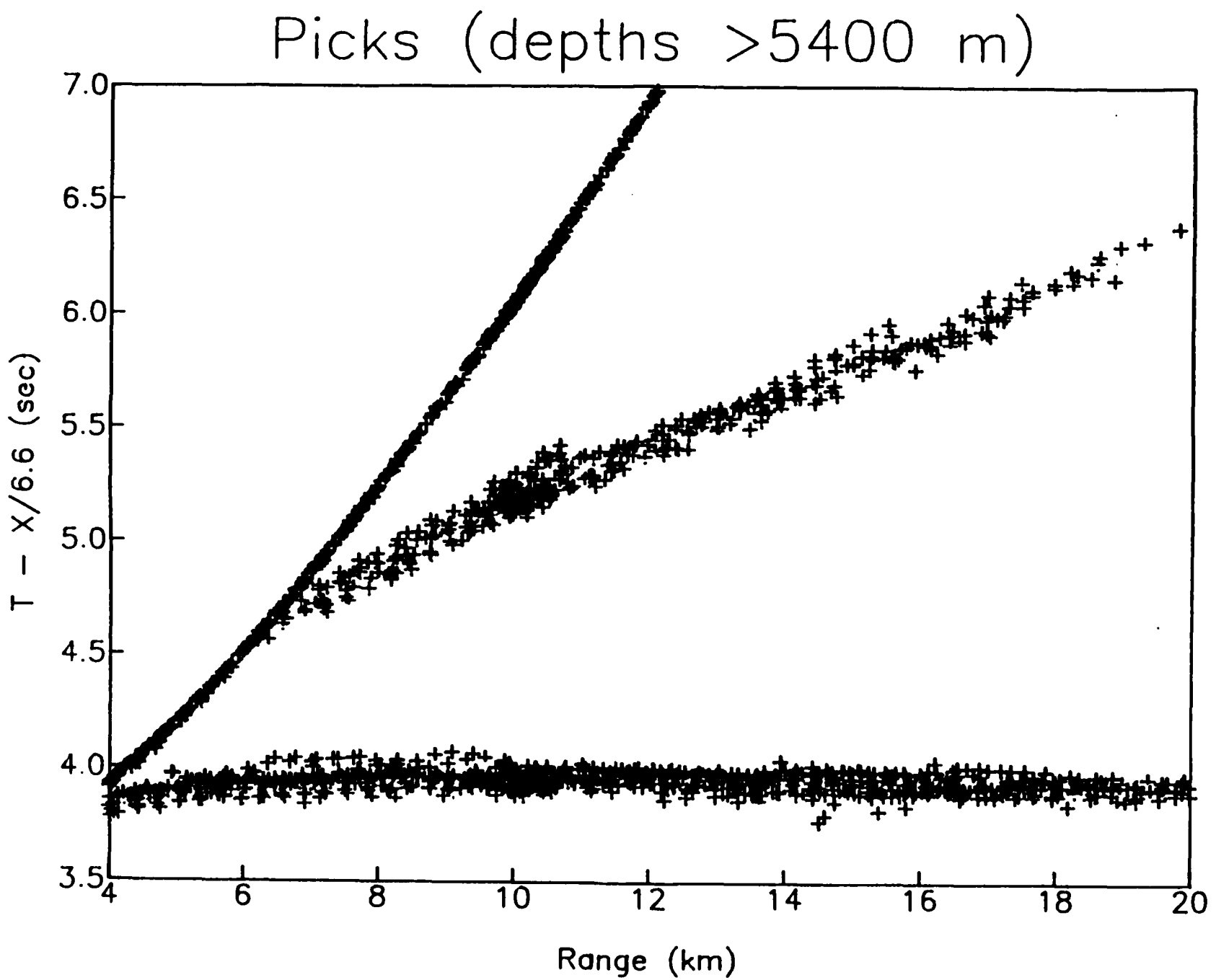

Picks (depths >5400 m)
T − X/6.6 (sec)
7.0
6.5
6.0
5.5
5.0
4.5
4.0
3.5
4
6
8
10
12
14
16
18
20
Range (km)

Fig. 11

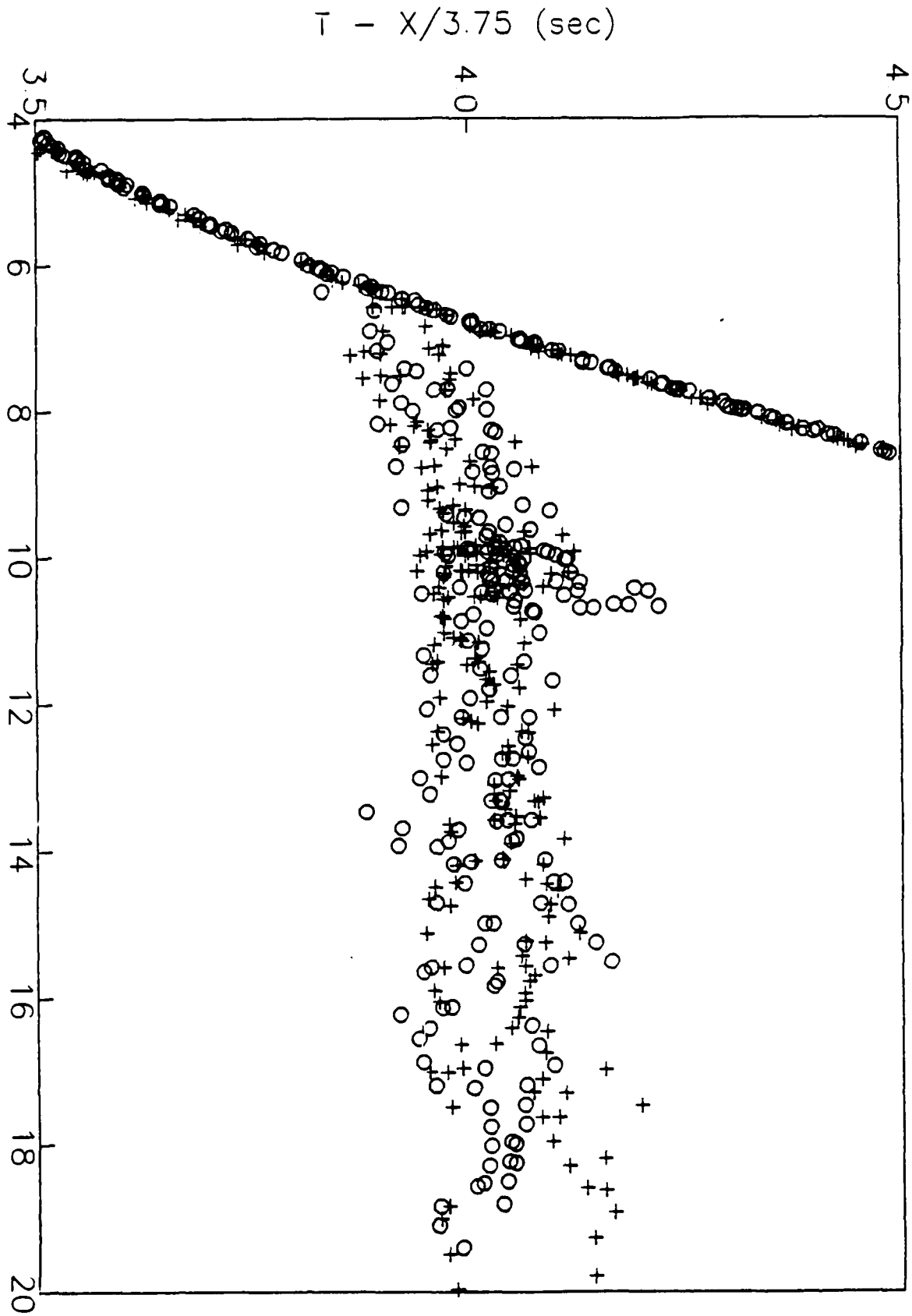

T − X/3.75 (sec)
3.5
4
4.5
Range (km)
6
8
10
12
14
16
18
20
Picks (depths >5400 m)

Fig. 12

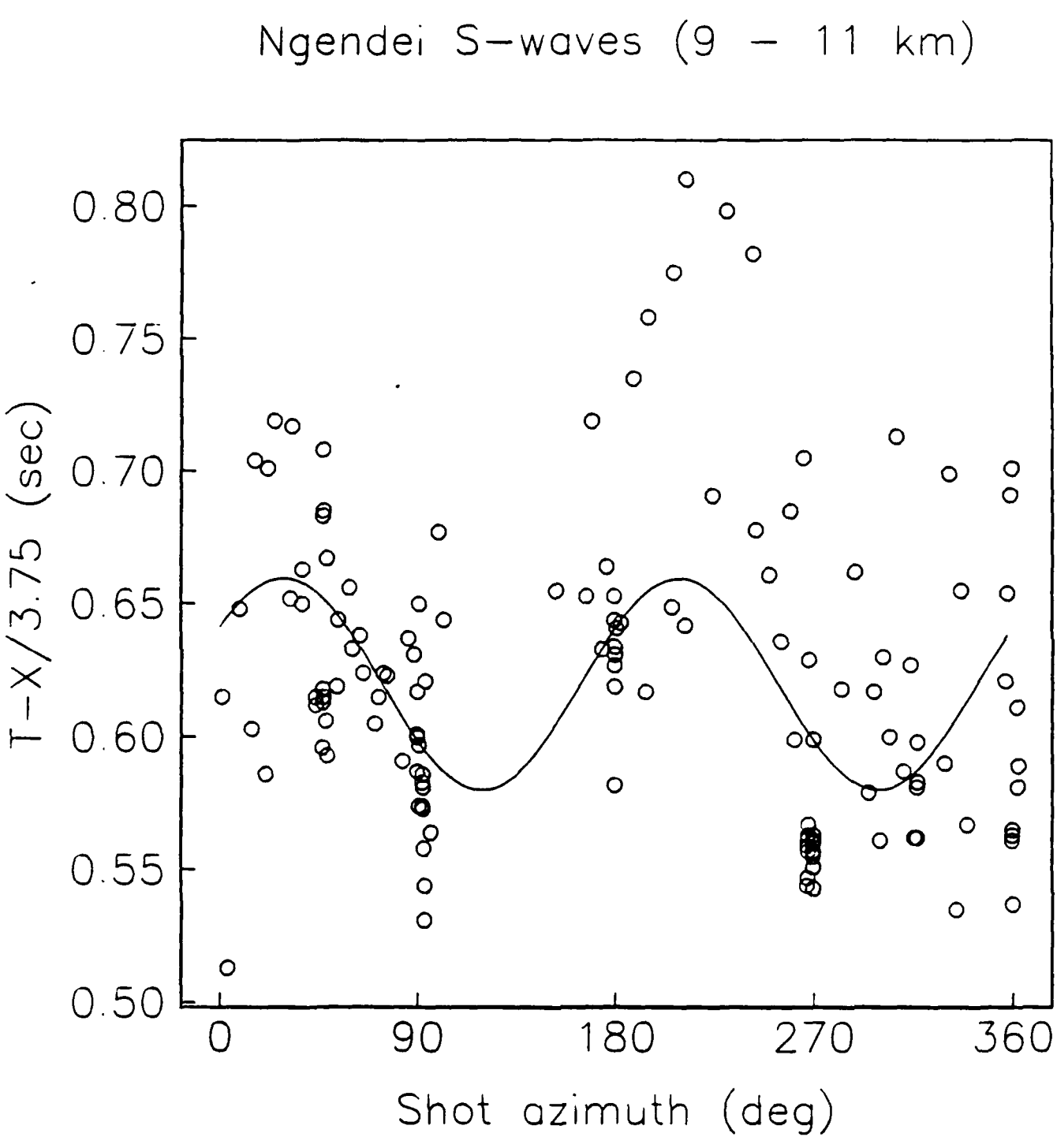
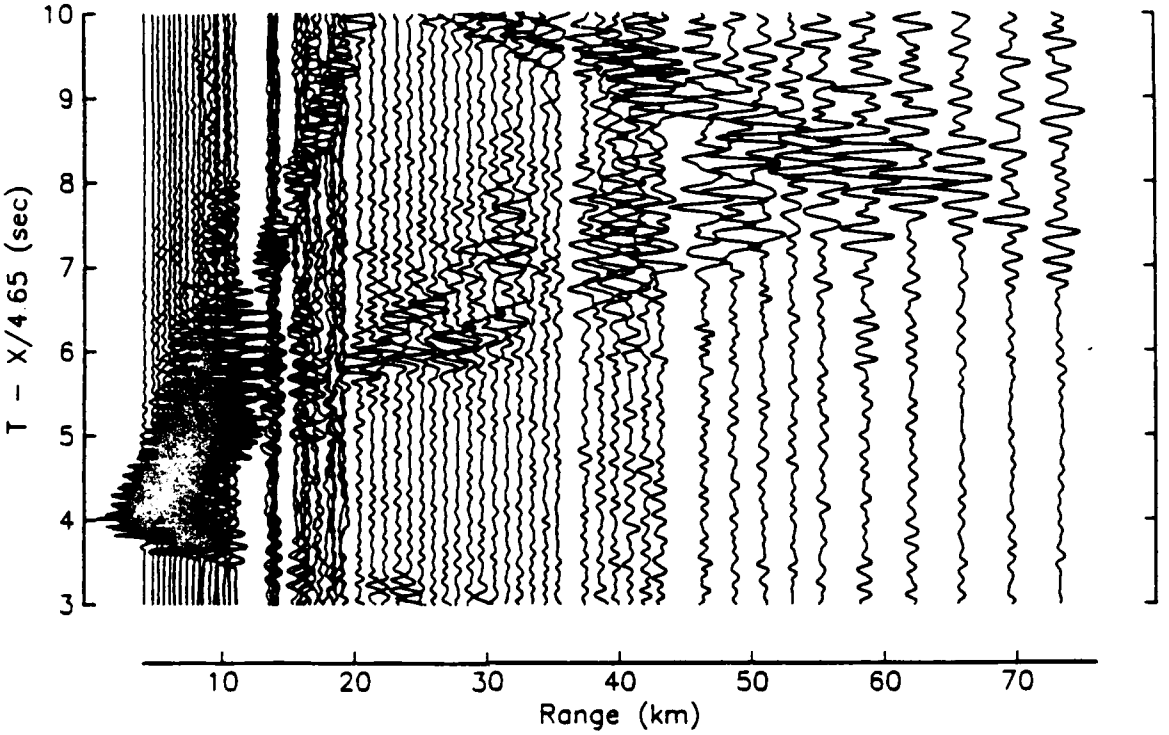

Ngendei S–waves (9 – 11 km)
T–X/3.75 (sec)
0.80
0.75
0.70
0.65
0.60
0.55
0.50
0
90
180
270
360
Shot azimuth (deg)

Fig 13

Line 4b (MSS)



Line 5b (MSS)

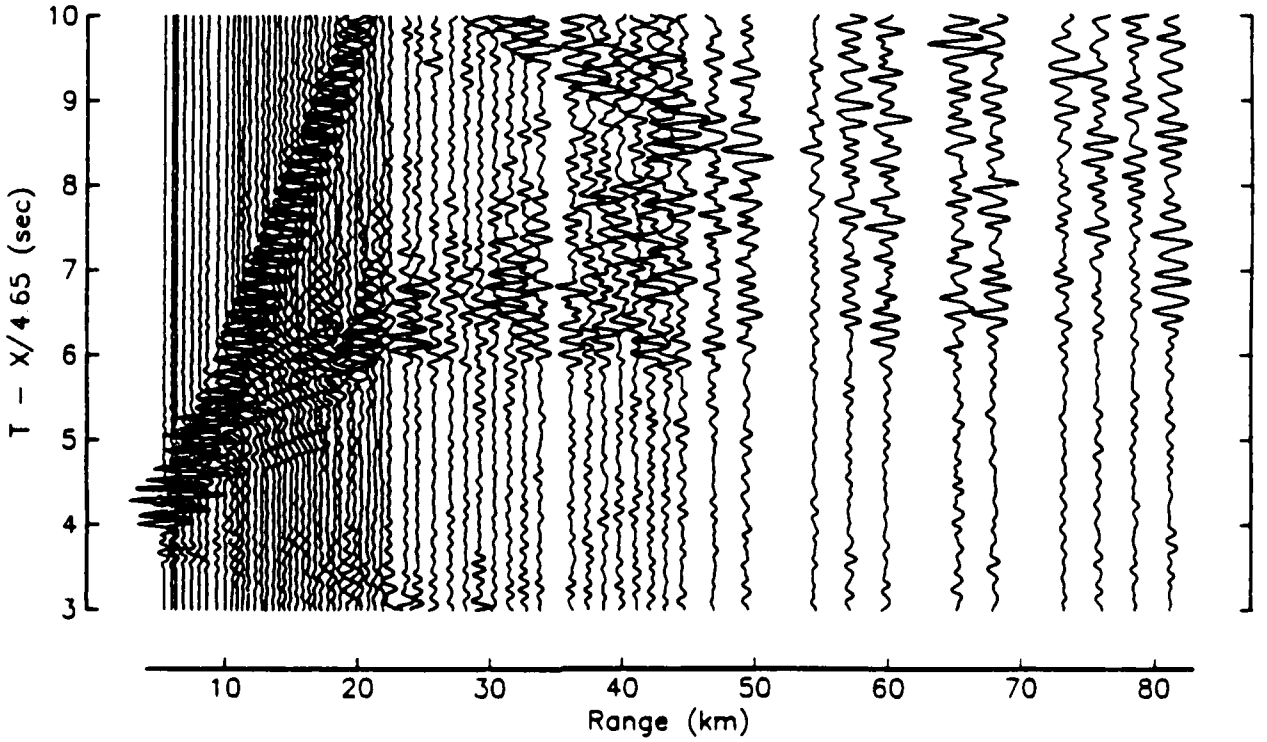
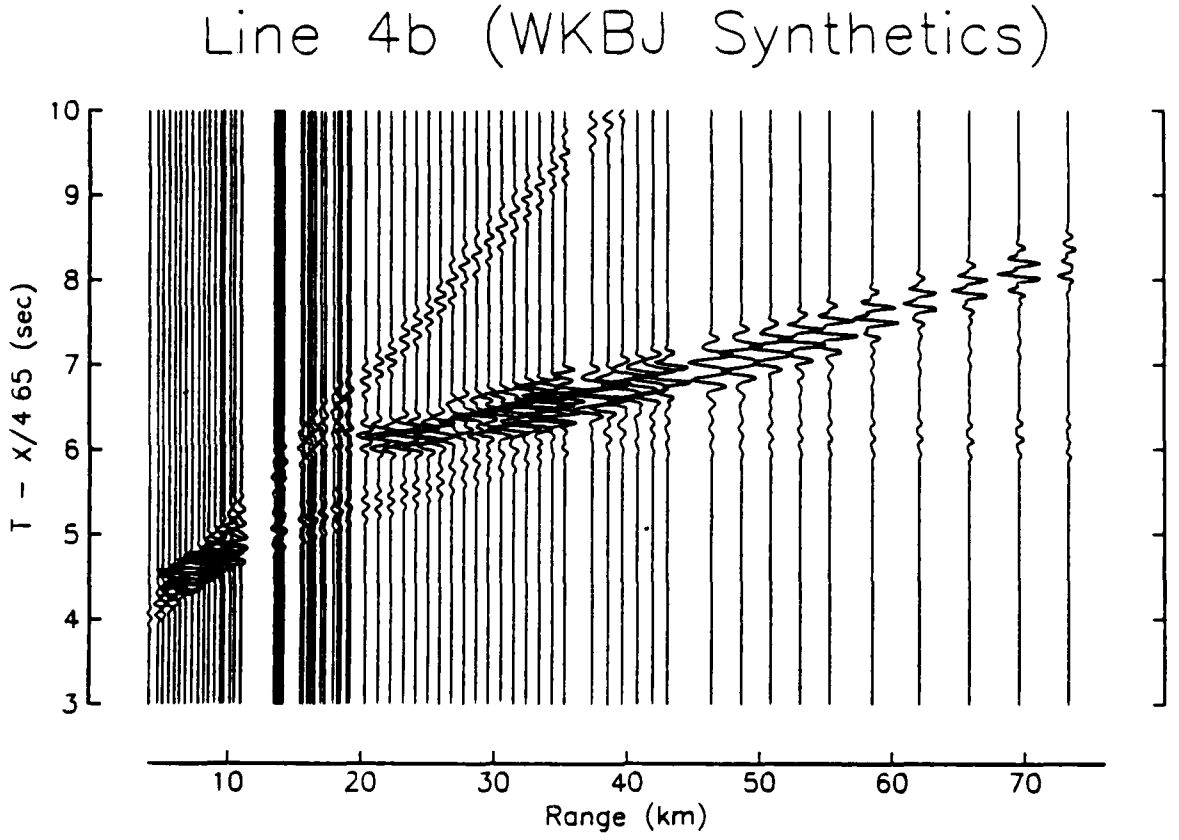


Fig 17


Line 4b (WKBJ Synthetics)
T - X/4 65 (sec)
10
9
8
7
6
5
4
3
10
20
30
40
50
60
70
Range (km)

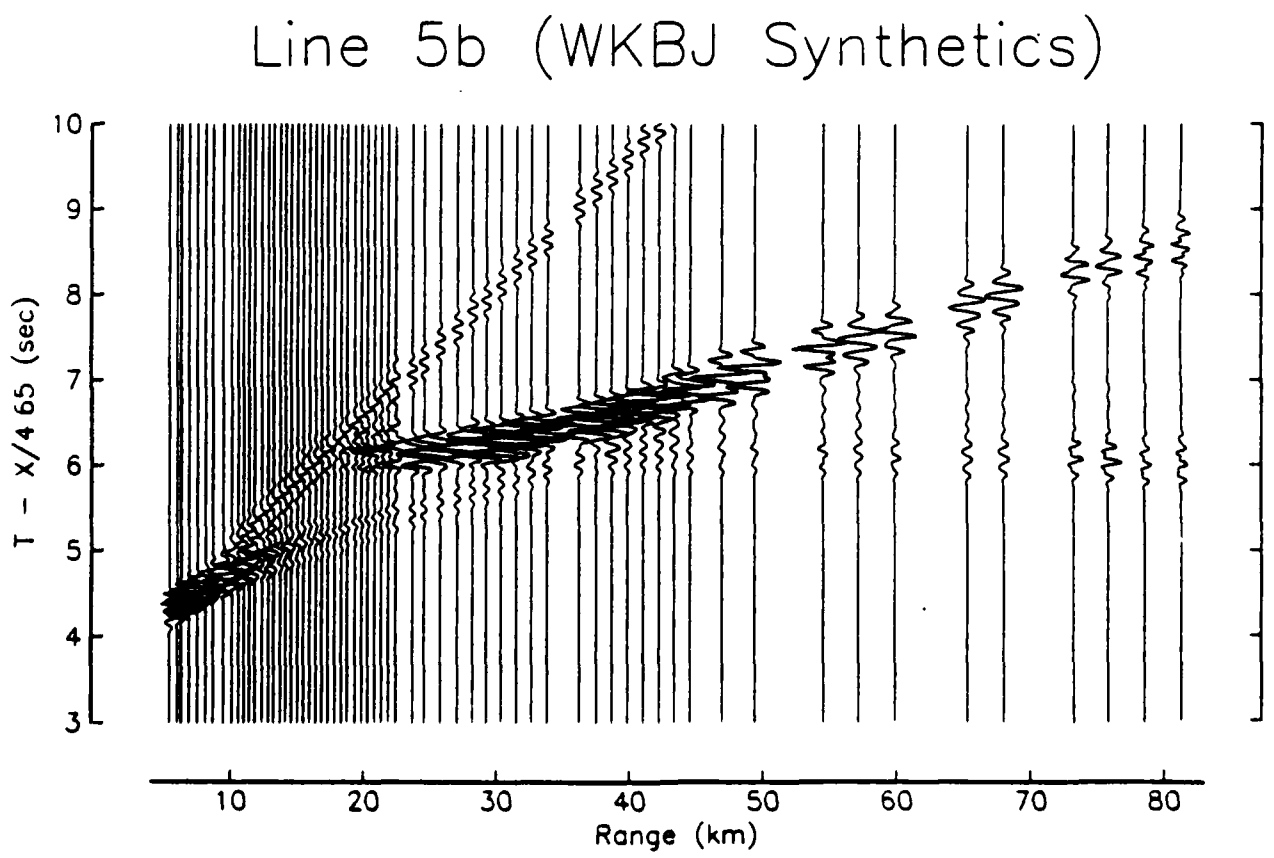

Line 5b (WKBJ Synthetics)
T - X/4 65 (sec)
10
9
8
7
6
5
4
3
10
20
30
40
50
60
70
80
Range (km)

Fig. 14b

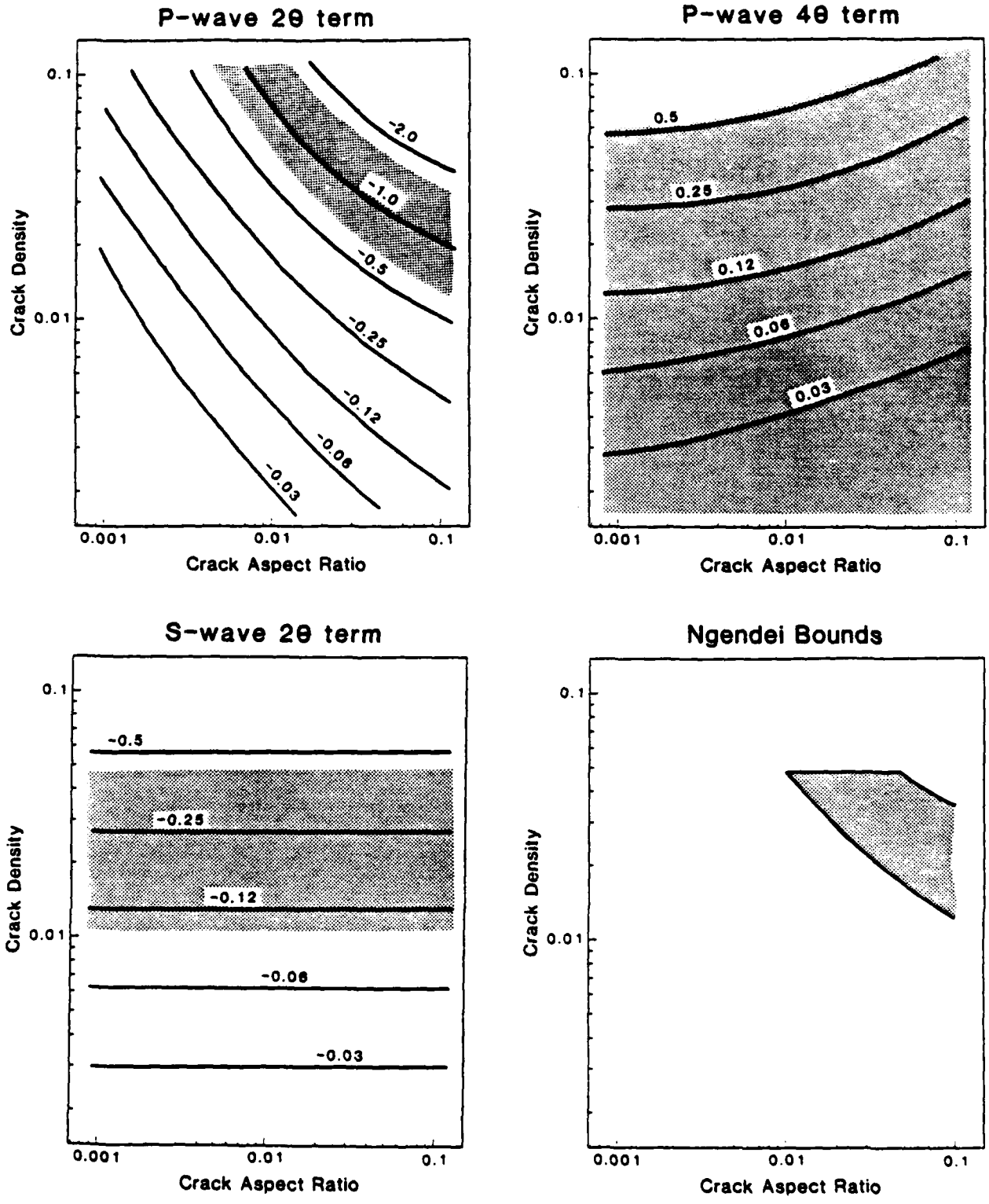
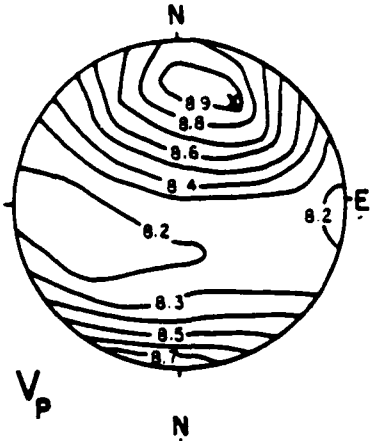

P-wave 2θ term
0.1
0.01
Crack Density
-2.0
-1.0
-0.5
-0.25
-0.12
-0.06
-0.03
0.001
0.01
0.1
Crack Aspect Ratio
P-wave 4θ term
0.1
0.01
Crack Density
0.5
0.25
0.12
0.06
0.03
0.001
0.01
0.1
Crack Aspect Ratio
S-wave 2θ term
0.1
0.01
Crack Density
-0.5
-0.25
-0.12
-0.06
-0.03
0.001
0.01
0.1
Crack Aspect Ratio
Ngendei Bounds
0.1
0.01
Crack Density
0.001
0.01
0.1
Crack Aspect Ratio

Fig. 15

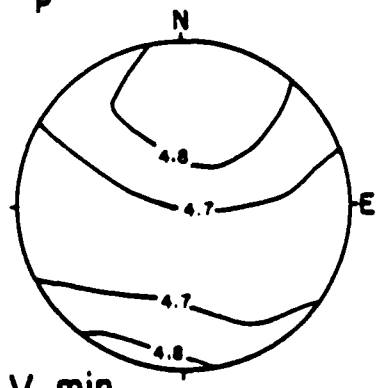
Anisotropy of Oman Harzburgite



V_P

P-waves

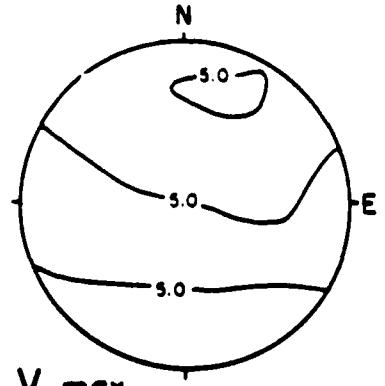
8.2 to 8.9 km/sec



V_S min

SV-waves

4.7 to 4.8 km/sec



V_S max

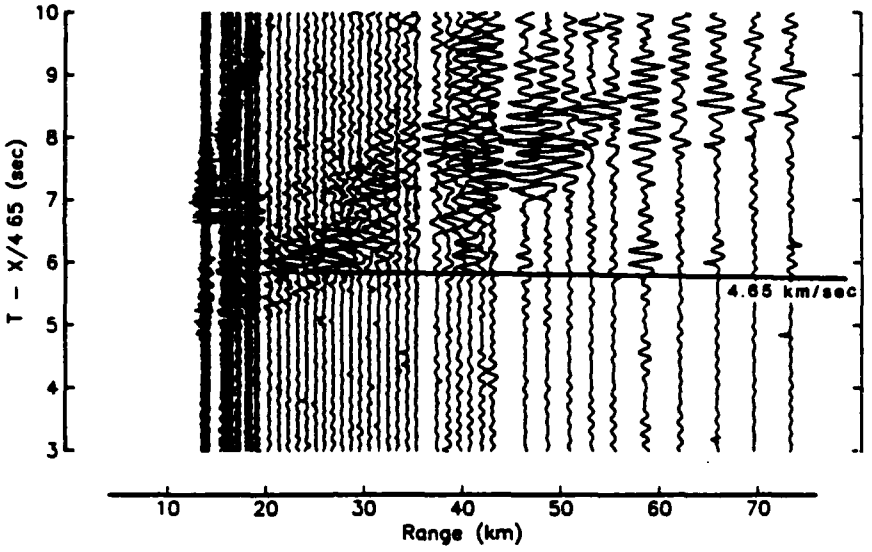
SH-waves

5.0 km/sec

from Christensen and Smewing, 1981

Fig 16

Line 4b (MSS horizontal)



Line 5b (MSS horizontal)

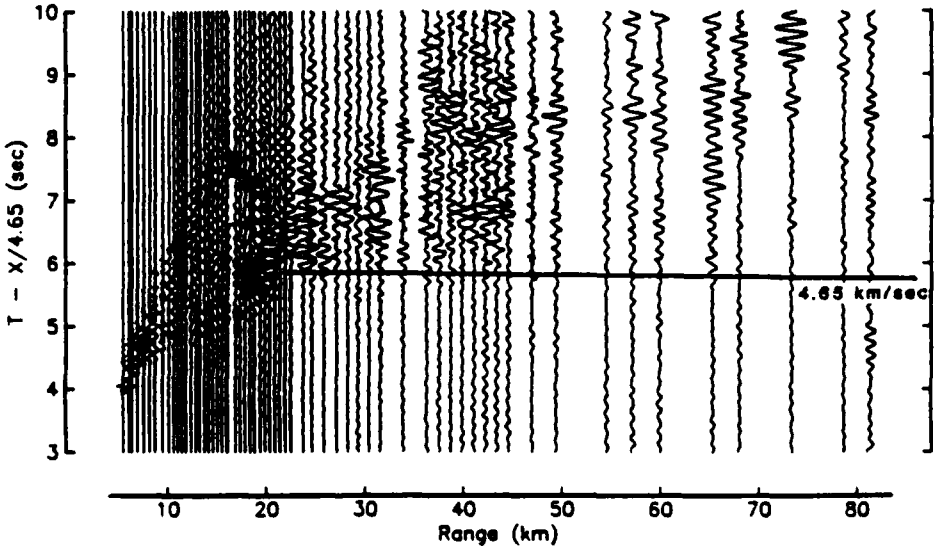


Fig. 17

CHAPTER 13

COMMENTS ON THE INFRASONIC NOISE THEORY OF ISAKOVICH AND KUR'YANOV AND ITS MODIFICATION BY WILSON

Richard G. Adair*

Institute of Geophysics and Planetary Physics,
Scripps Institution of Oceanography
La Jolla, California 92093

* Now at: Rockwell Hanford Operations, Energy Systems Group, Richland, Washington 99352

Comments on the infrasonic noise theory of Isakovich and Kur'yanov and its modification by Wilson.

Richard G. Adair[a)]

Institute of Geophysics and Planetary Physics A-025, Scripps Institution of Oceanography, La Jolla, California 92093

Received

The infrasonic noise theory of Isakovich and Kur'yanov and its modification by Wilson are reviewed and evaluated. The tractability of the theory's formulation depends upon two assumptions. The most crucial assumption is that the turbulent wind field, acting normally at the sea surface, linearly excites acoustic waves and wind waves in identical manners. This assumption is physically unreasonable. The second assumption is that the wind waves attenuate. Isakovich and Kur'yanov assume viscous attenuation, while Wilson incorporates the recent conjecture of Hasselmann that above a critical wind speed the attenuation is due to whitecapping and is quadratic in frequency. It is shown that due to incorrect implementation of Hasselmann's attenuation term, Wilson's expressions for the noise source and pressure levels are too low by a factor of $(2\pi)^{-1}$, or -16 *dB*.

---

a) Now at: Rockwell Hanford Operations, Energy Systems Group, Richland, Washington 99352

The purpose of this letter is to comment on the validity of Isakovich and Kur'yanov's[1] theory of infrasonic noise due to atmospheric turbulence near the ocean surface, and to clarify some aspects of Wilson's[2,3] revision of that theory.

A review of the conditions for acoustic wave generation by an ocean-surface source is first presented. The principle point of this review is that the source field must possess significant energy at angular frequencies ω and horizontal wavenumbers k such that $\omega \geq ck$, where c is the acoustic wave speed in the ocean. Contributions such that $\omega < ck$ attenuate exponentially with depth in the ocean.

Following this review, the linear theory of Isakovich and Kur'yanov, and Wilson's modifications of it are considered. It is argued that the basic premise of these theories is invalid.

It is furthermore shown that the source and noise levels predicted by Wilson are too low by a factor of $(2\pi)^{-2}$, or -16 dB, due to the incorrect implementation of an attenuation term.

1. SURFACE SOURCE CHARACTERISTICS

The source and the acoustic wavefield it generates may be decomposed into elemental Fourier components of the form:

$$A(\mathbf{k},\omega)\, e^{-i\omega t}\, e^{i(\mathbf{k}\cdot\mathbf{r} + k_z z)} \quad . \tag{1}$$

Here, $\mathbf{k}$ is the horizontal wavevector, $\mathbf{r}$ is the horizontal position vector, k_z is the vertical wavenumber, and z is the depth, taken to be *positive* downward. In the ocean, which shall be taken to be a homogeneous, isotropic layer with acoustic speed c,

$$k_z^2 = (\omega/c)^2 - k^2 \quad , \tag{2}$$

where $k = |\mathbf{k}|$. If k exceeds ω/c, then k_z is imaginary and the Fourier component attenuates with depth. In the deep ocean, therefore, only components such that $\omega \geq ck$ need be considered.

The foregoing implies that gravity-capillary waves cannot directly excite significant acoustic energy in the ocean since the dispersion relationship between the angular frequency σ and horizontal wavenumber χ do not satisfy $\sigma \geq c\chi$. This well-known surface wave relationship is:

$$\sigma^2 = \gamma\chi^3 + g\chi \quad . \tag{3}$$

γ is the kinematic surface tension ($\sim 75\ cm^3 s^{-2}$), and g is gravitational acceleration ($9.8\times10^2 cm\ s^{-2}$). *Figure 1* graphs $\sigma(\chi)$ and demarks the region of acoustic wave generation

in the frequency band 0.1 - 100 Hz. The acoustic and surface wave loci are clearly disparate.

On the other hand, it may be shown that the second-order interaction between nearly anti-parallel ocean surface waves of wavevectors $\chi + \delta$ and $-\chi$, $|\delta| \ll |\chi|$, and common angular frequency σ does generate acoustic energy (Hasselmann[4]; Hughes[5]). The wavevector δ and angular frequency 2σ of the excited pressure fluctuation are each the sum of the respective surface wave quantities. The magnitude of the resultant wavevector is sufficiently small to satisfy the condition $2\sigma \geqslant c\,|\delta|$. This non-linear wave interaction is the source of infrasonic noise in the band 0.1 - 1.0 Hz (see, e.g., Webb and Cox[6]; Kibblewhite and Ewan[7]; Adair et al.[8]).

2. THE INFRASONIC NOISE THEORY OF ISAKOVICH AND KUR'YANOV

In this theory, atmospheric turbulence is assumed to generate a pressure field which acts normally on the ocean surface. All excited motion is related to the turbulence through a linear boundary condition which may be expressed as:

$$\varsigma(\mathbf{k},\omega) = \beta(\mathbf{k},\omega)\, \tau(\mathbf{k},\omega) \quad . \tag{4}$$

The function β embodies the boundary condition relating the source field τ to the ocean surface height spectrum ς. At a given frequency, the low-wavenumber components of this pressure field generate wind waves, while its 'acoustic' components excite acoustic waves.

Isakovich and Kur'yanov adopt a functional form for the source field τ and explicitly evaluate it in terms of the empirically-known wind wave frequency spectrum by integrating *Equation (4)* over wavevector. In this manner, the acoustic properties of the hypothesized source are inferred from its non-acoustic properties. The integral, which is singular at wavenumbers corresponding to gravity-capillary waves [see *Equation (3)*], is made tractable by incorporating wave attenuation (the wave frequency is made complex), thereby removing the singularities from the real wavenumber axis. Isakovich and Kur'yanov assume viscous attenuation, for which the imaginary part of the frequency is $2\nu\chi$, where ν is the effective water viscosity and χ is the wavenumber which satisfies the *Equation (3)* (see Phillips[9]).

3. VALIDITY OF ISAKOVICH AND KUR'YANOV'S THEORY

A serious objection must be raised against this model of infrasonic noise. Isakovich and Kur'yanov employ a source function which is hypothesized for wind waves, and extrapolate it without justification or comment to all values of frequency and wavevector. This implicitly assumes that identical physical processes are operative in both the acoustic ($\omega \geqslant ck$) and wind wave ($\omega^2 \approx \gamma k^3 + gk$) regimes, which is highly unlikely. Wind waves are a nonlinear resonance phenomenon of gravity-capillary waves in which the wind and ocean surface

mutually distort each other, with resultant characteristics specific to the wind wave regime. (A discussion of the physical mechanisms of wave generation is beyond the scope of this letter. An excellent summary of the subject is given in Phillips[9].) There is no evidence which suggests that a similar resonance phenomenon exists for acoustic energy in the ocean. It is therefore unlikely that a single function can describe the spatial behavior of the source over the entire frequency - wavenumber plane.

If it is true that different functional forms should be used in the two regimes, then the strategy of Isakovich and Kur'yanov for inferring acoustic properties of the source and noise from the wind wave spectrum cannot succeed. This conclusion may be drawn from consideration of the wind wave spectrum $\varsigma(\mathrm{k},\omega)$ in conjunction with the boundary condition *Equation (4)*. The sharpness of the wind wave resonance is well-modeled by a delta-function dependence in wavevector $\delta(\mathrm{k}-\chi)$, where $|\chi|$ satisfies the gravity-capillary wave dispersion relationship, *Equation (3)*. The boundary condition, clearly indifferent to the source's acoustic portion, yields information only at $\chi(\sigma)$. Inclusion of wave attenuation, which would broaden the resonance peak somewhat, does not substantially affect this argument.

4. WILSON'S MODIFICATION OF ISAKOVICH AND KUR'YANOV'S THEORY

While the foregoing discussion casts serious doubt on the validity of Isakovich and Kur'yanov's theory, its explication is nonetheless useful for the purposes of comparison. Wilson's[2,3] modification of the theory, which adopts the same source function as before, is therefore considered.

Wilson[2] more precisely evaluates the integral of the boundary condition *Equation (4)*, and employs recently proposed forms of the wind wave spectrum and wave attenuation. In a subsequent erratum, Wilson[3] points out several notational and algebraic errors in his original paper[2], most importantly in the equations which specify the source field and mean-squared noise spectra. (The corrected equations are recapitulated in the Appendix of this letter.)

Some uncertainty exists regarding the absolute levels of infrasonic noise predicted by Wilson (see: Cato[10]; Wilson[11]; and Kibblewhite and Ewan[7], pp. 991, 992-993). Cato[10] notes that Wilson's original expressions for these spectra are too low by "about 20 dB". Although Wilson[3,11] acknowledges this deficit, which is due to the omission of a factor of the kinematic surface tension γ ($\sim$75, or +19 dB), he claims that it is offset by a factor of $(2\pi)^{-2}$, or -16 dB, resulting from his incorrect implementation of the attenuation term, α_0. Wilson originally specified this term as:

$$\alpha_0 = 2.5\times10^{-4}\omega^2 \tag{5}$$

citing Wu et al.[12], but subsequently claimed that frequency f rather than angular frequency $\omega=2\pi f$ should have been used. Since the source and mean-square noise spectra are both proportional to α_0 (see Appendix), Wilson's net correction is only $+3\ dB$.

Wilson's use of frequency rather that angular frequency in *Equation (5)* is inconsistent with the literature. The form of the wave attenuation in *Equation (5)* is due to Hasselmann[13], who found that if the attenuation is a quasi-linear effect, then it is proportional to ω^2. Hasselmann's expression for the parameter of proportionality depends upon wind speed and fetch, and the peak frequency of the wind wave spectrum. Wu et al.[12] (see also: Wu et al.[14]) inferred the value of this parameter from laboratory experiments. Their results, while not well constrained, ranged between 1.7×10^{-4} and 5.4×10^{-4}. Evaluation of Hasselmann's expression using reasonable field values also yields a value on the order of 10^{-4}. These results imply that Wilson's original use of ω for the attenuation α_0 was correct, and that his source values should be increased by 19 dB, as Cato originally contended.

ACKNOWLEDGEMENTS

The author thanks Chip Cox and John Orcutt for useful discussion and review. This research was supported by DARPA contracts F49620-79-C-0019 and AFOSR-84-0043.

APPENDIX

Wilson's[2,3] corrected expressions relating the ocean height power spectrum $H(\omega)$ to the source power spectrum $P(\omega)$ and the mean-squared power spectrum in the water $p^2(\omega)$ are:

$$P(\omega) = \frac{3\gamma U \rho^2 \alpha_0}{\pi F(\omega)}\ H(\omega) \tag{A1}$$

and

$$p^2(\omega) = \frac{U^2}{5.7c^2}\ \frac{3\gamma U \rho^2 \alpha_0}{\pi F(\omega)}\ H(\omega)\ , \tag{A2}$$

where U is the free stream wind speed, ρ is the water density ($1\ g/cc$), α_0 is an attenuation factor which is discussed in the main text, γ is the kinematic surface tension (T/ρ in Wilson's notation), and c is the acoustic wave speed in water ($1.5\ km\,s^{-1}$). The function $F(\omega)$ is:

$$F(\omega) = -\mathrm{Re}\left[(\chi_2^2 + g/3\gamma)^{-1}\right]\ . \tag{A3}$$

χ_2 is a solution of the cubic equation:

$$\chi_2^3 + (g/\gamma)\chi_2 - \Omega^2/\gamma = 0 \ , \tag{A4}$$

$$\Omega = \omega - i\alpha_0 \ ,$$

such that $\mathrm{Im}(\chi_2)>0$. This root is given by:

$$\chi_2 = s_1 w + s_2 w^* \ . \tag{A5}$$

The asterisk denotes the complex conjugate, and:

$$s_{1,2} = \left[r \pm (q^3+r^2)^{1/2}\right]^{1/3}$$

$$q = g/3\gamma$$

$$r = \Omega^2/2\gamma$$

$$w = e^{i2\pi/3} \ .$$

In evaluating s_1 and s_2, care should be taken to compute the proper complex cube roots. An appropriate constraint in this regard is:

$$s_2 = q/s_1 \ .$$

The expression for χ_2, *Equation (A5)*, differs slightly from that given by Isakovich and Kur'yanov, and by Wilson. These authors replace Ω^2 by its linear approximation in α_0, i.e. $\omega^2 - 2i\omega\alpha_0$. In principal, it is no more difficult to evaluate *Equation (A5)* using the former than the latter.

Wilson uses the wave height spectrum $H(\omega)$ of Toba[15] (see also: Mitsuyasu[16]):

$$H(\omega) = 0.02 u_* \frac{2\pi}{\chi\omega^2} \ , \tag{A6}$$

where χ satisfies the free surface-wave dispersion relationship *Equation (3)*, and where u_* is the friction velocity. As Cato[10] observes, Wilson apparently uses the empirical relationship $u_* = 0.04U$ to evaluate *Equation (A6)*.

References

1. M. A. Isakovich and B. F. Kur'yanov, "Theory of low-frequency noise in the ocean," *Sov. Phys. Acoust. 16*, 49-5, 1970.
2. J. H. Wilson, "Very low frequency (VLF) wind-generated noise produced by turbulent pressure fluctuations in the atmosphere near the ocean surface," *J. Acoust. Soc. Am. 66*, 1499-1507, 1979.
3. J. H. Wilson, "Erratum: 'Very low frequency (VLF) wind-generated noise produced by turbulent pressure fluctuations in the atmosphere near the ocean surface,' [J. Acoust. Soc. Am. 66, 1499-1507 (1979)]," *J. Acoust. Soc. Am. 69*, 1517-1518, 1981.
4. K. Hasselmann, "A statistical analysis of the generation of microseisms," *Rev. Geophys. 1*, 177-210, 1963.
5. B. Hughes, "Estimates of underwater sound (and infrasound) produced by nonlinearly interacting ocean waves," *J. Acoust. Soc. Am. 60*, 1032-1039, 1976.
6. S. Webb and C. Cox, "Pressure and electric fluctuations on the deep seafloor: Background noise for seismic detection," *Geophys. Res. Letters 11*, 967-970, 1984.
7. A. C. Kibblewhite and K. C. Ewans, "Wave-wave interactions, microseisms, and infrasonic ambient noise in the ocean," *J. Acoust. Soc. Am. 78*, 981-994, 1985.
8. R. G. Adair, J. A. Orcutt, and T. H. Jordan, "Low-frequency noise observations in the deep ocean," *J. Acoust. Soc. Am., in press*, 1986.
9. O. Phillips, *Dynamics of the Upper Ocean*, Cambridge University Press, 2nd ed. (1980).
10. D. H. Cato, "Comments on 'Very low frequency (VLF) wind-generated noise produced by turbulent pressure fluctuations in the atmosphere near the ocean surface,' [J. Acoust. Soc. Am. 66, 1499-1507 (1979)]," *J. Acoust. Soc. Am. 70*, 1783-1784, 1981.
11. J. H. Wilson, " Rebuttal to 'Comments on 'Very low frequency (VLF) wind-generated noise produced by turbulent pressure fluctuations in the atmosphere near the ocean surface,' by Douglas H. Cato', " *J. Acoust Soc. Am. 70*, 1785-1786, 1981.
12. H.-Y Wu, E.-Y. Hsu, and R. L. Street, "The energy transfer due to air-input, non-linear wave-wave interaction and white-cap dissipation associated with wind-generated waves," *Stanford University Dept. of Civil Engineering Tech. Rept. No. 207* (February, 1977).
13. K. Hasselmann, "On the spectral dissipation of ocean waves due to white capping," *Boundary Layer Meteorol. 6*, 107-127, 1974.

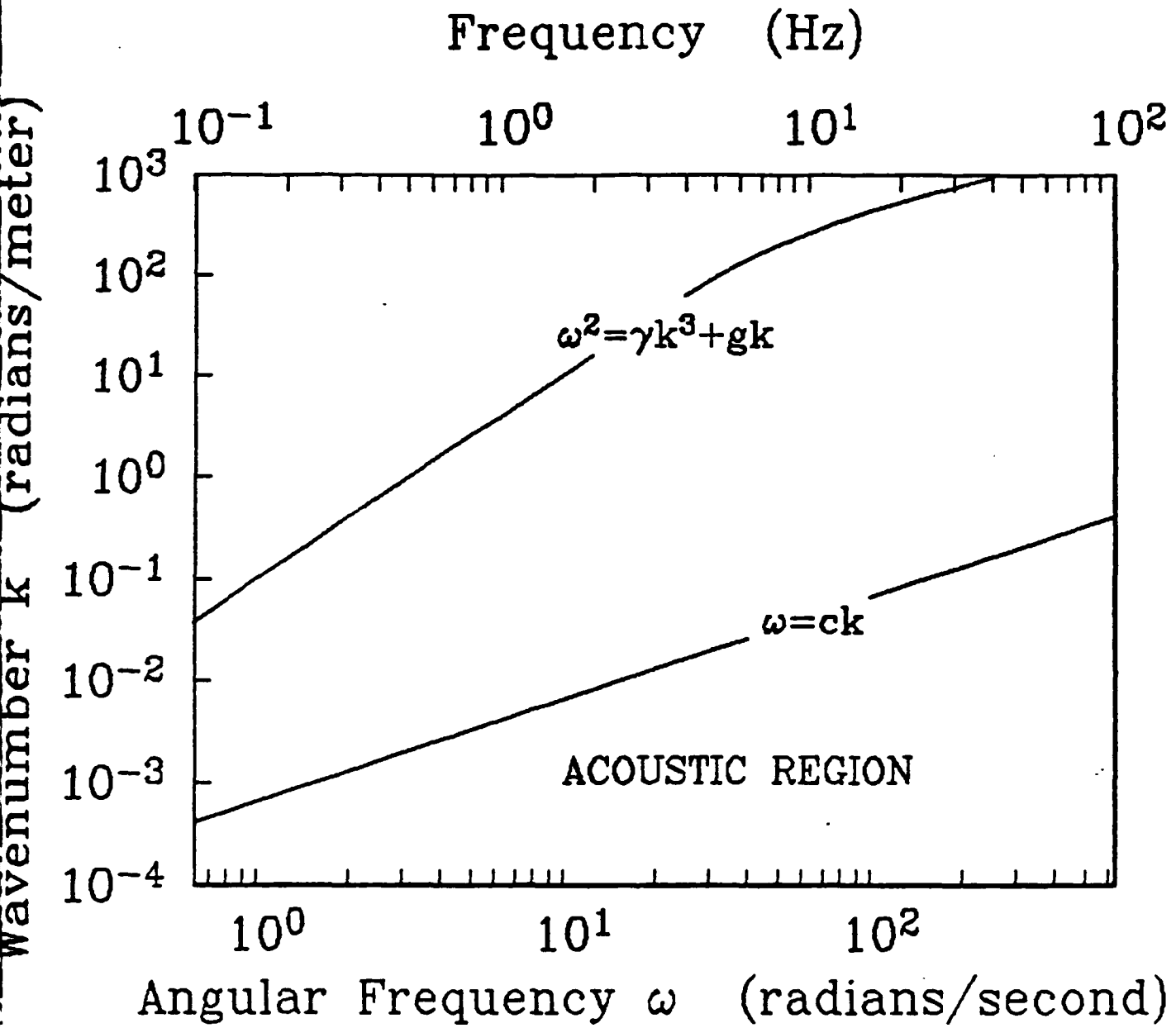
14. H.-Y. Wu, E.-Y. Hsu, and R. L. Street, "Experimental study of nonlinear wave-wave interaction and white-cap dissipation of wind-generated waves," *Dynamics Atmos. Oceans 3*, 55-78, 1979.

15. Y. Toba, "Local balance in the air-sea boundary process, III. On the spectrum of wind waves" *J. Oceanogr. Soc. Japan 29*, 209-220, 1973.

16. B. Mitsuyasu, "Measurement of the high-frequency spectrum of wind-generated waves," *J. Phys. Ocean. 7*, 881-891, 1977.

FIGURE CAPTIONS

Figure 1. Dispersion diagrams for gravity-capillary waves (upper curve) and acoustic waves (lower curve) in the angular frequency (ω) - wavenumber (k) plane. The region of this plane such that $\omega \geqslant ck$ delineates $\omega - k$ values which support free acoustic waves in the ocean.


Frequency (Hz)
10^{-1}
10^{0}
10^{1}
10^{2}
10^{3}
10^{2}
10^{1}
10^{0}
10^{-1}
10^{-2}
10^{-3}
10^{-4}
Wavenumber k (radians/meter)
$\omega^2=\gamma k^3+gk$
$\omega=ck$
ACOUSTIC REGION
10^{0}
10^{1}
10^{2}
Angular Frequency ω (radians/second)

CHAPTER 14

LOW-FREQUENCY NOISE OBSERVATION IN THE DEEP OCEAN

Richard G. Adair* and John A. Orcutt

Institute of Geophysics and Planetary Physics,
Scripps Institution of Oceanography
La Jolla, California 92093

* Now at: Rockwell Hanford Operations, Energy Systems Group, Richland, Washington 99352

Low-frequency noise observations in the deep ocean.

Richard G. Adair and John A. Orcutt

Institute of Geophysics and Planetary Physics, Scripps Institution of Oceanography, La Jolla, California 92093

Thomas H. Jordan

Department of Earth, Atmospheric, and Planetary Sciences, Massachusetts Institute of Technology, Cambridge, Massachusetts 02139

Received

Simultaneous measurements of ocean-bottom infrasonic, and ocean-bottom and sub-bottom seismic noise in the frequency band 0.1 - 20 Hz are presented. The data were obtained in 5.5 km-deep water in the South Central Pacific with a triaxial borehole seismograph and six triaxial ocean-bottom seismographs having externally-mounted hydrophones. The borehole sensors were emplaced 54 meters within basement rock overlain by 70 meters of pelagic clay. In the band 0.1 - 1 Hz, noise propagation as seismic modes trapped in the seafloor is supported by observed spectral coherences, cross-phases, and ratios between ocean-bottom pressure and vertical ground motion, and by the relatively lower noise levels in the borehole. Noise variations in this band are clearly correlated with changes in local wind direction and speed, presumably through ocean-bottom pressure fluctuations caused by nonlinear wind wave-wind wave and wind wave-swell interaction.

INTRODUCTION

In principal, seismic seafloor and acoustic ocean motion are related through kinematic boundary conditions at the benthic interface. One may therefore reasonably conclude that ocean-bottom seismic and infrasonic noise are related in source and character. This relationship is confirmed by observations of these two types of ambient noise. Measurements of seismic noise at the ocean bottom reveal the presence of the ubiquitous microseism peak (actually an agglomeration of peaks) over the microseism band (periods between 1 - 10 seconds) (Bradner et al.[1] and Latham and Sutton[2]). Ocean-bottom pressure measurements of high resolution over the microseism band, of which very few are published (Latham et al.[3], Nichols[4], and Cox et al.[5]) also display the microseism peak. Observed amplitude and phase relationships between the ocean-bottom pressure and vertical-component seismic noise are consistent with those of normal modes trapped near the ocean-seafloor interface (Latham and Nowroozi[6]).

Over the microseism band an intimate relationship between microseismic noise and non-linear surface gravity wave interactions has been both hypothesized (Longuet-Higgins[7] and Hasselmann[8]) and observed (Haubrich et al.[9], Latham and Sutton[2], Kibblewhite and Ewan[10] and Cox et al.[5]). This non-linear interaction occurs between opposed gravity waves of the same period and produces significant ocean-bottom pressures fluctutions of half the gravity wave period. The microseism peaks are the manifestation of this phenomonenon.

Although regional swell is most frequently identified as the primary source of microseisms in the deep ocean, recent observations have emphasized the role played by local wind-generated waves (Kibblewhite and Ewan[10]). Hasselmann[8] predicts a spectral form for ocean-bottom pressure fluctutations $\propto f^{3} S^{2}(f/2)$ at frequency f, where S(f) is the gravity wave spectrum. The asymptotic form of so-called equilibrium wind-generated waves is $S(f) \propto f^{-5}$ (Pierson and Moskowitz [11], Hasselmann et al.[12]) or, in some circumstances, f^{-4} (Kahma [13]). Thus, a fall-off for well-developed wind waves $\propto f^{-5}$–f^{-7} would be expected and, in fact, is observed (Cox et al.[5], Latham et al.[3], Figure 6, and Nichols[4]).

This paper presents ocean-bottom and sub-bottom observations from a recent ambient noise experiment in the South Central Pacific in which the dominant mechanism of ambient noise generation was clearly wind-related. The growth of spectral peaks

and generally increased levels over the microseism band in both seismic and acoustic measurements followed sharp changes in wind direction. Activity in the microseism band abated as the wind persisted or died away. Amplitude and phase relationships between pressure and vertical seismic motion at the microseism periods imply that a portion of the noise propagated as trapped modes of the ocean-seafloor elastic system. Spectral peaks at periods corresponding to acoustic reverberations in the water-sediment column suggests that some of the ambient noise may be due to (leaking) organ-pipe modes or, more likely, trapped modes of the seafloor.

These observations constitute the first comparison of simultaneous ocean-bottom and sub-bottom seismic noise and ocean-bottom acoustic noise over the microseism band in the deep ocean.

I. EXPERIMENT DESCRIPTION

The Defense Advanced Research Projects Agency developed a marine borehole seismograph, the Marine Seismic System (MSS), for seismic discrimination applications. The successful test of an MSS prototype tethered to the D/V Glomar *Challenger* on Deep Sea Drilling Project (DSDP) Leg 78B (Ballard et al.[14]) led to deployment of the fully-operational MSS on DSDP Leg 91, which composed the first portion of the Ngendei Experiment.

A primary objective of the Ngendei Experiment was the appraisal of the relative seismic signal and noise characteristics at a marine borehole site and proximate ocean-bottom site. This behavior was at issue because the first generation of ocean-bottom seismograph (OBS) efforts during the 1960's revealed that ambient seismic noise levels in the microseism band were typically 10-20 dB higher at ocean-bottom sites than at nearby land sites. In the microseism band, seismic noise at land sites is dominated by fundamental mode surface waves, the amplitude of which diminishes with depth into more rigid basement rock (Sorrells[15]). Since marine seismic noise is similarly composed, it was thought that the same advantage might obtain at a marine borehole site over an ocean-bottom site.

The MSS sensors were deployed in DSDP Hole 595B, located midway between New Zealand and Tahiti at 28°49.34′ S, 165°31.61′ W. Further details of the Ngendei Experiment may be found in Volume 88/91 of the Initial Reports of the DSDP.

II. INSTRUMENTATION AND OPERATIONS

Ocean Bottom Seismographs

The six OBS's are modifications of the four-component, digital event-recorders described by Moore et al.[16] (Orcutt et al.[17]). Output from three components of ground motion (one vertical and two horizontal) and a hydrophone are amplified, bandpassed, and digitized with a 12-bit word at 128 samples/second (sample/s). The gain of each channel is 2^N, where N=0,1,...,9. A channel's gain exponent N is modified only when the long-term average of its digital output, corrected for DC offset, falls outside pre-defined bounds of a few least significant bits.

Semiconductor memory, nominally 13-seconds long per channel, continuously accumulates the four channel data in a cyclically overwritten buffer to avoid the mechanical shaking and electrical transients of recorder operation. Software writes events to tape at scheduled times or when the short term average of vertical component amplitudes exceeds a long term average threshold. Additional RAM boards extended the 13-second buffers of several OBS's to 59 seconds.

The OBS's employed two seismometer responses *(see Figure 1a)*, selectable only prior to deployment. The 'teleseismic' response emphasizes lower frequencies more than the 'refraction' response in order to increase the sensitivity of the OBS event-triggering algorithm to moderate-amplitude, high-frequency depleted earthquake signals. The 'refraction' and 'teleseismic' capsules employed the same hydrophone response (*Figure 1a*).

The seismometers are the 1-Hz free period Mark Products L-4-3D triaxial set, and the hydrophone is an Ocean and Atmospheric Sciences, Inc., model E-2PD deep-water sensor. A bouyant aluminum sphere mounted on a detachable, dish-footed tripod houses the OBS instrumentation. Explosive bolts, detonated either by an acoustic or programmed command, free the instrumentation sphere, which then floats to the surface for recovery.

Marine Seismic System

The MSS is discussed in more detail in Adair et al.[18] The MSS comprises a borehole instrumentation package connected by coaxial cable to either an ocean-bottom recording unit or to two shipboard recording systems employed for diagnostic checkout

and recording redundancy. One of the shipboard recording systems, referred to as the Teledyne system, specifically monitors the borehole package, while the other, the Gould system, emulates the ocean-bottom recording unit. A special tool at the end of the drill string carries the sensor package to the seafloor, although simple lowering of the mechanically-strong coaxial cable, 'wireline' deployment, provides an alternate means to achieve this end. To date, only drill string deployments have been employed, although successful recovery of the borehole package has been achieved by wireline.

The MSS sensors are four Teledyne model S-750 seismometers configured as a triaxial set (two orthogonal horizontals and one vertical) and a redundant backup vertical component. The backup sensor is located 175.5 cm below the primary vertical sensor. Output from the three primary sensors are filtered in mid-period (0.5-10 seconds) and short-period (0.05-2 seconds) bands while output from the backup sensor is passed through the short-period band only. The resultant seven data streams are then digitized and transmitted to the recording devices via coaxial cable. For convenience, the sensors and data channels are labeled in subsequent discussion. The horizontal sensors are X and Y, and the primary and backup verticals are Z and B, respectively. The prefixes 'S' and 'M' will refer to the passband of a particular channel.

Data recorded on the Teledyne system are continuously gain-ranged to yield a 21-bit dynamic range with 14-bit resolution. No low-pass (anti-alias) filter is employed other than the roll-off of the instrument response. The mid-period and short-period bands are digitized at 4 and 40 sample/s, respectively, although either of the two short-period vertical channels may be digitized at 80 sample/s to the exclusion of the other.

Output recorded by the ocean-bottom recorder and its shipboard counterpart are oversampled 256-fold, transmitted to the recorder, digitally-convolved with a low-pass filter, resampled at the proper rates of 4 sample/s and 40 sample/s for the mid-period and short-period bands, respectively, and buffered to tape as 24-bit integers with 24-bit resolution. The data are oversampled to insure that the roll-off of the instrument response prevents aliasing prior to application of the digital filter. The transfer function of the digital low-pass filter is nearly flat to 75% of the ultimate Nyquist frequency, and thereafter falls at approximately 750 dB/decade. The low-pass filter coefficients are computed in an identical manner for both passbands. The dashed lines in *Figure 1b* illustrate the augmentation due to the low-pass filter

Operations

The first 20 days of the 60-day long Ngendei Experiment comprised a seismic refraction experiment, during which the OBS's recorded refraction signals and teleseismic signals with two distinct arrays, and the MSS operated with its two shipboard systems. The remaining 40 days were devoted to a teleseismic experiment during which the OBS's formed a single array for earthquake and noise recording, and the MSS employed its ocean-bottom recording system.

The D/V Glomar *Challenger* conducted MSS installation and shipboard recording operations. The Scripps Institution of Oceanography R/V *Melville* tended the six OBS's and recovered all instrumentation. *Figures 2* and *3* show instrumentation locations throughout the experiment. In these figures, octogons centered on ellipses depict estimated OBS locations and their 95% confidence bounds based on least-squares modeling of satellite and acoustic ranging data (Creager and Dorman[19]). Diamonds and arrows denote OBS drop points computed from satellite navagation and *Melville* radar ranging of *Challenger*. The borehole location is computed relative to the best satellite fix of *Challenger's* location.

During the refraction experiment, four OBS's were placed 0.6-0.7 km from the MSS site *(Figure 2a)*, and two at approximately 30 km *(Figure 2b)*. The former quartet of capsules employed the 'refraction' seismic response, 13-second event memory, and scheduled event recording, while the latter pair employed the 'teleseismic' response, 59-second event memory, and triggered event recording with scheduled noise samples at three-hour intervals.

The borehole package was emplaced at the bottom of DSDP Hole 595B, approximately 54 meters within a basaltic basement overlain by a 70-meter thick layer of zeolitic pelagic clays bearing hard stringers of porcellanite and chert near its base. The respective compressional and shear wave speeds of the sediment layer are 1.6 (Kim et al.[20]) and 0.116 km/s (Sereno and Orcutt[21]). The underlying basement structure is adequately modeled as normal oceanic crust (Whitmarsh et al.[22]).

The borehole package was not clamped in place in Hole 595B. The package's holelock/cable isolation mechanism was found to damage the coaxial cable and was therefore not employed. Comparison of MSS and OBS waveforms indicate that MSS sensor coupling with the ground was adequate. A coil of the coaxial cable payed out on

the seafloor aided in cable-motion isolation.

During the teleseismic experiment, the six OBS's were redeployed in a triangular array with single capsules forming two 25-km legs at approximate right-angles to the south and east of the MSS site *(Figure 3a)*. The other four capsules were clustered within 3 km to the west and north of the MSS in a trapeziform array *(Figure 3b)*. All OBS's employed the 'teleseismic' response, and triggered event recording, two with 13-second memory buffers and four with 59-second buffers. Daily noise events were recorded at Universal Time midnight. The MSS ocean-bottom recording system failed two days after entering the water due to a water leak.

Successful recovery of all OBS's and the MSS recording system took place from *Melville* over the period 22-26 March, 1983. Following a two-day shipboard recording period, the MSS recovery mooring was redeployed with a dummy load replacing the recording system. Both the borehole package and recovery mooring are still in place for future use.

III. NOISE DATA

Totals of 119, 43, and 83 hours of seismic data were obtained from the Teledyne system, the Gould ocean-bottom recording system, and its shipboard counterpart, respectively. During the refraction experiment, 114 and 70 hours of shipboard data were recorded on the Teledyne and Gould systems, respectively. OBS's recorded a total of 1400 noise events at 740 distinct times, 140 concurrently with MSS data.

Various MSS data channels were unavailable at certain times. The horizontal sensor Y malfunctioned throughout the entire Ngendei experiment for unknown reasons and provided no usable data. A shipboard source of electrical interference contaminated the subsequently-disconnected Gould channel SZ. A Gould electronics failure in its borehole package bay disabled Gould channel MZ at the start of the teleseismic experiment. Finally, as mentioned above, one of the Teledyne short-period Z channels was not available whenever the other recorded at 80 sample/s.

IV. DATA QUALITY

Data quality was assessed with both time- and frequency-domain criteria, the latter applied to power, cross, and coherence spectra.

Reliable spectral estimates were computed in the manner described by Welch[23] and Carter et al.[24]. Non-overlapping, de-meaned segments of digital data were tapered with a normalized Hanning window and Fourier transformed. The resulting spectra were averaged to achieve a reduction of estimate variance. Power spectra, defined only for non-negative frequencies, are normalized so that the total power in the Nyquist-frequency bandwidth equals the time-domain variance, a normalization which essentially folds the power of negative frequencies into the positive.

Estimates of statistical reliability were calculated under the assumption that the data derived from a stationary, Gaussian stochastic process. Power spectral estimates are then distributed as χ^2 random variables with 2N degrees of freedom, where N is the number of spectra averaged to obtain the estimate (see, e.g. Bendat and Piersol[25]).

Cross-spectra between different time series are calculated in order to estimate their coherence and cross-phase. The coherence shall be used as a measure of the degree to which the time series are linearly related. The coherence spectrum, actually the magnitude-squared coherence spectrum, is defined as the ratio between the squared cross-spectrum magnitude and the power spectra of the constituative time series. A useful application of the coherence is to define some threshold coherence value below which the estimate is no different from zero. In other words, we wish to determine the conditional cumulative probability $P(\hat{C} < T \mid C)$ that our coherence estimate $\hat{C}$ is less than the threshold value T given the actual coherence C. The complicated statistics of the magnitude-squared coherence are essentially those of the linear-regression correlation coefficient (Carter et al.[24]; Fischer[26]), and the expression for P involves a sum of hypergeometric functions. If the actual coherence C is zero, this expression is quite simple. Then, P is given by (Carter et al[24])

$$P(\hat{C} < R \mid C = 0) = 1 - (1 - R)^{N-1}, \tag{1}$$

where P(–) is the probability that the estimate $\hat{C}$ does not exceed the value R given the the actual coherence C and N is the number of spectra averaged in the coherence estimate. Thus, the threshold coherence R is given at the 100P % confidence level by

$$R = 1 - (1 - P)^{\frac{1}{N-1}}. \tag{2}$$

In computing spectral estimates from OBS data, the number of spectra averaged, and stationarity must trade-off because OBS noise samples are available only at discrete times: N must be large enough to yield estimate stability and useful error bounds, but

not so large as to sample over a time interval such that the noise field has statistically evolved. N=10, a 30-90 minute interval, was found to be generally optimal. The 95% confidence interval is then -2.0 dB and +2.7 dB. This trade-off is not very important for MSS data since they were continuously recorded except during brief interuptions. However, where comparisons of simultaneous observations are desired, the statistics and frequency resolution of the MSS estimates were made similar to those of the OBS.

Linear regressions of Gould data against Teledyne data in conjunction with sensor calibrations revealed a 3 dB shortfall of Gould amplitudes. The calibrations also show that instrument response below 0.2 Hz is not good for any MSS channel.

Figure 4 compares power spectral density estimates of simultaneous vertical-component Teledyne and Gould data with instrument noise spectra which have not been corrected for instrument response. The peaks above 8 Hz in the SB spectra are ship-generated. Peaks in the SB Teledyne spectrum *(Figure 4c)* which are absent in the SB Gould spectrum *(Figure 4b)* are manifestations of aliasing in the Teledyne data due to inadequate high-frequency filtering. Gould and Teledyne spectra have comparable values near the Nyquist frequency, indicating probable malfunctioning of Gould's low-pass filter.

Also shown in *Figure 4* are estimates of system noise, provided by H. B. Durham of Sandia Laboratories. The system noise is not significant over the entire short-period passband for either Teledyne or Gould data. The flat spectrum of quantizing noise for the Teledyne data, associated with uniformly-distributed round-off errors of digital representation (see e.g. Bendat and Piersol[25] pp. 231-232), has a level near 10^{-2} counts^2/Hz, well below the Teledyne signal level. Estimates of Gould's digitizing noise spectrum, that of a delta modulator, are not available. The MZ spectrum *(Figure 4a)* is similarly untainted by system and sampling noise. The MZ instrument response rolls-off sufficiently at high frequencies to avoid aliasing.

Spectral coherences (*Figure 5*) further delineate frequencies usable for ambient noise estimates. Coherences exceeding 0.28, illustrated in *Figure 5*, with a dash line, are considered significant at the 95% level. Mid-period coherences *(Figure 5a)* typically exceed 0.95 below the low-pass filter knee at 1.5 Hz except at 1 Hz, where it drops sharply over a very narrow band of frequencies. The sharp drop is due to energy present in the Gould data but not the Teledyne, and may be related to the Gould digitizing scheme. Gould

and Teledyne SB coherences *(Figure 5b)* exceeds 0.8 between approximately 0.2 and 4.0 Hz. The coherence at higher frequencies declines amidst peaks due to ship-generated signals. The sharp drops at approximately 2 and 4 Hz are similar to that at 1 Hz in the mid-period coherence. The frequencies bounding the short-period band of high coherence varied a great deal during the MSS deployment, but generally were those shown in *Figure 5.* Coherence estimates between SB and SZ Teledyne data *(Figure 5c)* were similar. Differences at frequencies greater than 4 Hz are probably due to the combined effects of aliasing and actual signal differences over the 175.5-cm sensor separation. The high coherence between the Gould and Teledyne data at the Nyquist frequencies indicates a possible deficiancy in the Gould low-pass filtering scheme.

OBS's employing the refraction response can measure lower-amplitude ground motion at high frequencies than those employing the teleseismic response. The refraction response was specifically designed to 'whiten' the ambient signal in the presence of typical deep-sea microseismic noise (Moore et al.[17]), while the teleseismic response was designed to low-pass it. Filtered high-frequency amplitudes are consequently less than that represented by a least significant bit as recorded with the teleseismic response. *Figure 6* compares spectra measured with the different OBS responses (upper curves) and shows the corresponding spectra of least-count noise (lower curves). The spectra, corrected for instrument response, were not measured simultaneously. Although most of the data composing the teleseismic capsule's spectrum (solid upper curve) were recorded after ship departure, their spectral levels exceed ship noise levels measured with a refraction capsule (dashed lower curve) at most frequencies. In the teleseismic spectrum, sampling noise clearly dominates at frequencies greater than 15 Hz, and is probably significant in the range 7-18 Hz.

The lowest valid frequency of OBS microseismic measurements is taken to be 0.1 Hz. At lower frequencies, least-count and system noise dominate. The system noise was inferred from the lack of estimate stability over a wide range of numbers of spectra averaged to compute power density estimates.

Ship-generated noise must be estimated on a case-by-case basis because it depends on ship speed, activity and range. Generally, sharply distinct peaks superimposed on a broadband level characterize ship-generated noise. In the Ngendei data, most peak frequencies appear to be multiples of some fundamental, indicating that propellor cavita-

tion caused the peaks (e.g. Urick[27]). *Challenger* generated peaks at multiples of 10 Hz while maintaining station, and two others at approximately 6.5 and 7.5 Hz while under way. *Melville* generated peaks at multiples of 6 and 9 Hz. *Figure 7* shows the growth of a peak at 18 Hz due to *Melville's* proximity to the MSS.

Figure 8a illustrates ship-generated noise with a comparison of vertical-component power density spectra, corrected for gain but not instrument response, of OBS Phred data recorded before (solid curve) and after (dashed curve) both ships departed. The capsule, located 1.6 km west of the borehole, employed the teleseismic response. The measurement prior to ship departure was made as both *Challenger* and *Melville* hove to within 2 km of the OBS. In this instance, ship-generated noise clearly dominates the spectrum at all frequencies above approximately 4.5 Hz. After ship departure, least-count noise dominated above 7 Hz, although the lowest frequency at which it dominated varied by ± 1 Hz since the level depends on OBS gain.

Some ambiguity exists concerning ship noise in the MSS data. Because the ocean-bottom recorder failed two days after its deployment when *Challenger* was 13 km away drilling Hole 596 and *Melville* was en route to Tahiti, MSS noise measurements in the complete absence of ships are not available. However, *Challenger* was briefly silent c 0510Z, 13 Feb, while monitoring an ocean- bottom navigational transponder, thus providing a sample of low ship noise for the MSS. *Figure 8b* compares the MSS spectrum of this time period with that measured a short time later when *Challenger* began using its dynamic positioning system thrusters. Also shown in *Figure 8b* is an estimate of short-period system noise which has been scaled to fit the 'quiet' spectrum. The good fit suggests that above 7 Hz system noise dominates the spectrum.

The dominance of ship-generated noise is in many instances diagnosed by an abrupt change in spectral slope, such as is seen in *Figure 8* at approximately 4 Hz. On this basis, it is apparent from these and other spectra that ship noise may be important at frequencies as low as 2 or 3 Hz in both the OBS and MSS data.

In summary, reliable spectral estimates of ambient seismic noise are available from MSS mid-period data between 0.2 and 1.5 Hz; from MSS short-period data between 0.2 and 7 Hz; and from OBS data between 0.1 and 7 Hz. These bands are subject to the variability described above due to ship proximity, and OBS gain range and instrument response. At frequencies greater than 7 Hz, sampling noise dominates OBS teleseismic

data, so that lower bounds on ocean-bottom microseismic noise levels must be established using data recorded with the refraction response.

V. RESULTS AND DISCUSSION

Spectral Noise Characteristics

Figures 9 - 12 compare displacement power densities for all available components, in units of *nanometers*^{2}*/ Hz* ($nm^2/\ Hz$) for simultaneous MSS and OBS data. The data were obtained at 5- and 10-minute intervals over a 70-minute period. Spectra are averages of 10 individual spectra obtained from approximately 13-seconds of data. The OBS, Suzy, was 0.6 km north of the MSS site. Based on considerations mentioned above, ship noise is assumed to dominate these spectra above 4 Hz.

The spectra all display the ubiquitous microseism peak near 0.2 Hz, where the observed noise levels are comparable, approximately $10^8\ nm^2/\ Hz$. At higher frequencies, ambient ocean-bottom microseismic noise levels exceed the borehole levels by 5-30 dB (*Figures 9* and *10*). Common to the spectra, though not prominent in all of the OBS spectra, are peaks centered on 0.5 and 0.7 Hz. At other frequencies, horizontal noise levels generally greatly exceed vertical levels (*Figure 11*). In contrast, horizontal levels in the borehole approximately equal the vertical levels (*Figure 12*). Latham and Sutton[2] find similar depth variation for the computed displacements of low-order trapped modes in an oceanic crust model, suggesting that these observations are consistent with the noise comprising such modes.

The ocean-bottom pressure spectrum measured simultaneously with the above spectra also displays the microseism peak *(Figure 13)*. The fall-off towards higher frequencies decreases with frequency from the microseism peak.

The microseism peak and a 0.4 Hz-wide band centered at 1 Hz display high coherence and a cross-phase of approximately 180° *(Figure 14 (a) and (b))* between the pressure and vertical displacement. These observations are diagnostic of the type of seismic waves comprising the microseism peak. At the ocean-bottom, the pressure and vertical displacement of the trapped modes of the ocean-seafloor elastic system have a cross phase of 180° (Bradner [28]; Schneider et al.[29]). On the other hand, plane waves exhibit a cross-phase of 90° (Schneider et al.[29]).

The spectral ratio of pressure and velocity amplitude is another quantitiy diagnostic of composition. If, for example, the noise consisted of body waves traveling from afar, then the low compressional wave speed of the sediment would result in nearly vertical incidence of these plane waves at the ocean-bottom. For vertically-traveling plane waves, the pressure-particle velocity ratio is constant with frequency and equals the product of density ρ and acoustic speed α in the water (Schneider et al.[29]), $1.5x10^6$ in MKS units. For trapped modes, this ratio may vary with frequency and exceed $\rho\alpha$ (Latham et al.[3] and Latham and Nowroozi[6]). *Figure 14 (c)* plots the ratio between the pressure and vertical-component velocity power density spectra, normalized by $(\rho\alpha)^2$. Over the two bands of high coherence, this ratio is on the order of 10, rather than one, suggesting that in this instance they represent trapped seismic modes. Thus, in this case the practice of comparing seismic ground velocities V(f) to a 'plane-wave equivalent' pressure P(f) via the relation $P = \rho c V$ is quite incorrect.

Figures 15-16 shows the coherence and cross-phase between the vertical and hydrophone channels of OBSs Suzy and Lynn, seperated by 0.6 km, for the same time interval as above. Again, energy at the microseism peak is highly coherent. The cross-phase at these frequencies is not significantly different from zero, implying either simultaneous arrival of microseism energy at the two capsules or a wavelength much larger that the capsule seperation. Latham et al.[6] calculate the dispersion for trapped modes in an ocean-bottom structure similar to that of the Ngendei site. At these frequencies the fundamental mode has a phase velocity C_p of 1.0 - 1.5 km/s, corresponding to a wavelength $\lambda = C_p / f$ on the order of 5 km. The capsule separation, roughly $\lambda / 10$, is too large to account for the observed small cross-phases, which rules-out oblique arrival of the microseism energy from a distant source. It therefore appears that the microseism source location in this instance is either local or along a line that is approximately normal to a line defined by the OBSs.

Temporal Noise Variations and Noise Sources

It has been generally observed that the sea state affects microseismic and infrasonic noise levels. Ample evidence is found that the microseism peak is due to non-linear interaction of opposed ocean surface waves of a given frequency. The interaction generates acoustic waves ~~which~~ with fluctuations of twice the waves' frequency (Hasselmann[8]). This has been conclusively demonstrated for swell reflected from a shoreline (Haubrich et

al.[9]), and for wind-waves (Kibblewhite and Ewan[10]; Webb[30]). Decklog observations provide observations pertinent to local and distant noise source discrimination. *Figure 17* summarizes *Challenger* decklog observations of wind and swell between 24 January and 13 February, 1983 (Julian dates 24-44) at two-hour intervals except for 8-10 hours swell gaps corresponding to local nighttime, and for hourly observations during days 33-37. The prevalent swell arrived from the south and had 6-7 second periods. The highest-amplitude swell had periods between 8-10 seconds, predominantly 9 seconds, and arrived from the south between dates 29-31 and 34-35. Very little northerly swell was observed. The wind direction changed both suddenly and gradually, the latter being marked by smooth changes in wind speed.

Figure 18 shows the variation of OBS Phred vertical-component acceleration spectra with time at three-hour intervals except for gaps due to triggered event recording. The spectra, single realizations corrected for instrument response, are computed from 58 seconds of data. The noise clearly changes with time, particularly at the prominent peaks near 0.2 and 0.5 Hz, which have comparable levels. *Figure 18(b)* plots the time-variation of the power in a 0.2 Hz band centered on these peaks, along with wind (*Figure 19(a)*) and swell (*Figure 19(c)*) observations over the same period. Abrupt increases in the power of both peaks, e.g. days 28.0, 30.0 and 33.0, coincide in several instances with sudden changes in wind direction. The onset of high-amplitude 9-second swell coincides with the wind change and power increases at day 30.0, but opposing 9-second swell, probably masked by other swell, were not observed. The onset at day 33 of the high-speed wind episode from the SSE coincides with a large power transient of the 0.5 Hz peak and a gradual ramping of power of the 0.2 Hz peak. Noise observations of 13-seconds length collected at three-minute intervals from the 'refraction' OBS's near the MSS site during day 33 show the peak at 0.5 Hz building quickly over the course of an hour. Power for both peaks gradually diminished as the wind weakened and wound northward. OBS Phred pressure spectra varied similarly with time. The clearly correlated behavior of the ambient noise and the wind as a major source of microseisms.

The observed variations of the wind are clearly related to those of the noise in *Figure 19*. A sharp change in the wind vector immediately preceeds, to within the 2-hour resolution of the decklog, noise increases at frequencies greater than the microseism peak band. Hasselmann[8] shows that the direct conveyance of pressure from the atmosphere at these frequencies is unlikely, leaving only the non-linear interaction of wind-generated

gravity waves or of wind-waves with background swell as a likely source for the seismic variations. In the case of wind wave interaction only, Hasselmann[8] derives the following expression for the spectral density $S_p(f)$ of the ocean-bottom pressure fluctuations at frequency f:

$$S_p(2f) = 8\pi \frac{\rho^2 g^2}{c^2} \omega^3 S_W^2(f) \int_0^{2\pi} G(\theta) G(\theta+\pi)\, d\theta \ , \tag{3}$$

where $\omega = 2\pi f$, $S_W(f)$ is the wave height power density, ρ and c are the density and sound speed of water, g is gravitational acceleration at sea level, and $G(\theta)$ is the angular dependence of the wind wave spectrum. $S_p(f)$ may be thought of as a forcing function for seismic wave generation. Note that the non-linear interaction between exactly-opposed waves of frequency f (cf the angular integrand in *Equation (3)*) leads to the double-frequency dependence 2f of the ocean-bottom pressure fluctuations. Implicit in *Equation (3)* is a white wavenumber spectrum which contributes only at phase speeds exceeding the scund speed of water, that is for wavenumbers $\leqslant \omega / c$.

A large body of observations (Pierson and Moskowitz[11]; Hasselmann et al.[12]) support self-similar form for the wind wave spectrum $S_W(f)$ of.

$$S_W(f) \propto f^{-5} e^{-\frac{5}{4}(\frac{f_m}{f})^4}, \tag{4}$$

The function described in *Equation (4)* falls exponentially for $f \leqslant f_m$ and as f^{-5} for $f \gg f_m$, where f_m is the peak frequency. Empirically, f_m decreases and power density increases with time under the influence of a steady wind. Tyler et al.[31] find that $G(\theta)$ is adequately described by

$$\cos^q(\theta / 2), \tag{5}$$

where q is a function of frequency and $\theta = 0$ corresponds to the mean wind direction.

A more detailed view of this interplay may be obtained from the continuously-collected MSS data. *Figure 20* shows the temporal variation of mid-period vertical acceleration in the borehole using data from Teledyne channels MZ. Averages of 14 spectra computed from consecutive 128-second samples, nearly 30 minutes total data, form the individual spectra of *Figure 20*. The dominant feature of these spectra is the microseism peak near 0.2 Hz, which with time steadily migrated towards lower frequencies, and grew larger in amplitude and narrower in width. Note the 'saddle' in the peak's amplitudes near day 41 coinciding with with generally-increased levels at higher frequencies. In contrast to the ocean-bottom accelerations, levels at the 0.5 Hz peak (*Figure 18*

(b)) are an order of magnitude lower than those at 0.2 Hz. Other peaks are observed at 0.35, 0.65, and 0.80 Hz (*Figure 20, detail*).

Figure 21(b) compares the temporal variation of power for the microseism ('primary') and 0.5 Hz ancillary peaks of *Figure 20.* Power was estimated by integrating over 0.10 Hz-wide bands centered on 0.22 and 0.50 Hz. Power variations in these two bands are roughly parallel until c. day 40.7, after which they were complimentary, corresponding to the microseism peak's 'saddle'. The power of these peaks decreased in an unknown manner early in the MSS shipboard recording period, then began growing c. day 39.0. Power in the ancillary band diminished during day 39, but resurged c. day 40.0. Power in both bands changed little in the half-day preceding day 40.7, then decreased in the primary band and increased in the ancillary band. At c. day 41.0, power leveled-off in the microseism peak band and generally increased at higher frequencies, which peaked c. day 41.2. The *rate* of power growth in the two bands increased c. day 41.5, so that primary power increased and ancillary power fall-off slowed. By the end of the shipboard recording period, power in both bands attained levels comparable to those observed c. day 40.5.

Figures 21 (a) and *(c)* show weather observations during the MSS shipboard data collection period, which began just as the epoch of the strongest winds observed during the Ngendei Experiment was concluding. Southerly swell of 6-7 second period dominated most of the time although northwesterly swell briefly dominated c. day 41 *(Figure 21 (c)).* The wind, on the other hand, varied a great deal (*Figure 21 (a)).* A moderate northeasterly wind blew during most of days 37 and 38 at a nominal 10 knots. During day 39, the wind was confused, though still northeasterly. The wind blew northwesterly throughout day 40, and southwesterly for the rest of the shipboard recording period. The highest wind speeds during the MSS shipboard recording period, 18 knots, accompanied the shift in wind direction from northwest to southwest at day 41.0.

The available data permit only a gross description of the sea. However, the forgoing discussion of wind-wave evolution permits drawing reasonable inferences of the wind-wave behavior from *Challenger* decklog observations. The increases in noise power at frequencies greater than those of the microseism band which follow soon after sharp changes in the wind vector are probably due to the wind degrading the pre-existing wave field. The subsequent power increases at these frequencies evident in *Figure 21*, c. days

39.0, 40.0, and 41.0 are due to the newly-evolving wind wave field.

The behavior of the microseism peak band is not as easily explained by the available data. The growth of power throughout days 38 and 39, as well as the shift towards lower frequencies apparent in *Figure 20* suggests an evolving wind wave source. Similarly, the fall during day 40 and subsequent rise during day 41 suggests the demise of the old wave regime and domination of the new regime in response to winds which blew approximately 90°, then 180° with respect to the old wind.

If steady wind waves were soley responsible for the observed seismic noise variations, *Equation (4)* implies that a fall-off of the wind-wave spectrum would result in an ocean-bottom pressure spectrum $\propto f^{-7}$, rather than the observed f^{-5} (*Figure 13*). However, the ragged fall-off observed in all spectra suggests either that the seafloor responded resonantly to the wind-wave forcing, or that a steady sea-state was not achieved. Sharp peaks at approximately 0.35, 0.5, 0.65, and 0.8 Hz were observed in the borehole data. It will be recalled that the peaks at 0.5 and 0.65 Hz were prominent in one or more of the OBS spectra in *Figure 11*.

The presence of equispaced peaks in ocean-bottom microseisms has also been reported by Bradner and Dodds[32], who attributed them to so-called 'organ-pipe' modes due to the near-vertical reverberations of acoustic waves between the sea surface and the sediment-basement interface. Organ-pipe modes belong to a class of seismic waves known as 'leaking' modes, in which the seismic energy radiates away into the deepest structure. In constrast, a 'trapped' mode remains confined within the capping crustal structure. Abramovici[33] found qualitative agreement between conspicuous peaks in the microseism observations of Bradner and Dodds [32] and calculations of organ-pipe mode dispersion curves and transfer functions. Organ pipe modes are an important constituent of the seismic phase P_n observed in the ocean which, in this context, is composed of P waves traveling almost entirely in the upper mantle before turning sharply to the vertical in the sediment (Sereno and Orcutt[21]). The resulting spectral peaks occur at frequencies $f_n = (2n+1)\ df\ /\ 2$, $n = 0,1,2, \cdots$, where df, the separation between peak frequencies, is the reciprocal of the two-way travel time of a single reverberation. At the MSS site[21], $df = 0.135$, close to the observed 0.15 Hz peak spacing in the microseism data. However, these modes are damped in time t by the term $e^{\ln(R)(t\ /\ \tau)}$ (Rosenbaum[34]), where R is the reflection coefficient for normally-incident plane waves at the sediment-basement

interface, and $\tau = 1/\ df$ is the two-way travel time of a single reverberation. R is given by

$$R = \frac{\rho_2\alpha_2 - \rho_1\alpha_1}{\rho_2\alpha_2 + \rho_1\alpha_1} \quad , \tag{6}$$

where the subscripts 1 and 2 refer to the sediment and basement, respectively, and where ρ and α denote density and compressional wave speed, respectively. For the MSS site, $\rho_1 = 1$, $\rho_2 = 2.7$ g/cc, and $\alpha_1 = 1.6$, $\alpha_2 = 5.0$ km/s (Shearer, personal communication). We find, then, that successive reverberations are damped by a factor of $e^{-4.2} = 1.5 \times 10^{-2}$. If we assume constructive interference of successive reverberations, the net contribution is found from the geometric series in the damping to be only 1.015 times the initial amplitude. It appears unlikely, therefore, that organ-pipe modes contribute significantly to the *local* generation of microseisms.

On the other hand, some crustal structures exhibit regular peak spacing for trapped modes because, as Rosenbaum[33] and Haddon[34] show, they are essentially continuations of leaking modes. At some transitional phase speed, the trapped mode spacing is approximately that of the organ-pipe modes. Modeling the relative contributions to the ambient noise of these complementary wave types will be the topic of further research.

VI. CONCLUSIONS

The observations reported here constrain the source mechanisms and propagation modes of infrasonic and microseismic noise in the deep ocean. High coherences, 180° cross-phases, and ratios between displacement and pressure at frequencies below 1 Hz imply a trapped wave propagation mode. Modeling of these measurements, as well as the horizontal-component measurements, may further constrain the wave type, although a definitive experiment to measure the wavenumber spectrum may be required.

Episodic variations of the wind direction and speed correlate with changes in both acoustic and microseismic noise. In particular, a peak at 0.5 Hz responded immediately to sudden changes in wind direction, both in ocean-bottom and sub-bottom observations. The microseism peak is also affected by the wind, an observation that is in contrast to multitudes of previous reports focusing attention on swell as the chief agent of noise generation. The mechanism for transferring energy from wind to microseisms is presumably the non-linear interaction of wind-generated waves. Spectral shapes and the temporal evolution of the pressure and displacement spectra support this hypothesis.

ACKNOWLEDGEMENTS

The authors thank Chip Cox for helpful discussions. W. Menke provided useful comments. This research was supported by DARPA contracts F49620-79-C-0019 and AFOSR-84-0043.

REFERENCES

1. H. Bradner, J. G. Dodds and R. E. Foulks, "Investigation of microseism sources with ocean-bottom seismometers, J. Geophys. Res. 69, 4339-4348 (1964).
2. Gary V. Latham and George H. Sutton, "Seismic measurements on the ocean floor, 1. Bermuda area," J. Geophys. Res.71 2545-2572 (1966).
3. Gary V. Latham, Rockne S. Anderson and Maurice Ewing, "Pressure variations produced at the ocean bottom by hurricanes," J. Geophys. Res. 72, 5693-5704 (1967).
4. R. H. Nichols, "Infrasonic ambient ocean noise measurements: Eleuthera," J. Acoust. Soc. Am. 69, 974-981 (1981).
5. Charles Cox, Thomas Deaton and Spahr Webb, "A deep-sea differential pressure gauge," J. Atmosph. Oceanic Tech., 1, 237-246 (1984).
6. Gary V. Latham and Ali A. Nowroozi, "Waves, weather, and ocean bottom microseisms," J. Geophys. Res. 73:3945-3956 (1968).
7. M. S. Longuet-Higgins, "A theory of the origin of microseisms," Phil. Trans. Roy. Soc., A. 243, 1-35 (1950).
8. K. Hasselmann, "A statistical analysis of the generation of microseisms," Rev. Geophys. 1 177-210 (1963).
9. R. A. Haubrich, W. H. Munk and F. E. Snodgrass, "Comparative spectra of microseisms and swell," Bull. Seism. Soc. Am.53 27-37 (1963).
10. Alick C. Kibblewhite and Kevin C. Ewans, "Wave-wave interactions, microseisms, and infrasonic ambient noise in the ocean," J. Acoust. Soc. Am. 78, 981-985 (1985).
11. Willard J. Pierson, Jr., and Lionel Moskowitz, "A proposed spectral form for fully developed wind seas based on the similarity theory of S. A. Kitaigorodskii," J. Geophys. Res. 69, 5181-5190 (1964).
12. K. Hasselmann, T. P. Barnett, E. Bouws, H. Carlson, D. E. Cartwright, K. Enke, J. A. Weing, H. Gienapp, D. E. Hasselmann, P. Kruseman, A. Meerburg, P. Müller, D. J. Olbers, K. Richter, W. Sell and H. Walden, "Measurement of wind-wave growth and swell decay during the Joint North Sea Wave Project (JONSWAP)," Ergänzungsheft zur Deutschen Hydrographischen Zeitschrift Reine A(8 °) (12), 122 pp (1973).

13. Kimmo K. Kahma, "A study of the growth of the wave spectrum with fetch," Journ. Phys. Ocean. 11, 1503-1515 (1981).

14. J. A. Ballard, C. C. Mulcahy, R. C. Wallerstedt and E. L. Kiser, "The borehole seismic experiment in Hole 395A: Engineering and installation," in *Initial Reports of the Deep Sea Drilling Project*, edited by R. D. Hyndman, M. H. Salisbury, et al.(U. S. Government Printing Office, Washington, 1984), Vol. 78, pp. 743-758.

15. Gordon G. Sorrells, "A preliminary investigation into the relationship between long-period seismic noise and local fluctuations in the atmospheric pressure field," Geophys. J. R. Astr. Soc. 26, 71-82 (1971).

16. R. D. Moore, L. Dorman, C.-Y. Huang and D. L. Berliner, "An ocean bottom, microprocessor based seismometer," Mar. Geophys. Researches 4, 451-477 (1981).

17. J. A. Orcutt, R. D. Moore and T. H. Jordan, "Description and performance of the Scripps ocean bottom seismographs during the Ngendei Experiment," *In*: The Initial Reports of the Deep Sea Drilling Project, Volume 88/91 (in press).

18. R. G. Adair, M. M. Harris, J. A. Orcutt, and T. H. Jordan, "Description and performance of the Marine Seismic System during the Ngendei Experiment," *In*: The Initial Reports of the Deep Sea Drilling Project, Volume 88/91 (in press).

19. K. C. Creager and L. M. Dorman, "Locations of instruments on the seafloor by joint adjustment of instrument and ship positions," J. Geophys. Res. 87, 8379-8388 (1982).

20. I. I. Kim, D. K. Smith, J. A. Orcutt, T. H. Jordan, and H. W. Menard, "Seismic reflection site survey: Correlation with physical properties, Leg 91, Deep Sea Drilling Project," *In*: The Initial Reports of the Deep Sea Drilling Project, Volume 88/91 (in press).

21. T. J. Sereno and J. A. Orcutt, "The synthesis of realistic oceanic P_n wavetrains," J. Geophys. Res., 90, 12755-12776 (1985).

22. R. B. Whitmarsh, J. A. Orcutt, T. H. Jordan, P. M. Shearer, and R. G. Adair, "Velocity Bounds on the seismic structure of Late Jurassic (157 Ma old) crust and upper mantle in the Southwest Pacific Basin from downhole observations at Deep Sea Drilling Project Hole 595B," *In*: The Initial Reports of the Deep Sea Drilling Project, Volume 88/91 (in press).

23. P. D. Welch, "The use of fast Fourier transform for the estimation of power spectra: A method based on time averaging over short, modified periodograms," IEEE Trans. Audio Electro-acoust. **AU-15**, 70-73 (1967).

24. G. C. Carter, C. H. Knapp, and A. H. Nuttall, "Estimation of the magnitude-squared coherence function via overlapped fast Fourier transform processing," IEEE Trans. Audio Electroacoust. **AU-21**, 337-344 (1973).

25. J. S. Bendat and G. G. Piersol, *Random data: Analysis and measurement procedures*, (John Wiley, New York, 1971).

26. R. A. Fischer, "The general sampling distibution of the multiple correlation coefficient," Proc. Roy. Soc., Ser. A **121** 654-673 (1928).

27. R. J. Urick, *Principals of Underwater Sound* (McGraw-Hill, New York, 1983), 3rd edition.

28. H. Bradner, "Pressure variations accompanying a plane wave propagated along the ocean bottom," J. Geophys. Res. **68**, 3465-3471 (1962).

29. W. A. Schneider, P. J. Farrell, and R. E. Brannian, "Collection and analysis of Pacific ocean-bottom seismic data," Geophysics, **29**, 745-771 (1964).

30. Spahr Chapman Webb, *Observations of Seafloor Pressure and Electric Field Fluctuations*, Ph.D. thesis, University of California (1984).

31. G. L. Tyler, C. C. Teaugue, R. H. Stewart, A. M. Peterson, W. H. Munk and J. W. Joy, "Wave directional spectra from synthetic aperture observations of radio scatter," Deep-Sea Res. **21**, 989-1016 (1977).

32. H. Bradner and J. G. Dodds, "Comparative seismic noise on the ocean bottom and on land," J. Geophys. Res., **69**, 4339-4348 (1964).

33. F. Abramovici, "Diagnostics, diagrams, and transfer functions for oceanic waveguides," Bull. Seism. Soc. Am., **58**, 427-456 (1968).

34. J. H. Rosenbaum, "The long-time resonse of a layered medium to exlosive sound," J. Geophys. Res., **65**, 1577-1613 (1960).

35. R. A. W. Haddon, "Computation of synthetic seismograms in layered earth models using leaking modes," Bull. Seismol. Soc. Am., **74**, 1225-1248 (1984).

FIGURE CAPTIONS

Figure 1 Displacement responses of (a) ocean-bottom seismograph (OBS) and (b) Marine Seismic System (MSS) instrumentation used during the Ngendei experiment. (a) OBS seismometer and hydrophone responses. Two responses were available for the OBS's (ocean bottom seismographs). (b) The Gould MSS mid-period and short-period responses differ from the Teledyne responses by the low-pass digital filter shown with dashed lines.

Figure 2 Locations of the MSS and six OBS's during the refraction experiment. See text for explanation of symbols. (a) Configuration of the four capsules which recorded refraction signals (Juan, Karen, Lynn, and Suzy). (b) Configuration of the two OBS's which concurrently recorded teleseismic signals in a triggered mode (Janice and Phred).

Figure 3 (a) and (b): Locations of the OBS's during the teleseismic experiment. See text for explanation of symbols.

Figure 4 Spectral power density estimates of typical MSS noise samples compared to system noise levels. The spectra, given in counts^2/Hz, have not been corrected for instrument response. (a) Gould Channel MZ. (b) Gould channel SB. (c) Teledyne channel SB.

Figure 5 Coherence spectra, corrected for alignment, between (a) Teledyne and Gould channel MZ, (b) Teledyne and Gould channel SB, and (c) Teledyne channels SZ and SB.

Figure 6 Comparison of noise spectrum obtained with the teleseismic (solid upper curve) and refraction (dashed upper curve) OBS responses. The corresponding instrument-corrected sampling noise spectra (lower curves) are also shown.

Figure 7 Demonstration of *Melville's* ship noise during the period 034:0430-035:0000 (Julian date). (a) Smoothed, integrated OBS Suzy vertical component power density between 17.9 and 18.2 Hz. (b)*Melville's* range from the MSS site.

Figure 8 Illustration of ship noise in the (a) OBS and (b) MSS data. Solid spectra were observed when ships were nearby and operational, and the dashed spectra when ships were completely absent (OBS) or still nearby (MSS). MSS data are not available at any time when ships were completely absent.

Figure 9 Simultaneous vertical-component displacement power densities at the ocean bottom (dashed line) and in the borehole (solid line).

Figure 10 Simultaneous horizontal-component displacement power densities at the ocean bottom (dashed line) and in the borehole (solid line).

Figure 11 A comparison of simultaneous vertical (solid) and horizontal (dashed) power densities in the borehole.

Figure 12 A comparison of simultaneous vertical (solid) and horizontal (dashed) power densities at the ocean-bottom.

Figure 13 Ocean-bottom pressure measurements concurrent with the displacement spectra of Figures 9-12.

Figure 14 (a) Coherence and (b) cross-phase between OBS Suzy channels Z (vertical) and P (hydrophone). The cross-phase, plotted in multiples of π, has been corrected for instrument response phase. (c) The ratio between OBS Suzy pressure and vertical ground velocity power densities, normalized by the product of density and acoustic speed in the water.

Figure 15 (a) Coherence and (b) cross-phase between the vertical channels of OBS's Suzy and Lynn, as for Figure 14.

Figure 16 (a) Coherence and (b) cross-phase between the hydrophone channels of OBS's Suzy and Lynn, as for Figure 14.

Figure 17 *Challenger* decklog observations of (a) wind and (b) swell depicted as vectors with origin at the time of measurement, lengths proportional to wind speed (knots) or swell height (feet), and direction that of the measurement. The swell measurements are plotted at a level corresponding to swell period.

Figure 18 Variation with time of OBS Phred vertical-component acceleration power in the frequency band 0.1 - 1.0 Hz.

Figure 19 Temporal variation of (b) peaks at 0.2 and 0.5 Hz of the OBS Phred data shown in Figure 18 compared with (a) wind and (c) swell observations shown in Figure 17.

Figure 20 Temporal variation of vertical accleration in the borehole in the frequency bands 0.1 - 1.0 Hz and 0.4 - 0.9 Hz (detail).

Figure 21 Temporal variation of (b) peaks at 0.2 and 0.5 Hz of the MSS data shown in Figure 20 compared with (a) wind and (c) swell observations shown in Figure 17.

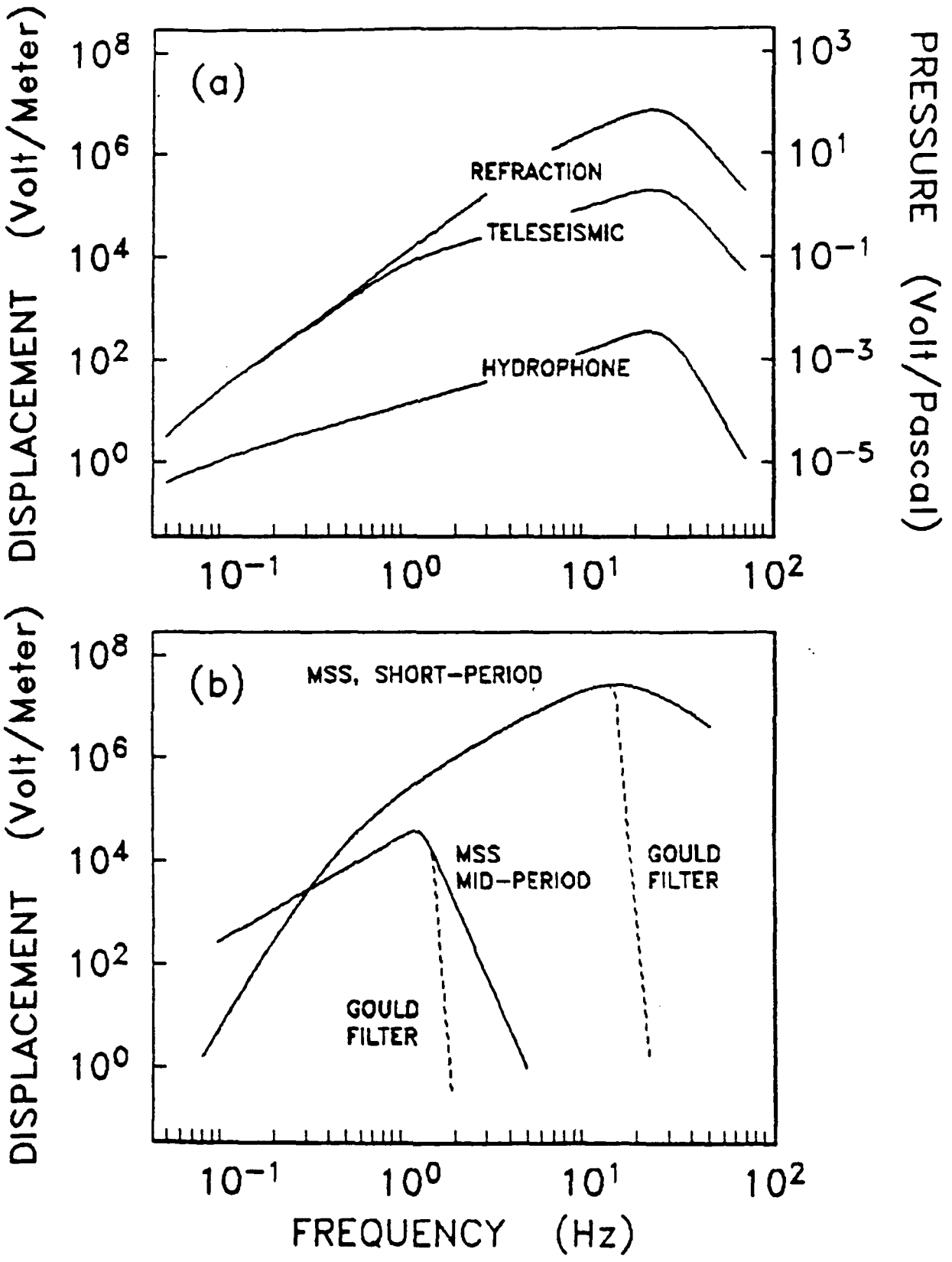

(a)
REFRACTION
TELESEISMIC
HYDROPHONE
DISPLACEMENT (Volt/Meter)
PRESSURE (Volt/Pascal)
10^8
10^6
10^4
10^2
10^0
10^3
10^1
10^{-1}
10^{-3}
10^{-5}
10^{-1}
10^0
10^1
10^2
(b)
MSS, SHORT-PERIOD
MSS
MID-PERIOD
GOULD
FILTER
GOULD
FILTER
DISPLACEMENT (Volt/Meter)
FREQUENCY (Hz)

FIGURE 1

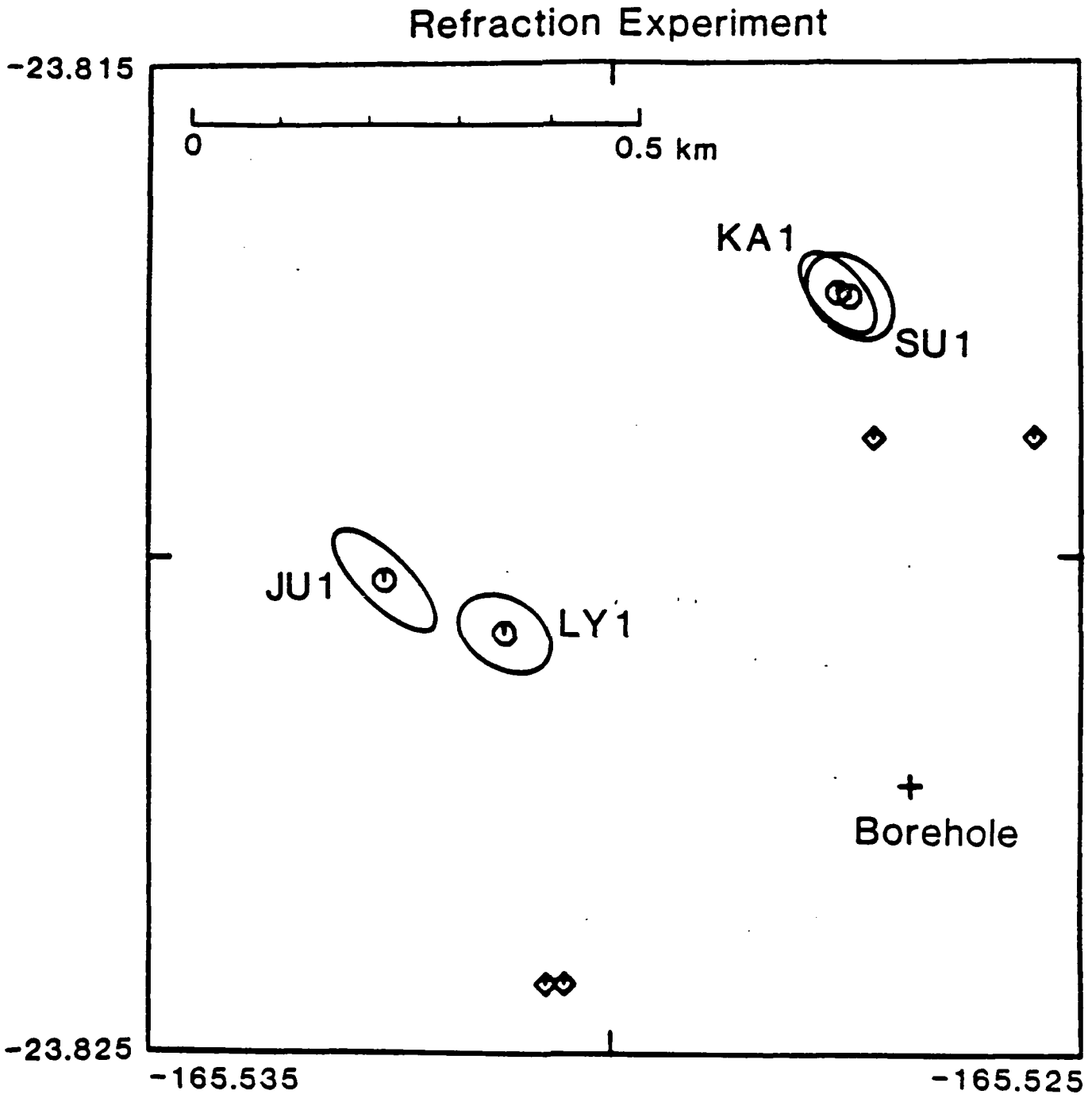

OBS Locations
Refraction Experiment
-23.815
0
0.5 km
KA1
SU1
JU1
LY1
Borehole
-23.825
-165.535
-165.525

FIGURE 2 (a)

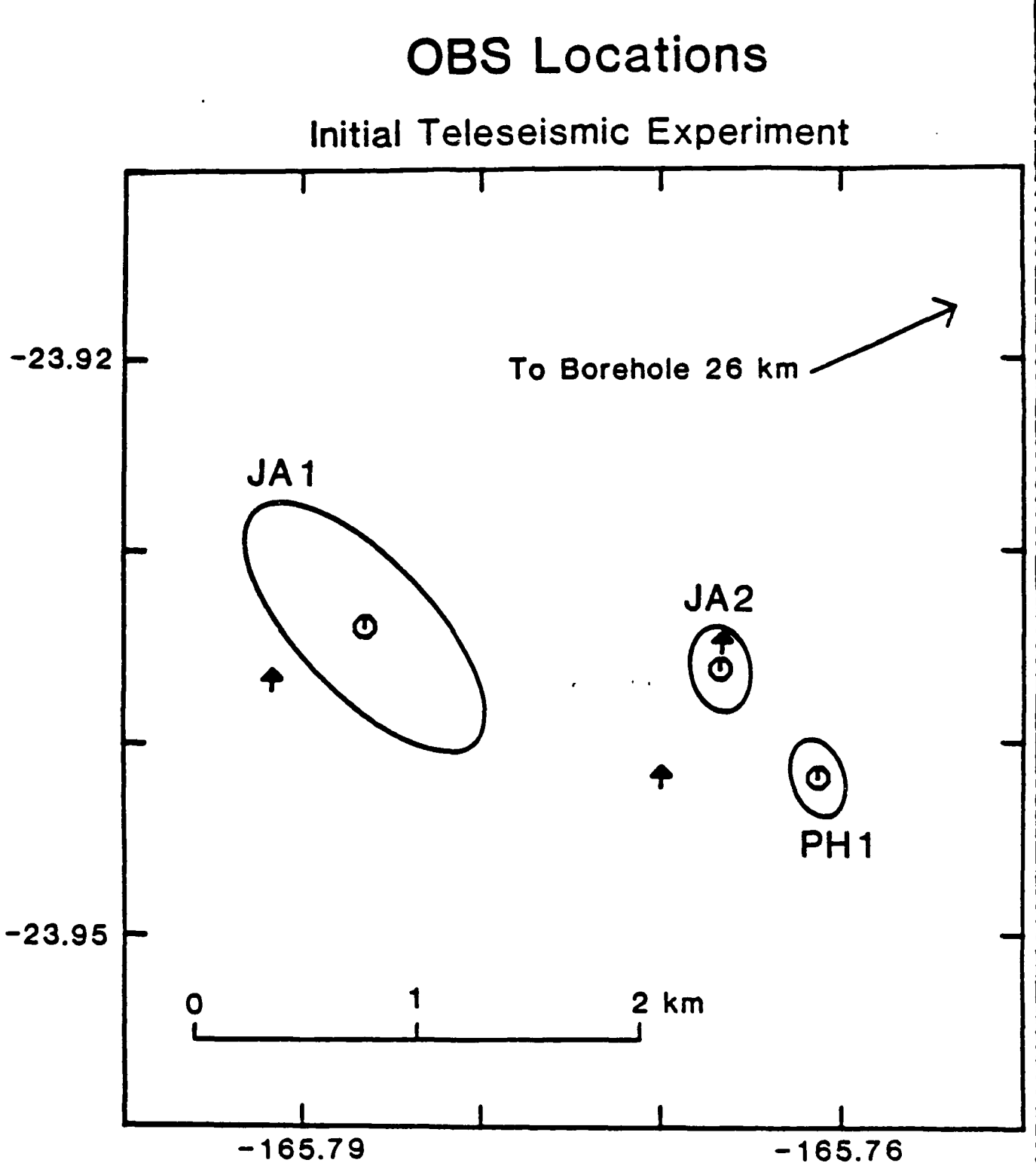

OBS Locations
Initial Teleseismic Experiment
-23.92
-23.95
To Borehole 26 km
JA1
JA2
PH1
0
1
2 km
-165.79
-165.76

FIGURE 2 (b)

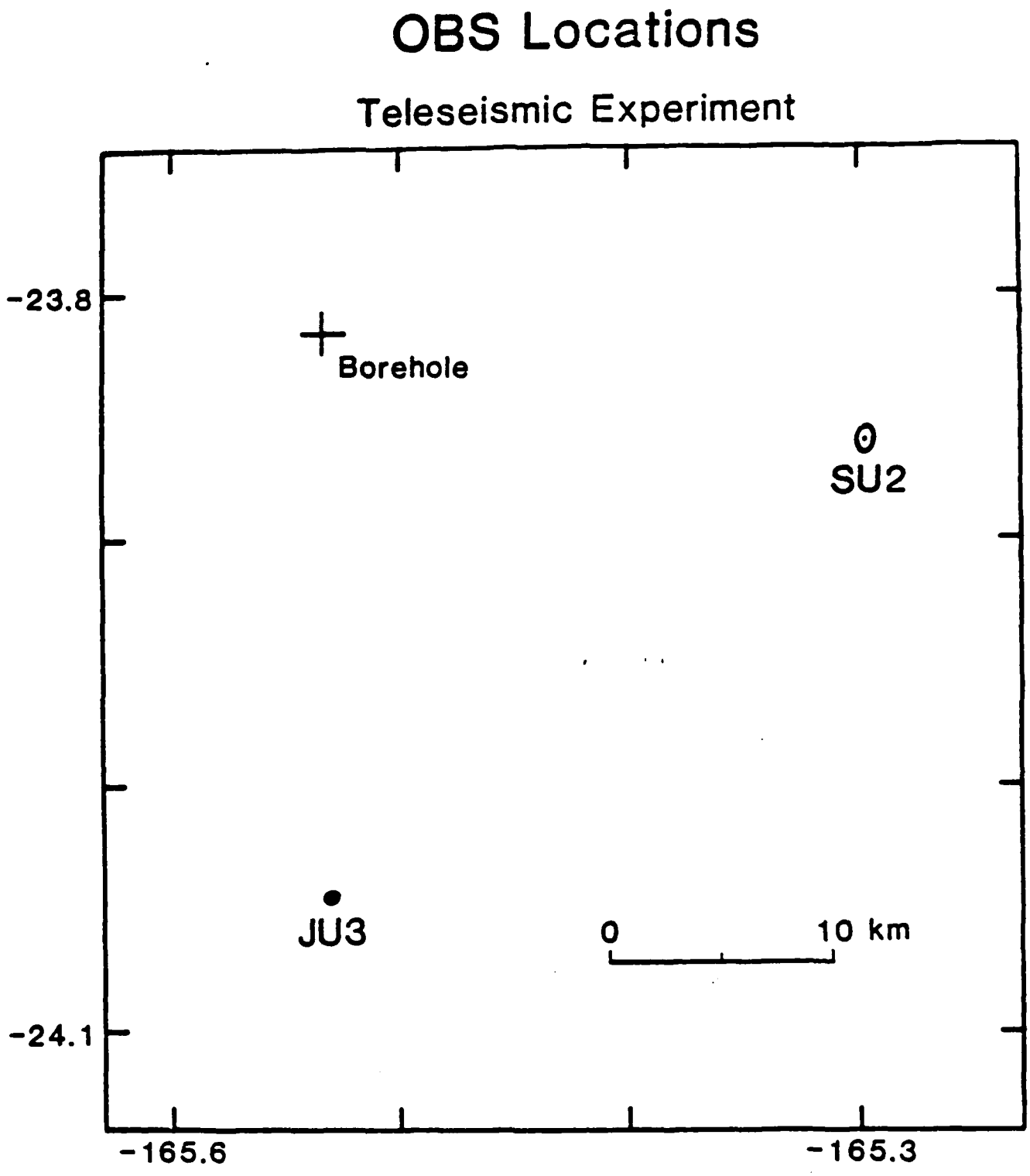

OBS Locations
Teleseismic Experiment
-23.8
Borehole
SU2
JU3
0
10 km
-24.1
-165.6
-165.3

FIGURE 3 (a)

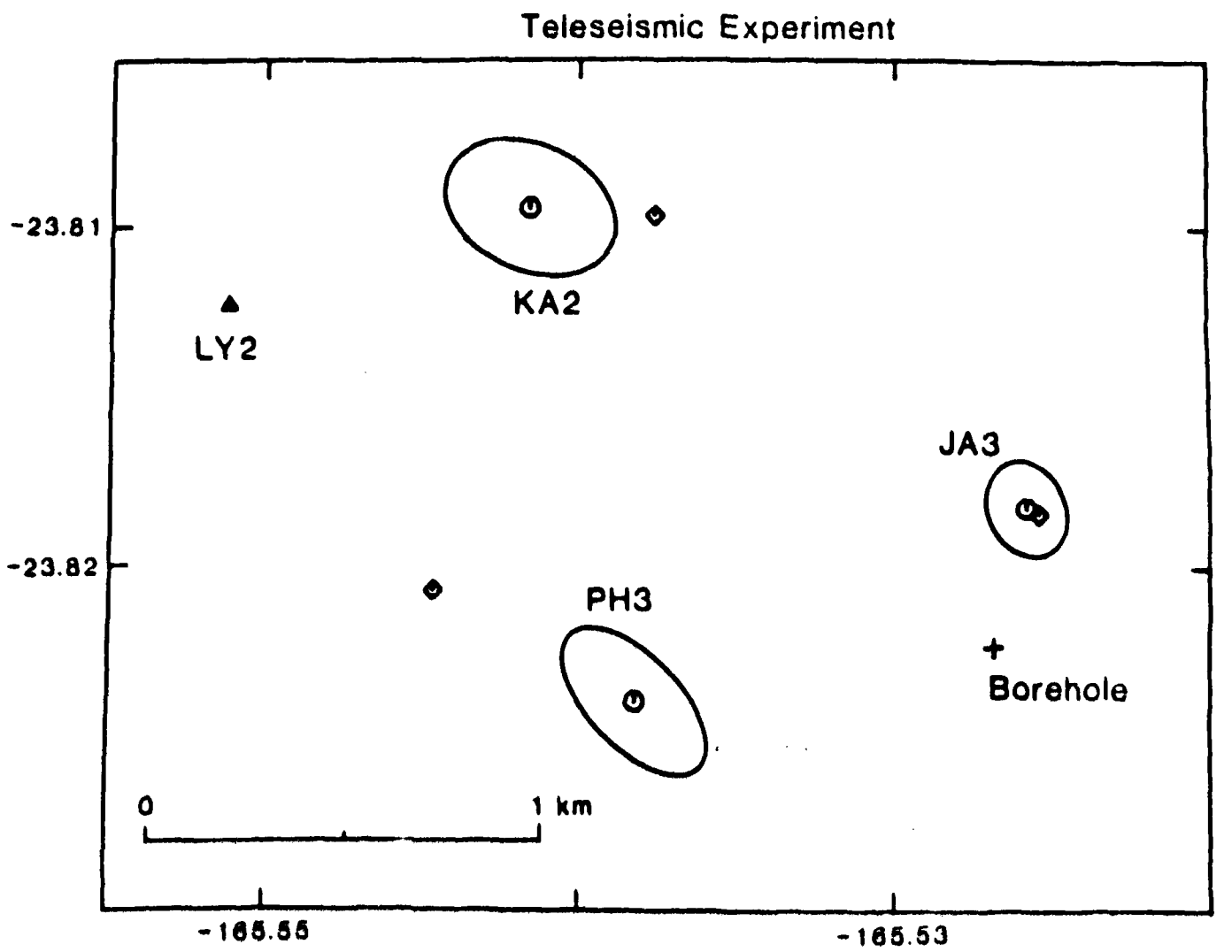

OBS Locations
Teleseismic Experiment
-23.81
-23.82
KA2
LY2
JA3
PH3
Borehole
0
1 km
-165.55
-165.53

FIGURE 3 (b)

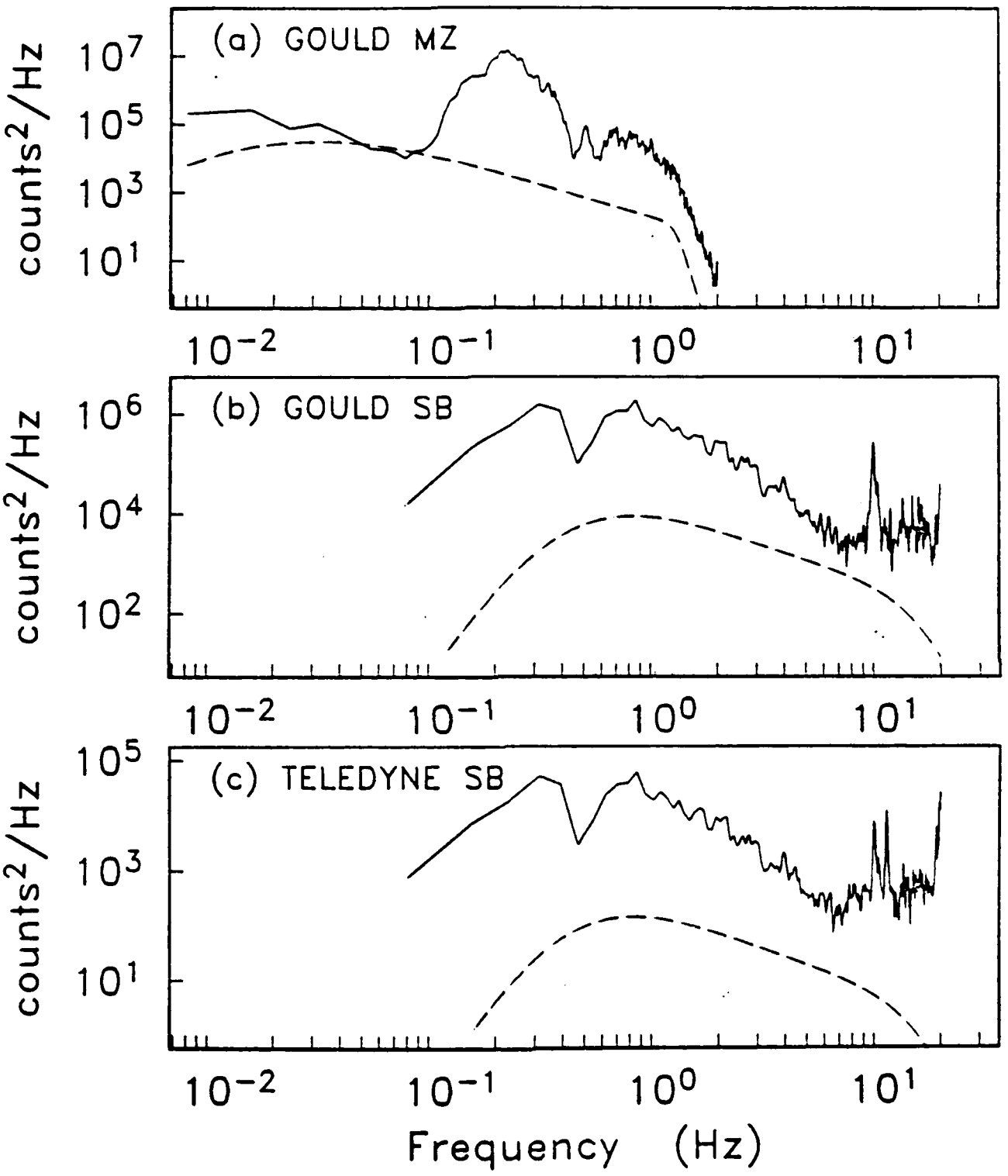

(a) GOULD MZ
(b) GOULD SB
(c) TELEDYNE SB
counts²/Hz
10⁷
10⁵
10³
10¹
10⁶
10⁴
10²
10⁵
10³
10¹
10⁻²
10⁻¹
10⁰
10¹
Frequency (Hz)

FIGURE 4

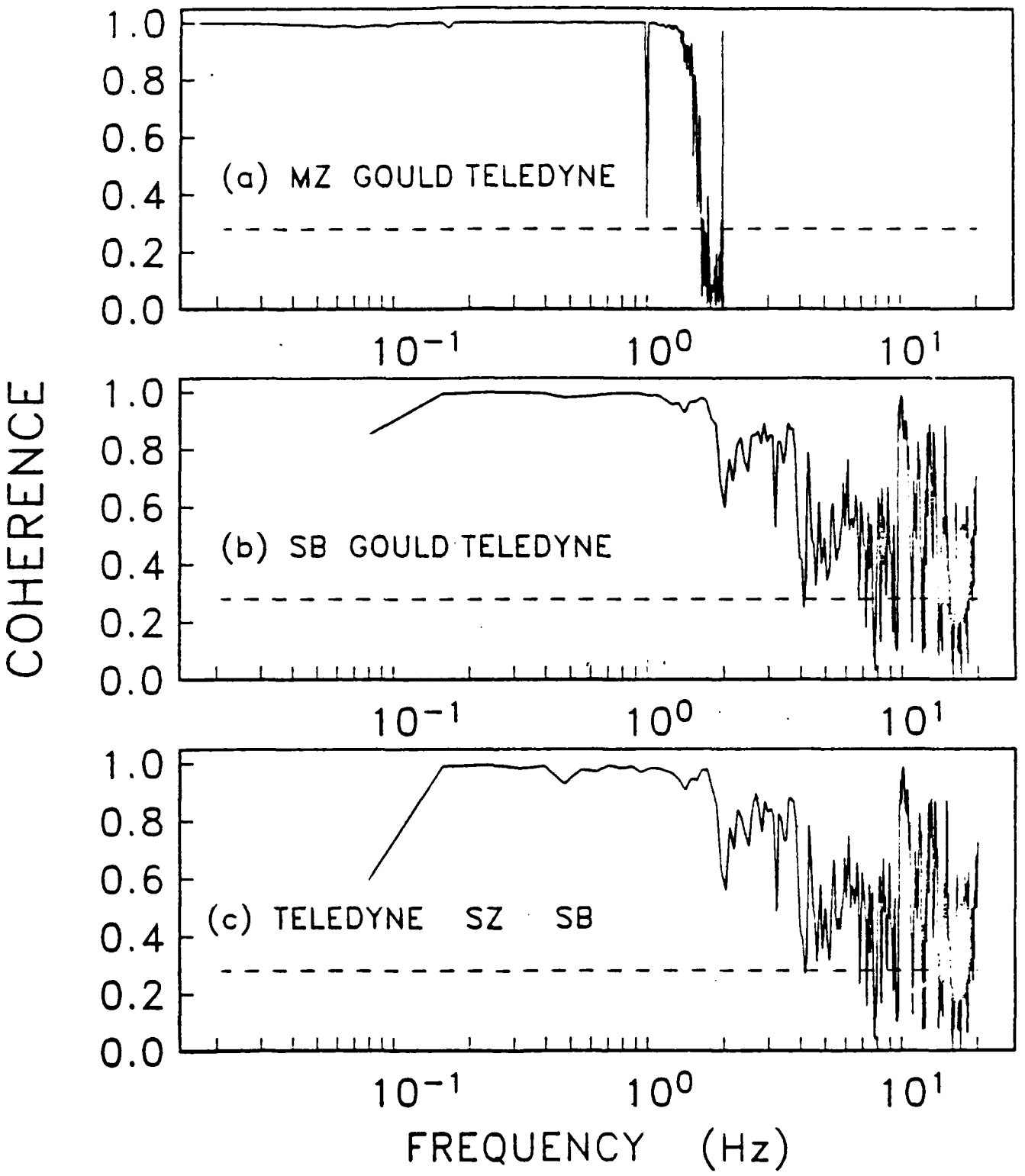

COHERENCE
1.0
0.8
0.6
0.4
0.2
0.0
(a) MZ GOULD TELEDYNE
(b) SB GOULD TELEDYNE
(c) TELEDYNE SZ SB
10^{-1}
10^{0}
10^{1}
FREQUENCY (Hz)

FIGURE 5

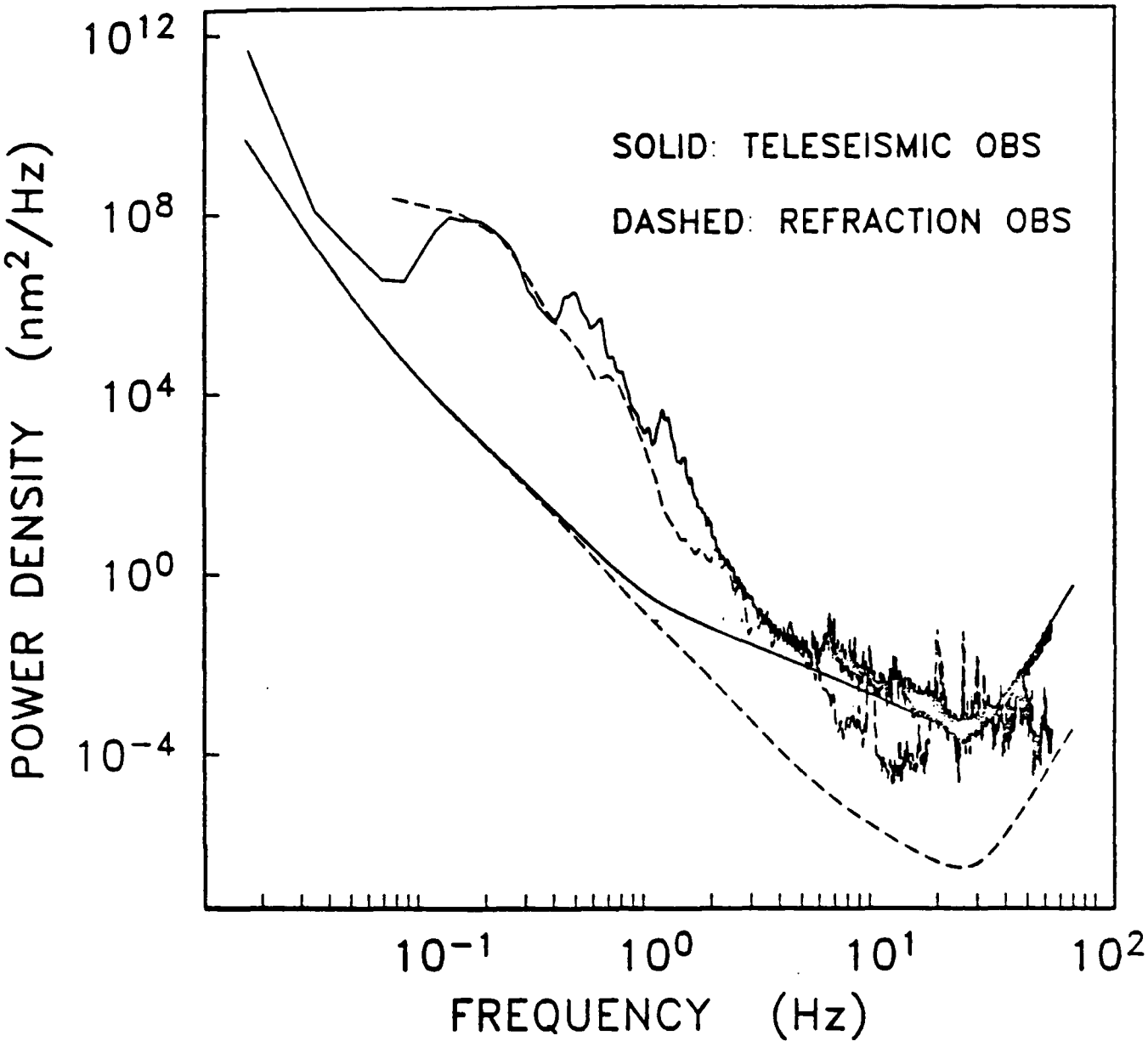

SOLID: TELESEISMIC OBS
DASHED: REFRACTION OBS
POWER DENSITY (nm²/Hz)
10¹²
10⁸
10⁴
10⁰
10⁻⁴
10⁻¹
10⁰
10¹
10²
FREQUENCY (Hz)

FIGURE 6

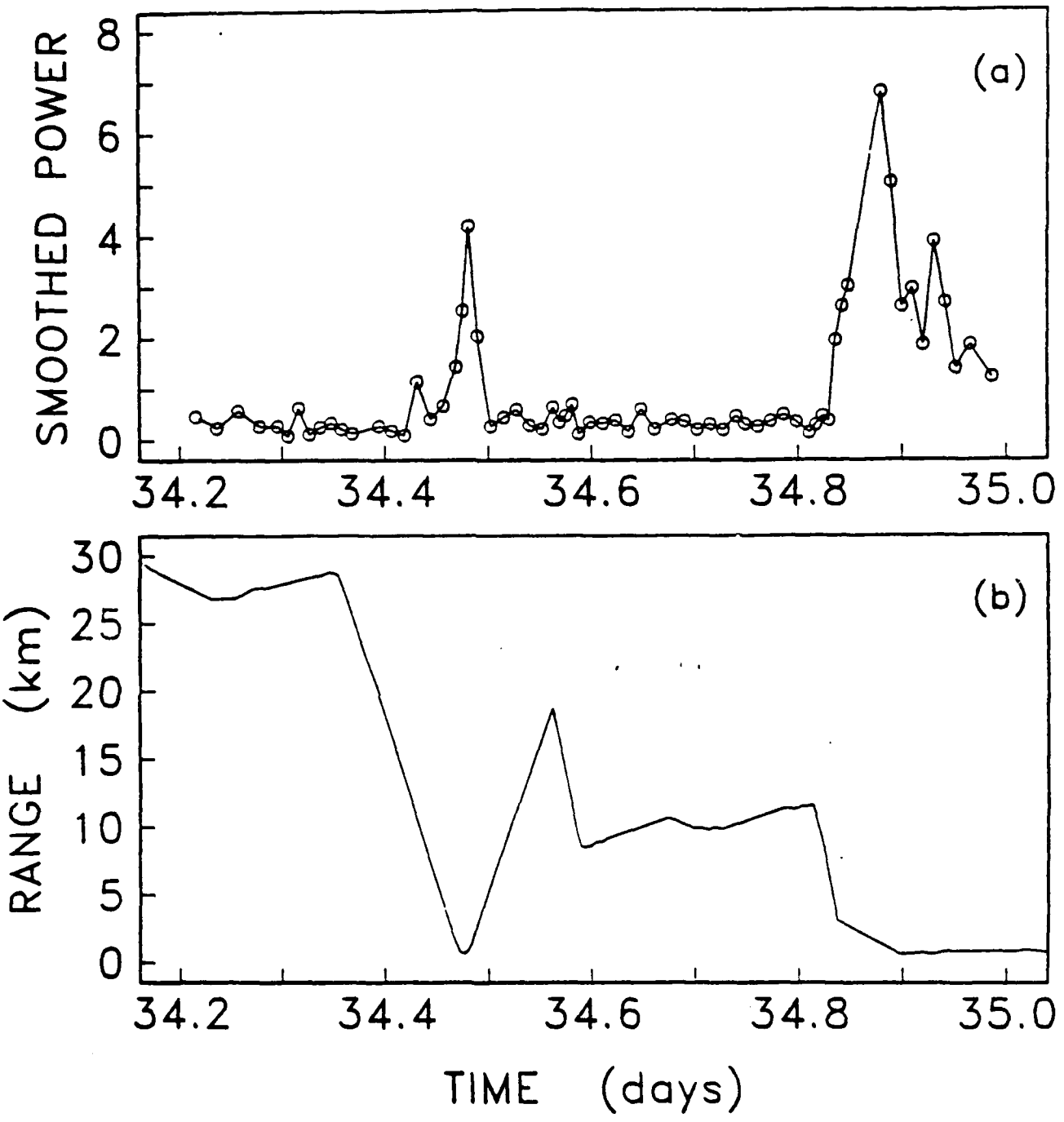

SMOOTHED POWER
0
2
4
6
8
(a)
34.2
34.4
34.6
34.8
35.0
RANGE (km)
0
5
10
15
20
25
30
(b)
34.2
34.4
34.6
34.8
35.0
TIME (days)

FIGURE 7

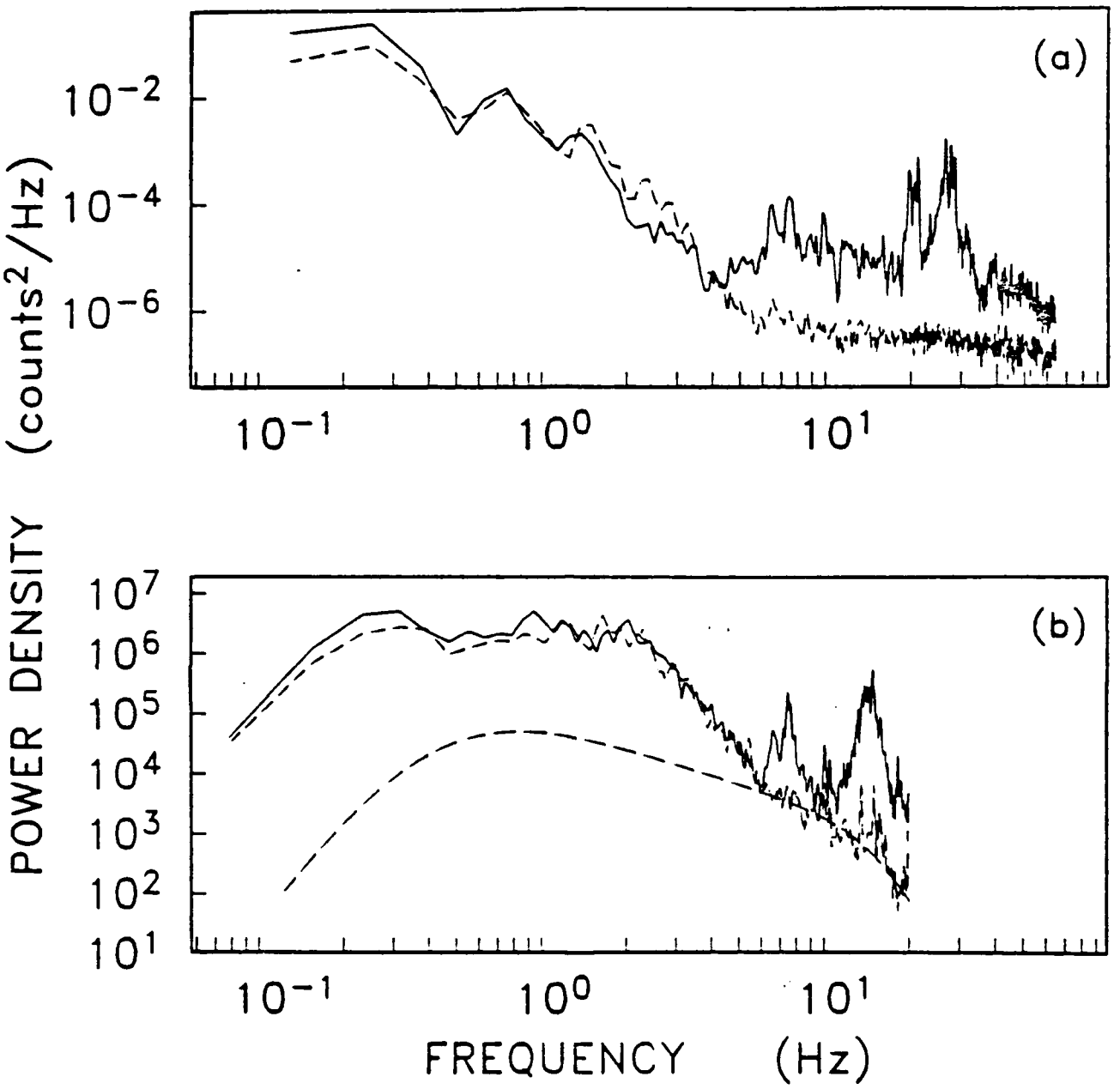

(a)
10^{-2}
10^{-4}
10^{-6}
10^{-1}
10^{0}
10^{1}
POWER DENSITY (counts^2/Hz)
(b)
10^{7}
10^{6}
10^{5}
10^{4}
10^{3}
10^{2}
10^{1}
10^{-1}
10^{0}
10^{1}
FREQUENCY (Hz)

FIGURE 8

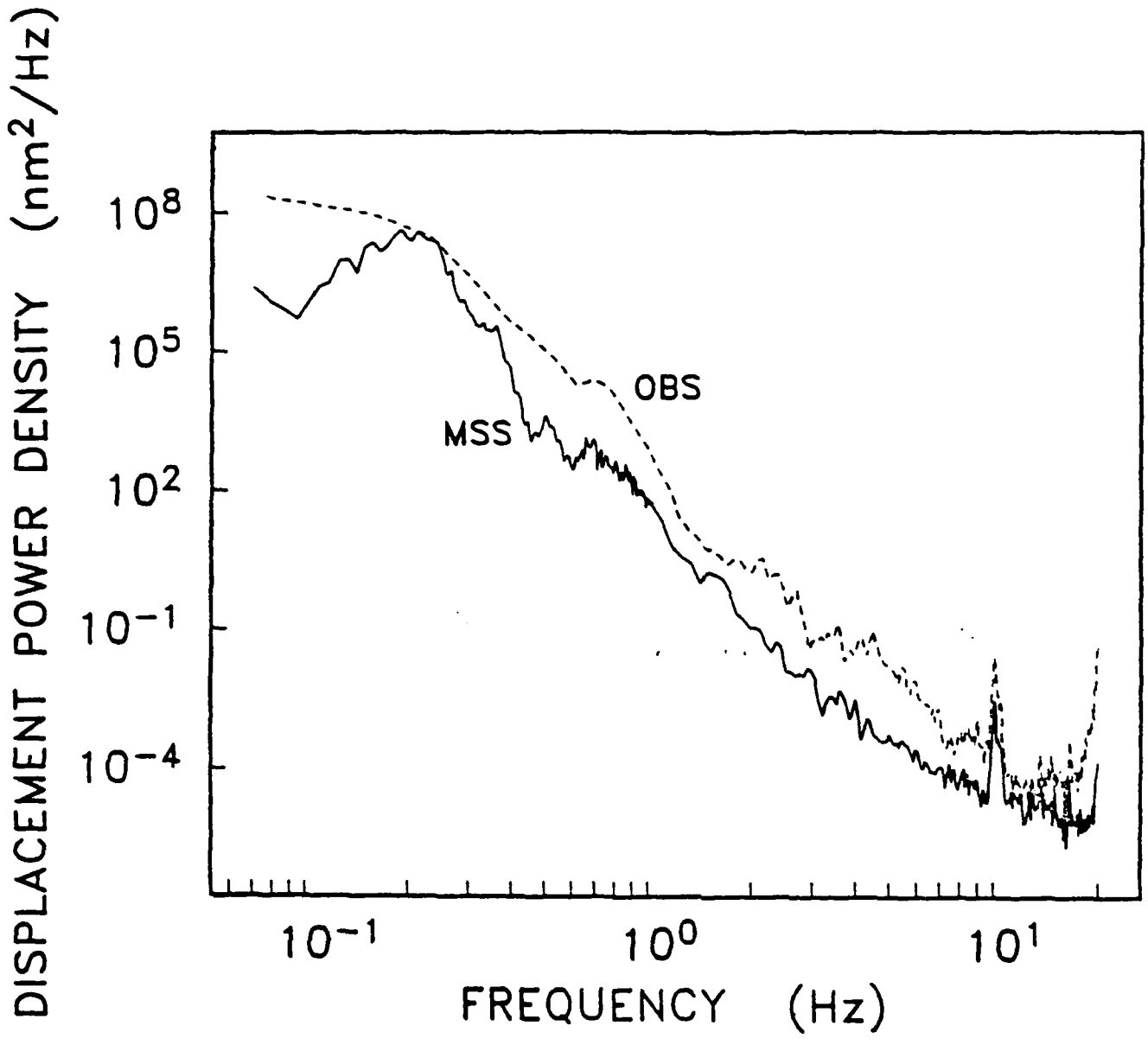

DISPLACEMENT POWER DENSITY (nm²/Hz)
10⁸
10⁵
10²
10⁻¹
10⁻⁴
OBS
MSS
10⁻¹
10⁰
10¹
FREQUENCY (Hz)

FIGURE 9

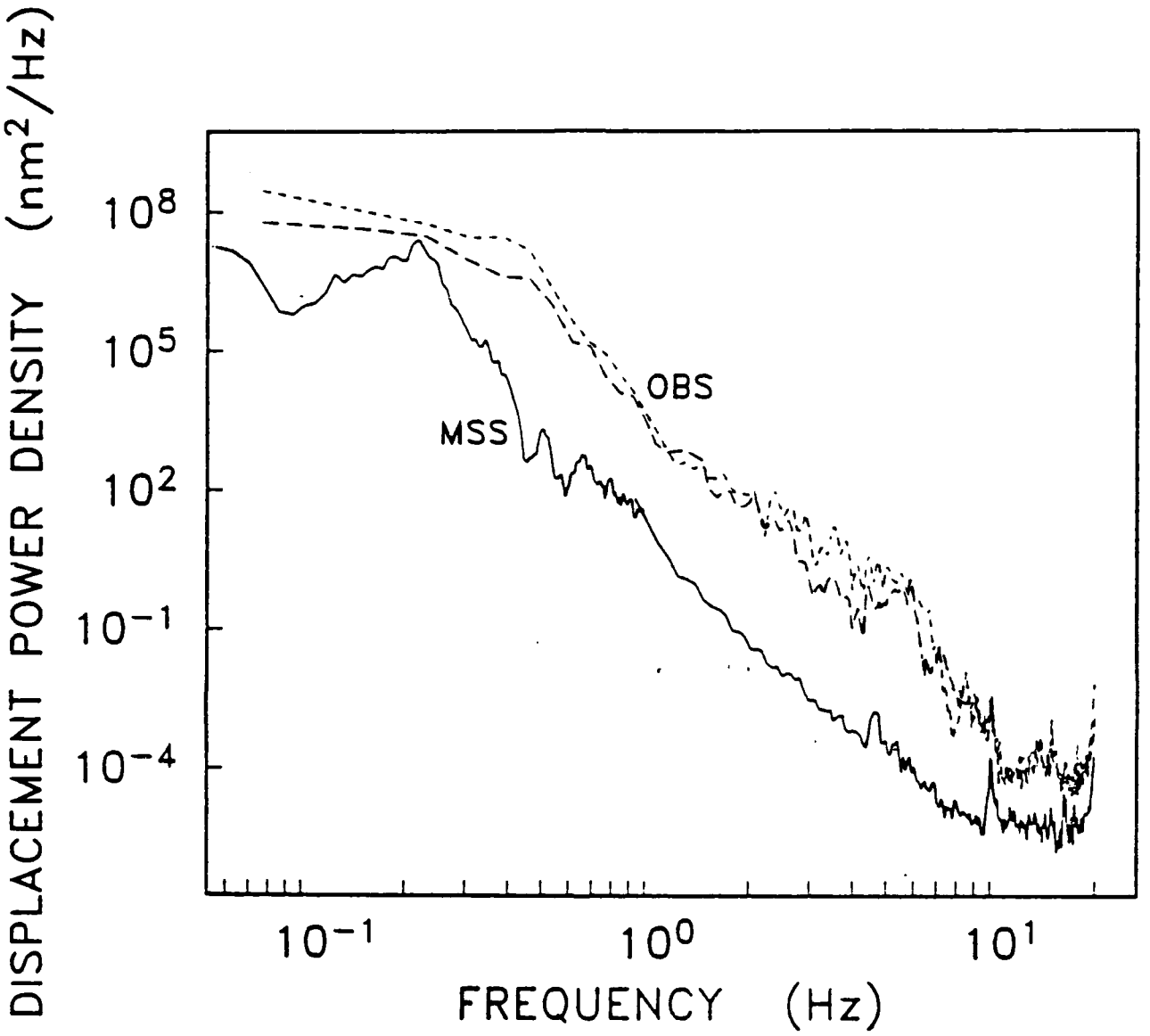

DISPLACEMENT POWER DENSITY (nm²/Hz)
10⁸
10⁵
10²
10⁻¹
10⁻⁴
OBS
MSS
10⁻¹
10⁰
10¹
FREQUENCY (Hz)

FIGURE 10

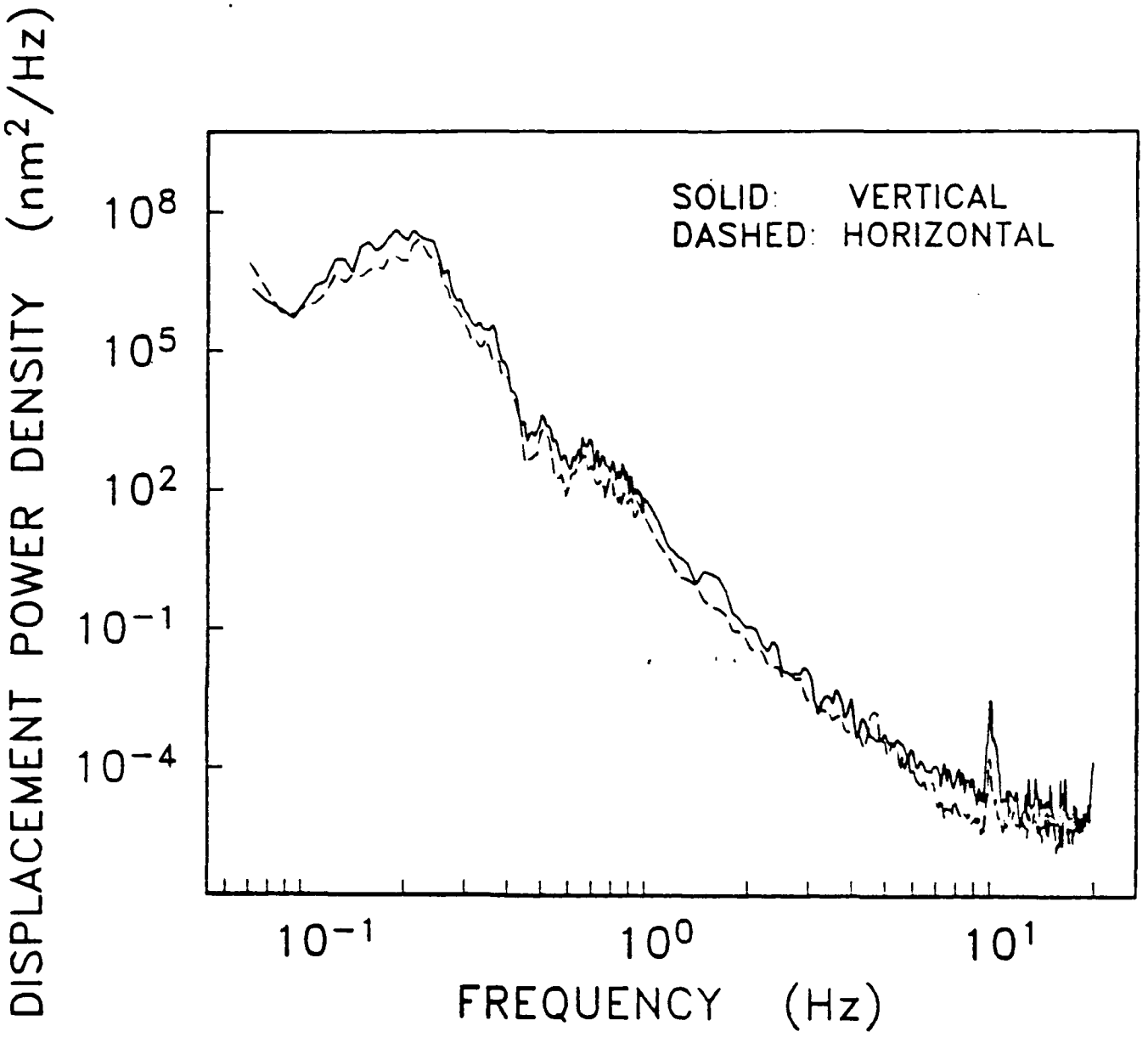

DISPLACEMENT POWER DENSITY (nm²/Hz)
10⁸
10⁵
10²
10⁻¹
10⁻⁴
SOLID: VERTICAL
DASHED: HORIZONTAL
10⁻¹
10⁰
10¹
FREQUENCY (Hz)

FIGURE 11

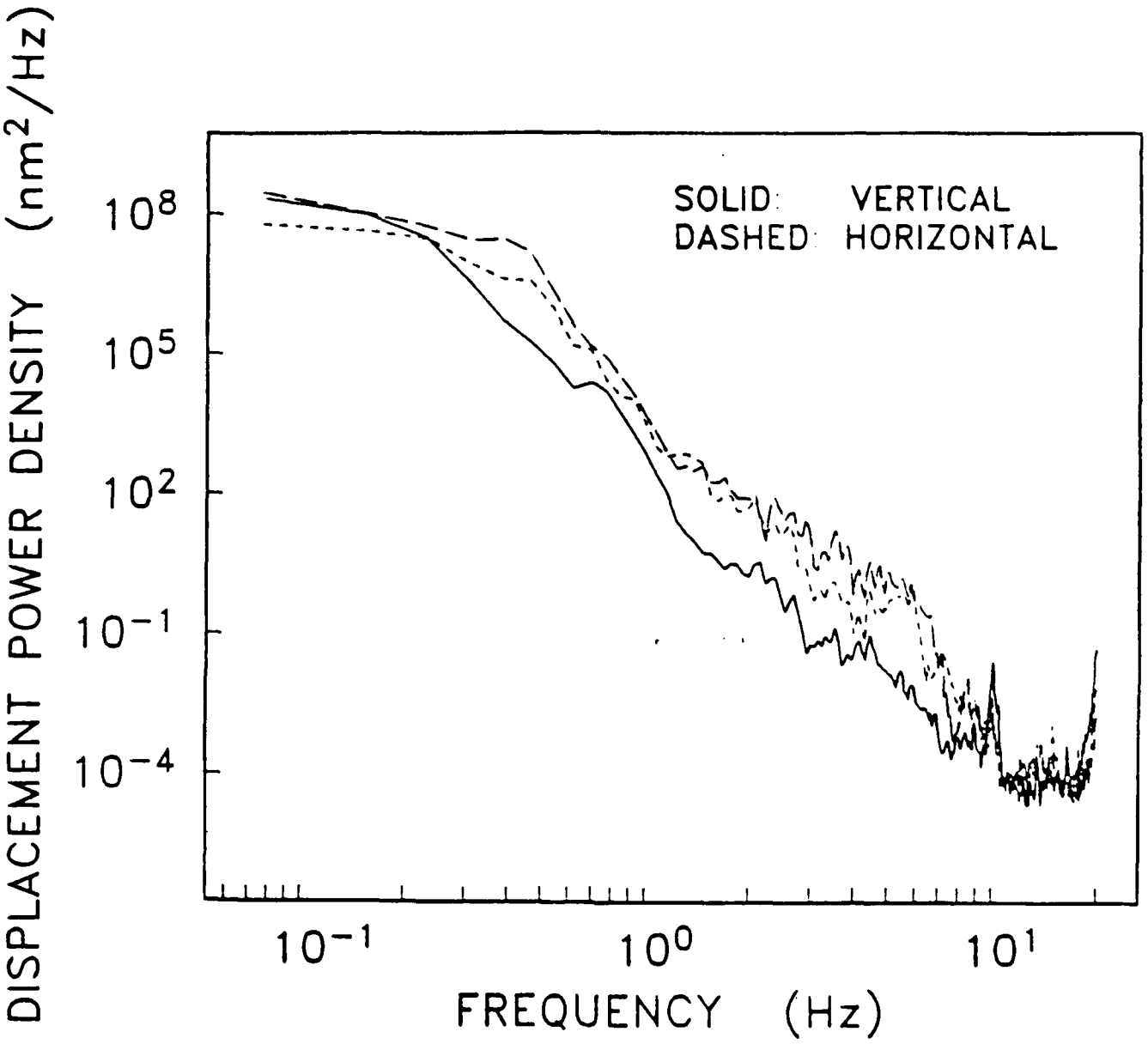

DISPLACEMENT POWER DENSITY (nm²/Hz)
10⁸
10⁵
10²
10⁻¹
10⁻⁴
SOLID VERTICAL
DASHED HORIZONTAL
10⁻¹
10⁰
10¹
FREQUENCY (Hz)

FIGURE 12

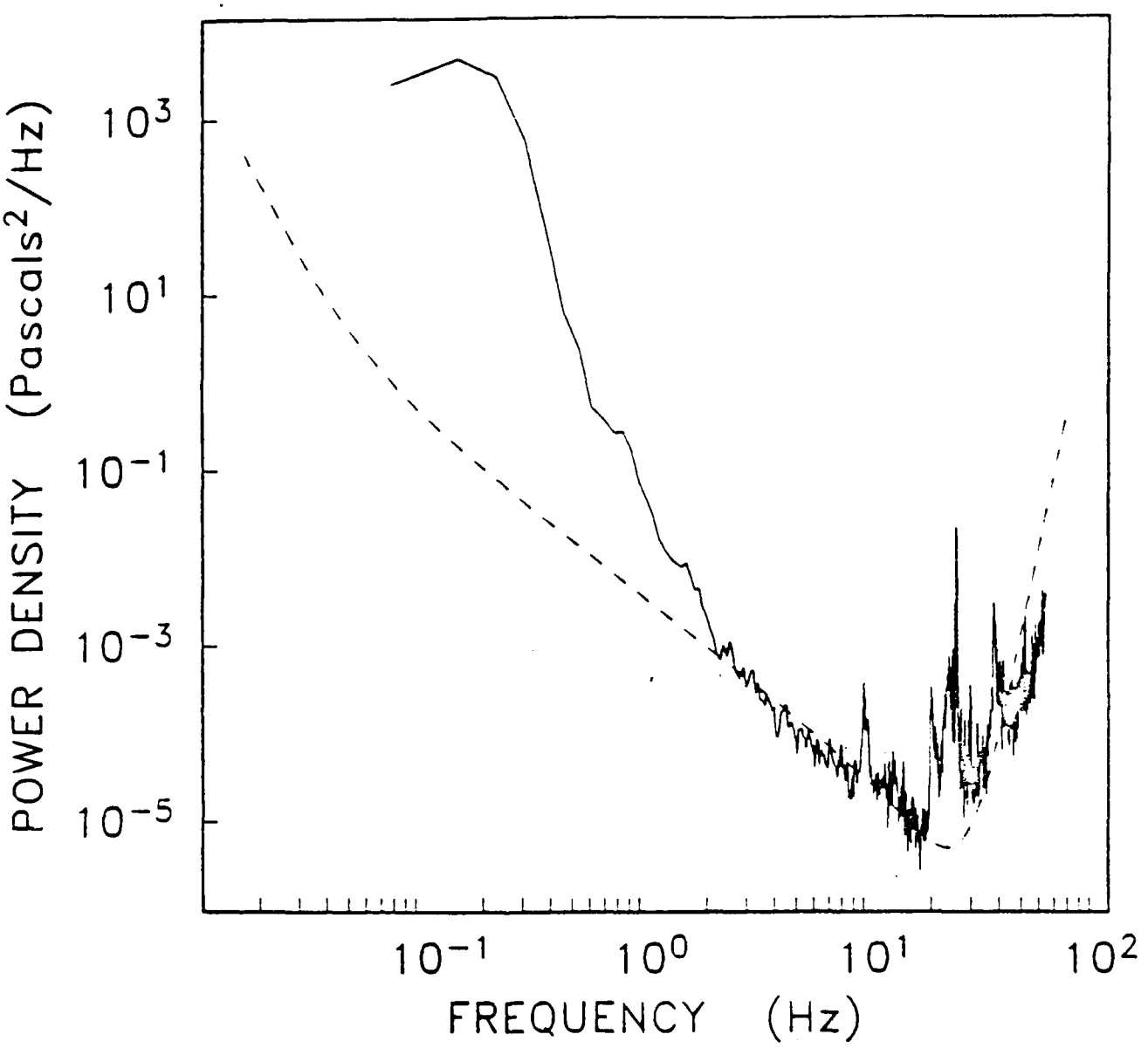

POWER DENSITY (Pascals²/Hz)
10³
10¹
10⁻¹
10⁻³
10⁻⁵
10⁻¹
10⁰
10¹
10²
FREQUENCY (Hz)

FIGURE 13

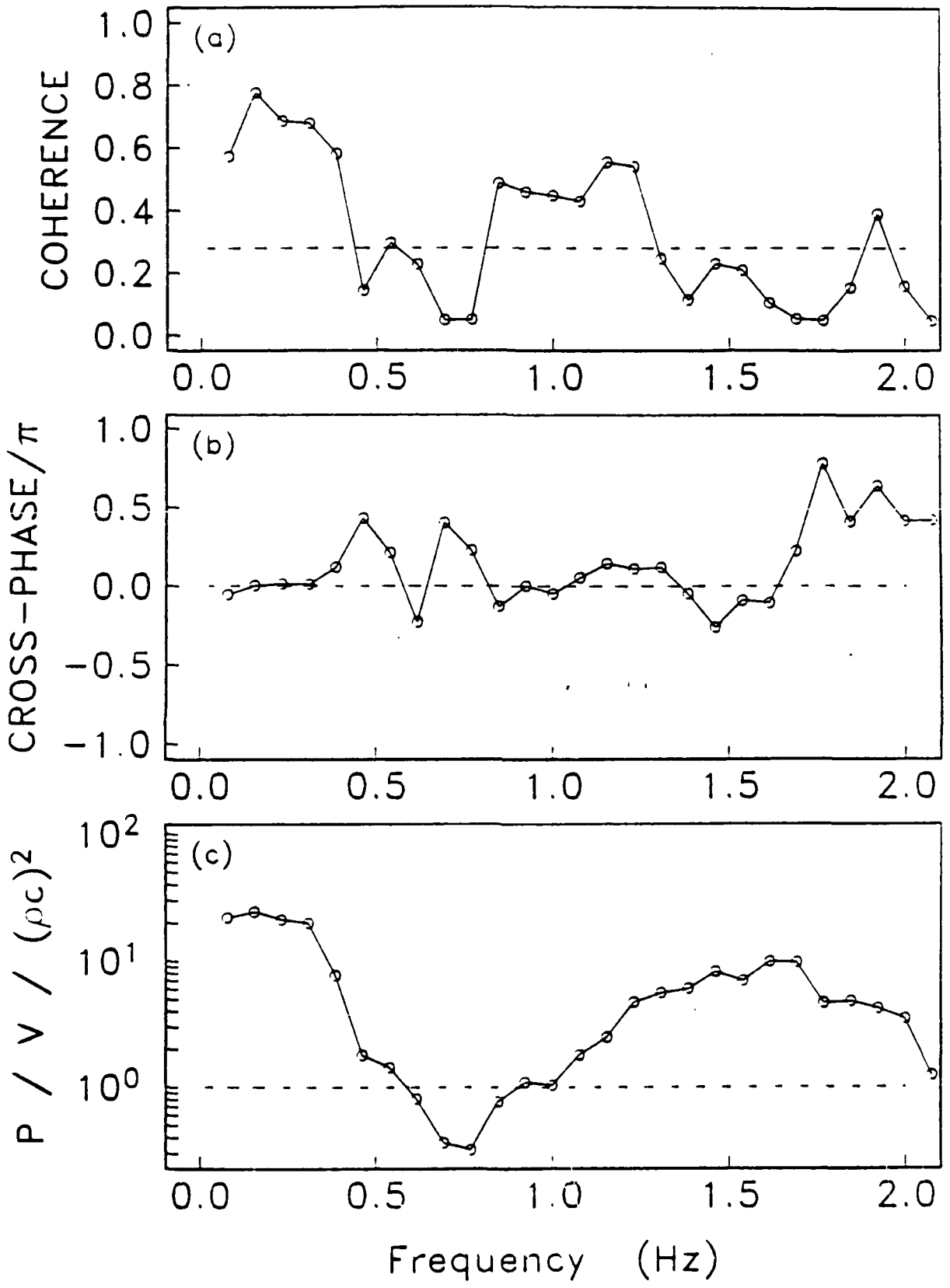

(a)
COHERENCE
1.0
0.8
0.6
0.4
0.2
0.0
0.0
0.5
1.0
1.5
2.0
(b)
CROSS-PHASE/π
1.0
0.5
0.0
−0.5
−1.0
0.0
0.5
1.0
1.5
2.0
(c)
P / V / (ρc)²
10²
10¹
10⁰
0.0
0.5
1.0
1.5
2.0
Frequency (Hz)

FIGURE 14

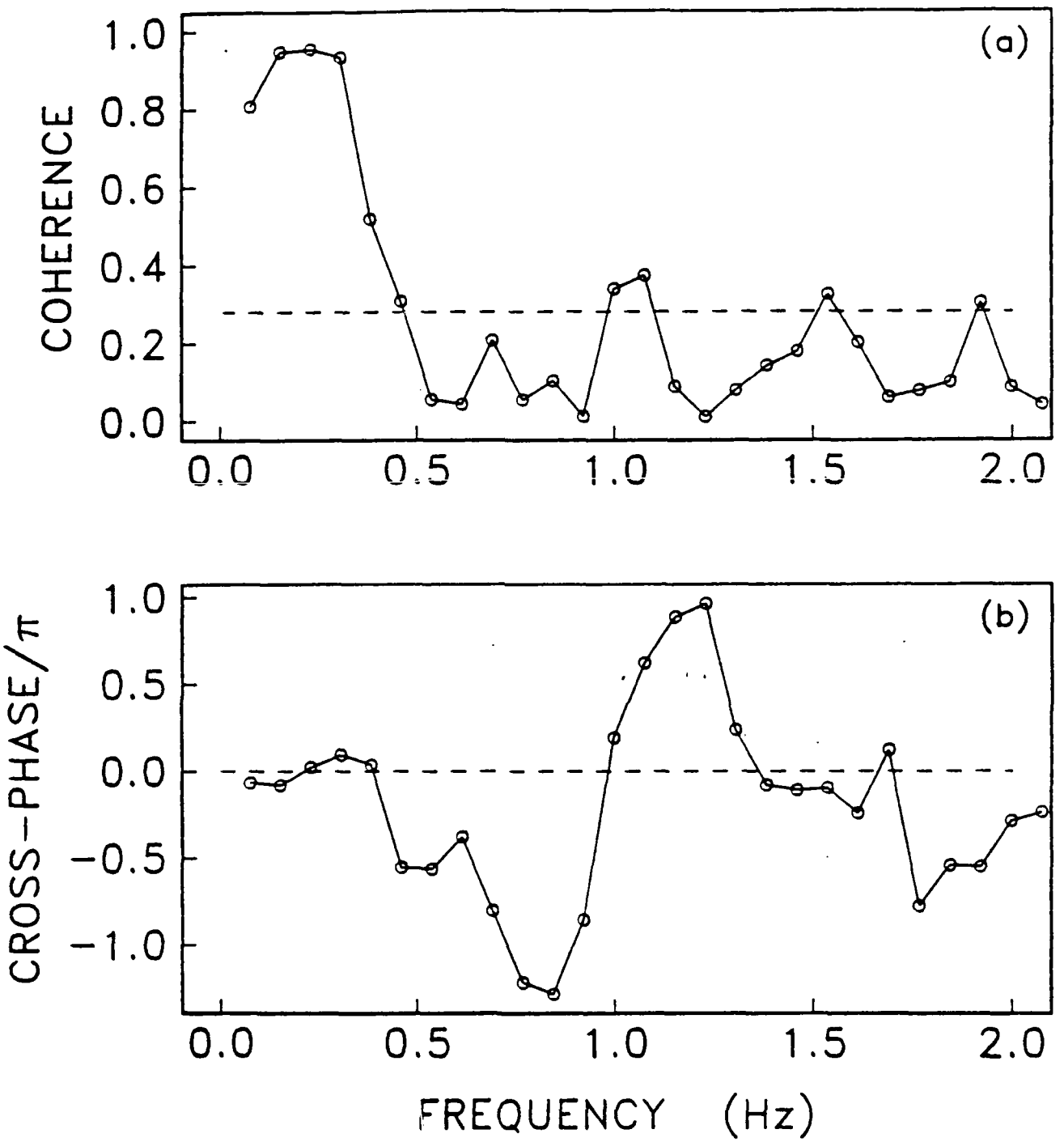

(a)
COHERENCE
1.0
0.8
0.6
0.4
0.2
0.0
0.0
0.5
1.0
1.5
2.0
(b)
CROSS-PHASE/π
1.0
0.5
0.0
−0.5
−1.0
0.0
0.5
1.0
1.5
2.0
FREQUENCY (Hz)

FIGURE 15

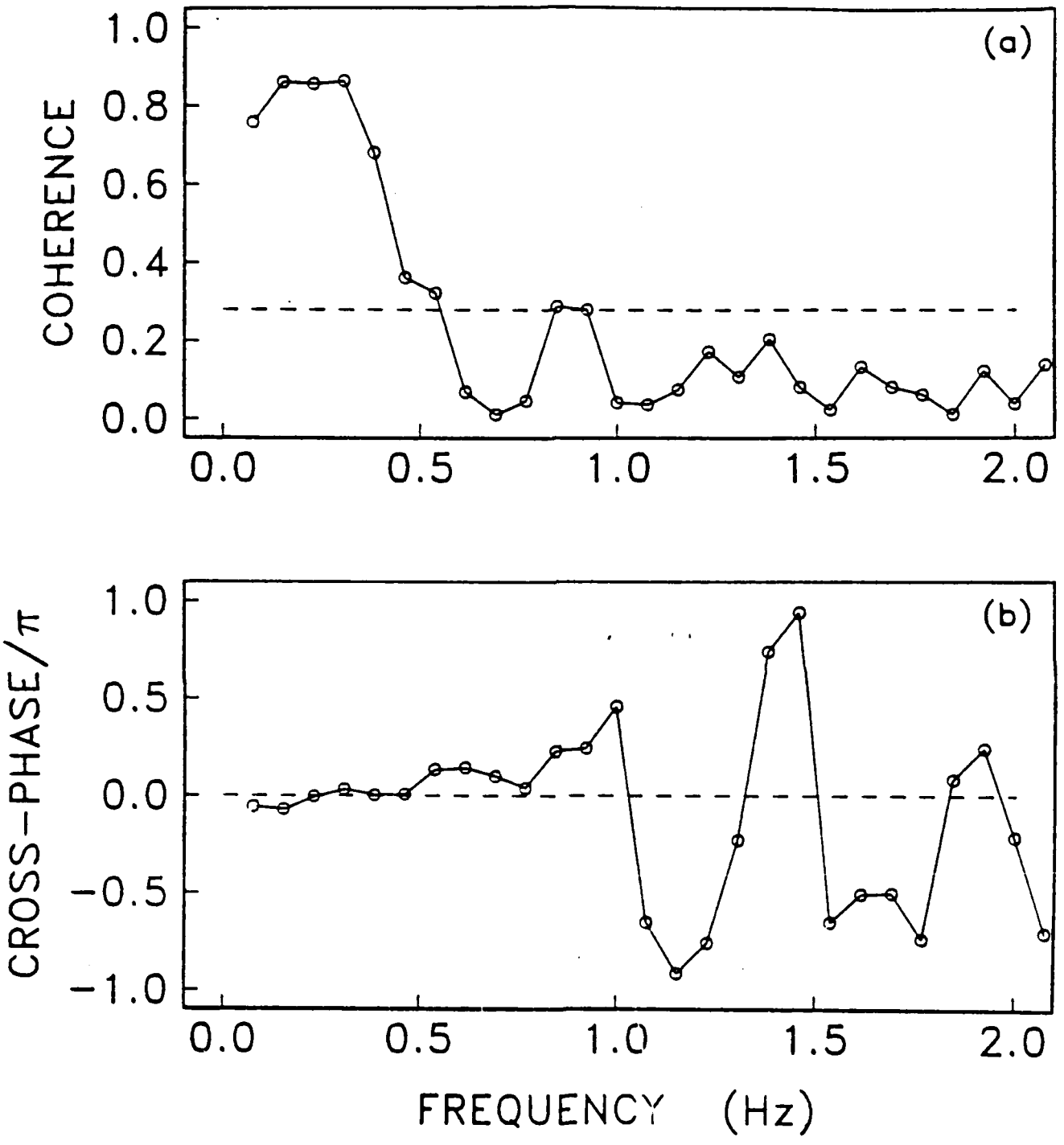

(a)
COHERENCE
1.0
0.8
0.6
0.4
0.2
0.0
0.0
0.5
1.0
1.5
2.0
(b)
CROSS-PHASE/π
1.0
0.5
0.0
−0.5
−1.0
0.0
0.5
1.0
1.5
2.0
FREQUENCY (Hz)

FIGURE 16

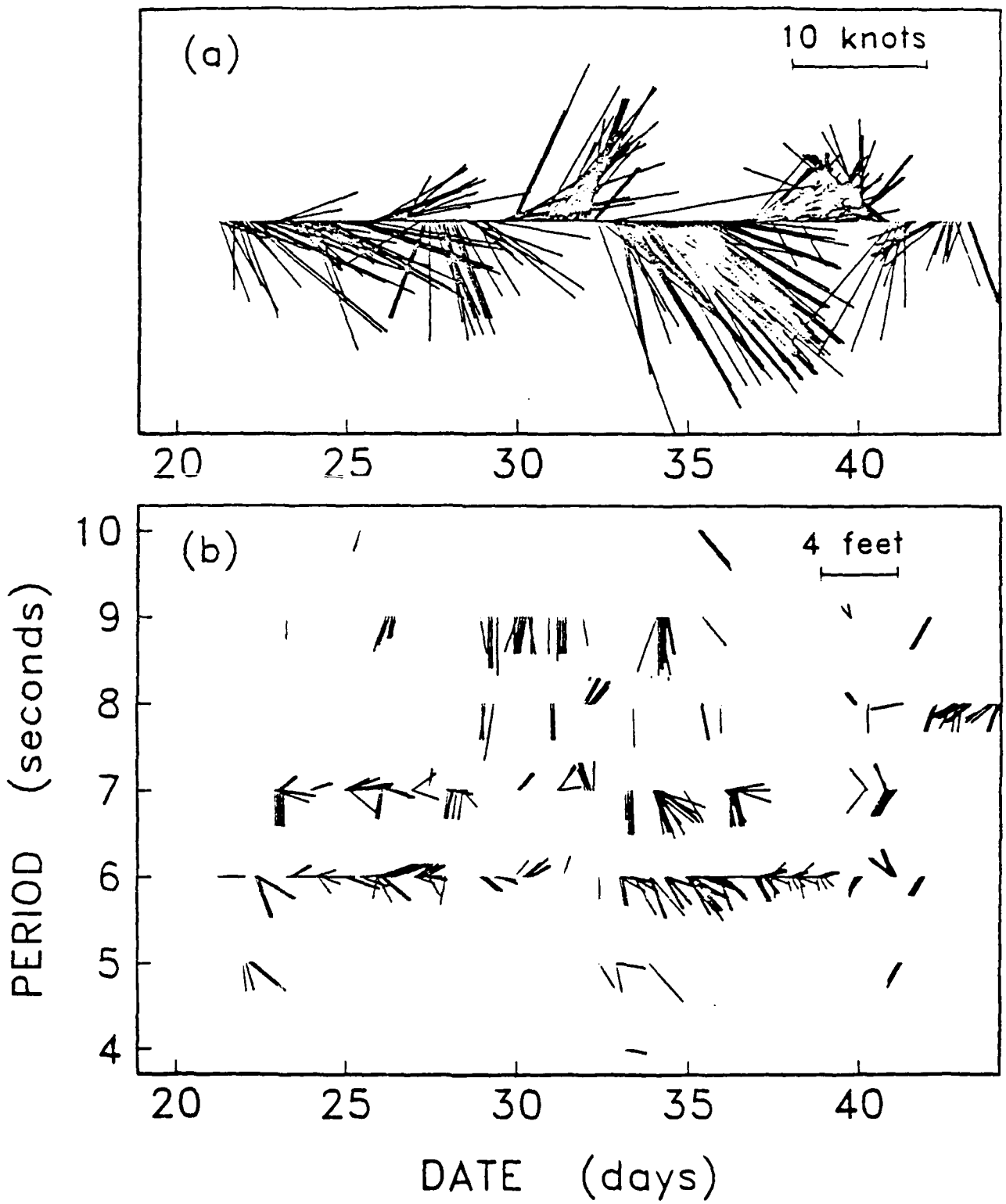

(a)
10 knots
20
25
30
35
40
(b)
4 feet
PERIOD (seconds)
10
9
8
7
6
5
4
20
25
30
35
40
DATE (days)

FIGURE 17

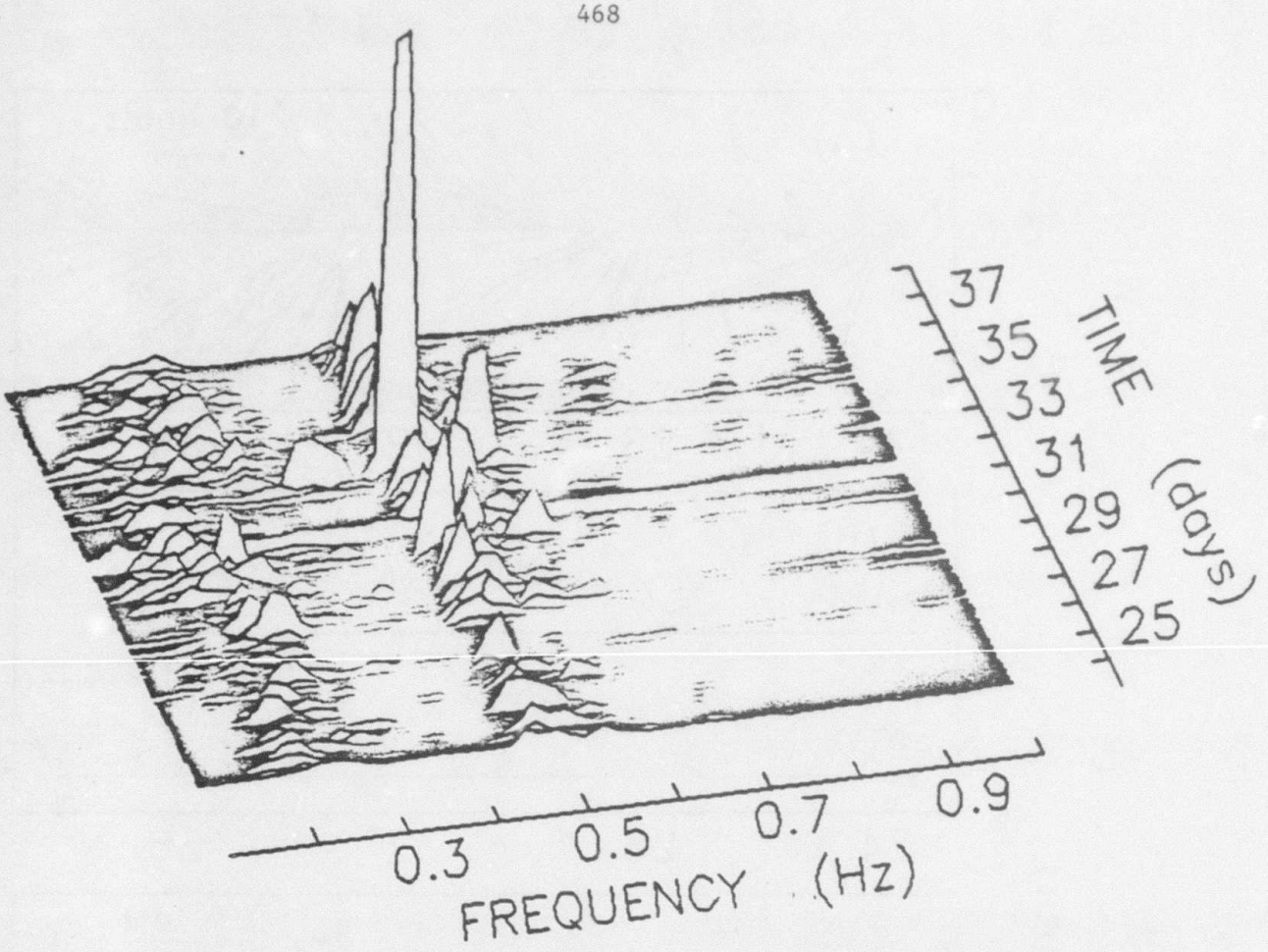


FIGURE 18

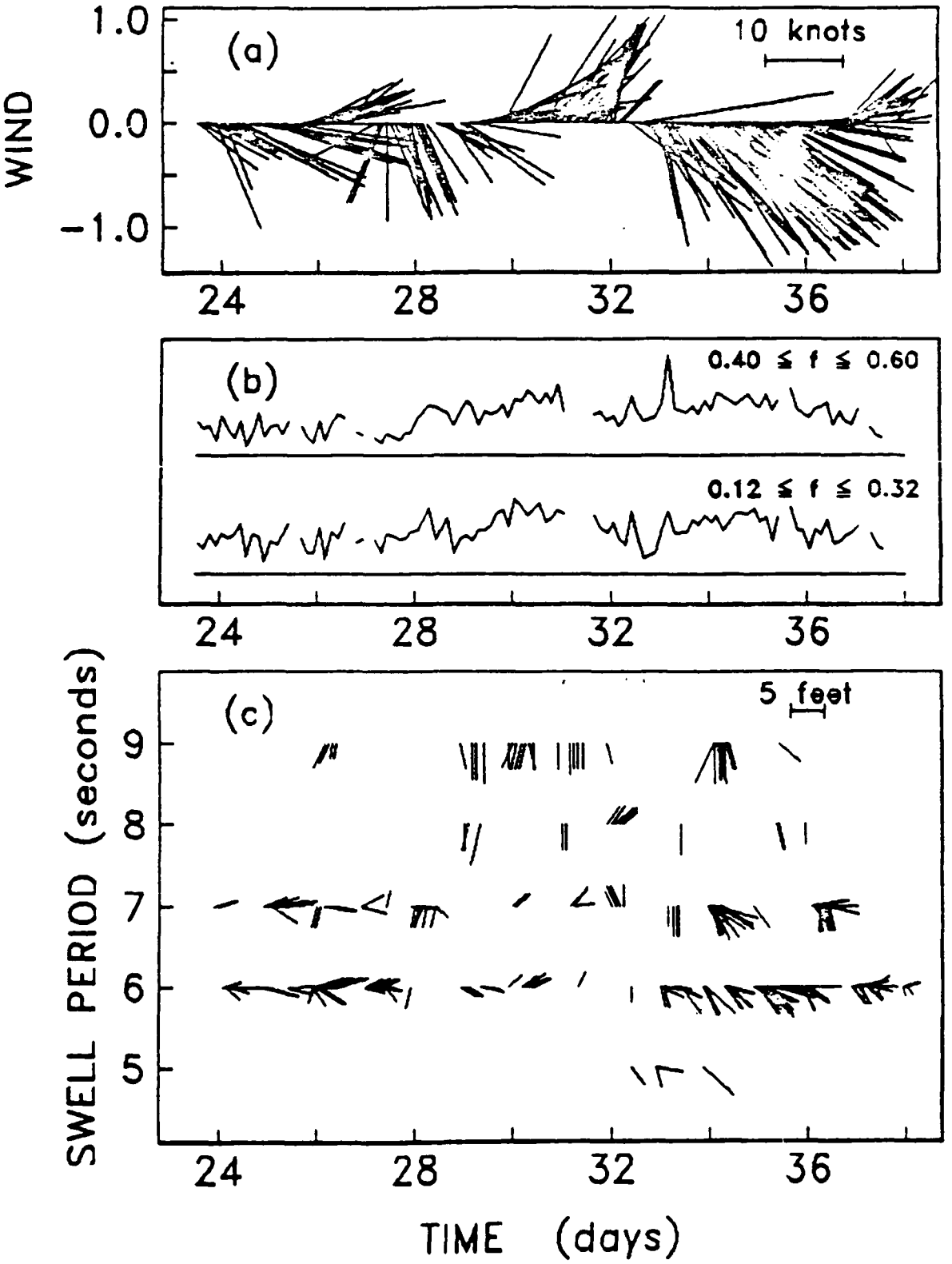

(a)
10 knots
WIND
1.0
0.0
-1.0
24
28
32
36
(b)
0.40 ≤ f ≤ 0.60
0.12 ≤ f ≤ 0.32
24
28
32
36
(c)
5 feet
SWELL PERIOD (seconds)
9
8
7
6
5
24
28
32
36
TIME (days)

FIGURE 19

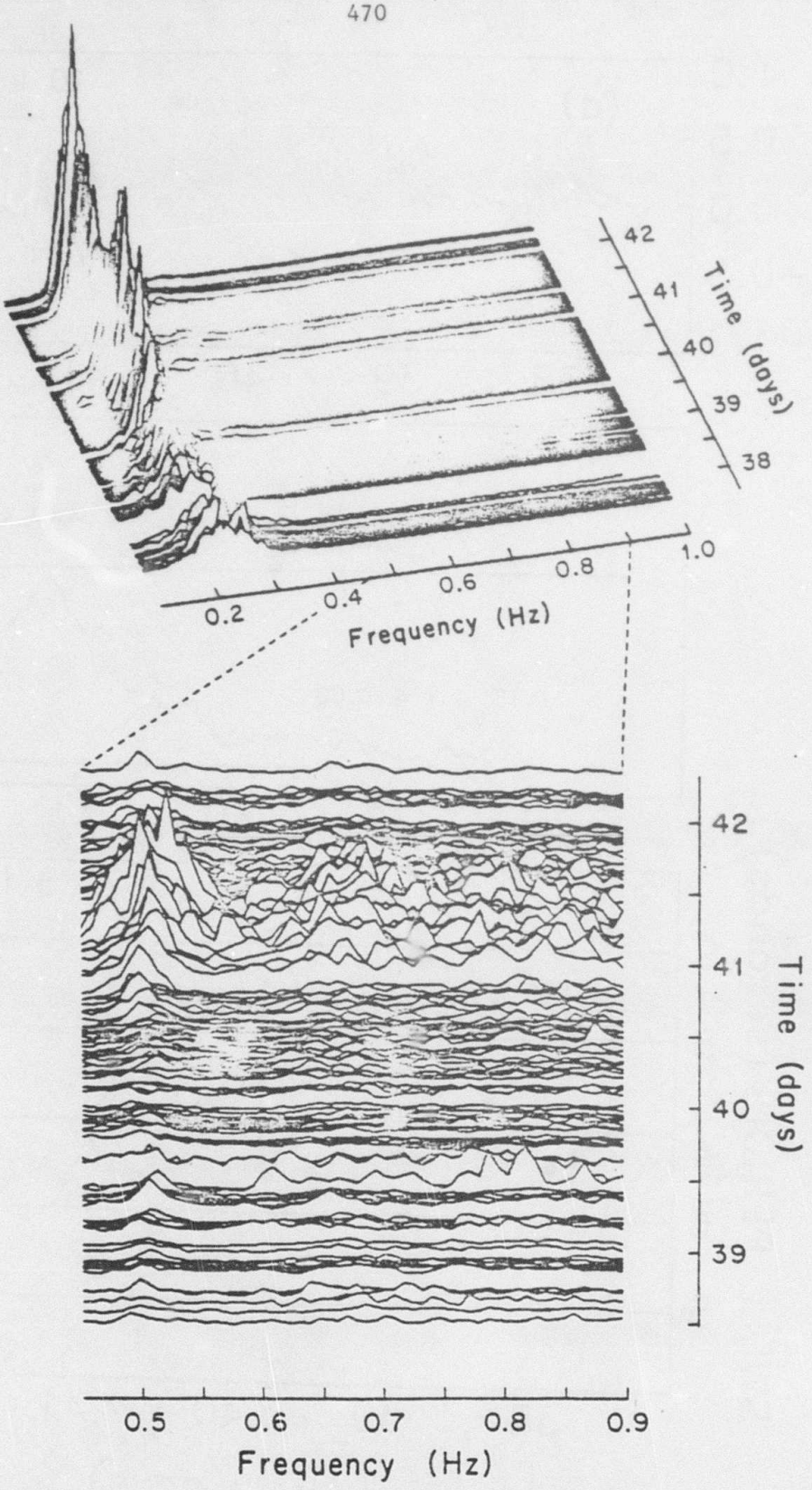

42
41
40
39
38
Time (days)
0.2
0.4
0.6
0.8
1.0
Frequency (Hz)
42
41
40
39
Time (days)
0.5
0.6
0.7
0.8
0.9
Frequency (Hz)

FIGURE 20

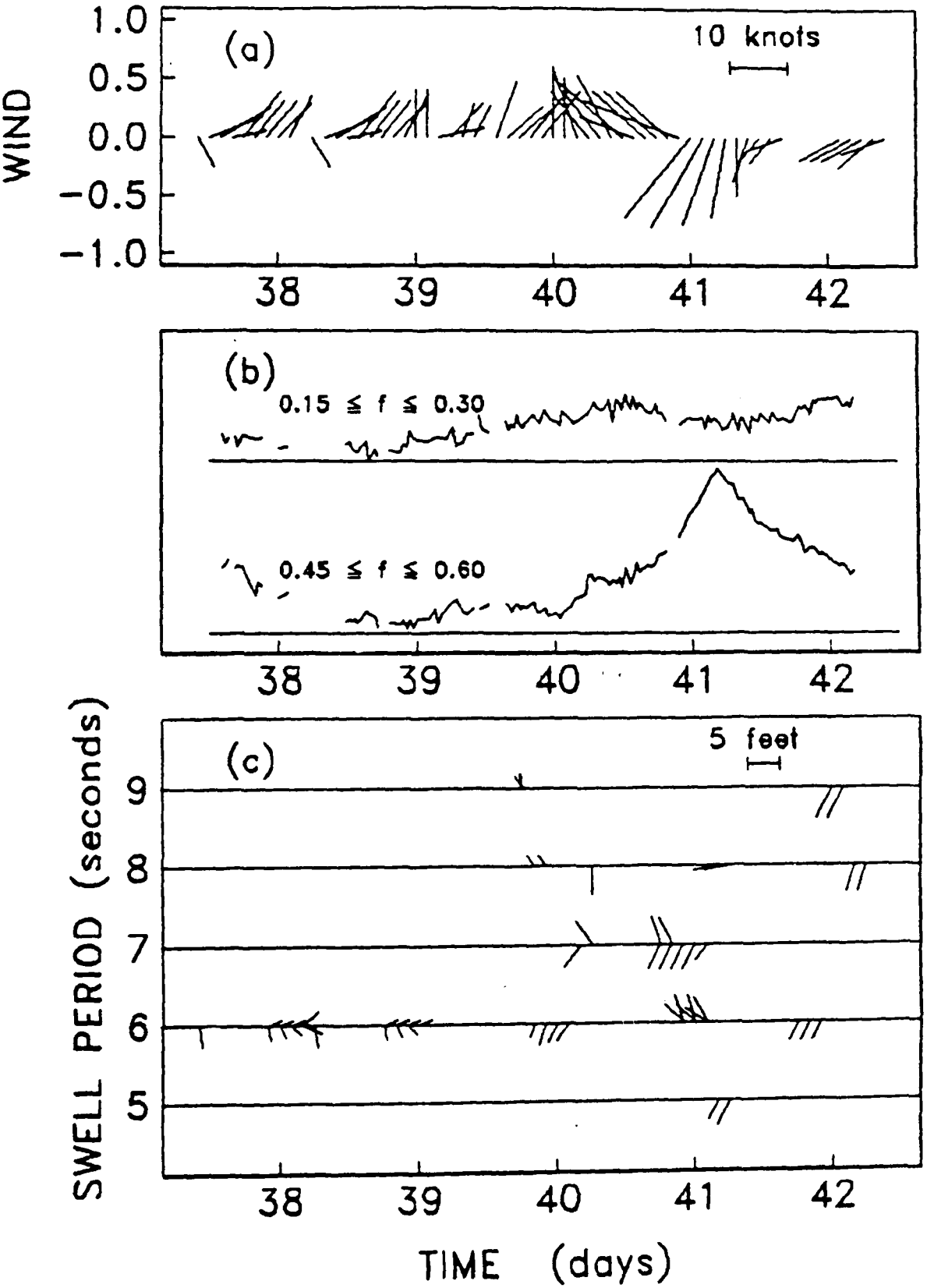

(a)
10 knots
WIND
1.0
0.5
0.0
−0.5
−1.0
38
39
40
41
42
(b)
0.15 ≤ f ≤ 0.30
0.45 ≤ f ≤ 0.60
38
39
40
41
42
(c)
5 feet
SWELL PERIOD (seconds)
9
8
7
6
5
38
39
40
41
42
TIME (days)

FIGURE 21

CHAPTER 15

MSS and OBS DATA FROM THE NGENDEI EXPERIMENT IN THE SOUTHWEST PACIFIC

John A. Orcutt

Institute of Geophysics and Planetary Physics,
Scripps Institution of Oceanography
La Jolla, California 92093

and

Thomas Jordan

Department of Earth, Atmospheric and Planetary Sciences
Massachusetts Institute of Technology
Cambridge, MA 02139

AGENDA SECTION: Earthquake or Explosion: Where Are We Now?

PAPER TITLE: MSS and OBS Data from the Ngendei Experiment in the Southwest Pacific

PAPER AUTHORS: John Orcutt and Thomas H. Jordan

SUMMARY: An extensive set of noise, explosion, and earthquake data was collected by the Marine Seismic System (MSS) and ocean bottom seismometer (OBS) arrays during the 1983 Ngendei experiment in the Southwest Pacific Basin. The MSS was emplaced in a drill hole 124 m below the sediment-water interface. Noise levels in the frequency band 0.5-2.0 Hz observed on the MSS were 20-30 dB less than those recorded on the OBSs, consistent with models in which seafloor noise propagates primarily as interface waves. The refraction data require directional anisotropy in the upper crust and uppermost mantle; the latter implies a fossil seafloor-spreading direction of N30°E in this part of the Pacific. Clear Sn phases, with an apparent velocity of 4.7 km s^{-1}, are observed in the refraction data. A number of earthquake signals at regional and teleseismic distances were recorded by the MSS and OBSs. Intermediate-focus and deep-focus events from the Tonga-Kermadec seismic zone show complex P arrivals; these provide new information about the attenuation and velocity structure of the oceanic upper mantle. In particular, the sub-lithospheric mantle beneath the Ngendei site is highly attenuating, with an average apparent Q_P of about 300. Because of this attenuation, the detection threshold of the MSS for distant ($\Delta > 30°$) teleseismic events is relatively high ($m_b \simeq 5.0$). At regional distances ($\Delta < 15°$), however, where signals propagate through the high-Q lithospheric waveguide, events with body wave magnitudes as small as 4.0 are well recorded on the MSS, and the detection threshold is lowered to about 3.7.

During January-April, 1983, the D/V Glomar Challenger and the R/V Melville deployed and recovered the NORDA/DARPA Marine Seismic System (MSS) and a six-element ocean bottom seismometer (OBS) array at a site in the southwest Pacific (23°49'S, 165°32'W), approximately 900 km east of the Tonga Trench. The expedition was named NGENDEI after a Polynesian deity associated with volcanoes and earthquakes. Instrument emplacement and recovery were accomplished as planned, and the major scientific objectives were achieved; three basic types of seismological data - noise, refraction, and earthquake - were successfully recorded by both the MSS and the OBS array.

The data analysis program has four primary objectives: (a) comparison of noise levels and signals recorded by the MSS and OBS sensors to assess the signal-to-noise improvement attainable by burial of seismometers below the sediments in a deep-ocean environment, (b) use of noise data to investigate the mode of noise propagation on the sea floor and to test physical models of noise generation in the deep ocean, (c) analysis of refraction data to study the structure of the crust and upper mantle, in particular, the anelastic and anisotropic structure of the oceanic lithosphere, and (d) use of earthquake data to examine the propagation of seismic signals to regional and teleseismic distances over purely oceanic paths and to constrain elastic and anelastic models of the sub-lithospheric mantle.

NOISE DATA

The comparison of absolute values of seismic noise at the sea floor, as measured by the OBSs, with values recorded by the sub-bottom MSS is a major component of this study. The MSS was deployed in DSDP hole 595B at a depth of 124 m below the sediment-water interface, approximately 54 m into basaltic basement. It was anticipated that noise levels would decrease substantially with depth of burial given the working hypothesis that high-frequency (~1 Hz) noise travels largely as a fundamental-mode Stoneley wave along the sea floor. The Leg-78B deployment of the MSS yielded results which supported this hypothesis (Adair et al., 1984), but a full-fledged test of noise models was not possible with the data from this experiment because of the lack of OBS array measurements at the time of MSS recording.

Figure 1 depicts the response of the OBS and MSS instrumentation employed during Ngendei. The MSS mid-period channel has a much lower gain than the short-period channel. The high end of the MSS short-period response was substantially modified over that illustrated by the Gould anti-aliasing FIR filter, which essentially eliminated all energy above about 18 Hz. The Nyquist frequency was 20 Hz for the MSS and 64 Hz for the OBSs.

Figure 2 illustrates the absolute ground-motion noise levels for the period beginning at 0635 Z on 8 February 1983. The spectra from the MSS and Suzy (one of the OBSs) were stabilized by stacking ten spectral realizations from contiguous, tapered windows of 13-second duration. Both the Glomar Challenger and the Melville were on station near the drill site at this time; a 10 Hz peak associated with the thrusters on the Challenger can be seen in both data sets. The spectra differ by only a small amount in the vicinity of the microseism peak at 3-4 s period, but the difference increases at higher frequencies, reaching approximately 30 db at a frequency of 2 Hz. Figure 2 also shows several continental noise spectra for comparison. The Brune-Oliver upper bound is taken from Brune and Oliver (1959), as normalized by Melton (1976), and represents the highest noise levels expected for a continental site. The MSS/OBS levels are lower than this bound (the penetration of the bound at a frequency of 0.17 Hz by the Suzy spectrum is largely owing to the increasing OBS electronic instrument noise generated by low-power CMOS amplifiers). The Lajitas, Texas, spectrum, the lowest ever documented on continents (Herrin, 1982), and the very quiet Queen Creek, Arizona, measurement (Melton, 1976) are also plotted. (The Queen Creek spectrum, as noted by Herrin (1982), is nearly identical to Lajitas at frequencies below about 0.7 Hz.) The Ngendei noise levels are higher than at these continental sites but, above 1 Hz, are substantially less than those of average continental stations. The uncorrected noise levels before and after Challenger departure are illustrated in Figure 3; substantial improvements are realized in the OBS levels at frequencies above 3 Hz and in the MSS levels above 10 Hz.

REFRACTION DATA

The seismic refraction experiment conducted at the Ngendei site consisted of a star pattern (4 split profiles) with legs extending to approximately 60 km range. Two legs, normal to one another, were extended to 250 and 150 km to evaluate deeper lithospheric structure. Figures 4 and 5 illustrate the MSS and OBS data for one of the lines; topographic corrections have been applied.

The OBS seismograms show clearly the high-frequency noise generated by Challenger (cf. Figure 3) and, because of the broader bandwidth of the OBS response (Figure 1), contain substantially more energy at high frequencies. The OBS signals fell below the noise level beyond a range of about 70 km, whereas the MSS yielded observable signals out to 250 km.

Figures 6 and 7 contrast two of the distant events from the refraction line in Figures 4 and 5. The OBS and MSS seismograms have been aligned by a correction for the depth differences. The two data sets are nearly identically in phase with the MSS appearing largely as a filtered version of the OBS data. The OBS data have higher signal amplitudes after the arrival of the initial compressional wave; we attribute this signal to reverberations within the gelatinous sediment layer.

The gross velocity structure of the crust at this site is typical of the older parts of the Pacific Basin. Strong compressional-wave anisotropy (8.0 to 8.4 or 8.5 km s^{-1}) is observed in the uppermost mantle, with a direction of maximum velocity (and, by inference, a fossil direction of seafloor spreading) oriented 30° east of north. An anisotropy of somewhat smaller magnitude is required by the data for the shallow crust. The direction of crustal anisotropy is rotated by almost exactly 90° from the mantle anisotropy; we propose the former is associated with the sheeted dike complex underlying the surface volcanics, as hypothesized from the ophiolite model of oceanic crustal structure. Clear Sn phases are observed on the MSS profiles and are characterized by a phase velocity near 4.7 km s^{-1}. The phase velocity appears to be independent of azimuth.

TELESEISMIC AND REGIONAL EVENTS

Approximately five days of MSS data were recorded on the deck of the D/V Glomar Challenger during its occupation of Site 595. At the end of this period, which included the refraction experiment and engineering tests of the MSS, the downhole sensors were connected via an electromechanical cable to the Gould Bottom Processing Package (BPP), and the continuously recording BPP was deployed for a planned 45-day experiment. The six-element OBS array was recovered by the R/V Melville and redeployed for simultaneous recording of teleseisms (triggered) and ambient seismic noise (at preset intervals) over this period. All six OBSs functioned nearly perfectly, but, unfortunately, the extended MSS experiment was cut short by a power failure in the BPP only 40 hours after its deployment.

Nevertheless, a number of earthquake signals from events at regional and teleseismic distances were recorded by the MSS, and the analysis of these signals is providing new information about seismic wave propagation in the ocean basins. During the five days of on-deck recording, for example, 64 natural seismic events occurred which were large enough to be identified on the low-gain, strip-chart recorders used for real-time monitoring of the MSS. Most of these were regional events from various depths in the Tonga-Kermadec seismic zone.

Figure 8 shows a typical shallow-focus (h = 52 km) earthquake from the Kermadec Trench. The initial arrival (Figure 9) is dominated by high-frequency, incoherently scattered energy characteristic of Pn propagation

through the high-Q oceanic lithosphere at this distance (12.5°). Waveforms from deeper events are more complex. Figures 10 and 11, for example, display an earthquake at about the same distance (12.9°) with a focal depth of 293 km. In this case the initial wave group is not Pn but rather comprises the P waves triplicated by interaction with the 400-km discontinuity. Because the sub-lithospheric mantle beneath this part of the Pacific Basin is highly attenuating, these arrivals are relatively depleted in high frequencies. After ~10 s, however, the amount of high-frequency energy increases, corresponding to the arrival of the Pn wave refracted up and around the corner of the descending slab. (Similar signals were observed by Oliver and Isacks (1967) and Barazangi et al. (1972) at the WWSSN station on the island of Rarotonga and were used as evidence for the existence of subducted lithosphere during the development of the plate-tectonic model.)

The spectral ratios of these two types of signals give quantitative information on the differences in attenuation along lithospheric and sub-lithospheric paths. An analysis of OBS records from the intermediate-focus Tonga earthquake of 1/26/83 (Δ = 14°, h = 238 km), which show similar arrivals, yields an apparent differential attenuation of $\Delta Q_P^{-1} \simeq 2.5 \times 10^{-3}$. Assuming the attenuation is frequency independent and the Q_P of the lithosphere is ~1000 (Oliver and Isacks, 1967), we obtain an average quality factor for the sub-lithospheric path of $\bar{Q}_P \simeq 300$.

The effect of this relatively high attenuation in the upper mantle beneath the Ngendei site is manifested in the spectral content and amplitudes of teleseismic P waves from events at distances greater than 30°. Figure 12 shows the P and pP waveforms from an intermediate-focus earthquake (m_b = 5.7) at Δ = 61°, which again are relatively depleted in high frequencies. The detection capabilities of the MSS with respect to earthquakes located by the National Earthquake Information Service are summarized in Figure 13. No events with body-wave magnitudes below 5.1 were detected at distances beyond about 30°.

At regional distances, however, where signals propagate through the high-Q lithospheric waveguide, this threshold is considerably reduced. All events at distances less than 30° located by the NEIS were observed on the MSS (unless the record was obscured by refraction shots or other earthquakes). In addition, many smaller, unlocated events from the Tonga-Kermadec seismic zone with S-P times less than 170 s ($\Delta \lesssim 15°$) were recorded with a good signal-to-noise ratio. We estimate the detection threshold for shallow-focus events at these distances to be of the order of 3.7.

CONCLUSIONS AND RECOMMENDATIONS

The Ngendei seismic experiment has demonstrated the capability of the MSS and OBS instruments to record earthquakes at regional distances in the deep-ocean environment. These events, especially the intermediate-focus and deep-focus earthquakes, show waveform complexities which are proving useful in constraining attenuation and velocity models of oceanic upper-mantle structure. As demonstrated by Hales et al. (1980), the signals from deeper events yield information about upper-mantle structure not attainable from shallow-focus sources, and additional experiments to collect these data should be conducted. For this purpose, arrays of OBSs distributed on profiles normal to the Tonga-

Kermadec Trench and operated for intervals of 30-90 days would provide the density of coverage required for detailed modeling work.

Acknowledgements. We thank the captains, crews, and scientific parties of the D/V Glomar Challenger and R/V Melville for their efforts during the complex field operations of the Ngendei seismic experiment. R. Adair, M. Burnett, P. Shearer, C. Van Bruggen, and R. Whitmarsh assisted in the preparation of these results. This research was sponsored by the Defense Advanced Research Projects Agency, the Office of Naval Research, and the Air Force Office of Scientific Research under contracts ONR-N0014-83-K-0151 and AFOSR-84-0043.

References

Adair, R.G., J.A. Orcutt and T.H. Jordan, 1984. Analysis of ambient seismic noise recorded by downhole and ocean bottom seismometers on Deep Sea Drilling Project Leg 78B, Initial Reports Deep Sea Drilling Project, in press.

Barazangi, M., B. Isacks, and J. Oliver, 1972. Propagation of seismic waves through and beneath the lithosphere that descends under the Tonga Island Arc, J. Geophys. Res., 77, 942-958.

Brune, J.N. and J. Oliver, 1959. The seismic noise of the earth's surface, Bull. Seism. Soc. Am., 49, 349-353.

Hales, A.L., K.J. Muirhead and J.M.W. Rynn, 1980. A compressional velocity model for the upper mantle, Tectonophysics, 63, 309-348.

Herrin, E., 1982. The resolution of seismic instruments used in treaty verification research, Bull. Seism. Soc. Am., 72, 561-567.

Melton, B.S., 1976. The sensitivity and dynamic range of inertial seismographs, Rev. Geophys. Space Phys., 14, 93-116.

Oliver, J., and B. Isacks, 1967. Deep earthquake zones, anomalous structures in the upper mantle, and the lithosphere, J. Geophys. Res., 72, 4259-4275.

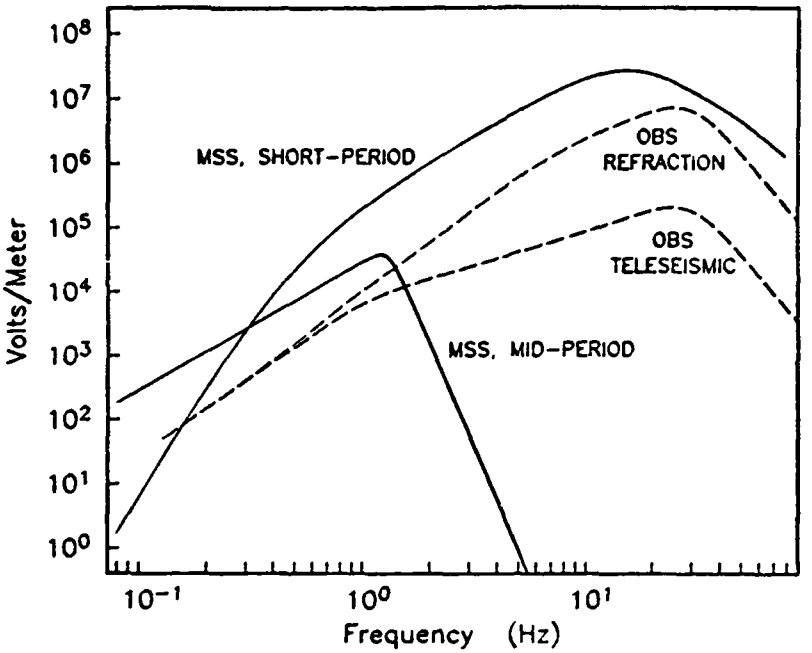


Figure 1. A comparison of the MSS and OBS response functions used in the Ngendei experiment. The MSS Nyquist frequency was 20 Hz; the response of the MSS was modified by a low pass FIR filter (not shown) to prevent aliasing. The OBS response is broader band and has a Nyquist frequency of 64 Hz.

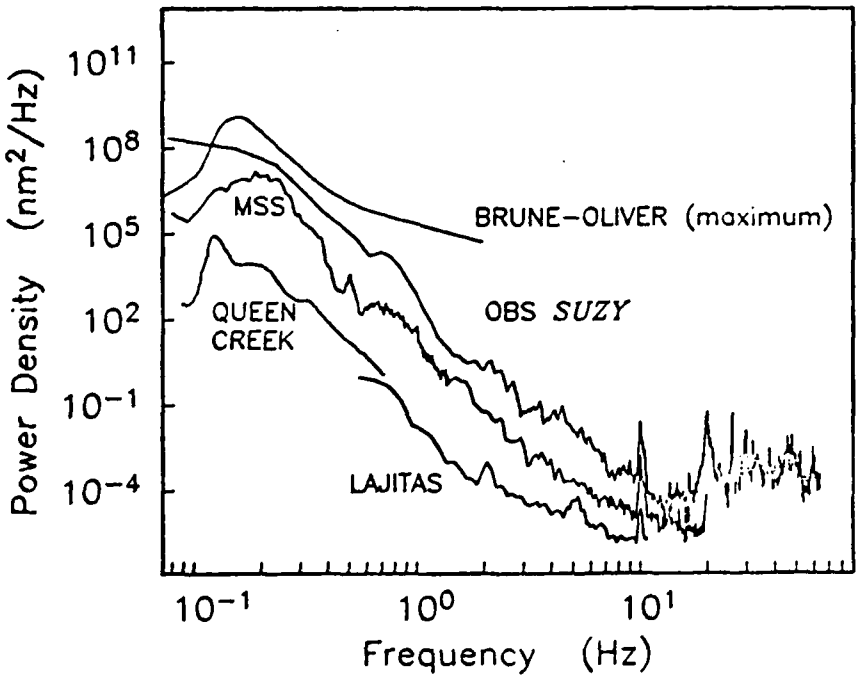


Figure 2. Power spectra of simultaneous sea-floor noise estimates for the MSS and OBS Suzy. These power spectra are compared to the Brune and Oliver continental upper bound and to two extremely quiet continental measurements described in the text. The 10-Hz and 20-Hz (overtone) peaks are ship noise from the D/V Glomar Challenger.

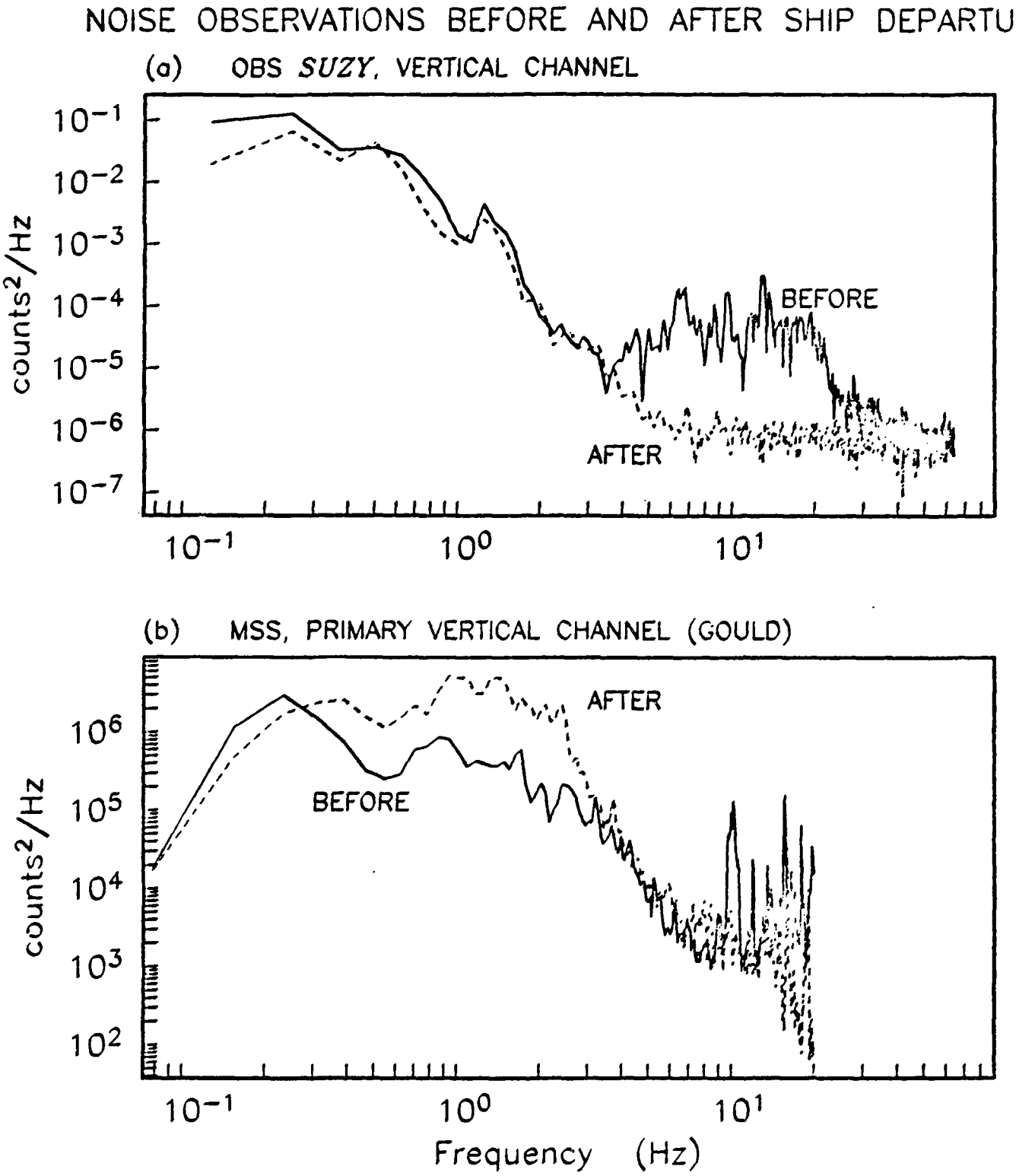


Figure 3. Power spectra, uncorrected for instrument response, illustrating the effect of ship noise on estimates such as those in the previous figure. At the sea floor, the ship noise is a significant contributor above a frequency of 3 Hz. The flat spectrum from OBS Suzy above a frequency of 8 Hz in the absence of ships is due to the digitizing noise associated with a 12-bit A/D converter.

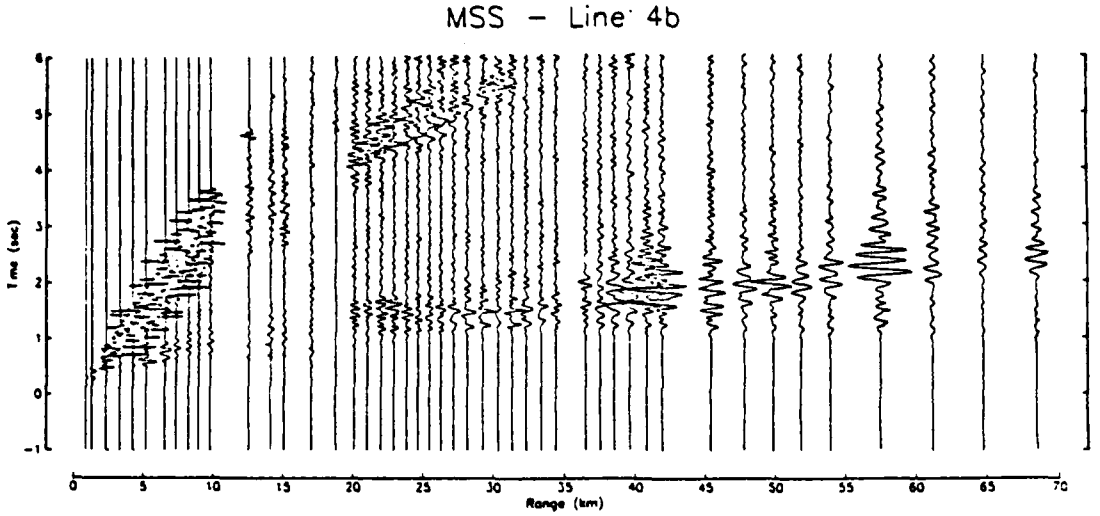


Figure 4. Marine Seismic System data from an explosion seismology line extending from the MSS/OBS array to the southwest reduced at 8 km s^{-1}. The MSS began its first recording when the epicentral distance was about 20 km; The events between 0 and 20 km were shot at a later time and, hence, cannot be directly compared to the OBS records in Figure 5. The crossover between Pn and crustal phases occurs at about 35 km. Note the large shear waves arriving at later times.

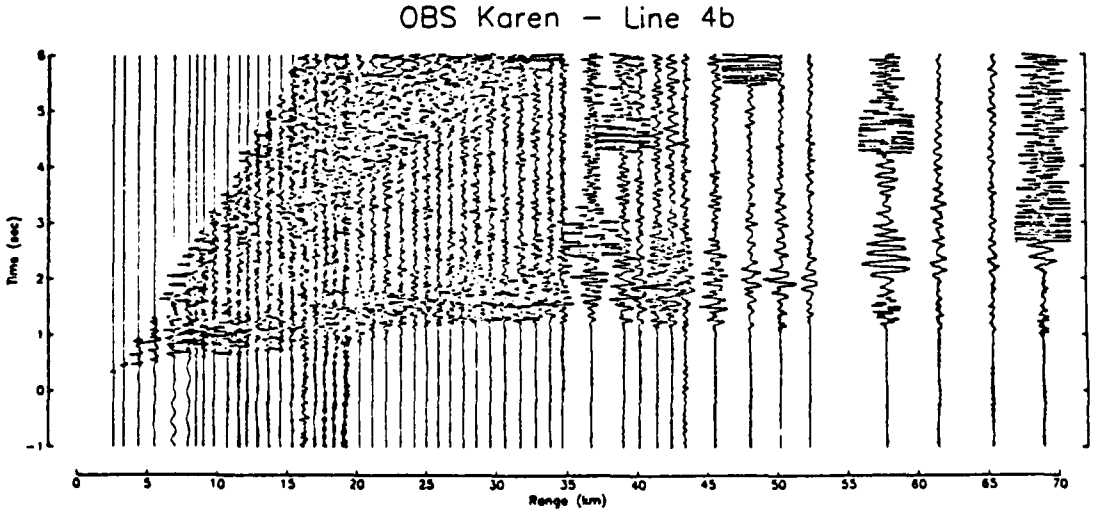


Figure 5. Same as Figure 4 as recorded by an OBS. The OBS records are noisier due to the presence of the D/V Challenger, and sediment reverberations contaminate the later portions of the record. The large impulses in some records (e.g. at 36.5 km) are caused by tape recorder turn-on transients after the OBS CMOS memory buffer had been filled.

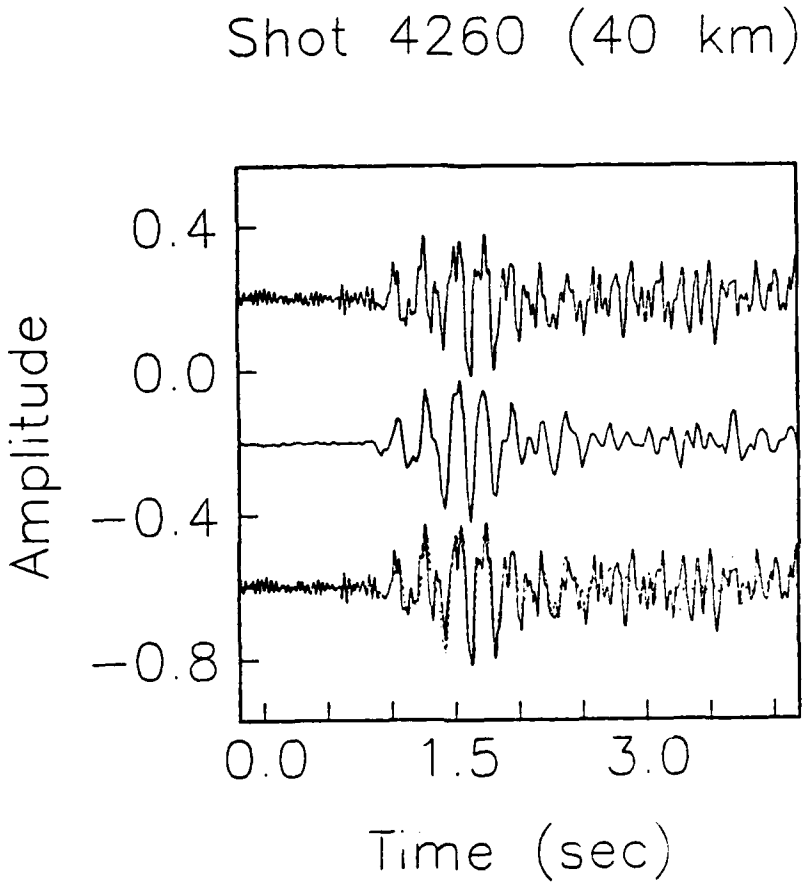


Figure 6. An event from profile 4B as recorded by an OBS (top trace) and the MSS (middle trace). The OBS record, with a greater bandwidth, contains a great deal of noise from D/V Challenger. The two seismograms are overlain in the bottom trace to emphasize the coherence of the P wave. The coherence deteriorates after 1.0-1.5 s as low-velocity shear-wave reverberations in the sediment are sensed by the OBS.

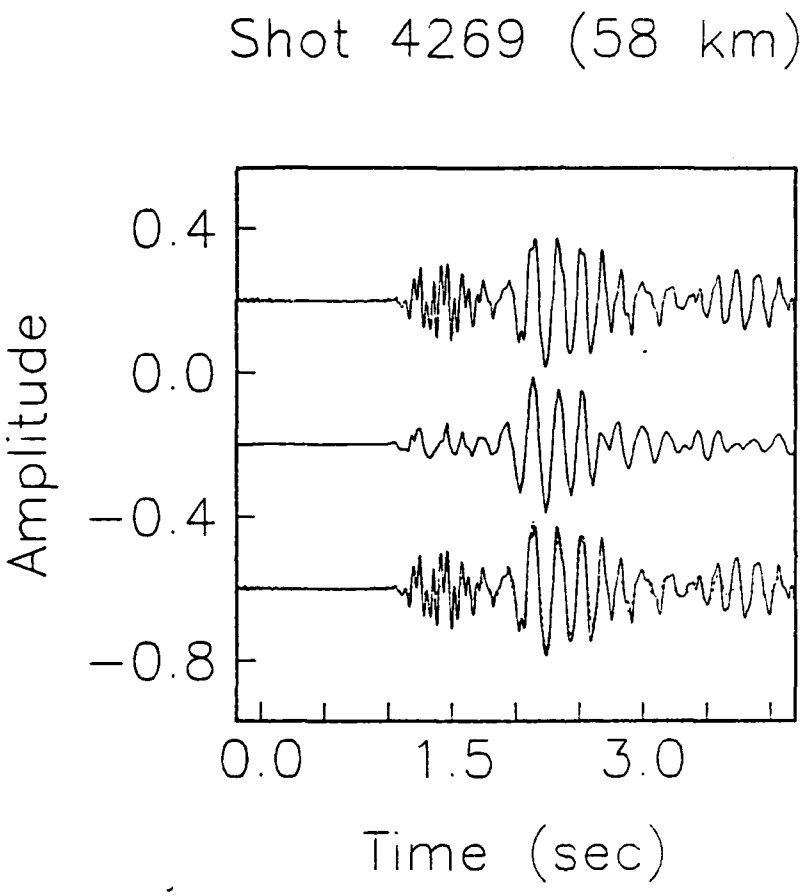


Figure 7. Another trace from profile 4B. The initial arrival is Pn while the large second arrival is a "reflection" from the Moho. Again the MSS appears as a low-passed version of the OBS data.

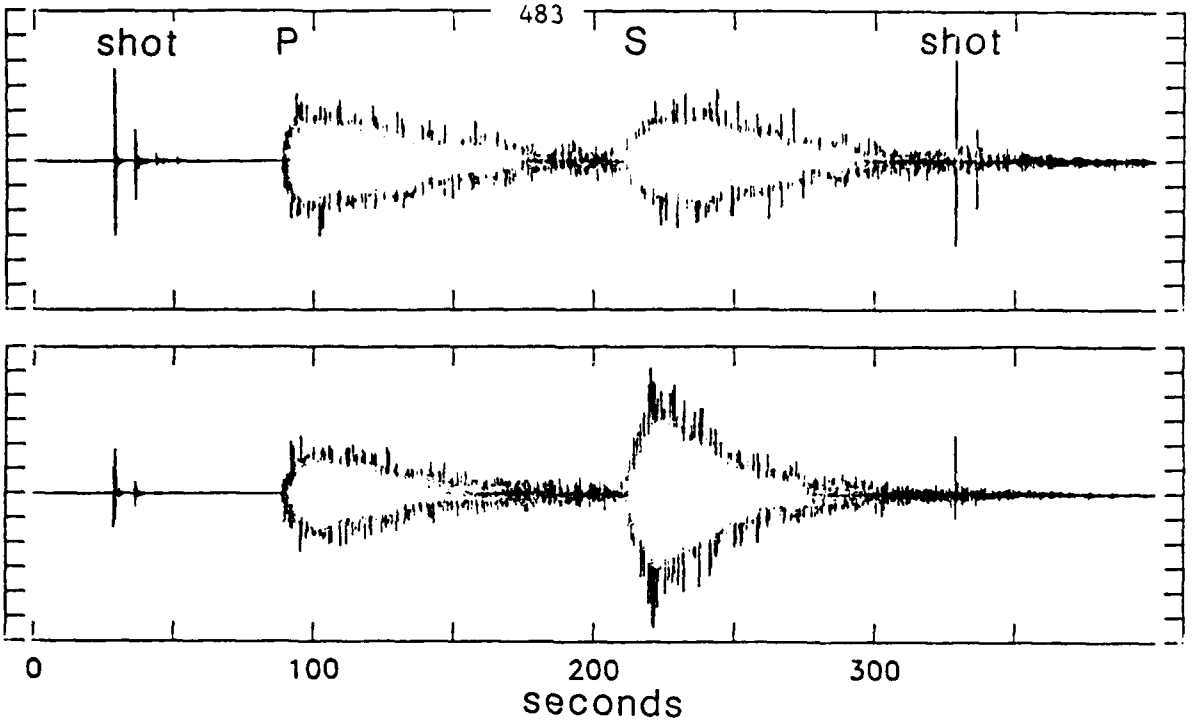


Figure 8. Short-period vertical (top panel) and horizontal (lower panel) seismograms recorded on the MSS from the shallow-focus (h=52 km) Kermadec earthquake of 7 Feb 83 (m_b = 6.0, Δ = 12.46°). Time is in seconds after 18:24:34.49 Z; tic-mark interval on vertical axis is 5 x 10^4 counts. Spikes near 30 s and 300 s are refraction shots.

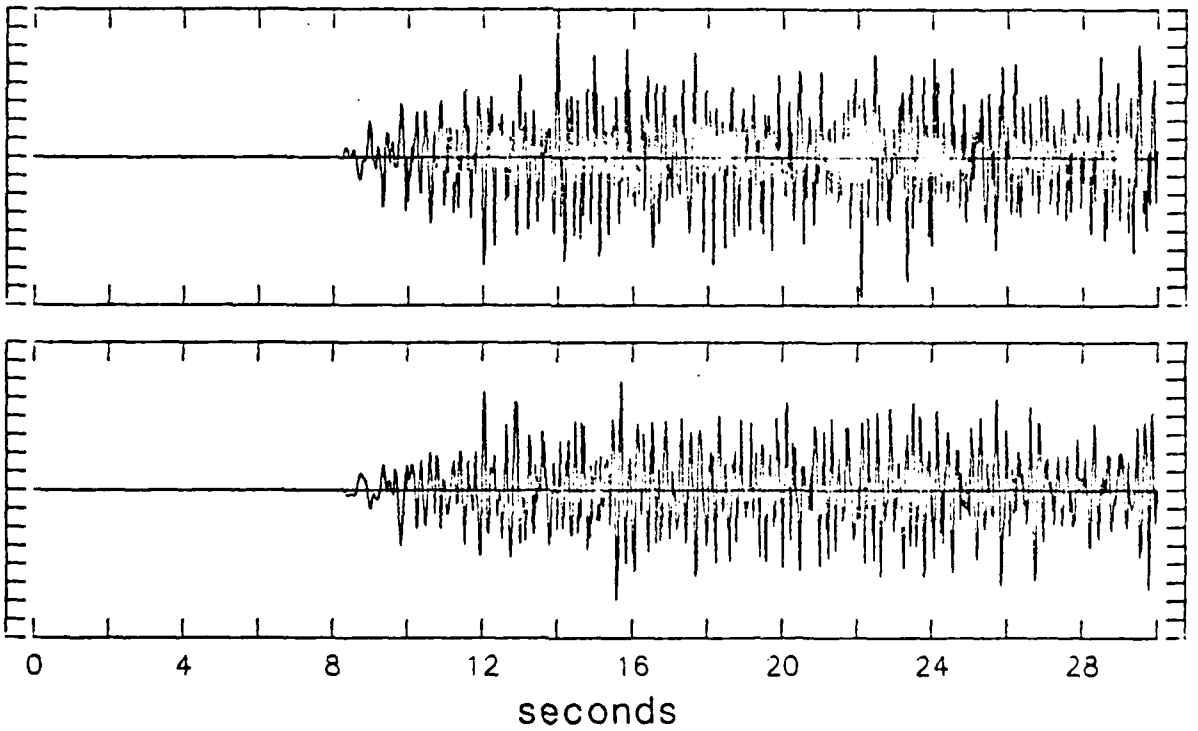


Figure 9. Short-period vertical (top panel) and horizontal (lower panel) seismograms from the shallow-focus earthquake of Figure 8, showing P-wave arrival on expanded time scale. Time is in seconds after 18:25:54.49 Z; tic-mark interval on vertical axis is 2 x 10^4 counts. The high-frequency, incoherently scattered energy observed on this record is characteristic of oceanic Pn at this distance (Δ = 12.46°).

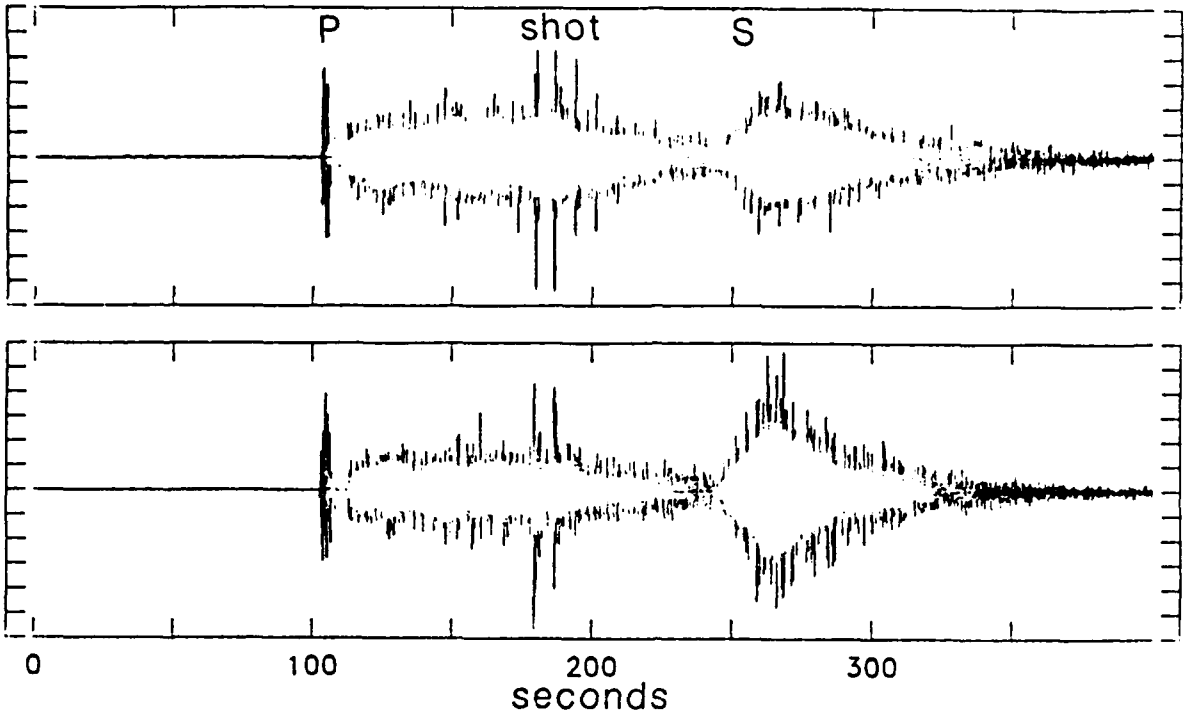


Figure 10. Short-period vertical (top panel) and horizontal (bottom panel) seismograms recorded on the MSS from the intermediate-focus (h = 293 km) Kermadec earthquake of 7 Feb 83 (m_b = 5.0, Δ = 12.91°). Time is in seconds after 17:57:04.49 Z; tic-mark interval on vertical axis is 5 x 10^3 counts. Spikes between 175 s and 205 s are arrivals from a refraction shot.

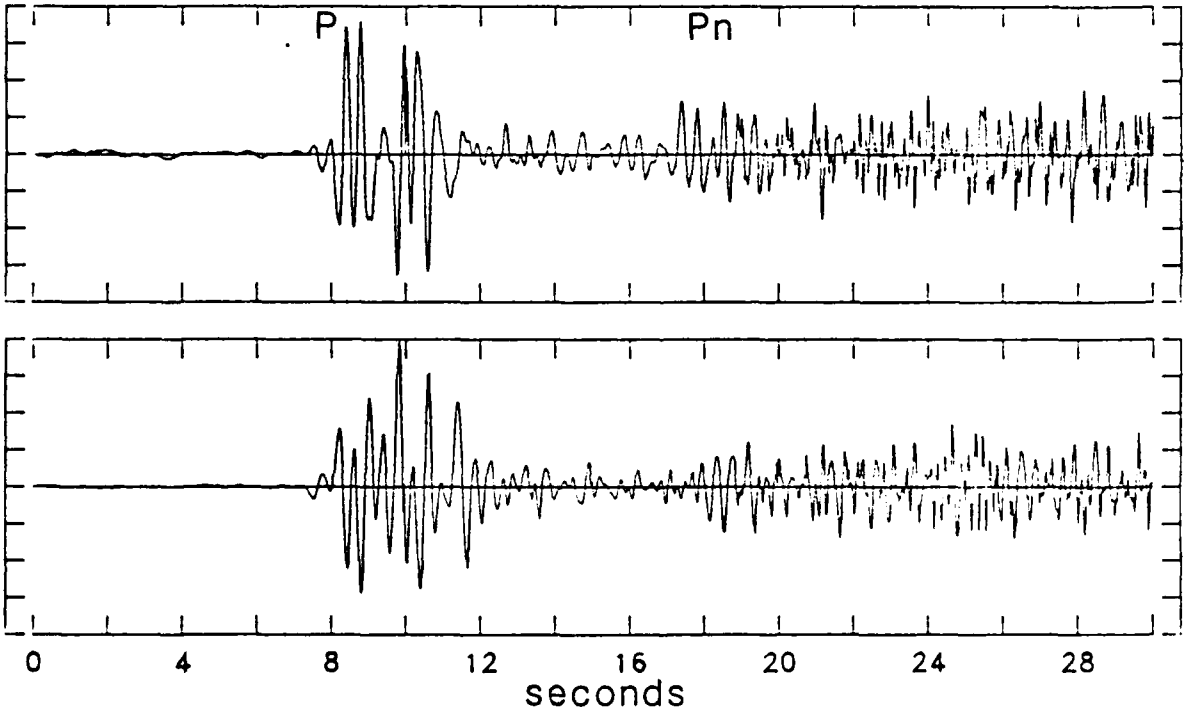


Figure 11. Short-period vertical (top panel) and horizontal (lower panel) seismograms from the intermediate-focus earthquake of Figure 10, showing P-wave arrivals on expanded time scale. Time is seconds after 17:58:39.49 Z; tic-mark interval on vertical axis is 5 x 10^3 counts. Complex P waveform between 7 s and 12 s is a triplication from the 400-km discontinuity. Arrivals following 18 s are Pn waves refracted up and around the corner of the lithospheric waveguide; their enrichment in high frequencies relative to P is indicative of the low Q of the sub-lithospheric mantle beneath the Southwest Pacific Basin.

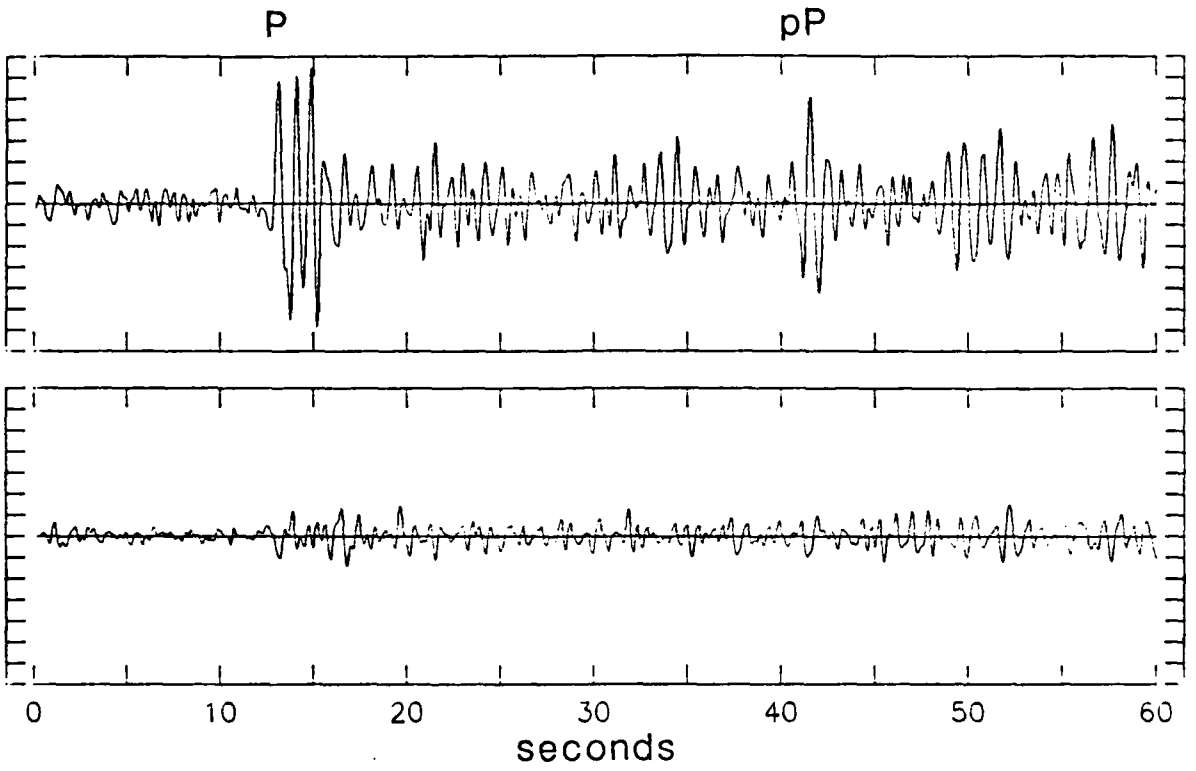


Figure 12. Short-period vertical (top panel) and horizontal (lower panel) seismograms recorded on the MSS at a distance of 61.2° from a teleseism in the Marianas Islands (13 Feb 83, h = 105 km, m_b = 5.7), showing P and pP arrivals. Tic-mark interval on vertical axis is 5 x 10^3 counts.

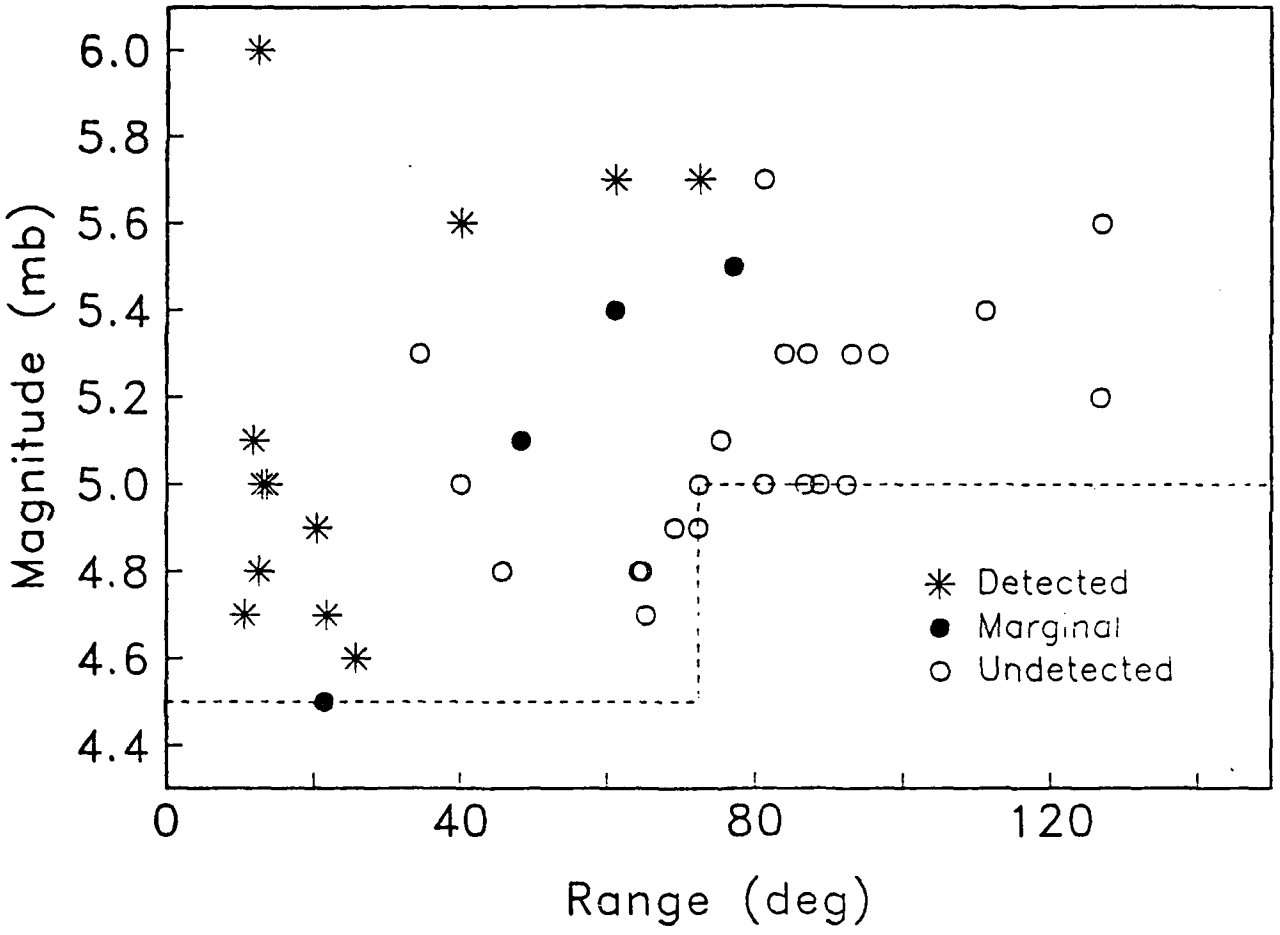


Figure 13. Diagram of body-wave magnitude versus epicentral distance showing NEIS-catalogued earthquakes detected by the MSS. Each symbol represents an earthquake located by the NEIS in the time interval of MSS recording (6 Feb 83, 14:37 Z through 13 Feb 83, 15:11 Z). Stars are events recorded with good signal-to-noise ratio; closed circles are marginal detections with signal-to-noise ratios near unity; open circles are events undetected by the MSS. Events with $m_b < 4.5$ at $\Delta \leq 72^\circ$ and $m_b < 5.0$ at $\Delta > 72^\circ$ were not included in the sample, nor were those whose signals were obscured by refraction shots and local earthquakes or whose records were missing because of deployment operations and engineering tests. As discussed in the text, the detection threshold for regional events ($\Delta \lesssim 15^\circ$) is less than magnitude 4.0.

CHAPTER 16

SYNTHETIC P_n AND S_n PHASES AND THE FREQUENCY DEPENDENCE OF Q OF OCEANIC LITHOSPHERE

Thomas J. Sereno, Jr. and John A. Orcutt

Institute of Geophysics and Planetary Physics,
Scripps Institution of Oceanography
La Jolla, California 92093

Submitted to J. Geophys. Res., July 1986

ABSTRACT

The oceanic lithosphere is an extremely efficient wave guide for high frequency seismic energy. In particular, the propagation of the regional to teleseismic oceanic P_n and S_n phases is largely controlled by properties of the oceanic plates. The shallow velocity gradient in the sub-Moho lithosphere results in a nearly linear travel time curve for these oceanic phases and an onset velocity near the material velocity of the uppermost mantle. The confinement of P_n / S_n to the lithosphere imposes a constraint on the maximum range that a normally refracted wave can be observed. The rapid disappearance of S_n and the discontinuous drop in P_n / S_n group velocity beyond a critical distance, dependent upon the local thickness of the lithosphere, is interpreted as a shadowing effect of the low Q asthenosphere. Wave number integration was used to compute complete synthetic seismograms for a model of oceanic lithosphere. The results were compared to data collected during the 1983 Ngendei Seismic Experiment in the southwest Pacific. The P_n / S_n coda is successfully modelled as a sum of leaky organ-pipe modes in the sediment layer and oceanic water column. While scattering is present to some degree, it is not required to explain the long duration and complicated nature of the P_n / S_n wave trains. The presence of extremely high frequencies in P_n / S_n phases and the greater efficiency of S_n than P_n propagation are interpreted in terms of an absorption band rheology. A shorter high frequency relaxation time for P waves than for S waves results in a rheology with the property that $Q_\alpha > Q_\beta$ at low frequency while $Q_\beta > Q_\alpha$ at high frequency, consistent with the teleseismic P_n / S_n observations. The absorption band model is to viewed as only an approximation to the true frequency dependence of Q in the oceanic lithosphere for which analytic expressions for the material dispersion have been developed.

INTRODUCTION

The oceanic lithosphere is an extremely efficient wave guide for high frequency seismic energy. The oceanic P_n and S_n phases (more recently designated P_o and S_o for ocean P and ocean S by *Walker*, 1982) propagate entirely within this wave guide and are commonly observed on ocean bottom seismometer records in the distance range of 5° to 30° (Figure 1). Three distinguishing characteristics are used to identify these phases.

(1) An onset that generally fits a travel time curve that is linear with an inverse slope near the material velocity of the uppermost mantle. The onset is quite often emergent with a gradual build up to an energy maximum that propagates near basal crustal velocities.

(2) The development of a high frequency wave train of extremely long duration (1-2 minutes). The P_n coda extends into the onset of S_n and generally has a longer duration than the S_n coda (*McCreery*, 1981; *Walker, et. al.*, 1983).

(3) Extremely low spatial attenuation. Frequencies as high as 15 Hz for P_n and 20 Hz for S_n have been reported at a distance of 3300 km for travel paths under the western Pacific (*Walker, et al.*, 1983). Estimates of the effective quality factor, Q, indicate a nearly elastic rheology for the oceanic lithosphere and losses in shear wave energy less than those in compressional wave energy (*Walker, et al.*, 1978; *Sutton, et al.*, 1978).

While the confinement of P_n and S_n to the oceanic lithosphere is relatively well established (*Oliver and Isacks*, 1967; *Isacks and Barazangi*, 1973; *Stephens and Isacks*, 1977; *Menke and Richards*, 1980), no commonly accepted theory for the mode of propagation of these phases exists.

It is generally accepted that P_n and S_n are in some sense guided phases yet the depth and nature of the proposed wave guide is still the subject of debate. The propagation of P_n within a wave guide immediately below the Moho has been suggested based on the group velocity of the P_n onset and the linearity of the travel time curve as a function of distance (*Sutton and Walker*, 1972; *Sutton, et al.*, 1978). The nomenclature, P_n, was developed from these models in analogy with the shorter range P_n headwaves.

Talandier and Bouchon (1979) proposed that the propagation of P_n occurs in a low velocity channel within the subcrustal lithosphere. For rays with phase velocities

between the minimum channel velocity and the velocity bracketing the channel, this provides an efficient wave guide. A problem exists, however, of getting energy into and out of the channel. Aside from tunneling, which is important mainly for low frequencies, the source must be located within the channel itself or energy must be scattered into it. Also, because P_n is observed throughout most of the Pacific basin, this model would require a fairly continuous sub-Moho low velocity zone to exist in much of the oceanic lithosphere.

It has also been suggested that P_n and S_n propagation takes place within a sub-Moho, high Q wave guide (*Walker*, 1977*a*; *Walker, et al.*, 1978; *Sutton et al.*, 1978). *Walker, et al.* (1978) estimated the effective quality factors for P_n and S_n with travel paths in the northwest Pacific for two separate earthquakes yielding P_n values of 3700 ± 200 and 8400 ± 1300 and S_n values of 8500 ± 600 and $19{,}100 \pm 3700$. In fact *Walker* (1977*a*) reports dual wave guides in this region because observed velocities near 7.87 km/s for distances in excess of 30° are significantly less than shorter range velocities of 8.33 km/s. He proposed that the slower wave guide was more efficient and therefore propagated the high frequency energy to longer ranges.

The propagation of high frequency energy between thin, high-velocity lenses in the lower lithosphere was suggested by *Fuchs and Schulz*, (1976). Their model consists of a finely layered oceanic lithosphere in which the thin lenses, embedded within material with "normal" mantle velocities, provide an effective wave guide for P_n / S_n wave propagation. The reflections between the lenses occur at post-critical incidence and losses are largely confined to low frequencies which tunnel through the lenses. This model predicts the long coda of these phases due to the many different propagation paths between the lenses. The authors suggest that the same mechanisms which induced preferred orientation in anisotropic minerals (ie. creep in the regional stress field) are also responsible for the horizontal orientation of the lenses.

A study of S_n propagation in terms of normal modes was conducted by *Stephens and Isacks* (1977). They concluded that S_n can be modelled as a sum of "lid modes," with group velocity maxima near the velocity of the uppermost mantle, which develop at high mode numbers and short periods. Sphericity alone is sufficient to provide a wave guide for S_n and particle motion is restricted largely to depths above the low velocity zone of the upper mantle. Because of leakage of low frequency energy, the wave guide is efficient only for high frequencies.

A similar interpretation for oceanic P_n phases was made by *Menke and Richards*, 1980. They modelled P_n as a sum of whispering gallery phases with upward reflection

points at the Moho and turning points deep within the oceanic lithosphere. The entrapment of P_n in the lithosphere lid avoids the depletion of high frequency energy which occurs when a normally refracted P wave crosses the low Q asthenosphere. The individual rays of the whispering gallery are labelled WGn where n is the number of upward reflections at the Moho. Rays turning in the lower lithosphere selectively lose their low frequencies through tunneling into the asthenosphere. This model also predicts the discontinuous drop in P_n group velocity at large epicentral ranges (*Walker*, 1977*a*; *Walker*, 1981) where WG1 has a turning point below the low velocity zone and WG2 is the first arrival of P_n. This model does not, however, predict the long coda of P_n. The infinity of rays in the whispering gallery all arrive just a few seconds after WG1. The authors attribute the long coda to scattering from heterogeneity along the propagation path. The model also underestimates the amplitude ratio of P_n to P by a factor of 10.

A serious problem with any P_n / S_n wave guide that does not include the oceanic water column is that, to be observed by an ocean bottom seismometer or hydrophone, it must be leaky but at the same time efficient. This is the case for any sub-Moho wave guide, propagation between thin, high-velocity lenses or a whispering gallery at the crust-mantle boundary.

Two mechanisms for the development of long P_n and S_n codas have been proposed. While both scattering and layer resonance contribute to the seismic coda there has been considerable debate as to which of the two is the dominant mechanism in oceanic P_n and S_n phases. Numerical models involving the development of long coda by net forward scattering in a medium including a random distribution of small scale heterogeneities have been developed (*Richards and Menke*, 1983; *Menke and Chen*, 1984). The scattering properties of a single thin layer embedded between two homogeneous halfspaces are considered and then an ensemble average over many such layers yields the response in a randomly layered medium. The coda of P_n is then presented as a product of the interaction of seismic energy in this complex medium.

Gettrust and Frazer (1981) pointed out that, by using reflectivity for a simple oceanic lithosphere structure, a coda 20 s long could be generated in the absence of scattering. They attribute the coda to a combination of free surface reflections and multiple bounces in the crust.

In this paper (and two earlier papers on P_n (*Sereno and Orcutt*, 1985*a*,*b*)), we contend that the propagation of high frequency oceanic P_n and S_n phases can be explained rather simply as a refraction from the lower oceanic lithosphere while the subsequent coda is predominantly a result of near-receiver sediment and water reverberations.

Complicated oceanic lithosphere models are not needed to explain the gross characteristics of these high frequency phases. The attenuation properties of P_n and S_n are interpreted in terms of an absorption band rheology. A shorter high frequency relaxation time for P waves than for S waves results in a rheology with the property that $Q_\alpha > Q_\beta$ at low frequency while $Q_\beta > Q_\alpha$ at high frequency. The development of a substantial P_n / S_n coda due to sediment and ocean layer resonances is presented first while the effects associated with the propagation paths of the first arrivals are treated separately.

P_n / S_n CODA

We have shown, in a previous paper (*Sereno and Orcutt*, 1985*b*), that the development of complicated P_n and S_n codas can be achieved in the absence of scattering. Wave number integration (*Apsel*, 1979) was used to compute synthetic seismograms for a realistic oceanic lithosphere model. The synthetic P_n and S_n wave trains result from the propagation of leaky organ-pipe modes in the oceanic water column and sediment layer. Spectral peaks associated with acoustic modes in the water column and both compressional and shear wave modes in the sediment layer were observed in the synthetics and in data collected during the 1983 Ngendei Seismic Experiment in the southwest Pacific (23°49′ S, 165°32′ W). In this investigation, we have computed complete synthetics for a model of the Ngendei site for direct comparison to the data. Furthermore, the propagation path of the first arrivals of P_n and S_n, as well as implications for properties of the oceanic lithosphere, are described in a more quantitative manner. In particular, constraints on the rheology of the oceanic lithosphere are suggested.

Ngendei model. The oceanic lithosphere model used in the computation of the synthetic seismograms was chosen on the basis of a refraction study conducted during the 1983 Ngendei Seismic Experiment in the southwest Pacific (23°49′S, 165°32′W). An ocean bottom seismometer (OBS) array was located approximately 900 km east of the Tonga trench and recorded numerous regional oceanic P_n phases which were available for comparison to the synthetics. The Ngendei site was also the location of hole 595B of Deep Sea Drilling Project (DSDP), leg 91. The depth of the oceanic water column at the site is 5.55 km and, from core sample measurements, the sediment thickness is 70 m with a compressional velocity of 1.6 km/s (*Kim, et al.*, 1986). The model is listed in Table 1. A single source depth of 15 km was used in the computation and the receivers were on the sea floor at epicentral ranges of 500 to 1500 km.

Each of the Green's functions were computed at 16385 frequency points extending to a Nyquist frequency of 12.8 Hz. The number of slowness points required by the integration at a single frequency was typically of the order of 1800. The fine frequency sampling was necessary to avoid temporal aliasing.

Figures 2, 3, and 4 display the full set of Green's functions for the Ngendei model at a range of 1000 km. Group velocities of 8.1 and 4.65 km/s are indicated by vertical lines in the top figure. Vertical displacement for an arbitrarily oriented double-couple source is obtained through linear combination of the four stress tensor elements in Figure 2 (*Sereno*, 1986; *Shaw and Orcutt*, 1984). Similarly, radial displacement is obtained through linear combination of the Green's function in Figure 3 and transverse displacement is obtained from the Green's functions in Figure 4.

Examination of the Green's functions for vertical displacement (Figure 2) and radial displacement (Figure 3) indicates that the vertically polarized component of S_n is strongly dependent upon the source mechanism. Only sources that include a substantial fraction of the shear stress Green's functions will yield strong S_n signal levels. For example, an explosion source, which is obtained through linear combination of the diagonal elements of the stress tensor (*Sereno*, 1986), would generate only a very weak S_n signal.

Figure 5 illustrates vertical and radial displacement at the sea floor at a range of 1000 km for a sub-Moho thrust fault. The fault used had a dip of 25°, a rake of 270°, and an azimuth relative to the receiver of 60°. The synthetic radial component oceanic P_n and S_n phases very closely resemble data collected at the Ngendei site. The substantial coda of these phases is modelled as a sum of leaky organ-pipe modes in the oceanic water column and sediment layer. Shear wave resonance is particularly prominent on the horizontal component due to the steep incidence of the rays at the receiver. The impulsive character of the water reverberations in the synthetic vertical component P_n wave train does not, however, emulate the data. The vertical component coda results predominantly from compressional wave reverberation in the oceanic water column and sediment layer. Due to the low impedance contrast at the ocean-sediment interface for compressional waves, the sediment modes are extremely leaky and die out long before the arrival of the next water multiple. Clear water multiples *are* observed in data and several factors could reduce the discreteness of these reverberations. Three possible explanations of the discrepancy are scattering, coupling of vertical and horizontal components, and a frequency dependent Q. These alternatives will be discussed in the attenuation section.

The acoustic velocity of the water layer, ≈ 1.5 km/s, is substantially lower than typical crustal velocities. This results in a high impedance contrast between the water

column and oceanic crust. Rays can therefore be trapped in the uppermost part of the structure, even with high incidence angles, without significant energy loss. Thus a resonance in the water column can be established which, for high phase velocities, can be characterized as a sum of leaky organ-pipe modes (*Aki and Richards*, 1980; p. 330). Additionally, the extremely high value of Q in the oceanic water column renders the loss of energy due to anelasticity insignificant. The result is a long reverberatory wave train for oceanic structures due to near-receiver resonance.

A further complication to seismograms recorded in a marine environment arises from the blanket of low velocity oceanic sediments covering most of the world's ocean floor. The surface layers of sediment have very low rigidity and a density near that of water. Shear wave velocities are typically a few hundred meters per second (*Hamilton*, 1976) and compressional velocities are only slightly greater than the acoustic velocity of the overlying water column. The sediments act as an extremely efficient wave guide for shear wave propagation and as a leaky wave guide for compressional wave propagation. The impedance contrast for shear waves at both the ocean-sediment and sediment-crust interfaces is quite high, even for near-vertical incidence. The shear wave energy is thus trapped in the sediment layer as a sum of organ-pipe modes. Compressional waves have a much lower impedance contrast at the ocean-sediment interface and therefore propagate as extremely leaky organ-pipe modes in the sediment layer. Due to the much shorter two-way travel time through the sediment layer, as opposed to the water column, the sediment reverberations do not substantially increase the length of the time series. They do, however, severely complicate the waveforms.

As illustrated by *Sereno and Orcutt* (1985*b*), the importance of reverberations within the oceanic water column and sediment layer in the development of a substantial P_n / S_n coda is most effectively demonstrated in the frequency domain. It was shown that the power spectrum of a wavelet reverberating in a single layer contains peaks at frequencies given by

$$f_n = (2n+1)\frac{df}{2}, \quad n = 0,1,2,... \tag{1}$$

where $df = 1/T$ and T is the time between multiples. In the case of near-vertical incidence T can be approximated by the two-way travel time in the layer and (1) represents the eigenfrequencies for organ-pipe modes. The $df/2$ offset of the spectral peaks is due to a π-phase shift between multiples. The width of the spectral peaks is related to the temporal decay rate of the wave train. There are several factors which can

influence this parameter, the most important of which are the impedance contrast at the boundaries of the layer and the time between multiples. The temporal decay rate due to propagation within a leaky wave guide is the amount of loss per reflection, governed by the impedance contrasts, divided by the time between multiples. Anelasticity can also effect the decay rate of the wave train, however its main effect is to reduce the high frequency content between successive multiples rather than the amplitude.

The development of the P_n coda will be discussed first and the S_n coda will be treated subsequently. Compressional wave reverberations are strongest on the vertical component due to the steep incidence of the rays at the receiver. Water reverberations, which actually occur between the free surface and the base of the sediments, are schematically illustrated in Figure 6*a*. Three points are to be drawn from this figure:

(1) The time between multiples is between 7.4 and 7.5 s yielding a spectral peak spacing of less than 0.14 Hz.

(2) The reflection coefficients at both interfaces are quite high (-1 at the free surface and 0.78 at the sediment-crust interface for a phase velocity of 8 km/s) resulting in narrow spectral peaks.

(3) The reflection coefficient at the free surface is negative inducing the π-phase shift between multiples.

Compressional wave sediment reverberation is schematically illustrated in Figure 6*b*. In this case:

(1) The time between multiples is only 0.0875 s resulting in an extremely wide spectral peak spacing. For the Ngendei site this spacing is 11.43 Hz.

(2) The impedance contrast at the ocean-sediment interface is quite small for compressional waves. Thus the sediment layer acts as an extremely leaky wave guide for compressional wave propagation and the peaks associated with sediment reverberation have a large characteristic width.

(3) The reflection coefficient at the ocean-sediment interface is negative yielding the π-phase shift between multiples.

These features are clearly illustrated in the synthetic vertical component power spectrum displayed in Figure 7. A Hanning window was applied over the first 80 s of the vertical component synthetic P_n wave train of Figure 5*a* prior to computing the spectrum. Figure 7*a* contains the first 3.0 Hz of the spectrum with vertical lines indicating predicted frequencies of resonance within the oceanic water column. Figure 7*b* is the full spectrum and displays a broad uplifted region centered at 5.7 Hz due to compressional wave reverberation in the sediments. A perhaps more convincing demonstration of the P wave sediment reverberation contribution to the P_n coda comes from examination of the frequency-ray parameter wave field. Figure 8 is the modulus of the vertical normal stress, $k\sigma_{220}(\omega,p)$, for the Ngendei structure. The broad feature centered at 5.7 Hz is due to the fundamental leaky organ-pipe mode in the sediment layer. This dependence was verified by increasing the layer thickness by a factor of 2 and recomputing the wave field. The eigenfrequency spacing decreased by a factor of two and the contributions of the fundamental and first higher modes were both contained in the 12.8 Hz band.

The spectral characteristics of sediment and water layer resonances observed in the synthetic P_n wave trains are also clearly seen in the Ngendei data. Figure 9 illustrates the presence of compressional wave reverberation in the P_n coda. Figure 9*a* plots hydrophone data and Figure 9*b* illustrates the first 3.0 Hz of the P_n power spectrum. Vertical lines indicate predicted eigenfrequencies of water layer resonance. Figure 9*c* is vertical component data and Figure 9*d* is its power spectrum. The vertical lines indicate the predicted eigenfrequencies for leaky compressional organ-pipe modes in the sediment layer. The wide spacing and large characteristic width, due to the low impedance contrast at the ocean-sediment interface, agree with predictions for P wave sediment resonance. The water reverberation peaks, which are separated by less than 0.2 Hz (Figure 9*b*), when plotted on a scale extending to 64 Hz appear rather incoherent as in Figure 9*d*. The isolated peaks at 34.3 and 50.7 Hz are due to instrument noise. Comparison of Figure 9 with Figures 7 and 8 quite clearly demonstrates the presence of water and compressional wave sediment resonance in the vertical component P_n data.

Shear wave sediment resonance, while observable on the vertical component, is strongest on the horizontal component due to the steep incidence of the rays. Figure 10 is a schematic illustration of shear wave sediment reverberation. In this case:

(1) The two-way travel time for shear waves in the sediment layer is 1.2 s yielding an eigenfrequency spacing of 0.83 Hz.

(2) For shear waves the impedance contrasts at both interfaces are quite large resulting in a rather narrow spectral width.

(3) The reflection coefficient at the sediment-crust interface is negative inducing the π-phase shift between multiples.

Figure 11 is the power spectrum of the radial component P_n wave train of Figure 5*b*. The eigenfrequencies of shear wave sediment resonance are delineated by vertical lines. Figure 12 is the modulus of the horizontal normal stress, $k\sigma_{221}(\omega,p)$, for the Ngendei structure. The conspicuous ridges separated by 0.83 Hz are shear wave sediment organ-pipe modes which can be easily verified by changing the layer thickness and recomputing the wave field. The spacing, width, and rapid decay with increasing mode number (due to the low value of Q_β in the sediment layer) all agree with predictions for S wave sediment reverberation. Figure 13 is a comparison of the first 3.0 Hz of the synthetic horizontal component power spectrum to data spectra. Figure 13*a* is the synthetic P_n spectrum of Figure 11 after including the OBS instrument response and a source spectrum of the form (*Aki and Richards*, 1980; p.823)

$$|S(f)|^2 = \frac{|S(0)|^2}{\left(1+\frac{f}{f_c}\right)^4} \qquad (2)$$

In (2), f_c is the corner frequency and was assigned a value of 0.8 Hz. Figure 13*b* is the synthetic spectrum without including the instrument response. Figure 13*c* is the first 3.0 Hz of the power spectrum of horizontal component data taken at the Ngendei site and 13*d* was obtained by removing the instrument response. The OBS instrument response calibration has been shown to be reliable above 0.1 Hz (*Adair, et al.*, 1986). In Figures 13*a*-13*d*, dashed vertical lines indicate predicted eigenfrequencies of shear wave sediment organ-pipe modes for a shear wave sediment velocity of 116 m/s. The instrument response is a strongly increasing function of frequency in this band and therefore has the effect of severely attenuating the first shear wave sediment resonance peak. The dominant resonant frequency of the horizontal component OBS data thus arises from the first higher organ-pipe mode in the sediment layer. The fundamental mode is strongly attenuated by the instrument and the absence of higher modes may be due to the rather low value of Q_β in the sediment layer. In the synthetics, a rather high value of 100 for Q_β in the sediment layer was used, possibly accounting for the strength of the higher

modes. Note, however, that a linear scale was used in this figure.

The oceanic S_n coda is similarly characterized as a sum of organ-pipe modes in the oceanic water column and sediment layer. Figure 14 is an example of OBS horizontal component data collected at the Ngendei site. A strong, high frequency onset ($t \approx 97$ s) followed by a monochromatic shear wave sediment resonance, typical of marine horizontal components, characterize the oceanic S_n phase.

To demonstrate the importance of layer resonance in the development of a substantial S_n coda, spectral estimates of the synthetic radial and transverse component S_n wave trains were computed. Figure 15*a* is the power spectral estimate of the radial component S_n wave train. The propagation of shear wave organ-pipe modes in the sediment layer is manifested in the spectrum as a set of equally spaced peaks separated by 0.83 Hz. The predicted eigenfrequencies for these modes are delineated in Figure 15*a* by vertical lines. The alignment of the peaks with the predicted frequencies clearly demonstrates the presence of shear wave sediment resonance in the S_n coda. The finely spaced peaks in this diagram, separated by less than 0.2 Hz, are due to compressional wave reverberation in the oceanic water column. The spacing of these peaks is the reciprocal of the time between multiples for a phase velocity near 4.7 km/s. Figure 15*b* is the power spectral estimate of the synthetic transverse component S_n wave train. The predicted eigenfrequencies of shear wave sediment resonance are again delineated by vertical lines. The transverse component S_n coda consists only of a sum of shear wave organ-pipe modes in the sediment layer in that *SH* propagation is independent of the overlying water column.

The shear wave sediment resonance can also be seen in the frequency-ray parameter wave fields. Plotted in Figure 16 is

$$k\sigma_{211}(\omega,p) + k\sigma_{231}(\omega,p) \tag{3}$$

which, when multiplied by a Bessel function of order one and integrated, yields

$$\Sigma_{rz1}(\omega) - \Sigma_{\theta z1}(\omega). \tag{4}$$

$\Sigma_{\theta z1}$ (Figure 4) is a Green's function for transverse displacement and therefore contains only S_n. Σ_{rz1} (Figure 3) has a strong S_n phase and only a very weak P_n signal level. The wave field in Figure 16 is therefore a good approximation to the actual

decomposition of the S_n phase into the contributions from different ray parameters. Initially it was thought that the S_n coda would be strongly contaminated by the presence of crustal P phases with phase velocities between the compressional velocity of the lowermost crust and that of the uppermost crust. Figure 16 illustrates, however, that the dominant contribution to S_n, especially at high frequency, arises from a narrow range of ray parameters near the reciprocal of the shear wave velocity of the uppermost mantle. Contributions from lower ray parameters, associated with crustal P phases, are significantly smaller in amplitude. The conspicuous ridges in Figure 16, separated by 0.83 Hz, are shear wave sediment organ-pipe modes. The excitation of the peaks by these resonances is easily verified by changing the layer thickness and recomputing a section of the wave field.

Shear wave sediment resonance in S_n data collected at the Ngendei site is demonstrated in Figure 17. This figure is a comparison of the first 3.0 Hz of the synthetic radial component power spectrum to data spectra. Figure 17*a* is the synthetic S_n spectrum of Figure 15*a*. Figure 17*b* is the synthetic spectrum without including the instrument response. Figure 17*c* is the first 3.0 Hz of the power spectrum of horizontal component data taken at the Ngendei site and 17*d* was obtained by removing the instrument response. In Figures 17*a*-17*d*, dashed vertical lines indicate predicted eigenfrequencies of shear wave sediment organ-pipe modes for a shear wave sediment velocity of 116 m/s. As was the case for the P_n coda, the dominant resonant frequency of the horizontal component S_n OBS data arises from the first higher organ-pipe mode in the sediment layer. Note that a linear scale was used in this figure.

In this section it has been demonstrated that the development of long P_n / S_n codas is due primarily to resonance within the oceanic water column and sediment layer. Other aspects of P_n / S_n propagation, such as the linearity of the travel time curve, the discontinuous drop in group velocity at large epicentral ranges, and the presence of extremely high frequencies are consequences of the entrapment in the oceanic lithosphere. These propagation effects are discussed in the following section.

PROPAGATION PATH

The presence of a sharp contrast in the attenuation properties of the oceanic lithosphere and underlying asthenosphere is well documented (*Oliver and Isacks*, 1967; *Barazangi, et al.*, 1972; *Smith*, 1972; *Anderson and Hart*, 1978*b*). Extremely high frequencies in the oceanic P_n phase observed at teleseismic distances (*Walker, et al.*, 1978; *Sutton, et al.*, 1978) thus indicate that the phase does not penetrate the low Q asthenosphere.

That P_n velocity increases with increasing age of the lithosphere has been suggested by numerous authors (*Hart and Press*, 1973; *Chinn, et al.*, 1980; *McCreery*, 1981). This result is expected for rays that remain in the lithosphere in that as the plate ages it cools and compacts yielding slightly higher velocities. Further evidence for the confinement of this phase to the lithosphere comes from the inefficiency of propagation across tectonic features such as mid-ocean ridge systems (*Walker*, 1977*b*; *McCreery*, 1981; *Walker*, 1982). Lateral variations in lithosphere thickness and properties are strongest in these tectonic regions and a resulting change in the nature of P_n propagation across such boundaries is expected.

Similarly, the onset of the oceanic S_n phase is a shear wave that propagates entirely within the lithosphere and does not penetrate the low Q asthenosphere (*Molnar and Oliver*, 1969; *Hart and Press*, 1973; *Isacks and Barazangi*, 1973; *Stephens and Isacks*, 1977; *Chinn, et al.*, 1980). The strongest evidence for the confinement of S_n to the oceanic lithosphere is the presence of extremely high frequencies at teleseismic distances (*Walker, et al.*, 1978; *Sutton, et al.*, 1978). Estimates of the effective quality factor of S_n greatly exceed those of a normally refracted S wave that has crossed the low Q asthenosphere. Furthermore, the efficiency of S_n propagation is greatly reduced across tectonic features, such as mid-ocean ridge systems or the concave side of Island arcs (*Molnar and Oliver*, 1969; *Walker*, 1977*b*; *McCreery*, 1981). The increase in S_n velocity as a function of lithosphere age (*Hart and Press*, 1973; *Walker*, 1977*b*) constitutes further evidence that the propagation of S_n is controlled by properties of the lithosphere.

Normal mode theory for a layered medium (*Kennett*, 1983) was used to compute dispersion curves and partial derivatives of phase velocity with respect to material velocity as a function of depth for the Ngendei model. The decomposition of the seismic wave field into a discrete set of modes is an extremely useful tool for the interpretation of various parts of the seismogram. The radial and transverse components of S_n are similar in character with the most notable exception being that water layer resonance is an important part of the radial component S_n coda while it is absent from the transverse component. Nevertheless, the study of Love waves alone can yield useful information about the propagation of S_n.

The phase velocity dispersion curves for the first 50 Love wave modes are presented in Figure 18. The most obvious feature of this diagram is the tessellating behavior of the dispersion curves. Kinks in these curves develop in response to layer resonance and crustal propagation. The nearly vertical structure in Figure 18 is due to shear wave organ-pipe mode propagation in the sediment layer. Crustal propagation is manifested as nearly horizontal features in the dispersion curves, especially at high frequency. This

disruption in the regular spacing of the eigenfrequencies, due to first order discontinuities in model parameters, is referred to as a *solotone* effect (*Kennett*, 1983). Dashed horizontal lines indicate layer velocities in the model (Table 1). The sediment, uppermost crust, lowermost crust, and mantle shear wave velocities are shown. The summation of the excitation functions of these modes yields a superposition of relatively non-dispersed crustal and mantle body waves with an extended shear wave sediment resonance. Figure 19 is an expanded view of the high frequency, high phase velocity portion of the dispersion curves. Love wave modes 25-49 are included. Because the algorithm includes only locked modes, the curves are truncated at a phase velocity equal to the highest shear wave velocity of the model, 4.693 km/s. The nearly horizontal features at phase velocities of 4.678 and 4.664 km/s are *solotone* effects from model discontinuities in the mantle (see Table 1).

Group velocity is related to phase velocity via

$$u(T) = \frac{C(T)}{1+\frac{T}{C}\frac{dC}{dT}} \tag{5}$$

where u is group velocity, C is phase velocity, and T is period. Therefore group velocity maxima develop at the nearly horizontal portions of the phase velocity dispersion curves. Figure 19 thus indicates that high frequency, higher mode Love waves have group velocity maxima near the shear wave velocity of the uppermost mantle. It is also found that these modes have particle displacements largely restricted to the sub-Moho portion of the oceanic lithosphere. Figure 20 contains the partial derivative of phase velocity with respect to material velocity as a function of depth, at a frequency of 5.0 Hz, for a variety of Love wave modes. The Moho depth is indicated by a solid horizontal line at 12.2 km. The mode number for each curve is shown on the bottom. The lower order modes, at high frequency, sample mainly the oceanic crust while the higher modes sample an increasing fraction of the high Q, sub-Moho portion of the lithosphere. These higher modes constitute the high frequency onset of S_n and have phase velocities very nearly equal to the group velocity of ≈ 4.65 km/s. This is also demonstrated in Figure 16 which shows the high frequency contribution to S_n is confined mainly to high phase velocity, higher modes.

These results are in agreement with those of *Stephens and Isacks* (1977) who concluded that S_n could be modelled as a sum of "lid modes" with group velocity maxima near the material velocity of the uppermost mantle which develop at high mode numbers

and short periods. These modes have phase velocities restricted between the sub-Moho shear wave velocity and that at the base of the lithosphere. Particle displacement is largely confined to depths above the low velocity zone of the upper mantle. Longer period energy, on the other hand, samples the low Q asthenosphere and therefore they concluded that the lithosphere wave guide is efficient only at short periods. The locked mode approximation is, however, inappropriate for the computation of synthetic S_n phases in that the coda is dominated by leaky organ-pipe mode propagation in the water column and sediment layer.

A discontinuous drop in P_n group velocity, observed by *Walker* (1981) in the northwest Pacific, at a range of 30° can be explained as a shadowing effect of the low Q asthenosphere. The confinement of P_n to the oceanic lithosphere, required by the high apparent Q, imposes a constraint on the maximum range a normally refracted wave, without upward reflection points, can be observed. At ranges less than 30°, the first arrivals of P_n are normally refracted waves in the lithosphere while at longer ranges they contain a free surface reflection. This is similar to the whispering gallery phase interpretation presented by *Menke and Richards* (1980) except that in their model the upward reflection point is at the Moho rather than at the free surface.

This phenomenon is demonstrated in Figure 21*b* which displays the group velocity of P_n as a function of epicentral distance for the velocity model shown in Figure 21*a*. The model consists of a 200-km-thick lithosphere lid overlying a thin low velocity zone. The 400 and 670 km discontinuities are included. The model is the PEM-O model of *Dziewonski, et al.* (1975) for depths greater than 270 km. The discontinuous break in group velocity at a distance of 30° (Figure 21*b*) represents the crossover between a ray normally refracted in the lithosphere and one that contains a free surface reflection, similar to the seismic phase PP. In order to accommodate a crossover distance of 30°, a homogeneous lithosphere with thickness of 200 km is required.

A lithosphere thickness of 200 km is substantially higher than estimates based on thermal models, flexural studies or surface wave interpretation. The elastic lithosphere thickness, calculated from the flexure caused by loading, is typically between 25 and 40 km for a crustal age of 100 million years (*Watts, et al.*, 1980). Thermal models based on half-space cooling define the lithosphere thickness as the depth to the melting point isotherm, between 1200° C to 1300° C (*Parker and Oldenburg*, 1973). The depth to the 1200° C isotherm for a crustal age of 100 million years can be calculated from *Parker and Oldenburg* (1973) to be 94 km. *Parsons and Sclater* (1977) indicate, however, that the $t^{1/2}$ dependence of lithosphere thickness predicted by plate cooling is valid for crustal ages less than 60 to 80 million years but approaches an asymptotic value for older crust.

Watts, et al. (1980) demonstrate that the elastic lithosphere thickness is consistent with thermal models as the depth to the 300 ° C to 600 ° C isotherm. The *seismic lithosphere* is defined as the depth to the shear wave low velocity zone of the upper mantle. These studies generally result in a higher estimate of the lithosphere thickness than either thermal or flexural studies. Using the dispersion of Love and Rayleigh waves in the period range of 17 to 167 s. *Forsyth* (1975) estimated a lithosphere thickness of 60 km for a crustal age of 10 million years. Assuming a $t^{1/2}$ dependence, this would yield a lithosphere thickness of 190 km for 100 million year old crust. *Forsyth* (1975), however, reports a slower increase in thickness with age than $t^{1/2}$, increasing to only 70 km in the 20 to 50 million year age zone (in agreement with the results of *Parsons and Sclater* (1977)). Attempts to determine lithosphere thickness from long range explosion experiments have been largely unsuccessful. Two possible exceptions are the work of *Hales,et al.* (1970) and *Asada and Shimamura* (1976). *Asada and Shimamura* (1976) investigated the fine scale P wave velocity structure of the western Pacific lithosphere using data collected during the Longshot Experiment (September, 1974). They reported a lithosphere thickness, as defined as the depth to a very thin P wave low velocity layer, of 80 km. *Hales, et al.* (1970) similarly obtained the depth to a P wave velocity inversion of 80 km in the Gulf of Mexico, a region with an uncertain tectonic history. The lithosphere thickness, as defined by the discontinuous drop in P_n group velocity, is an estimate of the depth to a low Q zone. The relationship between depths to a particular isotherm, the low velocity zone, and a low Q zone is obscure. While 200 km exceeds other estimates of lithosphere plate thickness, it is clear that the same parameter is not being measured. Furthermore, the nature of P_n propagation up and around the corner of the descending slab is not well understood and it is quite possible that the epicentral range is not indicative of the true shadowing distance.

Walker's (1981) observations of P_n group velocity as a function of epicentral range are reproduced in Figure 22*a*. The measured group velocities of P_n having travel paths in the northwest Pacific for events with focal depths less than 100 km are shown. The group velocity of P_n is shown to be greater in the distance range of 12 ° to 30 ° than for distances outside this range. The means for each of the three distance ranges, 0 ° to 12 °, 12 ° to 30 °, and > 30 °, are indicated by solid lines and the dashed lines represent one standard deviation. Figure 22*b* is a superposition of the apparent group velocity curves of Figure 21*b* on the means and standard deviations of *Walker* (1981). Note, however, that the apparent group velocity curves fit the measured data points even better than *Walker's* (1981) bands. The low group velocity of P_n at distances less than 12 ° can be attributed to shallower turning points in the lithosphere and the break at 30 ° is the

shadowing effect of the low Q asthenosphere.

The confinement of S_n to the lithosphere produces a shadowing effect at large epicentral ranges. The maximum distance that S_n can propagate, without upward reflection points, is governed by the thickness and velocity gradient of the oceanic lithosphere. At longer ranges, a normally refracted S wave will penetrate the low Q asthenosphere and the first arrival of S_n will contain an upward reflection point, a shallower turning point, and a correspondingly lower group velocity. Previously, it was found that an upward reflection point at the free surface for the oceanic P_n phase at distances greater than 30° was consistent with the discontinuous drop in P_n group velocity reported by *Walker* (1981) in the northwest Pacific (see Figure 22). *Walker* (1981) also reports a discontinuous drop in S_n group velocity at a range of 30°; however, it is of much smaller magnitude than that observed for P_n. The upward reflection coefficient for shear waves at the ocean-sediment interface is typically much greater than for compressional waves. Furthermore, shear waves don't propagate in the water column and thus it is expected that the upward reflection point for S_n at long ranges is at the ocean-sediment interface rather than the free surface. Propagation through the water column can add in excess of 7 s to the travel time for P_n, resulting in a more severe reduction in group velocity.

The shear wave velocity model used to compute S_n group velocity as a function of range is shown in Figure 23. For this analysis the important parameters are lithosphere thickness and velocity. It was found, for P_n, that a homogeneous lithosphere with a compressional wave velocity of 8.1 km/s and a thickness of 200 km was consistent with *Walker's* (1981) observations (see Figures 21 and 22). The model in Figure 23 contains a 200 km thick homogeneous lithosphere with a shear wave velocity of 4.68 km/s. *Walker's* (1981) S_n observations are presented in Figure 24*a*. Figure 24*b* is a comparison of the computed S_n group velocity as a function of range to the means and standard deviations shown in Figure 24*a*. As was the case for P_n, the lower group velocities at ranges less than 12° are due to shallower turning points in the lithosphere. The discontinuous drop in group velocity near 30° represents the crossover between a ray normally refracted in the lithosphere and one that contains an upward reflection point at the ocean-sediment interface. In order to accommodate a crossover distance of 30°, a homogeneous lithosphere with a thickness of 200 km is required. *Walker's* (1981) observations were for travel paths in the northwest Pacific, a relatively old portion of oceanic lithosphere. According to thermal models (*Parsons and Sclater*, 1977), a thick lithosphere is expected for this region.

Chinn, et al. (1980) similarly explain the rapid disappearance of the oceanic S_n phase at distances greater than 16° along ray paths in the eastern part of the Nazca Plate as a shadowing effect of the low Q asthenosphere. This oceanic plate is relatively young (50 Ma) in comparison to the northwest Pacific (100 Ma) and would have a smaller lithosphere thickness. This accounts for the shorter shadowing distance (16°) observed for S_n in this region as compared to the cutoff in the northwest Pacific (30°). *Chinn et al.* (1980) point out that for a homogeneous lithosphere, its thickness is related to the cutoff range of S_n by

$$h = R\,[1-\cos(\Delta_c/2)] \tag{6}$$

where h is the lithosphere thickness, R is the radius of the Earth, and Δ_c is the S_n angular cutoff distance. A cutoff distance of 16° yields a plate thickness of 62 km for the Nazca Plate and a cutoff distance of 30° results in a 217 km thick plate in the northwest Pacific. Direct measurement of these transition or cutoff regions, through the use of ocean bottom seismographs, probably represents the most accurate means of measuring lithosphere thickness at different ages by seismic methods.

A further consequence of the confinement of P_n to the lithosphere is the presence of low frequency forerunners. At large epicentral ranges, a normally refracted P wave with turning point below the low velocity zone is expected to precede the oceanic P_n phase. This relationship is shown in Figure 21c which is the travel time curve for P_n (solid) versus normal refracted P with turning point below the base of the lithosphere (dashed) for the model in Figure 21*a*. The curves diverge at an approximate range of 25° where the normal refracted arrival constitutes the commonly observed low frequency P_n forerunner (*Latham and Sutton*, 1966; *Ouchi*, 1981; *Sereno and Orcutt*, 1986). Because the forerunner has penetrated the low Q asthenosphere, it is characterized by a much lower dominant frequency than P_n. An example is illustrated in Figure 25. The complicated waveform between 2 and 4 s is a triplication from the 400 km discontinuity. For deep events, the appearance of forerunners occurs at shorter distances as the rays comprising P_n must propagate up and around the corner of the descending slab (*Barazangi, et al.*, 1972).

Molnar and Oliver (1969) report that for ranges less than 20°, travel time curves for S_n and S are indistinguishable and, in fact, that they are the same phase. For distances beyond 25° they found that S_n and S travel time curves are significantly different. For these longer ranges, S penetrates the low Q asthenosphere into high

velocity material and arrives before the S_n phase. *Barazangi, et al.* (1972) similarly report the arrival of low frequency, normally refracted S_n forerunners. The much lower dominant frequency of S_n forerunners is indicative of the low Q of the sub-lithosphere mantle.

The suggestion that a descending slab can act as a wave guide to propagate the high frequency oceanic S_n phase was made by *Isacks and Barazangi* (1973). The travel time of S_n agrees with propagation up around the corner of the descending slab. Their model consists of a transformation of the basaltic oceanic crust to a thin, high velocity, eclogite layer as the slab descends to greater depths. Thus the upper flank of the slab provides an effective reflecting surface and, in combination with a velocity gradient within the slab, could provide an efficient wave guide for the propagation of high frequency seismic energy.

The wave guide for oceanic P_n and S_n includes the entire oceanic lithosphere. The enrichment of the high frequency content of P_n / S_n, relative to normal refracted arrivals, is indicative of a low Q asthenosphere. Figure 26 summarizes the model presented here for P_n / S_n wave propagation. At ranges less than a critical distance, determined by the thickness of the lithosphere, the first arrivals are coincident with waves turning in the oceanic lithosphere. For distances greater than the critical distance, they contain an upward reflection, a shallower turning point, and therefore a lower group velocity. A normal refracted P wave constitutes the low frequency forerunner to P_n and is illustrated in Figure 26. The attenuation properties of both the oceanic P_n and S_n phases are the subject of the next section.

ATTENUATION

In a previous paper (*Sereno and Orcutt*, 1985*b*), synthetic seismograms computed for a model representative of typical oceanic lithosphere (Table 2) were presented. The complete synthetic seismograms for this model featured realistic P_n phases, however, the synthetic S_n phase did not emulate data. The only arrival near 4.65 km/s was composed entirely of horizontally polarized shear waves and had a much lower dominant frequency than is typical for oceanic S_n phases. The absence of a strong, high group velocity S_n signal suggests that the mantle shear Q used in the computation of these synthetics, 225, was too low. Figure 27 displays curves of

$$| I(f) \exp\left(\frac{-\pi r f}{u Q}\right) \tag{7}$$

where $|I(f)|$ is the OBS instrument response, r is epicentral range, u is group velocity, and $\overline{Q}$ is the path averaged Q. In Figure 27 this function is plotted for a range of 3300 km, a group velocity of 4.7 km/s, and varying $\overline{Q}$ values. *Walker, et al.* (1983) report observable S_n signal levels at a frequency of 20 Hz and a range of 3300 km, drawn as a dashed vertical line in Figure 27. Due to the cutoff character of these diagrams, clearly a value of 225 for Q_β is insufficient to explain the high frequency content of the data. The curves in Figure 27 assume a flat source spectrum and would display an even lower frequency cutoff for a temporally extended source mechanism. Similar results were obtained by *Oliver and Isacks* (1967) by estimating the amplitude response of an attenuating medium as proportional to $\exp(-f/f_c)$ where $f_c = \overline{Q}/\pi t$ is the cutoff frequency of an equivalent low pass filter for travel time, t. They obtained a value of 1000 for $\overline{Q}$ of oceanic lithosphere. Applying the same technique, *Molnar and Oliver* (1969) obtained values of 3000-7000 for $\overline{Q}$ for travel paths between the West Indies and North America and *Isacks and Stephens* (1975) report a value of 4000 from hydrophone recordings at Bermuda.

As a result of the above considerations, the Q values were increased in the Ngendei oceanic lithosphere model used to compute synthetic seismograms (Table 1). A value of 1000 for Q_β in the sub-Moho portion of the lithosphere was adopted, in better agreement with published values. The full set of Green's functions for the Ngendei model is shown in Figures 2-4. Examination of Σ_{rz0} (Figure 2), Σ_{rz1} (Figure 3), and the transverse components, $\Sigma_{\theta z}$ and $\Sigma_{r\theta}$ (Figure 4) quite clearly demonstrates the presence of a high group velocity, high frequency S_n onset followed by a substantial coda.

Figure 28 is synthetic horizontal displacement, rotated 25° clockwise from the radial direction, due to a thrust fault source at an epicentral range of 1000 km computed for the two models. The synthetic seismogram for the *typical* oceanic lithosphere model, with a mantle shear Q of only 225, is shown in Figure 28*a*. Figure 28*b* displays the corresponding result for the Ngendei model, which had a value of 1000 for the mantle shear Q. The only S_n arrival in Figure 28*a*, near the mantle shear wave velocity, is a low frequency, low order mode. The higher modes responsible for the high frequency S_n onset are too severely attenuated by the rather low Q_β value. The presence of a high frequency S_n phase at 4.65 km/s is quite apparent for the Ngendei model (Figure 28*b*) followed by a lower frequency shear wave sediment resonance. The difference in the P_n coda of the two seismograms is due to the drastically different sediment properties used in the two models. Neither the OBS instrument response nor a source-time function have been included in either seismogram.

The oceanic lithosphere is an extremely efficient wave guide for high frequency seismic energy. The oceanic P_n and S_n phases propagate entirely within this wave guide and therefore their attenuation properties are, to a large extent, controlled by the rheology of the oceanic plates. The propagation of frequencies as high as 15 Hz for P_n and 20 Hz for S_n to a distance of 3300 km (*Walker, et al.*, 1983) suggests extremely high Q values for the lithosphere (see Figure 27). *Walker, et al.* (1983) estimated the effective quality factors of P_n and S_n with travel paths in the northwest Pacific for two separate earthquakes yielding P_n values of 3700± 200 and 8400± 1300 and S_n values of 8500± 600 and 19,100± 3700.

Two important aspects reported for P_n and S_n wave propagation are the observations that Q is an increasing function of frequency beyond 1-2 Hz (*Butler, et al.*, 1985) and that Q_{S_n} is greater than Q_{P_n} (*Walker, et al.*, 1978; *Sutton, et al.*, 1978). *Butler, et al.* (1985) report Q_{S_n} values of 500 at 2.5 Hz and 3000 at 22 Hz and Q_{P_n} values of 300 at 2.5 Hz and 1500 at 17.5 Hz for travel paths in the northwest Pacific recorded by the Wake Island hydrophone array. *Aki* (1980*a*) reports a similar frequency dependence of Q_β for the lithosphere between 1 and 25 Hz.

First, some of the complications involved in estimating the quality factors of P_n / S_n propagation are illustrated. Estimates of Q_{P_n} and Q_{S_n} for the synthetics computed for the Ngendei model were obtained using a two-station spectral ratio method. In this case, the intrinsic $Q(z)$ profile is frequency-independent and $Q_\alpha = 2Q_\beta$. The results of the Q estimation can be compared directly to the model to test the applicability of the spectral ratio method, in the case of *perfect data*, to P_n and/or S_n wave trains. Next, the frequency dependence observed for Q_{P_n} and Q_{S_n} and the relative efficiency of S_n to P_n propagation is examined. To accomplish this, an absorption band rheology with a distribution of relaxation times was incorporated into the wave number integration algorithm.

Estimation of Q_{P_n} and Q_{S_n}. The most recently published values of Q_{P_n} and Q_{S_n} are those of *Butler, et al.* (1985). A 1600 km long ocean bottom hydrophone array at Wake Island recorded an m_b = 6.6 Kuril earthquake which occurred at an angle of 7° to the trend of the array. P_n and S_n data, covering a distance range of 2740 to 4125 km, were used to obtain the Q estimates. Their results indicate a frequency dependence of both Q_{P_n} and Q_{S_n} and more efficient propagation of S_n than P_n. The authors offer two possible explanations of the greater efficiency of S_n propagation relative to P_n. First, the propagation of P_n as a leaky mode could bias the Q_{P_n} estimate to a lower value. Second, bulk attenuation is important in the western Pacific lithosphere.

In an effort to distinguish between these two possibilities, estimates of the quality factors for the synthetic P_n and S_n phases, computed for the Ngendei model (Table 1), were obtained using a two-station spectral ratio method. Compressional waves turning in the sub-Moho lithosphere propagate as leaky modes in that they continuously radiate shear wave energy to the deeper part of the structure. Thus Q_{P_n} estimates based on the spatial decay of the amplitude spectrum will be consistently biased to lower values. Propagational effects of this sort are included in the wave number integration algorithm and, if leaky mode propagation is responsible for the observed relative efficiency of S_n to P_n propagation, then the result should be reproduced in the synthetic phases.

Spectral Ratios. In order to estimate an apparent Q, the seismic amplitude spectrum is modelled as

$$A(f,r) = S(f)\, I(f)\, T(f,r)\, r^{-m} \exp\left(\frac{-\pi f r}{u\bar{Q}}\right) \tag{8}$$

where $A(f,r)$ is the spectral amplitude at frequency f and range r; $S(f)$ is the source spectrum, $I(f)$ is the instrument response; $T(f,r)$ is the crustal transfer function; r^{-m} is geometric spreading ($m=1/2$ for for cylindrical spreading and $m=1$ for spherical spreading); the last term represents plane wave anelastic attenuation for a pulse travelling a distance r at group velocity u. The natural logarithm of the ratio of the amplitude spectra at two ranges, r_1 and r_2, from a common source and recorded by instruments with the same response functions can be expressed as

$$\ln\left[\frac{A(f,r_2)}{A(f,r_1)}\right] = \ln\left[\frac{T(f,r_2)}{T(f,r_1)}\right] - m \ln\left[\frac{r_2}{r_1}\right] - \frac{\pi f}{u\bar{Q}}(r_2 - r_1). \tag{9}$$

In equation (9), the term for which the least information can be gathered is the ratio of the crustal transfer functions. In general, it is assumed that for rays turning in the mantle, which have steep incidence in the crust, the crustal transfer functions at the two sites are approximately equal. This allows the removal of this term from equation (9). This can, however, lead to a serious instability in the Q estimate for P_n and/or S_n. The crustal transfer function for P_n / S_n phases is dominated by properties of the sediment layer. For example, Figure 7*b* is the power spectrum of the first 40 s of the synthetic vertical component P_n wave train. The rapid roll-off at frequencies greater than 10 Hz is due to a cosine-squared taper applied to the spectrum prior to time domain synthesis.

The dominating feature of the spectrum is the broad uplifted region centered at 5.7 Hz which is due to P wave sediment resonance (see Figure 8). The presence of P wave sediment reverberation in the crustal transfer function would actually cause a *negative* value to be obtained for Q based on the spectral slope at a single station. The spectral ratio from neighboring stations should, theoretically, remove this effect if the sediment properties at the two sites are equivalent and if the receiver spacing is small enough. At the same time, however, to distinguish high Q values, the spectral ratio at either very high frequencies or for a large receiver separation is required for anelastic attenuation to have a measurable effect. Two problems associated with a large receiver spacing are

(1) The sediment properties at the two sites are less likely to be equivalent.

(2) The rays constituting the first arrivals of P_n / S_n will have different phase velocities at the two sites and therefore different incidence angles in the sediment layer.

The first of these could result in an oscillatory spectral ratio. For example, if the sediment layer at site 1 had a thickness of 70 m and a compressional velocity of 1.6 km/s, then the resonant frequency of the fundamental organ-pipe mode is 5.7 Hz. If the thickness is 100 m at site 2, the fundamental mode eigenfrequency will be 4.0 Hz. The resulting spectral ratio is biased to a higher value near 4 Hz and to a lower value near 5.7 Hz than is indicative of the actual path averaged Q value. The second problem arises even when the sediment properties at the two sites are equivalent. The resonant frequency of the fundamental organ-pipe mode is given by $1/2T$ where T is the time between multiples. Clearly the time between sediment multiples is dependent upon the incidence angle of the rays in the layer. The corresponding shift in the eigenfrequency of the fundamental sediment organ-pipe mode results in the same problem as that of a difference in sediment properties between the sites.

The problems associated with an inadequate knowledge of the crustal transfer function are accentuated by the extremely high Q values required for the lithosphere to explain the high frequency content of P_n and S_n data. The spectral ratio, after assuming the crustal transfer functions at the two sites are equivalent, can be written as

$$\ln\left[\frac{A(f,r_2)}{A(f,r_1)}\right] = -m\ln\left[\frac{r_2}{r_1}\right] - \frac{\pi f}{uQ}(r_2 - r_1) \qquad (10)$$

or for power spectra, $P(f,r)$,

$$\ln\left[\frac{P(f,r_2)}{P(f,r_1)}\right] = -2m\ln\left[\frac{r_2}{r_1}\right] - \frac{2\pi f}{u\bar{Q}}(r_2-r_1). \qquad (11)$$

From (11), the path averaged Q estimate can be obtained by one of two methods. First, the slope of the spectral ratio can be used to estimate $\bar{Q}$ directly. Second, an assumption of the geometric spreading can be used to obtain $\bar{Q}$ at a particular frequency without estimating the slope. The apparent Q from either technique can be, in some cases, drastically different from the intrinsic Q of the medium. For example, tunneling of low frequency energy into the low Q asthenosphere could impart a frequency dependent shift in the spectral ratio causing Q to be overestimated. Leaky mode propagation would result in a more rapid spatial decay of the spectrum than pure geometric spreading and intrinsic anelasticity. This would not alter the slope of the spectral ratio, but would cause an underestimate of $\bar{Q}$ based on the spatial decay of the spectrum.

Figure 29 is a power spectral ratio of the vertical component P_n wave trains at ranges of 900 and 1100 km. A Hanning window was applied to the first 40 s of the records prior to computing the spectral estimates. The instability of the ratio is due to the inequality of the crustal transfer functions at the two ranges. Equation (11) was used as an analytic prediction of the spectral ratio. The four solid lines were generated, from (11), assuming cylindrical spreading ($m=1/2$), a group velocity of 8 km/s. and varying $\bar{Q}$ values. From top to bottom the values used for $\bar{Q}$ are 5000, 2000, 1000, and 500. The dashed line indicates the analytic result for $\bar{Q}$ = 2000, assuming spherical spreading ($m=1$). From the slope of the spectral ratio, $\bar{Q}$ values less than 1000 can be ruled out, however it becomes very difficult to distinguish a Q of 2000 from one of 5000. Comparing the four solid lines, it is shown that a careful error analysis would never produce equal confidence above and below the $\bar{Q}$ estimate. The intrinsic Q_o of the mantle (Table 1) is 2000 which is, at least, consistent with the spectral ratio. Broader band data is required to further refine the estimate.

The dashed line in Figure 29, indicative of spherical spreading, is below the mean value of the spectral ratio over the entire frequency band. This suggests that cylindrical spreading is more representative of the spatial decay of P_n. This is to be expected in that P_n is confined to the lithosphere and propagates to teleseismic distances resulting in an aspect ratio as high as 30:1.

Figure 30 is a power spectral ratio of the synthetic radial component S_n wave trains at ranges of 900 and 1100 km. The solid lines were obtained using (11) assuming cylindrical spreading ($m = 1/2$), a group velocity of 4.7 km/s, and varying $\bar{Q}$ values. From top to bottom the $\bar{Q}$ values are 5000, 2000, 1000, and 500. The dashed line represents $\bar{Q}$ = 1000 and spherical spreading ($m = 1$). The estimate, even in the case of *perfect data*, is highly oscillatory, however a $\bar{Q}$ value of 1000 for cylindrical spreading is consistent with the spectral ratio. More importantly, comparing Figures 29 and 30, the efficiency of P_n propagation exceeds that of S_n for the Ngendei synthetics.

These results indicate that the observation of greater efficiency of S_n than P_n is not a propagation effect, but rather an intrinsic property of the lithosphere. In the following section, it will be shown that the attenuation properties of P_n / S_n propagation can be explained in terms of an absorption band rheology with a distribution of relaxation times.

Absorption Band Rheology. Surface wave and normal mode studies have shown that a Q essentially independent of frequency throughout much of the seismic frequency band is consistent with the data (*Anderson and Archambeau*, 1964; *Knopoff*, 1964). More recently, however, short period body wave studies indicate that Q increases with frequency (*Anderson and Hart*, 1978*a*; *Aki*, 1980*a*; *Aki*, 1980*b*; *Lundquist and Cormier*, 1980; *Anderson and Given*, 1982; *Clements*, 1982; *Der et al.*, 1982; *Ulug and Berckhemer*, 1984; *Bache, et al.*, 1985; *Butler, et al.*, 1985). To approximate the true frequency dependence of Q in the oceanic lithosphere, an absorption band rheology with a distribution of relaxation times has been adopted (*Liu, et al.*, 1976; *Zener*, 1948). This has the advantage of providing an analytic expression for the complex material velocity that is easily incorporated into the wave number integration algorithm.

Prior to examining the synthetic seismograms computed for a lithosphere structure that includes an absorption band rheology, further motivation for allowing Q to be frequency dependent is presented. The synthetic horizontal component P_n and S_n wave trains (Figures 3-5) very closely resemble data collected during the 1983 Ngendei Seismic Experiment. The impulsive character of the water reverberations in the synthetic vertical component P_n wave train does not, however, emulate the data (Figures 2 and 5). Three possible explanations for the discreteness of the synthetic vertical component P_n wave train, relative to the data, were mentioned previously. One of these was coupling of the vertical and horizontal components in the OBS instrumentation. If the OBS vertical component seismometer is excited by horizontal ground motion, the discreteness of the arrivals would be obscured by the shear wave sediment resonance. If this was the case, the dominant lower frequency of the vertical component P_n wave train should coincide

with a shear wave sediment organ-pipe mode. The strong low frequency resonance in the vertical component data is not, however, coincident with the shear wave sediment resonance frequencies observed in horizontal component data. The horizontal component resonance coincides with the first higher shear wave organ-pipe mode in the sediment layer (≈ 1.2 Hz). The dominant frequency of the vertical component data is, however, approximately 0.75 Hz which is in between the fundamental and first higher shear wave sediment modes. It is therefore not likely that the coupling of vertical and horizontal components is responsible for the drawn out character of the vertical component P_n data.

Scattering, as a mechanism to reduce the impulsive character of the water multiples, is not so easily dismissed. The development of water and sediment resonance peaks in the P_n and S_n spectra indicate, however, that scattering is of secondary importance in producing the substantial coda. Furthermore, strong coherence observed between OBS's at different sites argues against scattering as the dominant mechanism of coda generation (*Sereno and Orcutt*, 1985*b*).

A third possible explanation for the impulsive appearance of the synthetic vertical component P_n wave train involves a frequency dependent Q. The 0.75 Hz resonance in the vertical component data coincides with an organ-pipe mode in the water column with a particularly strong excitation function. The preferential excitement of this water mode is due to a combination of the instrument response, source spectrum, and Q effect. Figure 31*a* is the power spectrum of the synthetic vertical component P_n wave train after including the OBS instrument response and a source spectrum with f^{-2} asymptote and a corner frequency of 0.8 Hz. Figure 31*b* is the first 12.8 Hz of the power spectrum of vertical component P_n data collected at the Ngendei site. The obvious difference between the two spectra is the enrichment of power at frequencies between 0-2 Hz of the data relative to the synthetics. The lack of low frequency energy gives rise to the impulsive character of the synthetic P_n wave train.

One way to enhance the power level of the low frequencies relative to higher frequencies is to lower the Q. This, however, inhibits the propagation of extremely high frequencies to teleseismic distances which is required by the data. As an alternative, Q could increase with frequency thereby enhancing the power at frequencies between 0-2 Hz relative to frequencies between 3-5 Hz without severely attenuating frequencies in excess of 10 Hz. To approximate the true frequency dependence of Q in the oceanic lithosphere, we have adopted an absorption band rheology with a distribution of relaxation times. This is incorporated into the wave number integration algorithm (*Lundquist and Cormier*, 1980) by allowing the complex material velocity to be of the form

$$V_c(\omega) = V_e\left[1-\frac{1}{\pi Q_m}\ln\frac{1+\omega^2\tau_1^2}{1+\omega^2\tau_2^2}-i\frac{2}{\pi Q_m}\tan^{-1}\frac{\omega(\tau_1-\tau_2)}{1+\omega^2\tau_1\tau_2}\right]^{-\frac{1}{2}} \tag{12}$$

where V_e is the *elastic* velocity, Q_m is the minimum Q, and τ_1 and τ_2 are the low and high frequency relaxation times, respectively. Care must be taken in applying this equation in that the natural log term perturbs the real part of the complex velocity and can cause an unrealistic deviation in travel times. In the limit as this term approaches zero, the familiar expression for Q as a function of frequency for an absorption band rheology is obtained

$$Q^{-1}(\omega) = \frac{2}{\pi Q_m}\tan^{-1}\left[\frac{\omega(\tau_1-\tau_2)}{1+\omega^2\tau_1\tau_2}\right]. \tag{13}$$

As an example of the effect of an absorption band Q on the spectra, values for compressional waves of Q_m=200 and τ_2=0.05 s were used resulting in a linear frequency dependence of Q for frequencies greater than about 3.0 Hz. The low frequency relaxation time, τ_1, was arbitrarily set to 100 s, well out of the frequency range of interest. Figure 32*a* displays curves of the instrument response multiplied by a source spectrum with f^{-2} amplitude decay and corner frequency of 0.8 Hz multiplied by $e^{\frac{-\pi rf}{uQ}}$ for a range of 1000 km, a group velocity of 8 km/s, and varying Q values. The dashed curves represent constant Q values and for the solid curve the absorption band Q was used. Figure 32*b* displays the same curves to a frequency of 64 Hz. In order to enhance the low frequency energy of the synthetics without depleting the very high frequencies, Q must increase with frequency.

Synthetic seismograms were computed for a model of the Ngendei site that includes an absorption band rheology in the mantle portion of the lithosphere. The model differs from that in Table 1 only in the Q structure. The values of Q in the sediment layer were reduced by a factor of two and parameters for the absorption band in the mantle are listed in Table 3. The value of the low frequency relaxation time, τ_1, was set arbitrarily to 100 s, well out of the frequency band of interest. The important parameters are τ_2, the high frequency relaxation time, and Q_m, the minimum Q.

Figure 33 displays Q_α^{-1} (solid) and Q_β^{-1} (dashed) computed using (13) with the parameters in Table 3. At low frequencies, $Q_\alpha = 2Q_\beta$, a result consistent with normal mode and surface wave studies (*Anderson, et al.*, 1965). A shorter relaxation time, τ_2,

for P waves than for S waves results in a rheology with the property that $Q_\alpha > Q_\beta$ at low frequencies while $Q_\beta > Q_\alpha$ at high frequencies, consistent with teleseismic P_n / S_n observations. The circles in Figure 33 are the Q_{S_n} values reported by *Butler, et al.* (1985) and the triangles are their Q_{P_n} estimates.

The absorption band parameters in Table 3 are consistent with those obtained in continental lithosphere studies (*Lundquist and Cormier*, 1980; *Bache, et al.*, 1985). *Lundquist and Cormier* (1980), from compressional body wave spectra of shallow earthquakes, obtained an average value of 0.069 s for τ_2 in the upper mantle. From body wave spectra of deep earthquakes, the average τ_2 value for P waves was 0.088 s and for S waves, 0.145 s. *Bache, et al.* (1985) studied attenuation of teleseismic P waves for continental paths and concluded that intrinsic attenuation could be represented by an absorption band model with $0.04 \leqslant \tau_2 \leqslant 0.1$. The best fit to their data, covering the frequency band 1-8 Hz, resulted in $\tau_2 = 0.05$ s. Using data collected at the Warramunga Seismic Array in northern Australia, *Clements* (1982) modelled the frequency dependence of Q as

$$Q = Q_0(1+\tau\omega). \tag{14}$$

The resulting τ values were 0.110± .005 s for P phases and 0.46± .02 s for S phases. These numbers are not directly comparable to τ_2 in (13), however, $\tau_S > \tau_P$ is consistent with the Q model in Table 3.

The full set of Green's functions for the Ngendei absorption band model are displayed in Figures 34-36. The synthetics were computed at 16385 frequencies extending to a Nyquist frequency of only 6.4 Hz. Green's functions for vertical displacement are shown in Figure 34, radial displacement in Figure 35, and transverse displacement in Figure 36. Figure 37 is a comparison of vertical displacement computed for the absorption band model to that computed for the constant Q Ngendei model at a range of 1000 km. A sub-Moho thrust fault with a dip of 25°, a rake of 270°, and an azimuth relative to the receiver of 60° was used. The OBS instrument response and a source spectrum with f^{-2} amplitude decay and corner frequency 0.8 Hz were included. Introducing an absorption band Q has greatly reduced the impulsive character of the water reverberations, especially in the latter part of the wave train. The agreement of the synthetic vertical component P_n wave train with the data is greatly enhanced by allowing Q to increase with frequency.

In the frequency band, 0-6.4 Hz, the effect of incorporating the frequency dependent Q is to enhance the power level between 0 and 2 Hz relative to that between 3 and 5 Hz (Figure 32). Figure 38 is a comparison of the synthetic vertical component P_n spectra for the constant Q and the absorption band Q Ngendei models. Figure 38*a* is the first 6.4 Hz of the spectrum of the P_n wave train in Figure 37*a*. The spectrum of the absorption band Q P_n wave train (Figure 37*b*) is illustrated in Figure 38*b*. The absorption band Q synthetics were computed to a Nyquist frequency of only 6.4 Hz and the rapid decay of the spectrum beyond 4.4 Hz is due to a cosine-squared taper applied prior to time domain synthesis. Comparing this figure to Figure 31 illustrates that the absorption band Q synthetic P_n spectrum more closely resembles the data spectrum than that computed for the constant Q structure.

The computation of the broad band, full synthetic seismograms required to adequately analyze the effects of anelastic attenuation is inhibited by the substantial computational time that would be involved. As an alternative, phase velocity can be restricted to a small band around the material velocity of the uppermost mantle. Only a portion of the seismogram is synthesized and therefore a more sparse frequency sampling is adequate to avoid temporal aliasing. Synthetic P_n spectra were computed for the absorption band Q Ngendei model to a frequency of 40 Hz by restricting phase velocities between 7.0 and 25.0 km/s. Figure 39 displays the vertical component synthetic P_n power spectrum at a range of 900 km due to a sub-Moho thrust fault source. The same fault parameters were used as in Figure 37. The OBS instrument response and a source spectrum with f^{-2} amplitude decay and corner frequency of 0.8 Hz were included. The dashed curve superimposed on the spectrum is the function

$$|I(f)|^2 |S(f)|^2 \exp\left[\frac{-2\pi f r}{uQ(f)}\right] \qquad (15)$$

where $I(f)$ is the OBS instrument response, $S(f)$ is the source spectrum, r (=900 km) is the epicentral range, u (=8.0 km/s) is the group velocity, and $Q(f)$ is the absorption band Q computed from (13) using the parameters for P waves in Table 3. The importance of the crustal transfer function is apparent in this diagram. The broad ridges at 5.7, 17.1, 28.6, and 40 Hz are due to P wave sediment resonance. The suppressed amplitude of the spectrum for frequencies less than 3.0 Hz, relative to the simple dashed curve, is similarly due to the crustal transfer function. The fundamental compressional sediment organ-pipe mode eigenfrequency is 5.7 Hz resulting in a reduced

spectral amplitude for lower frequencies. The synthetic radial component P_n spectrum is shown in Figure 40. Shear wave sediment resonance is more prominent on the horizontal component due to the steep incidence of the rays. Therefore, the low frequencies are not suppressed due to P wave sediment resonance and the spectrum more closely follows the curve computed using (15). These figures demonstrate that the amplification of low frequencies ($\leq$ 2 Hz) without inhibiting the propagation of high frequencies ($\geq$ 20 Hz) can be accomplished with a frequency dependent Q.

Figure 41 is the power spectrum of vertical component P_n data collected at the Ngendei site. A Hanning window was applied to the first 64 s of the P_n data shown in Figure 9*c* prior to computing the spectral estimate. The dashed curve is the same as that shown in Figure 39. The P wave sediment resonances can be identified with those in the synthetic spectrum in Figure 39. Comparison with the dashed curve indicates that, while the low frequency spectral level is consistent with a frequency dependent Q, that dependence is not as strong as predicted by the absorption band model. An inadequate knowledge of the source spectrum at very high frequency could also contribute to the disagreement.

A similar analysis was conducted for S_n by computing the synthetic spectra to 40 Hz with phase velocities restricted between 4.0 and 5.0 km/s. Figure 42 is the resulting synthetic radial component S_n spectrum with the dashed curve computed from (15) for a range of 900 km, a group velocity of 4.7 km/s, and the absorption band Q function for shear waves listed in Table 3. The spectral shape agrees quite well with that predicted by (15).

The Q function for an absorption band rheology has a simple asymptotic form for high frequencies when $\tau_1 >> \tau_2$. In that case, from (13), the absorption band $Q(f)$ can be approximated by

$$Q(f) \approx \pi^2 Q_m \tau_2 f. \tag{16}$$

The condition, $\tau_1 >> \tau_2$, is satisfied for the model in Table 3 and therefore, at high frequencies,

$$\frac{Q_\beta}{Q_\alpha} \approx \frac{Q_m^\beta \tau_2^\beta}{Q_m^\alpha \tau_2^\alpha}. \tag{17}$$

Equation (17) results in a constant ratio of $\frac{Q_\beta}{Q_\alpha}$ 1.6 for the model in Table 3 at high

frequency. Because the ratio of compressional to shear wave velocity in the mantle is very close to this ratio, it is expected that for high frequencies, P_n and S_n should have very nearly equal spectral slopes. For example, Figure 43 displays curves of (15) plotted for P_n (dashed) and S_n (solid). For P_n, a group velocity of 8.0 km/s and the absorption band $Q(f)$ in Table 3 for P waves were used. Similarly, for S_n, a group velocity of 4.7 km/s and the absorption band $Q(f)$ in Table 3 for S waves were used. The spectra are almost identical for frequencies greater than 10 Hz.

This feature was also seen in the Ngendei data. Figure 44 displays the P_n spectrum of Figure 41 (top) and the S_n spectrum of the same event (below). The curves were offset for illustrative purposes but do, in fact, almost perfectly overlay one another. The near equivalence of the spectral slopes of P_n and S_n data is a strong indication that $Q_\beta > Q_\alpha$ at frequencies greater than 5-10 Hz and that the ratio of Q_β to Q_α is relatively constant to a frequency at least as high as 40 Hz.

In this section, it has been shown that the observations that Q_{P_n} and Q_{S_n} increase with frequency (*Butler, et al.*, 1985) and that $Q_{S_n} > Q_{P_n}$ (*Walker, et al.*, 1978; *Sutton, et al.*, 1978; *Butler, et al.*, 1985) can be modelled in terms of an absorption band rheology with the high frequency relaxation time for S waves greater than for P waves. The onset of a substantial frequency dependence in Q occurs at a higher frequency for P waves than for S waves, resulting in high $\frac{Q_\beta}{Q_\alpha}$ ratios at high frequency. The absorption band model is to be viewed as only an approximation to the true frequency dependence for which analytic expressions for the material dispersion have been developed. In fact, comparison of synthetic spectra to data collected at the Ngendei site indicate that the frequency dependence of Q is not as strong as that predicted by the absorption band model. While an array of instruments was not available at the Ngendei site to eliminate source spectra by the spectral ratio method, the Ngendei data are, at least, consistent with the reported teleseismic P_n / S_n observations.

Wave number integration automatically includes the effects of leaky mode propagation and tunneling of low frequency energy. Because the spectral ratios of the constant Q Ngendei synthetics yielded results consistent with the model parameters, it is not likely that these propagational effects are responsible for the observation, $Q_{S_n} > Q_{P_n}$. *Aki* (1980*a*) pointed out that thermoelastic relaxation results in peak absorption at a frequency K/d^2 where K is the thermal diffusivity and d is the average radius of the grains. For compressional waves, the high frequency relaxation time in the Ngendei absorption band (Table 3) is 0.05 s resulting in a peak absorption frequency of 3.18 Hz.

Assuming a thermal diffusivity of 10^{-6} m^2s^{-1} (*Aki*, 1980*a*), the average grain size involved in P wave anelastic attenuation is of the order of 0.6 mm. Similarly, the shear wave high frequency relaxation time is 0.16 s resulting in a peak absorption frequency of 1.0 Hz. The average grain size associated with S wave anelasticity is therefore of the order of 1 mm. P_n and S_n have steep incidence in at least the upper portion of the lithosphere and particle motions for compressional waves are perpendicular to those for shear waves. Therefore, the alignment of elongated grains, with aspect ratios near 0.6 to 1, could result in the larger average grain size involved in S wave attenuation than in P wave attenuation. The alignment of olivine grains, responsible for seismic velocity anisotropy, could cause transverse (or polarization) attenuation anisotropy resulting in a different frequency dependence of Q_α than Q_β in the oceanic lithosphere. *Mitchell and Yu* (1980) report resolvable polarization anisotropy in the oceanic lithosphere based on inconsistent Love and Rayleigh wave velocities for the same propagation direction. They found that polarization anisotropy is larger than azimuthal anisotropy throughout the Pacific lithosphere. They suggested that the accretion of crystals at the base of the lithosphere, as it ages and cools, with preferred vertical orientation, causes the observed polarization anisotropy.

Taylor, et al. (1986) report (Q_P/Q_S) ratios less than one at frequencies greater than 1 Hz for the basin and range province and the North American shield. They suggest that intrinsic absorption dominates at low frequency while scattering is responsible for the reduced (Q_P/Q_S) ratio at high frequency. The frequency at which attenuation due to scattering is strongest is inversely proportional to the scale length of the heterogeneity. If P and S waves interact with the same heterogeneities, a decrease in S to P attenuation is expected at high frequencies.

The observations indicate that both Q_α and Q_β in the lithosphere increase with frequency and the onset of that frequency dependence occurs at a lower frequency for S waves than for P waves. More work is required to distinguish between scattering and intrinsic anelasticity as the dominant mechanism of P_n / S_n attenuation at high frequency.

CONCLUSION

The propagation of the high frequency oceanic P_n and S_n phases can be explained rather simply as refractions from the lower oceanic lithosphere while the subsequent coda is predominantly a result of near-receiver sediment and water reverberations. Complicated oceanic lithosphere structures including low velocity channels, thin high-velocity

lenses, or a distribution of small scale heterogeneity are not necessary to explain the gross features of these high frequency phases.

The high frequency onset of S_n is modelled as a sum of higher modes with particle motions largely restricted to the sub-Moho portion of the lithosphere. The propagation of these modes to teleseismic distances requires a relatively high value for Q_β in the oceanic lithosphere.

The onset of P_n and S_n generally fit a travel time curve that is linear with an inverse slope near the material velocity of the uppermost mantle. Because the rays comprising these phases remain in the lithosphere, this implies only a very shallow velocity gradient is present within the oceanic lithosphere. The emergent onset is due to the gradual build up of energy within the uppermost resonating layers. The very low gradients observed in the oceanic lithosphere are consistent with low amplitudes observed in refraction experiments at large ranges and are responsible for the impractically large source sizes required for that work (*Orcutt and Dorman*, 1977).

The development of a long wave train is due primarily to resonance within the oceanic water column and sediment layer. Due to the large impedance contrast at the sediment-crust interface, the efficient propagation of leaky organ-pipe modes in these two layers results in a long reverberatory wave train. The sediments act as an extremely efficient wave guide for shear wave propagation and a leaky wave guide for compressional wave propagation. The P_n coda does not require a distribution of small scale heterogeneity within the oceanic lithosphere. While scattering is present to some degree, its main contribution to the observations most likely comes from the uppermost crust and not from an inherent property of the deeper part of the lithosphere. The extended length of the P_n coda is due primarily to water reverberation. The shorter duration of the S_n coda possibly results from the inefficiency of S to P conversion in the uppermost layers. The onset of S_n consists of a shear wave turning in the lithosphere and the coda is due to water and sediment resonance. Clearly water reverberation requires S to P conversion at either the sediment-crust or, less likely, the ocean-sediment interface which results in a significant amplitude reduction.

The discontinuous drop in group velocity observed by *Walker* (1981) in the northwest Pacific at an epicentral range of 30° can be explained as a shadowing effect of the low Q asthenosphere. The confinement of these high frequency phases to the oceanic lithosphere, required by their high apparent Q, imposes a constraint on the maximum range a normally refracted wave without upward reflection points can be observed. At ranges less than 30°, the first arrivals of P_n / S_n are normally refracted waves in the lithosphere while at larger ranges they contain an upward reflection. The magnitude of

this group velocity reduction is, however, substantially less for S_n than for P_n. This result is consistent with an S_n phase, at long ranges, that contains an upward reflection point at the ocean-sediment interface while P_n reflects off the free surface.

Chinn, et al. (1980) similarly explain the rapid disappearance of the oceanic S_n phase at distances greater than 16° along ray paths in the eastern part of the Nazca Plate as a shadowing effect of the low Q asthenosphere. This oceanic plate is relatively young (50 Ma) in comparison to the northwest Pacific (100 Ma) and according to thermal models (*Parsons and Sclater*, 1977), would have a smaller lithosphere thickness. This accounts for the shorter shadowing distance (16°) observed for S_n in this region as compared to the cutoff in the northwest Pacific (30°).

The predominance of high frequencies in the oceanic P_n and S_n wave trains is a direct result of the confinement of these phases to the high Q lithosphere. A perhaps more surprising result is that the apparent Q for S_n is greater than that for P_n (*Walker, et al.*, 1978; *Sutton et al.*, 1978) and both phases exhibit Q to be an increasing function of frequency (*Butler, et al.*, 1985). In this paper, we have presented evidence that this behavior can be modelled in terms of an absorption band rheology with high frequency relaxation times similar to those obtained in studies of continental lithosphere structure (*Lundquist and Cormier*, 1980; *Bache, et al.*, 1985). A shorter relaxation time for P waves than for S waves results in a rheology with the property that $Q_\alpha > Q_\beta$ at low frequencies while $Q_\beta > Q_\alpha$ at high frequencies, consistent with the teleseismic P_n / S_n observations. An intrinsic property of the lithosphere that could be responsible for the shorter relaxation time for P waves than for S waves is the preferred orientation of crystals in the lithosphere responsible for observed polarization anisotropy (*Mitchell and Yu*, 1980). This, of course, assumes that attenuation of P and S waves through the lithosphere is associated with grain-boundary relaxation. Scattering could also be responsible for the reduced Q_{P_n} / Q_{S_n} ratio and more work is needed to distinguish between this and intrinsic anelasticity as the dominant mechanism of P_n / S_n attenuation at high frequency.

The absorption band model is to be viewed as only an approximation to the frequency dependence for which analytic expressions for the material dispersion have been developed (*Lundquist and Cormier*, 1980). The introduction of attenuation in the wave number integration is accomplished by allowing the material velocities to be complex. The integration is conducted in the frequency domain and therefore the inclusion of frequency dependence to Q is easily accomplished once the analytic expression for the complex velocity is obtained.

REFERENCES

Adair, R. G., J. A. Orcutt, and T. H. Jordan, Low-frequency noise observations in the deep ocean, *J. Acoust. Soc. Am.*, in press, 1986.

Aki, K., Attenuation of shear waves in the lithosphere for frequencies from 0.05 to 25 Hz, *Phys. Earth Planet. Inter., 21*, 50-60, 1980*a*.

Aki, K., Scattering and attenuation of shear waves in the lithosphere, *J. Geophys. Res., 85*, 6496-6504, 1980*b*.

Aki, K., and P. G. Richards, *Quantitative Seismology: Theory and Methods*, W. H. Freeman, San Francisco, Calif., 1980.

Anderson, D. and C. Archambeau, The anelasticity of the earth, *J. Geophys. Res., 69*, 2071-2084, 1964.

Anderson, D., A. Ben-Menahem, and C. Archambeau, Attenuation of seismic energy in the upper mantle, *J. Geophys. Res., 70*, 1441-1448, 1965.

Anderson, D. and J. Given, Absorption band Q model for the earth, *J. Geophys. Res., 87*, 3893-3904, 1982.

Anderson, D. and R. Hart, Attenuation models of the earth, *Phys. Earth Planet. Inter., 16*, 289-306, 1978*a*.

Anderson, D. and R. Hart, Q of the earth, *J. Geophys. Res., 83*, 5869-5882, 1978*b*.

Apsel, R. J., Dynamic Green's functions for layered media and applications to boundary-value problems, Ph.D. thesis, 349 pp., Univ. of Calif., San Diego, La Jolla, 1979.

Asada, T., and H. Shimamura, Observation of earthquakes and explosions at the bottom of the western Pacific: structure of oceanic lithosphere revealed by Longshot Experiment, *Monogr. Am. geophys. Un., 19*, 135-153, 1976.

Bache, T., P. Marshall, and L. Bache, Q for teleseismic P waves from central Asia, *J. Geophys. Res., 90*, 3575-3587, 1985.

Barazangi, M., B. Isacks, and J. Oliver, Propagation of seismic waves through and beneath the lithosphere that descends under the Tonga island arc, *J. Geophys. Res., 77*, 952-958, 1972.

Butler, R., C. McCreery, L. N. Frazer, and D. Walker, High-frequency attenuation in the western Pacific, (abstract), *EOS, 66*, p. 305, 1985.

Chinn, D., B. Isacks, and M. Barazangi, High-frequency seismic wave propagation in western South America along the continental margin, in the Nazca plate and across the Altiplano, *Geophys. J. R. astr. Soc., 60*, 209-244, 1980.

Clements, J., Intrinsic Q and its frequency dependence, *Phys. Earth Planet. Inter., 27*, 286-299, 1982.

Der, Z., W. Rivers, T. McElfresh, A. O'Donnell, P. Klouda, and M. Marshall, Worldwide variations in the attenuative properties of the upper mantle as determined from spectral studies of short-period body waves, *Phys. Earth Planet. Inter., 30*, 12-25, 1982.

Dziewonski, A., A. Hales, and E. Lapwood, Parametrically simple earth models consistent with geophysical data, *Phys. Earth Planet. Inter., 10*, 12-48, 1975.

Forsyth, D., The early structural evolution and anisotropy of the oceanic upper mantle, *Geophys. J. R. astr. Soc., 43*, 103-162, 1975.

Fuchs, K., and K. Schulz, Tunneling of low-frequency waves through the subcrustal lithosphere, *J. Geophys., 42*, 175-190, 1976.

Gettrust, J., and L. N. Frazer, A computer model study of the long-range PN phase, *Geophys. Res. Lett., 8*, 749-752, 1981.

Hales, A., C. Helsley, and J. Nation, P wave times for an oceanic path, *J. Geophys. Res., 75*, 7362-7381, 1970.

Hamilton, E. L., Shear-wave velocity versus depth in marine sediments: a review, *Geophysics, 41*, 985-996, 1976.

Hart, R., and F. Press, S_n velocities and the composition of the lithosphere in the regionalized Atlantic, *J. Geophys. Res., 78*, 407-411, 1973.

Isacks, B., and M. Barazangi, High frequency shear waves guided by a continuous lithosphere descending beneath western South America, *Geophys. J. R. astr. Soc., 33*, 129-139, 1973

Kennett, B., *Seismic Wave Propagation in Stratified Media*, Cambridge University Press, Cambridge, 1983.

Kim, I. I., D. K. Smith, J. A. Orcutt, T. H. Jordan, and H. W. Menard, Seismic reflection site survey: Correlation with physical properties, leg 91, Deep Sea Drilling Project, *Initial Rep. Deep Sea Drill. Proj., 91*, in press, 1986.

Knopoff, L., *Q* , *Rev. Geophys., 2*, 625-660, 1964.

Latham, G., and G. Sutton, Seismic measurements on the sea floor, 1. Bermuda area, *J. Geophys. Res., 71*, 2545-2573, 1966.

Liu, H., D. Anderson, and H. Kanamori, Velocity dispersion due to anelasticity; implications for seismology and mantle composition, *Geophys. J. R. astr. Soc., 47*, 41-58, 1976.

Lundquist, G., and V. Cormier, Constraints on the absorption band model of *Q*, *J. Geophys. Res., 85*, 5244-5256, 1980.

McCreery, C., High-frequency *PN*,*SN* phases recorded by ocean bottom seismometers on the Cocos plate, *Geophys. Res. Lett., 8*, 489-492, 1981.

Menke, W., and R. Chen, Numerical studies of the coda falloff rate of multiply scattered waves in a randomly layered media, *Bull. Seismol. Soc. Am., 74*, 1605-1621, 1984.

Menke, W., and P. Richards, Crust-mantle whispering gallery phases: a deterministic

model of teleseismic P_n wave propagation, *J. Geophys. Res.*, *85*, 5416-5422, 1980.

Mitchell, B., and G. Yu, Surface wave dispersion, regionalized velocity models, and anisotropy of the Pacific crust and upper mantle, *Geophys. J. R. astr. Soc.*, *63*, 497-514, 1980.

Molnar, P., and J. Oliver, Lateral variations of attenuation in the upper mantle and discontinuities in the lithosphere, *J. Geophys. Res.*, *74*, 2648-2682, 1969.

Oliver, J., and B. Isacks, Deep earthquake zones, anomalous structures in the upper mantle, and the lithosphere, *J. Geophys. Res.*, *72*, 4259-4275, 1967.

Orcutt, J., and L. Dorman, An oceanic long range explosion experiment, *J. Geophys.*, *43*, 257-263, 1977.

Ouchi, T., Spectral structure of high frequency P and S phases observed by OBS's in the Mariana basin, *J. Phys. Earth*, *29*, 305-326, 1981.

Parker, R., and D. Oldenburg, Thermal models of ocean ridges, *Nature Phys. Sci.*, *242*, 137-139, 1973.

Parsons, B., and J. Sclater, An analysis of the variation of ocean floor bathymetry and heat flow with age, *J. Geophys. Res.*, *82*, 803-827, 1977.

Richards, P., and W. Menke, The apparent attenuation of a scattering medium, *Bull. Seismol. Soc. Am.*, *73*, 1005-1021, 1983.

Sereno, T., The propagation of high frequency seismic energy through oceanic lithosphere, Ph.D. thesis, 168 pp., Univ. of Calif., San Diego, La Jolla, 1986.

Sereno, T., and J. Orcutt, Synthetic seismogram modelling of the oceanic P_n phase, *Nature*, *316*, 246-248, 1985*a*.

Sereno, T., and J. Orcutt, Synthesis of realistic oceanic P_n wave trains, *J. Geophys. Res.*, *90*, 12755-12776, 1985*b*.

Sereno, T., and J. Orcutt, The propagation of P_n, Proceedings of the Ocean Seismo-Acoustics meeting, La Spezia, Italy, 1986.

Shaw, P., and J. A. Orcutt, Propagation of *PL* and implications for the structure of Tibet, *J. Geophys. Res.*, *89*, 3135-3152, 1984.

Smith, S., The anelasticity of the mantle, *Tectonophysics*, *13*, 601-622, 1972.

Stephens, C., and B. Isacks, Toward an understanding of S_n: normal modes of Love waves in an oceanic structure, *Bull. Seismol. Soc. Am.*, *67*, 69-78, 1977.

Sutton, G., C. McCreery, F. Duennebier, and D. Walker, Spectral analyses of high-frequency *PN*,*SN* phases recorded on ocean bottom seismographs, *Geophys. Res. Lett.*, *5*, 745-747, 1978.

Sutton, G., and D. Walker, Oceanic mantle phases recorded on seismographs in the northwestern Pacific at distances between 7° and 40°, *Bull. Seismol. Soc. Am.*, *62*, 631-655, 1972.

Talandier, J., and M. Bouchon, Propagation of high frequency P_n waves at great distances in the central and south Pacific and its implications for the structure of the lower lithosphere, *J. Geophys. Res.*, *84*, 5613-5619, 1979.

Taylor, S., B. Bonner, and G. Zandt, Attenuation and scattering of broadband *P* and *S* waves across North America, *EOS*, *67*, 199, 1986.

Ulug, A., and H. Berckhemer, Frequency dependence of *Q* for seismic body waves in the earth's mantle, *J. Geophys.*, *56*, 9-19, 1984.

Walker, D., High-frequency P_n phases observed in the Pacific at great distances, *Science*, *197*, 257-259, 1977*a*.

Walker, D., High-frequency P_n and S_n phases recorded in the western Pacific, *J. Geophys. Res.*, *82*, 3350-3360, 1977*b*.

Walker, D., High-frequency *PN*,*SN* velocities: some comparisons for the western,

central, and south Pacific, *Geophys. Res. Lett.*, *8*, 207-209, 1981.

Walker, D., Oceanic *PN / SN* phases: a qualitative explanation and reinterpretation of the *T*-phase, *Rep. HIG-82-6*, 19 pp., Hawaii Inst. of Geophys., Honolulu, 1982.

Walker, D., C. McCreery, and G. Sutton, Spectral characteristics of high frequency P_N,S_N phases in the western Pacific, *J. Geophys. Res.*, *88*, 4289-4298, 1983.

Walker, D., C. McCreery, G. Sutton, and F. Duennebier, Spectral analyses of high-frequency P_n and S_n phases observed at great distances in the western Pacific, *Science, 199*, 1333-1335, 1978.

Watts, A., J. Bodine, and N. Ribe, Observations of flexure and the geological evolution of the Pacific ocean basin, *Nature, 283*, 532-536, 1980.

Zener, C., *Elasticity and Anelasticity of Metals*, University of Chicago Press, Chicago, Ill., 1948.

Table 1. Ngendei Model

Layer	V_p, km/s	V_s, km/s	ρ, Mg/m^3	Q_α	Q_β	h, km
1	1.500	0.000	1.0000	50000	---	5.55
2	1.600	0.116	1.0096	200	100	0.07
3	5.000	2.757	2.7000	900	450	0.25
4	5.300	2.923	2.7600	900	450	0.20
5	5.600	3.088	2.8200	900	450	0.20
6	5.900	3.254	2.8800	900	450	0.20
7	6.200	3.419	2.9400	900	450	0.40
8	6.500	3.585	3.0000	900	450	0.70
9	6.800	3.750	3.0600	900	450	4.63
10	8.200	4.650	3.3400	2000	1000	30.0
11	8.225	4.664	3.3450	2000	1000	30.0
12	8.250	4.678	3.3500	2000	1000	30.0
13	8.275	4.693	3.3550	2000	1000	∞

Table 2. Oceanic Lithosphere Model [*Sereno and Orcutt*, 1985*b*]

Layer	V_p, km/s	V_s, km/s	ρ, Mg/m^3	Q_α	Q_β	h, km
1	1.5000	0.0000	1.0000	50000	---	4.0
2	2.0000	1.1548	1.0096	200	100	0.5
3	5.5000	3.1760	2.3350	450	225	1.0
4	6.4018	3.6962	2.6756	450	225	0.5
5	6.8032	3.9279	2.8265	450	225	2.0
6	7.4058	4.2759	3.0527	450	225	2.0
7	8.1654	4.7144	3.3232	450	225	31.6
8	8.1807	4.7233	3.2975	450	225	31.6
9	8.1961	4.7322	3.2717	450	225	31.6
10	8.2038	4.7366	3.2588	450	225	∞

Table 3. Absorption band parameters.

	Q_m	τ_1, s	τ_2, s
P waves	200	100	0.05
S waves	100	100	0.16

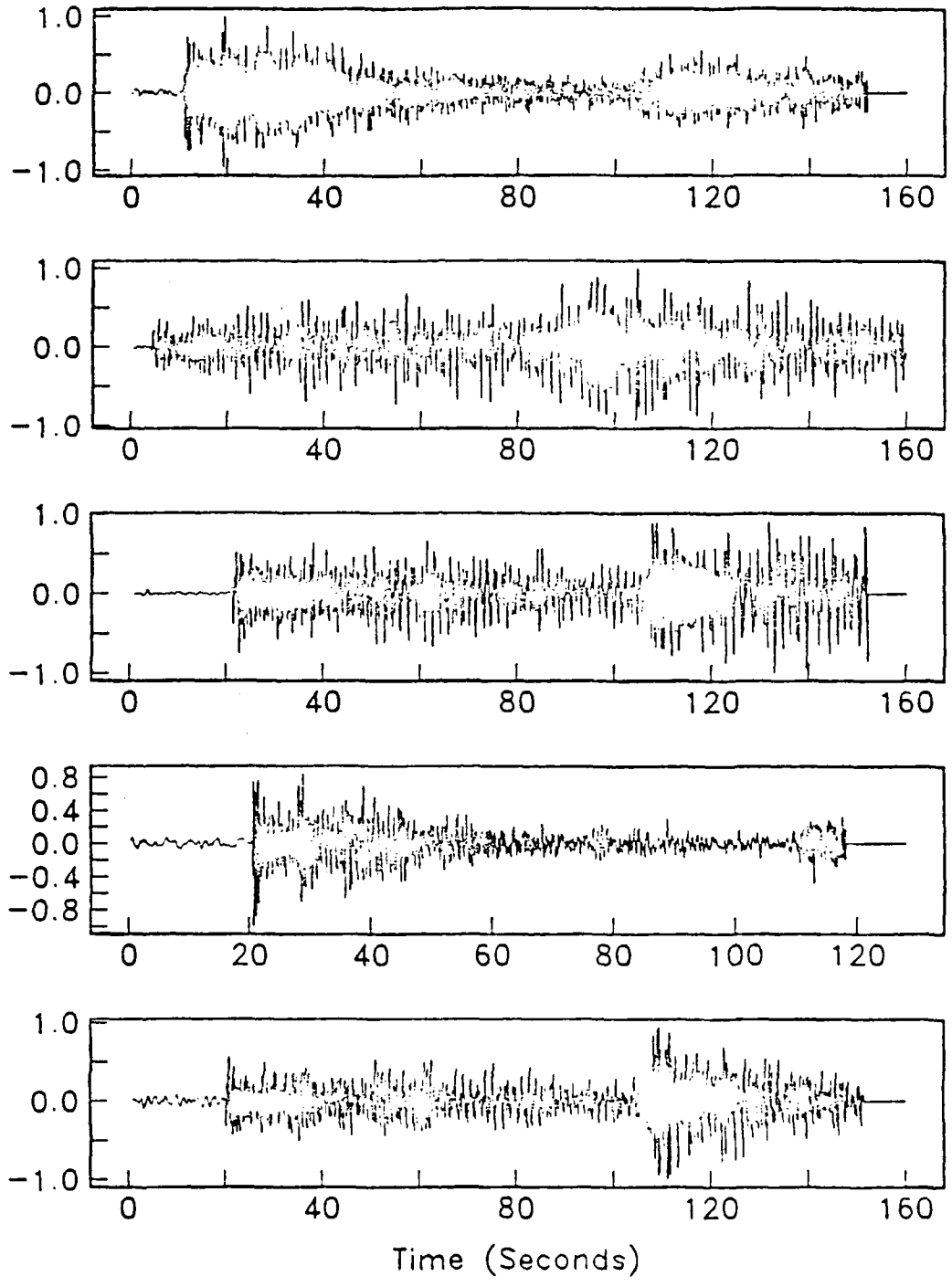


Figure 1. Examples of vertical component P_n, S_n data collected during the 1983 Ngendei Seismic Experiment in the southwest Pacific. The P_n wave train has a duration of 80-90 s and extends into the onset of S_n. Travel path lengths are of the order of 1000 km.

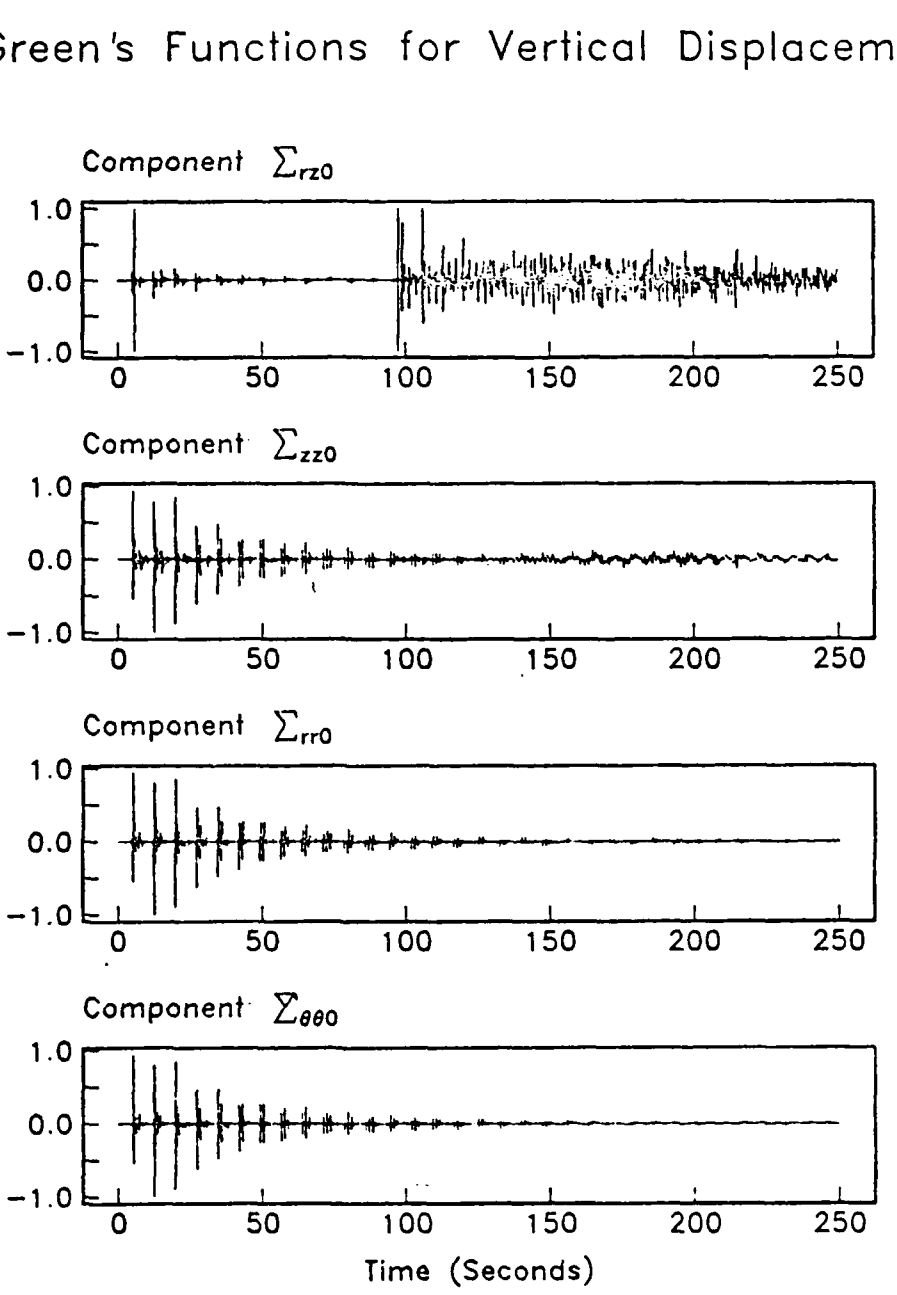


Figure 2. Green's functions for vertical displacement computed for the Ngendei structure. The four stress tensor elements for a vertical point force are shown, Σ_{rz0}, Σ_{zz0}, Σ_{rr0}, and $\Sigma_{\theta\theta0}$. Vertical displacement for an arbitrarily oriented double-couple source is obtained through linear combination of these four stress tensor elements.

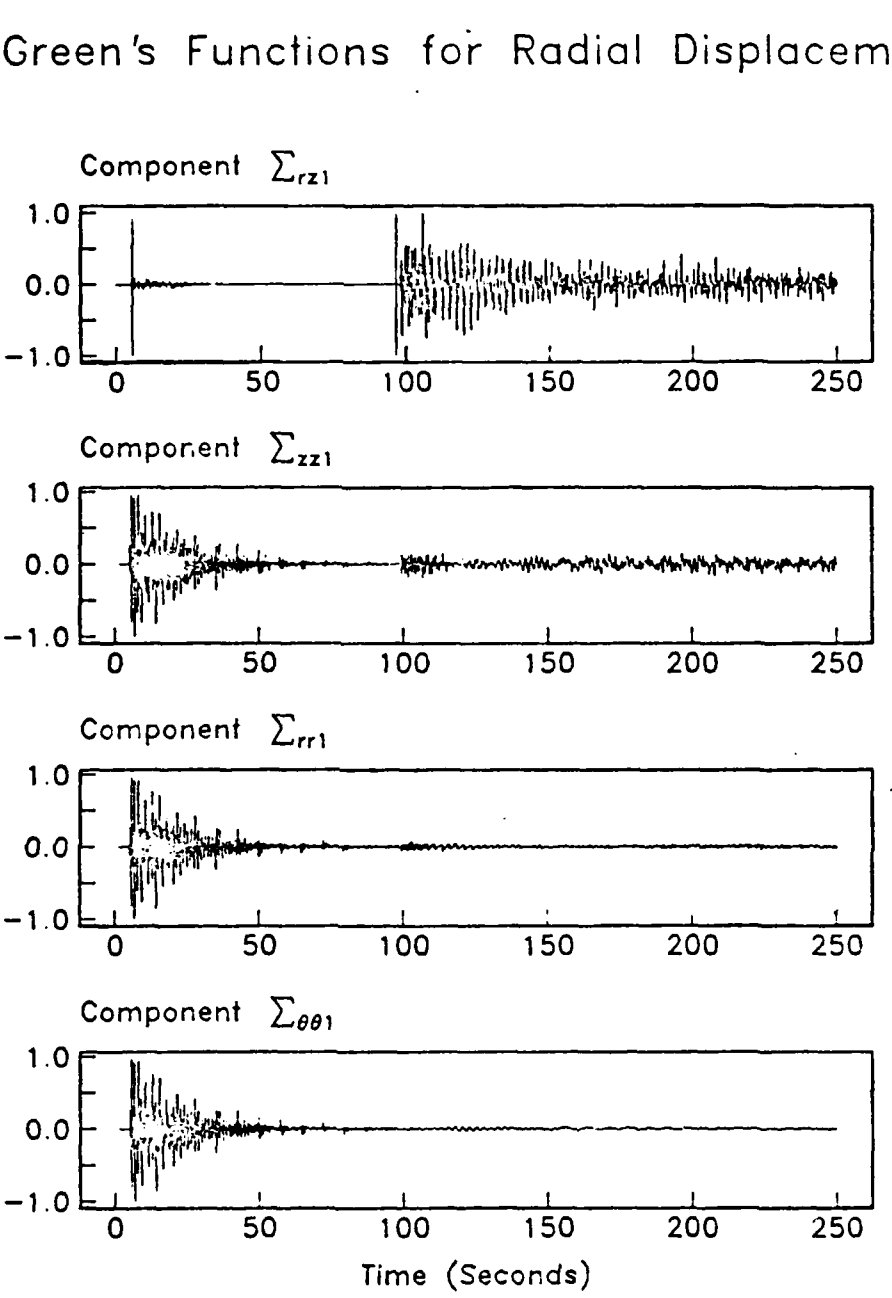


Figure 3. Green's functions for radial displacement computed for the Ngendei structure. Four stress tensor elements for a horizontal point force are shown, Σ_{rz1}, Σ_{zz1}, Σ_{rr1}, and $\Sigma_{\theta\theta1}$. Radial displacement for an arbitrarily oriented double-couple source is obtained through linear combination of these four stress tensor elements.

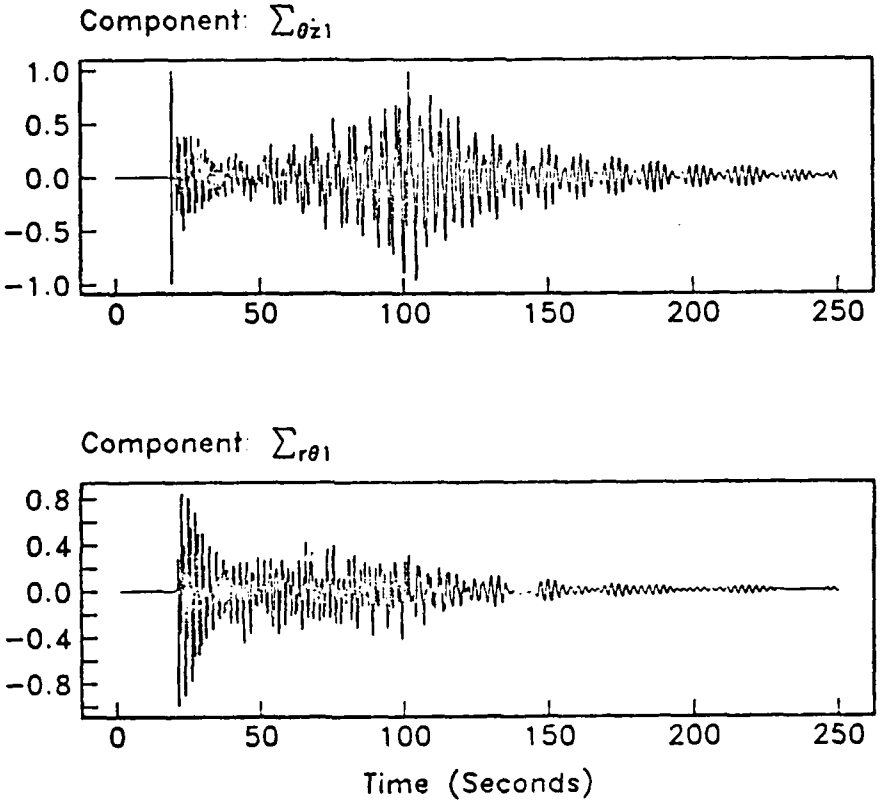


Figure 4. Green's functions for transverse displacement computed for the Ngendei st - ture. Two stress tensor elements for a horizontal point force are shown, $\Sigma_{\theta z1}$ and $\Sigma_{r\theta1}$. Transverse displacement for an arbitrarily oriented double-couple source is obtained through linear combination of these two stress tensor elements.

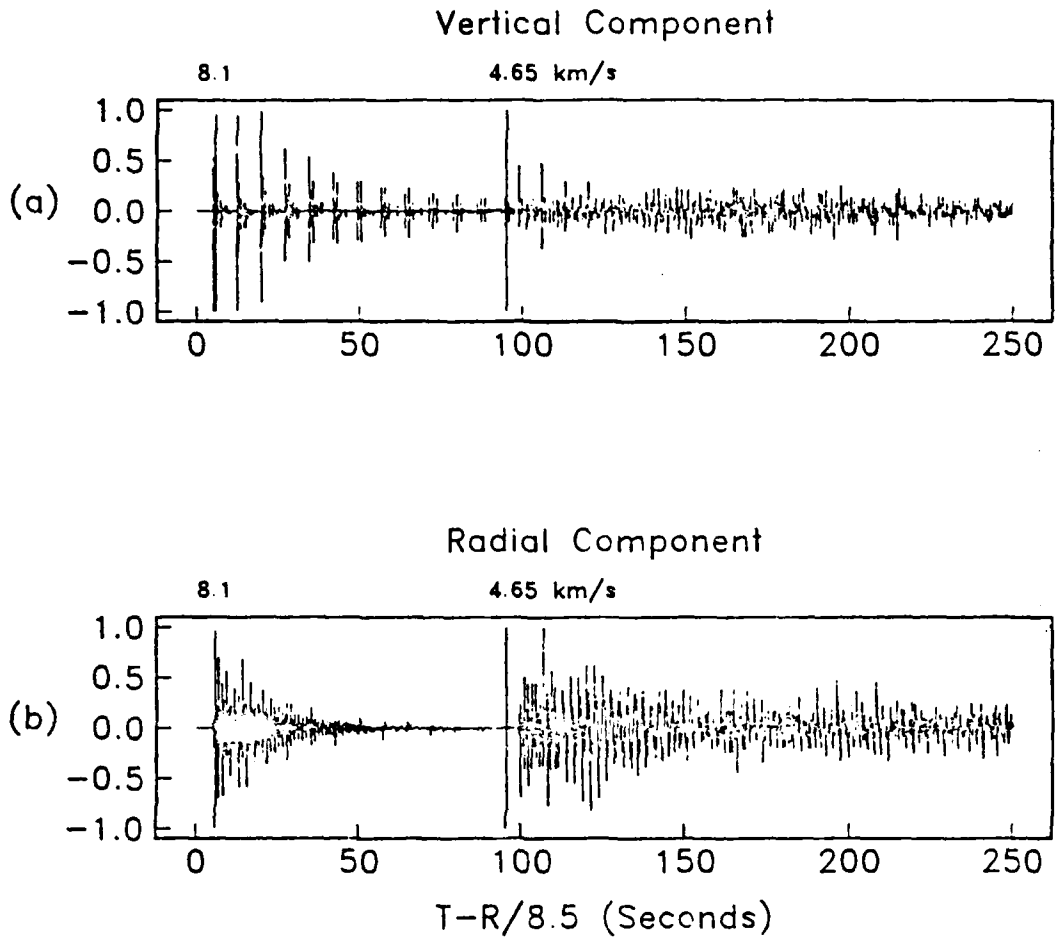


Figure 5. Synthetic P_n / S_n phases computed for the Ngendei structure. (*a*) Vertical displacement and (*b*) radial displacement for a thrust fault source at 15.0 km depth at an epicentral range of 1000 km. Velocities of 8.1 and 4.65 km/s are indicated.

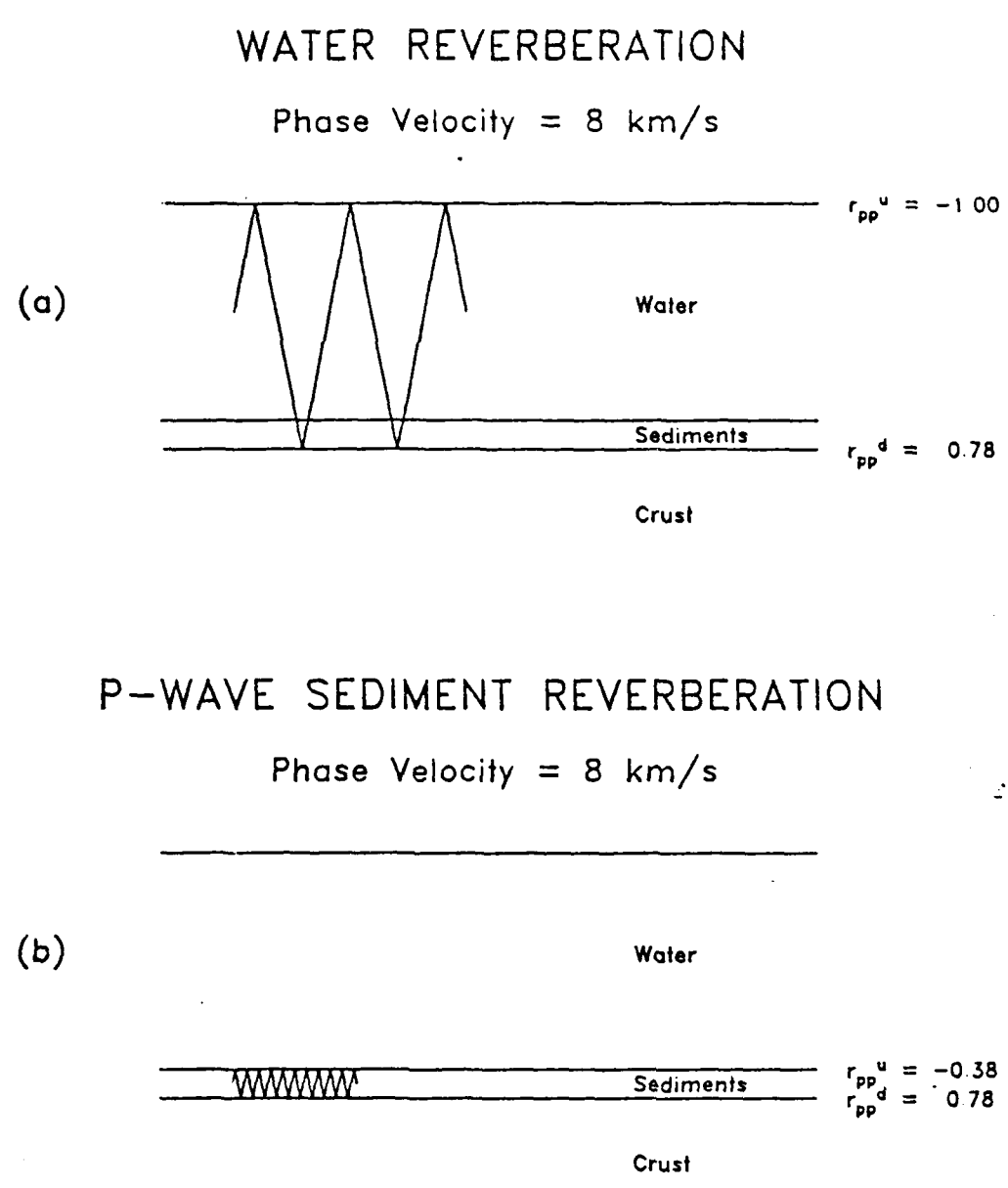


Figure 6. Schematic illustration of the compressional wave reverberation contribution to the P_n coda. (*a*) Water reverberation and (*b*) sediment reverberation. The reflection coefficients are given for a phase velocity of 8 km/s.

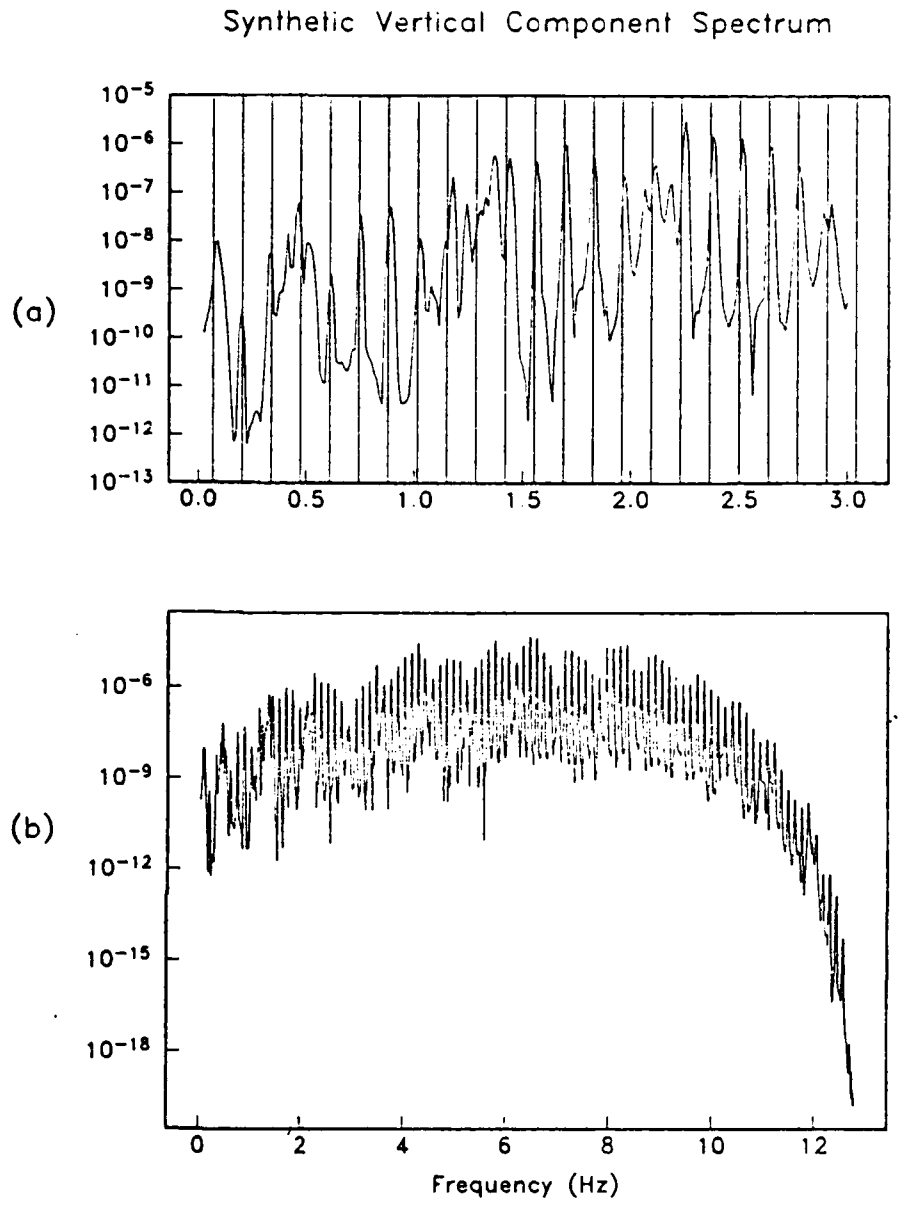


Figure 7. Power spectrum of the synthetic P_n wave train in Figure 5*a*. A Hanning window was applied over the first 80 s of the time series. (*a*) First 3.0 Hz of the spectrum with vertical lines indicating the predicted frequencies of water resonance peaks. (*b*) Full spectrum.

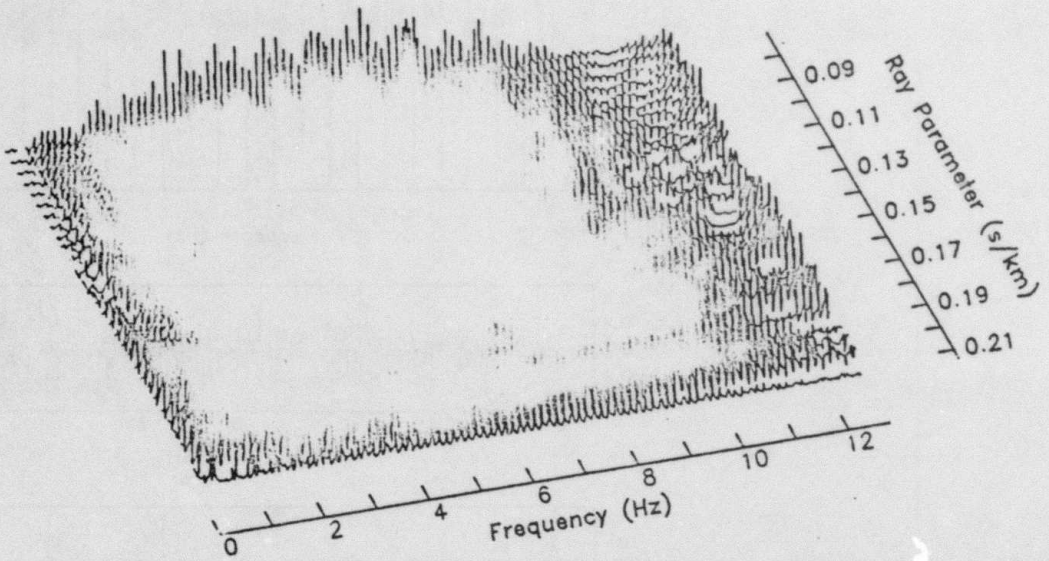


Figure 8. Modulus of the vertical normal stress, $k\sigma_{220}(\omega,p)$, for a source depth of 15 km for the Ngendei model.

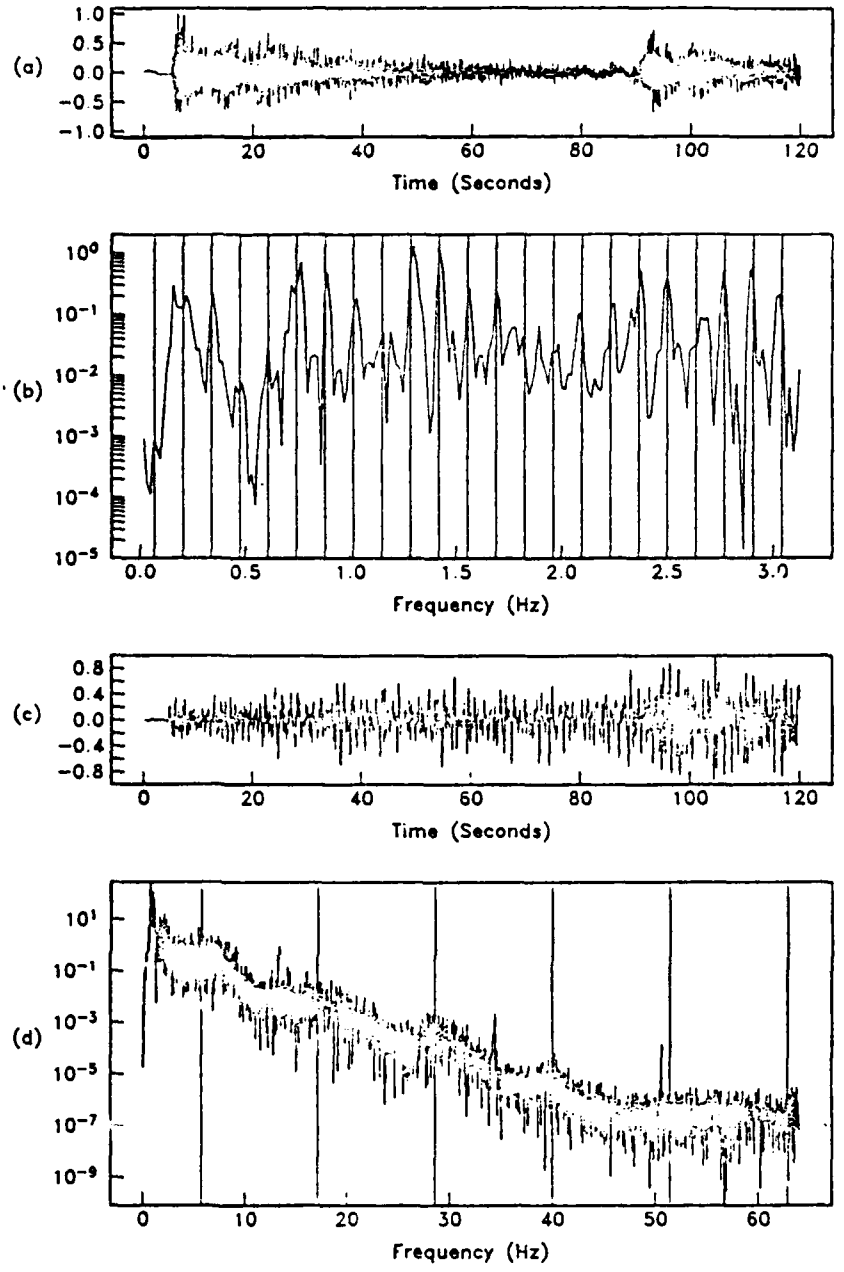


Figure 9. Data collected in the southwest Pacific during the 1983 Ngendei Seismic Experiment. (*a*) Hydrophone record; OBS Suzy, event 130 and (*b*) the first 3.0 Hz of its power spectrum with vertical lines at predicted eigenfrequencies of water layer resonances. (*c*) OBS vertical component data: OBS Karen, event 24 and (*d*) its power spectrum. Vertical lines indicate predicted resonance frequencies for P-wave sediment reverberation.

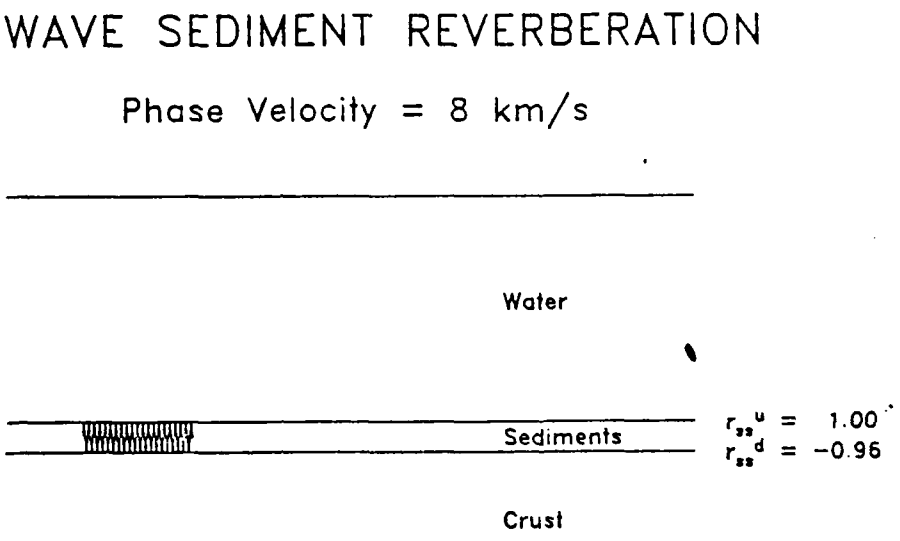


Figure 10. Schematic illustration of the shear wave sediment reverberation contribution to the P_n coda. The reflection coefficients are given for a phase velocity of 8 km/s.

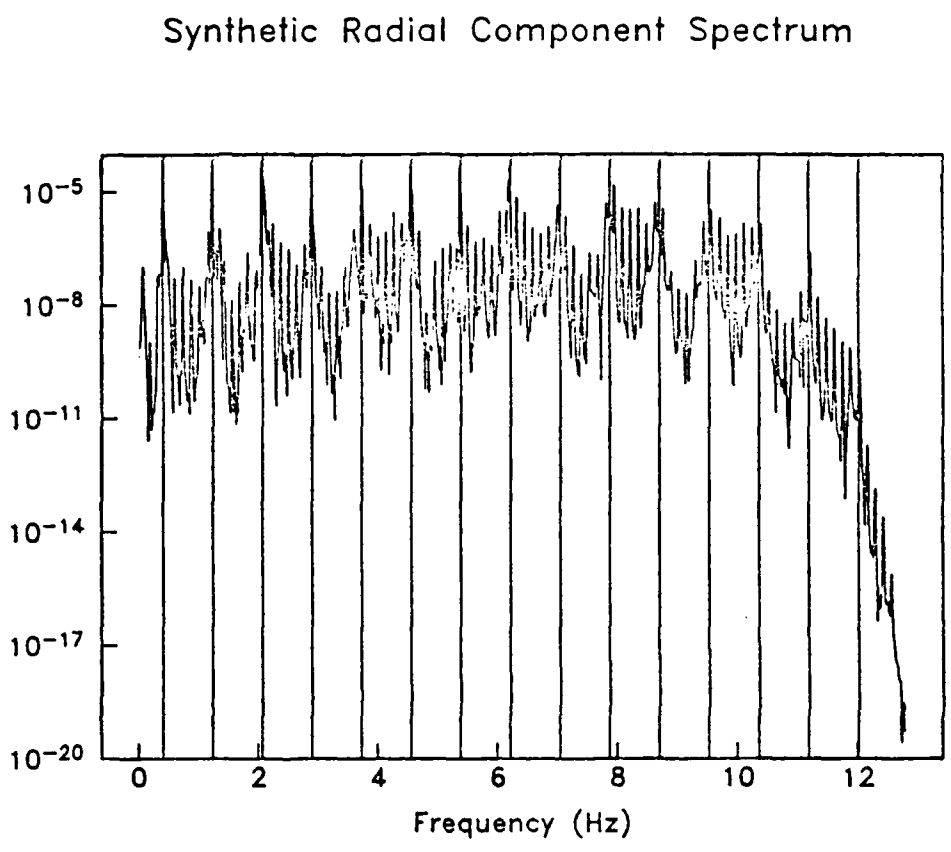


Figure 11. Power spectrum of the synthetic P_n wave train in Figure 5*b*. A Hanning window was applied over the first 80 s of the time series. Vertical lines indicate the eigenfrequencies for shear wave organ-pipe modes in the sediment layer.

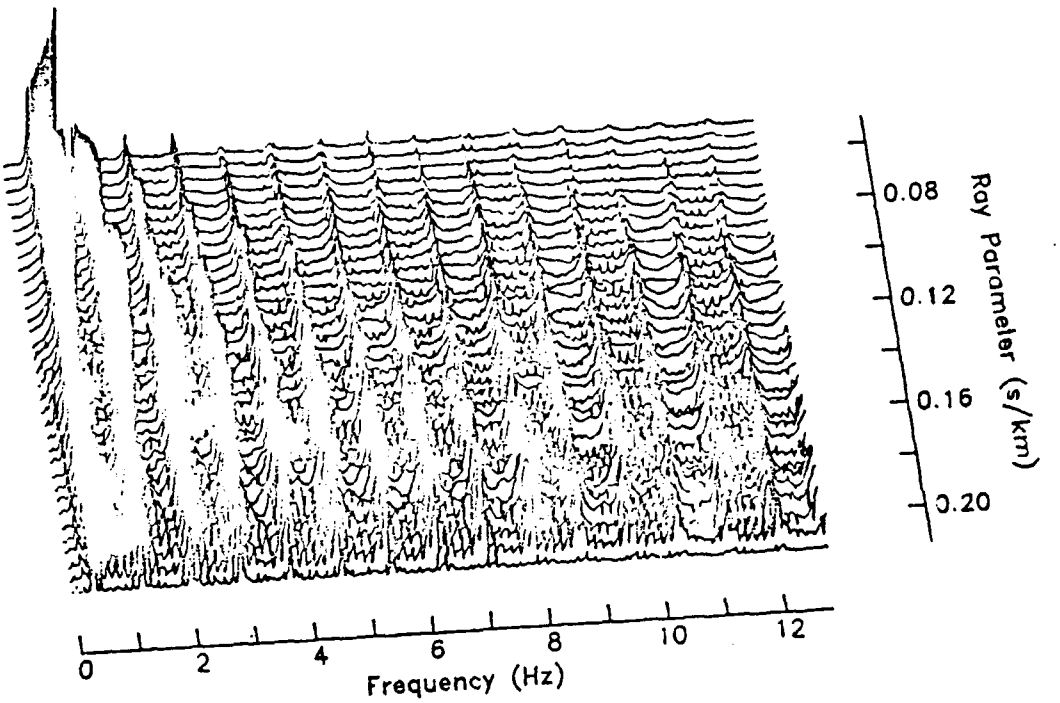


Figure 12. Modulus of the horizontal normal stress, $k\sigma_{221}(\omega,p)$, for a source depth of 15 km for the Ngendei model.

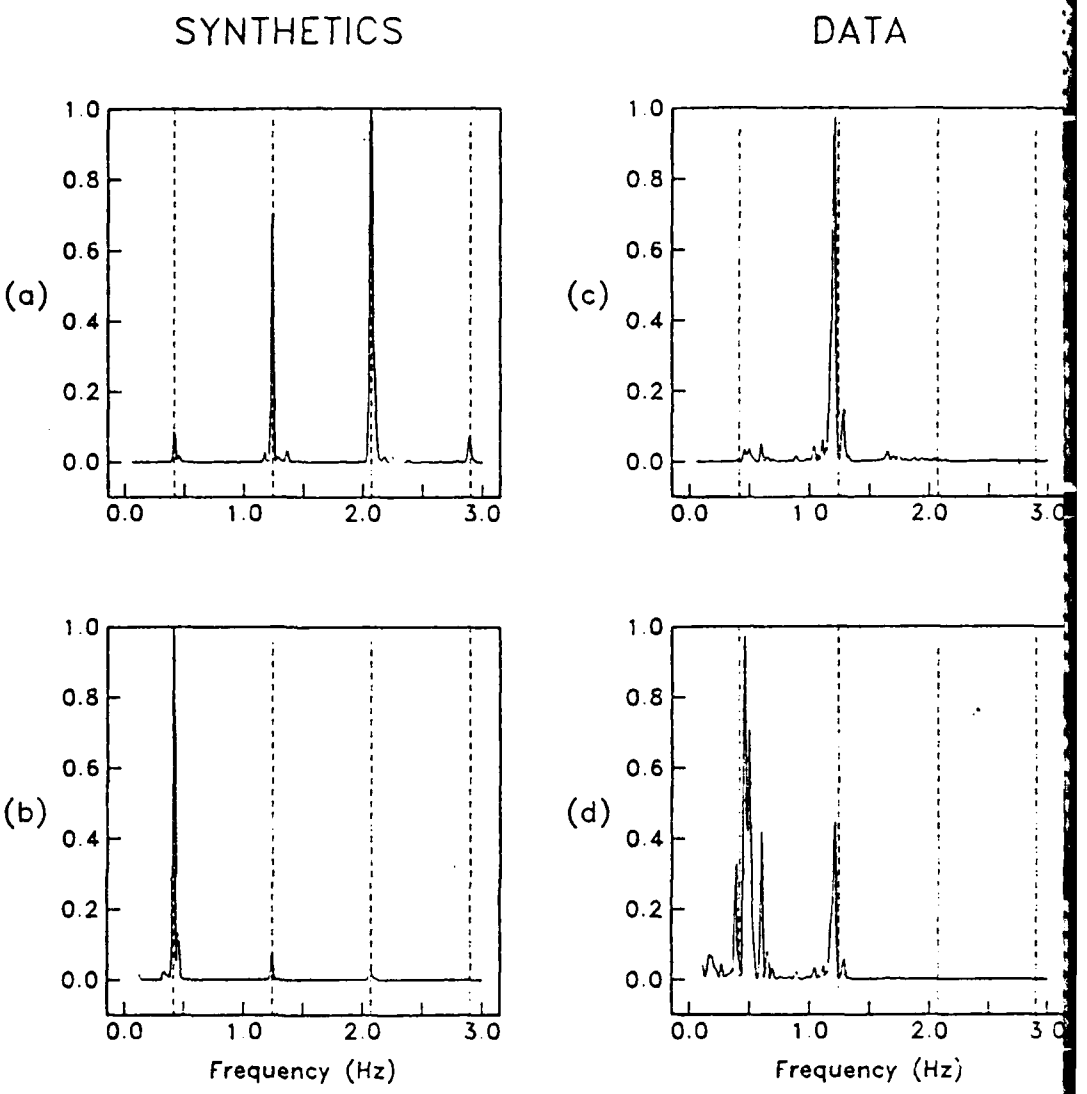


Figure 13. Power spectra illustrating shear wave sediment reverberations within the P_n coda. (*a*) First 3.0 Hz of the synthetic horizontal spectrum after including the OBS instrument response. (*b*) Synthetic spectrum of Figure 13*a* without including the instrument response. Power spectra of horizontal component data taken at the Ngendei site (*c*) before removing the instrument response and (*d*) after removing the instrument response. In Figures 13*a*-13*d*, dashed vertical lines indicate predicted frequencies of *S* wave sediment reverberation peaks. The peak amplitudes in each figure were scaled to a maximum amplitude of one. Note the linear scale used in these figures.

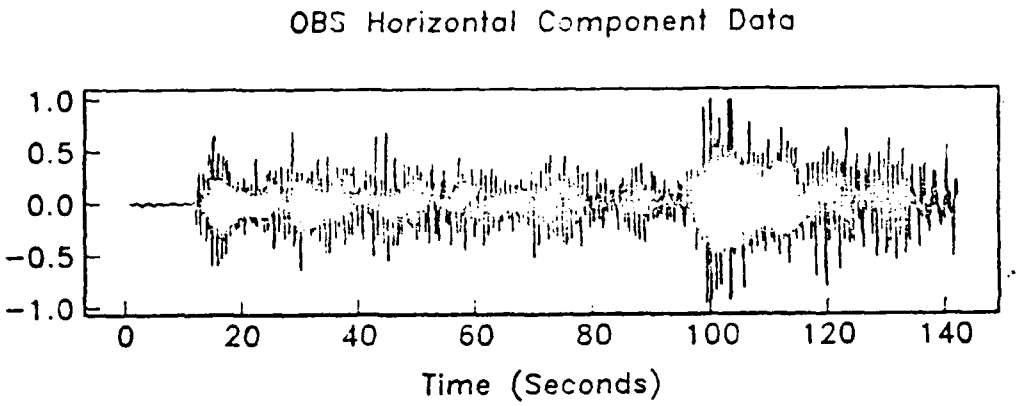


Figure 14. Horizontal component OBS data collected at the Ngendei site at a range of 920 km. OBS Suzy, event 25.

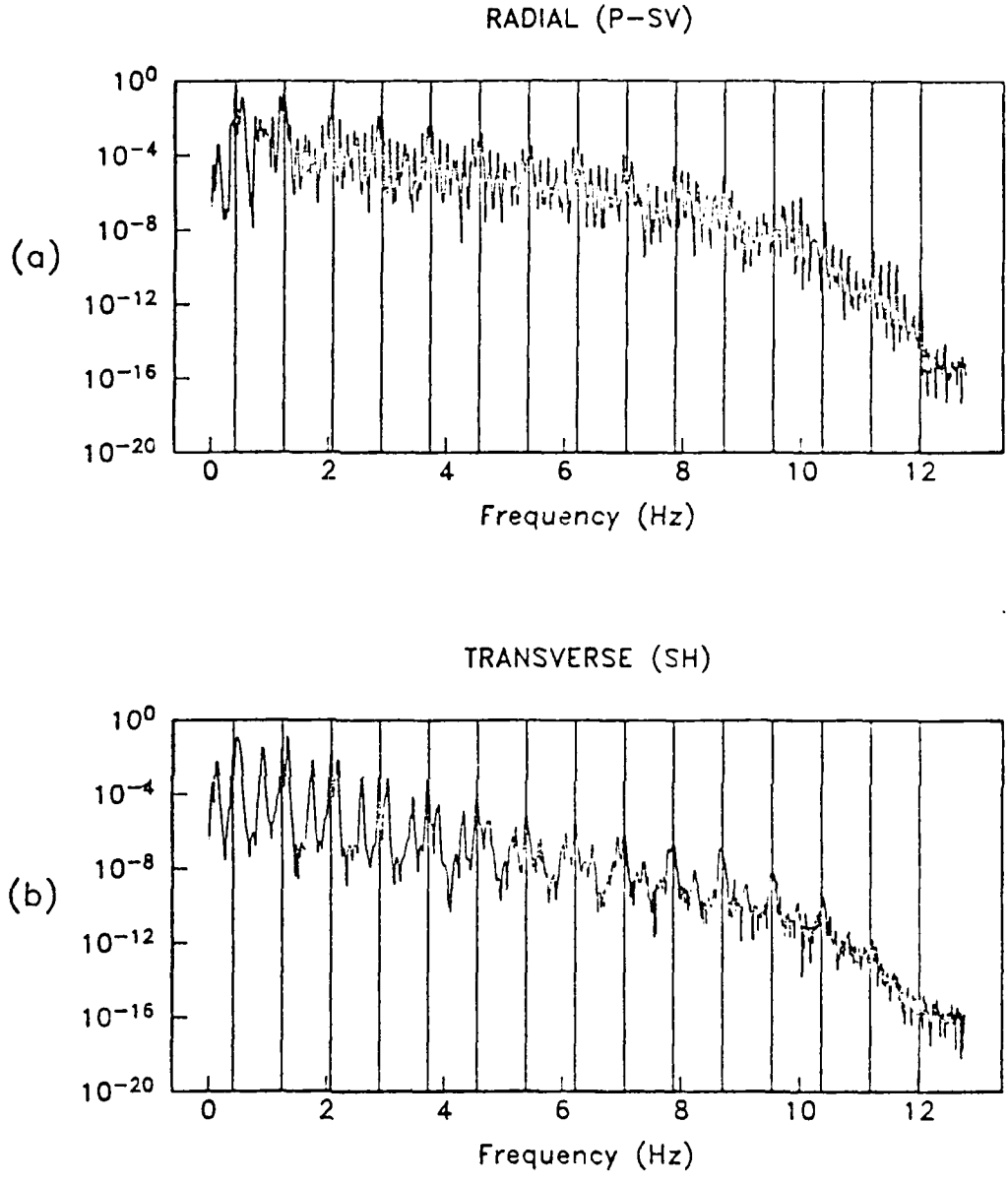


Figure 15. (*a*) Power spectrum of the synthetic radial component S_n wave train. (*b*) Power spectrum of the synthetic transverse component S_n wave train. Vertical lines in both diagrams are drawn at predicted eigenfrequencies of shear wave organ-pipe modes in the sediment layer.

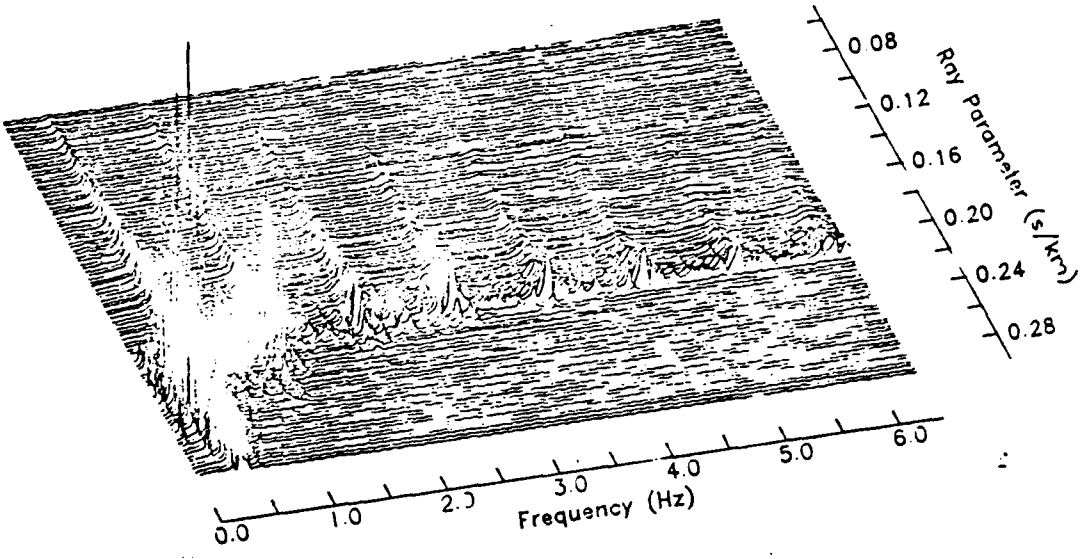


Figure 16. Frequency-ray parameter wave field, $k\sigma_{211}(\omega,p) + k\sigma_{231}(\omega,p)$, computed for the Ngendei model (Table 1).

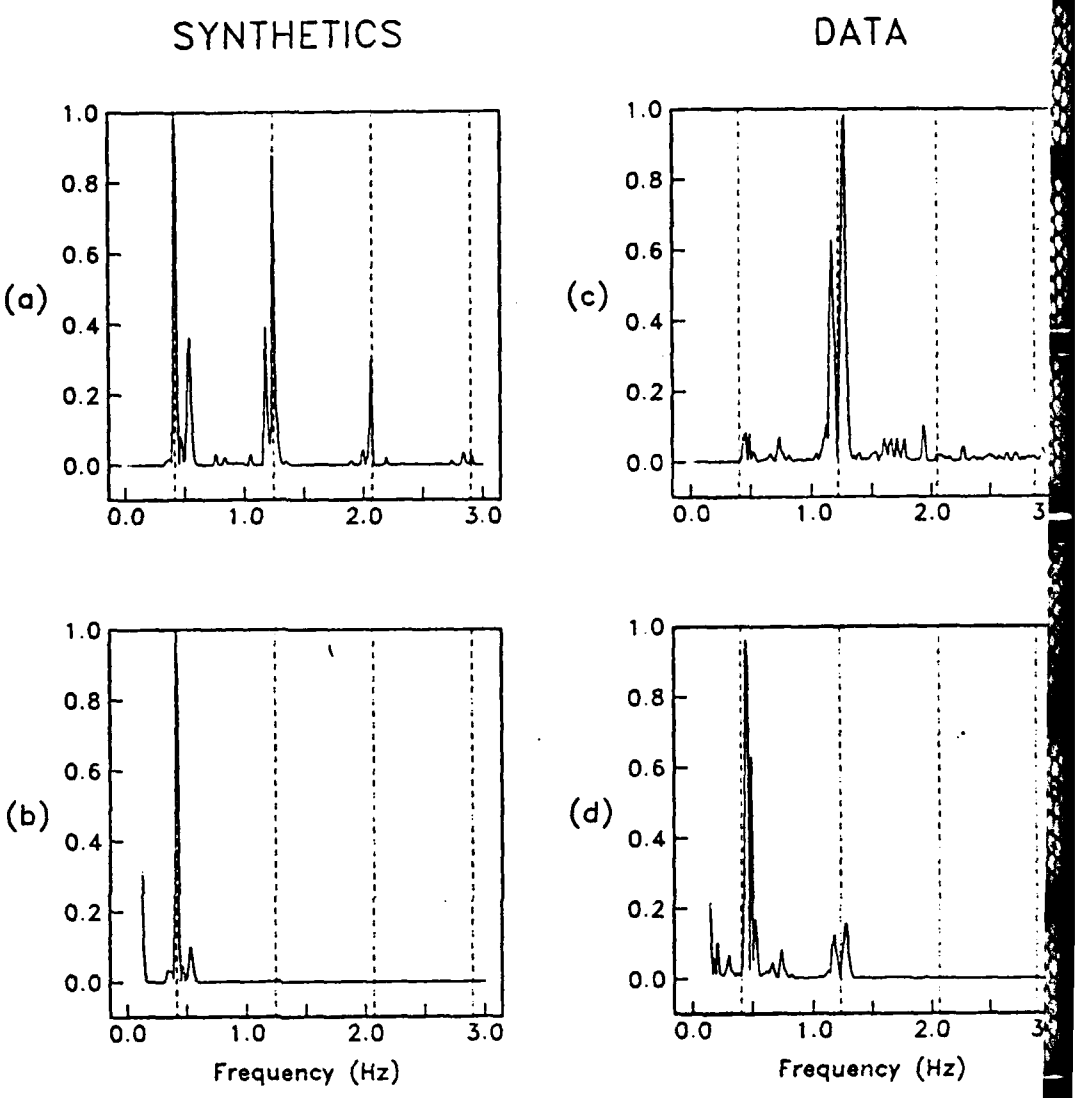


Figure 17. Power spectra illustrating shear wave sediment reverberations within the S_n coda. (*a*) First 3.0 Hz of the synthetic radial component spectrum of Figure 15*a*. (*b*) Synthetic spectrum of Figure 17*a* without including the instrument response. Power spectra of horizontal component S_n data taken at the Ngendei site (*c*) before removing the instrument response and (*d*) after removing the instrument response. In Figures 17*a*-17*d*, dashed vertical lines indicate predicted frequencies of *S* wave sediment reverberation peaks. The peak amplitudes in each figure were scaled to a maximum amplitude of one. Note the linear scale used in these figures.

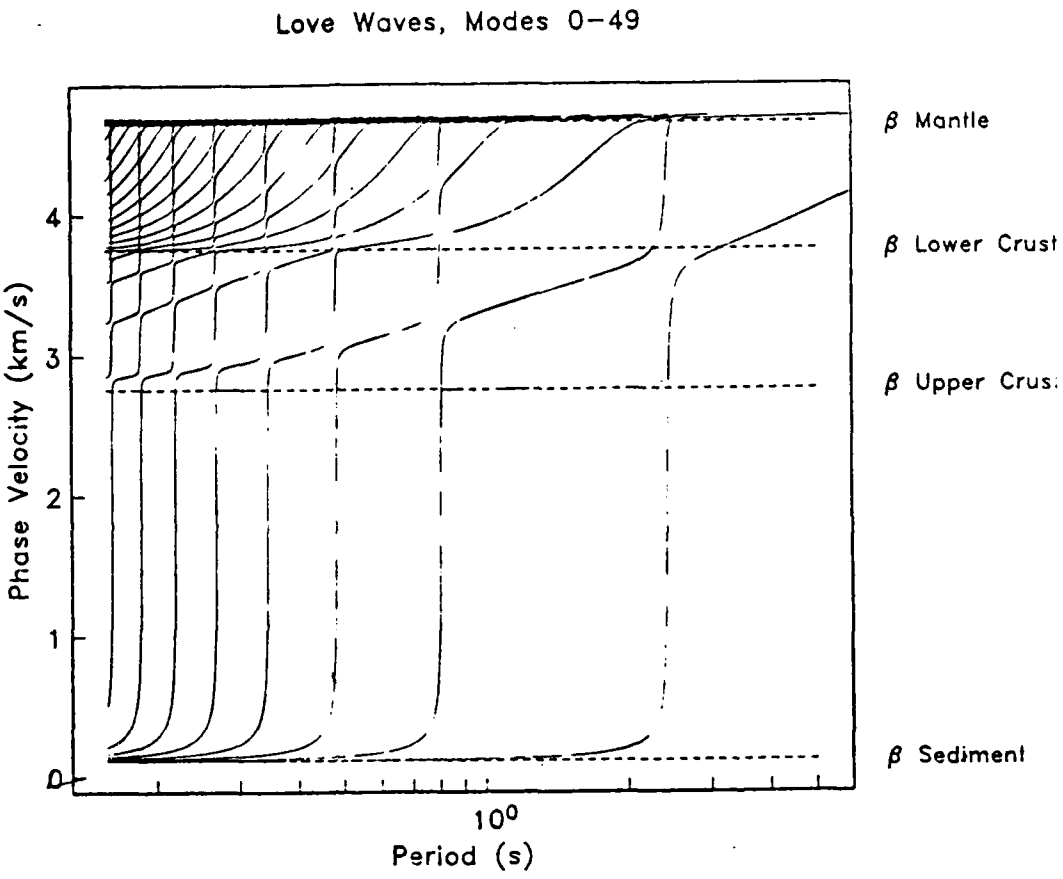


Figure 18. Phase velocity dispersion for the first 50 Love wave modes computed for the Ngendei model (Table 1). The fundamental mode is on the far right and mode number increases to the left. Dashed horizontal lines indicate layer velocities in the model.

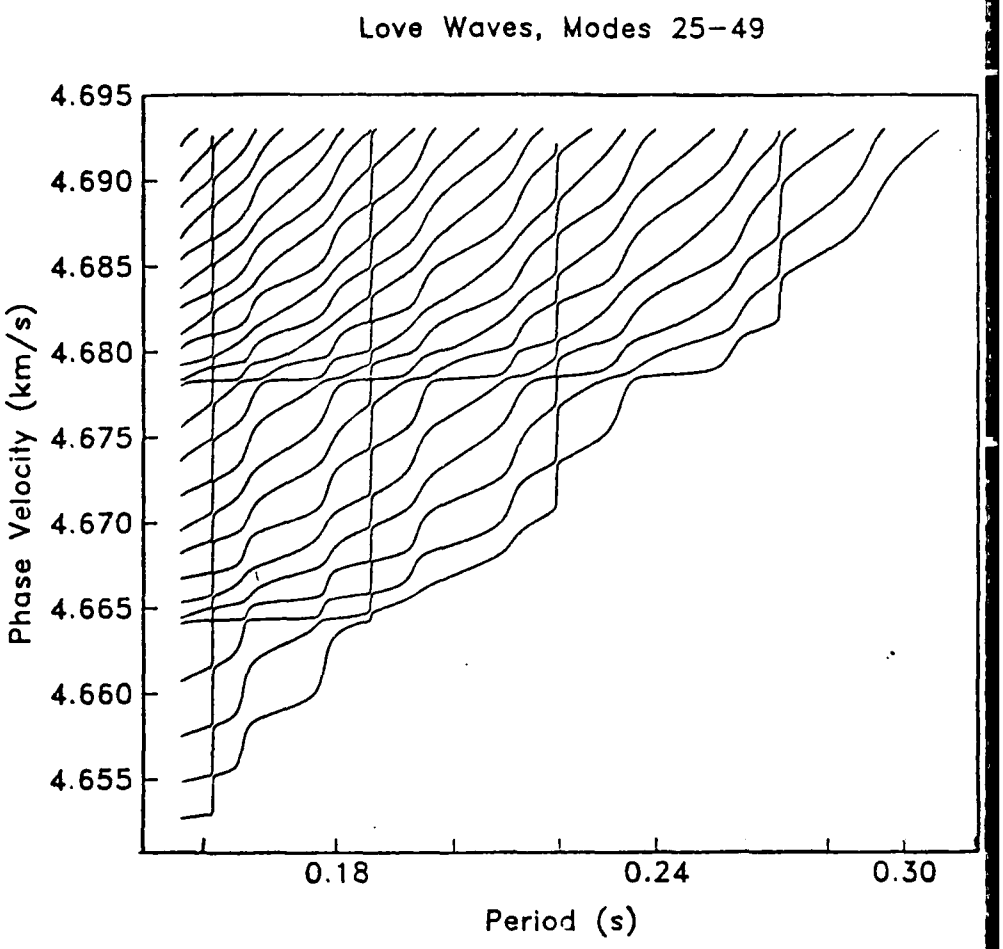


Figure 19. Phase velocity dispersion for Love wave modes 25-49 computed for the Ngendei model (Table 1).

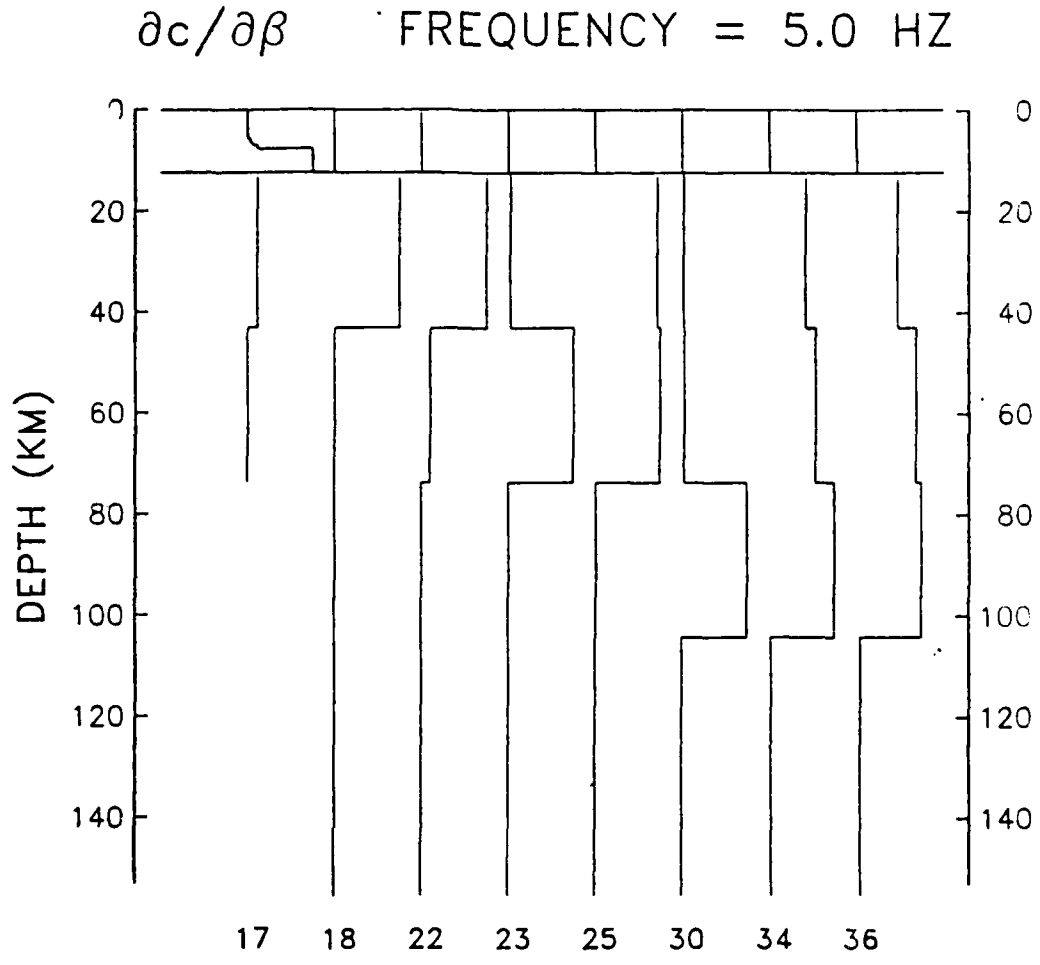


Figure 20. Partial derivatives of phase velocity with respect to material velocity, $\partial c / \partial \beta$, as a function of depth, at a frequency of 5.0 Hz, for several Love wave modes. Mode numbers are indicated on the bottom. The Moho is drawn as a solid horizontal line at a depth of 12.2 km. The function, $\partial c / \partial \beta$, is constant within any given homogeneous layer which results in the step-like appearance of the profiles.

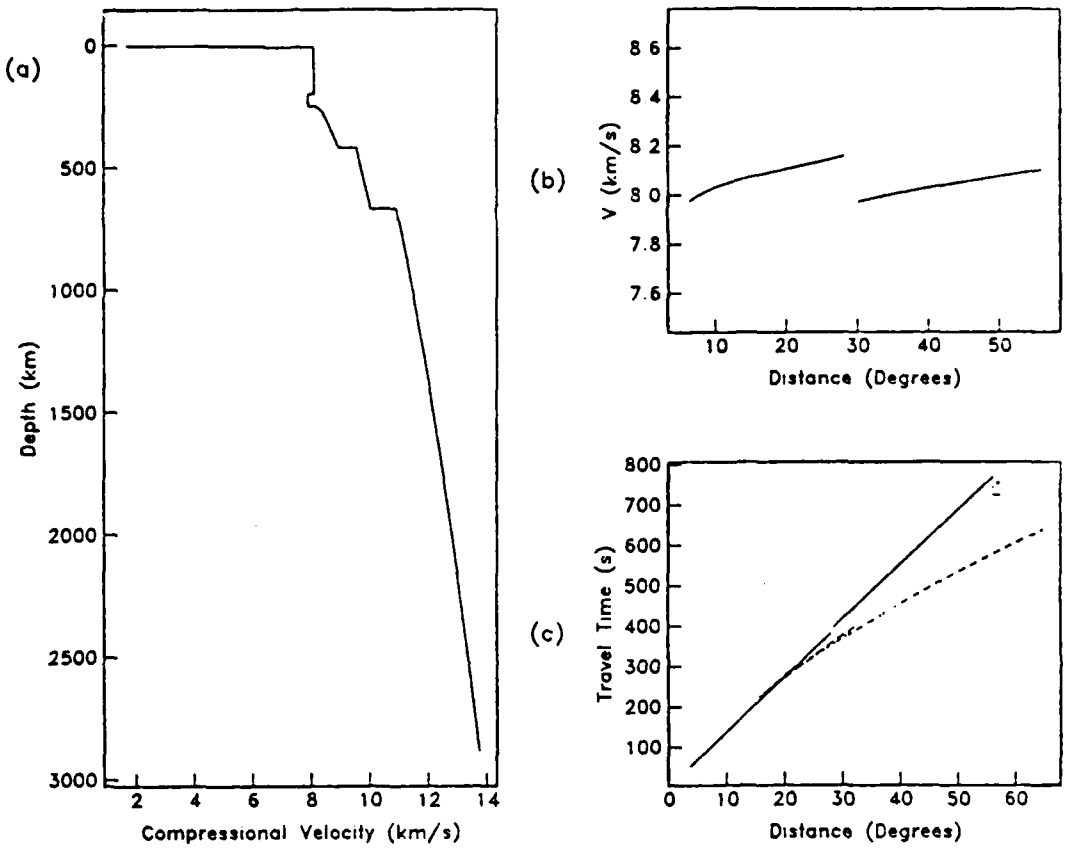
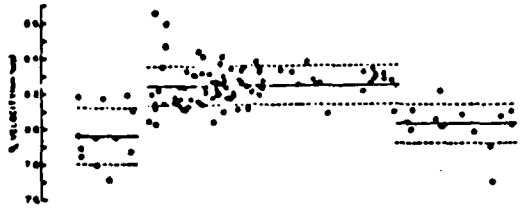


Figure 21. (*a*) Velocity model used to compute group velocities and travel times of P_n and normally refracted P. The results are shown for a surface source and receiver. (*b*) Group velocity of P_n as a function of epicentral distance for the model in (*a*). Group velocity has been defined as epicentral distance divided by total travel time. The discontinuous break at 30° represents the crossover between a ray normally refracted in the lithosphere and one that contains a free surface reflection. (*c*) Travel time curve of P_n (solid) versus normal refracted P with turning points below the base of the lithosphere (dashed) for the model in (*a*).

(a)



(b)

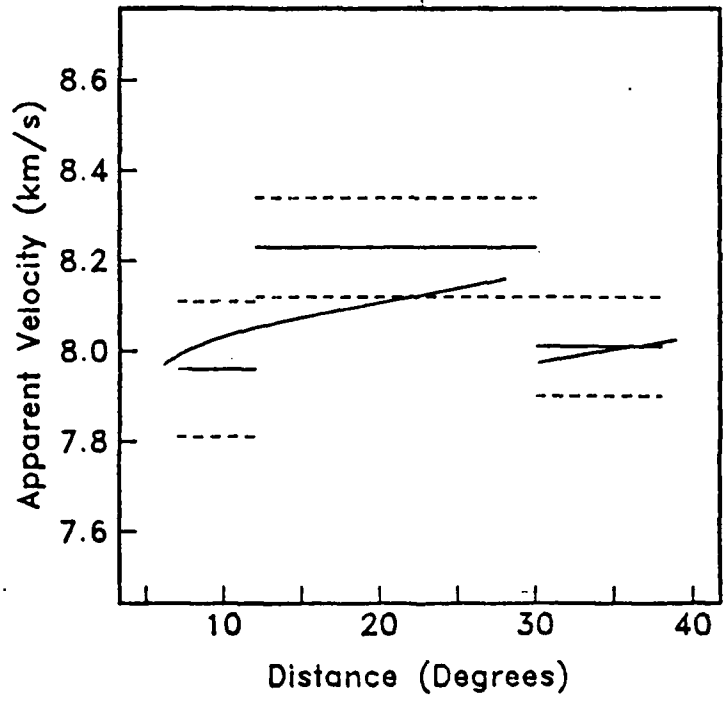


Figure 22. (*a*) Apparent group velocity versus epicentral distance for P_n phases with travel paths in the northwest Pacific (from *Walker*, 1981). Only events with focal depths $\leqslant$ 100 km were included. Means (solid) and standard deviations (dashed) are shown for the distance ranges $< 12°$, $12°$ to $30°$, and $> 30°$. (*b*) Comparison of *Walker's* observations to the P_n model proposed in this paper. The means and standard deviations from 22*a* have been superimposed on the apparent P_n group velocity curve of Figure 21*b*.

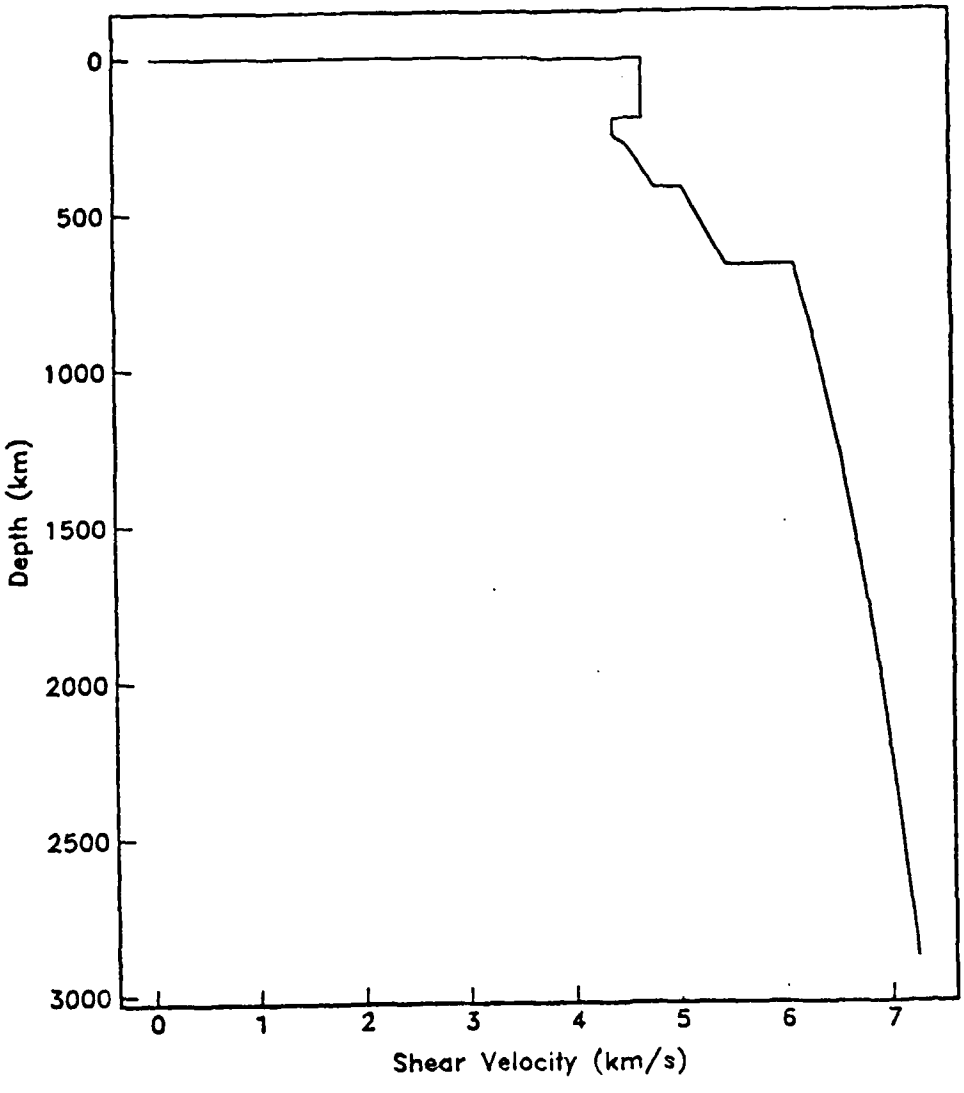
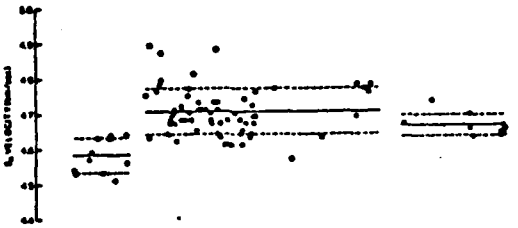


Figure 23. Shear wave velocity model used to compute S_n group velocity as a function of range.

(a)



(b)

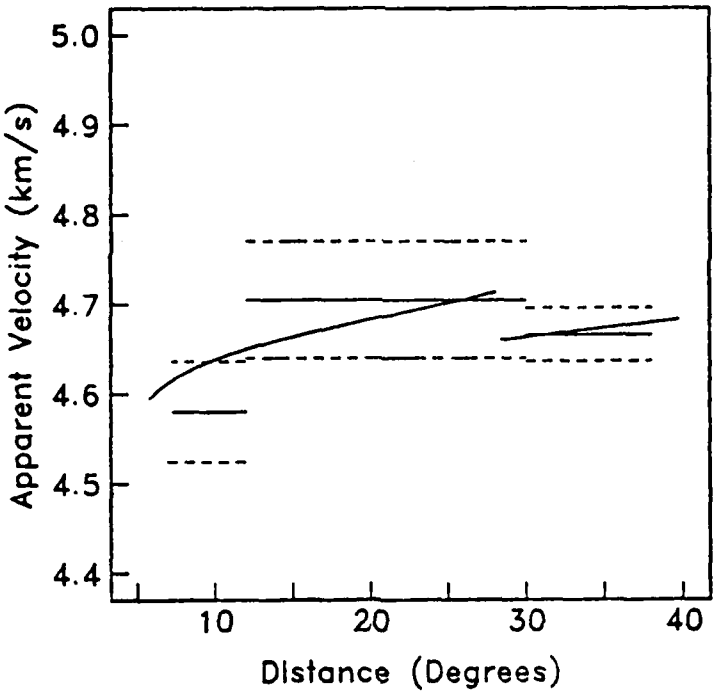


Figure 24. (*a*) Apparent group velocity versus epicentral distance for S_n phases with travel paths in the northwest Pacific (from *Walker*, 1981). Only events with focal depths $\leq$ 100 km were included. Means (solid) and standard deviations (dashed) are shown for the distance ranges < 12°, 12° to 30°, and > 30°. (*b*) Comparison of *Walker's* observations to the S_n model proposed in this paper. The means and standard deviations from 24*a* have been superimposed on the apparent S_n group velocity computed for the model in Figure 23. The drop in the mean S_n velocity at 30° is only 0.04 km/s whereas the corresponding drop in P_n velocity was 0.22 km/s.

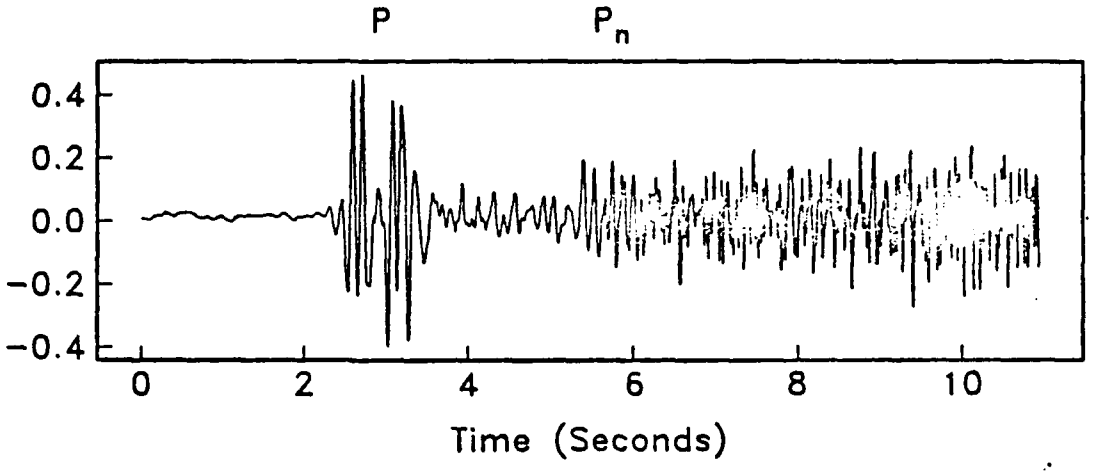


Figure 25. Vertical component seismogram recorded by a borehole seismometer at the Ngendei site. The focal depth of the event was 293 km in the Kermadec trench (m_b = 5.0, Δ = 12.91°). The complex P waveform between 2 and 4 seconds is a triplication from the 400 km discontinuity. Arrivals following 5.5 seconds constitute the P_n arrival. The enrichment in high frequency content of P_n relative to P is indicative of the low Q of the sub-lithosphere mantle.

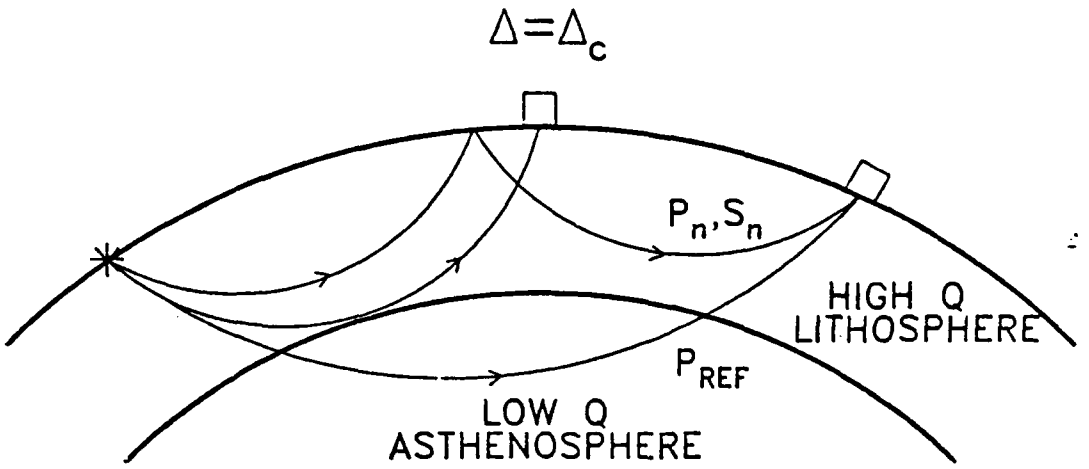


Figure 26. Schematic illustration of P_n / S_n wave propagation through the oceanic lithosphere. At ranges less than the cutoff distance, Δ_c, the first arrival of P_n or S_n is a normally refracted ray in the lithosphere. For distances greater than Δ_c, determined by the thickness of the lithosphere, the first arrivals contain an upward reflection. For long ranges, or deep events, P_n is preceded by a low frequency, normally refracted forerunner which has penetrated the low Q asthenosphere. This is indicated by P_{REF} in the diagram.

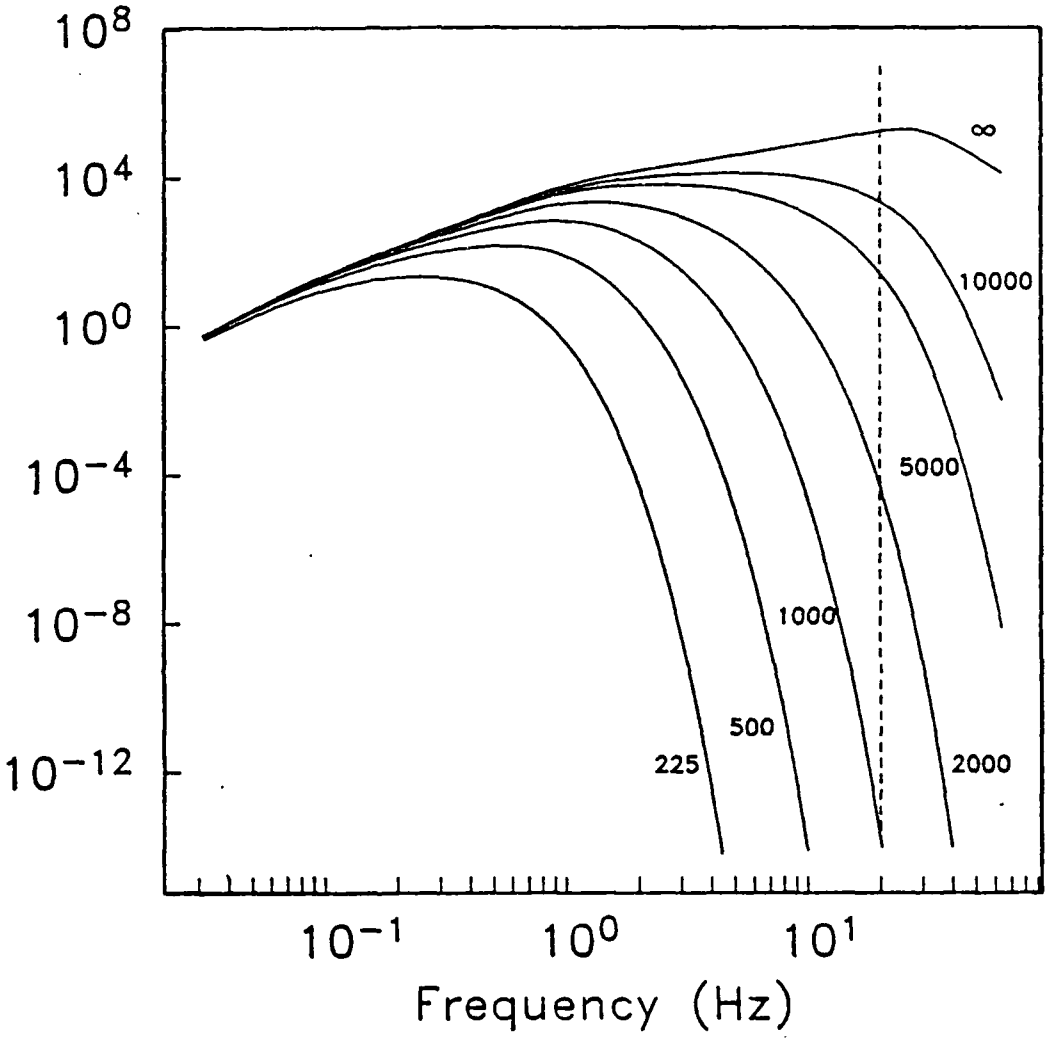


Figure 27. Curves of instrument response multiplied by $\exp\left(\frac{-\pi r f}{u\bar{Q}}\right)$ for a range of 3300 km, a group velocity of 4.7 km/s, and varying path averaged Q values. Each curve is labeled by its $\bar{Q}$ value and the curve labeled '∞' is the instrument response alone. The dashed vertical line is at 20 Hz and indicates detectable signal level in the S_n wave train at this range as reported by *Walker et al.* (1983).

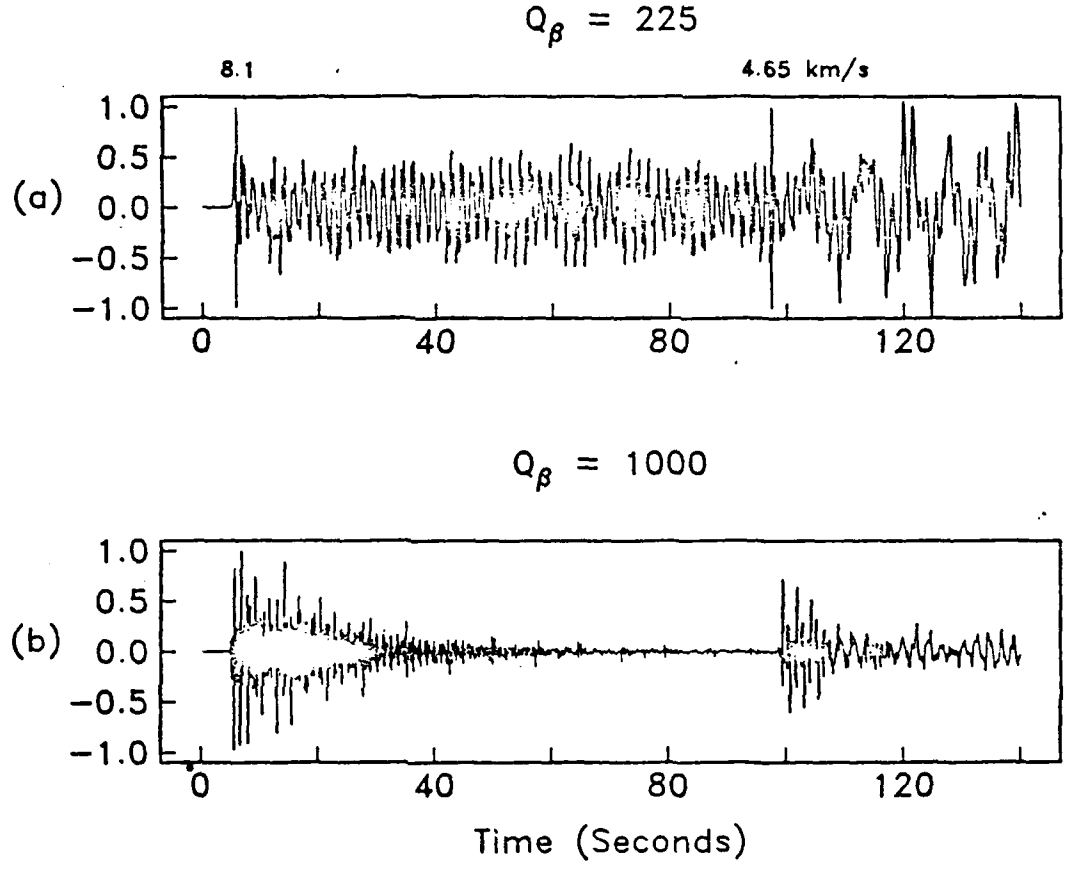


Figure 28. Synthetic horizontal displacement, rotated 25° clockwise from the radial direction, for the (*a*) *typical* oceanic lithosphere model (Table 2) and (*b*) Ngendei model (Table 1). Group velocities of 8.1 and 4.65 km/s are indicated in the top figure.

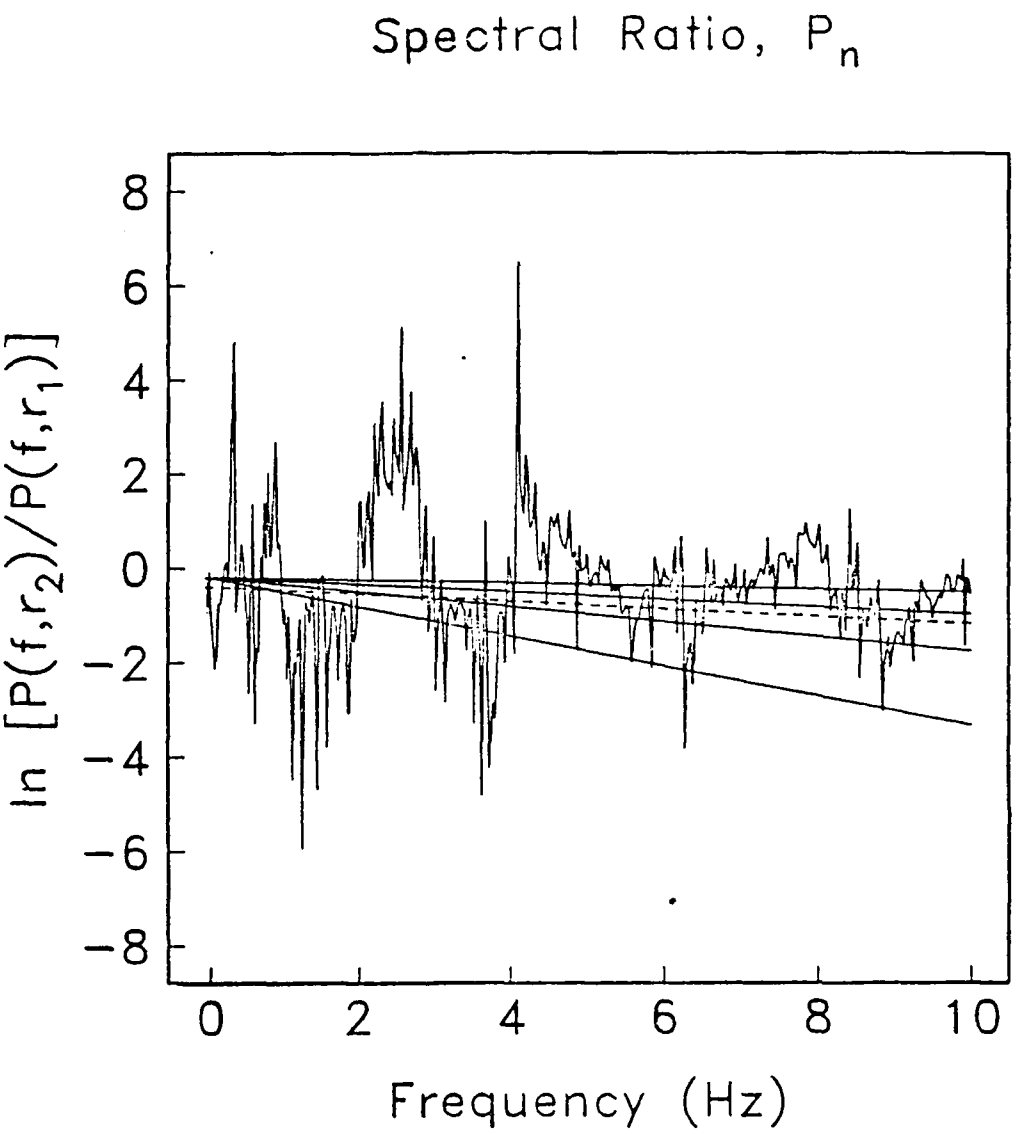


Figure 29. Spectral ratio of the synthetic vertical component P_n wave trains at ranges of 900 and 1100 km. The solid lines were obtained from (11) assuming cylindrical spreading, a group velocity of 8.0 km/s, and varying $\bar{Q}$ values. From top to bottom, the values of $\bar{Q}$ are 5000, 2000, 1000, and 500. The dashed line represents $\bar{Q}$ = 2000 and spherical spreading.

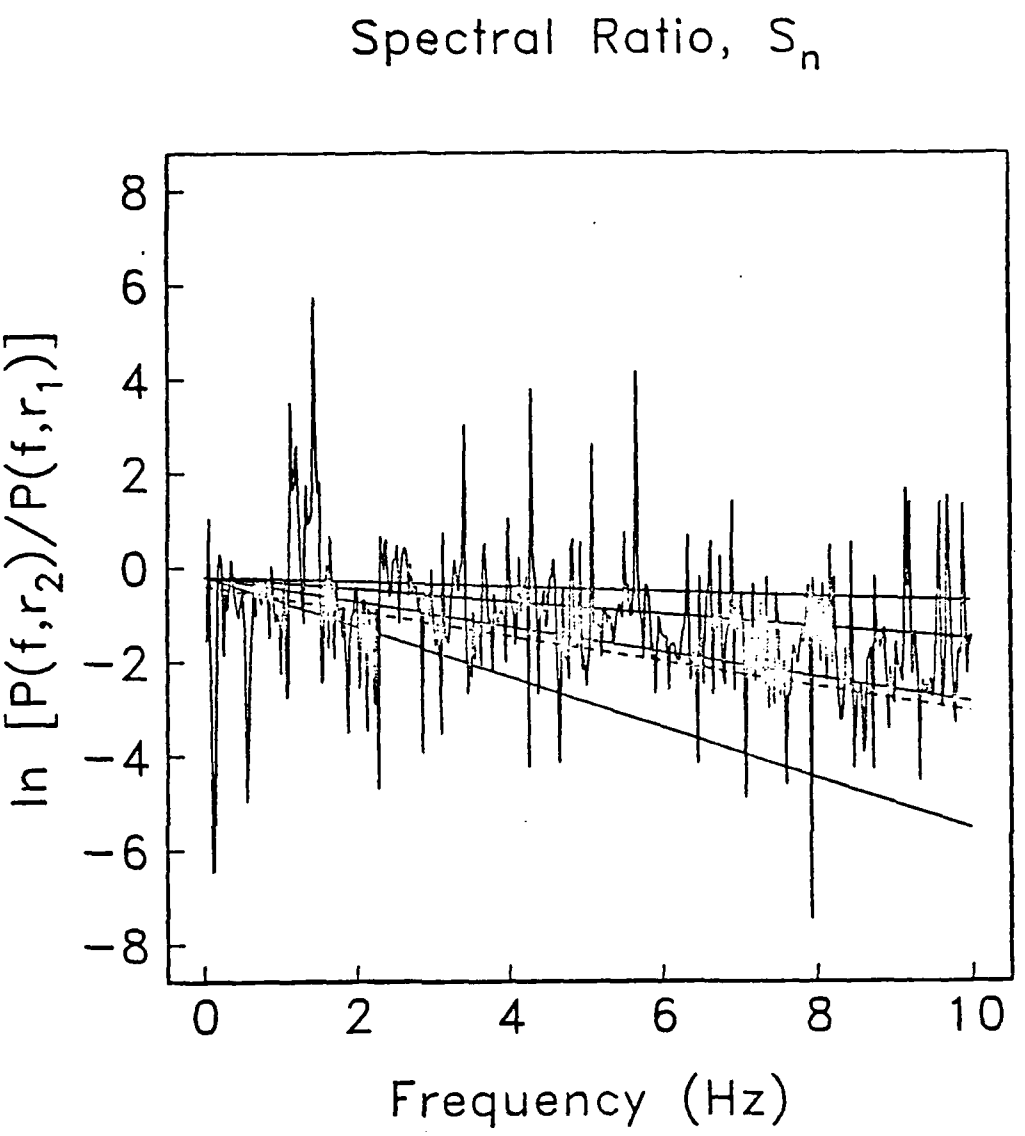


Figure 30. Spectral ratio of the synthetic radial component S_n wave trains at ranges of 900 and 1100 km. The solid lines were obtained from (11) assuming cylindrical spreading, a group velocity of 4.7 km/s, and varying $\bar{Q}$ values. From top to bottom, the values of $\bar{Q}$ are 5000, 2000, 1000, and 500. The dashed line represents $\bar{Q}$ = 1000 and spherical spreading.

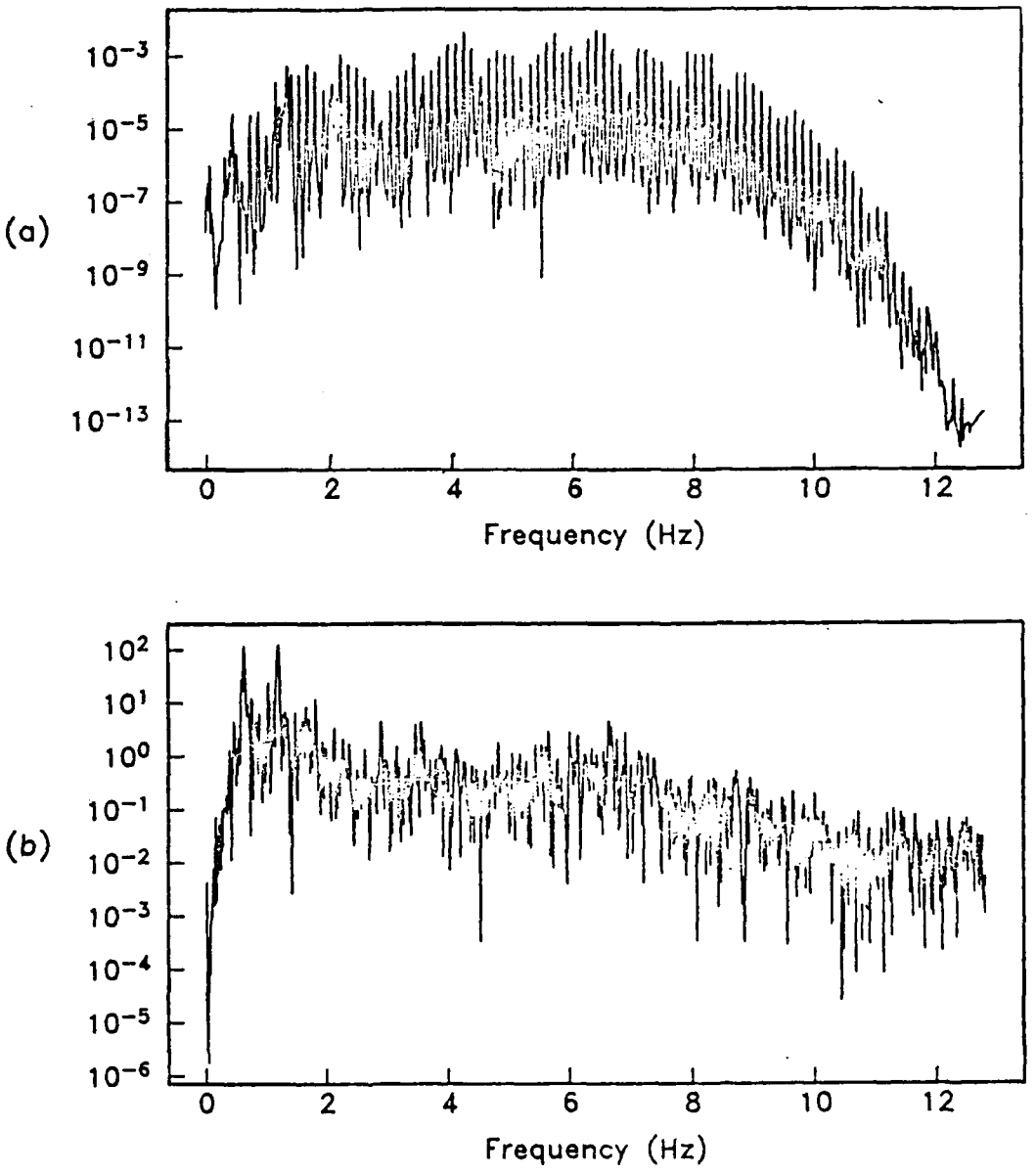


Figure 31. (*a*) Power spectrum of the synthetic vertical component P_n phase. (*b*) Power spectrum of vertical component P_n data collected at the Ngendei site.

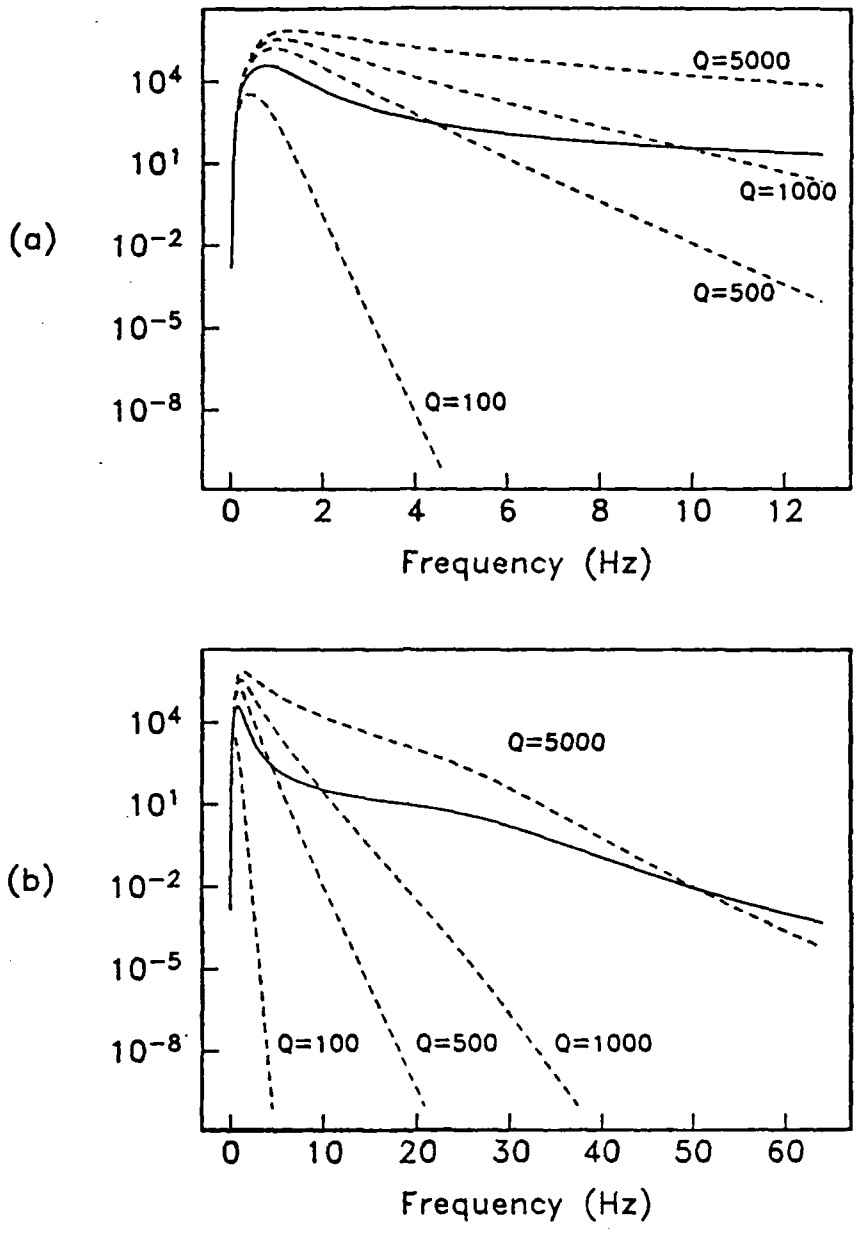


Figure 32. Curves of instrument response multiplied by a source spectrum with f^{-2} amplitude decay and corner frequency of 0.8 Hz multiplied by $e^{\frac{-\pi rf}{uQ}}$ for a range of 1000 km, a group velocity of 8 km/s, and varying Q values. The dashed curves are for constant Q and the solid curve represents the result for an absorption band Q model. First (*a*) 12.8 Hz and (*b*) 64.0 Hz of the spectrum.

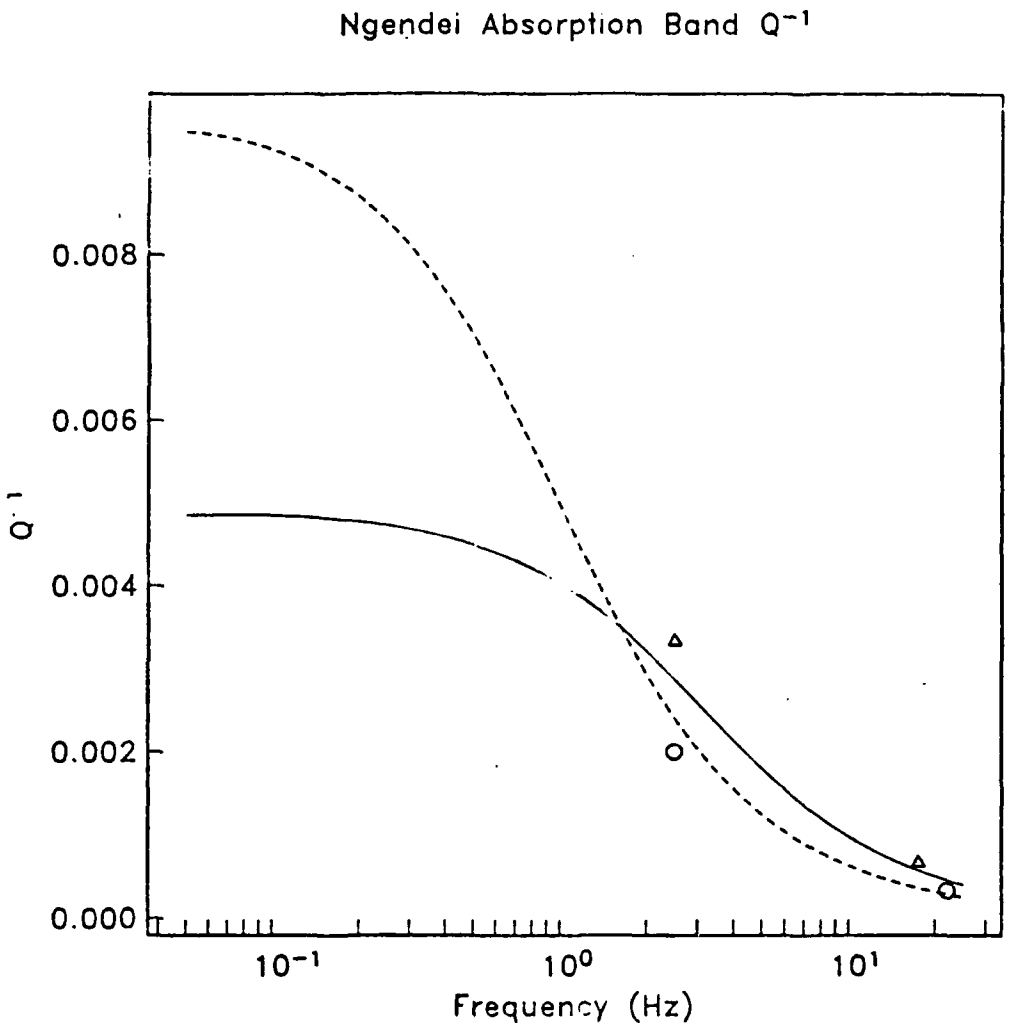


Figure 33. Upper mantle absorption band $Q^{-1}(f)$ used in the Ngendei model. Q_α^{-1} (solid) and Q_β^{-1} (dashed) were computed using (13) with the parameter values listed in Table 3. The circles are Q_{S_n} values reported by *Butler, et al.* (1985) and the triangles are their Q_{P_n} estimates.

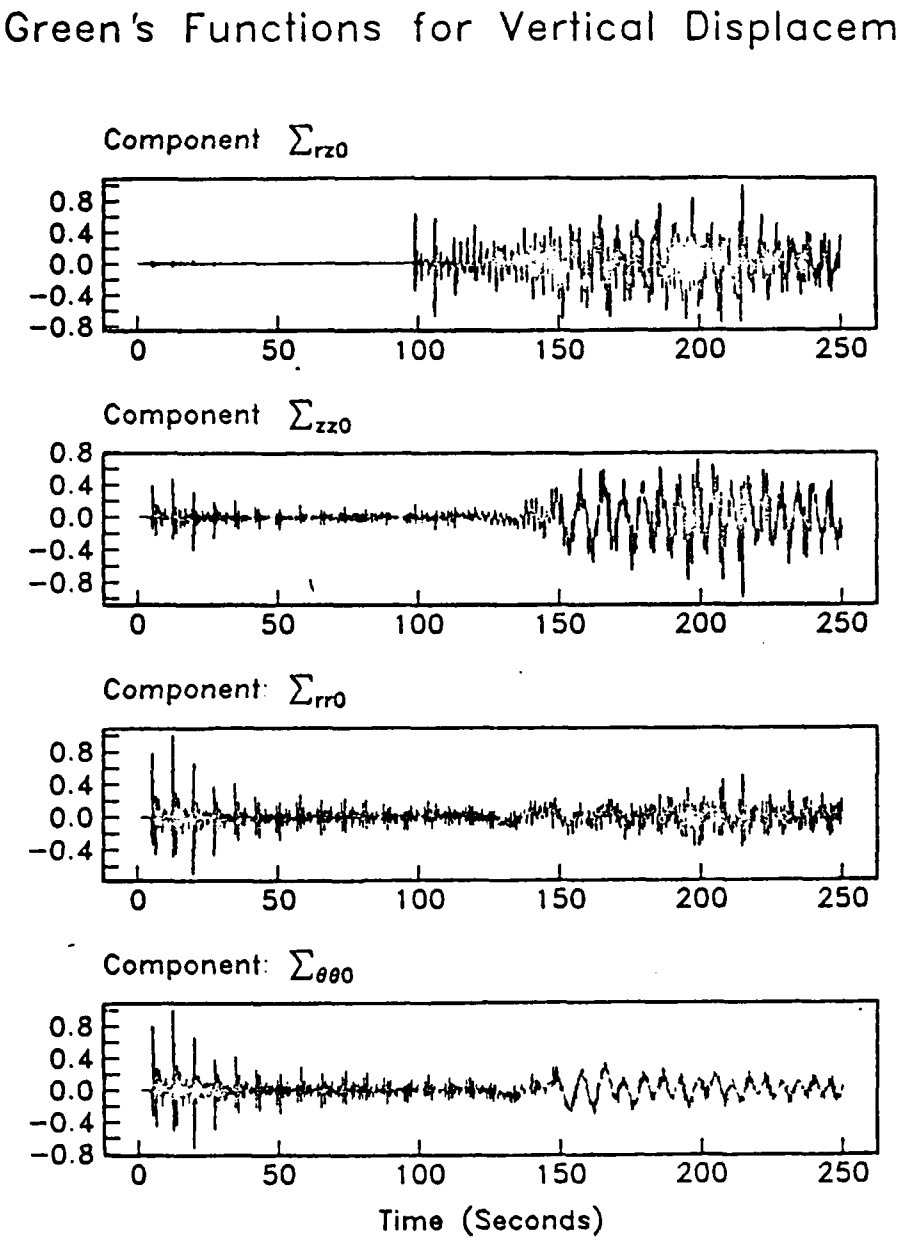


Figure 34. Green's functions for vertical displacement computed for the absorption band Q Ngendei structure. The four stress tensor elements for a vertical point force are shown, Σ_{rz0}, Σ_{zz0}, Σ_{rr0}, and $\Sigma_{\theta\theta0}$. Vertical displacement for an arbitrarily oriented double-couple source is obtained through linear combination of these four stress tensor elements.

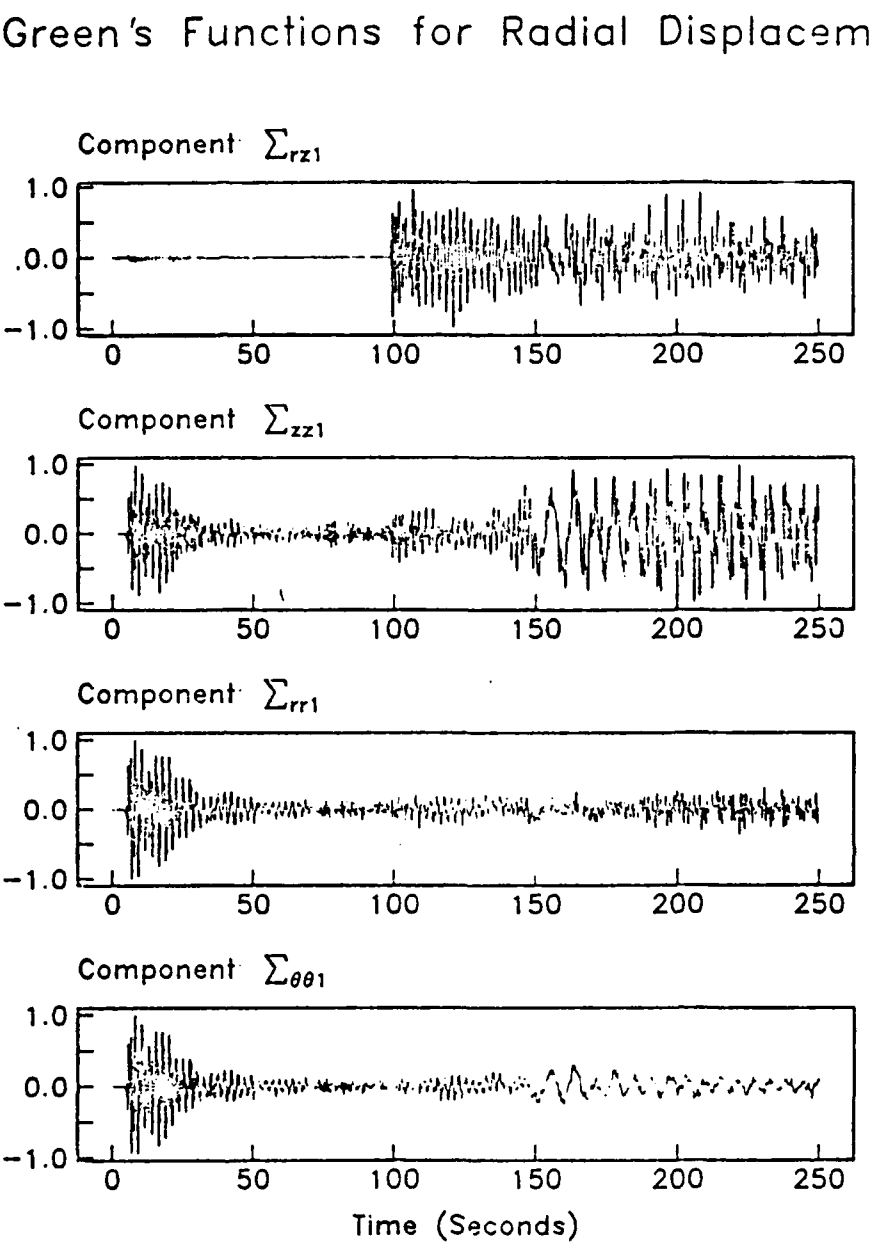


Figure 35. Green's functions for radial displacement computed for the absorption band Q Ngendei structure. Four stress tensor elements for a horizontal point force are shown, Σ_{rz1}, Σ_{zz1}, Σ_{rr1}, and $\Sigma_{\theta\theta1}$. Radial displacement for an arbitrarily oriented double-couple source is obtained through linear combination of these four stress tensor elements.

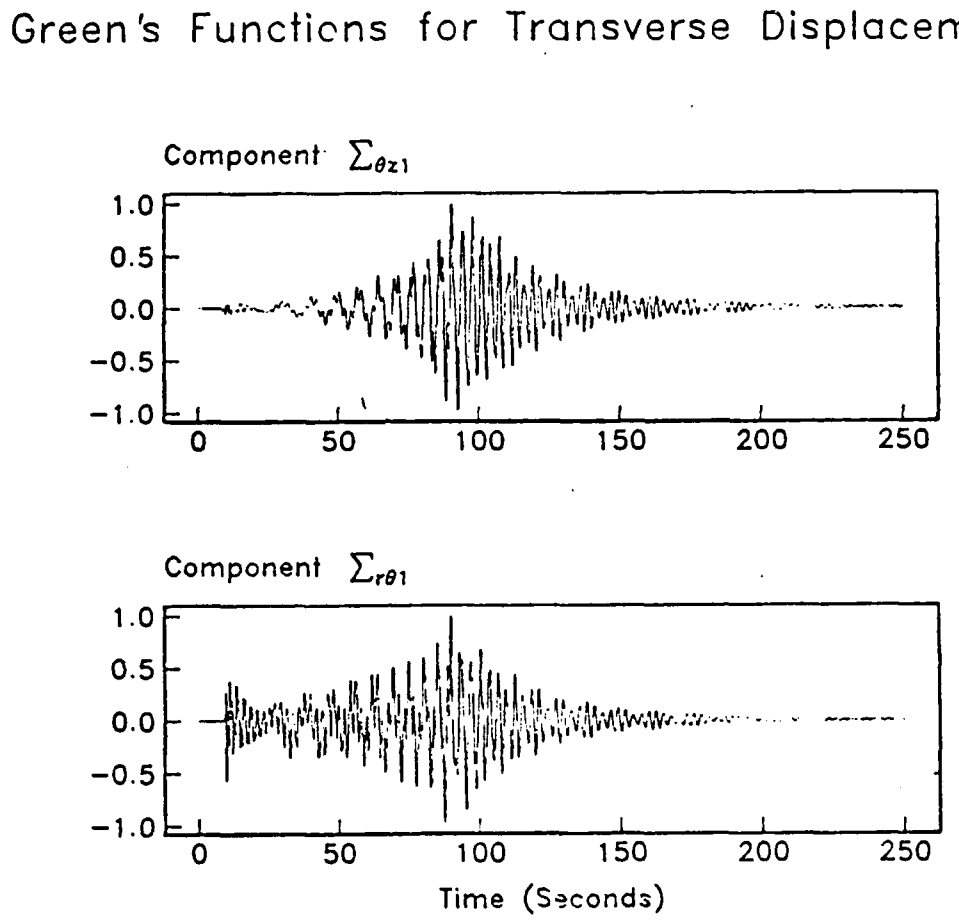


Figure 36. Green's functions for transverse displacement computed for the absorption band Q Ngendei structure. Two stress tensor elements for a horizontal point force are shown, $\Sigma_{\theta z1}$ and $\Sigma_{r\theta1}$. Transverse displacement for an arbitrarily oriented double-couple source is obtained through linear combination of these two stress tensor elements.

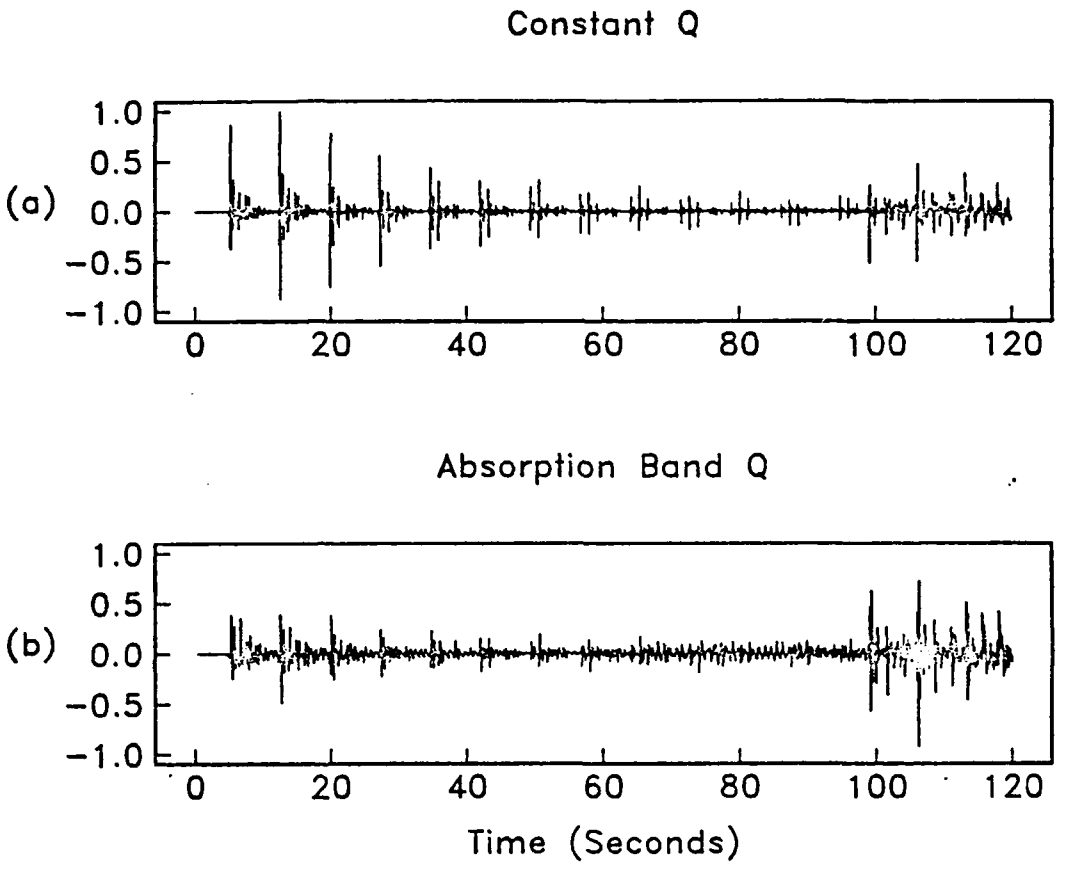


Figure 37. Comparison of vertical component synthetic P_n phases computed for (*a*) the constant Q Ngendei structure and (*b*) the absorption band Q Ngendei structure. The fault used had a dip of 25°, a rake of 270°, and an azimuth relative to the receiver of 60°. The OBS instrument response and source spectrum with f^{-2} amplitude decay and corner frequency of 0.8 Hz were included.

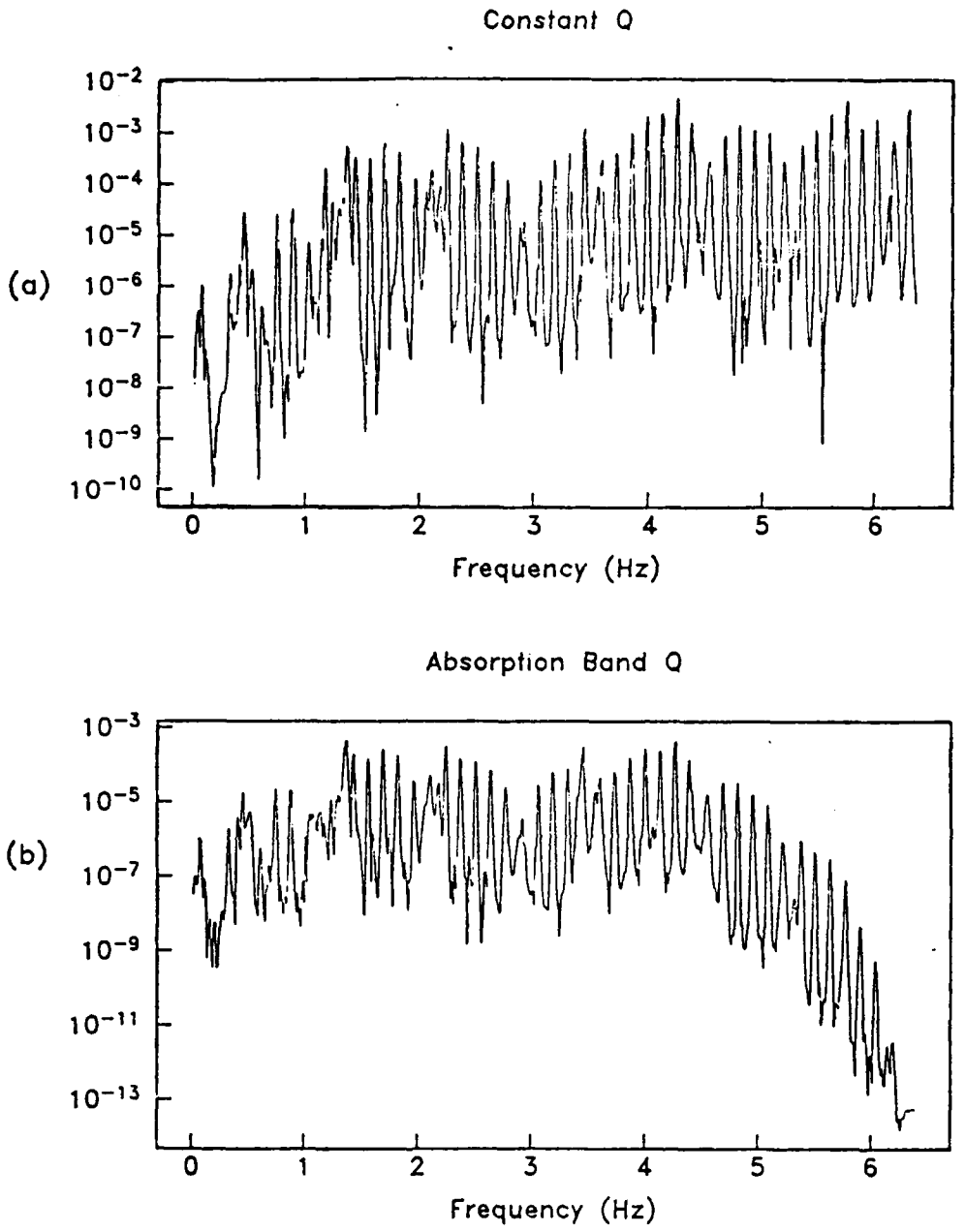


Figure 38. Power spectral estimates of the synthetic P_n wave trains in (*a*) Figure 37*a* (constant Q structure) and (*b*) Figure 37*b* (absorption band Q structure).

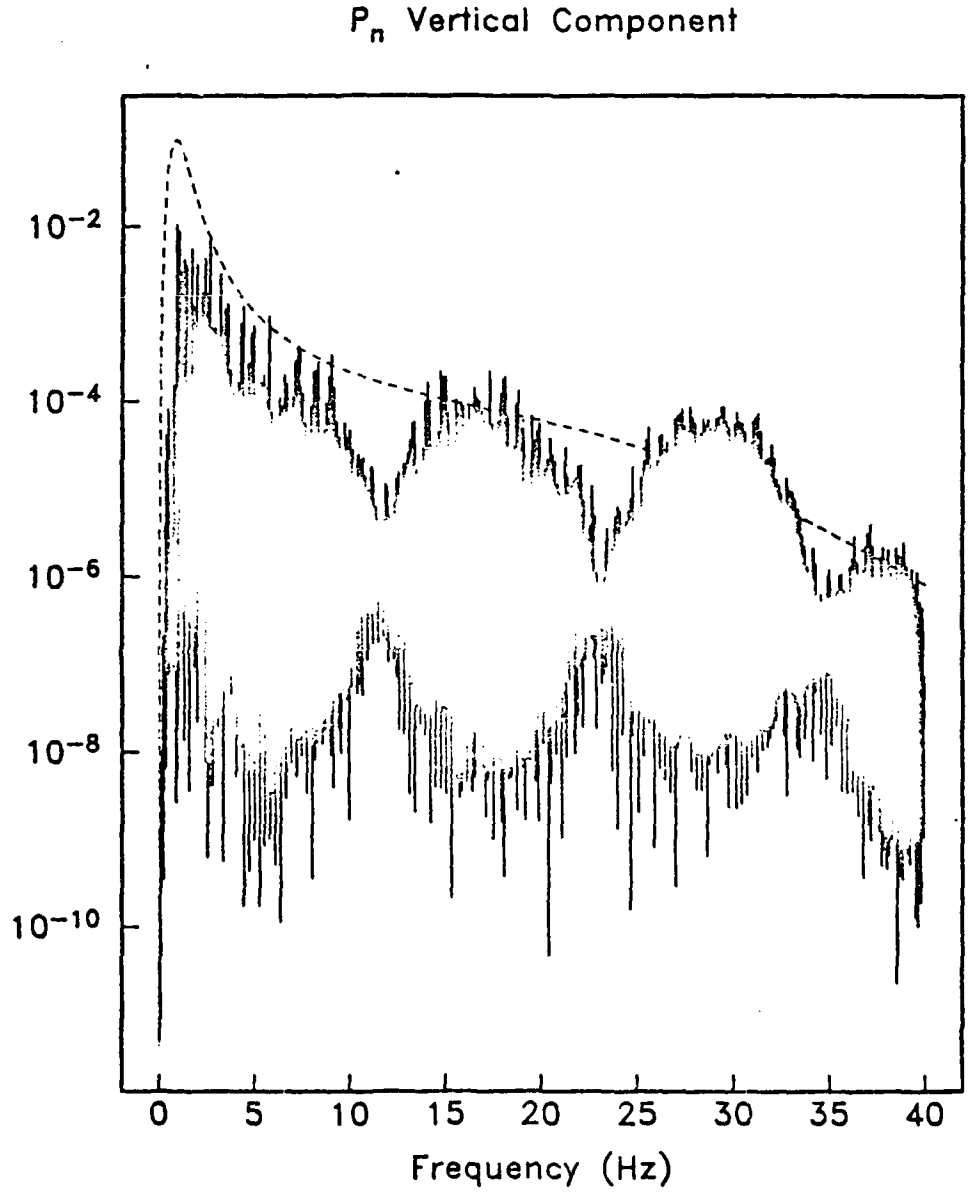


Figure 39. Synthetic vertical component P_n spectrum for the absorption band Q Ngendei model. Phase velocities were restricted between 7.0 and 25.0 km/s. The dashed curve was obtained from (15) for a range of 900 km, a group velocity of 8.0 km/s and the P wave absorption band $Q(f)$ listed in Table 3.

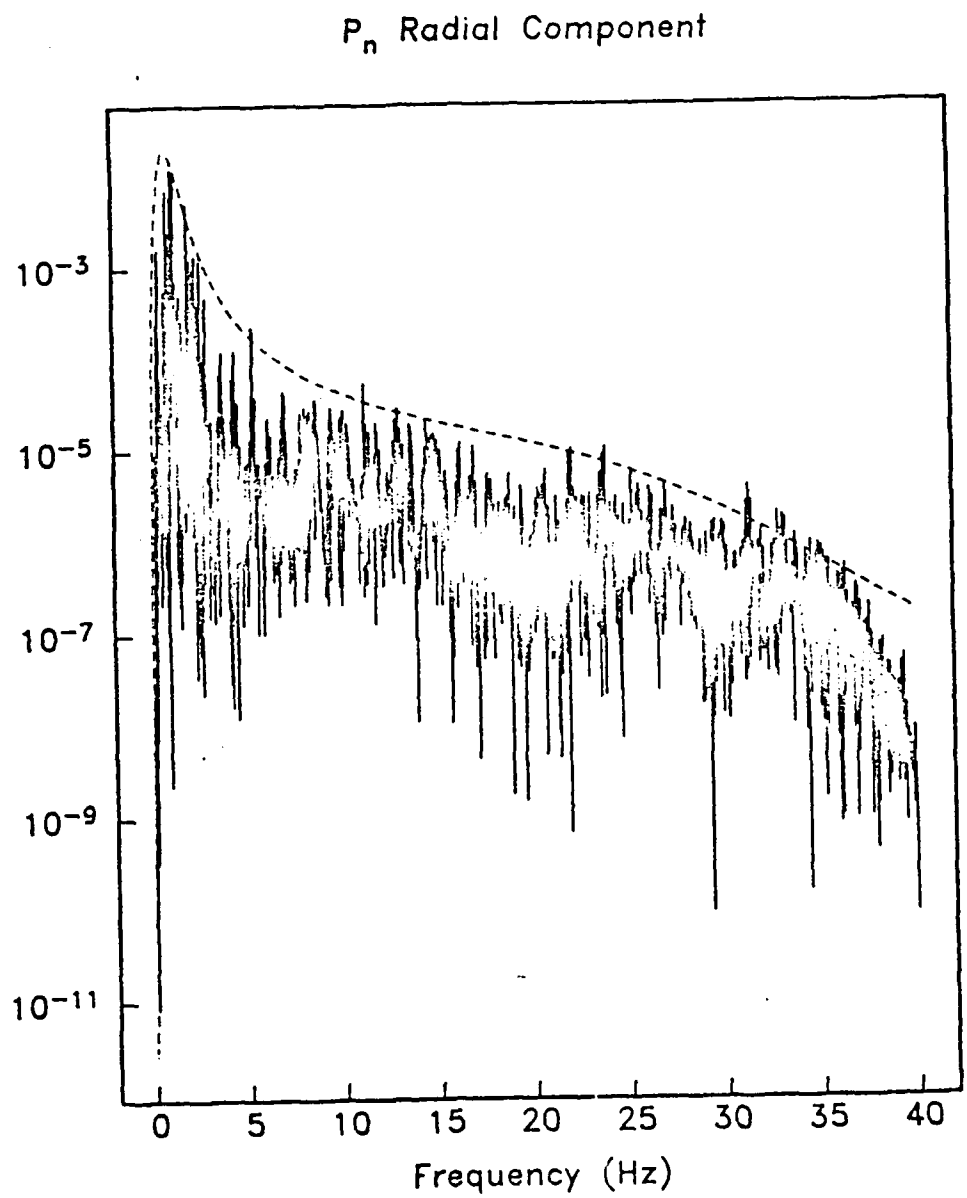


Figure 40. Synthetic radial component P_n spectrum for the absorption band Q Ngendei model. Phase velocities were restricted between 7.0 and 25.0 km/s. The dashed curve was obtained from (15) for a range of 900 km, a group velocity of 8.0 km/s and the P wave absorption band $Q(f)$ listed in Table 3.

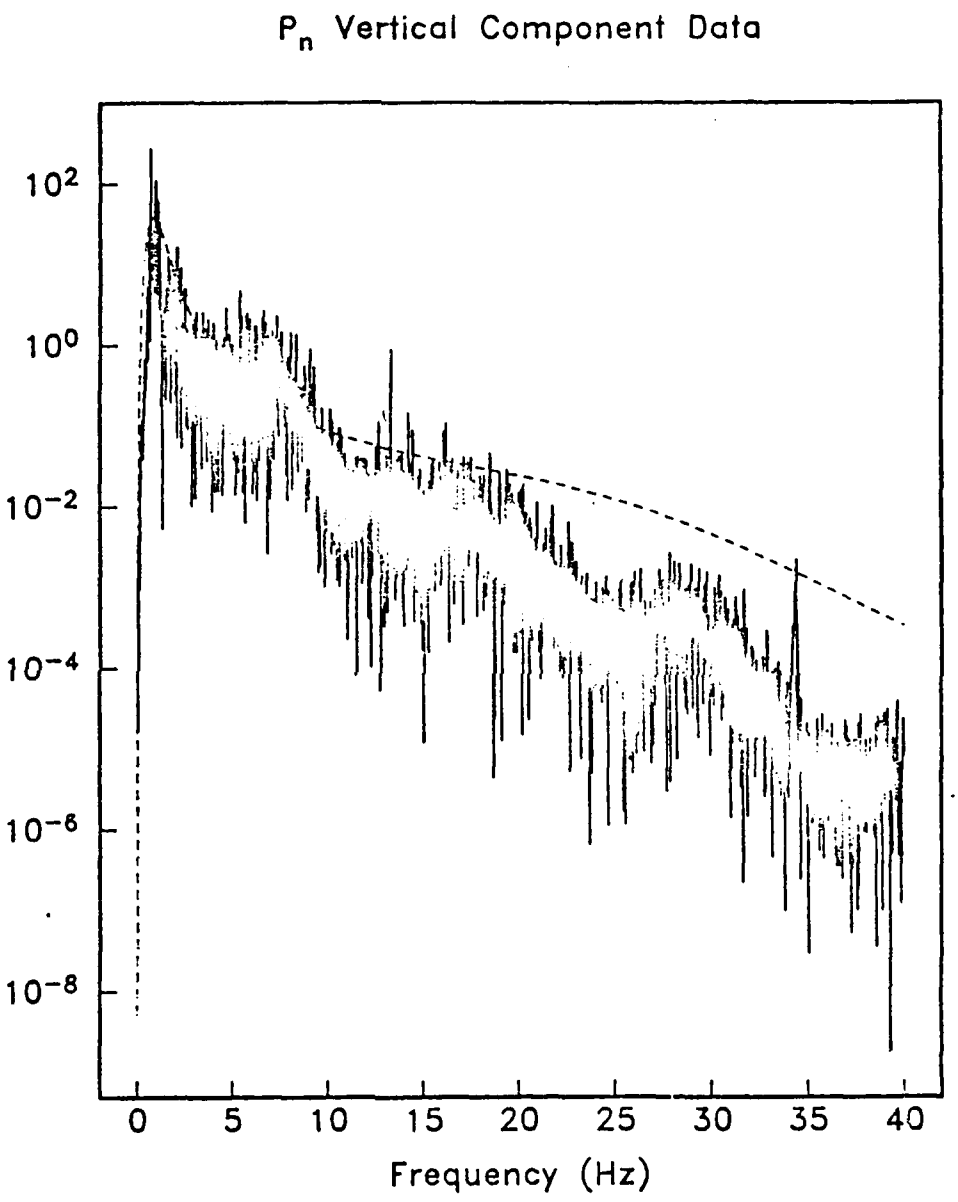


Figure 41. Power spectrum of the vertical component P_n data shown in Figure 9c. The dashed curve was obtained from (15) for a range of 900 km, a group velocity of 8.0 km s and the P wave absorption band $Q(f)$ listed in Table 3.

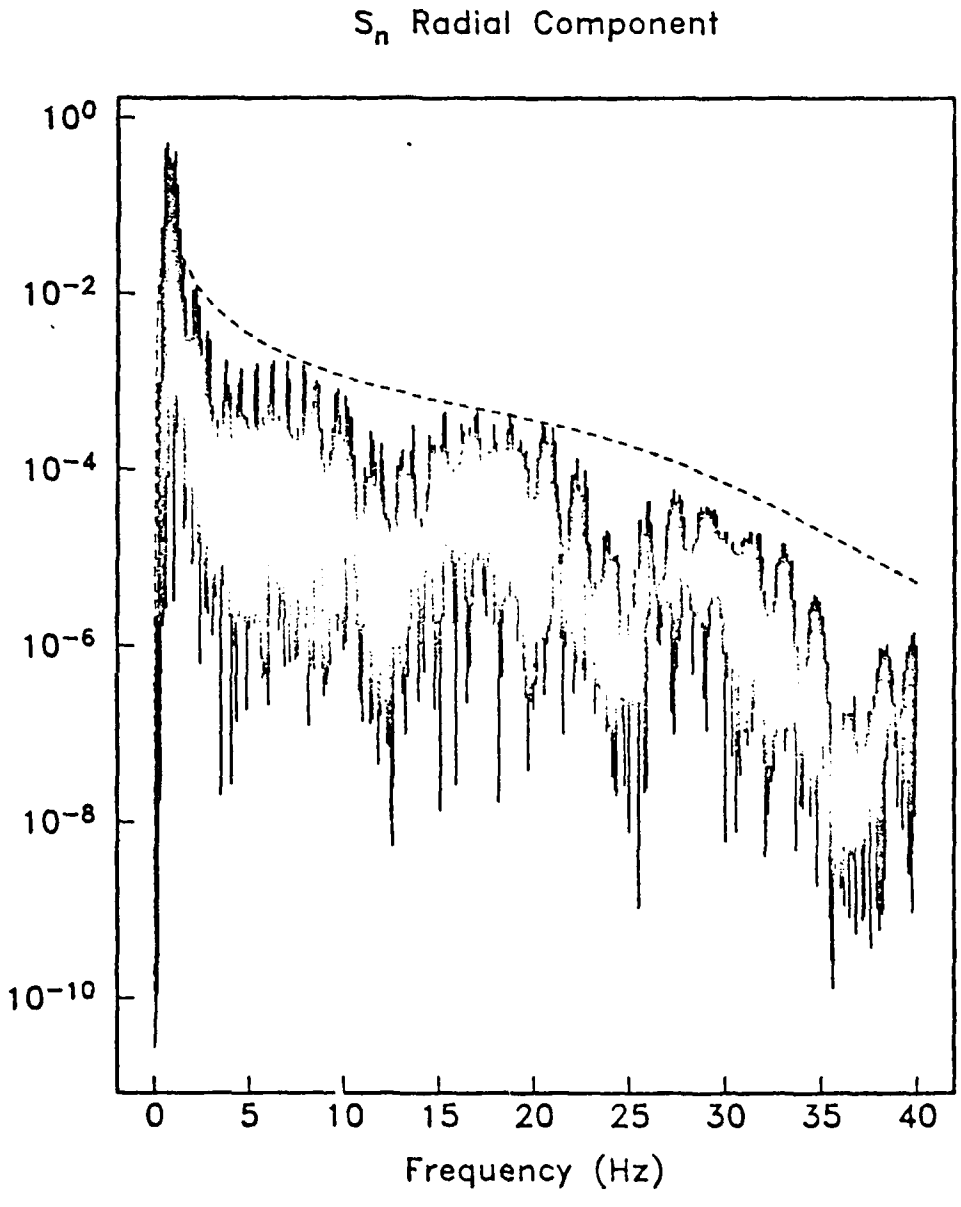
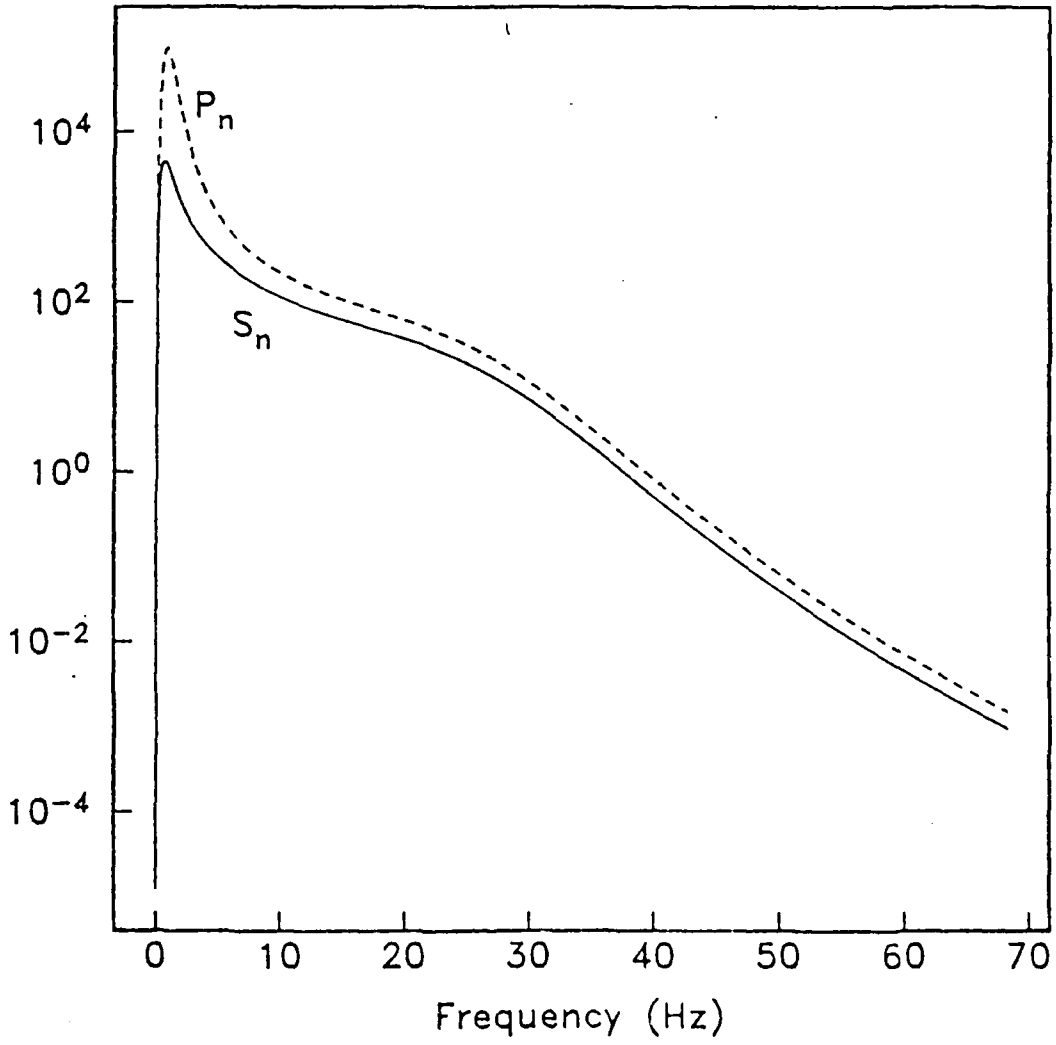


Figure 42. Synthetic radial component S_n spectrum for the absorption band Q Ngendei model. Phase velocities were restricted between 4.0 and 5.0 km/s. The dashed curve was obtained from (15) for a range of 300 km, a group velocity of 4.7 km/s and the S wave absorption band $Q(f)$ listed in Table 3.

Figure 43. Predicted power spectral amplitude computed using (15) for P_n (dashed) and S_n (solid). For P_n, a group velocity of 8.0 km/s and the P wave absorption band Q model of Table 3 were used. For S_n, a group velocity of 4.7 km/s and the S wave absorption band Q model of Table 3 were used. The source spectrum had a corner frequency of 0.8 Hz and a f^{-2} high frequency asymptote.



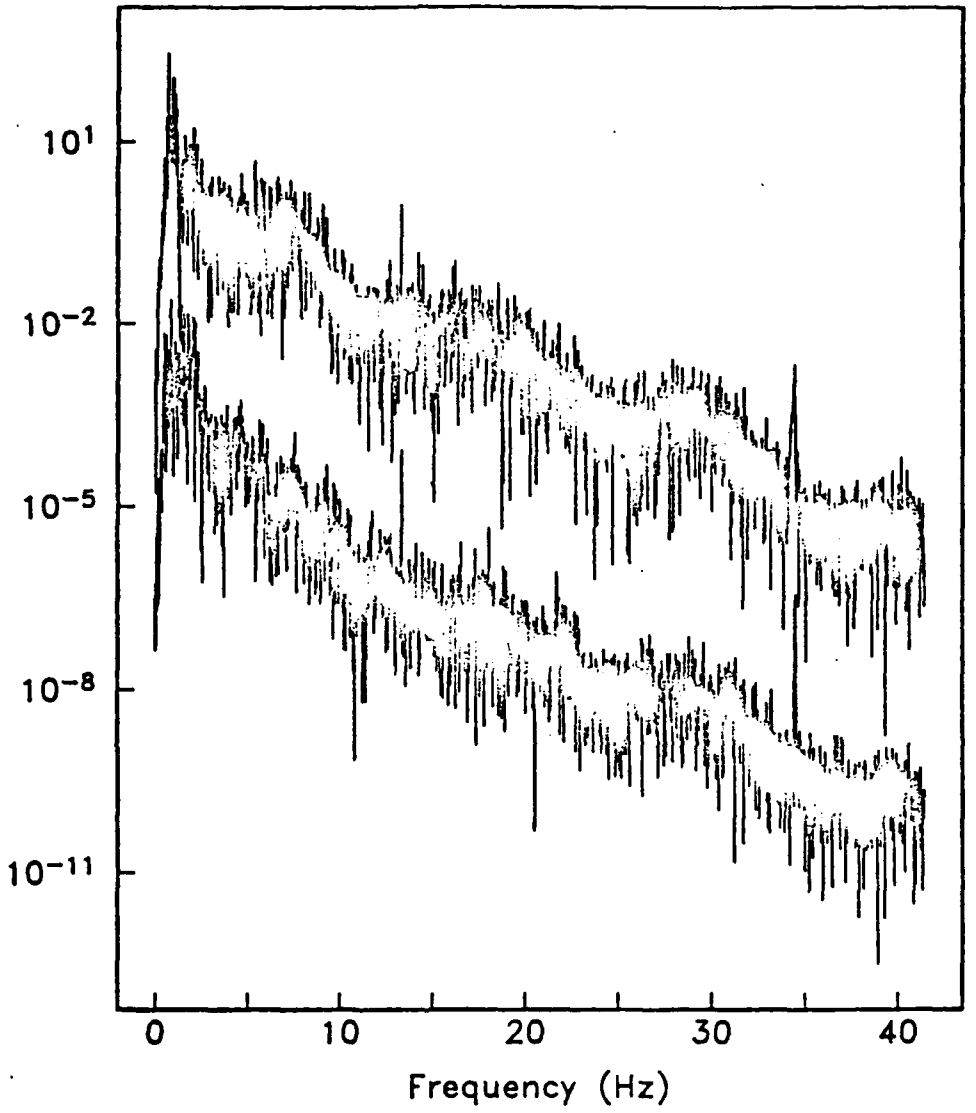


Figure 44. Comparison of spectra of vertical component P_n data (top) and S_n data (below) for the same event. The spectra were vertically offset for illustrative purposes.